KFA

Bilateral Seminars of the International Bureau

KERNFORSCHUNGSANLAGE JÜLICH GmbH

VIIIth

German-Yugoslav Meeting
on Materials Science
and Development

Ceramics and Metals

Edited by
Drago Kolar, Marija Kosec
and Johanna Krawczynski

Brdo pri Kranju
May 18–21, 1987

GERMAN-YUGOSLAV COOPERATION
IN SCIENTIFIC RESEARCH AND TECHNOLOGICAL DEVELOPMENT

GERMAN-YUGOSLAV COOPERATION
IN SCIENTIFIC RESEARCH AND TECHNOLOGICAL DEVELOPMENT

VIIIth GERMAN-YUGOSLAV MEETING ON MATERIALS SCIENCES AND DEVELOPMENT

CERAMICS and METALS

POWDER SYNTHESIS AND FORMING
SINTERING AND MICROSTRUCTURE
MECHANICAL PROPERTIES
THERMAL PROPERTIES
SURFACES AND INTERFACES
ELECTRICAL AND MAGNETIC PROPERTIES

Organizer of the VIIIth Meeting:
Institut Jožef Stefan, Ljubljana

Participating Institutions:

Boris Kidrić Institute of Nuclear Sciences, Vinča/Belgrade
Institute Jožef Stefan, Ljubljana

Universities of Belgrade, Ljubljana, Rijeka, Skopje, and Zagreb
University of Patras (GR)

Academy of Sciences and Arts of Bosnia and Herzegovina, Sarajevo
Serbian Academy of Sciences and Arts, Belgrade

Boris Kidrić Institute of Chemistry, Ljubljana

Energoinvest, Sarajevo
Skopje Steel Works, Skopje

Kernforschungsanlage Jülich GmbH
Kernforschungszentrum Karlsruhe GmbH

Max Planck Institut für Metallforschung,
Institut für Werkstoffwissenschaften, Stuttgart

Fritz Haber Institut der Max Planck Gesellschaft, Berlin

Universities of Aachen (RWTH), Clausthal (TU), Hannover and Karlsruhe

Herausgegeben von der Kernforschungsanlage Jülich GmbH
ZENTRALBIBLIOTHEK
Postfach 1913 · D-5170 Jülich
Telefon 02461/61-0 · Telex 833556-70 kfa d

Titelsatz: Graphische Betriebe der KFA

Druck: Wilhelm Dostall KG, Eschweiler

gleichzeitig Jül-Spez-446
ISBN 3-89336-001-8

INTRODUCTION

Within the Governmental Agreement on Cultural and Scientific Cooperation of 1969 between the Socialist Federative Republic of Yugoslavia and the Federal Republic of Germany, several Agreements were signed, i.e.

- the Agreement between YUZAMS[x)] and BMFT[xx)] (1975), as well as
- the Special Agreements between YUZAMS and KFA-Jülich[xxx)] (1977) and between KFA-Jülich and the Research Community of Slovenia (1978).

Within this legal structure, the VIIIth Meeting on Materials Sciences and Development was held in Brdo pri Kranju from May 18-21, 1987, in order to discuss on scientific results of on-going bilateral cooperation projects, and to pinpoint possible new areas of interest for future cooperation.

Indeed, since then, cooperation in the frame of existing projects has been deepened, complementary and coordinating aspects have been observed, and new fields of materials research have been entered into. Materials sciences is a key discipline for supporting developments in technologically-applied fields from the design of novel materials with ascribed or defined properties for new applications (f.i.in informatics) on the one hand, to the fruitful impetus in traditional fields of research and development, on the other hand. As such, this discipline is one of the main pillars of German-Yugoslav bilateral cooperation.

Within the range of competitive tension given by the need both for more basic-oriented research and for applicable results, a good balance has been maintained. Interest from the side of industrial firms for our work and during the VIIIth Meeting give proof of actual and prospective achievements of our common work, whereas endeavours to establish connections to the EUREKA-framework look promising.

Yugoslav institutions are definitely on their way to "Europe",

---

x) YUZAMS : Federal Administration for International Scientific,Educational, Cultural and Technical Cooperation, Belgrade
xx) BMFT : Federal Ministry for Research and Technology, Bonn
xxx) KFA-Jülich: Kernforschungsanlage Jülich GmbH, Jülich

and although participation in programmes of the European Communities like BRITE and EURAM have still to be organized along the line of Yugoslavia's participation on COST, the organisation of a Materials Science Seminar of the European Communities together with Yugoslavia in the second half of 1988 is as well an encouraging political sign as a justified stressing of this scientific discipline.

In this greater context, German-Yugoslav cooperative links form an inner core. They enable to introduce and test, to reject or verify developments, and above all to intensify mutual endeavours in the common projects, there were the work looks promising.

Selective deepening, considering the materials sciences cooperation in the frame of GER-YU bilateral cooperation as a whole, rather than uncritical widening, seems to be the most effective approach. Complementarity, not duplicity of efforts, is the demand, and the working and reporting on common projects therefore the ultima ratio of our joint endeavours.

It is with pride that the International Bureau of KFA-Jülich as the editing agency of the Proceedings of the VIIIth German-Yugoslav Meeting on Materials Sciences and Development herewith presents the original scientific contributions to the Seminar. They are compiled with the aim of further disseminating their contents. The manuscripts of the authors have remained unchanged, the liability therefore remains with them. The editing work has been done jointly between the Institute Jožef Stefan, Ljubljana, Professor Dr.Drago Kolar and Dr. Marija Kosec, and the International Bureau of KFA-Jülich. The Institute Jožef Stefan also was the organizer of the VIIIth Meeting, and we thank them for their many endeavours and for having chosen the beautiful setting of Brdo pri Kranju, where the Meeting was held.

The IXth Meeting will be organized in Stuttgart in April/May 1989.

Jülich, June 1988

(Johanna Krawczynski)

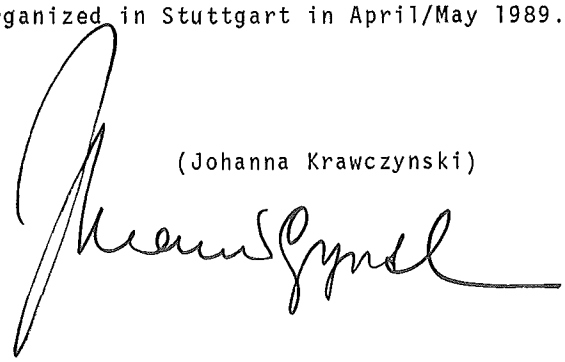

PREFACE BY THE ORGANIZING AGENCY, INSTITUTE JOZEF STEFAN

This volume contains the papers presented at the 8th German-Yugoslav Meeting on Materials Science and Development which was organized by the "Jožef Stefan" Institute, "E. Kardelj" University of Ljubljana, and held at Brdo pri Kranju near Ljubljana, Yugoslavia, in May 1987.

The meeting was organized within the framework of the German-Yugoslav agreement on technical and scientific cooperation, which was agreed upon in 1975. The aim of the meeting was to review the results achieved within joint projects and to acquaint the participants with the relevant studies carried out at the cooperating institutions during the last two years, i.e. since the last meeting in this series, which was held in Bad Herrenalb, Federal Republic of Germany, in april 1985.

General awareness of the importance of modern materials research and development is also reflected in bilateral Yugoslav-German meetings. The number of papers presented and the number of participants is steadily increasing, and set a new record at the Brdo Meeting.

Ample time was devoted to formal and informal discussions. Discussions were probably the most important aim of the meeting and were fully exploited. We firmly do believe that the exchange of ideas and the friendly but critical attitude will contribute to greater thoroughness and quality of the research work in progress.

The meeting was made possible with financial support from the Yugoslav and German authorities, whose assistance is gratefully acknowledged.

Drago Kolar Marija Kosec

TABLE OF CONTENTS OF LECTURES

L E C T U R E S

CERAMICS AND METALS

MATERIALS SCIENCE COOPERATION IN 1987[+)]

Johanna Krawczynski

International Bureau
Kernforschungsanlage Jülich

Structure of Lecture

1. General Viewpoints in the Advancement of Materials Sciences Research :

   Technological Challenges and "Awareness of Materials";

   Generalized Aims for the Advancement of R & D

2. The European Community Programmes

   B R I T E — Basic Research in Industrial Technologies for Europe

   E U R A M — European Research on Advanced Materials

3. The Materials Sciences Programme of the Federal Ministry for Research and Technology of the Federal Republic of Germany

4. Bilateral German-Yugoslav Cooperation in the Field of Materials Sciences

---

[+)] This overview is no original contribution in the scientific sense, but a summary of European Community and German programmes on materials sciences, mentioned in the literature.

Reference is also made to the information sheet issued by Kernforschungsanlage Jülich GmbH : "WHAT IS, WHY, WHO ORGANIZES, WHERE TO APPLY FOR, WHAT TO KNOW ABOUT ..... BILATERAL COOPERATION?"

The German-Yugoslav Bilateral Cooperation is on the German side sponsored by BMFT, the Federal Ministry for Research and Technology of the Federal Republic of Germany

1. General Viewpoints in the Advancement of Materials Sciences Research : TECHNOLOGICAL CHALLENGES AND "AWARENESS OF MATERIALS"

The necessities to save energy, preserve the environment, check the consumption of strategic materials and boost competitiveness on the world market have caused a technological upheaval which asks for the expansion (or contraction) of certain major industries until the year 2000 and which is essentially linked with (novel) m a t e r i a l s.

An "Awareness of Materials" has developed, determined by the importance of materials for technological innovation, observing necessities of rational use of materials and energy, cutting manufacturing costs (automation), control and elimination of pollution, and last not least the creation of more stable and rewarding new jobs as well as of new industries and technologies.
The "emergence of advanced materials" thereby encounters unequilibrated development of industrial sectors (multi-track level of development) and needs transnational R & D as a result of geographic and scientific "cross fertilization" requirements, advanced materials becoming more and more diversified and sophisticatedly structured, which complicates their use.

Multidisciplinary approaches have to be linked to complementary activities like studies of the market impact of new materials, standardization and calibration, production of components, establishment of data banks, organisation of training and refresher courses and of conferences, seminars and workshops.

GENERALIZED AIMS FOR THE ADVANCEMENT OF R & D

The aims for the advancement of R & D in the materials sciences are threefold : to produce technically usable knowledge, to purposeful develop novel materials and to predict properties of novel materials.

For the achievement of these goals, an intensive and consequent basic research should simultaneously be carried out with high-tech research, thus establishing an operation scheme "Application-oriented basic research / applied research / fundamental technical development". Scientific cooperation in the pre-competition field and an improvement of conditions for R & D as industrial capacities are regarded as its appropriate instruments.

The model to organize R & D effectively is in the Federal Republic of Germany called "Verbundforschung", which calls for a cooperation between research institutes and industry, an organisational linkage of working groups, a multidisciplinary approach, a pooling of capacities and a division of labour.

The working principles of "Verbundforschung" in the field of materials sciences are :

- "project finding" as an orginary task of research partners from industry, universities and R & D-institutions;
- promotion of R & D in a few selected key areas (or cross-section areas) of technological development, to increase long-term competitiveness of industry;
- quick transfer of applied basic research into industrial technology and application.

2. The European Community Programmes

B R I T E Basic Research in Industrial Technologies for Europe

E U R A M European Research on Advanced Materials

BRITE Under the second call for papers, which runs from 1985 to 1988, also project proposals on materials sciences were invited, having: at least one industrial partner, and participants from at least two EC-countries, in the following areas :

- Reliability, Wear and Deterioration
- Laser Technology
- Joining Techniques
- New Testing Methods, incl. New Destructive Testing, On-Line and Computer-Aided Testing

- CAD/CAM Mathematical Modelling
- Polymers, Composites, Other New Materials and Powder Technology
- Membrane Science and Technology
- Catalyst and Particle Technology
- New Production Technologies for Products made from Flexible Materials

As an example for the field of Polymers, etc., following sub-areas have been mentioned :

- Manufacturing Technology of Composites for Structural Applications
- Manufacturing Technology of Copolymers, Blends and Polymer Alloys for Structural and Engineering Applications
- Specific Functional Applications of Special Polymers
- Specific Functional Applications of Ceramics and Glasses
- Production, Compaction and Sintering of Powders for the Cost-Effective Manufacturing of Components
- Innovative Approaches to Process Control for Application in the Relevant Industries
- Studies of Mechanical and Physical Properties and Applications for New Products made of Polymers.

The sub-area of Manufacturing Technology of Composites focusses on following topics :

- New Reinforcing Materials
- Composites for Engineering Applications
- Polymers and Processing Systems for Specific Applications (for instance New Biocompatible Polymers)
- Development of Improved Ceramics
- Production, Compaction and Sintering of Powders (for instance High-Purity Sinter-Active Powders and Dense Silicon Nitride Ceramics)
- Non-Destructive Evaluation Methods for Advanced New Materials.

EURAM The List of Main R & D Topics of EURAM (1986-1989) comprises:

Metallic Materials
1. Aluminium Alloys
2. Magnesium Alloys
3. Titanium Alloys
4. Electrical Contact Materials
5. Magnetic Materials
6. Coating and Tooling Materials
7. Thin-Walled Castings

Engineering Ceramics
8. Optimization of Engineering Ceramics
9. Metal/Ceramic Interface
10. Composite Ceramics
11. High-Temperature Behaviour of Engineering Ceramics

Composite Materials

12. Organic Composites
    a) Thermoplastic Matrix
    b) Thermo-Setting Matrix
13. Composites with Metallic Matrix
14. Other Advanced Materials for Specific Application

3. The Materials Science Programme of the Federal Republic of Germany

The main technical aims of the MS-Programme are :

- High-Temperature Strength for Different Technical Applications
- High-Strength and Stiffness of the Materials to be used as Materials for Constructions in all Fields of Application
- High Abrasion Resistance and Hardness (taking into consideration the different possibilities of materials combination)
- High Chemical Corrosion Resistance
- Combination of Different Materials Properties according to the Existing Needs
- Technical Relevance for Applications
- Low Weight (if possible).

The German MS-Programme covers following areas :

1. Ceramics
2. Powder Metallurgy
3. Metallic High-Temperature Materials and Special Materials
4. New Polymers
5. Compound Materials

Two examples are given, one for the Area of Ceramics, one for that of Compounds.

CERAMICS 1. Powders : Continuation of Powder Production Techniques, especially

- Powders with a well defined (narrow) particle size distribution below a so-called "critical size"
- Production of very pure powders with well-defined compositions
- Production of fine crystalline and amorph powders
- Amelioration of the sinterability by means of additives

2. Dotation and defined texture (.....)
3. Process Development (.....)

COMPOUNDS 1. Fibre-Reinforced Plastics
Fibre-Reinforced Carbon

A) Improved Reinforcing Fibres (....)

B) Matrix Materials

Development of Materials with High Corrosion and "Environment" Resistance at given Temperatures having
- high impact strength
- developments of methods for cheap production of structural parts
- cheap mass production

2. Compound Materials with Metallic Matrices(....)

4. Bilateral German-Yugoslav Cooperation in the Field of Materials Sciences

Bilateral German-Yugoslav Cooperation takes place in a legal framework constituted by Agreements on the governmental and on the institutional level. Among the first, are the Agreement on Cultural and Scientific Cooperation signed on July 28,1969 between the two State Governments, and the Agreement on Cooperation in the Field of Scientific Research and Technological development, signed on May 23, 1977, between YUZAMS and BMFT.

On the institutional level,an Agreement between YUZAMS and KFA-Jülich, equally on Scientific Research and Technological Development, was signed on July 8,1977.

The ongoing projects take place in the following main research areas : Energy Research, Ecological Research, R & D for Health, Manufacturing Techniques, Biotechnology, Chemical Processing, Materials Sciences and Development, Physical Technologies and Basic Research. Roughly one third of the projects are running in the field of materials sciences. Project partners on the Yugoslav side are the Institute Jozef Stefan and the University of Ljubljana,

the Boris Kidric Institute of Nuclear Sciences, Vinča, and the Universities of Sarajevo, Skopje, Zagreb, Titograd and Belgrade.
On the German side, Kernforschungszentrum and University of Karlsruhe, the Institut für Werkstoffwissenschaften(PML) of the Max-Planck Institute in Stuttgart, KFA Jülich, the University of Erlangen and the Technical Universities of Aachen, Clausthal, Hamburg-Harburg, Karlsruhe and Munich are involved.
In the period 1985/1986 the budget rose by 20%; expenses of the International Bureau for materials science projects have doubled in this period. German delegations to Yugoslavia were four times as as numerous in 1986 as they were in 1984, stays of Yugoslav scientists in the Federal Republic of Germany rose by 50% in the same period. Project work has been accomplished in the field of powder metallurgy and structure-properties relationships (magneto ceramics, oxide ceramics, kinetics, thermophysical properties), engineering ceramics, sintering materials, grain growth, thermodynamics, carbon fibres, surface physics with special emphasis on corrosion problems, and physical-chemical processes,as well as metals.

The research and development priorities of the Federal Republic of Germany and of Yugoslavia practically being identical, both stressing also the field of materials sciences and development, a good basis for further intensification of the German-Yugoslav bilateral cooperation in this field of science and technology is existing. Special characteristics of bilateral cooperation projects are the stressing of partnership and a sharing of the work load, which ensures transparency of mutual efforts and also accounts for their effectivity.

The instrument of the German-Yugoslav Meetings on Materials Sciences and Development has since long proved its value to report on interesting new developments, and above all, on progress within on-going bilateral projects. At the same time, proposals for new projects can be discussed, existing project work deepened, and in this way technology transfer from research to industry further intensified.

Literature

Commission of the European Communities
Directorate-General for Science, Research and Development

B R I T E - Basic Research in Industrial Technologies for Europe

Project Synopses - Projects supported under the First Call for Proposals, 1985

Information Package for the Second Call for Proposals

E U R A M - European Research on Advanced Materials

Research Action Programme Materials

Raw Materials and Advanced Materials
1986-1989, Programme Description
IV. Advanced Materials EURAM

Bundesministerium für Forschung und Technologie, Bonn

M A T E R I A L F O R S C H U N G

Programm des Bundesministers für Forschung und Technologie

Bonn, 1985

Address of the International Bureau

Kernforschungsanlage Jülich GmbH
International Bureau
Postfach 1913
D-5170 Jülich

Bundesrepublik Deutschland

Telephone (99) 49 2461/613422,615791
Telex 833 556-30 kf d
Telefax (99) 49 2461/613635

CERAMIC PROJECT OF THE MAX-PLANCK-SOCIETY

Günter Petzow
Max-Planck-Institut für Metallforschung
Institut für Werkstoffwissenschaften
Pulvermetallurgisches Laboratorium
Heisenbergstr. 5, 7000 Stuttgart 80, FRG

It was powder metallurgy that started the German-Yugoslavian collaboration. And thus it was mostly work from the area of powder metallurgy that the Max-Planck-Institute for Metals Research contributed to this bilateral cooperation. It was not until a few years ago contributions of the materials area of advanced ceramics began to appear increasingly. This reflects a general tendency in the area of materials science, namely the growing significance of advanced ceramics. On one hand this new group of materials plays a key role in the development of new technological concepts, and on the other hand the advanced ceramics enter the competition with already established materials.

As well as other solid-state physics- and solid-state chemistry-oriented research institutes, the Max-Planck-Institute for Metals Research rapidly recognized the enormous significance of the new ceramic materials and started research on them already in the early seventies. It proved to be advantageous that ceramic processing basically followed the same steps as usually found in powder metallurgy, namely powder production, processing, shaping, and densification. Also many methods of characterization, all well established with the study of metallic materials, such as metallography, electron microscopy, and X-ray diffractometry, as well as mechanical, chemical, and thermal analyzing methods, could easily be adapted to the new class of materials. Thus it is not surprising that soon many of the metals-scientists at the Powder Metallurgical Laboratory of

the Max-Planck-Institute for Metals Research (PML) worked on ceramic materials besides metals and alloys. Internationally recognized results of these times are the development of multi-component alloy systems based on Si_3N_4, the discovery and understanding of transformation toughening, the dry-agglomeration, and the optimization of ceramic cutting materials.

For a long time the research on ceramic materials at the PML more or less was a "by-product", i.e. an official ceramic project did not exist at that time. Only at the end of 1984 the Senat of the Max-Planck-Society decided to take up ceramics research as a main activity at the Powder Metallurgical Laboratory of the Max-Planck-Institute for Metals Research. To this essentially three measures were decided upon:

- Construction of ceramics laboratories
- Research program and research team
- Establishment of a professor's chair

Construction of Ceramics Laboratories

The state of Baden-Württemberg and the Max-Planck-Society provided the funding for the annex to the PML.

After thorough planning in 1985, the construction began in March 1986 and was finished one year later in March 1987. Figure 1 gives an impression of the ceramics-annex, which is connected to the PML by several hallways. The three-story building has a total area of 2500 m^2, 750 m^2 of which are used as laboratories and offices, 1050 m^2 for technical support, 250 m^2 for locks and storage, and 450 m^2 for hallways, stairways, etc. At the center of the new building is a large laboratory hall that can be operated under clean-room conditions. Next to this hall are the measuring labs and powder-processing labs.

Fig. 1

Research Program and Research Team

Funding of the ceramic project is provided by a consortium of the companies Bayer AG, Daimler-Benz AG, Hoechst AG, and MTU within the framework of the materials research program (MATFO) of the Federal Ministry for Research and Technology (BMFT). 50 % of the funds come from industry and 50 % from the Federal Government. The project has a duration of seven years; after that it will be supported by the Max-Planck-Society.

The research team consists of six scientists, seven technicians, two clerks, and two mechanics. In addition to that, there will be guest-scientists, Ph.D. candidates, and postdocs, so that a total of about 35 people will work in the ceramics laboratory. An internationally renowned scientist will be engaged as the leader and director of the research team.

The Topic of the Project is

"Development of thermally and mechanically highly stressed ceramic materials with high reliability as basis for efficient components for engines and turbines."

The main points of the program are as follows:

1. Production and processing of high-purity ceramic powders.

   - Powder production: CVD, polymer pyrolysis, coprecipitation.
   - Alloying/doping: colloidal-chemical experiments, sol-gel, heterofloculation.
   - Chemical analysis/distribution analysis.

2. Microstructural reinforcement of advanced ceramics.

   - Transformation toughening (ZrO_2)
   - Whisker/fiber reinforcement (SiC-Wh)
   - Devitrivication ($Y_3Al_5O_{12}$)
   - Precipitation- and dispersion strengthening (Al_2O_3, BN).

3. Study of high-temperature properties (1000-1500°C).

   - Mechanical properties (toughness, creep, K_{Ic}).
   - Thermo-mechanical properties (thermal fatigue, thermal shock, thermal conductivity and thermal expansion).
   - Corrosion and wear.

Criteria for the evaluation of reliability and life time, especially of microstructurally reinforced ceramics.

4. Study of the thermodynamic phase equilibria in multi-component ceramic systems.

   - Calculation of phase diagrams (Si, Y, Al/O, C, N)
   - Simulation of extreme conditions
   - Design of new materials combinations.

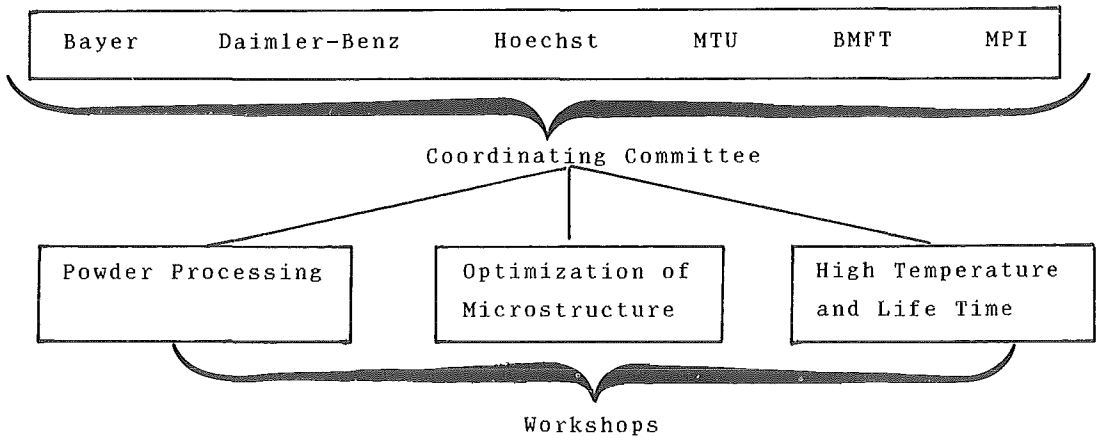

Fig. 2

The organizational structure of the project becomes clear from Fig. 2: A coordinating committee, consisting of one company representative each, controls the scientific-technological workshops made up of suitable delegates from all five consorts. The coordinating committee meets twice a year, the workshops meet as often as neces-

sary. The workshop "Materials Selection" determined the materials to be studied in detail and was discontinued its work for the time being. Figure 3 shows a summary of this materials selection.

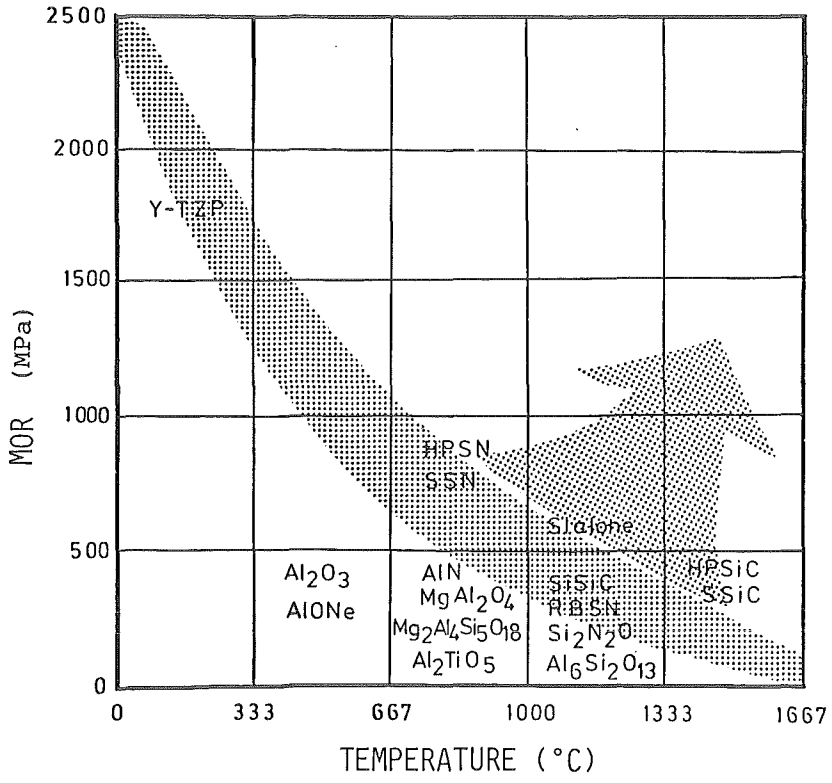

Fig. 3

The research team, the formation of which is nearly complete, has produced about 20 scientific publications and two patent applications at this time and collaborates smoothly with the industrial consorts. Special equipment available to the project, in addition to the clean-rooms, are measurement equipment to 1500°C. This enables a rapid assessment of the materials' development potential. Furthermore, computer-aided determination of constitution is of decisive significance.

Establishing of a Professor's Chair

The recently established chair for nonmetallic, inorganic materials, which is also located in the annex, is supplied with eight positions by the Ministry for Science and Culture of the state of Baden-Württemberg. This chair, which moreover is supported by a Feldmühle/Kyocera foundation, should remedy the pressing need for materials scientists in the faculty for chemistry with improved knowledge in the area of advanced ceramics. It is anticipated that the professor will begin his work in the summer semester 1988.

C E R A M I C S

POWDER SYNTHESIS AND FORMING

SILICON-CARBIDE MADE OF SILICON-ORGANIC COMPOUNDS

E. FITZER, M. KEUTHEN
Institut für Chemische Technik der Universität Karlsruhe
Kaiserstraße 12, D-7500 Karlsruhe, BRD

1. Introduction

Since 1975 YAJIMA and coworkers showed [1,2,3,4,5] the route from silicon-organic compounds to various silicon-carbide products. Some of the applications they proposed are to be

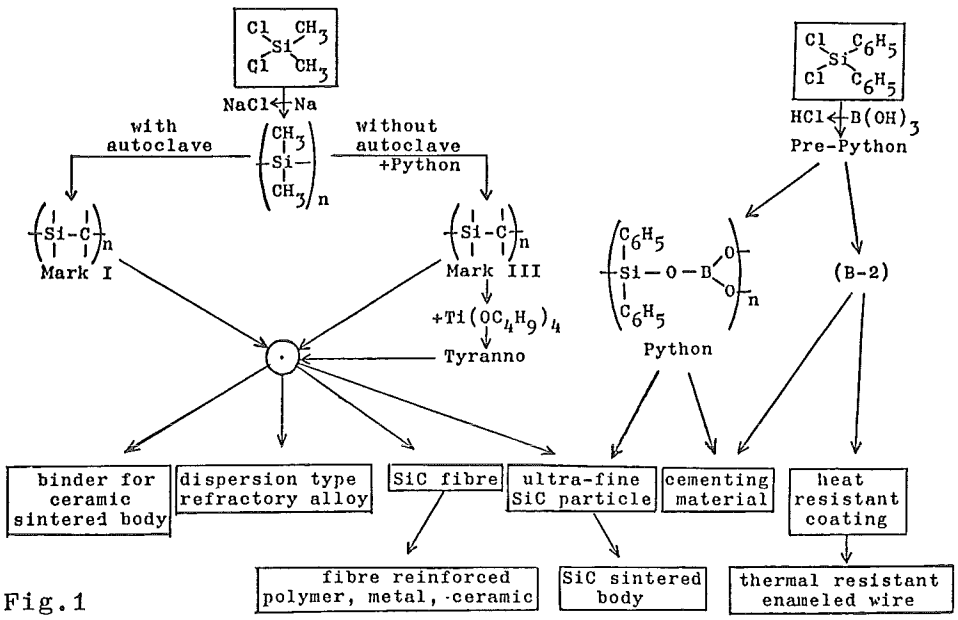

Fig.1

seen in Fig.1. One of their proposals which is already realized in industrial scale is the SiC-fibre, available under the trade mark NICALON®. The composition, the properties and the expected applications are shown in Table 1-3 due to ref.[5].

Table 1 Composition of Fibers

Fiber	Composition (wt%) Si	C	O	H
Mark I	46.8	38.1	0.82	7.40
Cured Mark I	44.4	31.0	15.5	5.30
SiC	50.5	31.6	10.3	0.06
SiC, heat-treated at 1250°C in air	51.3	23.9	18.5	0.02
SiC, commercial*	55.5	28.4	14.9	0.13

*Nicalon, Nippon Carbon Co., Ltd., Tokyo, Japan.

Table 2 Properties of SiC Fiber*

Tensile strength	2000–2500 MPa
Tensile modulus	1.8×10^5–2×10^5 MPa
Elongation	1.5–2.0%
Density	2.55 g/cm³
Filament diameter	13–15 μm
Cross section	Round
Filaments/yarn	500

*Nicalon.

In a recently published paper [7] a similar route from hydridopolysilazane to ceramics is proposed. Fig.2 shows the chemistry, Fig. 3-5 the properties of the resulting hydridopolysilazane HPZ due to ref. [7].

Table 3 Expected Industrial Uses of Continuous SiC Fiber

Category	Field	Uses
Heat-resisting material	Continuous furnace	Mesh belt
	High-temperature transport	Conveyor belt
	Melt refining, roll welding	Refractory curtain, molten metal filter, insulator support
	Environmental pollution countermeasures (dust removal, desulfuration and denitration of exhaust gas)	Packing, filter bag filter
	Chemical industry, nuclear power industry	Filter
	Automotive engineering (exhaust treatment)	Catalyst support
	Combustion equipment	Burner nozzle, wick
Fiber-reinforced metals	Space and aircraft machinery	Structural member, engine fixture, peripheral part of fan blade
	Automotive engineering	Engine part
Fiber-reinforced plastics	Space and aircraft machinery	Structural member
	Sporting goods	
Other reinforced materials	Ceramics, furnaces	Reinforcement for firebrick, ceramic, glass, and carbon
Other	Acoustic material	Speaker cone
	Business equipment	Brush for removal of static electricity

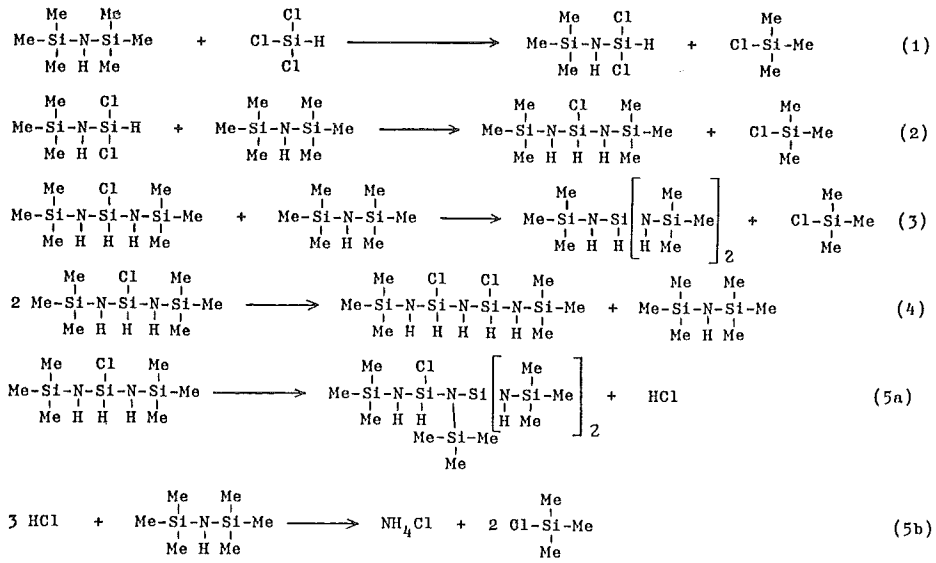

Fig.2 Preceramic Polymer Synthesis Me = methyl

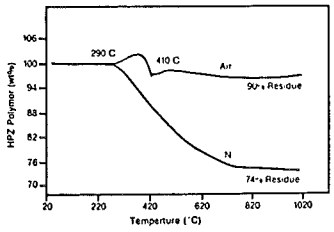

Fig.3 TGA of HPZ polymer in air and nitrogen.

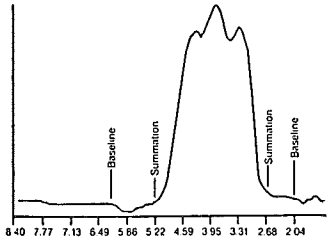

Fig.4 GPC of HPZ polymer.

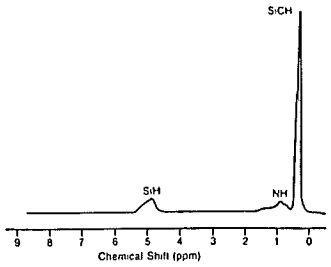

Fig.5 ^{1}H NMR spectrum of HPZ polymer.

2. Synthesis of SiC precursor according to the literature and thermal degradation to SiC

We started our own research in this field with the reproduction of the synthesis of silicon-organic compounds and their pyrolysis to SiC as reported in literature.

2.1 Preparation of silicon-organic precursors and thermal cross-linking to polycarbosilanes.

a) $(Me_2Si\text{-}CH_2)_2$ was made of $ClMe_2Si\text{-}CH_2Cl$ following a method described by Kriner[8]. (Reaction I)

Reaction I

$$H_2ClC\text{-}Si\,Me_2Cl + Mg \xrightarrow{THF} 50\%\ Me_2Si\langle CH_2\rangle_2SiMe_2 + 50\%\ \text{other products (useful carbosilanes as well)}$$

Me = methyl

Thermolysis of $(Me_2Si\text{-}CH_2)_2$ up to 200°C in sealed glass ampoules succeeded in a yield of nearly 100% of a resinous polycarbosilane with units like they are shown in Fig.6 and a molecular weight of 20 000 to 30 000, proved by NMR, elementary analysis, and gel permeation chromatography respectively as reported by Hill et al.[9] During the thermal decomposition in the range of 500-600°C this polymer forms volatile intermediates which cause the necessarity of pressure application, thus diminuishing the technical value of the process. Nevertheless the thermal decomposition of this polymer, its suitability and conditions of application as a SiC precursor for impregnations, coatings and composite materials is subject of present work.

Fig.6

b) $(SiMe_2)_6$ was made of Me_2SiCl_2 using a method of Carberry and West[10] (Reaction II). By the thermal decomposition of this product in an autoclave at 600°C and 5 MPa a brittle polycarbosilane of the density (xylol) = 1,32 g cm^{-3} was obtained.

Reaction II

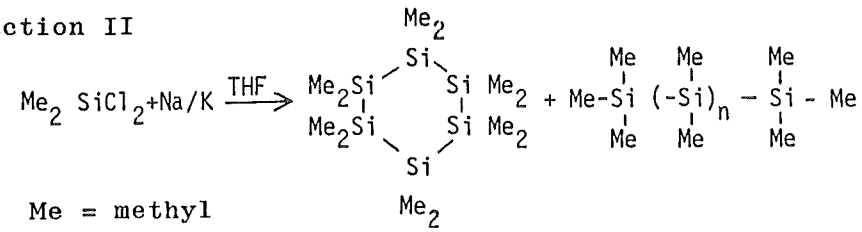

Me = methyl

2.2. Pyrolysis of polycarbosilane to silicon-carbide

The polycarbosilane reported in chapter 2.1.b was decomposed in the temperature range of 700-1400°C under 100 kPa argon atmosphere to more than 70% mass ceramic residue. After a temperature treatment of 1400°C this residue showed the x-ray pattern of ß-SiC (see Fig.9). The influence of the treatment temperature on the 20°C - density of the resulting ceramic is given in Fig.7.

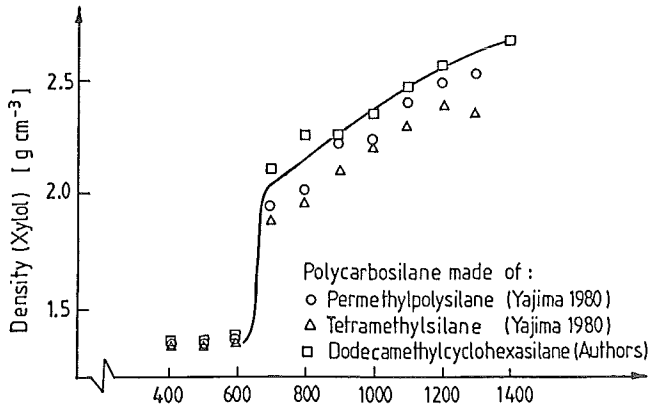

Fig.7

The glass-like structure of the product with few microscopic shrinking cracks and a surface similar those of glass-like carbon is shown in Fig.8. Fig. 9 demónstrates the crystallization effect of the material by the x-ray pattern after 1200, 1300 and 1400 °C temperature treatment.

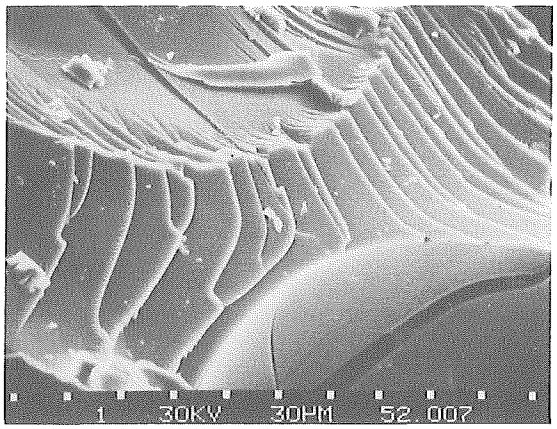

Fig.8

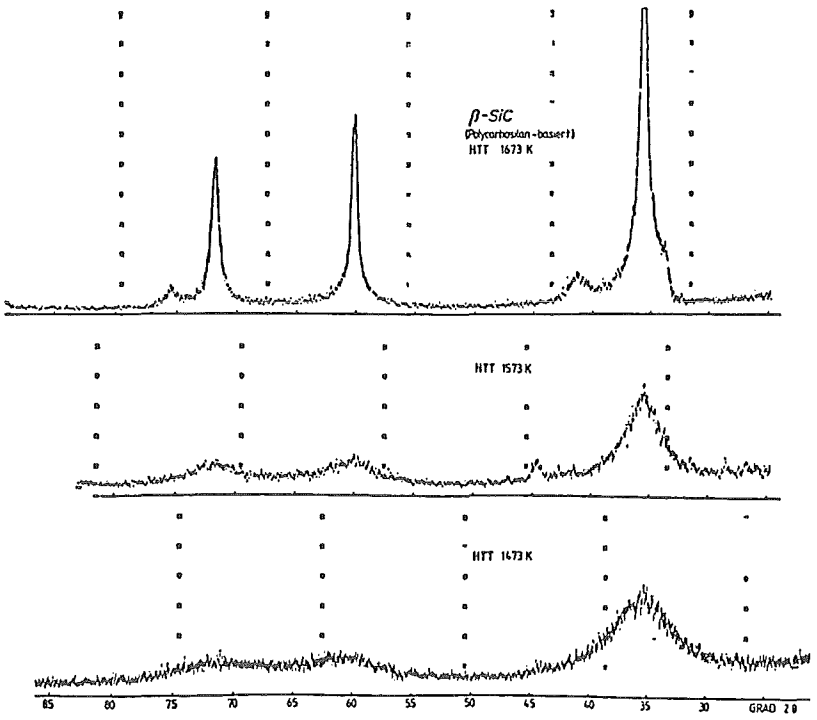

Fig.9

On the basis of the results of x-ray analysis and by using the Scherrer equation[11] and the method of Bartram[12], it was possible to calculate the increase of crystal size ref.[13] by temperature treatment. The results are given in Fig.10

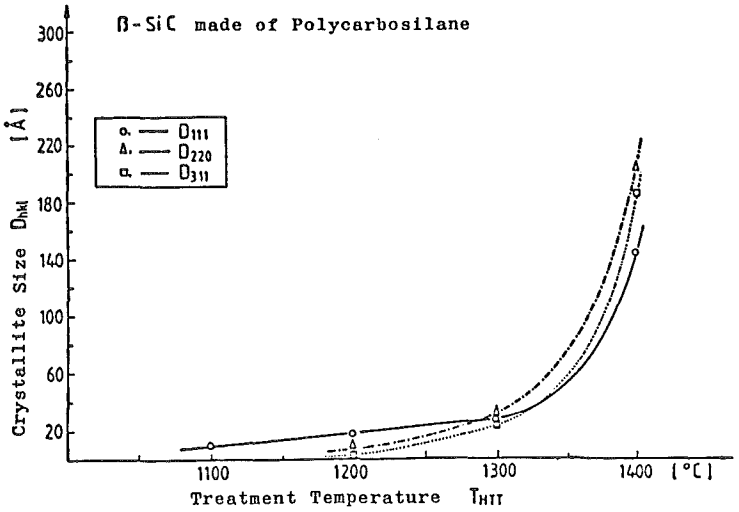

Fig.10

3. Experiments on the applicability of the SiC precursor

3.1 As liquid impregnants

Our first aim in the development of liquid, meltable or soluble SiC precursors was their use for densification of porous SiC-ceramic by impregnation and pyrolysis of the impregnated precursor to SiC. One of the basic questions in this research is the manner of pore filling during the impregnation step. In the case of melt impregnation with $(SiMe_2)_6$, the answer is given in Fig.11.

Preliminary studies[14] have shown, that porous granular silicon carbide bulk material can be improved in strength and oxidation resistance considerably by such methods.

As basis for modelling this process and a better understanding polygranular graphite with model pores was melt impregnated with $(SiMe_2)_6$.

Fig. 11 shows first respective results.

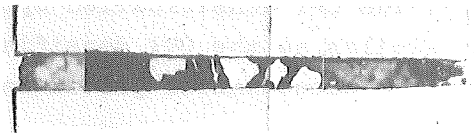

Passing pore $\emptyset$ = 400 μm

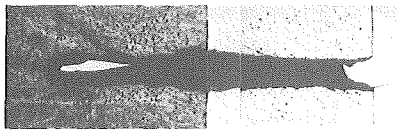

Dead end pore $\emptyset$ = 400 μm

Fig.11 Impregnation of model-pores in graphite with $(SiMe_2)_6$ at temperatures up to 300°C (Graphite with points, filler black, remaining porosity white or with points.)

3.2 Development of silicon carbide composites

The availability of meltable silicon organic SiC precursors offers the possibility to prepare SiC/SiC-composites following in principle the production route for C/C-composites. First experiments in preparation of SiC-whisker reinforced SiC are in progress (See Fig. 12) ß-SiC whiskers from TOKAI CARBON were used. After the first pyrolysis step, bulk samples with an overall density of 1.5 g/cm^3 and 40 vol% open pores were obtained. Such porous samples can be impregnated by liquid silicon organic compounds and reimpregnated after intermediate pyrolysis treatment. The work still in progress shows that densification by multiple impregnation/re-pyrolysis steps comparable with the method for fabrication of carbon composites is successful.

In parallel studies SiC/SiC composites with endless SiC-fibres are in work. Also in this case, the analogy to carbon/carbon composites technology is proved.

This method promises to be more successful as the conventional SiC/SiC fabrication methods. Hot pressing of the matrix for instance causes mechanical damage of the reinforcement fibres. Reaction sintering of an intermediate carbon binder matrix leads to a chemical attack on the reinforcement fibres because of the violent reaction at the process temperature around 1400°C.

Also cristallization of SiC fibres takes place under such process conditions [5,13]. The CVI densification by volatile methylchlorosilanes is similar as the CVI densifikation of carbon/carbon composites an uneconomical procedure.

1st step	Desagglomeration of whiskers	Solvation of $(SiMe_2)_6$
2nd step	Mixing	
3rd step	Removing of solvent	
4th step	Green bodies of ß-SiC whiskers in $(SiMe_2)_6$ matrix obtained by pressing at 20 MPa and 220-240°C	
5th step	Thermolysis of the samples obtained in the 4th step at 600-650°C and 5-8 MPa isostatic nitrogen pressure leads to green bodies of ß-SiC whiskers in polycarbosilan matrix	
6th step	Pyrolysis of samples obtained in the 5th step at 100 KPa argon pressure at 700-1000°C leads to ß-SiC whisker reinforced ß-SiC composites.	

Fig.12 Preparation of whisker reinforced SiC

References:

1. S.Yajima,J.Hayashi,M.Omori Chem.Lett.pp 931-934,(1975)
2. S.Yajima,K.Okamura,J.Hayashi Chem.Lett.pp 1209-1212,(1975)
3. S.Yajima,Y.Hasegawa,J.Hayashi,M.Jimura J.Mater.Sci.13 (1978)2569
4. Y.Hasegawa,M.Jimura,S.Yajima, J.Mater.Sci.15 (1980) 720
5. S.Yajima, Am.Ceram.Soc.Bull. 62 8 893 (1983)
6. E.Fitzer,R.Gadow Am.Ceram.Soc.Bull. 65 2 326 (1986)
7. G.E.Legrow,T.F.Lim,J.Lipowitz,R.S.Reaoch Am.Ceram.Soc.Bull. 66 2 363 (1987)
8. W.A.Kriner J.Org.Chem.29,1601 (1964)
9. C.Hill Diplom Univ. Karlsruhe
10. E.Carberry,R.West J.Am.Chem.Soc.91,5440 (1969)
11. P.Scherrer Göttinger Nachr. 2,98 (1918)
12. S.F.Bartram in Handbooksof X-rays,E.F.Kaelble ed.,pp 17-1 /17-13,McGraw-Hill,New York / 1967
13. R.Gadow Doctor Thesis Fak. Chemie Univ. Karlsruhe 1986
14. H.Strohmeier Doctor Thesis Fak. Chemie Univ. Karlsruhe 1981

SLIP CASTING OF FUSED SILICA

D.Kićević, B.Kostić,M.Gašić

Institute for Nuclear Sciences "Boris Kidrič" - Vinča
Institute for Materials
P.O.Box 522, 11001 Belgrade

Abstract

Slip casting is a very suitable forming process for making different products of fused silica, regarding their complex shape, size, firing shrinkage, porosity and other properties. One of the main problems in the processing of technical grade fused silica is the devitrification during sintering. The devitrification could be avoided by decreasing the sintering temperature and reducing the sintering time. To maintain high sintered density it is possible to use hot pressing or to increase green density. Usualy, good green density is achieved with well deflocculated slip and after extended casting time. The analysis of slip casting mechanism and rate equation for filtration model pointed out the way to accelerate the process of slip casting. Experiments with vibrocasting, pressure casting and casting of coarse grain slip showed that it is possible to obtain rather dense green cast samples with acceptable slip casting rate.

Introduction

Fused silica has various applications as refractory or technical ceramic material, due to its good thermophysical properties such as very low thermal expansion coefficient and high thermal shock resistance /1,2,3/. Most suitable forming process for fused silica ceramics is the slip casting. It allows making different products regarding their complex shape, size, firing shrinkage, porosity and other properties /2/. For technical grade fused silica ceramics one of the main problems in processing is the devitrification during sintering /4,5,6/. In order to avoid the devitrification it is necessary to decrease the sintering temperature and to reduce the time of isothermal sintering.

At the same time, to maintain high sintered density it is necessary, either to use the hot pressing /6/ or to improve the green density. Since hot pressing is rather costly and restricted to simple shape and moderate size, the better way to solve the basic problem is the increasing of the green density. In the usual slip casting process higher green density can be achieved with well deflocculated slip and after extended casting time /2/. For small size products, where rather fine grain slip is to be used, that would be even more pronounced. If both requirements, higher green density and shorter casting time, are to be fulfilled simultaneously, then the optimum should be a compromise between them. In this paper, through the analisys of slip casting mechanism and kinetics and the experiments with different slips, the aim was to find out possible combinations of process parameters which will alow faster slip casting and give higher green density.

Slip casting process analysis

Slip casting in the plaster moulds was first thought to be a diffusion process, i.e. governed by the rate of water diffusion into the capillaries of the plaster mould /7,8,9/. Later on, the filtration model was proposed /10,11/, indicating the flow of liquid through the porous cast layer as the governing process. This filtration mechanism can be described by the equation of Adcock and McDowell /10/, having a general form:

$$X = K\sqrt{\tau} \qquad (1)$$

where: X - thickness of the cast layer

τ - casting time

K - proportionality constant, which is a combination of many parameters:

$$K = \frac{2\,P\,G\,E^3}{5\,S_p^2\,\eta\,(Y-2)(1-E)^2} \qquad (2)$$

where: P - pressure drop across the cast layer

E - void fraction in the cast layer

S_p - specific surface of solids (by permeability measurements)

η - viscosity of the suspending medium

Y - volume of slip containing (1-E) volume of solids

G - gravitational constant

Analyzing these parameters and their influence on the process, it is clear that the possibilities to enhance the casting rate are the following: increasing casting pressure; lowering the viscosity; increasing slip density; lowering the specific surface of powder i.e. using corser grain slip; increasing porosity of the cast layer. Although some of this combinations will also influence the porosity of the cast layer it is likely to expect that vibrocasting, pressure casting and casting of coarse grain slip will give better results than simple drain casting. It should be pointed out also that the required particle size distribution, depending mainly on product's size, can make some additional constraints for other parameters.

General form of casting rate equation cannot be applied to the beginning og slip casting i.e. when the cast layer is not thick enough to make the higher resistance than the mould. Therefore, particularly for fused silica slip casting, some empirical equations were derived /12/:

1) drain casting

$$X = 0{,}1219\sqrt{\tau - 2{,}7} - 0{,}0528 \qquad (3)$$

where: X - thickness of cast layer (cm)
τ - time (min)

2) pressure casting

$$X = 0{,}0116\sqrt{\tau P} - 0{,}1194 \qquad (4)$$

where:
P - gauge pressure (kPa)

If coarser slip is used, higher rates could be expected.

Experimental

In order to investigate the possibilities of improving the casting rate and green cast density the following experiments were performed. Fused silica powder ("Elmin", nominal purity 99.5%) was wet ball milled with SiO_2 balls and then stabilized(25-40 h) to make slips with following properties:

- solid content: 82-89,7 w/o
- mean grain diameter: 15-20 μm (fine grain slip)
- density: 1,84-1,86 gcm^{-3} (1,86-1,94 gcm^{-3} for coarse grain slip)
- minimum viscosity*: 650-1000 mPa.s (4700 mPa.s for coarse grain slips)

* Brookfield rotational viscometer RVT

Casting rate was determined by simple, indirect method, after Pivinskiy /2/. This method is very useful for screening experiments and for relative measurements. It is based on the relation between cast layer thickness and volume of slip which is protruded in the mold cavity. Fig.1 shows the casting rate measuring cell and Fig.2 the apparatus for pressure casting.

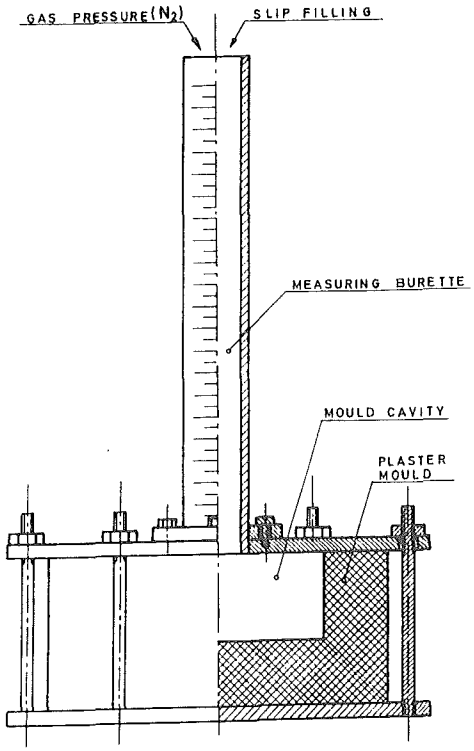

Fig.1. Casting rate measuring cell.

After casting, samples were dried and green cast density, as well as moisture, were calculated from weight and dimensional measurements.

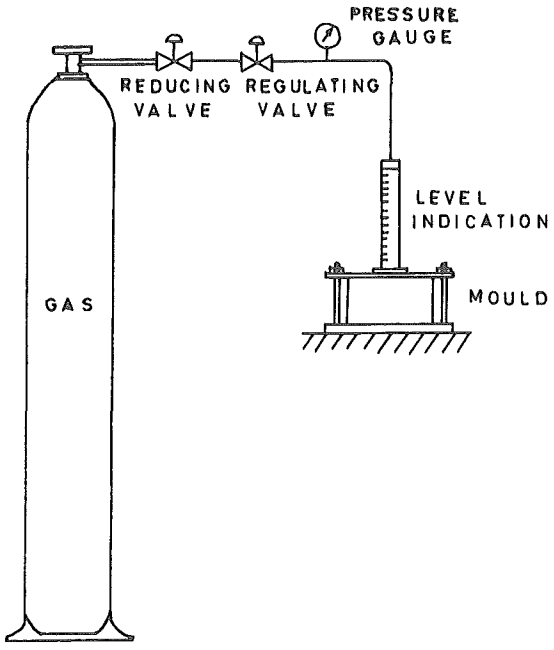

Fig.2. Laboratory apparatus for pressure casting.

Results and discussion

Casting rate (cast layer thickness versus casting time) for vibrocasting and casting of coarse grain slip, comparing to simple drain casting, is presented in Fig.3. In Fig.4 casting rates of coarse grain slips with different coarse fraction content were compared. The green cast density for each slip is indicated on respective curve. The influence of pressure on casting rate is given in Fig.5.

Moisture in green cast samples is presented in Fig.6 and Fig.7, as a function of coarse grain fraction and casting pressure.

These experimental results show that all investigated parameters, the casting pressure, vibrocasting and coarse grain slip, can improve the casting rate as well as maintain or even increase the green cast density. Also, the moisture in green cast samples is reduced either by higher casting pressure or by higher coarse grain fraction content. This will furthermore decrease the drying shrinkage and allow near net shape processing. Although results in figures

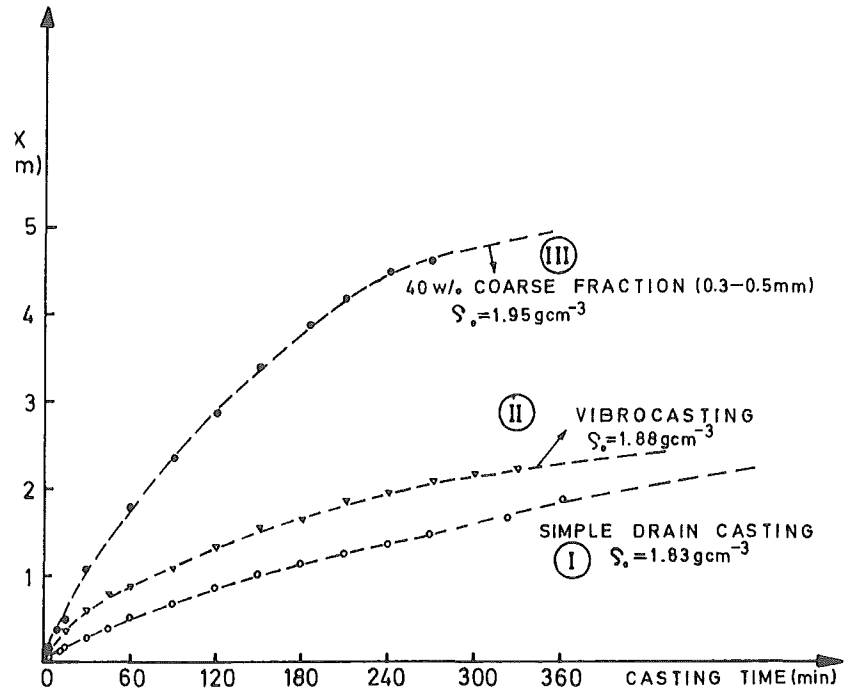

Fig.3. Casting rate of different slips and casting conditions.

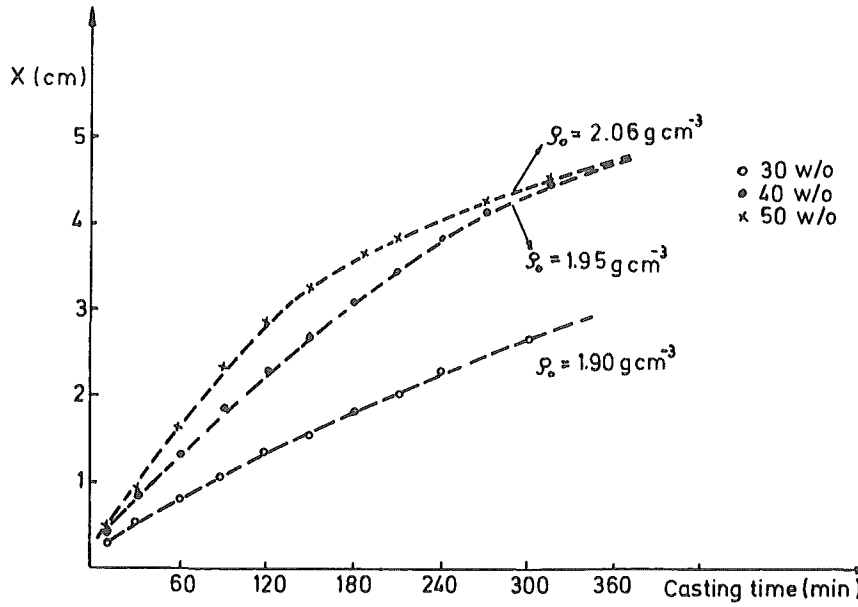

Fig.4. Casting rate for coarse grain slips with different coarse grain fraction.

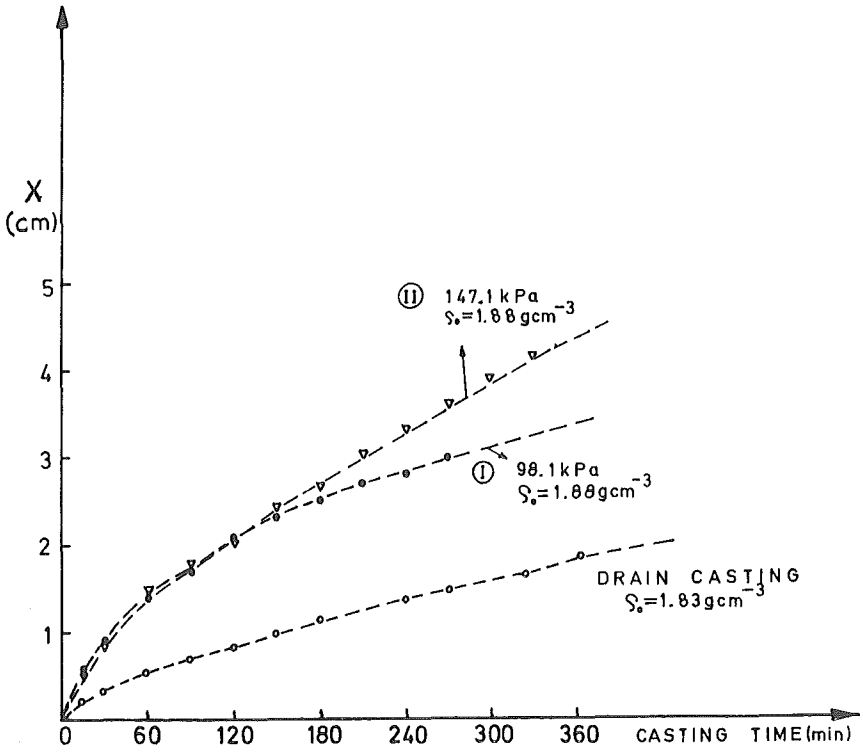

Fig.5. Casting rate for fine grain slip under different pressure.

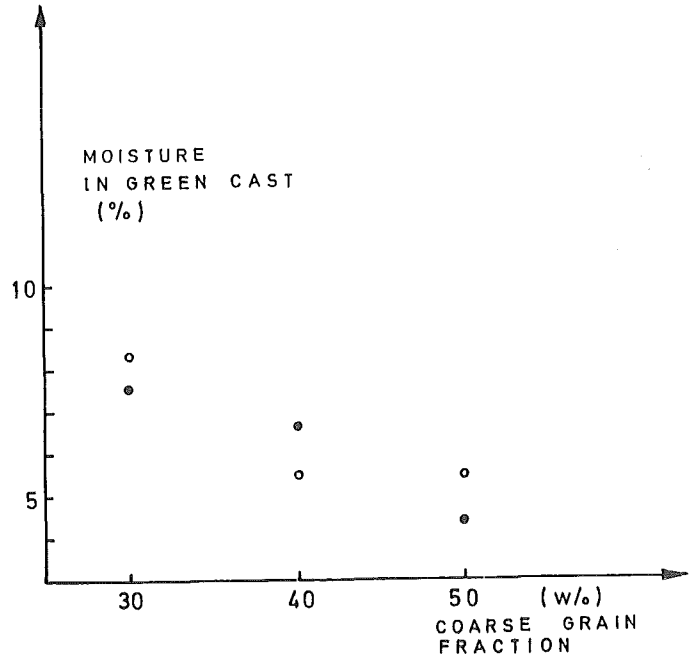

Fig.6. Moisture in green cast samples for different coarse grain fractions.

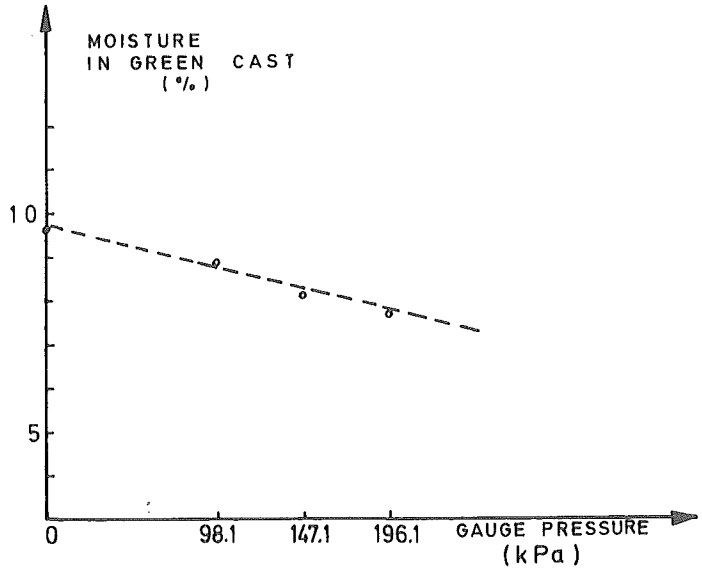

Fig.7. Moisture in green cast samples for different casting pressure.

would suggest even higher values of process parameters, it should be noted that such level is rather difficult to achieve because of great technological problems (slip workability). The obtained values (especialy for green cast density for coarse grain slips) are quite satisfactory and the requirements for green cast properties are fulfiled.

Regression analysis of casting rate data was used to obtain empirical rate equations, similar to equations (3) and (4), with high correlation coefficient (R^2):

simple drain casting

$$X - 0{,}1101 \sqrt{\tau} - 0{,}2507 \qquad (R^2 = 0{,}9842) \qquad (5)$$

vibrocasting

$$X = 0{,}0995 \sqrt{\tau} + 0{,}1758 \qquad (R^2 = 0{,}9753) \qquad (6)$$

pressure casting

$$X = 0{,}0198 \sqrt{\tau P} - 0{,}3336 \qquad (R^2 = 0{,}9766) \qquad (7)$$

casting of coarse grain slip

$$X = 0{,}3164 \sqrt{\tau} - 0{,}5116 \qquad (R^2 = 0{,}9941) \qquad (8)$$

Comparing the equation (7) and (4), it can be pointed out that the rate constant in (7) is higher than respective one in (4), resulting in faster casting. This is explained by the fact that equation (7) was obtained for

slip with mean particle diameter 15-20 μm and equation (4) for slip with mean particle diameter 7-8 μm. For coarse grain slip, even higher rate constant is obtained as a consequence of much higher particle diameter (0,1-0,5 mm).

Conclusions

On the basis of slip casting process analys and experimental results it can be concluded that casting rate of fused silica slips can be increased by vibrocasting, pressure casting and casting of coarse grain slip. All these methods will yield satisfactory green cast densities and, in some cases, even higher than those obtained by prolonged simple drain casting.

Empirical casting rate equations could be derived from casting rate data and compared to other empirical equations for fused silica slip casting.

References

1. Walton, J.D., Ceramic Age, 76 (1960) 2, 33-38; 76 (1960) 3, 23-38; 77 (1961) 5, 52-58; 77 (1961) 6, 53-58; 78 (1961) 1, 38-45.
2. Pivinskiy, Yu.E., Romashin, A.G., "Kvartsevaya keramika", Izd. Metallurgiya, Moskow, 1974., 243-256.
3. Ahjan, A.M., Refractories (in russ.), (1982) 4, 40-44.
4. Kićević D., Gašić M., in "Sintering - Theory and Practice", Materials Science Monographs 14, D.Kolar, S.Pejovnik and M.M.Ristić (Eds.), Elsevier Scientific Publ.Co., Amsterdam - Oxford - New York, 1982, 121-126.
5. Kićević D., Gašić M., Zec S., La ceramica, 38 (1985) 5, 16-22.
6. Kićević D., Gašić M., in "Contemporary Inorganic Materials": Progress in Ceramics, Metals and Composites", Proc. 7th German-Yugoslav Meeting on Engineering Materials Science and Technology, Bad Herrenalb, April 22-26, 1985., G.Ondrace, O.Vöhringer (eds.), KFA Jülich GmbH, 1985, 25-35.
7. Deeg, E., Ber. DKG, 30 (1953), 6, 129-138.
8. Ditzel, A., Mostetzky H., Ibid, 33 (1956) 1, 7-18.
9. Deeg, E., 6th Intern. Keram.Kongress Wiesbaden, 1958., 243.
10. Dal, P.H., Berden, W.J.H., Sci. of Ceramics 4, 1968, 113-131.

11. Adcock, D.S., McDowell, I.C., J.Am.Ceram.Soc., 40 (1957) 10, 355-362.

12. Fleming, J.D., "Fused Silica Design Mannual", Georgia Tech Engineering Experiment Station, 1964., Contract No. AT-(40-1)-2483 for U.S.A.E.C.

INJECTION MOULDING OF WHISKER-REINFORCED AL_2O_3-ZrO_2 CERAMICS

T.Kosmač*, D.Gorjan**, E.Lutz***, N.Claussen***

*"Jožef Stefan" Institute, Ljubljana, YU

** ISKRA Avtoelektro, Tolmin, YU

***Technische Universitat Hamburg-Harburg, FRG

INTRODUCTION

ZrO_2 toughened oxide ceramics represent a new class of high performance ceramic materials with significantly improved mechanical properties at low and intermediate temperatures(1). However, at higher temperatures (> 700°C) the efficiency of ZrO_2 toughening decreases drastically and vanishes almost completely above the m→t transformation temperature of ZrO_2 (i.e. > 1100°C). In addition, rather high creep rates in the oxide-based materials at elevated temperatures overshadow the benefit of ZrO_2 toughening(2), making both non oxides SiC and Si_3N_4 more competitive for high performance engineering application. In order to overcome these deficiences of toughened oxide ceramics, whisker of fiber reinforcement has recently received increasing interest(3), although other possibilities such as prevention of glassy intergranular films or incorporation of hard high modulus particles are also being thoroughly investigated(4).

Thus it was demonstrated that Al_2O_3-SiC whisker composites are very resistant to slow crack growth, high temperature creep and thermal shock(5,6). Furthermore, the room temperature fracture toughness of whisker-reinforced material was also found to be higher in comparison with the equivalent monolithic matrix material, particularly for the case where the fracture plane was perpendicular to the plane of the preferentially oriented whiskers resulting from hot pressing(3). Since fabrication of whisker-reinforced ceramics tends to avoid hot pressing techniques replacing it by conventional pressureless sintering + additional HIPing, desired whisker orientation should be ensured during the

shaping process. Here extrusion, tape casting, slip casting and injection moulding are forming techniques which could meet requirements. Considering that injection moulding offers versatility in complex shaping of both oxide and non-oxide powders(7), this forming technique seems to be very promising in the fabrication of whisker-reinforced ceramic parts.

A research project was therefore undertaken to study the influence of the whisker orientation which could be obtained by injection moulding on the mechanical properties of whisker - reinforced ceramics. In the present paper experimental results of injection moulding of an Al_2O_3-ZrO_2-SiC whisker mixture are presented. Special emphasis was put on the preparation of an appropriate ceramic slip which should ensure whisker orientation during the injection moulding.

EXPERIMENTAL WORK

The following materials were used for the slip preparation:

- Alumina: Alcoa CT8000 SG and Alcoa A-16 SG
- Zirconia: Dynazircon F (Dynamit Nobel)
- SiC whiskers: Tateho SCW1
- SiC powder: A - 10 (Starck)
- different organic acids as surfactants
- commercial organic vehicles for moderate temperatures (for example Products KX 1313 and Siliplast TP6000, Zschimer and Schwartz, Lahnstein)

The powder mixtures were attrition milled either for 4 h in water (CT 8000 based mixtures) or for 1 h in alcohol (A-16 based mixtures). After drying the powders were homogenized with a surfactant and organic vehicle by kneading and hot mixing at temperatures above the melting point of the organic vehicle. Due to extreme finess of powders, the procedure resulted in a highly viscous paste (viscosity in the range of 50000Pas) rather than in a free flowing liquid.

Ceramic injection moulding blends were filled in an adapted veterinary injection syringe, equipped with water heating coils as depicted in Fig 1a. The working temperature and pressure during injection moulding were both adjusted to the paste viscosity and ranged from 60 - 80 °C and 15-35 bars, respectively. The injection moulding test specimens were relatively simple thin walled rings with enlarged inner diameter at the top and bottom part, as shown on Fig.1b.

After injection moulding the specimens were dewaxed at 800 °C in a N_2 (heating rate 30 °C/h) and subsequently sintered for 2 h at 1600 °C in Ar (heating rate 300 °C/h).

RESULTS AND DISCUSSION

First compounding experiments were made using alumina CT 8000 SG + 20 wt% ZrO_2 + 5 wt% SiC whiskers, the powder mixture being attrition milled for 4 h in distilled water. After drying, the commercial organic vehicle (product KX 1313) together with 0.5% of stearic acid was admixed, proving to be very suitable for low pressure injection moulding of alumina-based ceramic powders. Surprisingly, sufficient plasticity in the system was reached only when as much as 26,5 wt% of organic vehicle was added, which corresponds to 62.5 vol%. Since usual filler contents in ceramic injection moulding blends range from 55-75 vol %, the amount of organic vehicle in our case was unacceptedly high. In order to find the main reasons for the observed behaviour, the composition of the powder mixture was systematically varied in such a way that the possible influence of a particular component should become visible. Since Alcoa CT 8000 SG alumina is not produced any more, we replaced it by Alcoa A-16 SG. To exclude the negative influence of moisture on the ceramic paste, the powder mixtures were attrition milled in isopropyl alcohol. The powder mixtures and appropriate ceramic binder blends were characterized, and the results of the measurements for the product KX 1313 and stearic acid combination are listed in Table 1. For some of the powder mixtures, (specimen numbers 1, 3 and 5 in Table 1) different commercial binder systems were also tested. In this context it is interesting to note that for a particular powder mixture the rheological properties of the ceramic paste were less sensitive to the major binder component but more to the amount of the surfactant. Thus, for example, by increasing the surfactant-to-binder ratio from 0.02 to 0.16, the powder loading was increased from 37.5 to 42%. From Table 1 one can also conclude that highly active ZrO_2 and SiC whiskers have more pronounced influence on the specific surface area and dry pressing ability, respectively, whereas the ceramic paste properties seemed to depend predominantly on the type of alumina as the major powder mixture constituent. The high specific surface area of powder mixture No. 5 (CT 8000 SG), together with rather large average Fisher SSS particle size and poor dry pressing ability indicated a strongly agglomerated powder composed of very fine crystallites. Microscopic inspection of the powders at high magnification confirmed our prediction, revealing two entirely different types of aluminas. The prime crystallite size of A-16 SG ranges from 0.1-2 μm (Fig.2), whereas the prime crystallite size in CT 8000 SG is one order of magnitude smaller (cca 50

nm), but they were stuck together forming hard agglomerates (Fig.3) which obviously could not be broken either by attrition milling or by dry pressing. It is therefore not surprising that the high specific area and large internal friction of the agglomerated powder demanded considerably higher amount of organic vehicle.

In order to estimate the possibility of whisker orientation by the injection moulding technique, the sintered test specimens were cut parallel and also perpendicular to the injection moulding direction and both intersections were metallographically prepared for microscopic investigations. Since an appropriate method for determination of whisker orientation has so far not been developed, our estimates are based on general impressions, obtained from the microstructural observations, rather than on results of exact measurements. Nevertheless, our preliminary results showed that whisker orientation was achieved with 11 wt% whisker loading in A-16 Alumina, whereas in the powder mixture CT 8000 SG + 20 % ZrO_2 + 5 % SiC it was considerably less pronounced or even negligible. Whisker orientation in A-16 SG + 11 % SiC was most pronounced in the layer close below the outer surface of the test ring along the injection moulding direction (Fig.4). In contrast, in the plane perpendicular to the moulding direction, orientation was observed only at lower working pressures, which also resulted in moulding defects. At higher pressures (i.e. higher shear rates) the orientation of whiskers was less pronounced in this plane.

These preliminary results fulfilled our expectations and represent a good basis for further experimental work in order to control whisker orientation by powder and ceramic based characteristics.

SUMMARY

Injection moulding was used to shape SiC whisker reinforced Al_2O_3-ZrO_2 ceramic parts.

High amounts of organic vehicle were needed to obtain sufficient plasticity in the case of firmly agglomerated powders. The presence of ZrO_2 and SiC whiskers have a more pronounced influence on the specific surface area and dry pressing ability of the powder mixture, whereas the paste characteristics are mainly determined by the properties of the major powder mixture constituent.

With 10% SiC whisker loading in a paste containing about 45% of organic vehicle, whisker orientation was observed and depended on the shear rate of the paste at the mould gate.

AKNOWLEDGEMENT

This work was supported by The Research Council of Slovenia and by Internationales Buro der KFA Julich.

REFERENCES

1. N. Claussen, Transformation Toughened Ceramics, Z. Wekstofftech. 13 (1982), 138-147, 185-196.
2. F. F. Laange, J. Mater. Sci. 17 (1982), 225-234.
3. P. F. Beeher, G. C. Wei, Toughening Behaviour in SiC-Whisker-Reinforced Alumina, J. Am. Ceram. Soc., 67 (1984), c-267-269.
4. N. Claussen, Strengthening Strategies for ZrO_2-toughened Ceramics at High Temperatures, J. Mat. Sci. Eng., 71 (1985), 23-38.
5. T. N. Tiegs, P. F. Becher, Sintered Al_2O_3-SiC-whisker Composites, Am. Ceram. Soc. Bull., 66 (1987), 339-342.
6. J. R. Porter, F. F. Lange, A. H. Chokshi, Processing and Creep Performance of SiC-Whisker-Reinforced Al_2O_3, ibid, 66 (1987), 343-347.
7. M. J. Edirisinghe, J. R. G. Evans, Review: Fabrication of Engineering Ceramics by Injection Moulding. I. Materials Selection, Int. J. High Tech. Ceramics, 2 (1986), 1-31.

Table 1: Characteristics of powders and appropriate ceramic slips using product K X 1313 (ZSCh)as organic vehicle (surfactant-to-binder ratio 0,02, slip viskosity 50.000 Pas)

Powders				Slips		
Powder composition (wt.%)	Surface area (m^2/g)	Mean * particle diameter (μm)	Green** density (%T.D.)	vol % organic vehic	Slip density g/cm^3	Green density (% T.D.)
A-16	10,3	-	-	42	2,69	58,8
A-16+20 ZrO_2	17,4	0,49	-	45	2,73	55,7
A-16+20 ZrO_2+II SiC powder	-	-	49,5	45,5	2,65	57,3
A-16+11 SiC whisker	-	-	48,0	41,5	2,64	60,0
CT 8000+20 ZrO_2+5 Sic whiscer	26,6	0,98	40,0	62,5	-	36,4
				58,0+	2,28+	45,0+

* Fisher SSS
** After uniaxal dry pressing
*** After dewaxing
\+ Surfactant-to-binder ratio 0,16

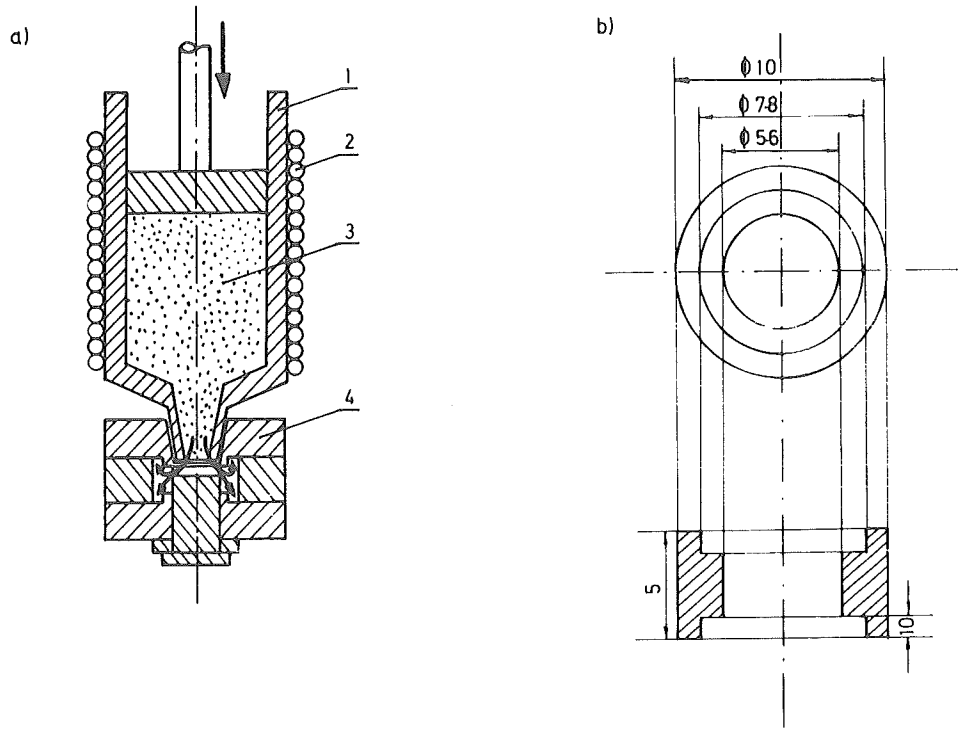

Fig.1: a) Laboratory injection moulding shematic. 1 - veterinary injection syringe, 2 - water heating coil, 3 - ceramic slip, 4 - metallic mould assembly
b) Sample geometry

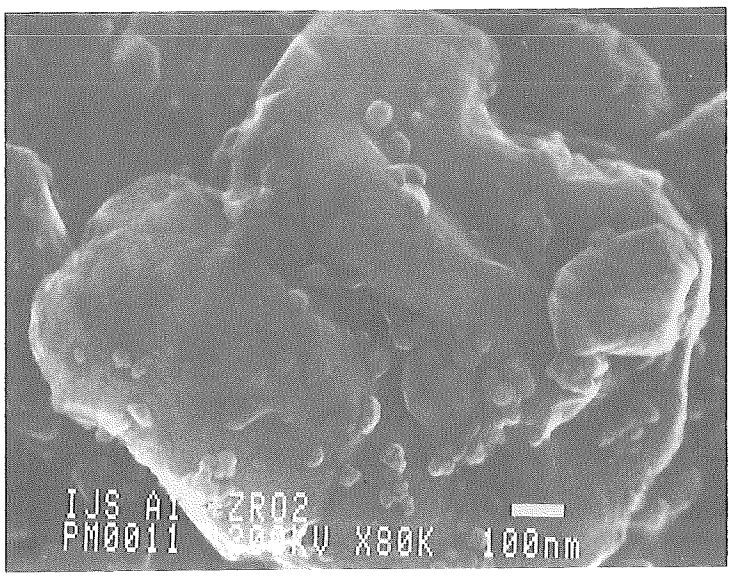

Fig.2: Morphology of A-16 SG + 20% ZrO_2 powder mixture after attrition milling (1 h in alcohol)

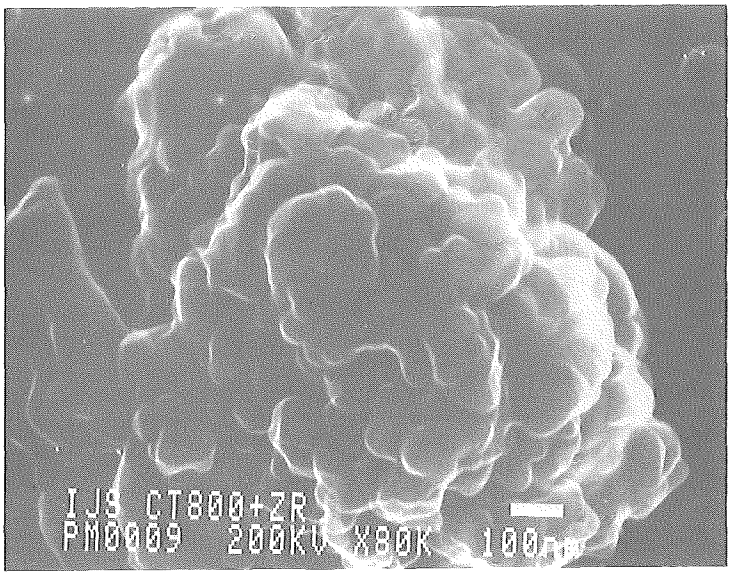

Fig.3: Morphology of CT 8000 SG + 20% ZrO_2 + 5 vol% SiC after attrition milling (4 h in water)

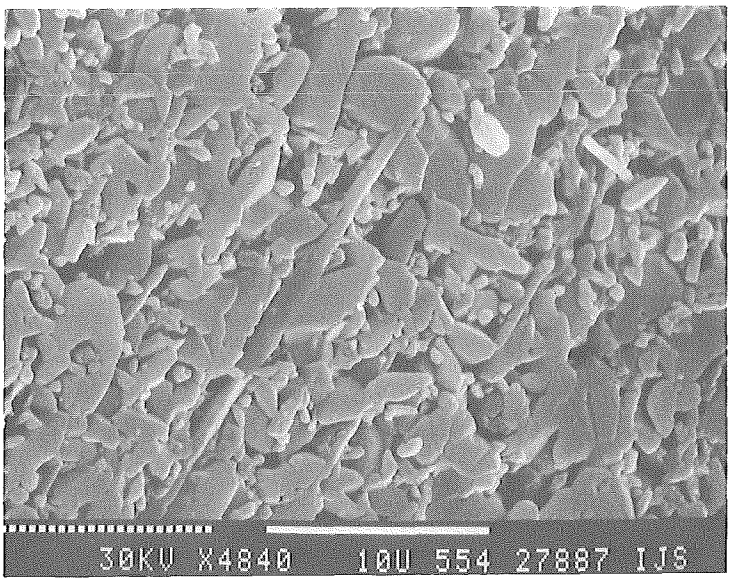

Fig.4: Microstructure of sintered composite A-16 SG + 11% SiC whiskers (chemically etched in hot H_3PO_4) with visible whisker orientation

C E R A M I C S

SINTERING AND MICROSTRUCTURE (1)

SINTERING AND HIPING WITH ADDITIVES

W.A.Kaysser, G. Petzow, and *M.Mitkov

Max-Planck-Institut für Metallforschung
Institut für Werkstoffwissenschaften
Heisenbergstr.5, D-7000 Stuttgart 80, West Germany

*Institute Boris Kidric, 11001 Beograd, Jugoslavia

Introduction

Todays world of powder metallurgy is characterized by pressureless or pressure assisted sintering of multicomponent parts and materials /1 Klar/. Preforms of ceramics or metallic powders are heated to high temperatures where shrinkage, grain growth, annealing recovery, compositional homogenization, and chemical reactions may occur to form new phases or compounds.

The powder metallurgical production route can be used to produce structural parts of accurate shape and size. Dimensional control and the required hardenability of sintered structural parts require knowledge of the diffusion processes leading to dimensional changes and homogenization /2 Petzow/.

The major objective to use the powder metallurgical route can also be the production of parts or semi-finishes of materials which are superior to the materials produced by casting. Only in a small number of materials are the properties of an inherent porosity used, e.g. in filters or self lubricating oil bearings. Most high-tech ceramics and most PM'materials are sintered with porosity elimination, as a goal. Of major interest for the production of these PM materials are therefore the mechanisms and processes that control densification and grain coarsening /3 Kaysser/.

Densification of semi-finishes or of parts of the materials may also be forced by pressure assisted sintering. Coarse powders are often used if the powder surfaces are subject to easy contamination or if the production of smaller powders is expensive. Pressure assisted sintering of fine powders is mainly used for materials which are difficult to densify by pressureless sintering, e.g. Si_3N_4 reinforced with SiC whiskers /4 Wei/.

Shrinkage and grain growth of ceramics and metallic materials and dimensional changes and homogenization of metallic structural parts are often manipulated by additives.

In the present paper the effect of additives on pressureless and pressure assisted sintering will be described using examples which cover some of the essential basic principles of interactions of additives with the host material.

2. Solid State Sintering and HIPing with a Small Amount of Additives

During the first and second stage of solid state sintering with small amounts of additives densification is accelerated by enhanced bulk or grain boundary diffusion /5 Kuzcynski, 6 Coble, 7 Brook/. Surface diffusion has to be kept small enough that sufficient driving force for densification, that means a high ratio of neck area to neck volume, is maintained. The surface diffusion must, however, also be large enough to keep the dihedral area of the neck close to the equilibrium shape /8 Ashby, 9 Exner/.

Classical examples of enhanced shrinkage by the addition of a small amount of an alloying element are W or Mo doped with Ni. The bulk diffusion of W(Ni) solid solution is far below a value which would influence solid state sintering at 1400°C to a measurable degree /10 Kaysser/. Two independent measurements confirm that the presence of Ni at W or Mo grain boundaries increases the grain boundary self diffusion coefficient of these materials /10 Kaysser, 11 Schintelmeister, 12 Amtenbrink/ by a factor 500 to 5000 in the case of W and by a factor of 25 in the case of Mo if Ni is present (Fig. 1a and b). Figure 2a and b shows the enhanced sintering of W or Mo if small amounts of Ni are present.

The third sintering stage is characterized by the transition of pore channels into isolated pores which lie along three or four-grain junctions or in the interior of the grains /14 Hsueh/. During the final stage of sintering both densification (pore shrinkage) and coarsening (pore coarsening and grain coarsening) occur simultaneously. Shrinkage occurs by migration of vacancies from the pores along the grain boundaries to vacancy sinks (grain boundaries and free surfaces). In the final stage there are two phenomena by which pores coarsen: by mass transfer between isolated pores and by pore coalescence during grain growth. Figure 3 shows a scheme proposed by Brook /15 Brook/ for pores which is extended for second phase inclusions. It shows fourteen mechanisms which may control the migration of a boundary. In all cases a decreasing pore size at a constant total porosity results in shorter efficient pathways and an increased mobility of the pores. Mechanisms 6 and 7 show two pathways wihich lead to coarsening of the pores by grain boundary or lattice diffsuion. It is obvious that small amounts of aditives can influence all these mechanisms including the intrinsic boundary movement (1) and the impurity drag (2). A second set of coarsening mechanisms is based on coalescence of pores by collision when the boundaries move /13 Kaysser/. Similar arguments are valid if instead of pores second phase inclusions are present at the grain boundaries (compare next section).

During grain growth, pores either remain at the boundaries or become separated and "trapped" inside the grains. Pores that are trapped usually shrink at much lower rates than pores which are at grain boundaries, since bulk diffusivity is much smaller than grain boundary diffusivity. Pore drag and pore grain boundary separation in W-0.15wt.%Ni after annealing at 1400°C for 3 h are shown in Fig.4a. There are two regimes where pores can remain attached to the grain boundaries (Fig.5a). Pores which are large enough are immobile but retard the motion of the boundary (pore control in Fig.5a) /14 Hsueh, 17 Brook, 16 Uematsu/. Pores which

are small enough move along with the grain boundaries without stopping their motion (boundary control in Fig.5a). The mechanisms of pore migration are shown in Fig.3. The intersection of the two regimes of pore-boundary interaction leads to a pore-boundary separation region with G* as the smallest grain size where grain boundary/pore separation occurs.

From Fig.5a the problem of manipulating final stage sintering by additives becomes obvious. Fast shrinkage at small grain sizes (yielding trajectories which pass below the separation field) requires a low surface diffusivity, D_{sv}, and a high grain boundary diffusivity, D_{gb} (D_{gb}+ perpendicular to the boundary plane can be shown to be related to the grain boundary self diffusion coefficient D_{gb}). To avoid grain boundary pore separation at medium grain size and smaller pore size the separation field has to be shifted to larger grain sizes which requires the opposite, high surface diffusion and low grain boundary diffusivity. Final stage sintering of W with Ni shows extensive grain boundary pore separation (Fig.4a) since both grain boundary and surface diffusion are increased by the presence of Ni at the grain boundaries (Fig.1a and /10 Kaysser/). Figure 4b shows the microstructure of Al_2O_3 which was doped with MgO /17 Kaysser/. In contrast to Ni doped W, the addition of MgO reduces the grain boundary mobility. Complete densification by pressureless sintering is possible /18 Bennison, 15 Brook/.

One possibility of increasing the flow of vacancies from pores at the grain boundaries to the sinks is by the application of an external pressure. When samples are subject to a high hydrostatic pressure as during HIP, the surface and grain boundary diffusion constants remain essentially constant, but the applied pressure gives much steeper gradients of the chemical potential of the vacancies and results in a faster vacancy flow towards the grain boundary sinks. The driving force for diffusional pore coarsening on the other hand remains unchanged.

Figure 6a clearly shows the grain boundary pore separation in a W-0.15wt.%Ni compact during prolonged sintering /13 - Kaysser/. The large pores are too immobile to remain attached to the grain boundaries. As shown in Fig.6b the application of 200 MPa at 1400°C changes the microstructure dramatically. In the wake of migrating grain boundaries all pores were eliminated. It can be shown that densification by other mechanisms, e.g. power law creep, which is most frequently observed in other systems and which depends on the bulk diffusivity, is small compared to the pore shrinkage by vacancy elimination at the grain boundaries /19 Kaysser/. The pore grain boundary breakaway diagram can be used for the HIP conditions after some additional kinetic considerations. If pores come into contact with a grain boundary they were subject to separation after a time interval t_c when the grain boundary has migrated into a position where the drag force of the pore is smaller than the pulling force of the grain boundary after a short time. During HIPing, pores which come into contact with a grain boundary may shrink during the time interval t_c to a size at which the attachment due to boundary control becomes dominating (Fig.5). As a result the pore migrates subsequently together with the moving boundary until it is completely eliminated (Fig.6b).

3 Solid State Sintering and HIPing with Additives Forming a Second Phase

Densification, dimensional control and homogenization can also be influenced by additives which are present as second solid phase. The additive may act as a fast diffusion path for the host atoms. The additive may also form inclusions on obstacles which retard densification and grain growth. The broad variety of possible chemical interactions between the solid phases yields a complicated influence on densification and dimensional control.

An example of a simple interaction is found in W-Cu /20 Lee/. At temperatures below 1100°C W powder does not sinter and the mutual solubility of W and Cu is negligible. Despite the insolubility, W-Cu compacts densify by solid state sintering during heating up to temperature in solid state (Fig.7). The densification rate increases with increasing volume content of Cu. In the vicinity of the Cu particles Cu is spreading on W particles. The comparison of shrinkage and microstructural development supports a two stage model where rapidly enlarging zones of low Cu content yield initial rearrangement and shrinkage (Fig.8a,α) whereas a second massive spreading of Cu from initial Cu particles leads to a local formation of denser Cu-W partilce aggregates and to a continuous macroscopic shrinkage after prolonged sintering when most aggregates form an interconnected network (Fig. 8a, β and Γ).

During final stage sintering the migration of grain boundaries may be retarded by second phase inclusions. If the bulk diffusion of the host material in the second phase inclusions is rapid the second phase inclusions will migrate with the grain boundaries and coalesce similar to pores (compare Fig.3). Figure 9a shows W-1wt.%Ni after sintering at 1400°C for 122 h. The "bell shape" of the inclusions indicates the drag of the moving boundaries on the second phase. As a consequence of the drag forces of the inclusions on the migrating boundary the grain growth rate is reduced if the Ni concentration exceeds the solubility limit of Ni in W at 1400°C (Fig.9b).

4 Liquid Phase Sintering

Additives may also form a liquid phase. A more complete description of the liquid phase sintering phenomena is given elsewhere /3 Kaysser/. In this paper the basic shrinkage phenomena and the mechanisms of melt penetration and liquid film migration will be described.

4.1 Densification

Densification during liquid phase sintering is based on rearrangement and shape change of the solid constituent particles (Fig.10) /21 Petzow/. The driving force for both phenomena results from a decrease in energy connected to the changes in the areas of the liquid/vapour, liquid/solid and solid/vapour interfaces during rearrangement and/or shape change. Melt may originate from low melting point particles or areas which have built low melting point compositions by diffusion during heating. With the condition of good wetting, the liquid phase is pulled by

capillary forces into particle necks and small pores. As a reaction to the capillary forces, particles are rearranged if their mobility allows it. This rearrangement of the solid particles is a necessary prerequisite for effective densification throughout the sintering process even during later sintering stages, when, for example the rates of particle shape change also limit the rearrangement rate. To distinguish clearly between rearrangement, which is essentially rate controlled by the mechanical movement produced by the capillary forces, and rearrangement, which is rate controlled by dissolution-reprecipitation processes, these particle movements are described as primary and secondary rearrangements /21 Petzow/. Shrinkage due to the shape change of the solid constituents always involves solution-reprecipitation processes and is therefore connected to secondary rearrangement in most cases.

4.2 Liquid Film Penetration

One of the main dissolution-reprecipitation processes leading to secondary rearrangement is the grain boundary penetration by the liquid phase. The penetration leads to skeleton disintegration, but also to contact dilatation, particle dilatation and subsequently to particle disintegration. Important consequences of grain boundary penetration are boundary alloying and liquid film migration.

Early grain boundary attack does not necessarily lead to densification. But if grain boundary attack is completed along all grain boundaries of a polycrystalline particle, particle disintegration and densification by secondary rearrangement may occur. This is illustrated in Fig.11a to c. In Al_2O_3-glass mixtures the shrinkage after particle disintegration due to secondary rearrangement could be separated from shrinkage due to primary rearrangement /23 Pejovnik/. Up to 1400°C, the shape and size of the polycrystalline Al_2O_3 spheres was maintained and only primary rearrangement occurred (Fig.11b). Above this temperature grain boundary attack and particle disintegration occurred (Fig.11c) and secondary rearrangement led to considerable additional shrinkage (Fig.11a) /2 Petzow, 23 Pejovnik/.

4.3 Liquid Film Migration

The penetration of melt along grain boundaries may also initiate liquid film migration. Liquid film migration is a general phenomenon which occurs under different conditions. In recent years boundary migration in metals and ceramics, which is associated with a noticable concentration change in the wake of the moving boundaries, has been investigated intensively. It is kown as diffusion induced grain boundary migration (DIGM) /23 Hillert/ and liquid film migration (LFM) /24 Yoon, 25 Handwerker/. If the solid in front of a migrating liquid film is not in equilibrium with the solute concentration of the boundary then solute will either deplete from or diffuse into this solid. When the boundary migrates at a constant velocity a steady state concentration profile will develop. The concentration gradients in the solid close to the liquid/solid interface will be very steep. If the lattice parameter changes with the concentration of the solute and coherency of the peripheral layers of the solid is main-

tained, coherency strains will arise. These coherency strains raise the free enthalpy of the stressed solid which is in contact with the boundary resulting in differences of the local concentration equilibria at either side of the liquid films. These differences cause a constant traverse of host atoms through the liquid film which results in the migration of the boundary.

The penetration of melt into contact areas and grain boundaries yields perfect conditions for LFM /3 Kaysser/. Figure 12 shows an area in a Fe particle after liquid phase sintering in the presence of Cu for 2 min. The thin liquid films have formed the bulges characteristic of LFM. Solid solutions of Fe-Cu have formed in the wake of the migrating boundaries /26 Kaysser/.

It must be emphasized that the bulk diffusivity of Cu in Fe is extremely small; thus, no solid solution formation is expected by bulk diffusion during the sintering times and temperatures applied usually in practice. The rapid homogenization is obtained by LFM.

In Fe-Cu the penetration of melt along grain boundaries is suppressed if sufficient carbon is present in the alloy. However, penetration of contact areas is possible. Figure 13 shows the microstructure of Fe-10Cu-0.4C after liquid phase sintering for 20 min at 1130°C. The thin liquid layers in the contact areas are shifted by liquid film migration. In the wake of the moving boundaries a saturated solid solution of Fe-Cu is left, which mainly contains the pearlite which preferentially formed in these areas during cooling due to the fact that the eutectoid of Fe-C forms at a higher temperature than the eutectoid of Fe-Cu-C /26 Kaysser/.

Liquid film migration influences the mechanical properties of a number of systems. It is well known that W and Mo embrittle if sintered with activators like Ni. The Ni segregates at the grain boundaries. If an appropriate heat treatment is done, then LFM produces bulged grain boundaries (Fig.14a) which mechanically interlock the grains. This tailored microstructure improves the mechanical properties considerably. Figure 14b shows the bend strength σ_B of Mo sintered as usual with Ni, and Mo sintered with Ni and heat treated to obtain LFM. Similar improvements might be possible in other systems susceptible to liquid film migration such as liquid phase sintered superalloys.

Acknowledgement

Part of the work was supported by the Internationales Buero of KFA Juelich and the Deutsche Forschungsgemeinschaft. We thank Prof.R.M.German for fruitful discussions.

Refernces

1. Metals Handbook, Ninth Edition, Volume 7, Powder Metallurgy, coordinator E.Klar, American Society for Metals, Metals Park,Ohio (1984).
2. G.Petzow and W.A.Kaysser, in Sintered Metal-Ceramic Composites, ed. G.S.Upadhyaya, Elsevier Science Publishers, Amsterdam (1984),51-70.
3. W.A.Kaysser and G.Petzow, Powder Metallurgy, 28(1985)145-150.
4. G.C.Wei and P.F.Becher, Am.Ceram.Soc.Bull., 64(1985)298-304.

5. G.C.Kuczynski, Trans AIME, 185(1949)169.
6. R.L.Coble, J.Appl.Phys., 32(1961)787.
7. R.J.Brook, J.Am.Cer.Soc., 52(1969),56.
8. F.B.Swinkels and M.F.Ashby, Powder Metallurgy, 23(1980)1-7.
9. H.E.Exner, Acta metall., in print.
10. W.A.Kaysser, M.Hofman-Amtenbrink and G.Petzow, in Sintering'85, eds. G.C.Kuczynski, D.P.Uskokovic, H.Palmour III and M.M.Ristic, Plenum Press, New York (1987), 121-132.
11. V.W.Schintelmeister and K.Richter: Planseeberichte für Pulvermetallurgie, 13(1970),3.
12. W.A.Kaysser, M.Hofmann-Amtenbrink and G.Petzow, Powder Metallurgy, 28(1985),199-206.
13. W.A.Kaysser, Y.S.Kwon, I.H.Moon and G.Petzow: unpublished.
14. C.H.Hsueh, A.G.Evans and R.L.Coble: Acta Metall., 30(1982),1269.
15. R.Brook,S.P. Howlett and Su Xing Wu, in "Sintering-Theory and Practice, eds. D.Kolar, S.Pejovnik and M.M.Ristic,"Material Science Monographs", Elsevier Scientific Publishing Company, Amsterdam, (1982),135-144.
16. K.Uematsu,R.M.Cannon,R.D.Bagley,M.F.Yan,U.Chowdry and H.K.Bowen,in Int. Symposium of Factors in Densification of Oxide Non-Oxide Ceramics, eds. H.Saito and S.Somiya, Hakone, Japan (1978),190.
17. W.A.Kaysser, M.Sprissler, C.A.Handwerker and J.E.Blendell, J.Am.Ceram.Soc., 70(1987)339-343.
18. S.J.Bennison and M.P.Harmer, J.Am.Ceram.Soc. 68(1985)C22-24.
19. W.A.Kaysser, M.Mitkov and G.Petzow: Proceedings "Colloquium on Unconventional Forming Processes in Powder Metallurgy", 19.-20. Sept., Paris (1984).
20. J.S.Lee,W.A.Kaysser and G.Petzow, in "Modern Developments in Powder Metallurgy", eds. E.N.Aqua and C.M.Whitman, MPFIF-APMI, Princeton,N.J., 17(1985)99-112.
21. G.Petzow and W.A.Kaysser, in Science of Ceramics 10, ed. H.Hausner, (Weiden, FRG, Deutsche Keramische Gesellschaft, (1980),269-280.
22. S.Pejovnik, D.Kolar, W.J.Huppmann and G.Petzow, in Sintering - Theory and Practice, eds. D.Kolar, S.Pejovnik and M.M. Ristic, Elsevier Scientific Publishers, Amsterdam (1982), 361-365.
23. M.Hillert and G.Purdy, Acta Metall. 26(1978)333-340.
24. D.N.Yoon, J.W.Cahn, C.A.Handwerker, J.E.Blendell and Y.J.Baik, in Interface Migration and Control of Microstructure, (Washington, NBS, 1985).
25. C.A.Handwerker, J.W.Cahn, D.N.Yoon and J.E.Blendell, in Atomic Transport in Alloys: Recent Developments, eds. G.E.Murch M.A.Dayananda, (Dayton, OH, TMS/AIME Publications,1985).
26. W.A.Kaysser, "Liquid Film Migration During Sintering of Fe-Cu," to be pulbished in Z.Metallkde.

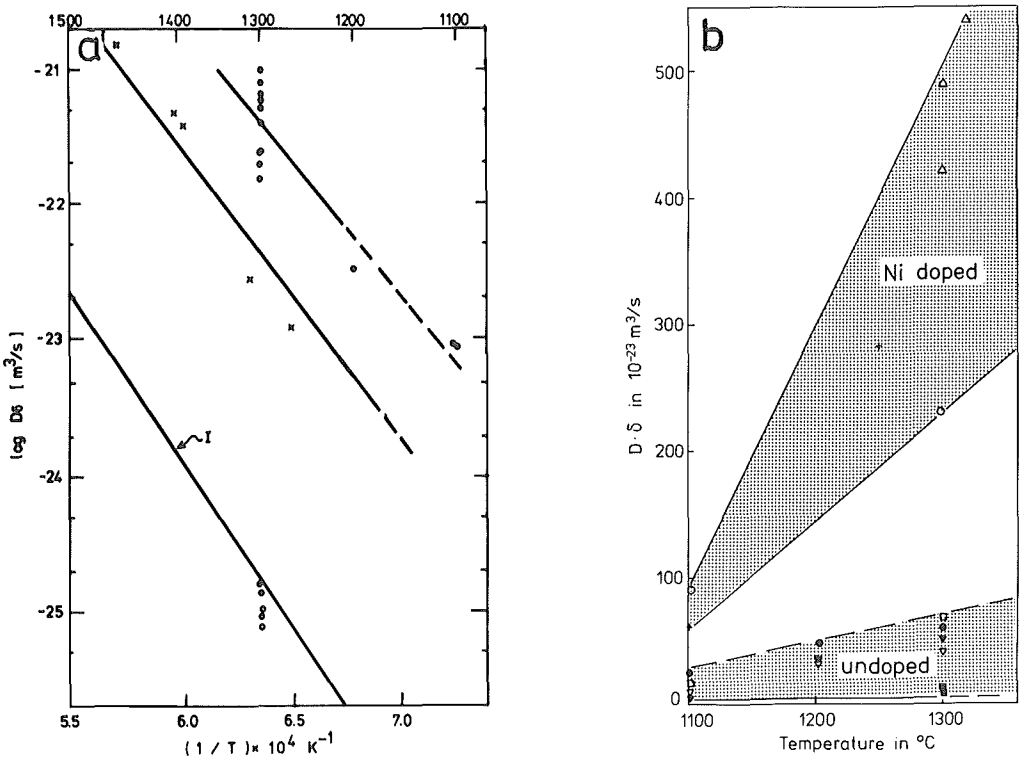

Fig.1a W; undoped I /11 Schintelmeister/, ● /12 Kaysser/; Ni-doped x /11 Schintelmeister/, o /12 Kaysser/.
Fig.1b Mo /12 Kaysser/.
Fig.1 Grain boundary self diffusion coefficients of undoped and Ni-doped W and Mo .

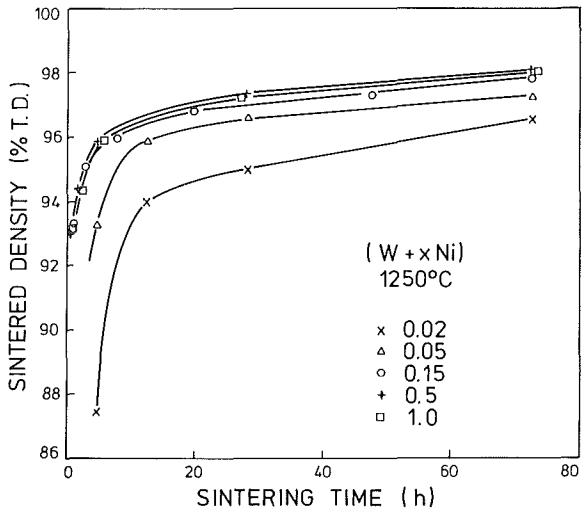

Fig.2a W-Ni compacts (200 MPa) during isothermal sintering at 1250°C (in wt.%, /13 Kaysser/).

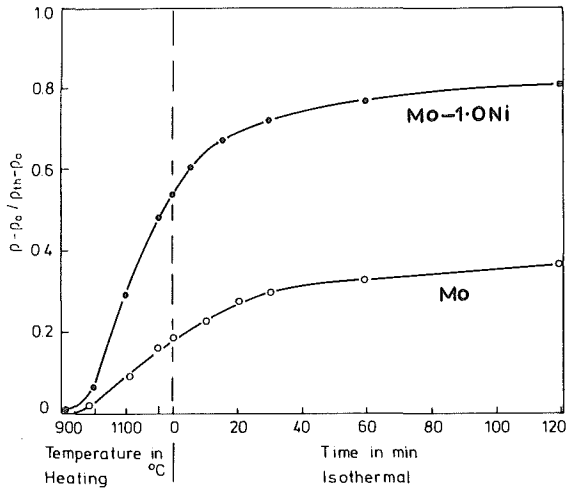

Fig.2b Mo-Ni compacts (200MPa) during heating to 1240°C and subsequent isosthermal annealing (ρ actual density, ρ_0 initial density, ρ_{th} theoretical density).
Fig.2 Shrinkage of Mo and W in the presence of Ni.

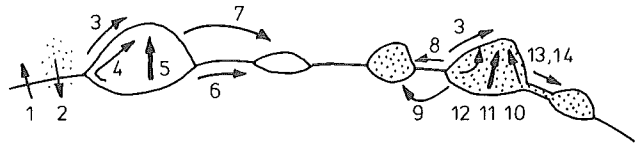

Fig.3 Mechanisms of grain boundary migration control. pores, second phase inclusions.

1 Intrinsic boundary movement, 2 impurity drag, 3 pore movement by lattice diffusion in the host material, 4 pore movement by surface diffusion, 5 pore movement by vapour transport, 6 pore coarsening by grain boundary diffusion, 7 pore coarsening by lattice diffusion, 8 inclusion coarsening by grain boundary diffusion, 9 pore coarsening by lattice diffusion, 10 inclusion movement by interface diffusion, 11 inclusion movement by grain boundary diffusion in the inclusion, 12 inclusion coarsening by lattice diffusion, 13 inclusion coarsening by interface diffusion, 14 inclusion coarsening by bulk diffusion in the second phase.

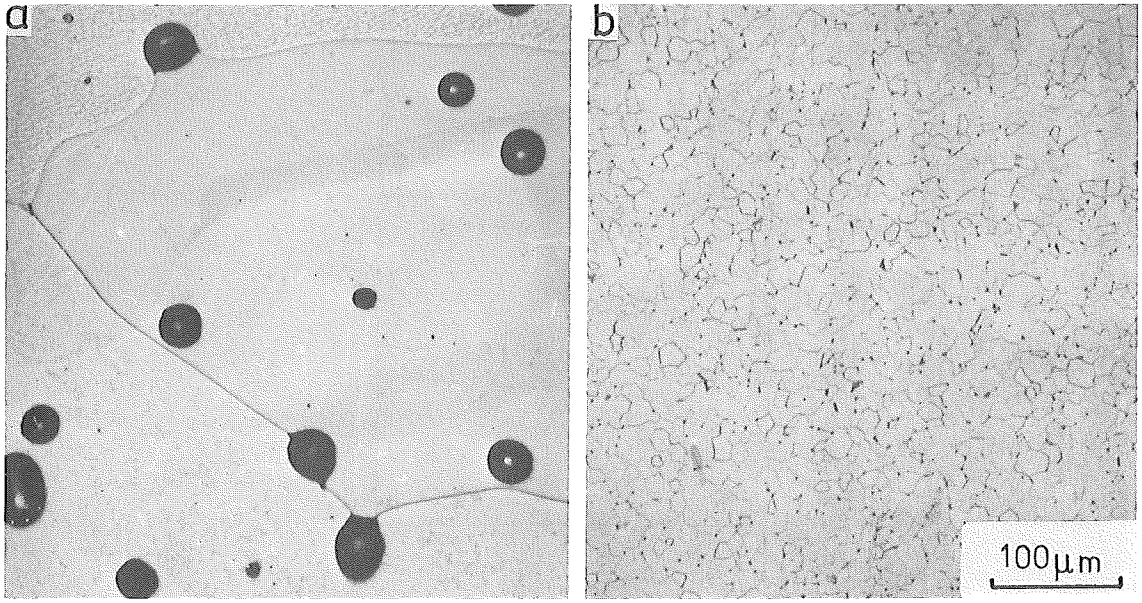

Fig.4a Microstructure showing pore drag and pore/grain boundary separation during final stage sintering of W-0.15Ni at 1400°C for 3h /13 Kaysser/.
Fig.4b Al_2O_3 doped with 0.1wt.% MgO after hot pressing at 1800°C for 5 min /17 Kaysser/.
Fig.4 Influence of Ni and MgO on complete densification of W and Al_2O_3.

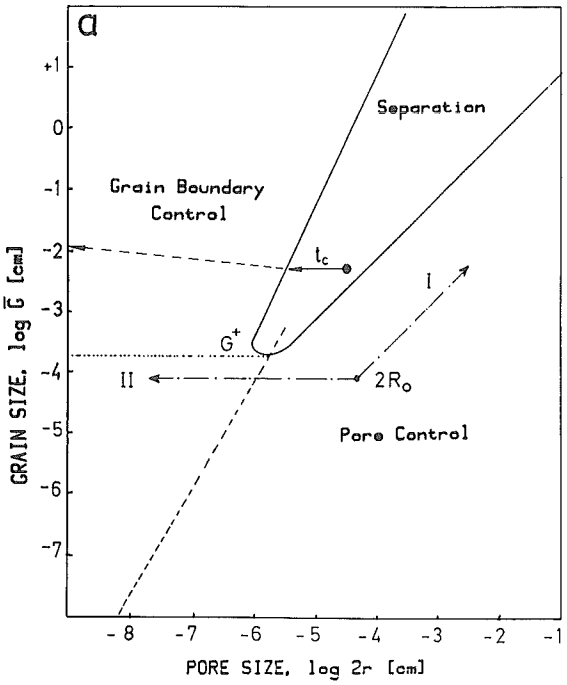

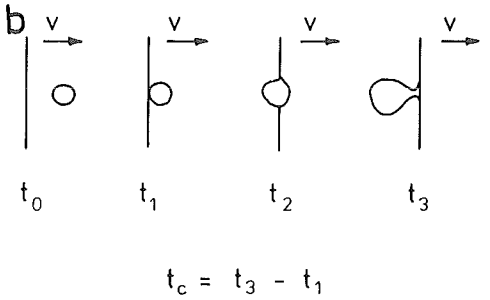

Fig.5

Pore/grain boundary separation during final stage sintering.

Fig.5a

Pore/grain boundary separation diagram. $2R_o$ is the initial grain size.

Fig.5b

Critical time t_c. A pore is passed by a grain boundary.

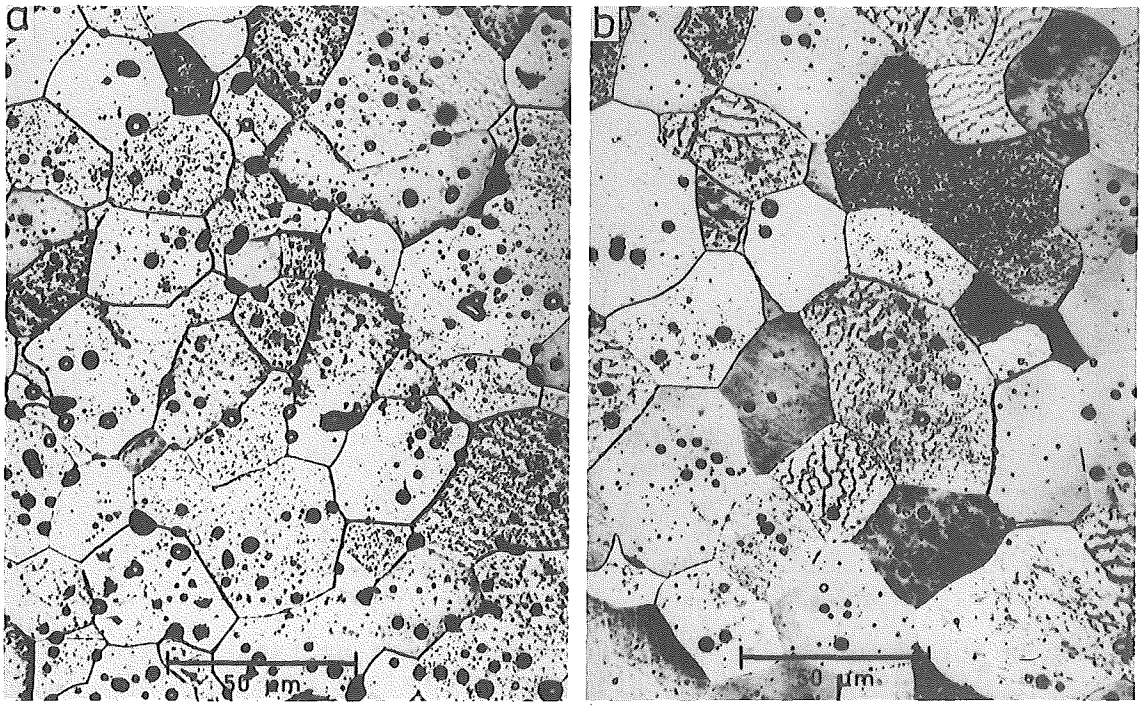

Fig.6a After sintering for 1h.
Fig.6b After sintering for 1h and subsequent HIPing at the same temperature for 1h at 200 MPa /13 Kaysser/.
Fig.6 Microstructure of W-0.15Ni after annealing at 1400°C.

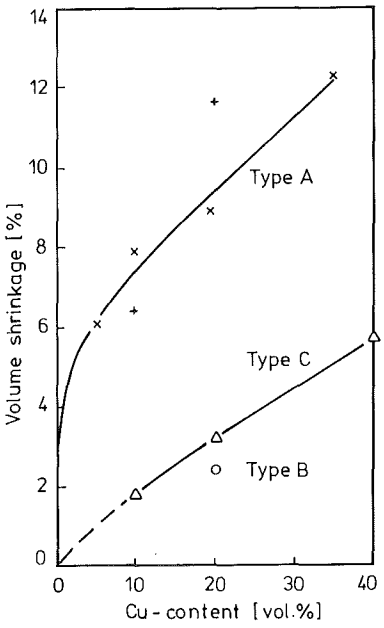

Fig.7

Volume shrinkage of W-Cu compacts after sintering at 1050°C for 1h /20 Lee/. A, B and C are W powders with an average particle size of 0.8, 5.0 and 2.4 µm.

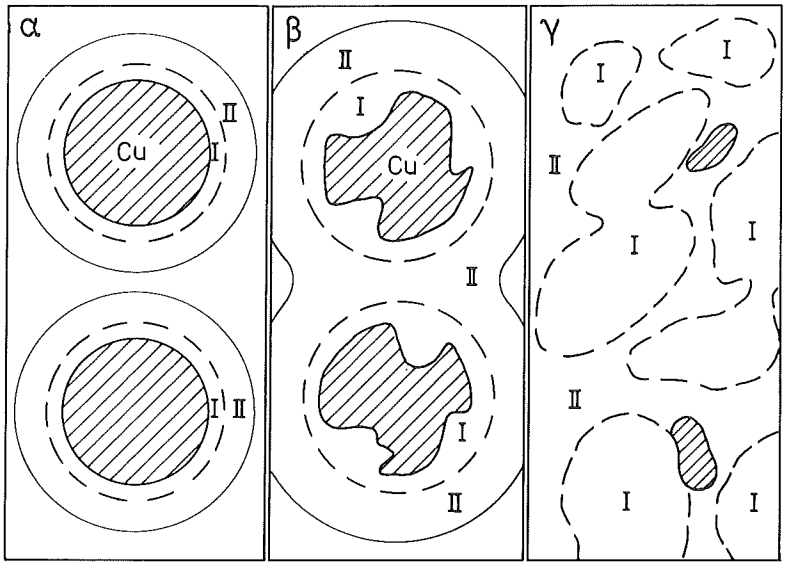

Fig.8a Shrinkage by aggregate formation starting from isolated individually shrinking aggregates (α). A zone (II) of rapidly spreading Cu is connecting the initial Cu particles (ß). As a subsequent step dense Cu rich aggregates (I) form (Γ) /20 Lee/.

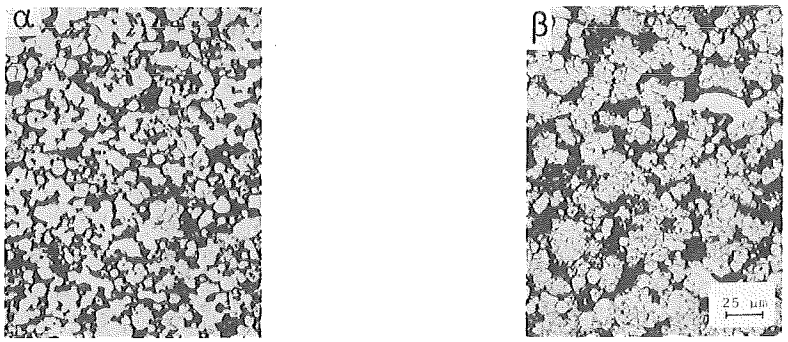

Fig.8b Enlargement of aggregates during sintering of W-10Cu at 1050°C for (α) 5 min and (ß) 16 h.

Fig.8 Spreading of Cu and aggregate formation in W-Cu compacts during solid state sintering (20 Lee).

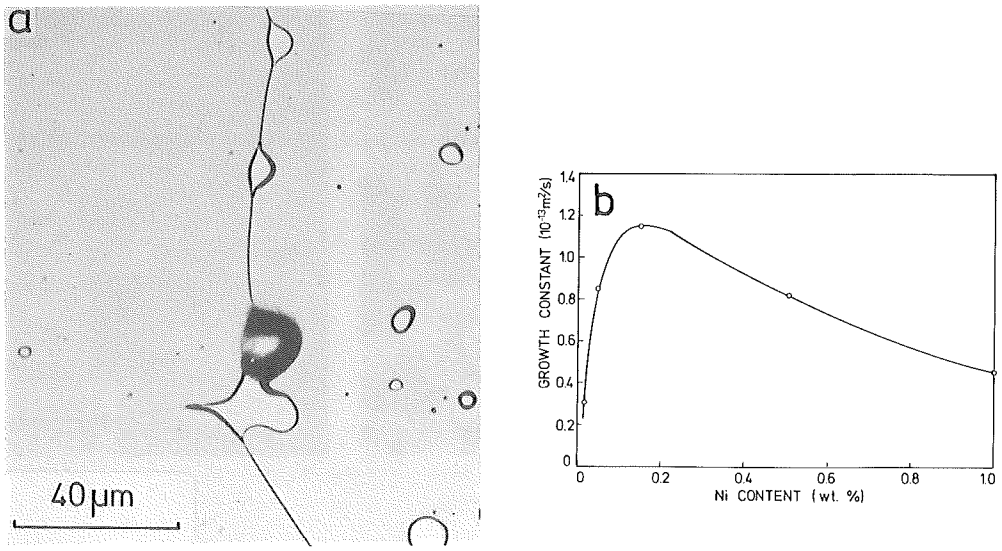

Fig.9a Second phase drag and separation of second phase inclusions from the boundary in W-1wt.%Ni after sintering at 1400°C for 122 h /13 Kaysser/.
Fig.9b Grain growth constants of W-Ni compacts during sintering at 1250°C.
Fig.9 Influence of a small amount of second phase with mutual solubility of the components on boundary drag and grain growth /13 Kaysser/.

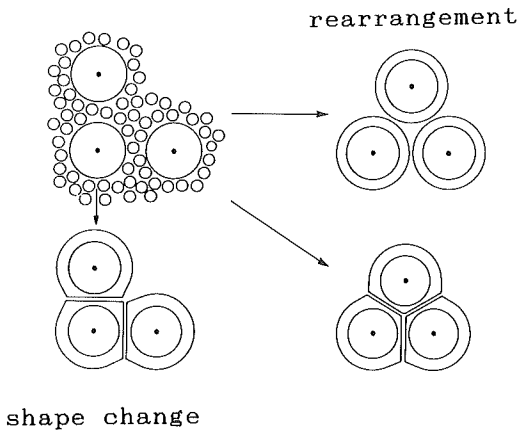

Fig.10 Shrinkage by rearrangement and shape change /21 Petzow/.

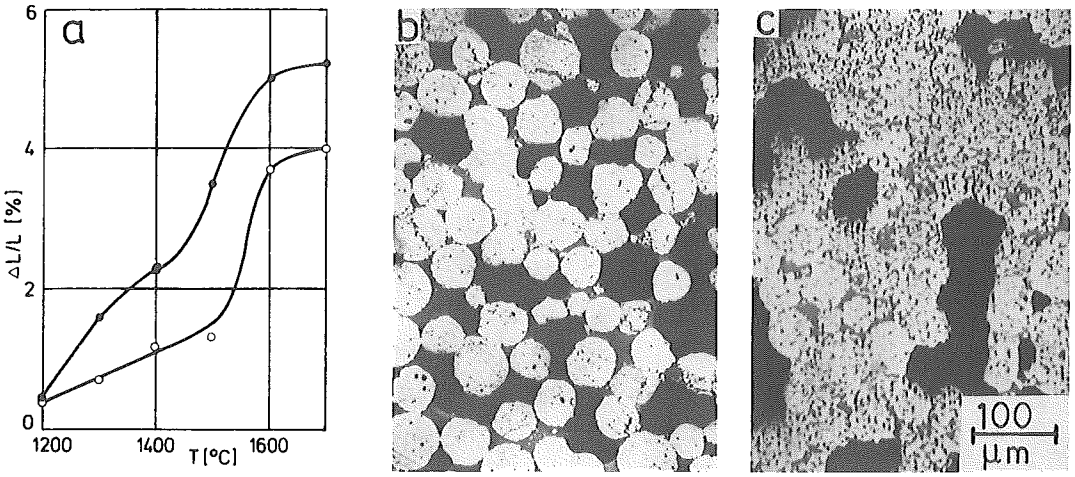

Fig.11 Microstructure and shrinkage during liquid phase sintering of Al_2O_3-alkali borate glass /2 Petzow, 22 Pejovnik/. a) - Shrinkage ° after 1 min, • after 120 min. b) - Microstructure after 1h at 1400°C. c) - Microstructure after 1h at 1700°C.

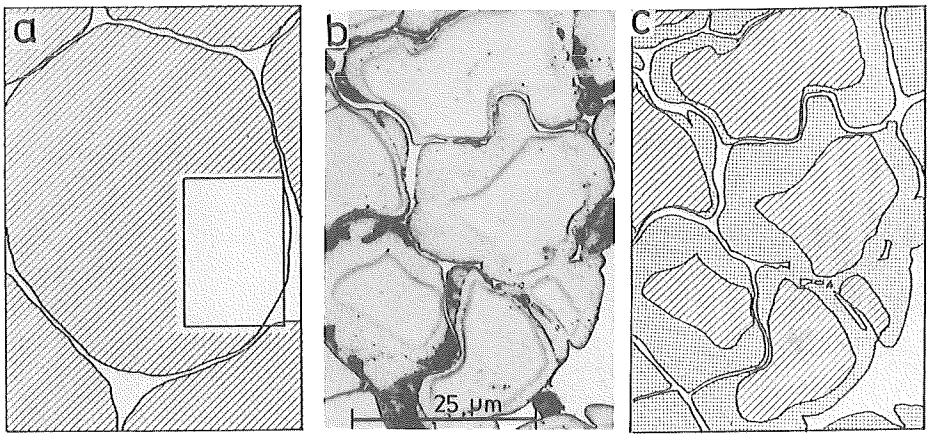

Fig.12a Overview, schematic
Fig.12b Microstructure
Fig.12c Formation of solid solution, schematic; white: melt, dotted: solid solution Fe(Cu), lined: unalloyed Fe
Fig.12 Liquid film migration in Fe-10Cu during liquid phase sintering at 1120°C /3 Kaysser/.

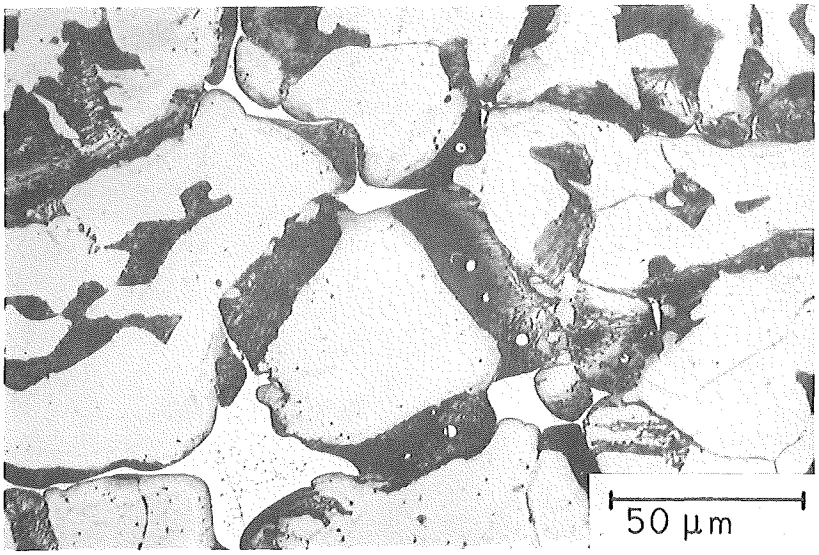

Fig.13 Liquid film migration in Fe-10Cu-0.45C sintered at 1150°C for 20 min /3 Kaysser/.

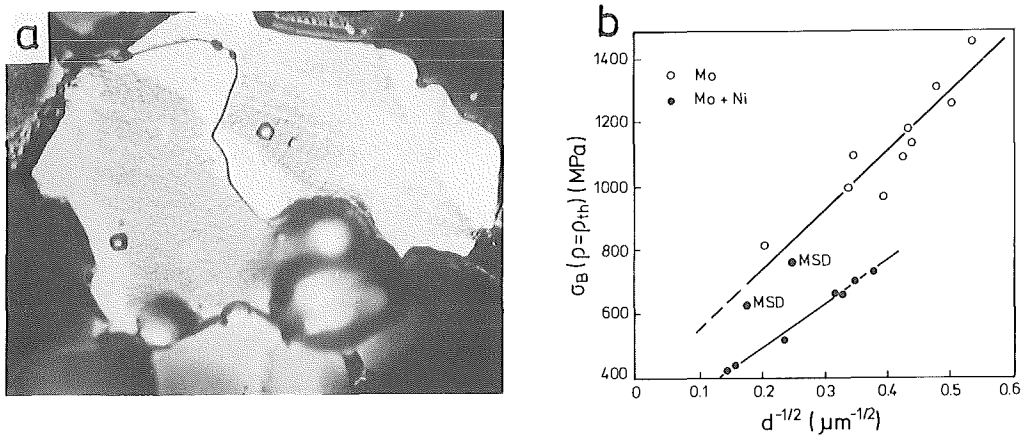

Fig.14a Microstructure
Fig.14b Bend strength; MSD cooling procedure resulted in bulged interlocking grain boundaries. d is the average grain size.
Fig.14 Microstructure and bend strength of Mo-Ni after slow cooling.

PREPARING AND SINTERING OF YTTRIA-STABILIZED ZIRCONIA

B.Pavlovski, L.Stojanovska, B.Jašmakovski
Faculty of Technology and Metallurgy, Skopje
91000 Skopje, Yugoslavia

INTRODUCTION

The high melting point and chemical inertness of stabilized zirconia are the basis for its extensive use as a refractory material.

The ionic conductivity and transformation toughening of zirconia have opened up such nonrefractory uses of zirconia as oxygen sensors, heaters, and extrusion dies.

Although zirconia has the potentially useful properties of high melting temperature and chemical inertness, the transformation from tetragonal to monoclinic symmetry produces cracking and even disintegration, which renders the material useless as a structural ceramic. The transition can be avoided by adding other oxides which stabilize the high temperature phase by forming solid solutions having the fluorite structure.

The most commonly used oxides to form solid solutions with zirconia are CaO, MgO, Y_2O_3, Sc_2O_3, rare earth oxides, because they exhibit a relatively high solubility in zirconia and are able to form fluoritetype phases with zirconia which are stable over wide ranges of composition and temperature.

The system ZrO_2-Y_2O_3 is one of the most intersting zirconia binary systems because of the relatively large cubic solid solution field (1,2,3,4,5,6).

The basic purpose in this work was to obtain a finaly-dispersed and homogeneous material which could be sintered at relatively low temperatures (7,8,9,10).

EXPERIMENTAL

The preparation of the tests was carried out by precipitation with amonium hydroxide using aquous solution of $ZrOCl_2$ and YCl_3. The flowdiagram of preparation sequence is shown in Figure 1.

A Zirconia-Yttria gel was precipitated from a zirconyl chlorite and Yttria chlorite. Zirconia and Yttria are added in exactly determined concentrates for obtaining partially stabilized zirconia with 3 mol.% Y_2O_3 and totally stabilized zirconia with 8 mol.% Y_2O_3. To effect precipitation, ammonium hydroxide was added. The amount of ammonium hydroxide was predetermined to give the pH=8,5. During precipitation, the solution was rapidly stirred. The obtained precipitate was collected by filtration and was washed with distilled water. The washed precipitate was dried in air at 120°C and calcined at 700, 800 and 900°C for 1 hr. in air.

The dried hydroxide and the calcined materials were examined with X-ray difractometer, transmission electron microscope (TEM) and thermal analysis (DTA and TGA).

The characteristic differential thermal and thermogravimetric curve, of zirconia with 3 mol% Y_2O_3, are given in Figure 2. A broad endothermic peak at 250°C is associated with a weight loss of physi-sorbed and chemi-sorbed water from the surface of the material. At 515°C the materials undergo an exothermic reaction. This reaktion is due to the rapid crystallizacion of the samples.

X-ray analysis of the dried hydroxide shows that the materials is amorphous (Figure 3). X-ray analysis of calcined zirconia-Yttria-hydroxide show a two phase system - cubic and monoklinic zirconia. (Figure 3).

The X-ray analysis of composition with 8 mol.% Y_2O_3, cacined at 800°C, show that the cubic phase was formed in the samples.

The calcined product was pulverized and then the morphologies and crystal textures were observed by transmission electron microscopy (TEM). The particles of samples were irregularly agregated and a number of large aggregates were observed by transmission electron microscopy. The aggregates seem to be composed of primary particles from 25 to 30 nm in diameter.

The calcined powders were cold-pressed at 60 MPa into disks (11 mm. in diameter by 3 mm. thick). The sintering of the obtained samples was carried out at temperature of 1300 and 1400°C for a period of 1 and 3 hours.

After sintering the tests were examined in order to determine the rate of sintering, the microstructure and phase composition. X-ray diffraction analysis was used for phase identification. Scans of 2θ between 27° and 32° were conducted to estimate the monoclinic/ (tetragonal + cubic) zirconia ratio, and scans between 55° and 62° were used to confirm the presence of the tetragonal and cubic phase.

In the tests of zirconia with 3 mol.% Y_2O_3 partially stabilized zirconia was obtained after sintering (Figure 4), while in the tests of 8 mol.% Y_2O_3 totally stabilized zirconia was obtained. (Figure 5).

Some characteristics of partially stabilized zirconia with 3 mol.% Y_2O_3, sintered at 1300°C, are given in Table 1.

Table 1. Some characteristics of partially stabilized Zirconia with 3 mol.% Y_2O_3, sintered at 1300°C

Sintering temperature	Shrinkage $\Delta l/l_o$	Monoklinic ZrO_2 (%)	Density (g/cm^3)
3h - 1300°C	16,3	30	4,41
1h - 1300°C	15,1	30	4,33

Microstructure of partially stabilized zirconia, sintered at 1300°C, was observed by scanning electron microscopy(Fig.6) It was observed that many dense large-grained (2-5 μm) zones existed within a fine-grained (0,5 μm) matrix. This structure could result from preferential intra-agglomerate sintering early in the sintering cycle. The densely packed aglomerates could achieve full density early in the cycle, Without pores to inhibit grain growt, the entire agglomerate could readily become a single grain. Meanwhile, the finegrained porous matrix continued to develop by normal sintering processes from a low-density compact of crystallites.

The samples of partially stabilized zirconia were tested for resistence to thermical shocks between 1300°C and 20°C. For showing the permanence of the cubic zirconia, after testing the resistance to thermal-shocks, with the use of X-ray diffraction, the phase composition of the samples was tested.

It can be concluded that the sintered partially stabilized zirconia, with 3 mol.% Y_2O_3, during the testing of resistance to thermo-shocks practically do not change their phase composition and as a result they have the best resistance to thermoshocks.

CONCLUSIONS

Reactive and homogeneous stabilized zirconia was prepared using a coprecipitation method from a solution of $ZrOCl_2$ and YCl_3. X-ray diffraction patterns of the dried hydroxide indicate that the materials is amorphous and that it transforms rapidly to a crystalline state at 515°C.

The calcined powders were cold-pressed at 60 MPa and the sintering of the obtained samples was carried out at temperature of 1300 and 1400°C.

After sintering the tests were examined in order to determine the microstructure and phase composition, The sample of partially stabilized zirconia were tested for resistence to thermical shocks between 1300 and 20°C,

REFERENCES

1. P.Duwez,F.H.Brown,F.Odell, J.Electrochem Soc.,98(9) 356-62 (1951)
2. Fu-K'ang Fan,A.K.Kuznetsov,E.K.Keler, Izv.Akad.Nauk SSSR, Ser.Khim., 1962,1141-46; ibid., 1963,No.4,601-10
3. D.K.Smith, J.Am. Ceram.Soc., 49(11) 625-27 (1966)
4. K.K.Srivastava, R.N. Patil, C.B.Choudhary,K.V.Gokhale, E.C.Subbarao, Trans.J.Br.Ceram.Soc., 73(3) 85-91 (1974)
5. H.G.Scott, J.Mater.Sci. 10(9) 1527-35 (1975)
6. V.S.Stubican,R.C,Hink,S.P.Ray, J.Am.Ceram.Soc., 61(1-2) 18-21(1978)
7. T. Sato,M.Shimada, J.Am.Ceram.Soc.67 (10) C212-213 (1984)
8. K.S.Mazdiyasni, C.T.Lynch,J.S.Smith, J.Am.Ceram.Soc. 48(7) 372-75 (1965)
9. K.Haberko, Ceramurgia 5(4) 148-54 (1979)
10. W.H.Rhodes, J.Am.Ceram.Soc., 64(1) 19-22 (1981)

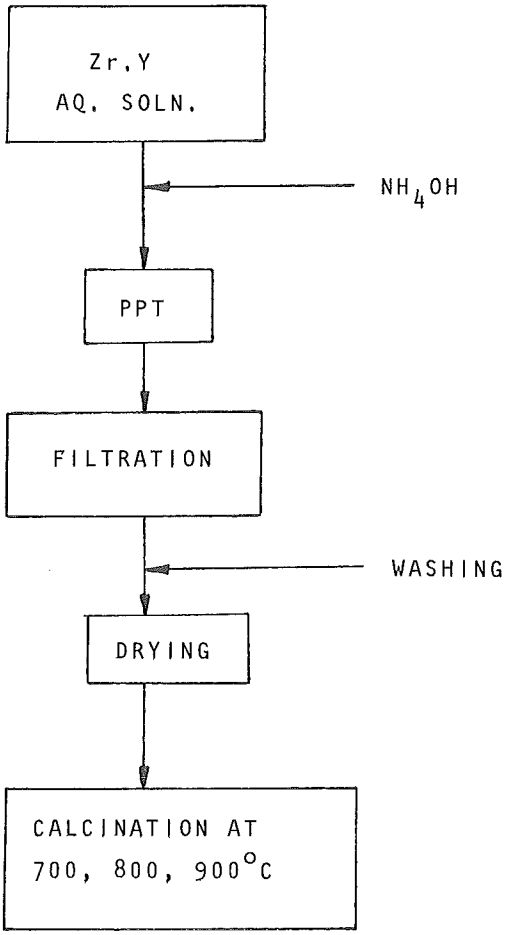

Fig.1. FLOW DIAGRAM FOR THE PREPARATION OF YTTRIA-STABILIZED ZIRCONIA

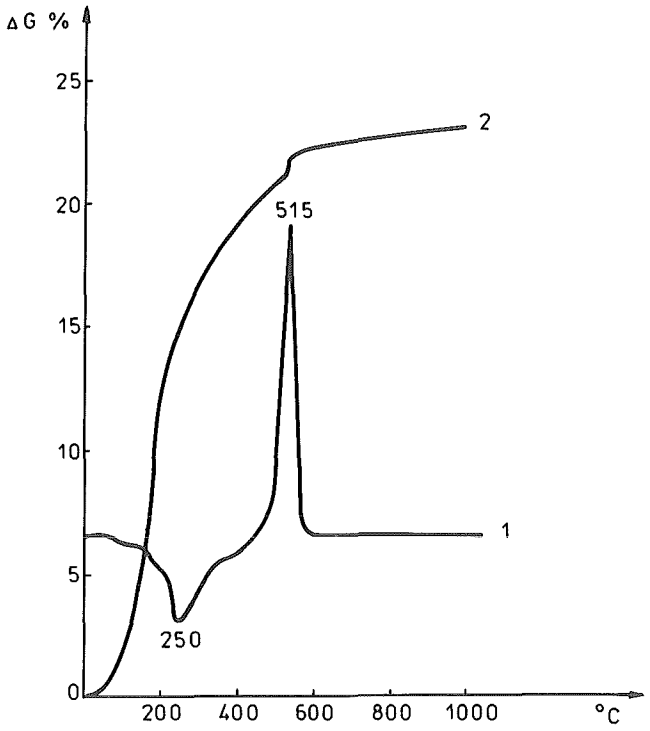

Fig. 2 1. DTA
2. Weight loss

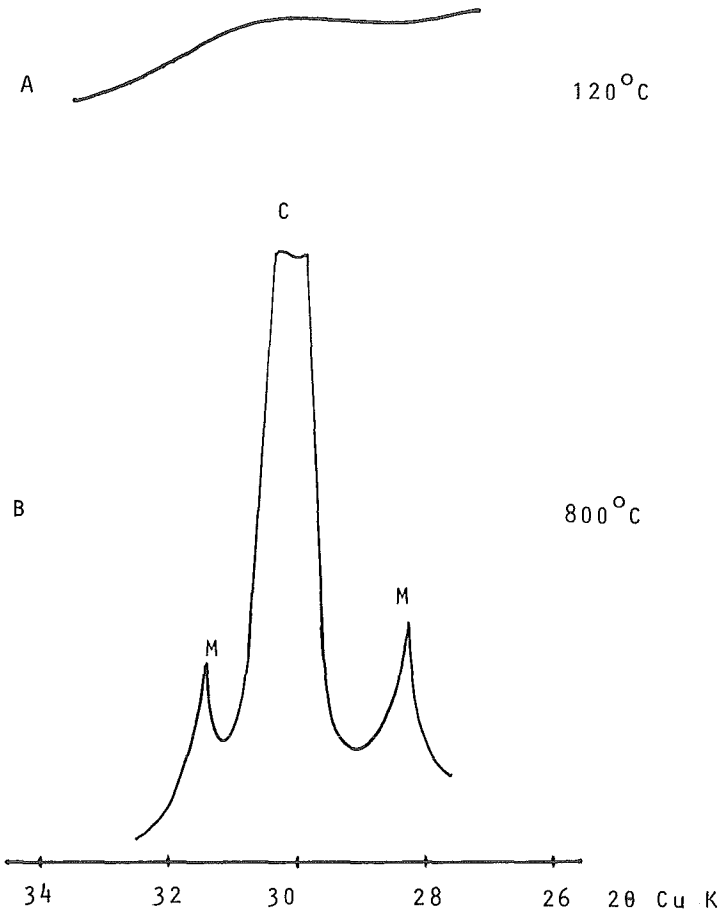

Fig.3. X-ray diffraction patterns of:

A) Amorphous precipitate at 120°C
B) Calcined at 800°C

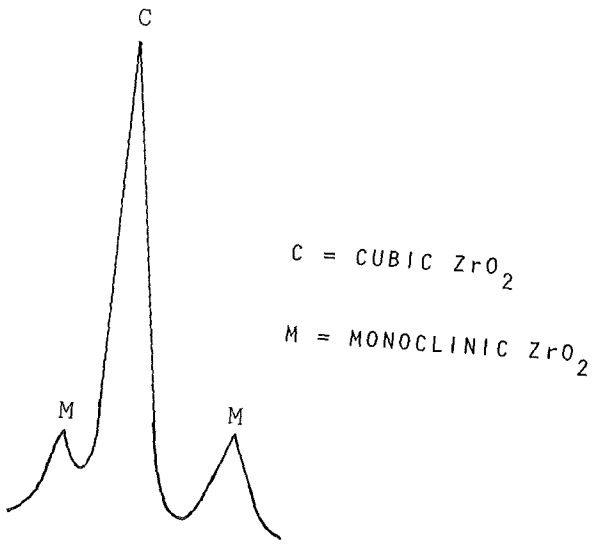

Fig.4.X-ray diffraction pattern of partially stabilized ZrO_2
ZrO_2 + 3 mol.% Y_2O_3, Sintered at 1300°C (3h)

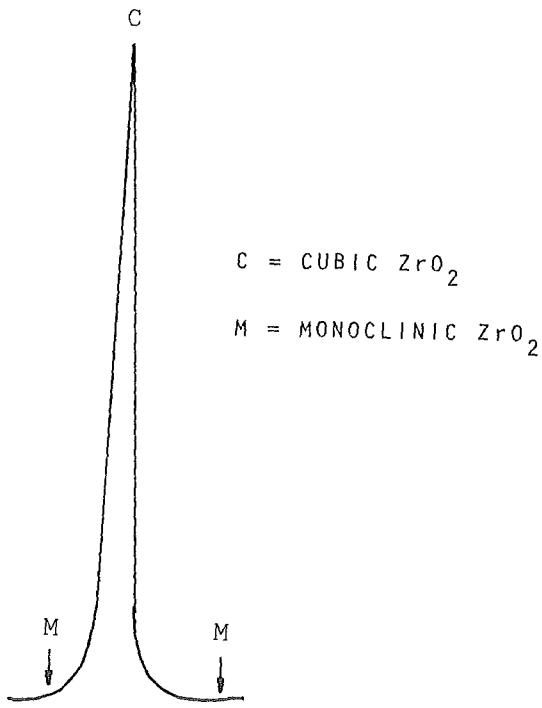

Fig. 5. X-ray diffraction pattern of "Fully stabilized
Zirconia" ZrO_2+8 mol.%Y_2O_3, Sintered at 1300°C (3h)

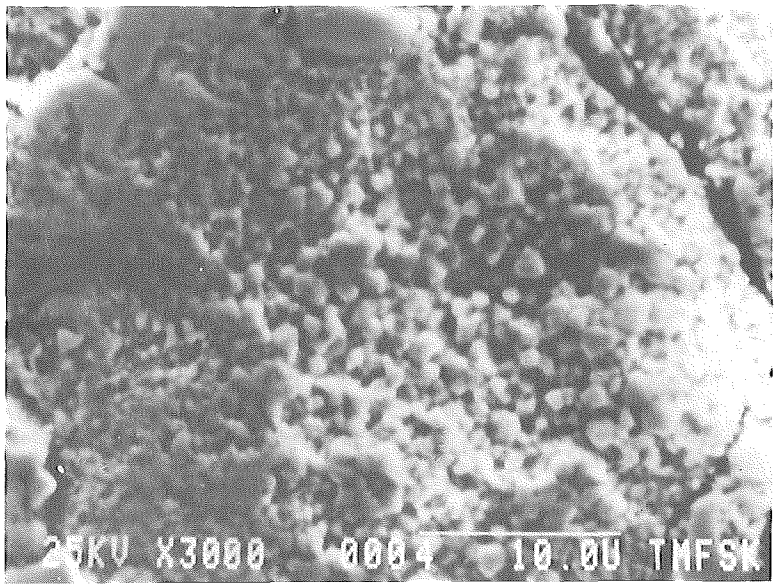

Fig.6. SEM micrograph of PSZ,with 3 mol.% Y_2O_3, sintered at 1300°C.

INVESTIGATIONS OF MULLITE-ZIRCONIA COMPOSITES

T. Fandel, W. Krönert

Institut für Gesteinshüttenkunde, RWTH Aachen
Mauerstraße 5, D-5100 Aachen

1. Introduction

One of the main disadvantages of ceramic materials is their brittleness. They can be toughened and strengthened by the dispersion of fine-grained zirconia particles into a ceramic matrix as it has been shown by several authors (1-6). The toughening originates from the volume and shape change associated with the martensitic tetragonal-to-monoclinic phase transformation of ZrO_2. The main toughening mechanisms are stress induced transformation toughening and formation of matrix microcracks, but also other mechanisms have been proposed, as for example solid solution effects (7).
During about the last ten years, the mullite-zirconia system has gained more interest (7-16). Due to its low thermal expansion, low thermal conductivity, creep resistance and high chemical stability, mullite is an interesting material for high technology applications. However it is difficult to obtain dense mullite because of its low sintering activity.
In order to obtain dense zirconia toughened mullite, most authors (8-13) investigated the reaction sintering of alumina and zircon according to the reaction:
$3\ Al_2O_3 + 2\ ZrSiO_4 \longrightarrow 2\ ZrO_2 + 3Al_2O_3 \cdot 2SiO_2$.
Most authors worked with attrition milling and isostatic pressing or hot pressing. A two-step sintering route had been suggested to separate the densification and reaction steps (8). Other authors (11-13) used sintering aids as MgO or CaO which caused the formation of a glassy phase. Also when sintering the components mullite and zirconia, most of the authors worked with attrition milling and isostatic pressing (14-16).
The aim of our investigations is to produce mullite-zirconia composites with good thermal and mechanical properties, esp. hot modulus of rupture and thermal shock resistance without complicated processing for refractory applications. Instead of reaction sintering , sintering of the components is applied. Here the results of these investigations concerning the densification and thermal expansion of mullite and mullite-zirconia composites are presented.

2. Raw Materials

The raw materials used in these investigatons are fused mullite, fused monoclinic zirconia and fused MgO-PSZ. The chemical analysis of the powders is given in table 1. The

cubic phase content in the PSZ was determined to be 67% using the equation of Porter and Heuer (17). The grain size distributions of the powders determined by a laser particle sizer are given in figure 1 showing cumulative mass percent versus mean grain diameter. Four different grain size fractions of mullite have been used: 0-2, 0-4, 0-10 and 0-20 µm, whereas only one fraction of monoclinic zirconia (0-2 µm) and PSZ (0-5 µm) have been considered. The morphology of the powders is shown in the SEM-micrographs (Fig. 2). Both mullite and zirconia consist of angular, irregular formed, sharpe-edged graines.

3.Experimental

The composition of the samples is given in table 2. Pure mullite and powder mixtures containing 10, 15 and 20 vol% zirconia were prepared with the different mullite grain sizes using monoclinic and partially stabilized zirconia. The powders were wet-ball-milled in plastic bottles for 6 hours with 1% of an organic binder on the basis of PVA. After drying the suspensions at 70°C, the powders were crushed , mixed with 1% of a lubricant, homogenized and finally sieve-granulated (500 µm sieve).
The so prepared powders were uniaxially pressed to cylindrical pellets (15 mm diameter * 5 mm) and bars (5 * 5 * 25 mm^3) with a pressure of 100 MPa. The samples were sintered in an electrical furnace at 1640°C/2h and 1590°C/12h. Heating and cooling rate was 120°C/h. The density of the sintered samples was determined using water replacement method. The phases were analyzed by XRD. Cubic/tetragonal to monoclinic phase ratio was calculated using the above mentioned equation. The microstructure was investigated by scanning electron microscopy and X-ray microanalysis. The thermal expansion and the transformation behaviour of the sintered samples were determined by dilatometric investigation up to 1500°C. Heating and cooling rate was 10°C/min.

4.Results and Discussion

The density of the sintered samples with monoclinic zirconia is shown in figure 3. The samples containing coarser mullite fractions have a very low density of about 62 to 70% of th.D., which is improved by the addition of zirconia, but is only weakly dependant of the sintering temperature. The finer mullite fractions are more reactive and their densification is clearly dependant of the sintering temperature and reaches more than 95 % of th.D. for mullite-zirconia composites. Fig 4 shows the microstructure of pure mullite samples. The 0-2 µm mullite fractions have a dense microstructure with closed porosity, whereas the 0-10 µm fraction is only weakly sintered at the edges of the grains and there is a continuous open porosity. The microstructure of mullite-zirconia composites is characterized by a homogeneous

dispersion of zirconia grains in the fine grained mullite matrix (Fig. 5a). In the coarser mullite matrix (Fig. 5b) there is still considerable porosity and the zirconia particles are mostly located within pores on the surface of mullite grains. Normally they are not completely embedded in a mullite matrix.
The thermal expansion of mullite shows a nearly linear slope (Fig. 6a), whereas the composites are characterized by the hysteresis of the martensitic monoclinic-tetragonal-monoclinic phase transformation of ZrO_2 (Fig. 6b). This hysteresis is smaller for the coarser mullite fractions (Fig. 6c). This can be explained by the higher porosity and the location of the ZrO_2-grains near to the pores, so that the volume change during the transformation does not result in a comparable volume change of the complete sample.
The addition of MgO-PSZ is accompanied by a drastic increase of the density and strongly dependant of the zirconia content (Fig. 7).
The densification is already achieved at 1590°C and not remarkably improved at higher temperature. The samples are almost dense (Fig. 8). XRD showed only small amounts of cubic zirconia in the sintered samples. Only about 5-9 % of the zirconia was stabilized, the rest was monoclinic. Also the thermal expansion (Fig. 6d) indicates that there is no stabilization, as the martensitic transformation is obvious. This indicates a destabilizing effect of the mullite matrix on MgO-PSZ. The destabilization of CaO-PSZ by SiO_2- and Al_2O_3-additions has been described by von Mallinckrodt (18). This destabilization is even increased by the presence of SiO_2 and Al_2O_3 together. This mechanism is active also in the case of mullite and MgO-PSZ.
The remarkable densification of the PSZ-containing specimens indicates the formation of a glassy phase which can also be seen at the micrographes. Moya (12) reported the formation of transient liquid phases in the system Al_2O_3-ZrO_2-SiO_2-MgO at temperatures lower than 1400°C, which is followed by a continuous liquid phase at 1450°C. So the stabilizing MgO in these samples is removed out of the ZrO_2 lattice and active as sintering aid by forming a liquid phase.

5. Conclusions

It has been shown that it is possible to get fine grained, nearly dense mullite-zirconia composites with homogeneous microstructure using fused mullite and zirconia powders and by a very simple processing suitable for refractory products. Neither attrition milling nor isostatic or hot pressing is necessary, but it is necessary to use fine- grained powders. MgO-PSZ is destabilized in the mullite matrix, but the densification is improved by the formation of a liquid phase.

References

1. N. Claussen, "Umwandlungsverstärkte keramische Werkstoffe", Z.Werkstofftech. 13, 1982, 138-147, 185-196
2. F.F. Lange, "Transformation-toughening", J. Mat. Sci. 17, 1982, 225-262
3. N. Claussen, "Transformation-Toughened Ceramics (TTC)" Ceramics in advanced energy technologies, D. Reidel Publ. Comp., 1984, 51-84
4. N. Claussen, M. Rühle, A.H. Heuer (Ed.), "Science and Technology of Zirconia II", Advances in Ceramics 12, Am. Ceram. Soc., 1984
5. E.P. Butler, "Transformation-toughened zirconia ceramics", Mat. Sci. Tech. 1, 1985, 417-432
6. A.H. Heuer, "Fracture-tough ceramics - the use of martensitic toughening in zirconia containing ceramics", Mat. Sci. Monographs 26, 1985, 264-278
7. M.J. Osendi, P. Miranzo, J.S. Moya, "Solid solution effects on the fracture toughness of mullite-ZrO_2-composites", J. Mat. Sci. Lett. 4, 1985, 1026-1028
8. N. Claussen, J. Jahn, "Mechanical Properties of Sintered, In Situ-Reacted Mullite Zirconia Composites", J. Am. Ceram. Soc. 63, 1980, 228-229
9. J.S. Wallace, N. Claussen, M. Rühle, G. Petzow, "Development of Phases in In Situ-Reacted Mullite-Zirconia Composites", Proc. Int. Conf. Surfaces and Interfaces, Plenum Publ. Corp., 1981, 155-165
10. P. Boch, J.P. Giry, "Preparation and Properties of Reaction-sintered Mullite-ZrO_2 Ceramics", Mat. Sci. Eng. 71, 1985, 39-48
11. P. Pena et al., "Effect of magnesia additions on the reaction sintering of zircon/alumina mixtures to produce zirconia toughened mullite", J. Mat. Sci. Lett. 2 1983, 772-774
12. J.S. Moya et al., "Multicomponent toughened ceramic materials obtained by reaction sintering", J. Mat. Sci. 20, 1985, 2011-2022, 2702-2718
13. J.M. Rincon, J.S. Moya, M.F. De Melo, "Microstructural Study of Toughened ZrO_2/Mullite Ceramic Composites obtained by Reaction Sintering with TiO_2 Additions", Br. Ceram. Trans. J. 85, 1986, 201-206
14. S. Prochazka, J.S. Wallace, N. Claussen, "Microstructure of Sintered Mullite-Zirconia Composites", Comm. Am. Ceram. Soc. 66, 1983, C-125-C-127
15. J.S. Moya, M.J. Osendi, "Microstructure and mechanical properties of mullite/ZrO_2 composites", J. Mat. Sci. 19, 1984, 2909-2914
16. G. De Portu, J.W. Henney, "The Microstructure and Mechanical Properties of Mullite-Zirconia Composites", Br. Ceram. Trans. J. 83, 1984, 69-72
17. D.L. Porter, A.H. Heuer, "Microstructural Development in MgO-Partially Stabilized Zirconia", J. Am. Ceram. Soc. 62, 1979, 298-305
18. D. von Mallinckrodt, "Einfluß von Verunreinigungen auf Sinterung und Stabilisierung von ZrO_2(CaO)", Ph.D. Thesis, TH Aachen, 1981

	Mullite	Zirconia	
		monoclinic	MgO-PSZ
SiO_2	25.43	1.10	0.540
Al_2O_3	74.36	0.027	0.041
ZrO_2	-	94.07	92.84
HfO_2	-	3.96	3.09
CaO	0.0001	0.0006	0.005
MgO	0.0014	0.006	3.34
Na_2O	0.347	0.005	0.004
K_2O	0.007	0.0007	0.001
TiO_2	0.05	0.05	0.150
Fe_2O_3	0.091	0.018	0.035

Table 1. Chemical analysis of the powders

Nr	Mullite (Vol%)	Zirconia (Vol%)
0	100	0
1	90	10
2	85	15
3	80	20

Table 2. Composition of the samples

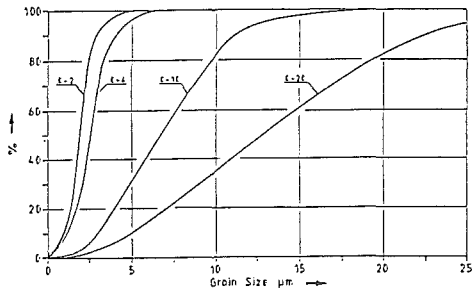

Grain Size Distribution of Mullite Powders

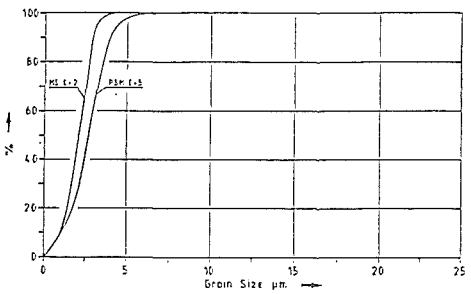

Grain Size Distribution of Zirconia Powders

Fig.1. Grain size disributions of the raw materials

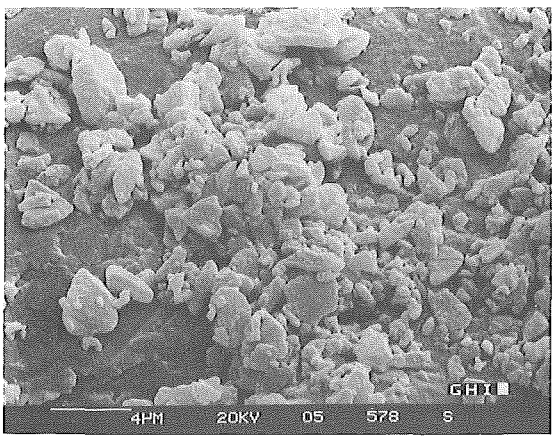

2a. mullite 0-4 µm

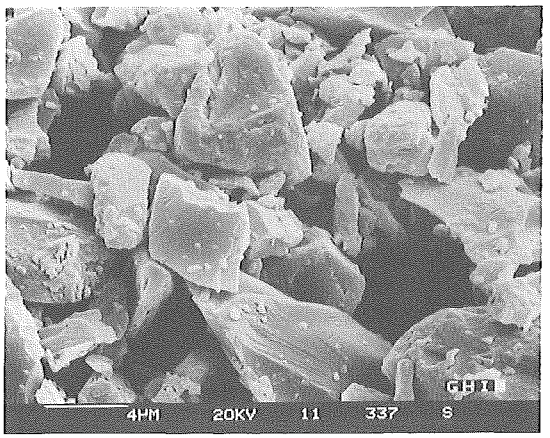

2b. mullite 0-10 µm

Fig.2. SEM-micrographs of the raw materials

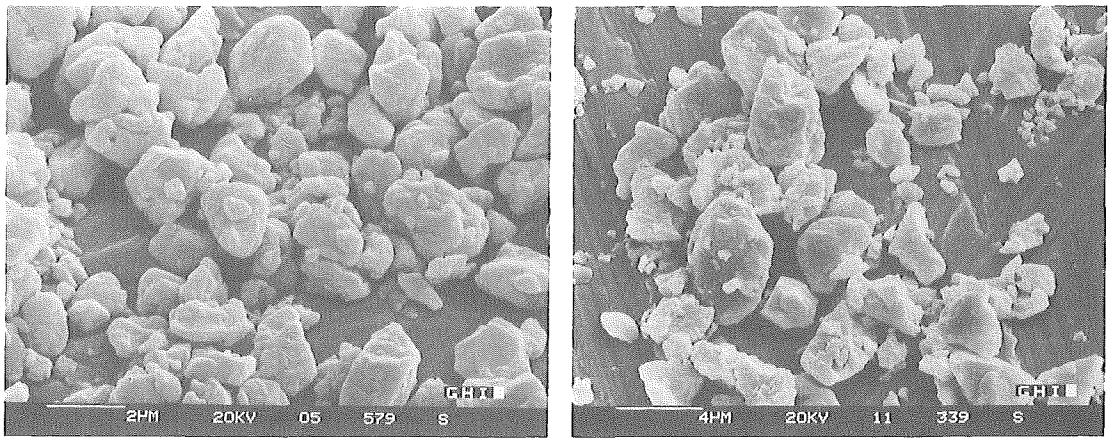

2c. mon. zirconia 0-2 µm

2d. MgO-PSZ 0-5 µm

Fig.2. SEM-micrographs of the raw materials

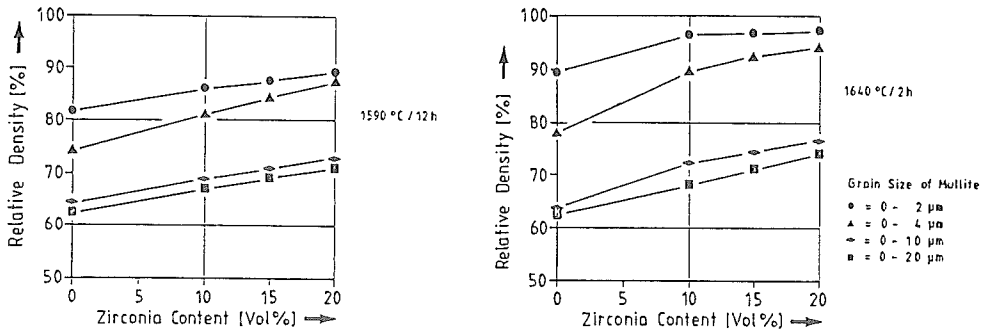

Fig.3. Density of sintered mullite-zirconia composites prepared with monoclinic ZrO_2 (0-2 µm)

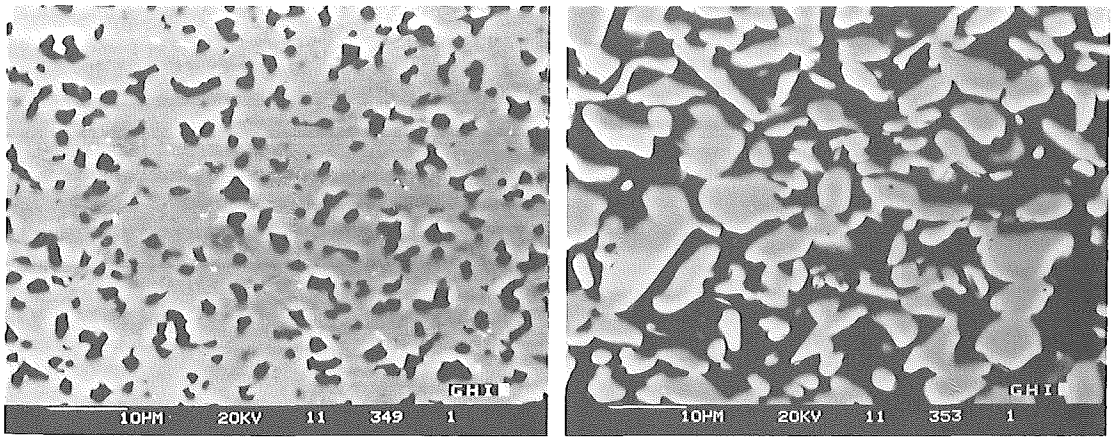

4a. mullite 0-2 µm, 1640°C/2h

4b. mullite 0-10 µm, 1640°C/2h

Fig.4. Microstructure of pure mullite samples

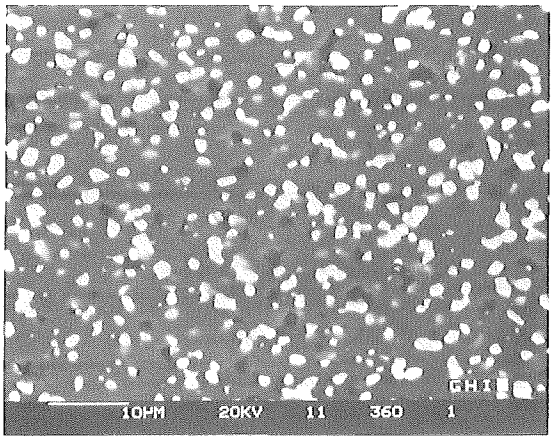

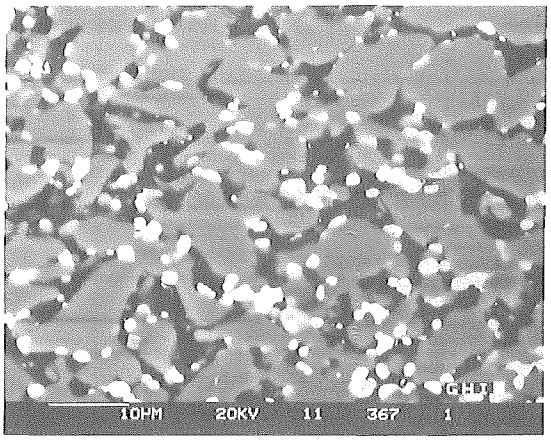

5a. mullite 0-2 µm 5b. mullite 0-10 µm

Fig.5. Microstructure of mullite-zirconia composites prepared with 15 vol% monoclinic ZrO_2, 1640°C/2h

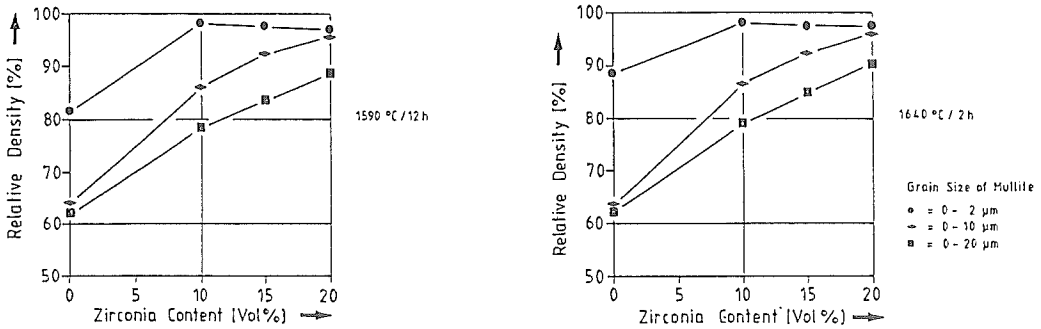

Fig.7. Density of mullite-zirconia composites prepared with MgO-PSZ

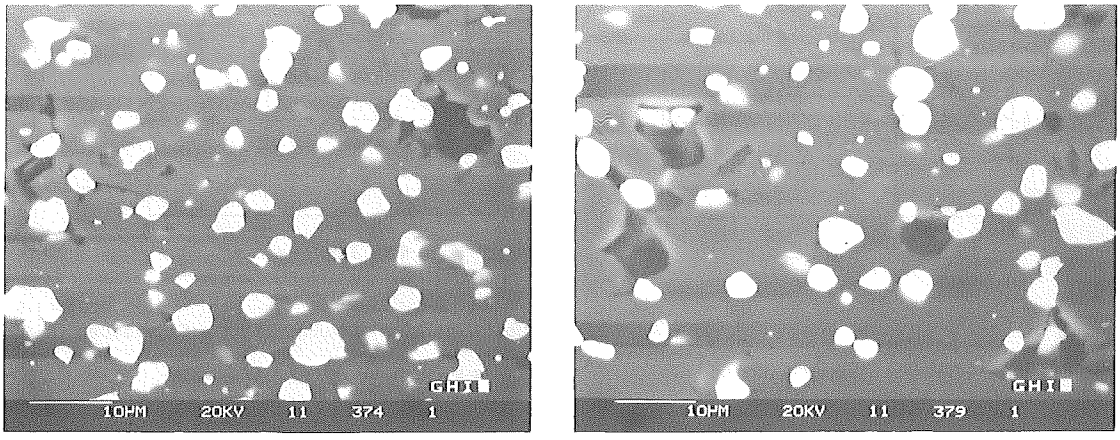

8a. mullite 0-2 µm 8b. mullite 0-10 µm

Fig.8. Microstructure of mullite-zirconia composites prepared with 15 vol% MgO-PSZ, 1640°C/2h

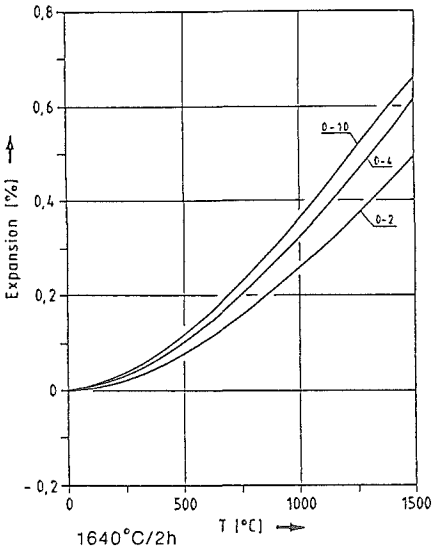

Thermal Expansion of Pure Mullite

6a.

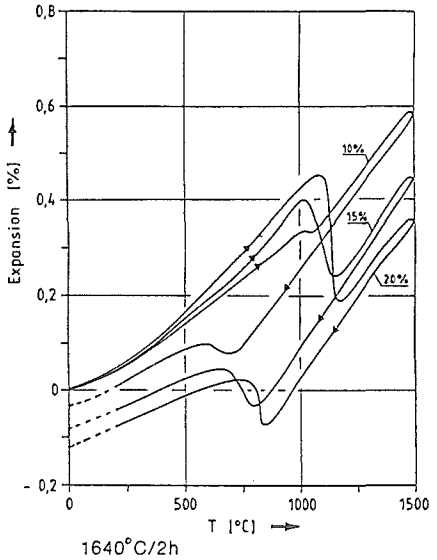

Thermal Expansion of Mullite-Zirconia Composites

as a Function of Zirconia Content

Mullite 0-2µm Zirconia(mon) 0-2µm

6b.

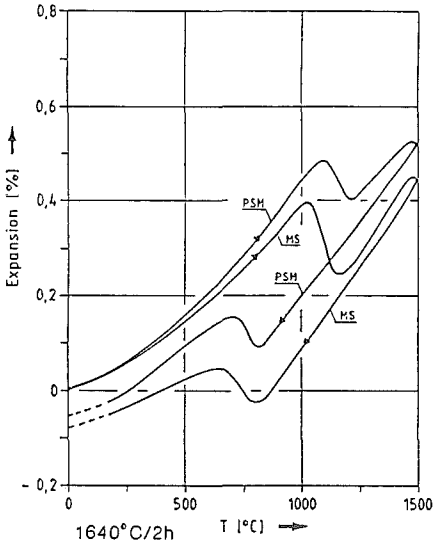

Thermal Expansion of Mullite-Zirconia Composites

85 Vol%Mullite 15 Vol% Zirconia

(monoclinic: MS; MgO-PSZ: PSM)

6c.

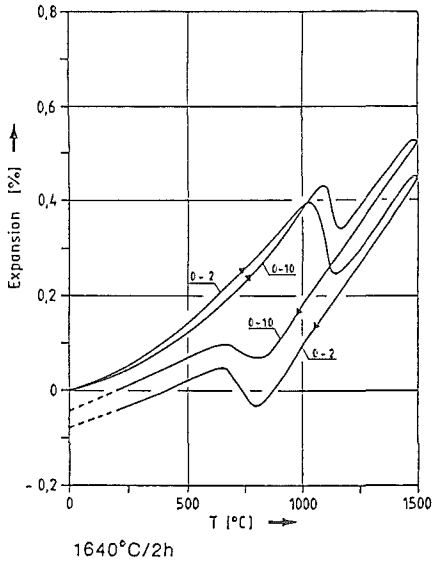

Thermal Expansion of Mullite-Zirconia Composites

as a Function of Mullite Grain Size

85 Vol% Mullite 15 Vol% Zirconia (mon)

6d.

Fig.6. Thermal expansion of pure mullite and mullite-zirconia composites

PREPARATION AND THERMAL EXPANSION OF Al_2TiO_5-TiO_2 SINTERED BODIES

I.Stamenković and G.Ondracek*
Institute of Nuclear Sciences "B.Kidrič"-Vinča, Belgrade
*Kernforschungszentrum and UNI, Karlsruhe

1. BACKGROUND

Aluminiumtitanate is already known as a commercial ceramic material[1]. To use it, however, as a host material in nuclear waste menagement and as a bioceramics its characteristic properties should be appropriatly developed. This is why we started to investigate the synthesis of Al_2TiO_5 material in the form of two-phase ceramics. As the modifying component TiO_2 was choosen because of its high corrosion resistance with respect to radwaste elements and because of its biocompactibility in the case of bioceramics.

Since with two-phase material we may always vary the properties by microstructural and content variations inbetween a certain region the present investigations covered the whole concentration range between the two phases permitting to get better insight into the property changes.

Investigated two-phase system up to the certain TiO_2 content we considered as a composite material built of Al_2TiO_5 matrix and TiO_2 particles as a dispersed component which thermal expansion difference is negative one and having the moderate value of $-6,4\ ^{o}C^{-1}$ (20-1200°C).

2. EXPERIMENTAL PROCEDURE AND DISCUSSION

2.1. Starting powders

TiO_2 powder of anatase crystal structure was used as a base material. Total TiO_2 content was 99.00 wt%. The complete crystal phase transformation anatase → rutile undergone at 1100°C in air during 2 hours.

Al_2O_3 powder - A16 of alpha structure and Al_2O_3 content 99.65 wt% was used in the experimental work.

Al_2TiO_5 synthesis. The equimolar mixture of alumina and titania having anatase structure was prepared by homogenization in ethyl-alcohol[2]. The MgO surplus of 2 wt% in the form of Mg-acetate was added to the slurry. After drying the mixture was cold pressed at 50 MPa and heated in air at 1420°C during 2 hours. Obtained material was wet milled and dried.

Characteristic properties of used powders are given in table I.

Table I: Characteristic properties of powders

Powder \ Property	X-ray structure	Surface area, m^2g^{-1}	Particle size range*, μm
TiO_2	anatase	7.3	<3
TiO_2	rutile	3.6	<7
Al_2O_3	alpha	1.2	<3
Al_2TiO_5	Al_2TiO_5**	0.9	<5

* Light microscope; ** Traces corundum

2.2. Preparation of Al_2TiO_5-TiO_2 ceramics

The mechanical mixtures of Al_2TiO_5 and TiO_2 were prepared by prolonged (5 hours) homogenization of starting oxides in plastic jars and using ethyl alcohol as dispersive liquid. After drying the mixtures were cold pressed at 100 MPa in the form of cylinders having the diameter of 12 mm and slabs 50x7x7 mm.

Table II. Compositions of Al_2TiO_5+TiO_2 cold pressed and sintered samples

Sample	vol.% AT*	vol.% T**	Green density gcm^{-3}	Linear shrinkage %	Density gcm^{-3}	Theoretical density %
1	100	0	2.05	3.2	2.66	71.7
2	88.9	11.1	2.35	5.2	2.80	74.7
3	77.5	22.5	2.33	7.7	3.23	84.5
4	67.8	32.2	2.40	10.9	3.53	91.0
5	53.4	46.6	2.34	12.0	3.63	91.6
6	40.8	59.2	2.38	13.3	3.79	94.0
7	27.7	72.3	2.34	14.2	3.86	94.1
8	14.1	85.9	2.31	14.5	3.93	94.2
9	0	100	2.20	15.3	4.03	94.6

*AT - Al_2TiO_5 **T - TiO_2-rutil

Final sample densification was performed by sintering in air at 1500°C and during 2 hours. Heating rate was 300°C/h and samples cooling was performed at a mean rate of 90°C/h. Samples exibited the colors like sample "1" white and "9" brownish.

Characteristic properties of pressed and sintered samples are given in table II.

When density values of sintered samples given in table II were plotted versus TiO_2 volumetric concentration, as shown on figure 1, it is evident that density curves are rather constant at TiO_2 contents above approximately 35 vol.% but not in the region below this. As already known from cermets and other two--phase materials the slope of sintered densities versus phase concentration expresses microstructural changes especially with respect to the matrix one: only below 35 vol.% TiO_2 the Al_2TiO_5 phase is acting the role of matrix component. Above this concentration a TiO_2 matrix exists.

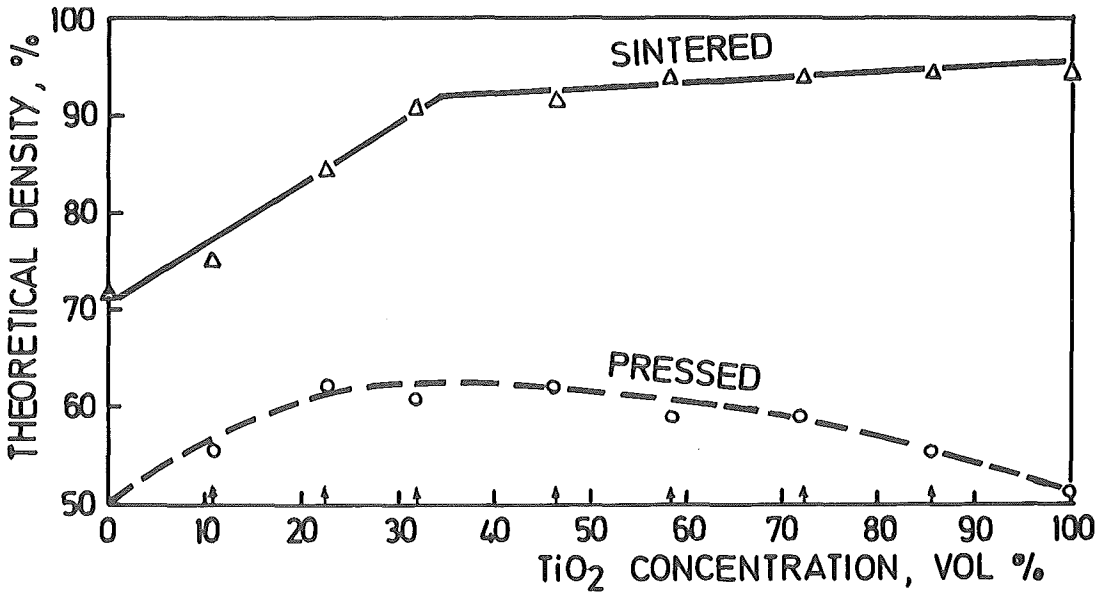

Figure 1. Density of Al_2TiO_5+TiO_2 bodies versus TiO_2 content

Microstructural analysis of sintered samples, some of SCAN micrographs are shown on figure 2, qualitatively gave the results consistent with previous ones. The samples composed of the lowest content of TiO_2 have fairly nonsintered Al_2TiO_5 matrix confirming its very poor sinterability. On the contrary, the samples having 35 vol.% of TiO_2 are characterized by interbonded TiO_2 particles due to its sintering temperature lower than Al_2TiO_5. Further microstructural analysis brought out that in all samples the cracking have occured stressing

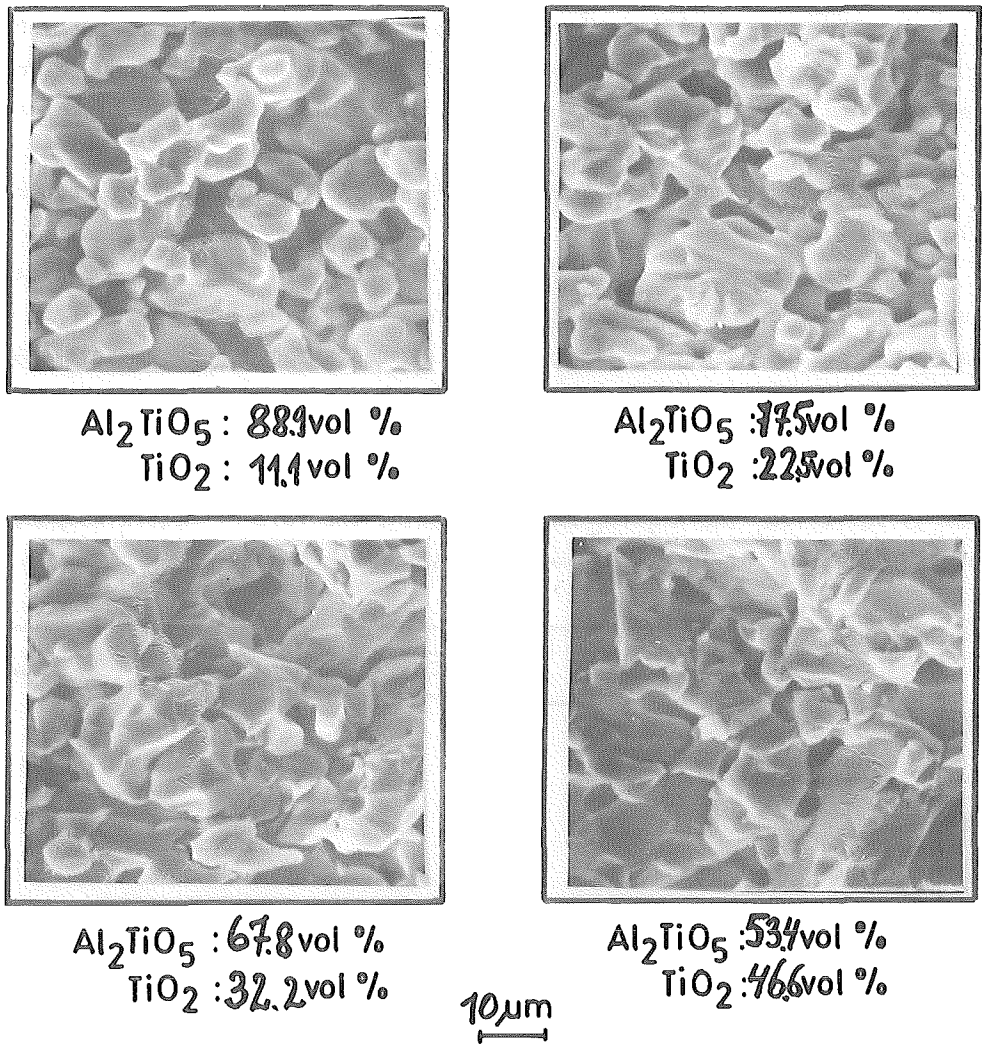

Figure 2. SCAN microscope micrographs of sintered Al_2TiO_5-TiO_2 samples

the limits influence by caracteristics of used starting powders and pressing--sintering procedure as a densification technique presently used.

Thermal expansion coefficient measurements, performed in air up to 1300°C and using heating-cooling rate of 10° per minute, were done over the whole TiO_2 concentration range just to get an imagination about the induced thermal stresses in the Al_2TiO_5-TiO_2 samples when cooling down from sintering temperature. The changes of mean expansion coefficients (20-1300°C) are shown on figure 3.

Obtained dilatograms, heating and cooling curves, were in evident accordance with those published by Persson et al[3] who investigated Al_2TiO_5 + (Al_2O_3 + + TiO_2) system.

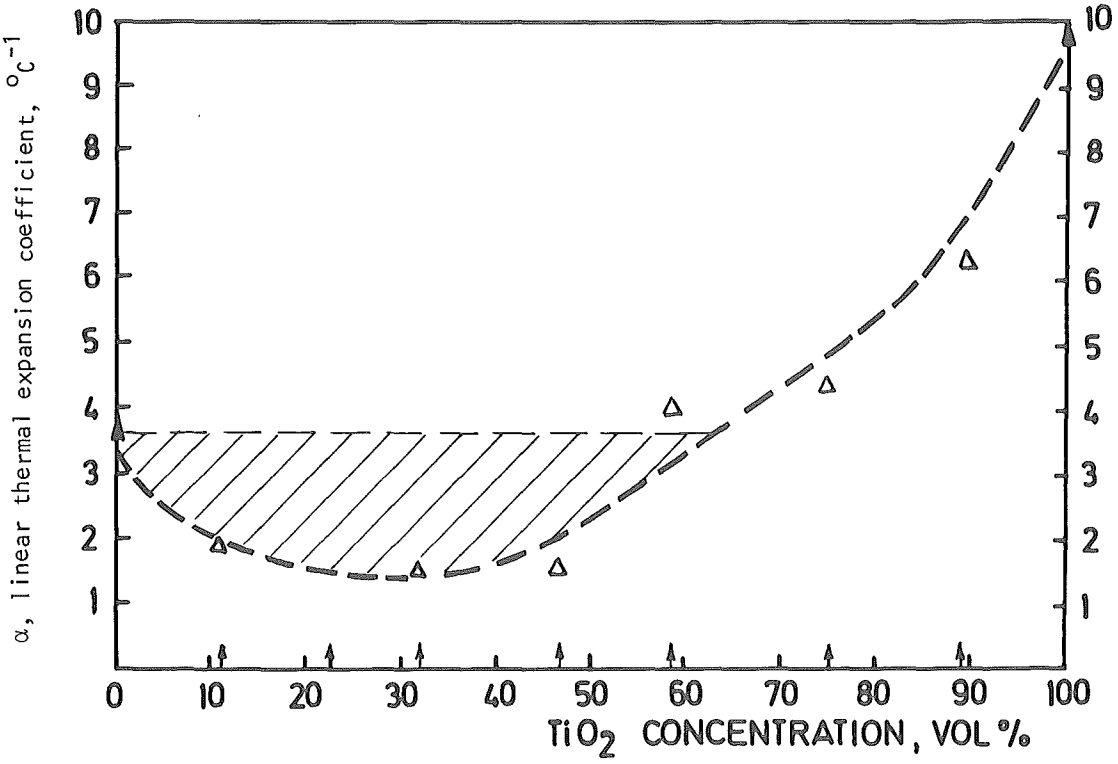

Figure 3. The effect of Al_2TiO_5-TiO_2 composition on linear thermal expansion coefficient

Suprising is so far from a theoretical point of view, that some values occured under the dotted line. The anomaly, possibly related with microstructural characteristics of investigated ceramic bodies and particulary with microarckings, is the subject of ongoing and future investigations.

3. THEORETICAL APPROACH

The procedure of increasing the matrix strength by incorporating the dispersed second phase having different thermoelastic and fracture properties was approved in a number of investigations. Strengthening was particularly evident if $\Delta\alpha$ was zero or slightly negative like composite glass - ZrO_2 (-2.9); if $\Delta\alpha$ demonstrated large negative values, like glass - Ni(-12) decohesion at interface and/or microcracking of matrix/dispersed particles occured.
What direction should be followed if we wanted to synthesize the Al_2TiO_5-TiO_2 ceramic body of increased strength? The present considerations are based on the model of matrix-dispersed particle having greater thermal expansion coefficient and Young's modulus than matrix.

The model system assumed that pre-existing cracks are of circular shape and nonreacting and crack extension under differential thermal condition occurs instantaneously, also.

Accordint to Wolsh's equation the effect of cracks on Young's modulus is correlated by:

$$E=E_o\left[1+\frac{16(1-\nu^2)NC^3}{9(1-2\nu)}\right]^1 \qquad (1)$$

E - Young's modulus of cracks containinig material; E_o - Young's modulus of cracks free material; ν - Poisson's ratio; C - crack length; N-Number of cracks per unit volume

Introducing the Davidge-Green's expression for the energy per unit volume of spherical particle subjected to uniform thermoelastic stress and Griffith's condition for crack extension Krstić[4] got the equation when not matrix cracking will occur:

$$\sigma_{FM} > \sigma_{FP}\frac{\emptyset}{2Eop} \qquad (2)$$

where: σ_{FM}, σ_{FP} - fracture stresses of matrix and dispersed particle; $\emptyset$ - expression relating Young's moduli of matrix (E_{om}) and particle (E_{op}) and Poisson's ratioes of matrix (ν_m) and particle (ν_p) of crack free components

Graphical presentation of equation 2, extrapolated for E_{op}/E_{om} values greater than 7, is shown on figure 4.

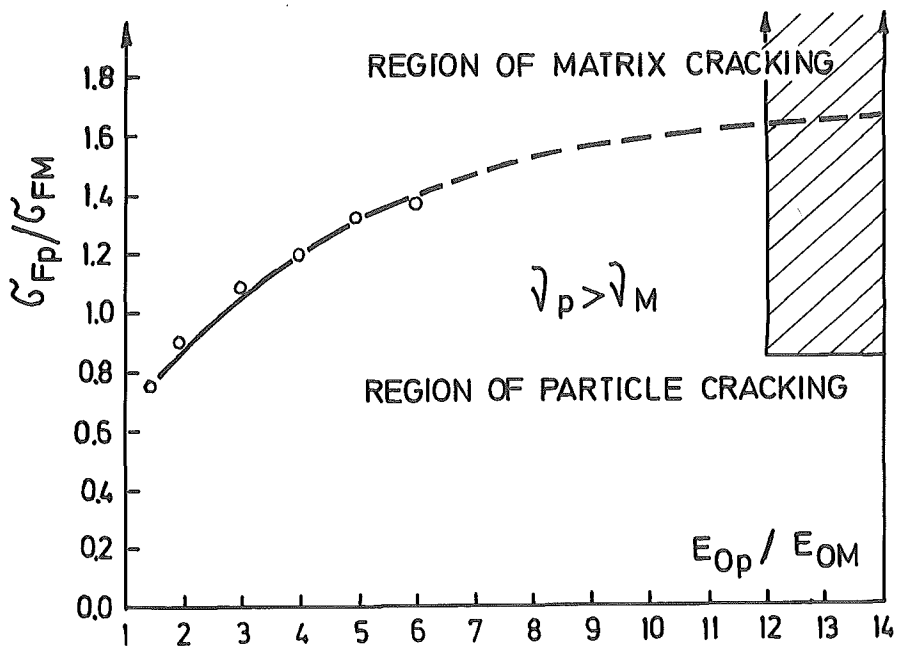

Figure 4. The effect of elastic properties and strength on circumferential cracking[4]

Taking into acount reported data for Al_2TiO_5 and TiO_2, as given in table III and using reported Young's moduli values as E_{om} and E_{op} will be

$$\frac{E_{op}}{E_{om}} = 12 - 14; \quad \frac{\sigma_{FP}}{\sigma_{FM}} = 0.8\text{-}9.5$$

Table III. Properties of Al_2TiO_5 and TiO_2 ceramics

Oxide	Young's modulus GNm^{-2}	Poisson's ratio 1	Tensile strength value Mnm^{-2}	Tensile strength grain size µm
TiO_2	282[5] 260[6]	0.265[5]	∿30-200[8]	200-5
Al_2TiO_5	22[7]	0.23[6]	21-37[9]	90-15

Corresponding area on diagram in figure 4 will be the hatched region. To achieve crack free matrix, according the extrapolated curve, the following strength ratio should be attained

$$\frac{\sigma_{FP}}{\sigma_{FM}} = 1.4\text{-}1.6 \quad \text{i.e. } \sigma_{FP} = (31\text{-}53)\ GNm^{-2}$$

Altering the strength ratio and/or strength values and/or elastic moduli of matrix/dispersed component could be teylored the composite material without matrix cracking. There are two lines of doit so:

a. by producing TiO_2 particles having the grains which size is correlated with specific and appropriate strength of this dispersed phase. Taking into account literature data, shown by diagram on figure 5, TiO_2 particles having grains between 50 and 150 µm should fit this purpose

b. decreasing the grain size of matrix phase ie increasing Al_2TiO_5 strength the need to lower TiO_2 particles strength needs to be less crucial and the composite synthesis is expected to be more feasible. According to the results of Cleveland and Bradt the critical Al_2TiO_5 grain size should be less than 1 µm to reach crack free and moderate strength of aluminiumtitanate.

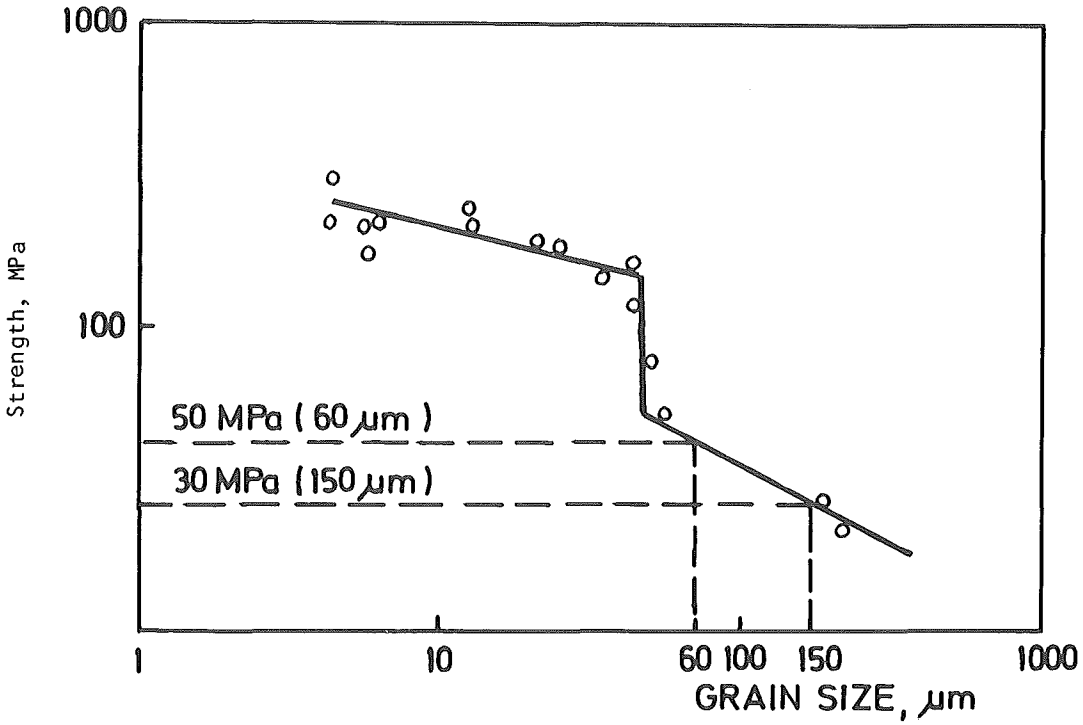

Figure 5. Strength of TiO_2 versus grain size[4]

REFERENCES

1. P.Valzer, H.Henrick, M.Langer "Ceramic components in Passinger-Car Diesel Engines" Materials and Design, 7, No 2 (1986) -.75-80
2. I.Stamenković, G.Ondracek, O.Vöhringer: "The Influecne of Eutectic Compositions on the Sintering Temperature of Alumina-Titania Ceramics" Ceramic Forum International, 64, Nr.5 (1987),p.154
3. M.Persson, L.Hermannson, R.Carlsson, Sci. of Ceramics, 11 (1981) p.479
4. V.D.Krstić et al. "Crack extension and arrest within the particle subjected to tensile thermoelastic stresses in brittle matrix composites", J.Mat.Sci. 19 (1984) p.4119
5. Data book "Engeneering properties of ceramic materials" Publ.by Am.Ceram. Soc., Columbus (1966)
6. Ondracek, G: Communication
7. J.J.Cleveland and R.C.Bradt "Grain size-microcracking relations for pseudobrookite oxides" J.Am.Ceram.Soc. 61 11 12 (1978) p.478
8. V.Krstić, et al. "Fracture of brittle solids in the presence of thermoelastic stresses", J.Am.Ceram.Soc. 67, 9 (1984), p.589
8. V.V.Kolomeicev, et al. "Synthesis, sintering and properties of aluminium titanate", Ogneupory, No.8 (1981) p.41.

C E R A M I C S

SINTERING AND MICROSTRUCTURE (2)

Microstructure Development in Alumina

Reijnen, P and KIM, H. D.
RWTH Aachen, W. Germany

1. Introduction

The role of sintering additives such as MgO or TiO_2 on microstructure development in Alumina is continuously discussed in the ceramic community. According to Coble (1), the rate determining step in the sintering of alumina is volume diffusion of cations, while rapid diffusion of oxygen ions takes place on the grain boundaries.
Small amounts of MgO (300 - 1000 ppm) are usually added to prevent discontinuous grain growth and higher final densities are obtained. Larger amounts of MgO reduce the sintering rate and grain growth as well due to formation of a second phase (spinel). The solid solution of MgO in Alumina leads to formation of oxygen vacancies and interstitial cations by which the ambivalent volume diffusion is enhanced. This mechanism is essentially different from the Coble model [Reijnen-Readey theory (2, 3) for the sintering of ionic solids]. The Reijnen-Readey-theory explains also the higher pore mobility and grain growth. The solid solution of TiO_2 in Alumina makes the material cation deficient and a lower sintering rate should be expected, when volume diffusion is the preponderant mechanism.
Experimentally it turns out that TiO_2 enhances the sintering rate and grain growth rate as well.
Reijnen (4, 5) pointed out that this is probably due to formation of a liquid phase together with Na_2O, an impurity which is difficult to avoid.
In this study we establish the phase relationships in the system Al_2O_3(bulk)-MgO-TiO_2-Na_2O using rather large amounts of impurities in order to be able to detect the phases by x-ray diffraction. According to the phase rule up to 4 condensed phases can coexist.

Sometimes upon cooling 5 solid phases are found. This is due to the decomposition of Al_2TiO_5 upon cooling which leads to a non-equilibrium phase assembly.
To avoid the take-up of Na_2O from the furnace atmosphere, the Na_2O free samples were sintered in specially prepared crucibles from pure Al_2O_3 doped with 1% MgO + 1% TiO_2 which could be closed with a lid of the same composition.
The most efficient way to avoid Na_2O contamination and to remove Na_2O impurities is the sintering in H_2, NH_3, or vacuum. In the vapour phase Na_2O is dissociated in Na and O_2. The strong reducing atmosphere reduces Ti^{4+} to Ti^{3+} or even Ti^{++} and makes the material aniondeficient.

2. Experimental

To a slurry of water and alumina, the required amounts of Mg acetate, Na_2CO_3 and Ti isopropylate (treated with HNO_3 to pH = 2) were added.
The slurry was dried under an infra-red lamp, while kept stirring. The dried powders were slightly ground and prefired at 1100 °C for 30 minutes in protective crucibles. The calcined powders were ground in a mortar and pressed.
Series of compacts were sintered in protective crucibles at 1500°C for 0,24h and 1600°C for 0,24h, 2,4h, 12h, 24h in an electrical furnace in air atmosphere. Families of compacts with and without Na_2O were sintered separately.
Samples with large amounts of additives were used for x ray diffraction analysis and microstructure analysis as well.
Samples with small amounts of additives were used for sintering studies.

3. Results and discussion

Fig. 1 shows th semiquantitative phase relationship in the system Al_2O_3(bulk)-MgO-TiO_2-Na_2O. (Samples sintered at 1600°C 12 hrs)

Density values for different sintering temperatures and soaking times are shown in fig. 2.

3.1 The system Al_2O_3 + xMgO or $yTiO_2$

Increasing amounts of $MgAl_2O_4$ and Al_2TiO_5 are found with increasing x and y: the solubilities of MgO or TiO_2 in the Al_2O_3 lattice are small.

The increasing amount of second phase $MgAl_2O_4$ reduces the sintering rate and grain growth of MgO containing samples. In TiO_2 containing samples the sintering behaviour is quite different, both grain growth and sintering rate are strongly enhanced. A large number of small pores are trapped within the grains and Ostwald ripening of the pores does not take place. This indicates a low value for ambivalent volume diffusion (cation deficient material). The presence of TiO_2 increases strongly grain boundary diffusion and grain growth, either by formation of a liquid phase (Na_2O impurity) or by solid segregation in the grain boundary region.

3.2 The system Al_2O_3 + 1 mol% Na_2O + xMgO or $yTiO_2$

Samples without MgO and TiO_2 show second phase ß Al_2O_3 ($Na_2O \cdot 11Al_2O_3$) which tends to strong Ostwald ripening, causing cracks around the ß crystals. This is explained by the easy way of sodium transport by the vapour phase within the sample. In adding MgO the Ostwald ripening of the ß phase is strongly suppressed. The second phase remains finely dispersed and hampers grain growth and sintering. This phenomenon is explained in the following way: MgO dissolves in the ß phase and lowers the Na vapour pressure. A small ß crystallite which has lost some Na obtains a higher MgO

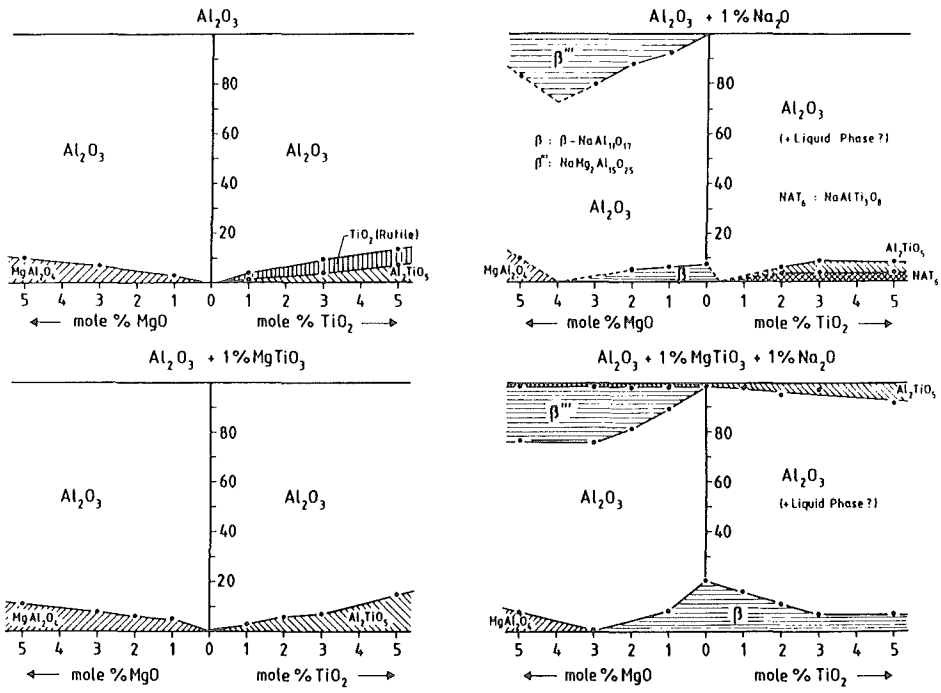

Fig. 1. Semi-quantitative phase relationship in the System Al_2O_3(bulk)-MgO-TiO_2-Na_2O drawn by the XRD analyses for the specimens sintered at 1600°C for 12 hours.

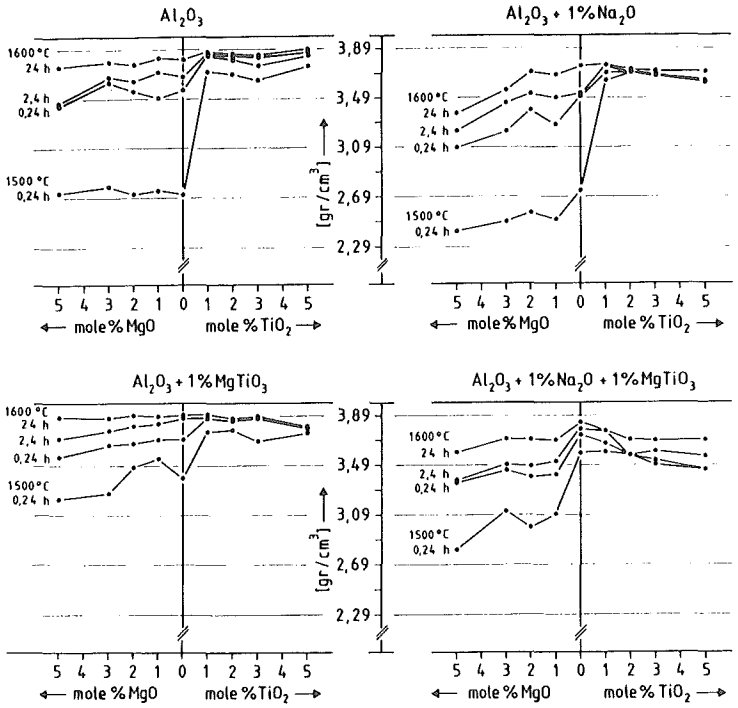

Fig. 2. Density values measured at different sintering temperatures and times

content which prevents a further evaporation of Na. This important effect will take place in all commercial alumina's which are sintered with MgO addition.

The samples containing Na_2O and TiO_2 contain $Na_2O \cdot Al_2O_3 \cdot 6TiO_2$ after cooling which is formed from a liquid phase. This liquid phase wets the grain boundaries and enhances the sintering rate and grain growth. Notice that the amount of liquid phase is approximately 10 times the amount of Na_2O .

3.3 The system Al_2O_3 + 1% $MgTiO_3$ + xMgO + y TiO_2

The solibility of $MgTiO_3$ in Alumina is considerably higher than the separate solubilities of MgO and TiO_2 because there is no deviation from stoichiometry.

With additional MgO the $MgTiO_3$ forms Mg_2TiO_4 and prefers to be in the spinel phase.
With additional TiO_2 the $MgTiO_3$ forms $MgTi_2O_5$ and remains dissolved in the Al_2TiO_5 phase. This is clearly indicated by the fact that the Al_2TiO_5 phase is not decomposed upon cooling. The outspoken effects of MgO and TiO_2 on the sintering of alumina are also found in these compositions.

3.4 The System Al_2O_3 + 1%$MgTiO_3$ + 1%Na_2O +xMgO or yTiO_2

The Na_2O combines in the presence of excess MgO in the ß phase and the ß''' phase ($Na_2O \cdot 4MgO \cdot 15Al_2O_3$) and TiO_2 is found combined whith Al_2O_3 as Al_2TiO_5. With excess TiO_2 the ß phase and Al_2TiO_5 is found. According to the phase rule a liquid can be present but the x ray diffraction method is not sensitive enough to detect small amounts of $Na_2O \cdot Al_2O_3 \cdot 6TiO_2$ which is formed from the liquid phase upon cooling.
With additional MgO (no liquid phase) the grains are small, the sintering density is low and with additional TiO_2 large grains and a higher density are formed.

4. Conclusions

The additions of MgO and TiO_2 have a strong effect on the sintering of alumina, but the presence of small amounts of Na_2O influence considerably the kind of phases formed.
All samples containing excess TiO_2 beyond the stoichiometric composition show enhanced sintering and grain growth, due to the formation of a liquid phase. The Na_2O is combined preferentially in the ß and ß'''phase as soon as excess MgO is present.

More detailed information is found in the doctor thesis of H.D. Kim, September 1987 RWTH Aachen, W. Germany

References

1a) Coble, R.L., " Sintering crystalline solids I. Intermediate and final stage diffusion models", I. Appl. Phys., 32, 787-92, (1961)

b) Coble, R.L., "Sintering crystalline solids. II. Experimental test of diffusion models in powder compacts", Ibid, 32, 793-99, (1961)

c) Paladino, A.E. and Coble, R.L., "Effect of grain boundaries on diffusion-controlled processes in aluminium oxide", ibid, 46, 133-36, (1963)

2a) Reijnen, P., "Non-stoichiometry and sintering of ionic solids", in Reactivity of Solids, Proc. 6th Int. Symp. Reactivity of Solids, P. 99-114, (1968)

b) Reijnen, P. "Sintering behaviour and microstructure of aluminates and ferrites with spinel structure with regard to deviation from stoichiometry", Sci, Ceram., 4, 169-88, (1968)

c) Reijnen, P., "Nonstoichiometry and Sintering in ionic solids", in Problems of Nonstoichiometry, Ed. Rabenau, A., North-Holland Pub. Co., P. 219-38, (1970)

3) Readey, D.W., "Mass transport and sintering in impure ionic solids", I. Am. Ceram. Soc., 49, 366-69, (1966)

4) Reijnen, P., "The impact of sintering theory on practical powder metallurgy", Mater. Sci. Res. 13, 355-75, (1980

5) Reijnen, P and Kim, H.D., " The influence of Na_2O on sintering and creep of alumina doped with MgO and TiO_2", cfi/Ber.DKG. 63 272-79, (1986)

SINTERING OF CaO AND MgO IN THE PRESENCE OF NON-EQUILIBRIUM LIQUID PHASE

E.Kostić, S.J.Kiss and D.Cerović
"Boris Kidrič" Institute of nuclear sciences, Vinča, POB 522,
11001 Belgrade, Yugoslavia

1. Introduction

During studying the sintering process of inactive alumina powders benefitial effect of additives forming equilibrium liquid phase at sintering temperature was found /1,2/.

In this paper we chose such systems within which liquid phase could be formed in the initial period of thermal treatment but under the conditions of chemical equilibrium at sintering temperature it should completely disappear. Only solid solutions sould be present in the sintered materials /3/. Systems CaO with CoO addition as well as MgO with manganese oxide addition which moreover in air atmosphere reacted with gas phase, were chosen. Results on the investigation of additive amount effect on density of sintered samples are presented. With samples having maximum density detailed microstructural as well as structural analysis were performed. Besides, the resistance of sintered materials to basic slag attack was investigated and these results are presented as well.

2. Experimental work

Mn_2O_3 was added to MgO powder "Kemika-Zagreb" by wet homogenization in non-aqueous alcohol. Additive amount was 1,2,3 and 8 wt.%.

To obtaine samples from CaO-CoO system we used $CaCO_3$ with addition of Co-acetate. Co-acetate was introduced through aqueous solution in the amounts of 1,2,4, and 8 wt.%, calculated to CoO. Dried mixtures were thermally treated at 1150°C to decompose carbonate. Product was kept in dessicator.

Green pellets were prepared by pressing mixtures and pure oxide powders for comparison, under the pressure of 70 MPa. Heating of green bodies was performed at 1600 and 1700°C for 2 hours. Samples sintered at 1700°C were slowely cooled, while the ones sintered at 1600°C were air quenched as well as slowely cooled.

Densities and open porosities were determined. The results on densities of samples, sintered at 1700°are given in Table I.

Table 1. Sintered density and open porosity as a function of addition amount at 1700^{o}-2^{h}

Addition amount	CaO		MgO	
(w%)	d (g/cm^3)	OP (%)	d (g/cm^3)	OP (%)
0	1.96	32.5	2.84	20.0
1	2.47	24.1	2.85	19.8
2	2.61	20.7	2.89	15.6
4	3.01	4.3	2.99	10.8
8	3.12	0.1	3.20	9.9

Additional investigations of microstructure, structure and resistance to basic slag attack were performed with samples containing 8% of additives, having maximum densities. Composition of the slag used for the experiments was: 39% CaO, 19%SiO_2, 17%FeO and 20%MnO.

Additive distribution in sintered samples as well as distribution of elements after slag attack were determined by electronprobe microanalysis.

3. Results and Discussion

3.1. Sintering process

On the basis of the experimental results on the investigation of density dependence on additive amount (Table I), it was found that density increased and open porosity decreased with increasing additive amount. Liquid phase was observed under the microscope only on the polished surface of sintered MgO-MnO samples, Fig.1a,1b. With samples on CaO basis fine-grained secondary crystalline phase can be observed, appearing along certain lines. In MgO samples, however, precipitates appear mostly within the grains. On thermally etched surfaces, Fig 2a,2b, it can be noticed that CaO grains are much bigger than in the case of MgO samples.

Mean grain size in CaO is 47 /um, and in MgO 12 /um. Within MgO and CaO grains the presence of precipitated phases can be observed. X-ray analysis of sintered samples obtained at 1600°C with 75 and 81% TD achieved for MgO and CaO respectively, did not prove the equilibrium was reached. Detected reaction pro-

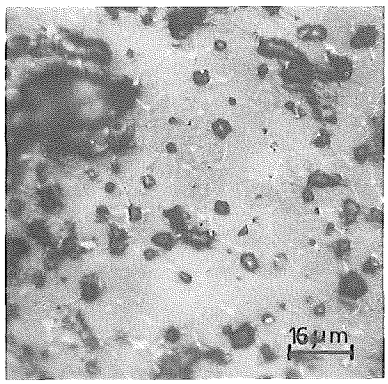

a) MgO(MnO)

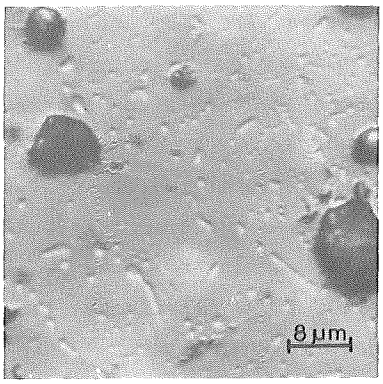

b) CaO(CoO)

Fig.1. Polished surfaces of the samples sintered at 1700°C - 2h

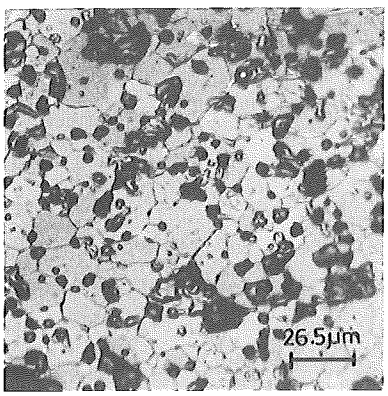

a) MgO(MnO)

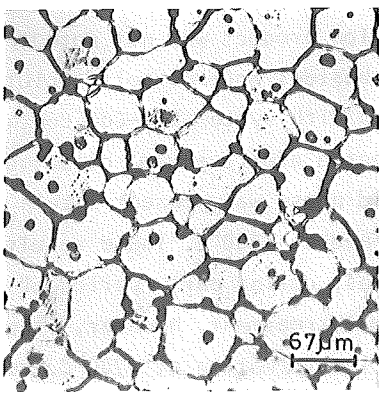

b) CaO(CoO)

Fig.2. Thermally etched surfaces of the samples sintered at 1700°C - 2h

ducts contained nonequilibrium phases for 1600°C. In sintered samples of the both systems at 1700°C only solid solutions phases were detected by X ray analysis. A comparison of X ray data of starting material with that obtained after sintering at 1600 and 1700°C points to the increase MnO content in MgO phase at higher temperature. The same appearence was not noticed with CaO samples obtained under above mention conditions. With the increase of MnO content in MgO phase the lattice spacing of obtained sintered materials was higher according to literature data too /3/.

Electron microprobe analysis of sintered samples MgO with 8w.% MnO was also done. An uniform distribution of MnO across the grain was detected with the increased content of Mn in precipitates within MgO grains, which were observed under the light microscope too. An increased amount of MnO was found in grain boundaries.

The presence of Co was detected both in grains and grain boundaries of CaO samples (Fig.3).

For both investigated systems it is common that additives during heating up period can form nonequilibrium liquid phase with host material. This liquid during following thermal treatment, under equilibrium conditions, disappears with subsequent formation of $(Mg_{1-x}Mn_x)O$ i.e. $(Ca_{1-x}Co_x)O$ solid solutions. Different reasons arise for liquid phase formation: with CaO-CoO system melting occurs by eutectic reaction between solid solutions, while with MgO-MnO system nonequilibrium liquid phase forms by melting either of additive or of the compound which may be found during heating up period.

Obtained results point to formation of $MgO.Mn_2O_3$ during heating up period in MgO-MnO system sintered at 1600°C. With samples sintered at 1700°C the mentioned reaction product was not detected, but nonequilibrium liquid has still been present besides MgO-MnO solid solution.

With system CaO-CoO containing 8% additives at 1600°C, the presence of unreacted additive was detected by x ray, but judging by densification data liquid phase was present within this system. Material without open porosity was obtained at 1700°C. These results prove that liquid phase was present in the samples, during early period of thermal treatment. In later stage of the used thermal treatment, however, liquid phase disappeared due to equilibrium solid solution formation at 1700°C. Detected precipitates result during the cooling period.

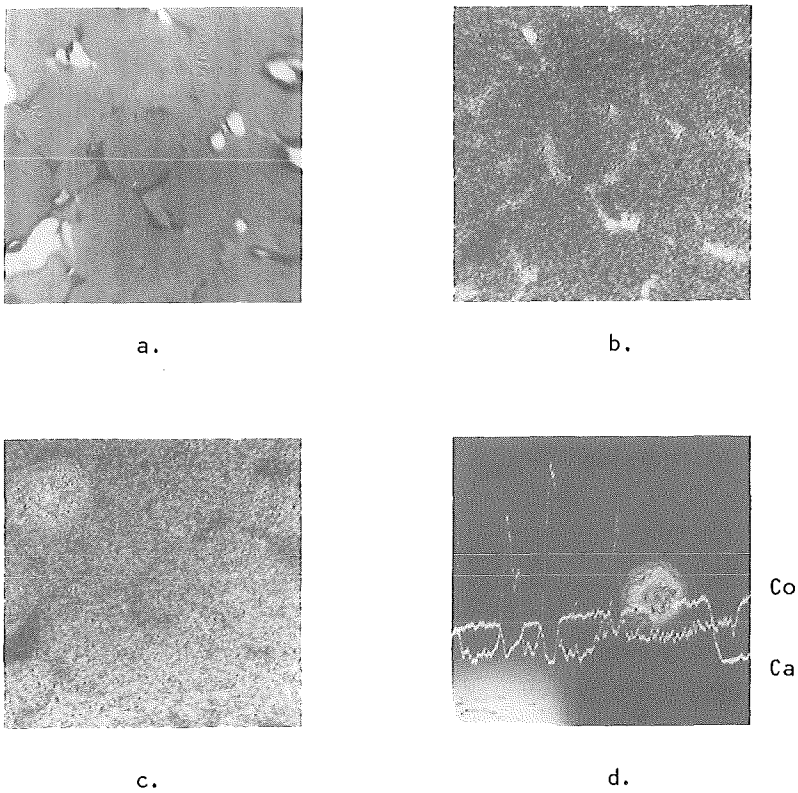

Fig.3. Electron microprobe analysis of sintered sample CaO + 8% CoO (1700°C, 2h), 150x

a - Electron image with the line L

b - Distribution of Co

c - Distribution of Ca

d - Distribution of Co and Ca along the line L

3.2. Interaction of samples sintered with 8% of additives with slag

Interaction between sintered samples and the slag was studied at 1400°C. Cross section of the reaction zones is given in Fig.4a and 4b.

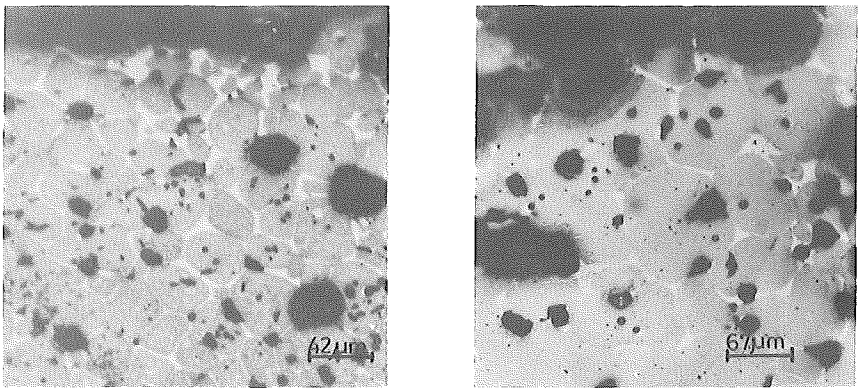

a) MgO-slag b) CaO-slag

Fig.4. Polished cross sections of the reaction zones

Rounding of the grains was observed in both systems in the area close to slag. Grain growth in reaction zones was observed too. Slag penetrates into material along grain boundaries what means that the interaction of slag and boundary phase is more pronounced.

Electron microprobe results showed that Fe was present within MgO grains as well as the increased Mn concentration in them, comparing with starting material. There are spots with extraordinary high Fe and Mn concentrations in MgO grains. Moving away from sample/slag boundary, liquid phase becomes poorer in Fe and Si. These results show that during the interaction Fe and Mn enter solid solution with MgO, forming $(Mg_{1-x-y}Fe_xMn_y)$ O phase. Precipitation of the phase on the basis of Mn and Fe oxides probably takes place on cooling. However, small amounts of CaO and Si were also detected within MgO grains which were close to slag. SiO_2 and CaO presence within MgO grains can only be explained by including of the slag or any silicate reaction product during MgO grain growth in the reaction zone (Fig.5).

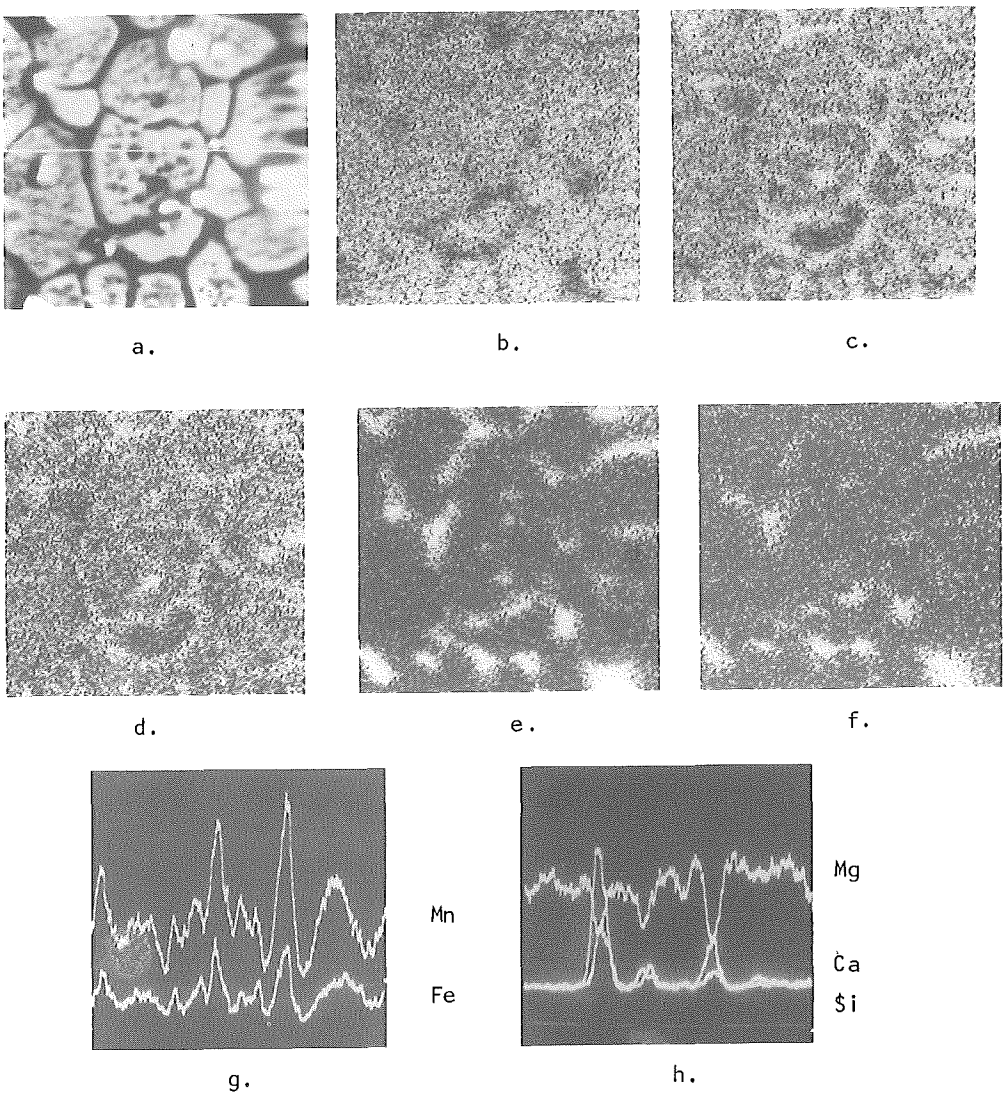

Fig.5. Electron microprobe analysis of reaction zone MgO sample / slag, 450x

Electron image with the line L (a).
Distribution of Mg (b); Mn(c); Fe (d); Ca (e) and Si (f)
Distribution of Mn, Fe (g) and Ca, Si, Mg (h) along the line L.

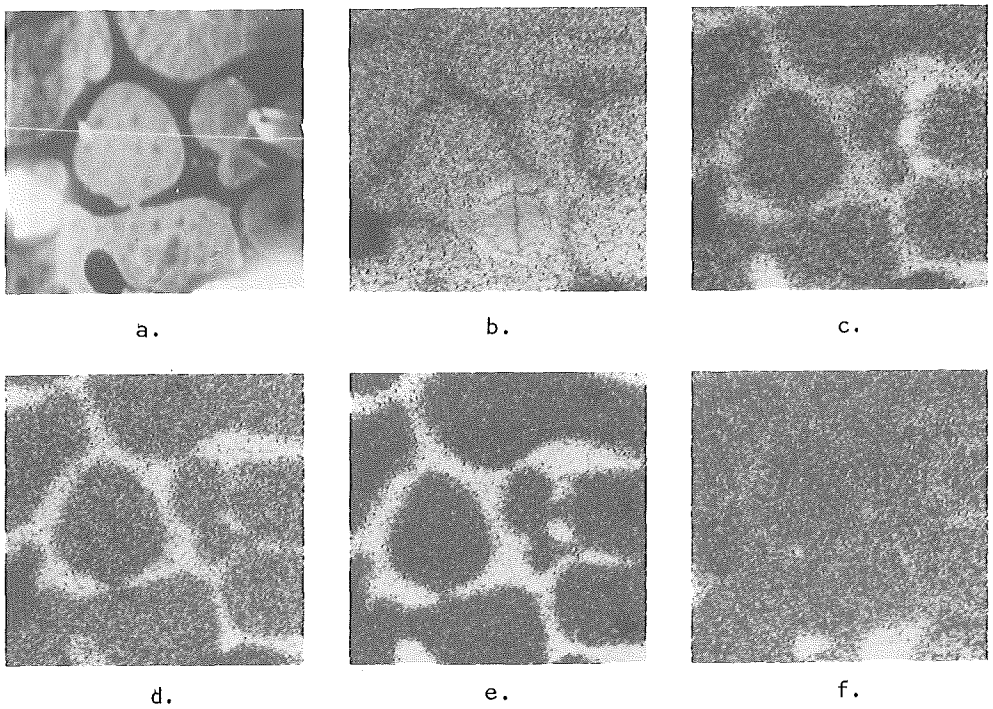

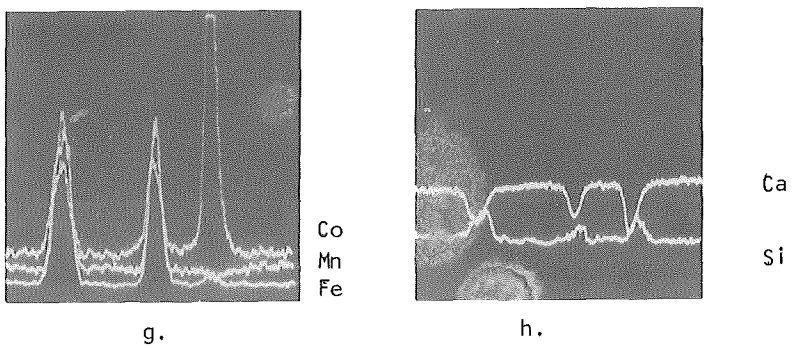

Fig.6. Electron microprobe analysis of reaction zone CaO sample/slag, 300x

Electron image with the line L, (a)
Distribution of Ca (b); Co (c); Mn (d); Fe (e) and Si (f)
Distribution of Co, Mn,Fe (g) and Ca, Si (h) along the line L.

According to electron microprobe analysis results, Fe was present only in the liquid phase of CaO-CoO system, meaning that CaO does not dissolve iron oxide. Some Mn oxide dissolution into CaO grains was observed. Mn concentration in the liquid decreases with moving away of the boundary surface. Liquid phase contains considerable amount of Co which points to dissolution of Co from precipitates situated in the grain boundaries in the liquid phase (Fig.6).

By comparison of changes caused during slag attack on investigated sintered samples we could conclude that CaO sample was more resistant to this attack. This may be due to high amount of CaO which was already present in the used slag.

4. Conclusion

According to obtained data we concluded:

1. The densification process was enhanced in CaO-CoO and MgO-MnO systems through the sintering in the presence of transient liquid phase. After sintering at $1700^{o}C - 2^{h}$ the liquid phase in the CaO-CoO system disappeared but in the MgO-MnO system it was still present.

2. Increased additive amount brought about more pronounced densification. This was more evident in CaO-CoO system in which material without open porosity was attained.

3. Intense grain growth was observed in both investigated cases, being more evident with CaO-CoO system.

4. Sintering process is in both investigated systems accompanied by solid solution formation from which during cooling secondary crystalline phases reprecipitate. These secondary phase were observed under the light microscope. Precipitated phases were very fine-grained and they could not be detected by X-ray.

5. Ceramic material on the basis of CaO was more resistant to basic slag attack.

References

1. Š.Kiš and E.Kostić, Approach to Equilibrium During Reactive Liquid Phase Sintering of Alumina, Interceram, 30 (1981), 4,408
2. E.Kostić, S.Bošković and Š.Kiš, Liquid Phase Sintering of Alumina Base Ceramics, Cont. Inorg.Materials '85, Ed.G.Ondrachek and O.Wöhringer, Pub. KFA, Jülich GmbH, 1985, p.79.
3. N.A.Toropov, V.P.Barzakovskij, V.V.Lapin i N.N.Kurceva, Diagrami sostojanija silikatnih sistem, Nauka, Leningrad, 1969, p.142 i 154.

SINTERING OF Si_3N_4 IN THE PRESENCE OF ADDITIVES FROM Y_2O_3-SiO_2-Al_2O_3 SYSTEM

S.Bošković
"Boris Kidrič" Institute of Nuclear Sciences, POB 522,
lab.170, 11001 Belgrade, Yugoslavia

Sintering process of Si_3N_4 in the presence of liquid phase from Y_2O_3-SiO_2-Al_2O_3 system was investigated. Starting composition of liquid phase was varied according to data in the phase diagram of Y_2O_3-SiO_2-Al_2O_3 system, in order to lower the temperature of liquid formation because it might exibit an influence on the sintering behaviour of Si_3N_4. Densification as well as phase analysis were followed as a function of composition and the amount of liquid phase, both in sintered and in hot pressed samples.

INTRODUCTION

It is known[1] that ceramics of very good quality can be produced using mixtures of Y_2O_3 + Al_2O_3 as sintering aid. However, there are also data[2] showing that very good materials on the basis of Si_3N_4 can be obtained using mixtures Y_2O_3 + SiO_2 and Y_2O_3 + SiO_2 + Al_2O_3 to promote densification, during hot pressing. There are no data on sintering course and the possibility to pressureless sinter above mentioned materials. We undertook this study to investigate the influence of additives from Y_2O_3-SiO_2-Al_2O_3 system on the densification during hot pressing and pressureless sintering of Si_3N_4.

EXPERIMENTAL

Starting α-Si_3N_4 powder, LC 12, Starck production was used. To that powder additives designated an 3, 5 and 8 were added in concentration range 10-20%. Additives composition is given in Table 1.

Homogenization of the host powder with additives was performed in vibratory WC mill, for 2 hours. Isostationally pressed samples under 147 MPa, were sintered and hot pressed at 1780°C.

Table 1: Composition of additives (wt.%)

Additive	Y_2O_3	Al_2O_3	SiO_2	T_m (°C)	Y_2O_3/SiO_2
3	60	16.6	23.4	1600	2,6
5	45	24.5	30.5	1400	1,5
8	32	22.0	46.0	1245	0,7

RESULTS AND DISSCUSION

The common way to enhance densification in series of published papers[3,4,5] is to use Y_2O_3+Al_2O_3 mixture to enhance densification, whereby content of either Y_2O_3 of Al_2O_3 were varied. This variation produces at sintering temperature not only different amount of liquid phase but also produces liquid of different composition. We used as additives compositions of invariant points in the Y_2O_3-SiO_2-Al_2O_3 system (Fig.1) which means that the composition of liquid was the same. It was only its amount which was varied during sintering. SiO_2 content in starting powder ∿3wt.%, was taken into consideration during calculation of additive compositions.

Al_2O_3 is added to Y_2O_3 usually to lower the temperature of liquid formation[3] in order to enhance densification. Al_2O_3, namely brings about viscosity decrease of the liquid.

In our case, as it can be seen, Al_2O_3 amount in additives does not very too much, especially not in additives 5 and 8, while the Y_2O_3/SiO_2 ratio varies from 2,6 to 0,7 respectively for additives 3, 5 and 8. (mol. ratio 0,7-0,2). Melting points of used additives decrease with decreasing Y_2O_3/SiO_2 ratio (i.e. with increasing SiO_2 content), from 1600° to 1345°C. Besides, these additives were chosen because they offer the possibility to keep Y_2O_3 level below 13% even if used in maximum concentration, to avoid formation of Y_2O_3. Si_3N_4 phase, which can be easily oxidized.

Hot pressing of samples having 10% of additives was performed at 1780°C. Densities of hot pressed samples do not differ too much e.q. they are 3,21:3,23 and 3,20 g/cm^3 for 3,5 and 8 additive respectively.

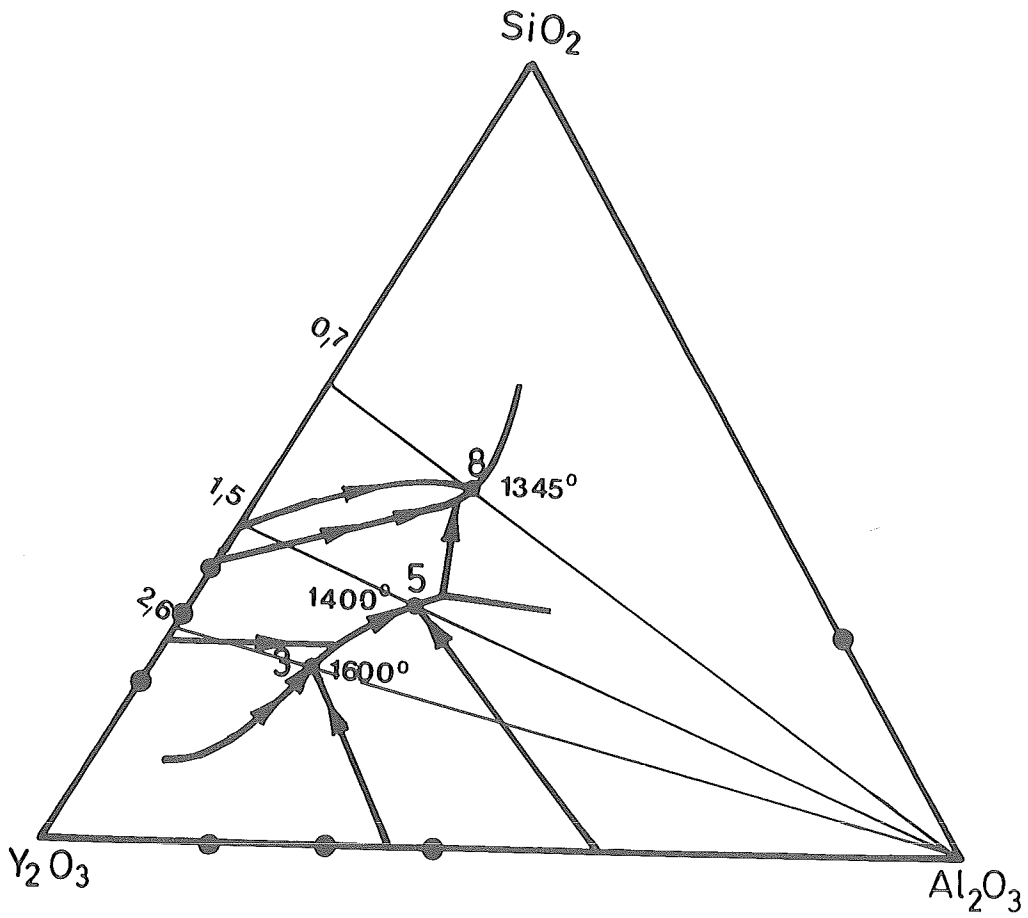

Fig.1. Compositions of additives from Y_2O_3-SiO_2-Al_2O_3 sistem[6]

X ray analysis was used to identify phases present in these samples (Fig.2). Only β-Si_3N_4 was present as a crystalline phase within samples having additives 3 and 5 with Y_2O_3/SiO_2 ratio 2,6-1,5, while with samples containing additive 8 (Y_2O_3/SiO_2 - 0,7), Si_2N_2O was detected in addition. This is to be expected because, composition of additive 8 is very close to Si_3N_4-SiO_2 join and the composition of synthesized ceramics lies within compatibility triangle I (Fig.3).

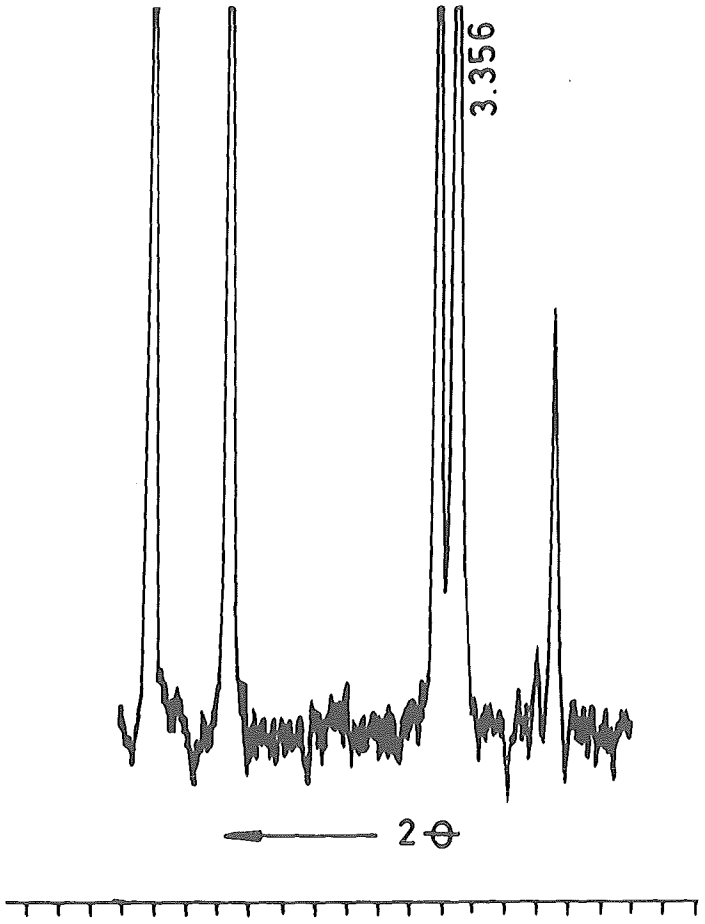

Fig.2. X-ray pattern of hot pressed sample with add.8.

Pressureless sintering was carried out at 1780-1800°C with samples having 10,15 and 20 wt.% of additives. Density change with additive concentration is given in Fig.4. Maximum densities are obtained with additive 4 having the highest melting temperature and the highest Y_2O_3/SiO_2 ratio. With additive 8 having the lowest melting temperature and the lowest Y_2O_3/SiO_2 ratio densities were very low and the open porosity was still present (Table 2). X-ray analysis of sintered samples showed that besides β-Si_3N_4 lines, Y_2SiAlO_5N (N-α-wollastonite) was present. With samples sintered in the presence of additive 8, besides N-α -wol-

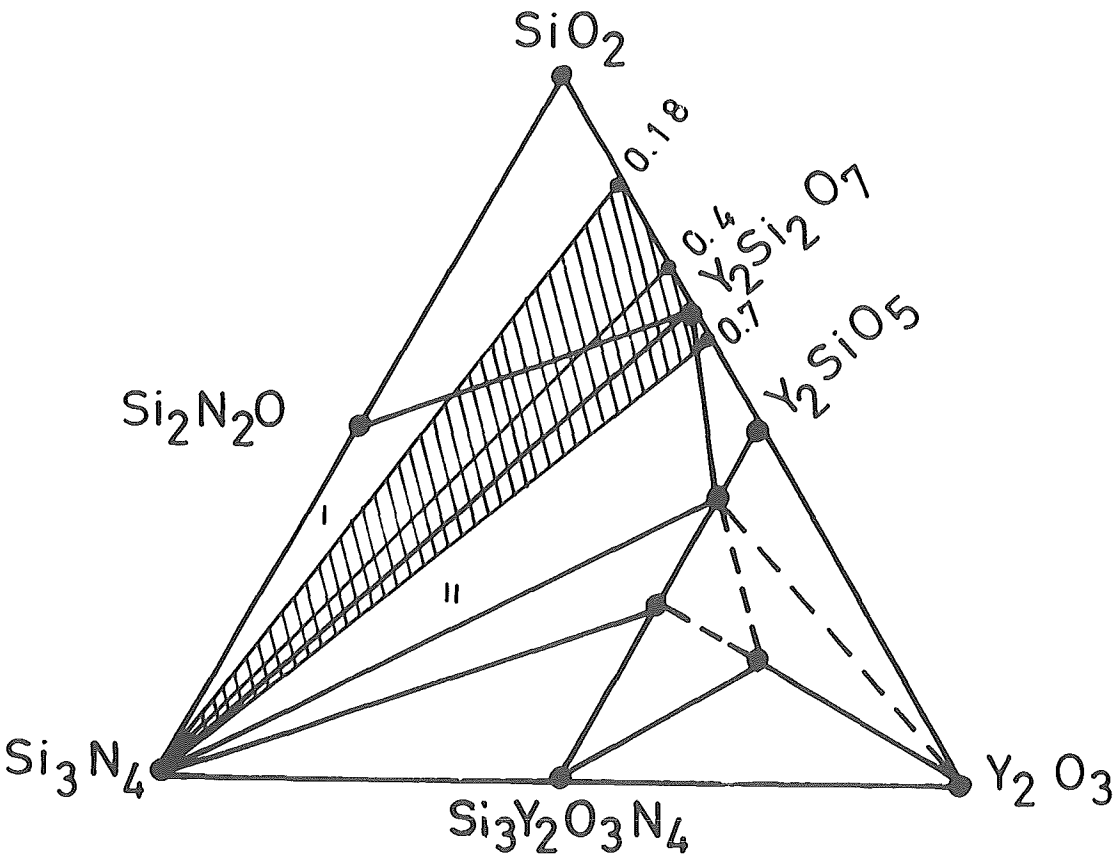

Fig.3. Si_3N_4-SiO_2-Y_2O_3 system[7] with additive range investigated.

lastonite, Si_2N_2O was present. Y_2SiAlO_5N content is very small,(Fig.5) but increases with increasing additive amount in all samples. Bearing in mind that this phase (stable up to 1100°C) crystallizes very easily from these liquids, because its composition lies within liquid phase field, the increase of its concentration with increas of additive amount is not unexpecting.

Si_2N_2O content, too, increases with increasing additive 8 amount. This compound is a reaction product between α-Si_3N_4 and SiO_2 from liquid phase[9]. Densification degree of samples containing additive 8 is low for several reasons. First, reaction of Si_2N_2O involves starting α-Si_3N_4 component and SiO_2 from the liquid phase, which means that liquid amount within these samples decreases due to chemical reaction development. This influences densification as it is well

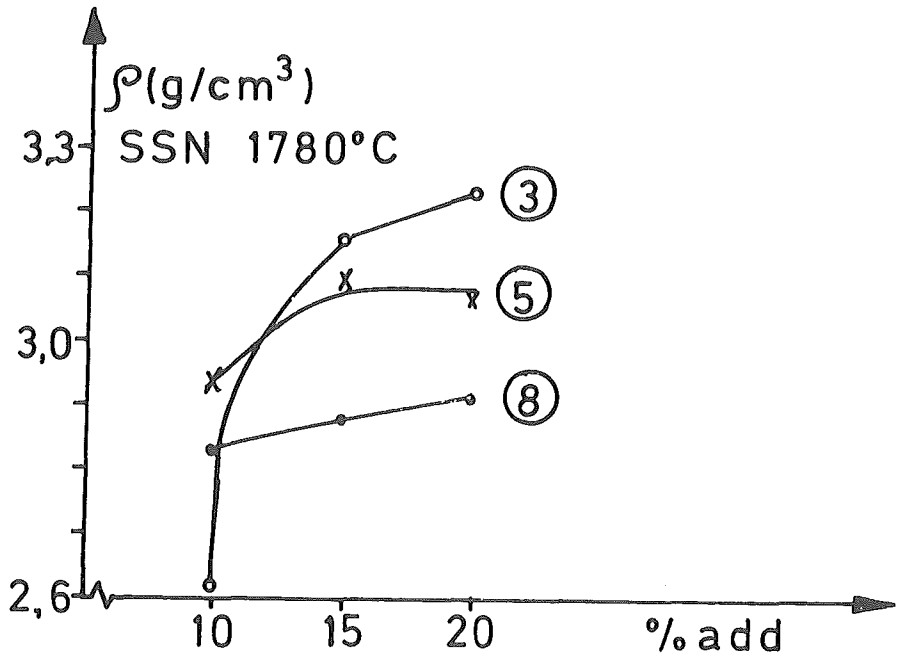

Fig.4. Density change with additive amount variation.

Table 2. Density and open porosity in sintered samples

add. conc.	additives					
	3		5		8	
	ρ	OP	ρ	OP	ρ	OP
10	2,62	13,8	2,93	0,20	2,83	0,7
15	3,16	0	3,08	0	2,88	0,7
20	3,23	0	3,06	0	2,91	0,6

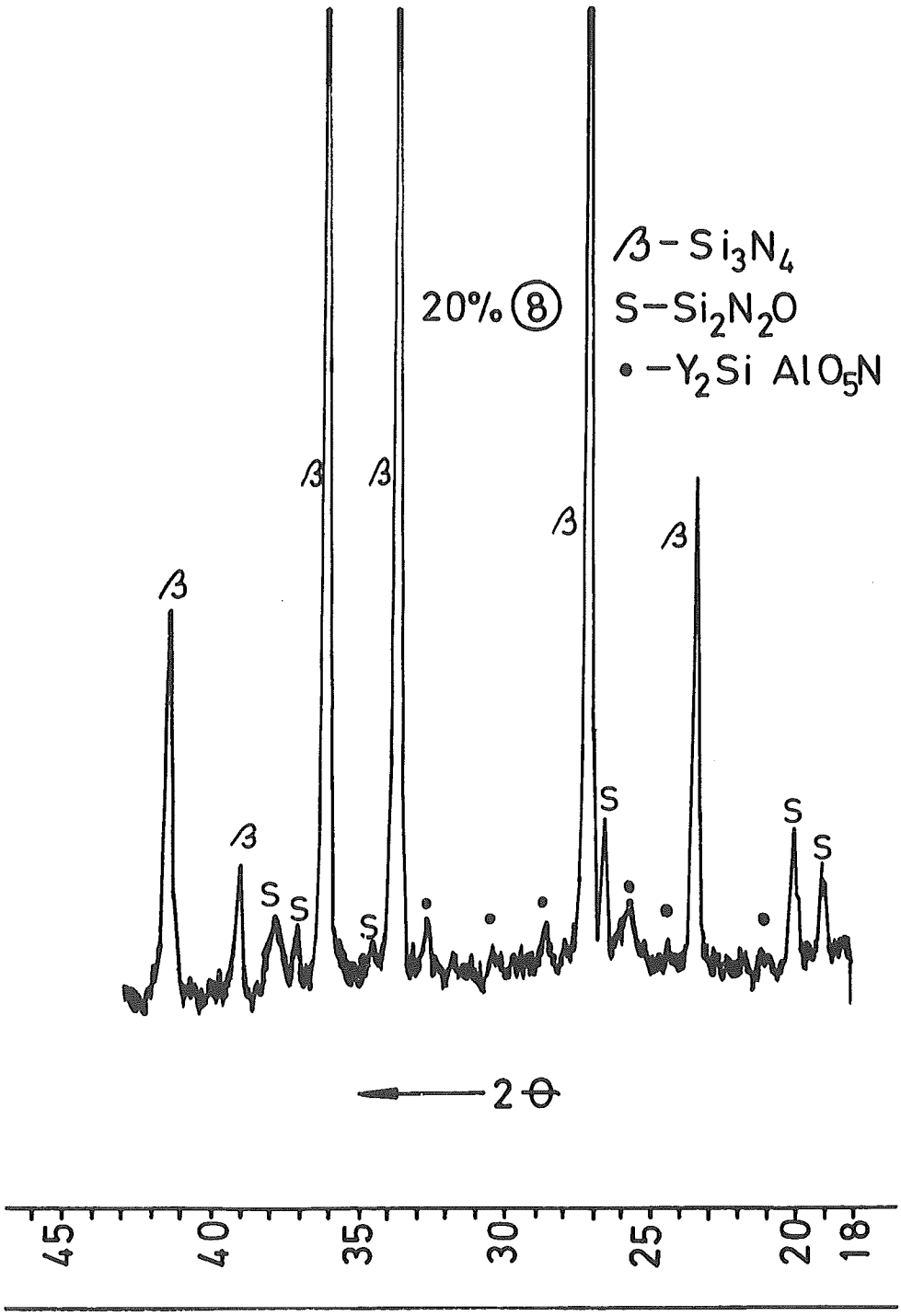

Fig.5. X-ray pattern of sintered sample having 20% add.8.

known. Besides, density of reaction product Si_2N_2O is lower than the one of Si_3N_4 which brings about decrease of sintered samples overall density. Besides, judging by SiO_2 content in the starting additive 8, this liquid may have highest viscosity, independent of its melting point[8].

Properties of the synthesized materials were measured, and summarized in Tab.3. According to these data one can see that materials having good properties can be obtained using additives having Y_2O_3/SiO_2 ratio less than 2,6. Differences in properties of pressureless sintered and hot pressed materials are ovious but it is also evident that good quality material can be obtained under described conditions, using additive 3 as sintering aid.

Table 3. Properties of hot pressed and sintered ceramics

Sample	ρ (g/cm^3)	OP (%)	X-ray	H_v (MPa)	K_{IC} ($MN/m^{3/2}$)
HPSN					
10% 3	3.21	0	-	20050	7.7
10% 5	3.23	0	-	20850	7.6
10% 8	3.20	0	Si_2N_2O	20830	8.0
SSN					
20% 3	3.24	0	Y_2SiAlO_5N	16000	7.6
20% 5	3.06	0	Y_2SiAlO_5N	13300	8.7
20% 8	2.91	0	Y_2SiAlO_5N + Si_2N_2O	10600	7.2

Lower hardness comparing with hot pressing materials are the consequences of high liquid content. Very low hardness of sample containing additive 8 is besides, the concequence of open porosity, as well.

CONCLUSION

These results represent only a part of our investigation on the system described. They show that it is possible to synthesize materials from this system by pressureless sintering procedure. Keeping the Y_2O_3/SiO_2 ratio within 2,6 and 1,5 limit one can synthesize single phase ceramics which can subsequently be heat treated to crystallize the existing glas. Chemical reaction takes place with additive having lower Y_2O_3/SiO_2 ratio, which exhibits negative effect on densification during liquid phase sintering. It was found also, that additive amount can be kept as low as 15% during pressureless sintering because already at 1780°C, open porosity was zero with additives 3 and 5. As far as additive 8 is concerned, one can imagine that good oxidation resistant materials could be obtained with this liquid composition after the condition for preparation of dense ceramics have been found.

REFERENCES

1. K.H.Jack, Non-Oxide technical and Engineering Ceramics, Ed. S.Hempshire, Elsevier Applied Science, London, 1986, p.1.
2. Ceramic Materials for Advanced Heat Engines, Noyes Publications New Jersey, 1985.
3. J. Smith and Quackenbush, Factor in Densification of Oxide and Non Oxide ceramics, 1978, Japan, p.426.
4. C.L.Quackenbush et all. Progress in Nitrogen Ceramics, 1983, p.669.
5. T.Hayashi et al., J.Mat.Sci., 21, (1986), 3501
6. N.A.Toropov et al. Phase diagrams, Vol.3, Nauka, Moscow, 1972.
7. W.Braue et al., Sci of Ceram 13, (1986) p.C1-341.
8. E.Kostić, S.Bošković, Accepted for publication in Interceram, 1987.
9. Z.K.Huang, P.Greil, G.Petzow, Ceramic International Vol.10, N.1, 1984,p.14.

MICROSTRUCTURE DEVELOPMENT IN SiC

T.Fetahagić[1] and D.Kolar[2]

[1]Energoinvest, CIRM, Sarajevo
[2]"Jožef Stefan" Institute, "Edvard Kardelj" University, Ljubljana

1. INTRODUCTION

It has been repeatedly shown that commercially available Acheson type α-SiC powders can be sintered to densities above 95% of theoretical density, provided that certain conditions are fulfilled, i.e. small grain size, controlled impurities and additions of appropriate amounts of boron and carbon (1,2).

It is also known that microstructure of sintered SiC is very sensitive towards amount of additives, sintering temperature and time.

Whereas optimum amount of additives depends on purity and activity of particular SiC powder, it has been generally shown that increase in carbon content results in smaller grain size (1,5), whereas a higher concentration of boron results in coarsening of the grains.

As expected, coarsening of SiC microstructure is also more pronounced at higher sintering temperatures. The temperature influence is less pronounced in α-SiC than in β-SiC where α to β transformation causes large platelike crystals of α-SiC to appear in a matrix of β-SiC at sintering temperatures in excess of 2000^{o}C (1,4). Grain growth in SiC is anisotropic.

In general, SiC is sintered at high temperatures (2000 °C-2100 °C) for a short time (20-30 minutes). It has been shown repeatedly that prolonged sintering does not cause further densification.

The purpose of this investigation was to obtain more data about grain growth and microstructure development in α SiC.

2. EXPERIMENTAL

The starting material was a commercial α SiC-powder (Alpha SiC, Grade A10 Starck). Fisher particle size of this powder was 0,64 μm, and the specific surface area by BET method 14m^2/g. The crystalline phases, identified by X-ray analyses were 6 H and 15 R. Boron or boron carbide and carbon were added as sintering aid. Amorphous B (Ventron) and B_4C (Schuhardt), particle size under 5 μm were directly introduced in the mixtures. Phenolformaldehyde resin solution in absolute alcohol served as a carbon source. After mixing in ethanol, the composition was dried and granulated through a 0,3 mm screen. The green samples (Φ=8, h=10 mm) were pressed in a steel die with the pressure of 400 MPa to green densities of 70 % (2 wt % oleic acid in aceton solution was used as pressing aid).

Sintering was performed in a furnace with a graphite heater in argon atmosphere at temperatures of 2040, 2080, 2100 and 2200 °C. Soaking time at temperature varied from 30 minutes to 8 hours. Densities of sintered samples were determined by Mercury pycnometry. Microstructures of sintered samples were studied after grinding, polishing and etching with Murakami solution. SEM and optical micrographs of samples were analyzed for porosity, grain size and grain size distribution.

Morphological characterization of SiC materials

Quantitative image analyses of SiC photomicrographs were carried out using Kontron MOP/AM 02 instrument. Average grain size and grain size distribution were determined by the lineal intercept method without correction. Anisotropy of grains was expressed as D_{max}/D_{min} ratio, i.e. ratio between the largest and the smallest diameter of analysed grain. For each grain, this value was automatically obtained by the help of appropriate software from measurements of the perimeter and the largest diameter, approximately the grain shape with an ellipse (3).

3. RESULTS AND DISCUSSION

Fig.1 shows the microstructure of 97,8% dense SiC (starting composition SiC A1O, 4% C, 0,3% B) after sintering at 2080°C for 30 minutes. Microstructure is composed of globular (equiaxed) grains, most of them within the range of 5-10 μm. Some large grains, exceeding 20 μm, may also be found and result from large particle size distribution in the starting powder, where particles above 10 μm are present in batches with average Fisher grain size 0,64 μm. Pores are located on grain boundaries.

Fig.2 shows the microstructure of 95,6% dense sample (ρ = 3,07 g/cm^3) of the same composition as Fig.1, after sintering at 2200°C for 30 minutes. Anisotropic grain growth results in large elongated grains. The longest grains exeed in cross section 200 μm in length and are 40-50 μm thick. Average intercept lengths of grains in SiC microstructures sintered at 2040, 2100 and 2200°C were 2.45, 4.28 and 14.78 μm, respectively (Fig.3). Grain growth is anisotropic. Fig.4 shows D_{max}/D_{min} ratio distribution in microstructures. Maximal D_{max}/D_{min} ratio values increase from 4,5 at 2040°C, 5.00 at 2100°C to 9.00 at 2200°C.

Histograms demonstrate increase in heterogeneity and anisotropy with increased grain growth. Pores are located within the large grains and on grain boundaries. Pore shape changed, too. Rounded pores at 2080°C changed to angular at 2200°C (Fig.5). The question arises whether the great difference in the microsttructure of SiC, sintered at 2080 and 2200°C, results from a continuous microstructure development or whether there is a change in grain growth mechanism.

In order to clarify this point, time dependence of microstructure development at various temperatures was investigated.

Fig.6 shows an average intercept length, measured on SiC microstructures after various sintering times at 2040 and 2080°C. Data presented confirm the already reported rapid densification of SiC above 2050°C. At 2080°C, density above 97,5% of the theoretical value is achieved already after 30 minutes at sintering temperature. Prolonged sintering does not cause (bring about) further densification. Lower temperature requires longer sintering time to achieve a high density, however, the average grain size of bodies, sintered at a lower temperature to the same density as bodies sintered at a higher temperature, is approximately twice as higher.

Dependence of average intercept length on sintered density is of the type GP^n = const, which has been observed frequently and supported theoretically (6) (Fig.7). Critical density for rapid grain growth is about 97%. However, this relationship holds only up to some limiting grain size which depends on temperature.

Grain growth in SiC is strongly anisotropic also at lower sintering temperatures, as demonstrated by histograms in Fig.8. D_{max}/D_{min} ratio increases with prolonged sintering from 1.43 to 2.66 at 2040°C and from 1.32 to 3.15 at 2080°C, respectively.

Although the comparison of mechanical properties with microstructural features was not the aim of this research, preliminary measurements confirmed negative influence of large grain size on bending strength of sintered SiC bodies.

4. CONCLUSIONS

Activated α-SiC powders with Boron and Carbon additives sinter rapidly to high densities. Typically, densities above 97% of the theoretical value may be achieved at 2080 °C in less than 30 minutes.

Microstructures of such samples consist of isometric grains with average grain size around 4 μm. The remaining pores are located at grain boundaries. After the high density is achieved, rapid grain growth takes place with linear time dependence and grain size distribution curve broadens. Above the average 10 μm size, the grain growth rate levels off and large pores appear within the grains.

5. REFERENCES

1. W.Bocker, H.Hausner. Powder Met. Int. 10, 2 87-89 (1978)
2. Y.Murata, R.H.Smoak, Densification of Silicon Carbide by the Addition of BN, BP and B C and Correlation to their Solid Solubilities, p.p. 382-399 in Factors in Densification and Sintering of Oxide and Non-Oxide Ceramics (ed Somiya Saito), Assoc. Sci. Doc. Inform., Tokyo, 1978
3. Underwood E.E., Quantitative Stereology, Adddison Wesley (1970)

4. S.Shinozaki, K.R.Knsman, Mat. Sci. Res. 11, pp. 641-652 641-652 in Processing of Crystalline Ceramics, ed by H.Palmour III, R.F. Davis and T.M.Hare, Plenum New York, 1978
5. T.Mizrah, M.Hoffmann, L.Gauckler, Preessureless Sintering of α-SiC, Powder Met. Int. 16, 5 217-220 (1984)
6. G.C.Kuczynski, Statistical Theory of Sintering, Z.Metallkunde, 67, 606-610 (1976)

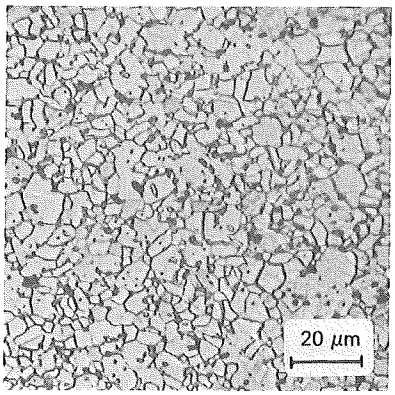

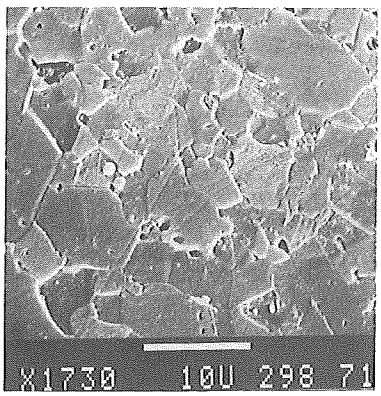

Fig. 1: Microstructure of 97,8% dense α SiC (SiC A10 + 0,5% B_4C + 4,0% C), sintered 30 min. at 2080°C

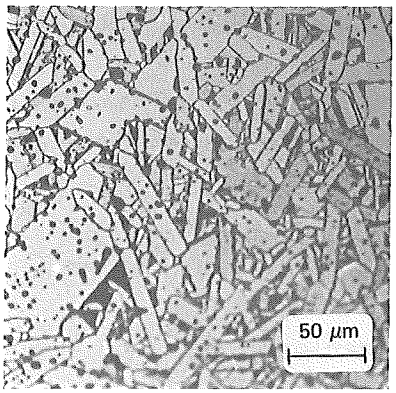

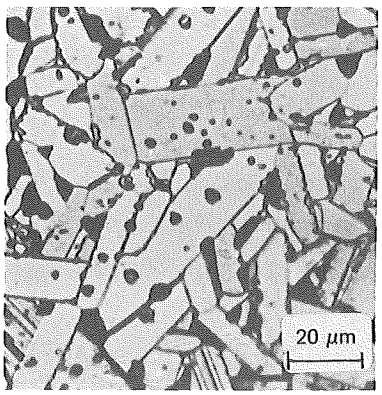

Fig. 2: Microstructure of 95,6% dense α SiC (SiC A10 + 0,5% B_4C + 4,0% C), sintered 30 min at 2200°C

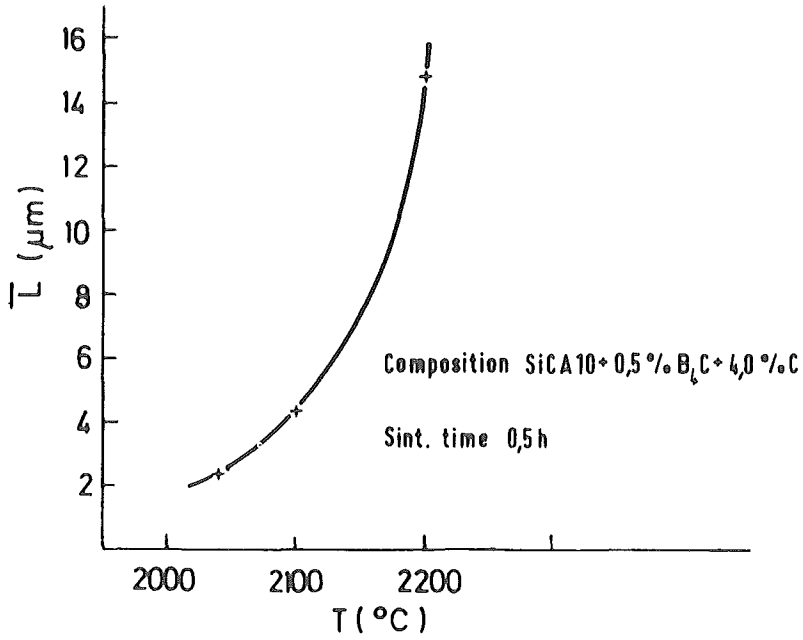

Fig.3: The effect of sintering temperature on the linear intercept length of SiC grains

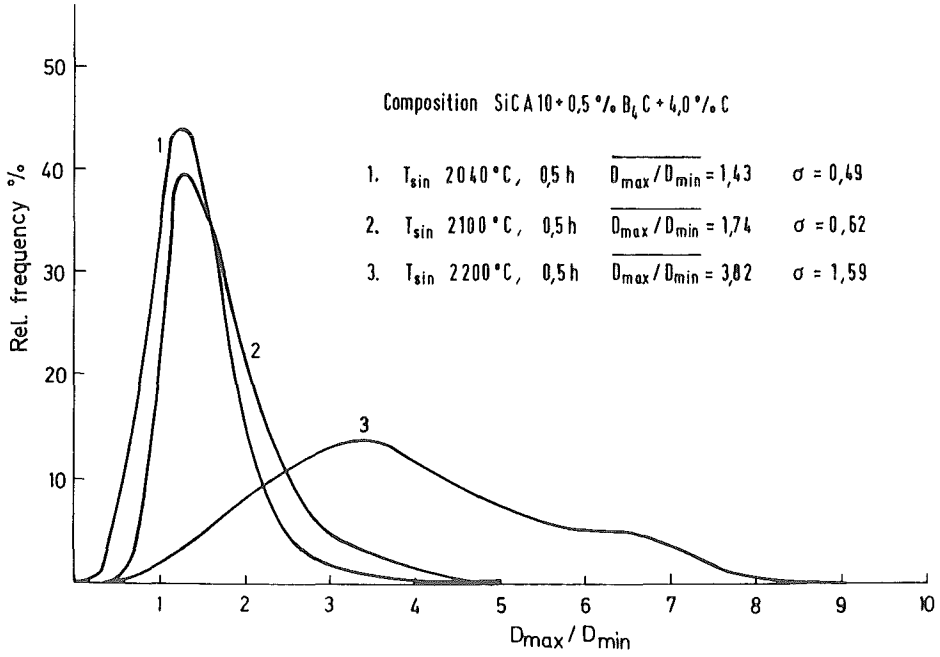

Fig.4: Influence of sintering temperature on D_{max}/D_{min} ratio distirbution in SiC

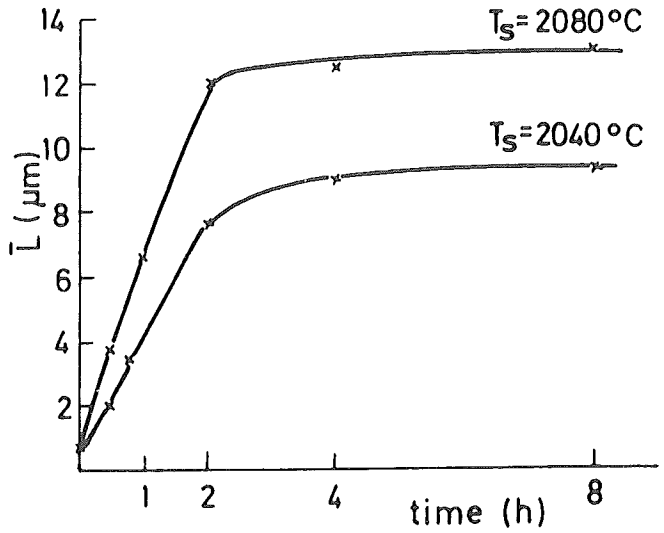

Comp. SiC A10+0,5 % B_4C+4,0 %C				
T (h)	T_S 2040		T_S 2080	
	ρ (g/cm³)	% t.g.	ρ (g/cm³)	% t.g.
0,5	2,97	92,52	3,16	98,44
0,75	3,12	97,19	—	—
1,0	—	—	3,16	98,44
2,0	3,15	98,13	3,16	98,44
4,0	3,14	97,81	3,15	98,13
8,0	3,14	97,81	3,14	97,81

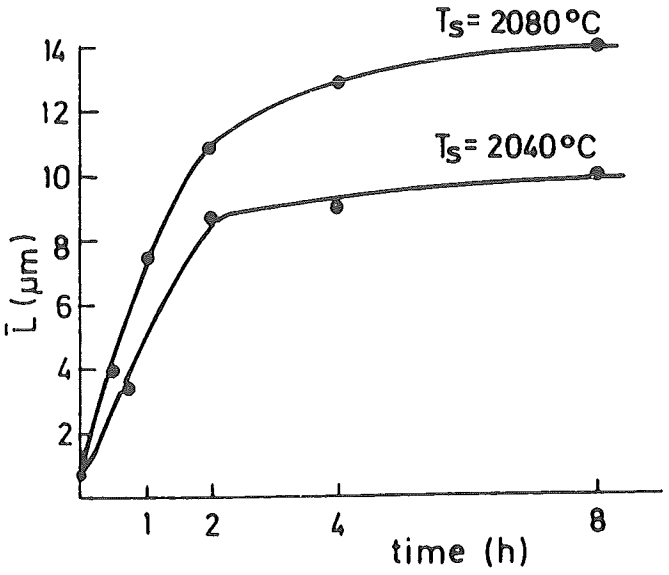

Comp. SiC A10+0,3 % B+4,0 % C				
T (h)	T_S 2040		T_S 2080	
	ρ (g/cm³)	% t.g.	ρ (g/cm³)	% t.g.
0,5	2,98	92,83	3,14	97,81
0,75	3,10	—	—	—
1,0	—	—	3,15	98,13
2,0	3,15	98,44	3,15	98,13
4,0	3,15	98,13	3,14	97,81
8,0	3,15	98,13	3,13	97,50

Fig. 6. Increase of the linear intercept length of SiC grains with sintering time

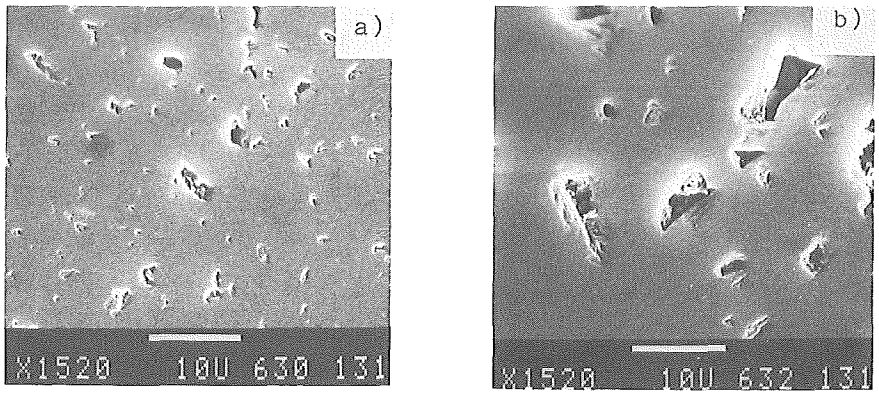

Fig. 5: Influence of sintering temperature on pore growth in SiC, sintered 30 minutes a) at 2080°C, b) at 2200°C

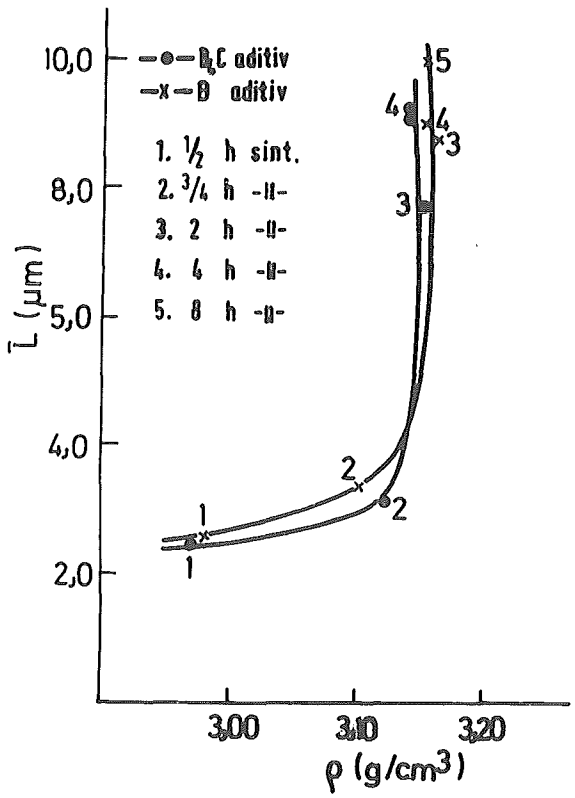

Fig. 7: Linear intercept length vs. sintered density in SiC

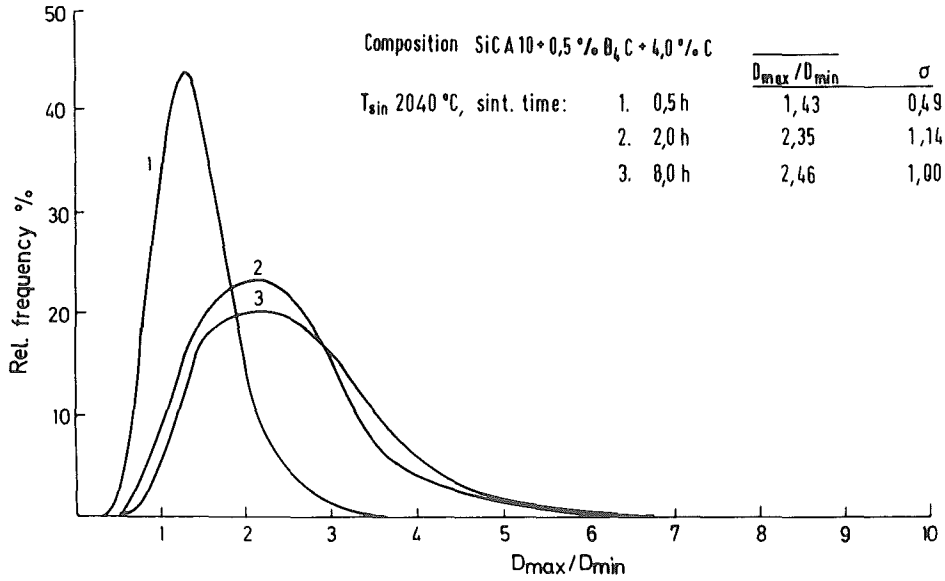

a)

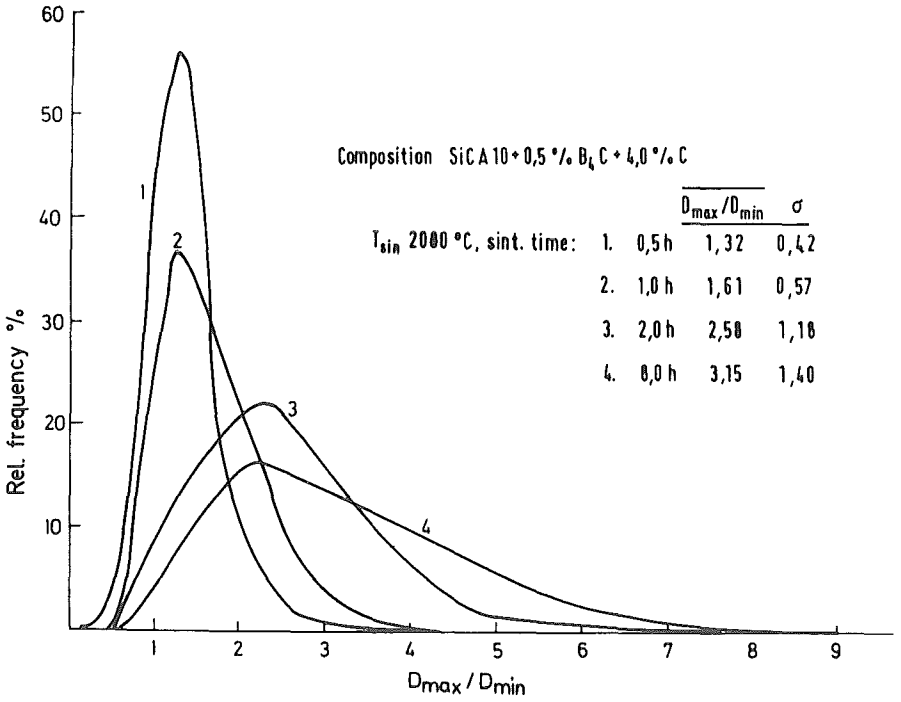

b)

Fig.8: Influence of sintering time on D_{max}/D_{min} ratio distribution
a) T_{sin} = 2040°C, b) T_{sin} = 2080°C

C E R A M I C S

MECHANICAL PROPERTIES

Fatigue in Ceramics

Georg Grathwohl
Universität Karlsruhe
Institut für Keramik im Maschinenbau
Institut für Werkstoffkunde II

Abstract

Fatigue in ceramics is a well-known problem; however, the specific cyclic fatigue phenomena are often not recognized. A short literature review is followed by the presentation of two methods of experimental analysis to identify true cyclic fatigue behaviour in contrast with static fatigue phenomena. Results are demonstrated for different ceramic materials and suggestions are made for the interpretation on the basis of possible cyclic fatigue mechanisms.

Introduction

For many applications in mechanical engineering the high-performance ceramics have to withstand cyclic mechanical stresses. Examples are given by ceramic components for automotive applications as piston pins, valves and rocker arm inserts. The durability of ceramic components is often determined by the occurrence of slow crack growth: microstructural defects as cracks or pores can be generated during service and grow until they reach their critical extension leading to the failure of the component. The relevant fatigue properties are often investigated in static or dynamic experiments where the strength of ceramic specimens is measured in dependence of time under load or as a function of the loading rate, resp. Static fatigue and dynamic fatigue properties are manifested by these methods. However, the fatigue behaviour due to the cyclic nature of the applied stresses is not evaluated by this way.

The question arises wether the fatigue behaviour of ceramics is influenced by the function of the applied stress. Is there a specific cyclic fatigue mechanism which is not to be activated in a static experiment. The existence of such a cyclic fatigue mechanism can be denied for an isotropic linear-elastic material, what was proved e.g. for soda lime glass [1]. The same situation was claimed to be valid also for polycrystalline ceramics such as Al_2O_3 [1], although a frequency effect was observed experimentally [2] leading to the suggestion of a specific cyclic fatigue mechanism. In various studies [3-7] the cyclic fatigue behaviour of Al_2O_3 was studied. Durability limits were found at 56 - 60 % of the short-term strength. At increasing temperatures a corrosion process including water vapour attack gets more important; thus, the kinetic of the stress corrosion process misses the influence of the type of the stress function. Nonoxide ceramics were mostly investigated at high temperatures, where the situation again may be changed due to the activation of plastic flow processes, creep and other time dependent microstructural processes. A compilation of fatigue data of ceramics is being elaborated [8].

The aim of this study concentrates on the phenomenon of cyclic fatigue at room temperature. Several ceramic materials were investigated by different methods in order to identify true cyclic fatigue processes.

Experimental results and analysis

Cyclic fatigue is investigated by the evaluation of Wöhler-type curves or other relations between the number of cycles to failure N_B and cyclic loading parameters. An example is presented in Fig. 1, where RBSN-specimens (RBSN = reaction bonded silicon nitride) are tested in cyclic flexural fatigue experiments with variable upper stress σ_0 and constant lower stress σ_u = 60 MPa. At the higher stress levels ($\sigma_0 \geq 240$ MPa) all tested specimens failed before the limit $N^* = 10^5$ was reached. At σ_0 = 200 MPa 13 specimens (out of 20 tested at this level) survived.

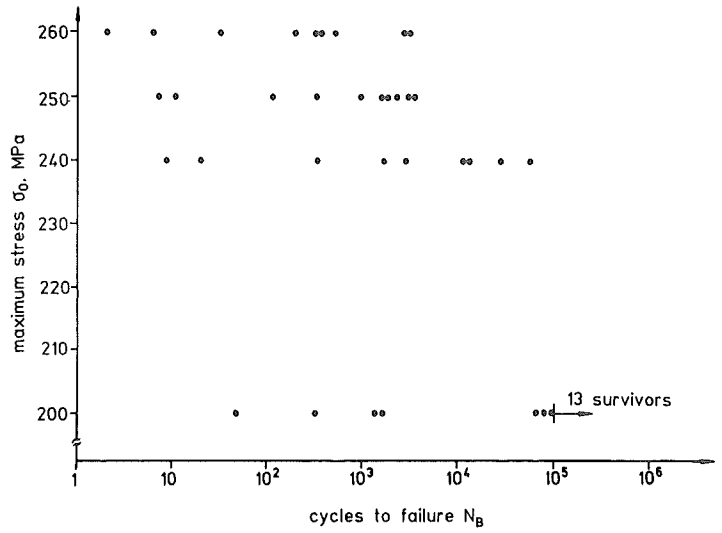

Fig. 1: Cyclic fatigue of RBSN in flexural tests, σ_u = 60 MPa

In order to decide whether these results can be understood in terms of slow crack growth only, the crack growth parameters were determined in separate dynamic tests. On the basis of the equation for slow crack growth $v = A \cdot K_I^n$, (v = crack growth rate, K_I = stress intensity factor, A, n = crack growth rate parameters) the relation between stressing rate $\dot{\sigma}$ and transverse rupture strength σ_B is given [9]

$$\sigma_B^{n+1} = B \cdot \sigma_c^{n-2} (n+1) \dot{\sigma} \qquad (1)$$

with B = const. and σ_c = original strength (without slow crack growth).
In Fig. 2 the Weibull-distributions of the strength of the RBSN-material determined at three different stressing rates $\dot{\sigma}$ are presented. Lower stressing rates lead to lower strength values.

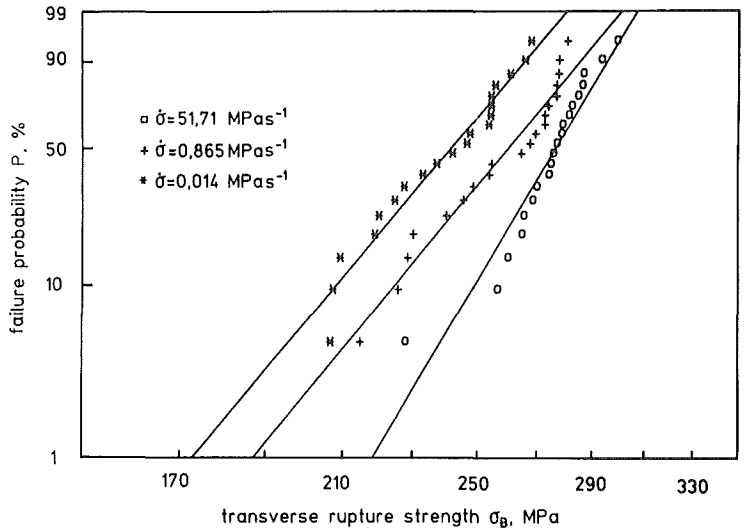

Fig. 2: Effect of stressing rate $\dot{\sigma}$ on the Weibull-distribution of the transverse rupture strength of RBSN

Expressing the inital strength σ_c as Weibull function the equation (1) can be written as

$$ln\ ln\frac{1}{1-P} = \frac{m(n+1)}{n-2} ln\ \sigma_B - \frac{m}{n-2} ln\dot{\sigma} + const. \qquad (2)$$

In an iterative regression analysis [9] or simplified by making use of (1) and introducing the mean strength $\bar{\sigma}$ or median strength $\tilde{\sigma}$ (Tab. 1) the parameter of slow crack growth can be evaluated. For the investigated RBSN-material n-values are found in the range between 50 and 64 [9].

Tab. 1: Characteristic strength values and Weibull modulus m of strength distributions of RBSN at various stressing rates

$\dot{\sigma}$ [MPa/s]	$\bar{\sigma}$ [MPa]	$\tilde{\sigma}$ [MPa]	m
$14 \cdot 10^{-3}$	239,7	244,6	12,6
0,865	257,4	266,4	13,0
51,71	275,1	277,2	17,7

Under the assumption that the crack extension is controlled by identical mechanisms under static and cyclic stress conditions, the lifetime under cyclic stresses can be calculated on the basis of the determined crack growth parameters. This may be done, e. g. for a stress function

$$\sigma(t) = \sigma_m + \sigma_a \cdot \sin \omega t \tag{3}$$

by introduction of a function g [1]

$$g(n, \sigma_a/\sigma_m) = \frac{1}{\lambda} \int_0^{\lambda} \left(\frac{\sigma(t)}{\sigma_m} \right)^n dt \tag{4}$$

with σ_a = stress amplitude
σ_m = mean stress
ω = frequency
λ = period.

This function (4) can be used for various stress functions, values for g are available from the literature [1]. Thus, the ratio between the lifetime under static stress t_B and under cyclic stress t_c can be calculated

$$\frac{t_c}{t_B} = \left(\frac{\sigma_n}{\sigma_m} \right)^n \cdot g^{-1} \tag{5}$$

In Tab. 2 the calculated number of cycles to failure N_C is compared with the experimentally measured mean number of cycles to failure N_B as presented in Fig. 1 for RBSN.

Tab. 2: Comparison of the measured mean numbers of cycles to failure N_B for RBSN with the calculated values N_C

σ_0 [MPa]	σ_u [MPa]	N_B	N_C
260	60	$8{,}3 \cdot 10^2$	$34{,}7 \div 66{,}6 \cdot 10^2$
250	60	$1{,}2 \cdot 10^3$	$25{,}3 \div 85{,}8 \cdot 10^3$
240	60	$1{,}25 \cdot 10^4$	$19{,}9 \div 116 \cdot 10^4$
200	60	$3{,}64 \cdot 10^4$*	---

*without survivors (see Fig. 1)

It is shown, that the measured values N_B represent lower numbers compared with the calculation at all levels of stress. The conclusion is drawn that the assumption of an identical fatigue mechanism in static and cyclic tests is not valid for this material. Cyclic stressing leads to an acceleration of the fatigue kinetics. Similar results are also found in a test serie with partially stabilized ZrO_2 [8].

In order to determine directly the differential crack growth behaviour in static and cyclic tests, bending specimens were loaded after they have been predammaged by a natural crack using the bridge indentation method [10,11]. These precracked specimens were then loaded, while the crack extension could be measured directly by an electric potential method. For this purpose the ceramic bending bars were coated by an electrical conducting TiC-layer [11]. By this method the different crack growth rates and the actual loading parameters (stress intensity factors) could be measured in the static and in the cyclic case. It was particularly interesting to determine the threshold condition for the crack extension in both cases.

This is illustrated in Fig. 3 by an experiment with a hot-pressed Si_3N_4-specimen. In the first part of the experiment the specimen was loaded in a flexural swelling mode with an upper stress intensity factor $K_{IS} = 3.6\ MPa\sqrt{m}$. After a period of very slow crack growth the crack growth rate increased very strongly during the first 10^5 cycles.

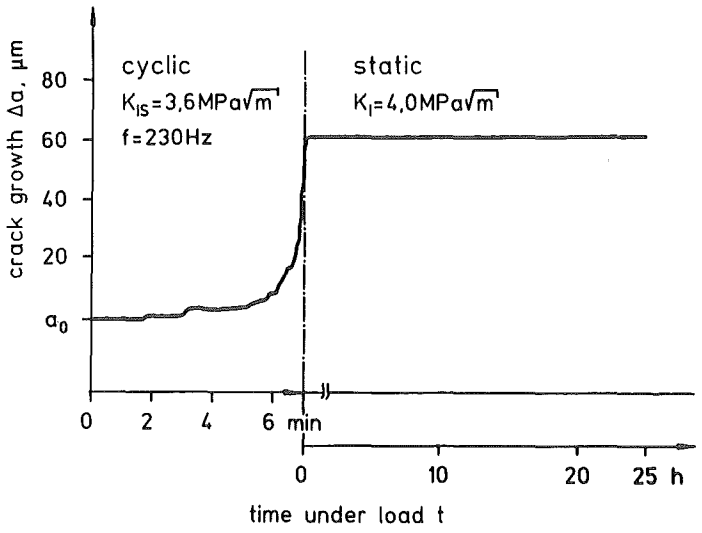

Fig. 3: Crack extension in a hot-pressed Si_3N_4-specimen at sinusoidal stressing condition in a flexural swelling test (K_{IS} = 3,6 MPa $\sqrt{m}$) and following crack stop at a static but higher stress intensity factor K_I = 4,0 MPa $\sqrt{m}$

The specimen was then loaded by a constant but higher stress intensity factor K_I = 4,0 MP$\sqrt{m}$; in this second part of the test no crack extension occured over 25 h. By this and similar experiments [11] it became evident, that the investigated ceramic materials can sustain a substantially higher load without any crack extension in the static tests than in the cyclic loading mode. The actual threshold values for crack extension were determined for this particular material as 5,3 and 3,5 MPa$\sqrt{m}$ in the static and in the cyclic case, resp. [11]. In materials with higher fracture toughness even larger differences between these threshold values were determined.

Conclusion

It has to be concluded, that specific cyclic fatigue mechanisms are active when ceramic components are loaded in a cyclic manner. There may further be a difference in the crack growth behaviour between a situation with alternating stresses and swelling (e.g. tension-tension) stresses. The relevant fatigue mechanisms are not completely understood so far and quantitative relations between the controlling microstructural features and the parameters of crack growth kinetics have to be elaborated. Some principles of the cyclic induced crack extension have been indentified [8]. These basic mechanisms include the participation of residual stresses which enable an additional crack growth step during the unloading phase. It has further to be realised that some features responsible for the R-curve behaviour of many new ceramics may suffer in a particular way by cyclic stresses.. The idea that the compression half-cycle in a tension-compression cycle is irrelevant for crack extension in ceramics may be wrong. There are several features which can explain additional crack growth when samples are loaded by alternating stresses: Elastic mismatch between both crack sides due to anisotropic stress relief during crack growth, asperities in the crack surfaces and volume increase e.g. due to phase transformation in the crack zone. All these phenomena have to be disqualified in an isotropic homogeneous, amorphous microstructure which is free of internal defects like glass; cyclic fatigue is then not observed. As ceramic microstructures differ from this state, cyclic fatigue becomes a problem with increasing importance.

References

[1] A. G. Evans, E. R. Fuller;
Crack propagation in ceramic materials under cyclic loading conditions.
Metall. Transact. 5 (1974) 27 - 33.

[2] D. A. Krohn, D.P.H. Hasselman;
Static and cyclic fatigue behavior of a polycrystalline alumina.
J. Am . Ceram. Soc. 55 (1972) 208 - 211.

[3] C.P. Chen, W.J. Knapp;
Fatigue fracture of an alumina ceramic at several temperatures.
in: Fracture Mechanics of Ceramics 2,

R.C. Bradt, D.P.H. Hasselman, F.F. Lange (Eds.)
Plenum, New York (1973) 691 - 707.

[4] W. Dawihl, E. Dörre, G. Altmeyer;
Über die Druck- und Biegeschwellfestigkeit von Sinterkörpern auf Aluminiumoxidgrundlage.
Ber. Dt. Keram. Ges. 42 (1965) 243 - 266.

[5] W. Dawihl, G. Altmeyer, E. Dörre;
Statische und dynamische Dauerfestigkeit von Aluminiumoxid-Sinterkörpern.
Z. Werkstofftech. 8 (1977) 328 - 330.

[6] L.S. Williams;
Fatigue and ceramics. in: Mechanical properties of engineering ceramics,
W. Wurth Kriegel, Hayne Palmour III (Eds.)
Interscience Publ. New York, London (1961) 245 - 302.

[7] S.J. Acquaviva, R. Chait;
Static and cyclic fatigue of ceramic materials. AMMRC TR 72 - 9, 1972

[8] G. Grathwohl;
Ermüdung von Keramik unter Schwingbeanspruchung. in preparation.

[9] G. Grathwohl, H. Iwanek, F. Porz, F. Thümmler;
Festigkeit und Lebensdauer von reaktionsgesintertem Siliziumnitrid bei verschiedenartiger thermischer und mechanischer Beanspruchung. in: Keramische Komponenten für Fahrzeug-Gasturbinen II, W. Bunk, M. Böhmer (Hrsg.) Springer-Verlag Berlin (1981) 357 - 384.

[10] R. Warren; B. Johannesson;
Creation of stable cracks in hardmetals using "bridge" indentation.
Powder Met. 27 (1984) 25 - 29.

[11] N. Brugger;
Zum Verhalten von Rissen in keramischen Werkstoffen unter statischer, langsam ansteigender und schwingender Belastung.
Dissertation, Universität Karlsruhe, 1987.

Young's modulus of elasticity: Measured values for multiphase metals and their calculation via the bound concept

G.Ondracek, Karlsruhe, and D.Windelberg, Hannover

1. Introduction

A *quantitative* description of microstructure should allow the formulation of a *quantitative* relationship between the manufacture and service parameters (or "material properties"). But it is much easier to examine the microstructure to establish the relationship between

manufacture and microstructure

and

microstructure and properties

(fig. 1).

Young's modulus will now be investigated.

The aim of these investigations is to forecast elastic properties. The theory should make it possible to produce "tailored" materials. For this many "principles" can be used - but not all of these are suitable (fig. 2).

MANUFACTURE	MICROSTRUCTURE	PROPERTIES
CASTING	SOLID STATE PHYS.	FIELD PROPERTIES
temperarure	Cristallographic	electr. cond.
rate of	TOPOLOGICAL	thermal cond.
freezing	number of	magn. perm.
pressure	grains	dielectric
atmosphere	edges	ELASTIC PROP.
	corners	elongation
POWDER	STEREOLOGICAL	Young's m.
size	grain volume	
mix speed	grain weight	permeability
temperature	connectivity	
atmosphere	isotropy	thermal shock

fig. 1

"FIRST PRINCIPLES"	
RELATIONS between	
• manufacture & microstructure	
• microstructur & properties	
lead to	
• manufacture & properties	
METHODS:	
MATHEMATICAL:	function of degree ≤ 3
STATISTICAL:	correlations
PHYSICAL	bound-concept
	model-concept
CHEMICAL:	process

fig. 2

It will be shown, that - in case of the bound concept - the statistical "Monte-Carlo-Method" leads to mathematical difficulties and inappropriate calculations, whereas mathematical analysis gives good results. In case of the model concept an iterative calculation of the Young's modulus is introduced.

2. Bound concept

Assuming a two-phase-material, physical arguments (especially those of HASHIN 1966) lead to "bound equations": All measured Young's moduli for concentrations between 0 and 100 % had to lie between the upper and the lower bounds (fig. 3+4).

In general bound equations of two-phase-material ("bound equations of first order") are applicable on field and elastic properties.

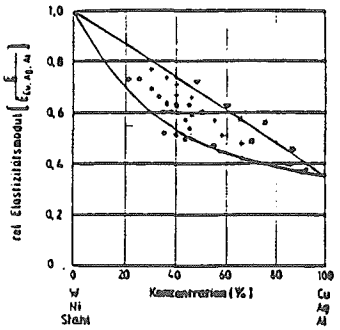

fig. 3

These equations are independent of material constants and give boundaries for the production of new materials in order to substitute less available or ecologically suspicious constituents in conventional engineering materials :

□ If the concentration cannot be changed, the upper or lower boundary of the property is usually attainable by variation the manufacturing parameters.

□ If the manufactoring parameters cannot be changed, the optimal material can be usually obtained by varying the concentration.

The area between upper und lower boundary must be minimalised to get an exact forecast.
For two-phased and isotropic material it is possible to calculate "second order boundary equations" (fig. 5): The area between upper and lower boundary is a little bit smaller than before. - But these equations depend on material constants, which means:
For two Poisson ratios ν_1 and ν_2 of the phases Π_1 resp. Π_2 and two Young's moduli E_1 resp. E_2 with $V := E_1 / E_2$ there exist two functions

$$E_{II} = E_{II}(V, \nu_1, \nu_2, c) \text{ and } E^{II} = E^{II}(V, \nu_1, \nu_2, c),$$

such that for a concentration c with $0 \leq c \leq 1$ the Young's modulus $E(c)$ can be determined by

$$E_{II} \leq E(c) \leq E^{II} \quad \text{for all c with } 0 \leq c \leq 1.$$

For example, the values of the Young's modulus of isotropic Al_3Ni-Al material lies within the expected range (fig. 6).

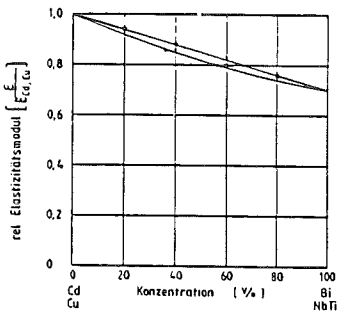

fig. 4

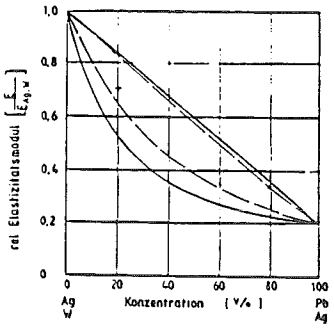

fig. 5

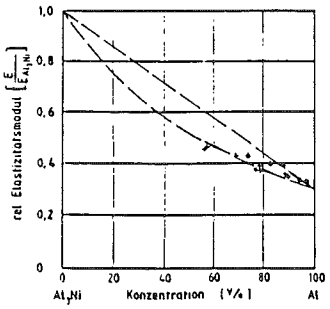

fig. 6

3. Problem of elimination

For general forecast of Young's modulus-values it is often not easy to determine the Poisson-ratios.Therefore it is necessary to eliminate the Poisson-ratios of the two phases. A greater area between the upper and lower boundary - but smaller than in case of first order - will be the result.
For eliminate the Poisson ratios ν_1 and ν_2 a necessary condition is the existence of pairs

$$MIN(V) := (\nu_{1,min}, \nu_{2,min})$$

and

$$MAX(V) := (\nu_{1,max}, \nu_{2,max})$$

with

$$E_{II}(V, \nu_{1,min}, \nu_{2,min}, c) \leq E_{II}(V, \nu_1, \nu_2, c) \quad \text{for all possible } V, \nu_1, \nu_2, c$$

and

$$E^{II}(V, \nu_{1,max}, \nu_{2,max}, c) \leq E^{II}(V, \nu_1, \nu_2, c) \quad \text{for all possible } V, \nu_1, \nu_2, c.$$

Limitations of coefficients are given by

$$V \geq 0 \quad , \quad 0 \leq c \leq 1 \quad , \quad 0 \leq \nu_1 , \nu_2 \leq 0.5$$

Here two methods for elimination are shown: a statistical and a mathematical concept. The methods lead to different results, but the statistical result is included in the mathematical result.

4. Statistical method

The Monte-Carlo-Method leads to four values for each ratio $V = E_1 / E_2$ of Young's moduli:

$$\nu_{1,min} = \nu_{1,min}(V) \quad , \quad \nu_{2,min} = \nu_{2,min}(V)$$
$$\nu_{1,max} = \nu_{1,max}(V) \quad , \quad \nu_{2,max} = \nu_{2,max}(V).$$

The points $MIN(V) = (\nu_{1,min} , \nu_{2,min})$ for different values of V are shown in fig. 7.

For each V there are unique determined points MIN (V) and MAX (V). The distribution of these points are at least functions which can be fittied in. But there is no sense in fitting points wich are calculated by the Monte-Carlo-Method only.

5. Mathematical method

By methods of 2-dimensional analysis it is well known that the partial derivations

$$D_1 := \partial E_{II}(V , \nu_1 , \nu_2 , c) / \partial \nu_1$$

and

$$D_2 := \partial E_{II}(V , \nu_1 , \nu_2 , c) / \partial \nu_2$$

vanish, if points (ν_1 , ν_2) are extremal to E_{II}. D_1 and D_2 are functions of sixth order in ν_1 and ν_2. Therefore this problem is solvable by geometric surfaces: For each V with $V < 1$ there exists not only one point MIN (V), but one of these points is included in all sets MIN(V).
Let c = 0.5. For each V the geometric surface D_1 as a function of (ν_1, ν_2) will cut the x-y-plane. In general, also D_2 will cut the x-y-plane. So at least the points of a cut of these three surfaces are the points MIN (V) (fig. 8).

Nevertheless the function E_{II} itself is interpretable as a geometric surface - for c=0.5 and V=constant (fig. 9). - It is easily be shown that the point MAX (V) is a absolute - and not a relative - maximum.

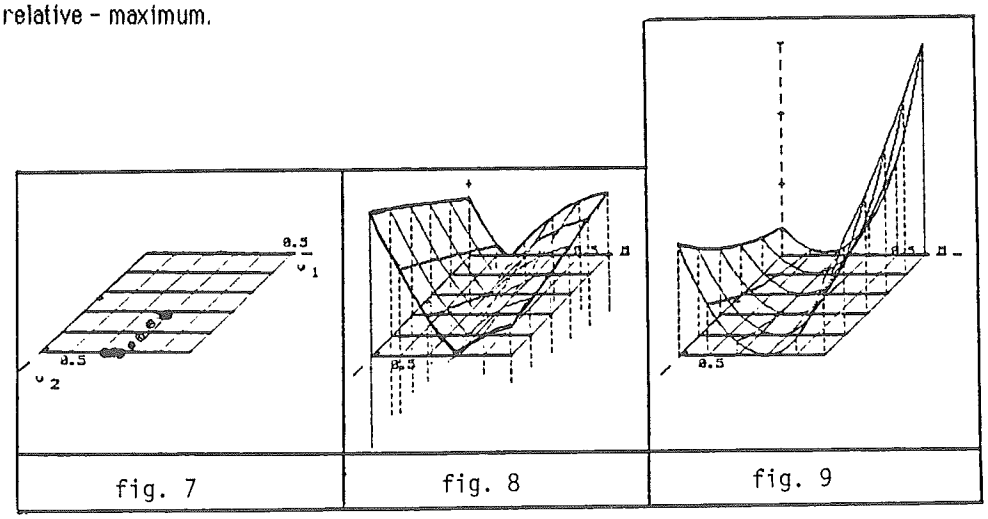

fig. 7 fig. 8 fig. 9

The points MIN(V) and MAX(V) can be chosen independently of V in this case.
Inserting the coordinates of these points in the boundary equations of second order results in equations characterizing the upper and the lower bounds of $\mathbf{E}(c)$ which have been tested in many materials (fig. 10).

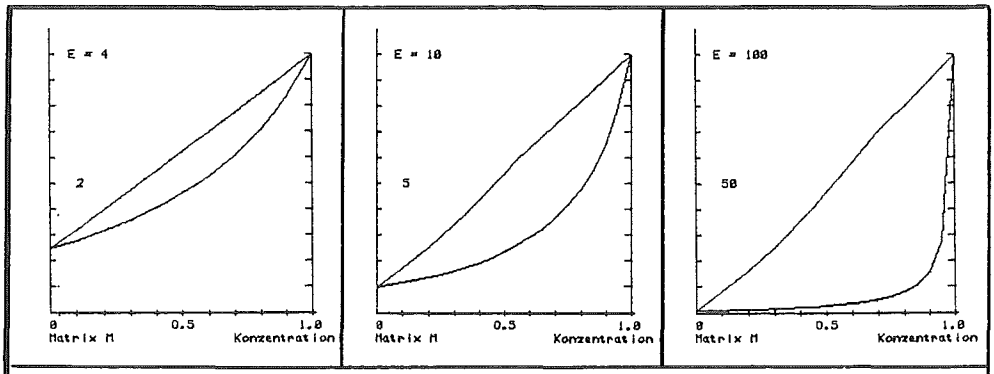

fig. 10

6. Model concept

For a "good" forecast *exact* values of $\mathbf{E}(c)$ are necessary (fig. 11).
Therefore the last step in this investigation is the introduction of the "model concept" (fig. 12).

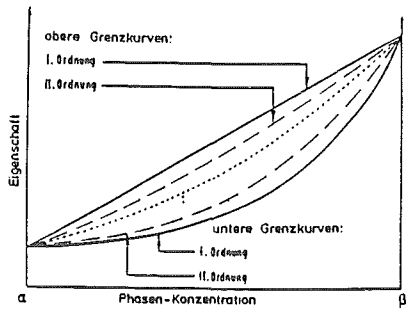

fig. 11

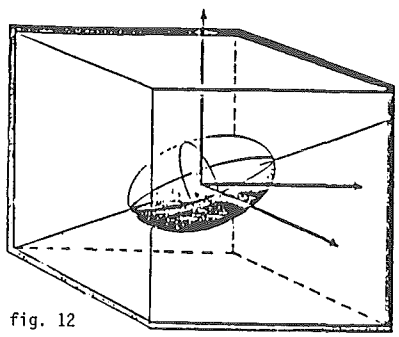

fig. 12

A two-phased material of phases Π_1 and Π_2 can be mathematically modelled by an ellipsoid of rotation, built of phase Π_2, which is embedded in a cube of phase Π_1.
This embedded ellipsoid has - in the model of the material -

- a defined ratio x/z of axis
- a defined angle δ between field direction F and axis of rotation
- a defined angle φ in the x-y-plane.

Looking at increasing concentrations - that is at different sizes of the embedded ellipsoid in fig. 12 -, there exists a bound concentration c_b, such that the ellipsoid lies within the cube if the concentration c is lower than c_b. (For instance: If $x/z = 3/4$, $\delta = 90^0$, $\varphi = 0^0$, then $c_b \approx 30\%$.)

Previous calculations of $E(c)$ show that, for this concentration c_b, Young's modulus for becomes infinite (fig 13).

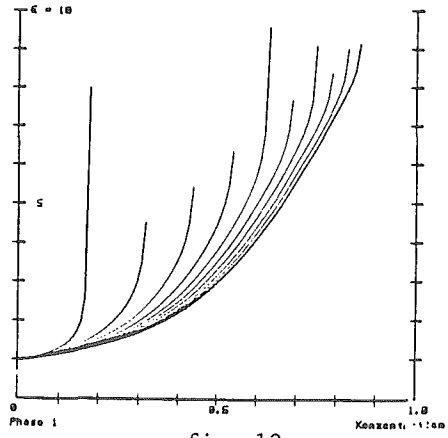

fig. 13

But engineering together with mathematical calculations lead to a method of substitution as shown in the six "steps" of fig. 14 [for $c_b > 30\%$]:

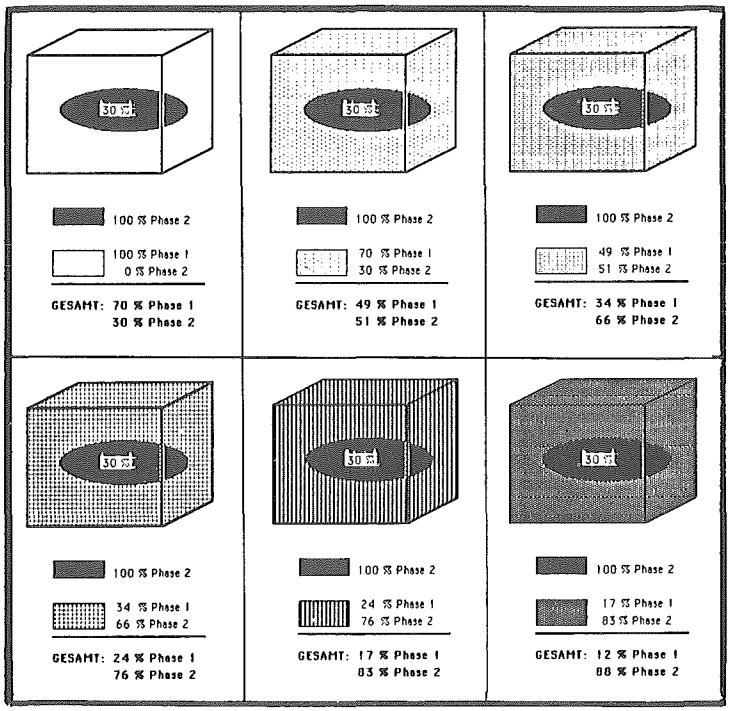

fig. 14

In all steps the embedded ellipsoid is of phase Π_2 and fills out 30 % of the cube, but the cube is made from different materials M in different steps:
In the first step M is of phase Π_1: so it is possible to calculate $E(30\%)$.

In the second step M is made of 30% of phase Π_2 and 70% of phase Π_1; calculations start at $E(30\%)$ - interpreted as $E^{(2)}(0\%)$. Calculations are possible up to $E^{(2)}(30\%) = E(51\%)$, and so on.

The result of these steps of calculation is shown in fig. 15.

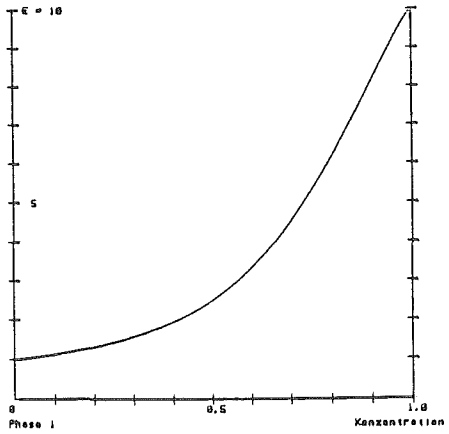

fig. 15

7. References:

Hashin,Z. :
Elasticity of Ceramic Systems.
In: Fulrath,R.M.; Pask, J.A.(eds.):
Ceramic Microstructures: their Analysis, Significance and Production .
Proc. of the 3rd Berkeley Int. Mechanics Conf. June 1966J

Ondracek, G:
Microstructure-thermomechanical-property correlations of two-phaseand porous materials
Materials Chemistry and Physics, 15 (1986), 281

STRENGTHENING OF SILICON NITRIDE CERAMICS

Peter Greil

Max-Planck-Institut für Metallforschung, Institut für Werkstoffwissenschaften, Pulvermetallurgisches Laboratorium, Heisenbergstraße 5, D-7000 Stuttgart 80,

Silicon nitride ceramics are being developed for their unique combination of excellent thermo-mechanical properties. Recently, silicon nitride is used as bearings and wear resistant components at high temperatures, in steel manufacturing and in heat engines. Increasing temperature and loading conditions, however, require the thermo-mechanical properties and their reliability to be improved.

Basic concepts for strengthening and toughening of sintered silicon nitride ceramics are solid solution formation, devitrification, phase transformation and particulate and whisker dispersion. The thermodynamic, kinetic and mechanical aspects of these concepts will be discussed. Recent results of property evaluation in strengthened silicon nitride ceramics will demonstrate the present state-of-the-art of this decisive class of materials and its role for the solution of future technological problems in the use of silicon nitride ceramics.

Introduction

High technology ceramics based on silicon nitride and oxynitrides are being developed for their unique combination of excellent material properties even at high temperature, Table I. Depending on the specific material composition as well as the manufacturing process a variety of 'silicon nitride alloys' exists which already entered important fields of thermo-mechanical application such as in steel manufacturing, as bearings, cutting tools and wear resistant components at high temperatures, and for structural components in heat engines. Silicon nitride plays a decisive role in the realization of new technologies as for example the development of a small gas turbine (T_{gas} ~ 1400°C) for passenger cars. Increasing temperature and loading conditions, however, require the thermo-mechanical properties to be improved. Large scale production of components with a more complex shape requires an increased reliability in order to minimize the failure probability during service. Figure 1 clearly demonstrates the benefit of improved Weibull modulus for the reduction of mean strength for various failure probabilities under a 500 MPa load.

Pressureless sintering of ultrafine silicon nitride powders containing sintering additives in a nitrogen atmosphere at 1700-1900°C is mainly used to obtain dense compacts. Almost all silicon nitride materials are therefore characterized by a multiphase microstructure, i.e. they contain at least two phases or more, a crystalline matrix phase and a secondary glassy or crystalline grain boundary phase. Thus microstructure homogenization for reliability and property improvement mainly implies a secondary phase control during powder processing, sintering and subsequent heat treatment. The secondary phase determines densification kinetics, pore and grain growth during sintering, and the chemical as well as mechanical properties of the dense material. Local stress and strain fields due to variation of thermal and elastic properties in a heterogeneous, multiphase microstructure are supposed to exert a particular influence on material damage in the low temperature regime whereas chemical gradients, impurities and in particular amorphous grain boundary phases dominate the high temperature material failure above 1000°C (1).

As a consequence, microstructure toughening and high temperature strengthening concepts involving solid solution formation, devitrification, transformation toughening and whisker reinforcement have been developed to increase the thermo-mechanical properties of Si_3N_4 and their reliability.

Controlled processing of multiphase Si_3N_4 materials

Chemical and physical homogeneity of the multiphase Si_3N_4 powder mixtures is a necessary condition to achieve dense and defect free microstructures upon pressureless sintering, gas pressure sintering or hipping. The homogeneous distribution of small quantities of sintering additives or higher contents of dispersed particles or whiskers in submicron Si_3N_4 powders can only be achieved in a liquid suspension. The stabilization of multiphase colloidal systems by electrolytes and surface active organic molecules is required in order to avoid differential flocculation and agglomeration of separate powder components, which otherwhise will form defects in the compacted material. The chemically homogeneous powder suspension allows the minimization of the total additive content and hence the reduction of grain boundary amorphous phase, which is particularly deleterious to the high temperature properties.

Introduction of impurity particles larger than 10-50 µm has to be excluded by using clean, dust controlled processing environment. Figure 2 shows the flaw size-rupture strength relationship for a semicircular surface crack geometry. Increased rupture strength is possible by reducing the flaw size (I) or raising the fracture toughness K_{Ic} (II). While the flaw size distribution is primarily dependent on the powder processing and sintering technology, toughening involves the controlled formation of special microstructures in order to dissipate elastic energy from a crack front. Composite microstructures of a Si_3N_4 matrix containing dispersed particles, whiskers or crystalline inclusions

precipitated from the glassy grain boundary phase ("in situ composites") have already demonstrated their potential for distinct toughness increase as will be shown later.

During sintering, a liquid is formed by reaction of the additives with the surface active oxygen on the Si_3N_4 particles, which promotes densification via a solution-diffusion-reprecipitation process. Pore elimination can be accelerated and grain growth retarded by appropriate heating procedure during sintering (Rate Controlled Sintering) (2), resulting in an improved microstructure homogeneity. Figure 3 shows the heating and density curve of a rate controlled sintered silicon nitride material which results in the pore free microstructure shown in fig. 4, although the total time of sintering was equivalent to the conventionally sintered, porous material.

Silicon nitride powders require sintering additives to obtain a rapid and complete densification. These additives, mainly Al_2O_3, Y_2O_3, MgO and AlN (3), form an oxynitride based liquid phase upon heating which accelerates all material transport processes. During cooling from the sintering temperature, part of this liquid phase remains as a glassy phase in the grain boundaries. At high temperatures, the intergranular glassy phase accelerates slow crack growth and grain boundary sliding resulting in an early failure of the sintered materials under load.

High temperature strengthening and toughening

Solid solution formation offers the possibility to produce dense materials with only minor amount of residual glassy phase by dissolution of a transient liquid phase in the Si_3N_4 crystal structure. Si_3N_4 forms a solid solution in the α- and ß-type crystal structure. ß-Si_3N_4-ss with Al and O as dissolved atoms is characterized by a constant cation to anion ratio of 3 to 4 and is represented by the general formula ß-$Si_{6-x}Al_xO_xN_{8-x}$ with $x < 4.2$ (4). Even though theoretically no glassy phase should remain in thermodynamic equilibrium, only in the system Si-Be-O-N almost glassy phase free solid solution ceramics have been formed (5).

While solid solution in the crystal structure of ß-Si_3N_4 has been found to exist only in a few Me-Si-O-N systems with Me = Al, Be, Ga, Ge (3), solid solution formation of α-Si_3N_4 was reported to exist in some quinary Me-Si-Al-O-N systems with Me = Mg, Ca, Y, Li, Mn and rare earth elements (6, 7). Table II summarizes some of the important quaternary and quinary Si-N-containing systems with the solid solutions found. Due to the localization of the creep deformation on the intergranular glassy phase improved creep resistance and stress rupture time will result in the solid solution ceramics with reduced amount of glassy phase and increased grain size. Figure 5 shows the temperature dependence of creep strain rate for various Si_3N_4 and Si_3N_4 solid solution ceramics.

Significant improvement of high-temperature rupture strength was achieved by devitrification of an appropriate grain boundary phase. Based on thermodynamic equilibrium between silicon nitride and a refractory second phase a variety of new and well defined material compositions has been investigated, Table III.

Controlled crystallization occurs between the glass transition temperatur T_g and the melting point T_m of the crystalline phase. The important rate controlling parameters are the viscosity of the melt/glass, crystallography, impurities and nucleants. The crystallizing phases are predominantly high symmetric oxides ($MgAl_2O_4$, $Y_3Al_5O_{12}$) or oxynitrides ($Y_{10}(SiO_4)_6N_2$, $Y_4Si_2O_7N_2$, $YSiO_2N$, $Y_2Si_3O_3N_4$) with crystal structures isomorphous to apatite, cuspidine, wollastonite or melilite. The heterogeneous nucleation of the precipitating phase can be promoted by a nucleant like TiO_2 or an epitaxial grain boundary orientation to a Si_3N_4 matrix grain. Figure 6 shows schematically the lattice

coincidence of $Y_3Al_5O_{12}$ growing on ß-Si_5AlON_7 with a grain boundary orientation of $(2130)_{ß}//(211)_{(Y3Al5O12)}$ (8). No residual amorphous layer could be observed in this grain boundary even by high resolution TEM.

After devitrification of the amorphous grain boundary phase creep resistance and high-temperature rupture strength is improved. Figure 7 shows the temperature dependence of the modulus of rupture of a reaction sintered Si_3N_4+$Y_3Al_5O_{12}$ ceramic after devitrification treatment. A distinct retention of the room temperature strength occurs as compared to the glassy phase rich material. During cooling thermal induced elastic misfit stresses develop at the boundary between the silicon matrix and the inclusion. Depending on the ratio of the thermal expansion considerable tensile or compressive stresses can be generated, which are supposed to interact with a propagating crack at low temperatures (9). Hence toughening can be induced by the controlled crystallization in an "in situ" composite material, as for example in Si_3N_4 solid solution ceramics with $LiAlSi_2O_6$ inclusions, where extensive crack deflection results in a 40 % toughness increment compared to the glass containing material (10).

While solid solution formation and devitrification involve a high temperature reaction process to form the "in situ composites", Si_3N_4 matrix composites containing particulates, whiskers or fibres have to be compacted without an inclusion-matrix reaction during high temperature sintering. The dispersed inclusions are incorporated in the Si_3N_4 matrix material to improve microstructure homogeneity and to generate a controlled stress-strain field in the matrix in order to make the crack propagation and matrix deformation more difficult. BN additions have been made to Si_3N_4 to improve the thermal shock and electrical behavior (11). ZrO_2-particulate-reinforced Si_3N_4 has been formed by hot pressing Si_3N_4 or Sialons with zyttrite (12). The resultant equiaxed microstructure contained cubic zirconia grains located at the grain boundaries of the ß-Si_3N_4 grains. The strength at 1370°C was found to be double that of hot pressed Si_3N_4 at the same temperature. The dispersion of SiC-particulates in sintered or hiped Si_3N_4 resulted in a distinct refinement of the microstructure with reduced grain and residual pore size in the composite (13). The strength controlling flaw size was also found to be minimized by SiC addition as long as full densification was achieved. Figure 8 shows the critical defect size in sintered and hipped Si_3N_4-SiC particulate composites calculated for various crack geometries.

Recently, Si_3N_4 composites reinforced with SiC whiskers are being developed for their superior fracture toughness over monolithic Si_3N_4. Slip casting or injection molding are used for aligning whiskers and HIP treatment for achieving dense matrices. Flexural strength values of 950 MPa and a fracture toughness up to 10 MPa m were reported (86 Kob). Crack deflection, matrix microcracking and a minor amount of whisker pull-out are supposed to be the relevant toughening mechanisms (86 Sha). Thus fracture energies of 150-200 J/m^2 are reached. A strong whisker-matrix interfacial bond was developed in these composites suggesting that even greater toughening enhancement is possible with SiC whiskers in a Si_3N_4 matrix by applying fabrication techniques and grain boundary glass compositions to weaken the interfacial bond and thus promote a larger amount of whisker pull-out.

Conclusions

Strengthening of Si_3N_4 ceramics is based both on the reduction of defect sizes by controlled processing of multiphase powders and microstructure toughening, mainly by composite formation. Physical and chemical contamination of the powders has to be excluded by environment controlled powder processing and manufacturing under clean conditions.

"In situ" composites made by reaction sintering and subsequent devitrification of the glass containing microstructures as well as single phase solid solution formation have demonstrated superior thermomechanical properties at high temperatures above 1000°C. The precipitation of refractory grain boundary phases offers the possibility to combine good sinterability with improved high temperature properties of multiphase, crystalline Si_3N_4 ceramics.

Particulate and whisker reinforced Si_3N_4 composites are supposed to achieve high fracture toughness materials with improved reliability. Although this type of composite materials suffer from weak sinterability resulting in porous microstructures, gas pressure sintering or post-hipping techniques at temperatures above 1800-1900°C have yield fully dense Si_3N_4 composites in complex shape.

Reference

1. B.S.B. Karunaratne and M.H. Lewis, High Temperature Fracture and Diffusional Deformation Mechanisms in Si-Al-O-N Ceramics, J. Mat. Sci. 15 (1980) 449-462.

2. H. Palmour III and D.R. Johnson. Phenomenological Model for Rate Controlled Sintering, in Sintering and Related Phenomena, ed. G.C. Kuczynski et al., Gordon Breach, N.Y. (1967) 779-791.

3. J. Weiss, Silicon Nitride Ceramics, Am. Rev. Mater. Sci. 11 (1981) 381-399.

4. K.H. Jack, Sialons and related nitrogen ceramics, J. Mat. Sci. 11 (1976) 1135-1158.

5. C. Greskovich, Hot-pressed ß-Si_3N_4 containing small amounts of Be and O in solid solution, J. Mat. Sci. 14 (1979) 2427 -2438.

6. S. Hampshire, H.K. Park, D.P. Thompson and K.H. Jack, α-SiAlON ceramics, Nature 274 (1978) 880-882.

7. Z.K. Huang, P. Greil and G. Petzow, Formation of α-Si_3N_4 solid solutions in the system Si_3N_4-AlN-Y_2O_3, J. Am. Ceram. Soc. 66 (1983) C96-97.

8. J.C. Bressiani, P. Greil and G. Petzow, Crystallization of Y-Al-Garnet in Pressureless Sintered ß-Sialon Materials in Ceramic Comp. For Engine, ed. S. Somiya, KTK Publ. Tokyo (1983) 228.

9. A.G. Evans and R.M. Cannon, Toughening of brittle solids by martensitic transformations, Acta Met. 14 (1986) 761-800.

10. S. Kobayashi, T. Kandori and S. Wada, Microstructure of Si_3N_4 composites reinforced with SiC whiskers, Yogyo-Kyokai-Shi 94 (1986) 903.

11. K.S. Mazdiyasni and R. Ruh, High/low modulus Si_3N_4-BN composite for improved electrical and thermal shock behavior, J. Am. Ceram. Soc. 64 (1981) 415-419.

12. S. Dutta and B. Buzek, Microstructure strength and oxidation of a 10 wt.% zyttrite-Si_3N_4 ceramic, J. Am. Ceram. Soc. 67 (1984) 89-92.

13. P. Greil, H. Tanaka and G. Petzow, Sintering and HIPping of Si_3N_4-SiC composite materials, to be publ. in Ceram. Int. (1986).

14. S. Kobayashi, T. Kandori and S. Wada, Microstructure of Si_3N_4 composites reinforced with SiC whiskers, Yogyo-Kyokasi-Shi 94 (1986) 903.

15. P.D. Shalek, J.P. Petrovic, G.F. Hurley and F.D. Grac, Hot-pressed SiC whisker/Si_3N_4 matrix composites, Am. Ceram. Soc. Bull. 65 (1986) 351-356.

Table I: Thermomechanical properties of Si_3N_4-materials.

Material	oxygen content	porosity	elastic mod.	fracture toughness	modulus of rupt. RT	Weibull factor	modulus of rupt. 1200°C
	(wt.%)	(%)	(GPa)	($MPam^{1/2}$)	(MPa)		(MPa)
RBSN	1-2	8-25	80-220	2-4	250-350	6-15	200-350
SRBSN	2-8	1-8	100-300	4-6	300-700	10-15	200-500
SSN	3-12	1-5	140-320	5-7	400-900	5-15	250-500
(Sialon	5-20	1-3	200-320	3-6	300-600	6-17	200-500)
HIP/HPSN	2-6	0.5-2	250-340	5-8	600-1300	10-20	300-800

Table II: Solid solution formation in Si_3N_4 systems.

Quaternary Systems	Solid Solution
Si-Al-O-N	ß-$Si_{6-x}Al_xO_xN_{8-x}$ (ß ss)
Si-Be-O-N	ß-$Si_{6-x}Be_xO_{2x}N_{8-2x}$

Quinary Systems	Solid Solution
Be-Si-Al-O-N	ß-$Si_{6-x-y}Al_xBe_yO_{x+2y}N_{8-x-2y}$
Li-Si-Al-O-N	ß ss + α-$Li_xSi_{12-x-y}Al_{x+y}O_yN_{16-y}$
Mg-Si-Al-O-N	ß ss + α-$Mg_xSi_{12-2x-y}Al_{2x+y}O_yN_{16-y}$
Y-Si-Al-O-N	ß ss + α-$Y_xSi_{12-3x-y}Al_{3x+y}O_yN_{16-y}$

ß:$Si_{6-x}Me^{n+}_xO_{(4-n)x}N_{8-(4-n)x}$ α:$Me^{n+}_xSi_{12-nx-y}Al_{nx+y}O_yN_{16-y}$

Table III: Phases precipitated in Si_3N_4 matrices.

Composition	Isomorphous	Example
oxides	spinel	$MgAl_2O_4$
	garnet	$Y_3Al_5O_{12}$
	perovskite	$Y_2Al_2O_6$
	whoelerite	$Y_4Al_2O_9$
oxynitrides	melilite	$Me_2Si_3O_3N_4$
	apatite	$Me_{10}(SiO_4)_6N_2$
	wollastonite	$MeSiO_2N$
	cuspidine	$Me_4Si_2O_7N_2$ Me=Y, Las, Ce, RE
silicates	cordierite	$Mg_2Al_4Si_5O_{18}$
	mullite	$Al_6Si_2O_{13}$

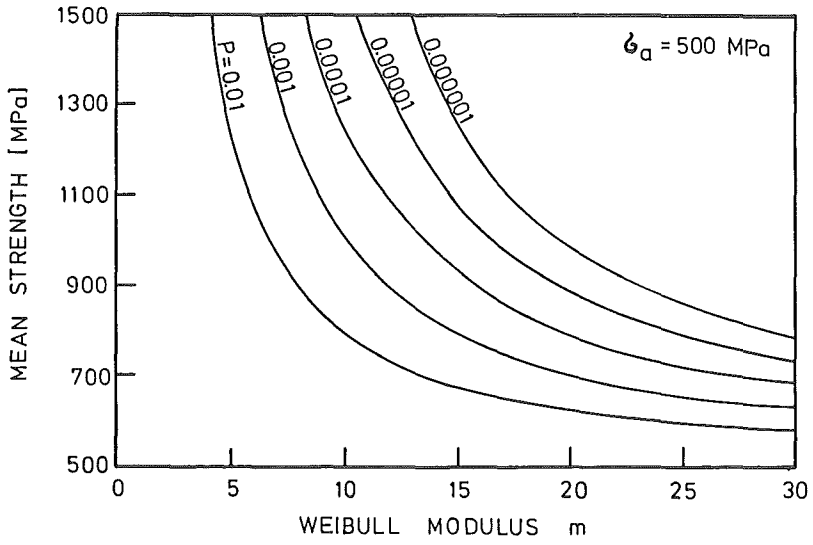

Fig. 1 Mean strength-Weibull modulus relationship for various failure propability levels under a 500 MPa load.

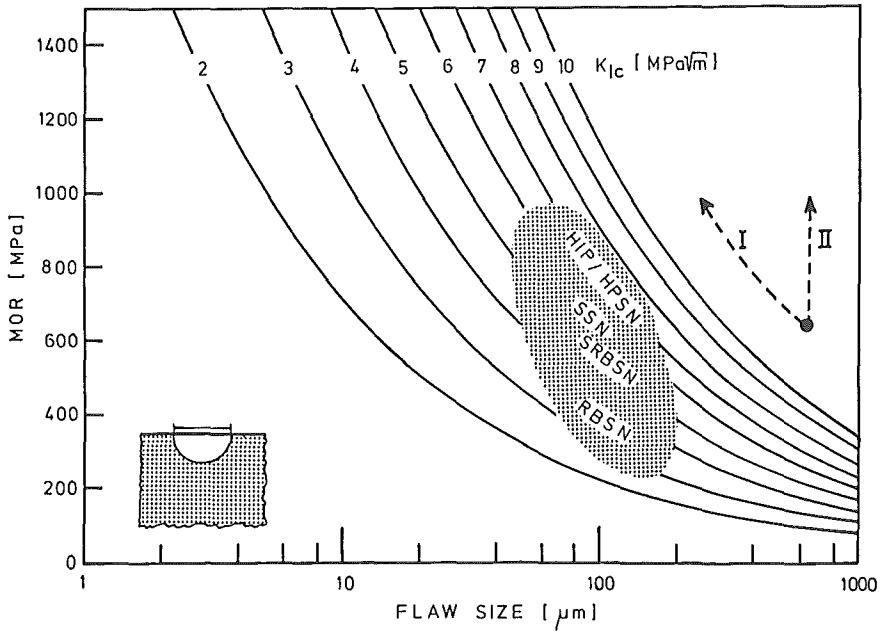

Fig. 2 Flaw size-modulus of rupture relationship for materials with different fracture toughness.

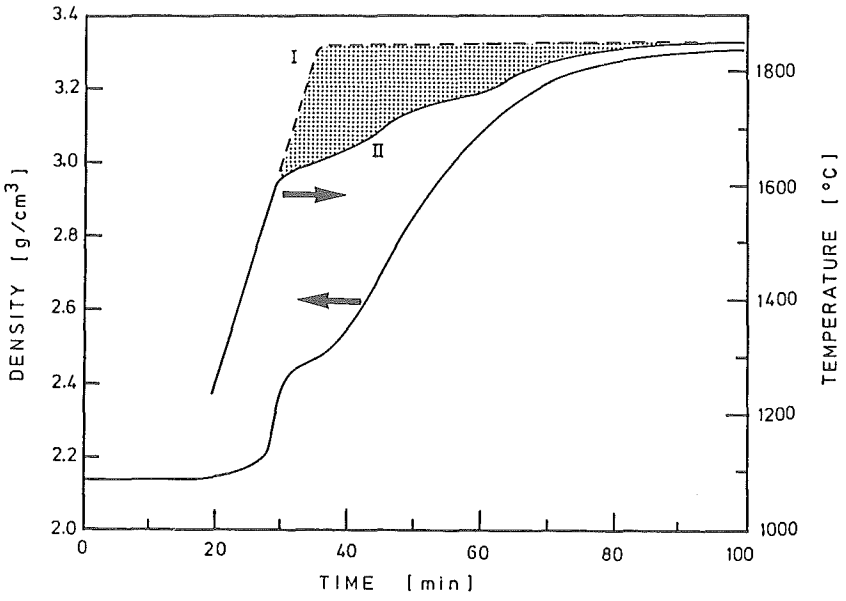

Fig. 3 Time dependence of temperature and density during sintering of a Y_2O_3-fluxed Sialon ceramic. I conventional isothermal sintering, II rate controlled sintering.

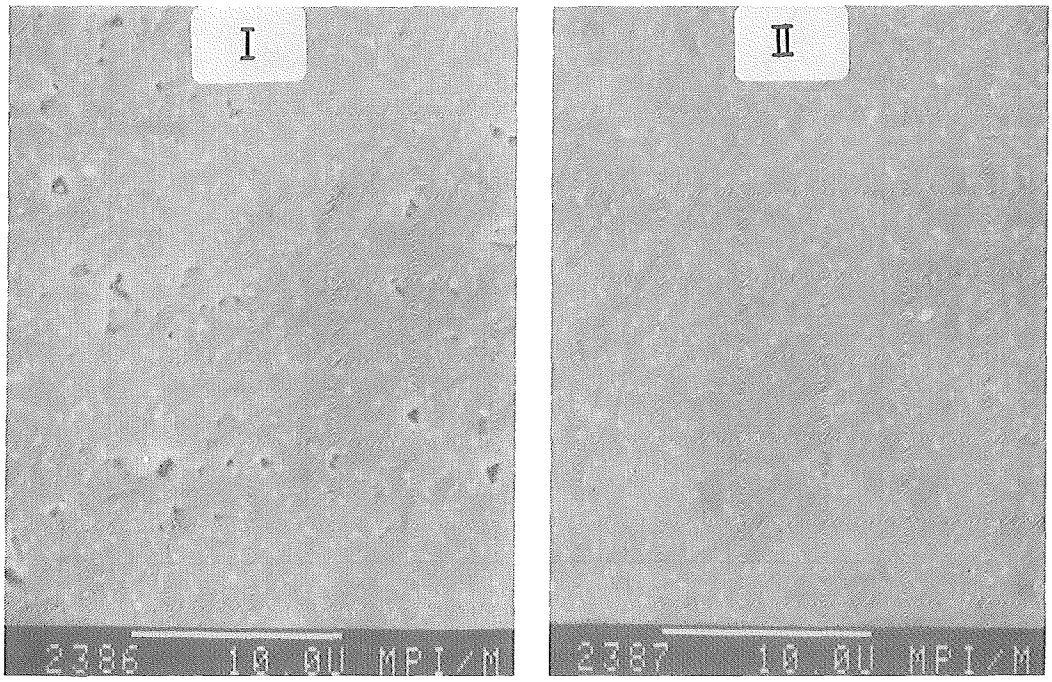

Fig. 4 SEM micrographs of a conventional I and rate controlled sintered II Y_2O_3-fluxed Sialon ceramic.

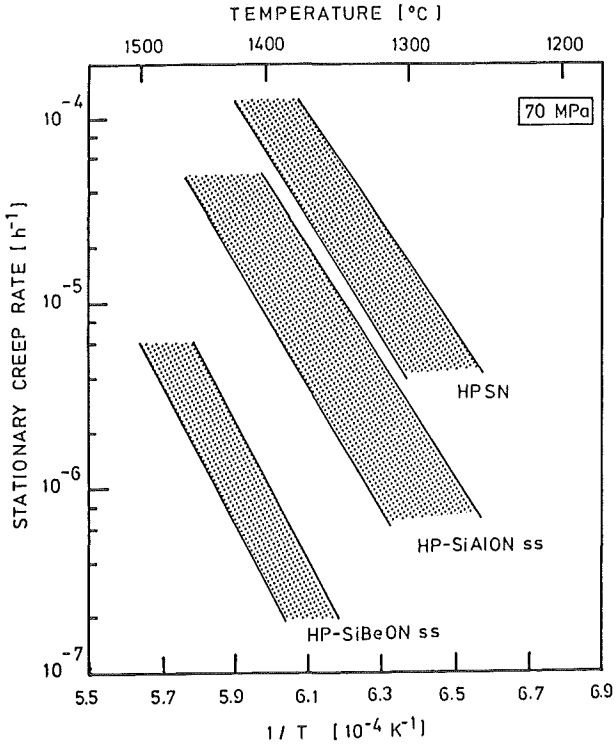

Fig. 5 Stationary creep rates of various hot-pressed Si_3N_4 and Si_3N_4 solid solution materials in dependence of temperature.

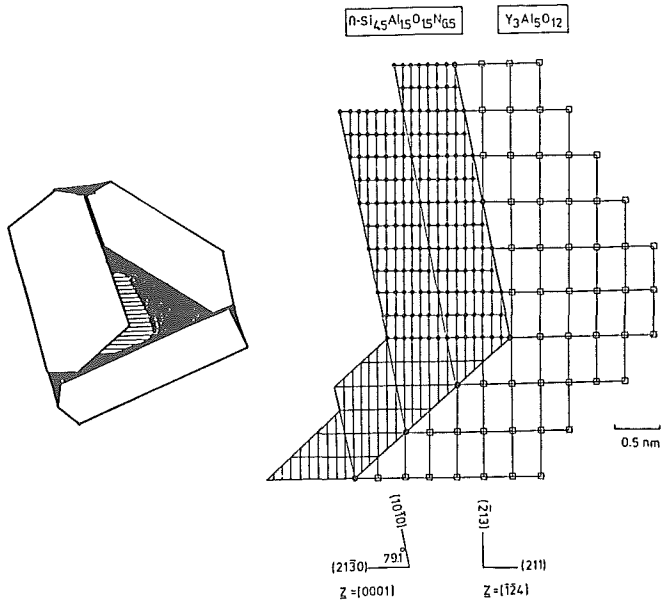

Fig. 6 Epitaxial grain boundary coincidence of a $Y_3Al_5O_{12}$ precipitation on a ß-Si_5AlON_7 crystal in a devitrificated Sialon ceramic.

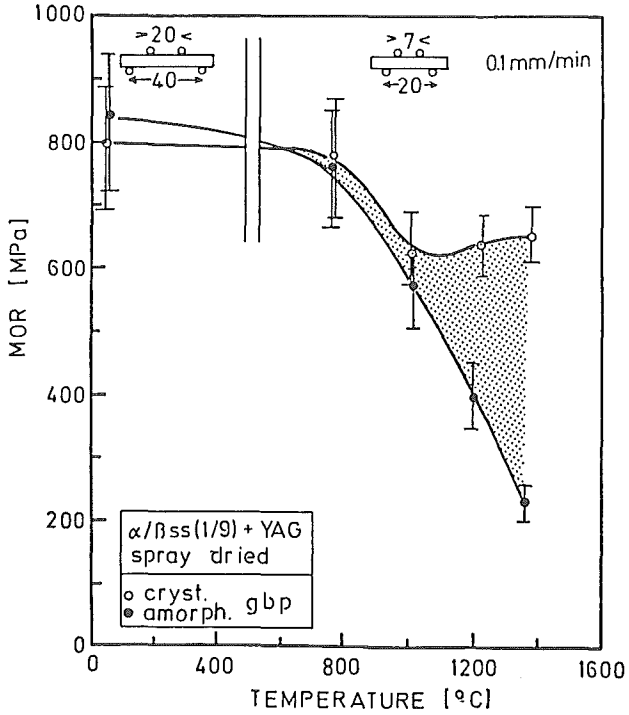

Fig. 7 Retention of high temperature strength after glass devitrification in a pressureless sintered Y_2O_3-fluxed Sialon ceramic.

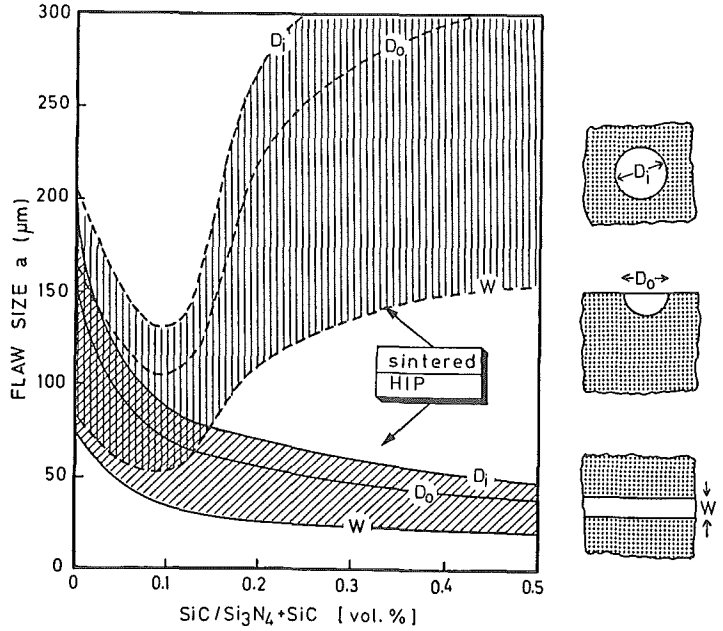

Fig. 8 Calculated flaw sizes of a sintered and a hiped Si_3N_4 composite as a function of the SiC particle content.

THE WEAR OF CUTTING TOOLS : THE CONTRIBUTION OF ABRASIVE WEAR

S. Novak, M. Komac
"J. Stefan" Institute, University of Ljubljana
61000 Ljubljana
Yugoslavia

INTRODUCTION

Besides corrosion, wear is a major cause of material wastage. It causes considerable concern in industry and great attention is now being given to its control. There are two main types of wear: thermo-mechanical, which involves processes like friction, abrasion, impact and fatigue, and thermo-chemical, which arises from chemical interactions between two materials ([1,2]). Abrasive wear caused by the ploughing of a hard surface or hard particles against a relatively softer surface is probably the most serious single cause of wear in engineering practice.

As a part of a programme exploring the wear behaviour of engineering materials, the wear resistance of WC and TiC hardmetals and ceramics when applied as cutting tools was examined. Thus diffusion couples were employed in order to estimate the contribution of chemical interactions at the chip-tool interface to the tool wear.

In the present study the abrasion resistance of hardmetal and ceramic cutting tools is evaluated. Generally, abrasive wear is not a dominant wear mode during cutting; however, its contribution to tool failure can be noticeable, especially if sliding conditions exist.

EXPERIMENTAL

The following materials were used in our investigations:

- TiC- based hardmetals:
  - TiC-MoC-Ni
  - TiC-NbC-Ni
  - Ti(C,N)-MoC-Ni
- WC- based hardmetals (8 - 15%Co)
- Al_2O_3
- Al_2O_3- TiC, Al_2O_3- TiN, Al_2O_3- TiB_2 composites
- SiC- whisker reinforced Al_2O_3

Abrasion wear resistance was evaluated using the pin-on-disc principle ([3]) by abrading the samples, which were in the form of cutting inserts (SNGN 120408) on a diamond wheel. The loads applied were in the range 0.1-0.3 MPa, the rotation speed 1430 rpm, and water was used as cooling liquid.

RESULTS AND DISCUSSION

The results obtained in the wear tests are represented as the volume wear loss versus the applied load (Fig.1). It is obvious that the tested samples fall into particular groups of materials in accordance with their chemical compositions: Al_2O_3 ceramics having the highest volume wear, followed by SiC whisker reinforced ceramics, TiC- based hardmetals, WC- based hardmetals and at the end, the most abrasion resistant material under the given test conditions, i.e. Al_2O_3 composite ceramics.
It is questionable what is the main reason for such behaviour, especially regarding the considerable differences between the wear resistance of Al_2O_3 and Al_2O_3 composite ceramics, and the surprisingly low wear resistance of SiC whisker reinforced Al_2O_3.

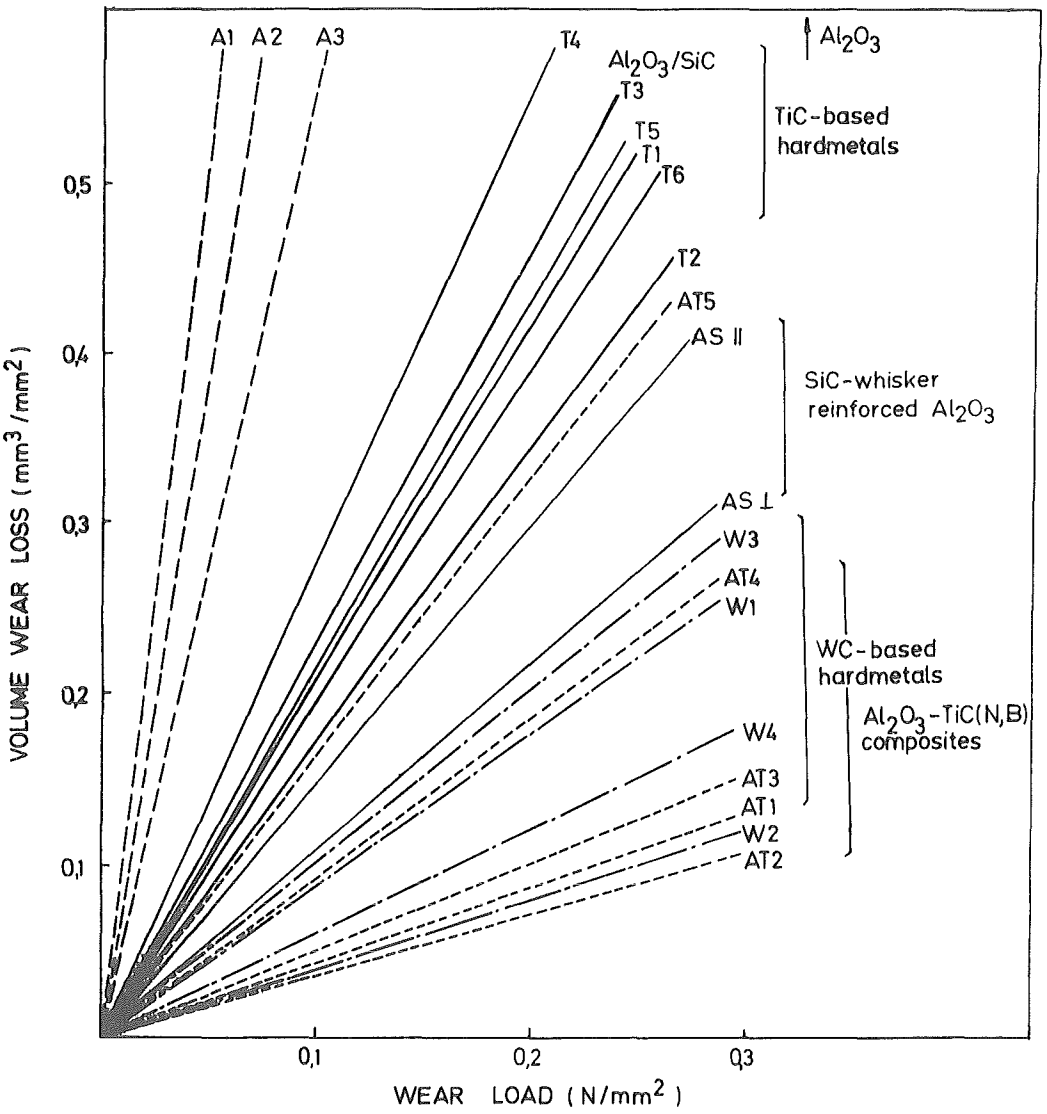

A1	Al_2O_3 1	W1	WC-TiC-Ta(Nb)C-8 Co
A2	Al_2O_3 2	W2	WC-TiC-10Co
A3	Al_2O_3 3	W3	WC-11Co
		W4	WC-15Co
*T1	TiC-MoC-25 Ni		
*T2	TiC-MoC-30 Ni	*AT1	Al_2O_3-TiN
*T3	TiC-NbC-15 Ni	*AT2	Al_2O_3-TiC
*T4	TiC-NbC-20 Ni	*AT3	Al_2O_3-TiB_2
*T5	Ti(C,N)-Mo_2C-30 Ni	AT4	Al_2O_3-TiC 1
*T6	Ti(C,N)-MoC-30 Ni	AT5	Al_2O_3-TiC 2
AS	Al_2O_3-SiC	*	experimental samples

Fig.1: Volume wear loss of different engineering materials as a function of wear load

It is generally accepted that abrasion wear is closely related to the mechanical properties of materials especially hardness (H) and fracture toughness (K_c) ([4]). Fracture mechanisms can cause much higher wear than plastic deformation mechanisms. If the material removal occurs by plastic deformations volume wear is proportional to 1/H, whereas in the case of brittle fracture it could be related to $1/H^{1/2}\ K_c^{3/4}$ ([5]).

As evident from figure 2 there is no functional relationship between volume wear vs. hardness.

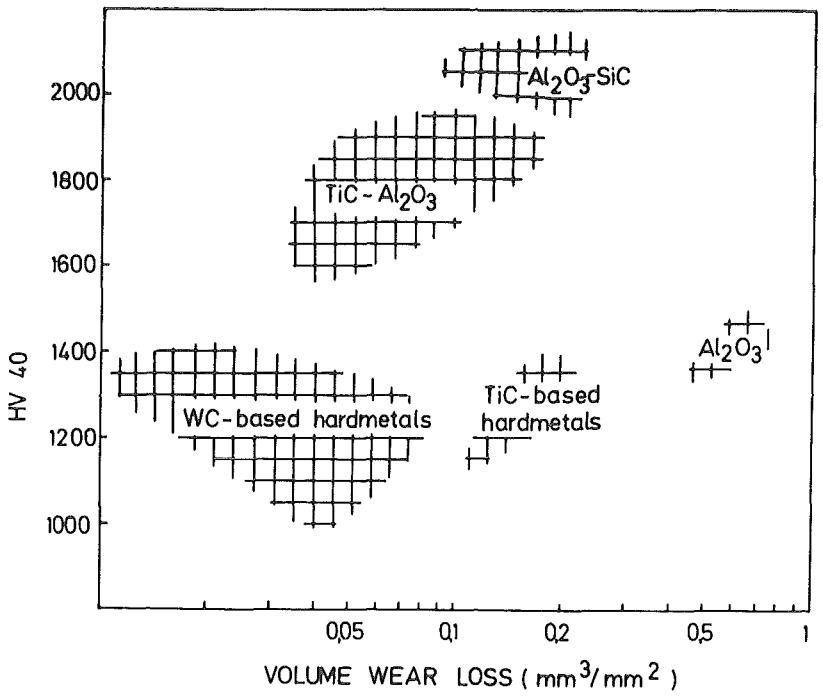

Fig. 2: Volume wear loss as a function of the Vickers hardness of the tested materials

Similarly, there is considerable scatter of the data, when plotting volume wear loss versus $K_c^{3/4}\ H^{1/2}$(Fig.3). This suggests that no simple relationship between wear and the mechanical properties of the tested materials exist. It implies that both plastic deformation mechanisms and fracture mechanisms contribute to material removal during abrasion.

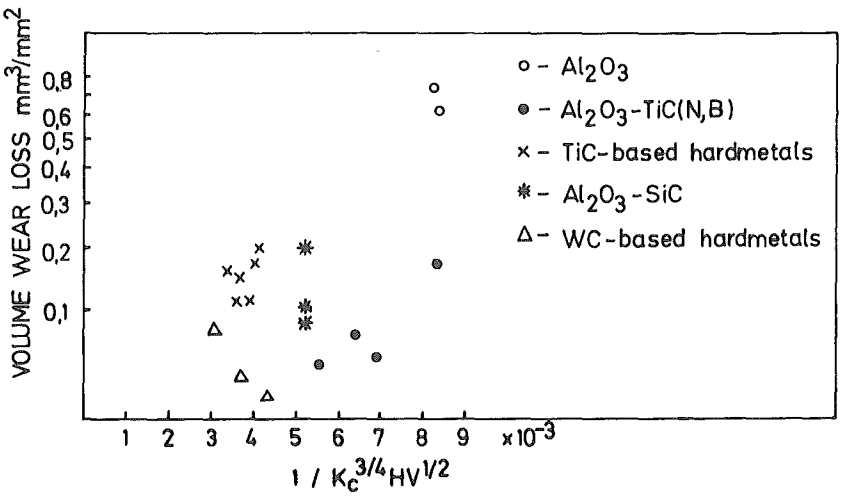

Fig. 3: Volume wear loss vs. $1/K_c^{3/4}\ H^{1/2}$

SEM analysis of the wear scar in an Al_2O_3 sample suggests that severe wear at room temperature occurs mostly by fracture mechanisms, that is by fragmentation of individual grains and extensive intergranular fracture (Fig.4). Low fracture toughness coincides with low critical indentation depth for fracture ([4])which is the reason for high volume wear.

In contrast, the appearance of worn surfaces of Al_2O_3- composite ceramics indicates that extensive plastic deformation has occurred (Fig.5). However, the dispersed hard inclusions of TiC, TiN or TiB_2 provide some protection against plastic deformation.

As mentioned above, the abrasion resistance of SiC- whisker reinforced Al_2O_3, which is known to have not only high hardness but relatively high fracture toughness too, is not as high as expected. This could be explained by the fact that the whiskers were preferentially aligned in a plane parallel to the plane of the lateral cracks which form during the action of hard abrasive particles.

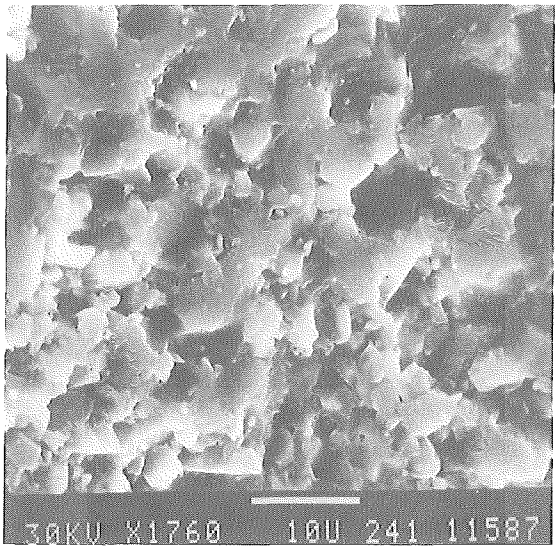

Fig.4: Worn surface of Al_2O_3

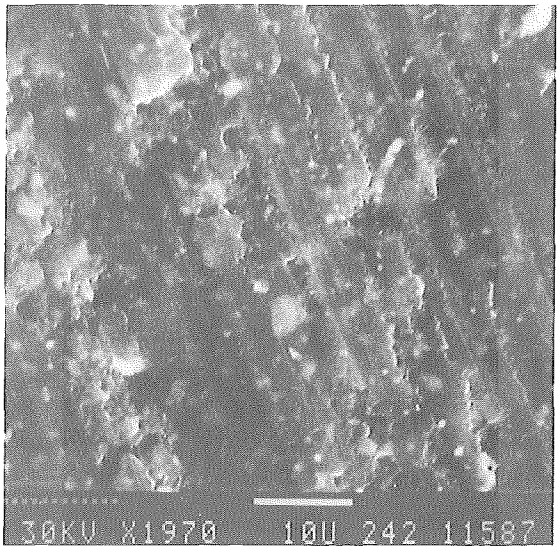

Fig.5: Worn surface of sample Al_2O_3- TiC composite

The abrasive wear resistance of WC- based hardmetals exceeds that of TiC- based hardmetals, primarily because of their good combination of hardness and fracture toughness. Worn surfaces of hardmetals differ in their appearance (Fig.6,7). Plastic deformation can be noticed in all cases. Isolated craters of several grains in diameter and fragmentation inside the craters is characteristic of the TiC-MoC-Ni sample (Fig.6).Worn surfaces of other samples exhibit a much more rugged appearance. In a sample with a lower binder content, wear scars are associated with extensive cracking ,while grain removal and grain fragmentation can be noticed in samples of TiC-TiN-MoC-Ni.

In contrast, abrasion of WC-Co resulted in a very smooth surface with some evidence of binder removal and chipping of carbide grains (Fig.7). EDS analysis of grooves in abraded TiC- and WC-based samples revealed the thin smearing of Ni binder metal,

implying that extrusion of the binder is an important mechanism in the loosening of the structure, similarly to the case of WC-Co alloys.

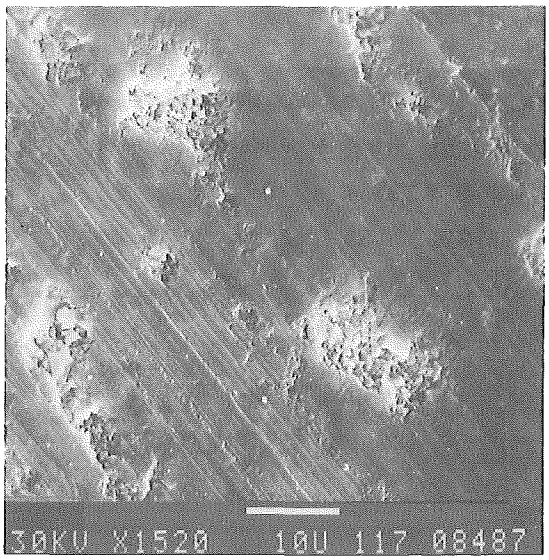

Fig.6: Worn surface of sample TiC-MoC-Ni

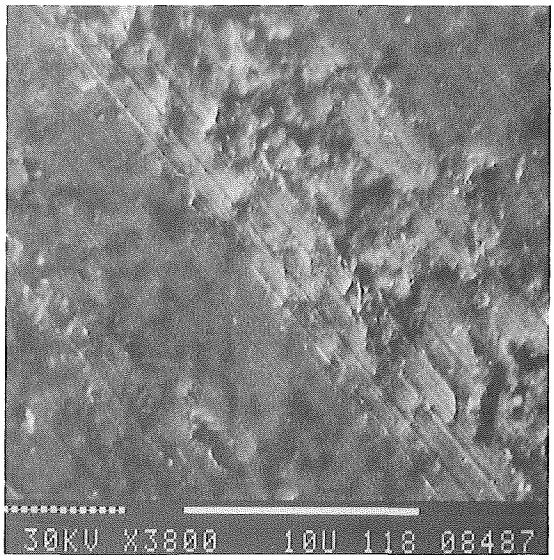

Fig.7: Worn surface of sample WC-Co

CONCLUSIONS

Both plastic deformation mechanisms and fracture mechanisms cause material removal during the abrasive wear of the investigated engineering materials. The predominant and rate controlling mechanisms differ for different groups of materials. Because material removal is a consequence both of plastic deformation and fracture mechanisms, there is no simple relation between wear and the mechanical properties of the investigated materials.

REFERENCES

1. A.R. Lansdown, A.L. Price, Materials to resist wear, ed.D.W. Hopkins et all, Pergamon Press, Oxford (1986)
2. N.P. Suh, Wear, 25 (1973) 111-124
3. E.A. Almond, L.A. Lay, M.G. Gee, Science of Hardmetals, ed. E.A. Almond et al, Adam Hilger LTD, (1984) 919-948
4. A.A. Torrance, J.M. d'Art, Wear,110 (1986) 49-59
5. M.A. Moore, F.S. King, Wear, 60 (1986) 123-140

Advanced Layer Materials

H. Holleck, H. Schulz
Kernforschungszentrum Karlsruhe
Institut für Material- und Festkörperforschung
Postfach 3640, 7500 Karlsruhe
Federal Republic of Germany

Introduction

The protection of materials by hard coatings is one of the most important and versatile means of improving component performance. We know a tremendous number of hard materials and therefore it is important to have criteria for the selection of the most suitable coating material for specific needs.

Problems with the material selection arise mainly because many desired properties such as good adherence at the substrate/layer interface and no surface interactions, or high hardness and high toughness of the layer cannot be obtained simultaneously. Increasing hardness and strength are mostly coneected with decreasing toughness and adherence.

Because of complex requirements multilayer coatings or multiphase coatings seem to be the best compromise. For these multiphase or multilayer coatings it is necessary to analyze the constitution of phase boundaries. For birttle bulk material systems it has been proved, that a high amount of interfaces can improve the toughness. It was obvious to examine the influence of high amounts of interaces also in coatings.

Preparation of nanodisperse coatings

Coatings with a high amount of phase boundaries, so called nanodisperse coatings, can be prepared by sequential or simultaneous sputtering (see Fig. 1). By sequential sputtering the substrates are moved between the cathodes on a rotating table. Beside sequential TiC-TiB_2-coatings (shown in Fig. 2) also sequential TiB_2-TiN and TiC-TiN-coatings were prepared. TiC and TiN are completely soluble in the solid state. TiB_2 forms two phase equilibria with TiC

and TiN. Coatings with a total thickness of 5 µm with 10, 100, 250, 500 and 1000 layer were prepared.

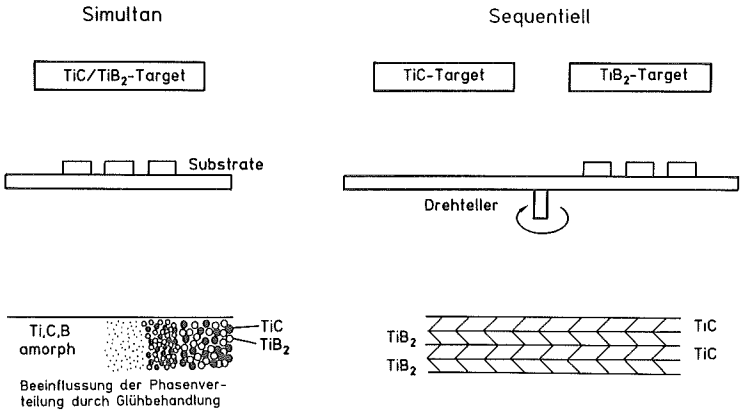

Fig. 1: Preparation of nanodisperse coatings.

The second possibility to prepare nanodisperse coatings is the sputter deposition from a multiphase target. Using a twophase TiC/TiB_2-target an amorphous Ti,C,B-coating results. After annealing in vacuum for 1 h at 1000 °C a two phase coating is formed. With the annealing procedure the phase dispersion can be controlled. Up to now only the amorphous Ti,C,B-coatings were examined in detail.

Constitution of sputtered phase transitions

The knowledge of the constitution of sputtered phase transitions is essential for the interpretation of the properties and the wear behaviour of sequential coatings. The constitution of phase transitions in sequential coatings was examined by Auger spectroscopy and X-ray analysis.

When sputtering TiC on TiN or TiN on TiC a sputtered mixed phase of Ti(C,N) is formed. The width of this zone was determined to be 3 to 4 nm. The X-ray diffraction pattern of a sequential TiC-TiN coating with 1000 layers shows strong Ti(C,N)-peaks and only small peaks of TiC and TiN (see Fig. 2).

When sputtering TiB_2 on TiC or TiN a sputtered Ti,C,B or Ti,N,B mixed phase is formed. The structures of these phases are not clear yet. On the Ti,C,B-phase TiB_2

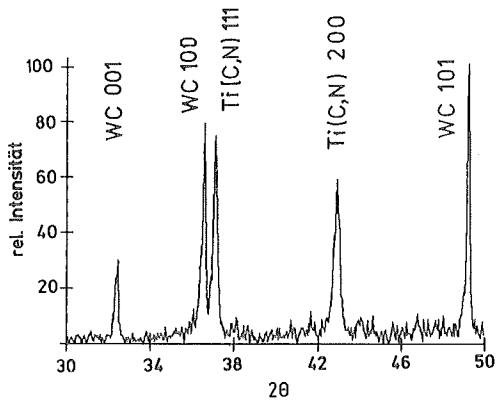

Fig. 2:
X-ray diffraction pattern of a 1000 layer TiC-TiN-coating.

grows up to about 5 nm and on the Ti,N,B-phase up to about 10 nm in an amorphous state.

In contrast to the amorphous growth of TiB_2 on TiC or TiN the phase transition from TiB_2 to TiC or TiN is completely crystalline. The atomic positions of Ti in the approximately 2 nm wide Ti,B,C and approximately 1 nm wide Ti,B,N mixed phase are the same as in the (001) plane of TiB_2. This is a presupposition for the observed epitactic growth of TiC and TiN on these mixed phases. Between the hexagonal TiB_2 and the cubic TiC or TiN many possibilities for coherence exist. In sputtered coatings only the coherence between the (001)-plane of TiB_2 with the (111)-plane of TiC or TiN was observed. These planes are the close-packed planes of the hexagonal and the cubic structure (see Fig. 3).

On the sputtered Ti,B,C-mixed phase TiC grows up to 20 nm with a [111]-texture. At a layer thickness of around 20 nm the crystal orientation changes to the (100)-plane, which is the standard orientation in TiC-monolayer coatings. TiN-coatings show a characteristic columnal grain structures. The orientation of some nuclei is influenced by the Ti, B, N mixing phase. A complete crystallographic growth in the [111]-direction as for TiC was not observed.

The different constitution of the phase transition in sequential coatings is also reflected also in the microstructure of fracture surfaces. Coatings with a high amount of amorphous phases, that means TiC-TiB_2- and TiB_2-TiN-coatings with 1000 layers show a smooth structural fracture. The completely crystalline 1000 layer sequential TiC-TiN coatings have a columnal microstrücture.

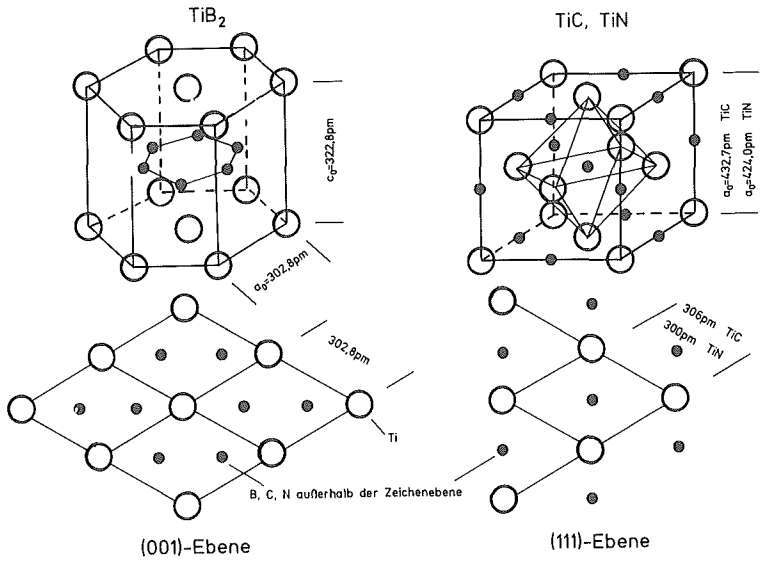

Fig. 3: Coherence between the (001)-plane of TiB_2 and the (111)-plane of TiC or TiN.

Properties of nanodisperse coatings

Since the structure of sequential coatings is partly clear now, the coating properties can be understood. Hardness, adherence, the toughness properties and the internal stresses of the coatings were investigated. The wear behaviour was examined in continious and interrupted cutting conditions against plain carbon steel. Hard metal was used as substrate. All coatings had a thickness of 5 µm.

The adherence of the coatings was tested with a scratch-test apparatus [4]. A quantitative measurement is not possible with this test. With an optimized sample pretreatment and advantageous sputtering conditions the adherence of the coatings is better than the strength of the coatings itself [5]. For the interpretation of the crack resistance of the coatings the internal stresses have to be known.

The hardness of sequential coatings is hardly influenced by the amount of phase transitions (see Fig. 4). The decrease of the hardness of the 1000 layer TiC-TiN-coating is due to the low strength of the grain boundaries of the radial crystals. The small decrease of the hardness of the 1000 layer TiC-TiB_2- and TiB_2-TiN-coatings is due to the increasing volume of amorphous coating zones. Simultaneously sputtered, amorphous TiC/TiB_2-coatings, that means coatings

sputtered from a two phase target show a lower hardness than monolayer TiC- or TiB_2-coatings, because of the missing long range order.

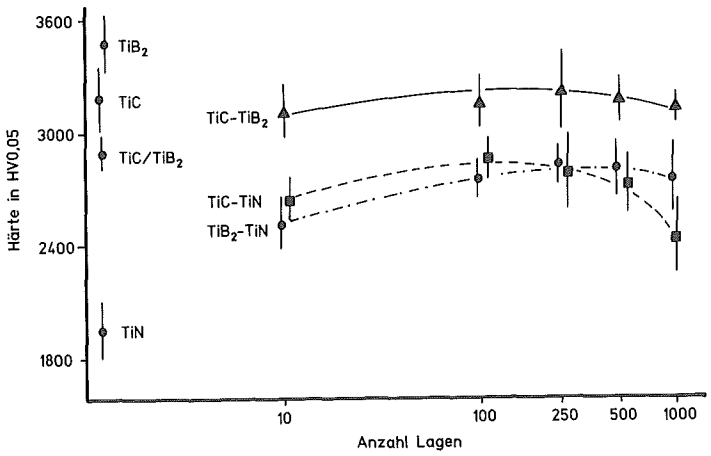

Fig. 4:
Microhardness of sequential coatings.

No standard testing method exists for the determination of the toughness of hard coatings. In our work the possibility was investigated to determine the coating toughness by the crack formation and crack propagation at Vickers indentations, so called Palmqvist method [6], and Hertzian indentation [7].

In sputtered coatings internal stresses are usually compressive. Cracks at the edges of Vickers indentation arise in a coating with compressive internal stresses only when cracks are also formed in the substrate. At Hertzian indentation a ring-shaped crack is formed when the substracte is plastically deformed. Because of the interaction of coating and substrate no absolute toughness value for the coating can be evaluated. A relative comparison of the toughness of various coatings is possible with both methods, if coatings with the same thickness on identical substrates are examined.

Sequential coatings show a strong dependence between the crack resistance and the amount of phase transitions (see Fig. 5). TiC-TiB_2- and TiB_2-TiN-coatings have the highest crack resistance with 100 monolayers. The crack resistance of TiC-TiN-coatings slowly increases from 10 to 250 monolayers. The decrease up to 1000 monolayers can be explained for TiC-TiN-coatings with a low strength of the grain boundaries. The decreasing crack resistance in TiC-TiB_2- and TiB_2-TiN-coatings is due to the increasing volume of the mixed phase and the amorphous TiB_2-phase. The crack resistance of monolayer and sequential coatings can be compared when considering the internal stresses.

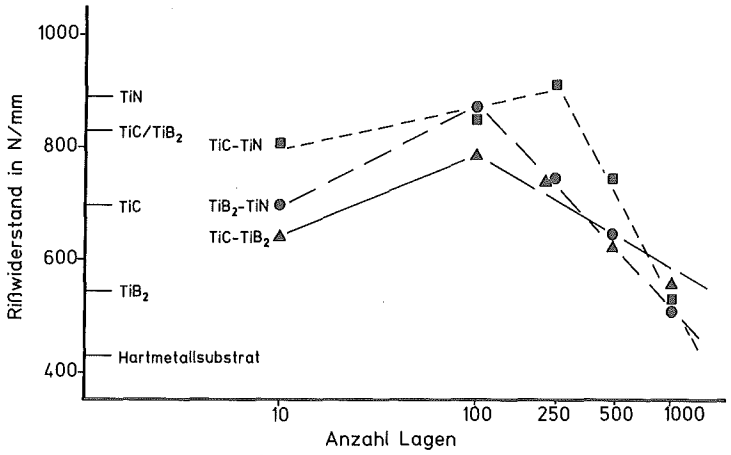

Fig. 5: Crack resistance of sequential coatings.

As a characteristic example for the dependence between crack resistance and the internal stresses coatings from the system TiB_2-TiN are shown in Fig. 6. The advantageous influence of the phase transitions on the crack resistance is shown with the 100 layer TiB_2-TiN-coating. The brittleness of the TiB_2-layers is nearly completely compensated by the dissipation of crack energy at the phase transition.

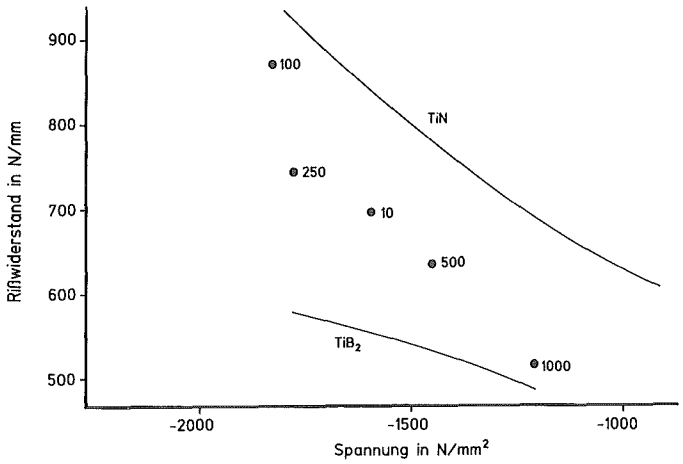

Fig. 6:
Comparison between the crack resistance of monolayer TiN, TiB_2 and sequential TiB_2-TiN-coatings in dependence of the internal stresses.

The wear behaviour of sequential coatings depends in a similar way as the toughness on the amount of phase transitions. The flank wear of monolayer and sequential TiC-TiB_2-coatings is shown in Fig. 7. Coatings with 100 phase

transitions have the lowest flank wear. This can be explained with the high crack resistance of the 100 layer coating. A direct correlation between the macroscopically measured crack resistance and the microscopic abrasive wear process could not be found. But the coating toughness is an important factor influencing the flank wear resistance.

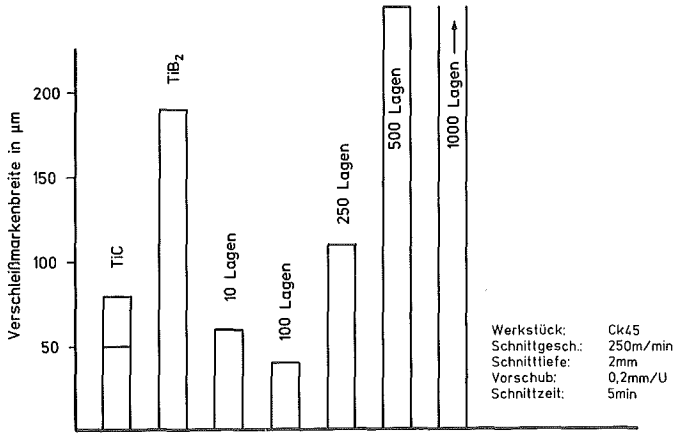

Fig. 7:
Flank wear of monolayer TiC, TiB_2 and sequential TiC-TiB_2- coatings by continuous cutting.

Especially under severe cutting conditions, for example at interrupted cutting, the advantage of sequential coatings against sputtered monolayer and CVD-coatings can be clearly shown, as demonstrated in Fig. 8. Only the CVD-samples with a monolayer TiN-coating could withstand the severe conditions of the bar turning test. Commercial CVD-samples with TiC-, TiC-TiN- and TiC-Al_2O_3-coatings failed after a few impacts. The sequential TiC-TiB_2- and TiC-TiN-coatings with 100 monolayers showed the lowest flank wear. The nonuniform flank wear of the sputtered coatings is due to the separated coating process for the rake and clearance face. With a uniform growth of the coating over the cutting edge the flank wear of sequential coatings could be three times smaller than for CVD-coatings.

Summarizing we can say, that the concept of introducing a high amount of phase boundaries in hard coatings is a promising development in the field of wear resistant coatings.

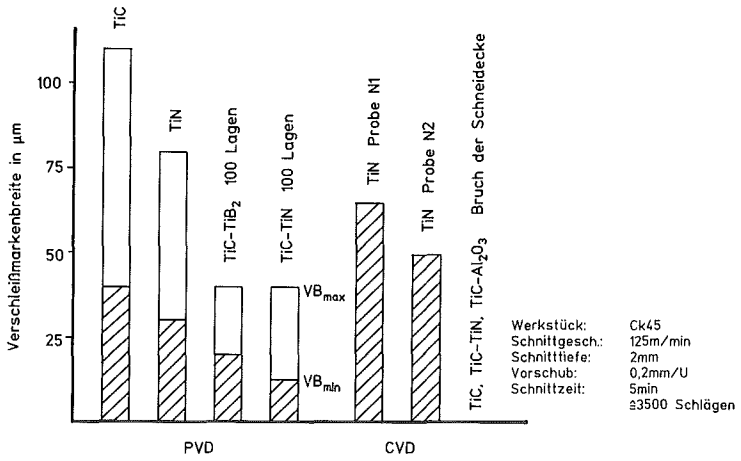

Fig. 8: Flank wear of PVD and CVD coatings by interrupted cutting.

Literature

[1] H. Holleck, Ch. Kühl, H. Schulz, J. Vac. Sci. Technol. A 3 (1985) 2345-2349

[2] H. Holleck, J. Vac. Sci. Technol. A4 (1986) 2661-2669

[3] H. Holleck, H. Schulz, "Advanced Layer Material Constitution", J. Vac. Sci. Technl. A5 (1987) in Press

[4] B. Hammer, A.J. Perry, P. Laeng, P.A. Steinmann, Thin Solid Films 96 (1982) 45-51

[5] H. Schulz, H. Holleck, Tagungsband PVD '86, Int. Conf. Darmstadt, 1986, 145-155

[6] S. Palmqvist, Arch. Eisenhüttenwesen 33 (1962) 1-6

[7] R. Warren, Acta Metallurgica 26 (1978) 1759-1769

PHASE TRANSFORMATION OF $Zr_xHf_{1-x}O_2$ IN ALUMINA MATRIX

F.Sigulinski
"Boris Kidrič" Institute of Nuclear Sciences, POB 522,
Lab.170, 11001 Belgrade, Yugoslavia

A_S temperature was determined on the basis of dilatometric measurements for different Al_2O_3+15 v/o ($Zr_xHf_{1-x}O_2$) compositions. It was demonstrated that A_S temperature is manifestation of soft lattice modes. Additional proof was obtained by IR results which pointed out that phase transformation (monoclinic - tetragonal) was indeed of soft phonon mode.

INTRODUCTION

In 1970, Patil and Subbarao[1] had observed by high temperature x-ray, during heating in temperature range 930-1100°C pretransformation region. In this region monoclinic peaks were enormously high and so they proposed existence of special vibrational modes. The region between 1100-1220°C they described as coexistency region - simultaneous existence of both monoclinic and tetragonal phases.However, they concluded also - that there is no pretransformation region during cooling.

In 1977 Burke and Garvie[2] assumed that phase transformation of zirconia and hafnia could be manifestation of soft phonon modes.

The equation they proposed is of the form:

$$T_H - T_Z = \frac{k}{\beta}\left(\frac{1}{M_Z} - \frac{1}{M_H}\right) \qquad (1)$$

where T is the transformation temperature and the subscripts, H, Z refer to hafnium and zirconium, k is force constant, β-correction factor and M is the cation mass.

Applied to solid solution of hafnia and zirconia one can obtaine following expression:

$$M_{SS} = (1-x)M_Z + M_H \qquad (2)$$

where x is mole fraction of hafnia. On substituting this expression in the equation (1) they obtained:

$$T_H - T_{SS} = \frac{k}{\beta}\left(\frac{1}{M_{SS}} - \frac{1}{M_H}\right) \qquad (3)$$

$$(1+Bx)T_{SS} = (BT_H+A)x + (T_H-A) \qquad (4)$$

where $B = \frac{M_H}{M_Z} - 1$ and $A = \frac{k}{\beta}\left(\frac{1}{M_H} - \frac{1}{M_Z}\right)$.

When applied to M_S transition temperature obtained by DTA (Ruh et al.[3]) linear relationship was obtained for $(1+Bx)T_{SS}$ dependence on mole fraction of hafnia, from whick k/β factor was determined. This factor could be used to calculate M_S temperature for any composition.

We were interested to investigate if the soft phonon modes was valid for A_S temperature? This was not proved up to now but it is what we inwestigated in this paper.

EXPERIMENTAL

Starting powders used in our experiments were alumina (Alcoa, USA), zirconia (Magnesium - Elektron, England) and hafnia (H.C.Starck, Germany). Homogenization of previously determined powder fractions was performed by attrition milling. Samples, Al_2O_3 + 15 $^v/o$ ($Zr_xHf_{1-x}O_2$) composites, where x=0,4-1,0; were obtained by isostatical pressing under 600 MPa, and by subsequent sintering at 1550^oC i.e. 1600^oC in air. Dilatometric measurement were performed in air with a heating /cooling rate of 10^oC/min.

RESULTS AND DISSCUSION

In Table 1 dilatometric data for A_S temperatures are shown.

Table 1. Dilatometric data for A_S temperatures

Mole fraction of ZrO_2	A_S (^oC)
1,0	1105
0,8	1257
0,5	1460
0,6	1522

If we apply the equation (3) to our case, we obtained following expression:

$$T_{SS}\ (Bx+1) = x(T_Z B+A) + T_Z - A \qquad (5)$$

where x is mole fraction of zirconia, $B = \frac{M_Z}{M_H} - 1$ and $A = \frac{k}{\beta}(\frac{1}{M_H} - \frac{1}{M_Z})$. Graphically presented the data show (Fig.1) linear relationship between $(1+Bx).T_{SS}$ and mole fraction of zirconia, from which we calculated the k/β ratio and A_S temperature for pure hafnia. We obtained

$$k/\beta = 1.076.10^2 \ \frac{K.kg}{mol} \qquad \text{and } A_S = 1955\ K.$$

We assumed that special vibrational modes must produced absorption band in far IR-spectra of monoclinic zirconia. This was indeed shown by Devitt and Baun[4] in the low frequency region (300 to 500 cm^{-1}). Namely, they faund absorption band at $\nu = 230\ cm^{-1}$.

Relation for wave number is:

$$\nu = \frac{1}{2\pi_c}\sqrt{\frac{k}{m_r}} \qquad (6)$$

where c is velosity of light, k is force constant, m_r is reduced mass and M_Z, M_o are masses of atoms (zirconium i.e. oxygen).

Using equation (6) we calculated force constant $k = 0.744.10^2$ N/m. Using this k and k/β values obtained earlier, we calculated $\beta = 0,687$ N.mol/m.kg.K.

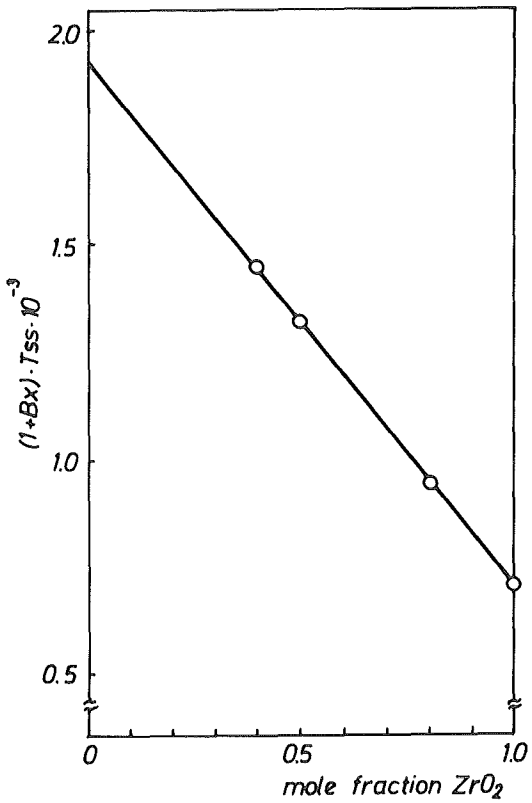

Fig.1. Relationship between $(1+Bx)T_{SS}$ and mole fraction of zirconia

To check this value we did the following:

$$M_H.0,687.(T_H-T_Z)= 0.744.10^2$$

we obtained T_H= 1985 K which is in good agreement with the one calculated from dilatometric data.

CONCLUSION

- As temperature is manifestation of soft phonon modes
- $k/\beta = 1{,}076.10^2$ K.kg/mol, makes possible to calculate A_S value for any composition.
- Using IR-data additional proof was obtained that phase transformation (monoclinic - tetragonal) was indeed manifestation of soft lattice modes.

REFERENCES

1. R.Patil and Subbarao, Acta Cryst. 26A (1970) 535
2. S.Burke and Garvie, J.Mater.Sci., 12 (1977) 1487
3. R.Ruh, H.J.Barret, R.F.Domogala and N.M.Tallan, J.Am.Ceram. Soc., 51 /1/ (1968) 23
4. N.T.McDevitt and W.L.Baun, J.Am.Ceram.Soc., 47 /12/ (1964) 622.

PREPARATION AND PROPERTIES OF HIGH STRENGTH CARBON FIBRES

S.Marinković, V.Rašković, S.Pejanović[1] and V.Pavlović

Boris Kidrič Institute, Vinča, Belgrade, Yugoslavia
[1]Institute of Chemistry, Technology and Metallurgy, Belgrade

1. Introduction

Carbon fibres today represent an unavoidable material in construction of airplanes, cosmic and balistic rockets, ships and boats, as well as of a number of sporting goods. Their biomedical applications are also becoming increasingly important.

Usage of carbon fibres is based on their unique properties - very high mechanical properties combined with low density, thermal and chemical stability and the fact that their mechanical properties do not decrease at high temperatures, up to 2500°C.

Several different precursors have been used for industrial production of carbon fibres, but at present about 90% of the total world production is based on polyacrylonitrile (PAN).

An essential improvement in quality of carbon fibres has been achieved recently thanks to everlasting research efforts since the discovery of the PAN-precursor-based procedure some 20 years ago. Fig.1 shows range of specific properties of plastic matrix composites reinforced with glass (GFRP), aramid (AFRP), boron (BFRP), and first and second generation carbon fibres (CFRP), together with new developments prognostic. The trend in development of new generations of carbon fibres, dictated mainly by the aerospace industry, has been to increase their strength and strain-to-failure, leaving modulus virtually unchanged. The increase in strength is an obvious demand, leading to further decrease in weight of structural components and/or decrease of their production cost. A relatively low strain to failure of carbon fibres has been a serious obstacle, preventing their wider use.

As far as modulus is concerned, there is no special need for its increase because it is high enough for majority of applications. For those applications where higher modulus is needed the intermediate or high-modulus

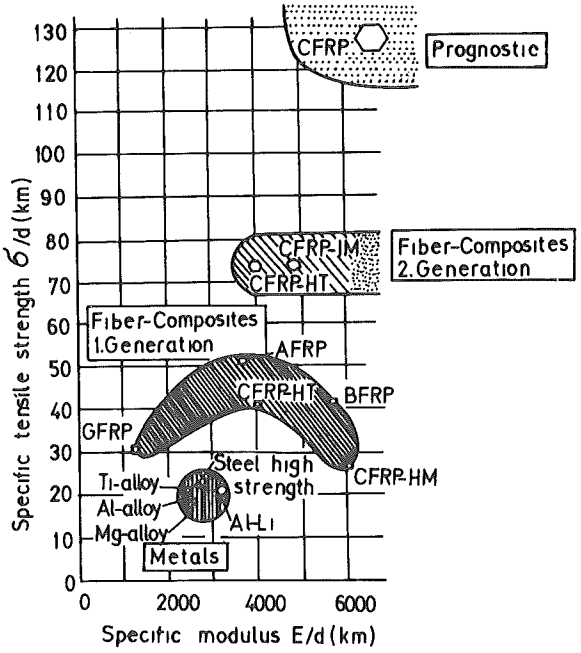

Fig.1. Specific strength and modulus of composites. Values apply in 0^{o} direction for, 0, +45, 0, -45 laminates with fibre-content 50 vol%.

carbon fibres can be used (with moduli up to 400 GPa or even higher), although their strength is lower than in the case of high-strength fibres.

The question is therefore, how to increase strength and strain to failure of carbon fibres. For a given structure and preferred orientation of the fibres, the modulus is determined, being an intrinsic property of the material. However, strength and strain to failure depend also on the flaws present in the fibres. Thus, supposing that structure of the fibres should not be essentially changed, the research efforts should be directed toward elimination of the flaws.

Research at Boris Kidrič Institute, Vinča has been directed to establish the process of continuous fabrication of high strength carbon fibres from the PAN precursor produced by the Yugoslav company OHIS.

2. Research at IBK-Vinča

Generally, the process of fabrication of carbon fibres from PAN precursor involves two essential steps: first step is stabilization of the starting polymer in order to prevent excessive loss of carbon during the second step, i.e. during carbonization of the stabilized fibres.

We have investigated two stabilization processes: air oxidation and SO_2 treatment.

Although the SO_2 treatment study revealed that this may be a very efficient process (1,2), air oxidation has been chosen because of the problems associated with the use of SO_2.

A study of air oxidation (3) showed, in agreement with other authors, that a long isothermal oxidation at a relatively low temperature (220°C) leads to a well stabilized cyclized polymer structure. The process was followed by IR spectroscopy (Fig.2), DT and X-ray diffraction analyses, showing that oxidation under this regime is practically completed.

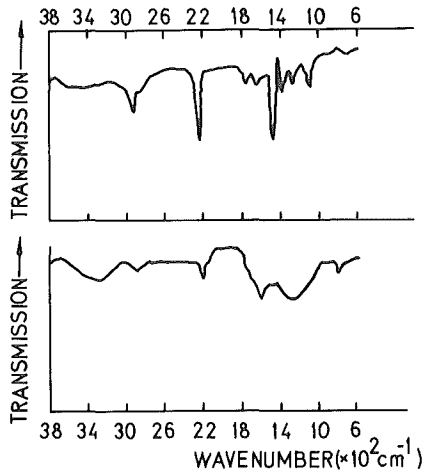

Fig.2. IR spectra of PAN fibres before (top) and after oxidation at 220°C for 5hr. Cyclization is indicated by intensity decrease of nitrile peak at 2240 cm^{-1}.

Further research has been mainly concerned with a possibility of shortening the process of oxidation. In order to achieve this goal, various temperature regimes coupled with various extension forces have been studied (4). Fig.3 shows temperature regime and relative elongation of PAN fibres

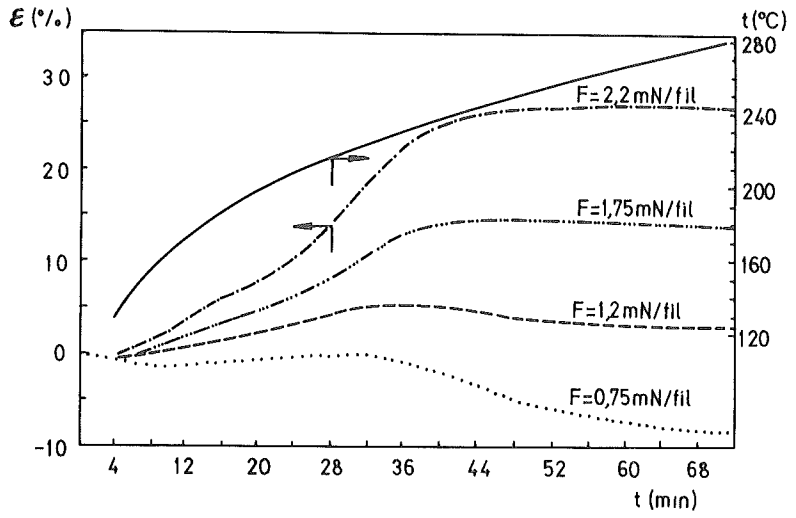

Fig.3. Heating regime and relative elongation of PAN fibres during oxidation under different stretching forces.

during the oxidation under different stretching forces. The results show that the lowest applied force is too low to prevent shrinkage of the fibres which is a consequence of cyclization. Higher force leads first to an extension of the fibres which increases up to a maximum after which some shrinkage takes place.

Such a behaviour is presumably a result of a superposition of two processes, i.e. of plastic deformation which increases with increasing force and temperature and cyclization leading to shrinkage the rate of which increases with temperature. The maximum is shifted toward higher temperature when the force is higher. This shift is a consequence of higher degree of cyclization needed to compensate the effect of higher stretching force.

Figure 4-a shows properties of the oxidized fibres as a function of applied stretching force. The diameter decreases, while breaking strength, modulus and strain to failure increase with increasing force.

Properties of carbon fibres obtained by carbonization of the fibres oxidized at different stretching forces are shown in Fig.4b. While diameter of the fibres and their elastic modulus are monotonously changed with increasing stretching force, strength and breaking elongation show a maximum for the force producing minimum extension in the process of oxidation.

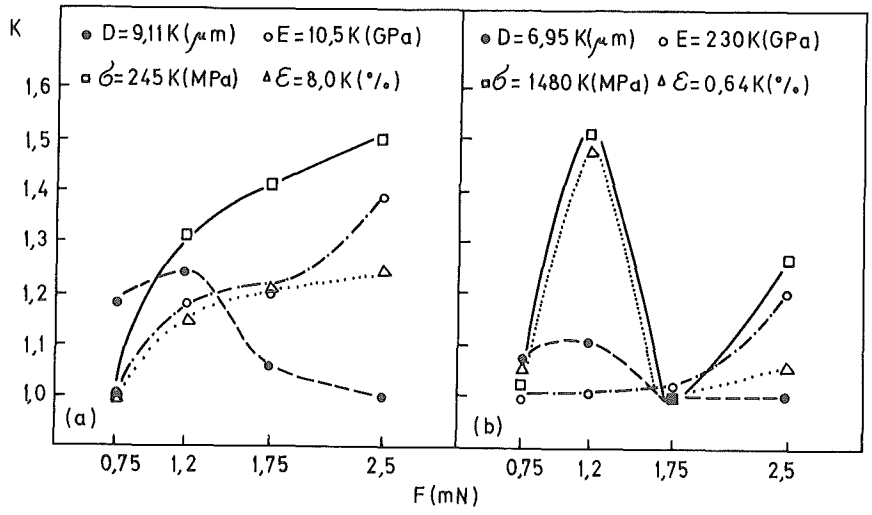

Fig.4. Properties of oxidized (a) and carbonized fibres (b) vs stretching force upon oxidation.

The decrease in strength and breaking elongation for higher stretching force may be explained by an increase in dimensions of the flaws already existing in the fibres.

The results of investigation of the stabilization by air oxidation enabled us to determine processing conditions on a large continuous experimental plant. High quality carbon fibres have been produced for a relatively short process time.

The carbon fibres obtained by the continuous process from the Yugoslav PAN precursor are compared with those obtained from the special acrylic fibres produced by Hysol-Grafil (Table 1). The table shows:

Table 1. Properties of carbon fibres produced from Yugoslav and imported special PAN

	Yugoslav PAN	Imported PAN
Diameter, μm	6,8	6,8
Strength, MPa	2850	3460
Modulus, GPa	220	220
Elongation, %	1.27	1.48

1. The fibres produced from the Hysol-Grafil presursor have mechanical properties similar to those of the commercial fibres produced by the company;

2. The fibres produced from the Yugoslav precursor have elastic modulus equal to that of the fibres produced from Hysol-Grafil precursor, indicating that structure is similar in both cases. However, carbon fibres produced from the Yugoslav precursor have lower strength and strain to failure which shows that these fibres contain more flaws.

References

1. V.Rašković and S.Marinković, Carbon 16, 351 (1978)

2. V.Rašković and S.Marinković, Proc. 5th London Intern. Carbon and Graphite Conf., London 1978, Soc.Chem.Ind.London, Vol.1, p.419

3. V.Rašković and S.Marinković, Carbon 13, 535 (1975)

4. V.Pavlović, Z.Lauševič, V.Rašković and S.Marinković, Proc. 4th Intern. Carbon Conf., Baden-Baden 1986, Arbeitskreis Kohlenstoff DKG, p.620.

C E R A M I C S

THERMAL PROPERTIES

THERMAL TRANSPORT IN PRESSURELESS SINTERED ALUMINIUM NITRIDE

A.Kranzmann, P.Greil and G.Petzow

Max-Planck-Institut für Metallforschung
Institut für Werkstoffwissenschaften
Pulvermetallurgisches Laboratorium
Heisenbergstr.5, 7000 Stuttgart 80, FRG

AlN powders of high purity were pressureless sintered in nitrogen at temperatures between 2020 K and 2370 K. The powders were sintered with MgO as a sintering additive and without additives, respectively. A maximum sintered density of 3630 kg/m³ was obtained by formation of AlN polytypes, 3170 kg/m³ with 1 wt.% MgO and 3210 kg/m³ without additives. After sintering a residual porosity of 2.2 vol.% was detected by SEM. A distinct increase of oxygen content was found by wet chemical analysis and XRD resulting in the anisotropic growth of platelike AlN polytypes in the sintered AlN material.

The measured quantities of heat conductivity were interpreted with common principles of heat conductivity in single crystals and compared with calculations based upon mixture theory. Both can sufficiently describe the heat transport.

Introduction

Since the development in electronic technology offers the possibilities of very small electric circuits the dissipation of heat is one of the main important problems. The heat sink material should be a electrical insulator and a good thermal conducting material. Since first descriptions of the thermophysical properties of AlN /1, 2/ this material became a main subject of substrate material investigations. Because of their high thermal conductivity ($\geq$ 100 W/(m*K)) AlN ceramics are developed for applications such as heat sink in power electronic circuits, LSI

and VLSI circuits /3, 4/. The alternative Beryllia ceramics are expensive and toxic. Silicon carbide has to be doped to reduce the density of free charges. For the further development of substrate materials the influences on thermal conductivity in ceramics should be exactly investigated.

Sample preparation

AlN powder Starck (A) with an oxygen content of 1.6 wt.% and 1 wt.% MgO were mixed and milled by attrition milling using alumina-milling-balls. Milling procedure lasted 5h with 1000 rounds per minute. The charge mass was 100 grams of AlN/MgO powder, 750 grams of milling balls and 200 ml iso-propanole. The same procedure was used to mill AlN without additive. The oxygen content of the AlN increased during milling from 1.6 wt.-% to 5.6 wt.%. This was analysed using inert gas fusion technique. To produce a sample sample with higher oxygen content the powder was hydrolized during milling. The milling in iso-propanol mixed with 3 vol.% water increased the oxygen content up to 15 wt.% /5/. The dried powders were sieved and compacted to (62 ± 2)% of the theoretical density of AlN by isostatic pressing with 640 MPa. The MgO doped material and the hydrolized material was pressureless sintered at 2020 K in nitrogen atmosphere. The heating rate was 20 K/min. The pure AlN material was fired up to 2370 K with the same heating rate. By formation of aluminium oxynitride polytypes, $Al_9O_3N_7$ and $Al_{23}O_{27}N_5$, the density of the sample with high oxygen content increased up to 3630 kg/m³ /6/. The residual porosity of the samples was in the range below (2.0 ± 0.2) vol.% as detected by SEM. Thirty percent the oxygen content decreased during sintering, which is assumed as a result of the reducing sinter atmosphere produced by the carbon heating element. Figure 1a shows the microstructure of the MgO doped sinter specimen. Pores appear often between two grains and decrease the contact area. Figure 1b shows the fracture surface of the pure AlN sample. Some platelike structures are visible. A x-ray analysis proofed that the 27R phase, $Al_9O_3N_7$,is formed. Because of the grain morphology it is assumed that the plate-like grains are 27R polytype. The fracture surface in Figure 1c shows such a plate in the fracture surface of a porous sample where it is not broken.

Measuring of thermal conductivity

Figure 2 is a cross section of the measuring cell. The system is working in steady state conditions. In the upper part (H) a quantity of heat is produced by electric heating of a hundred ohm resistance. The heat flows in vertical direction throughout the sample (S) to the heat sink at the bottom of the measuring cell. To isolate the system the experiment takes place in a vacuum better than 10^{-3} Pa. A protective heating system produces an equivalent temperature distribution as observed along the vertical axis of the sample. Isolation and protective heating reduce heat losses. All data are collected by a computerized twelve bit data system.

Measurement data and interpretation of the measurements

All data are shown in Figure 3. Even the higher porosity of the MgO doped sample did not decrease heat conductivity below the other observed values. The purer AlN materials show a very small temperature dependence of the thermal conductivity. The highly oxygen containing sample shows no temperature dependence in the observed temperature range. The main explanation of the big difference between the measured values is the oxygen content of the materials. By sintering with MgO as an additive some oxygen is gettered by forming a MgAl-spinel /7/. For explanation of the observed data some considerations of the influence of impurities in the AlN lattice are necessary. Unfortunately it is not possible to calculate the heat conductivity of crystals exactly with lattice dynamic theory. But in the case of pure III-V compounds such as AlN temperatures below a half of the Debye-temperature are in the region of umklapp- and normal-scattering processes of the various types of phonon scattering /8/. As mentioned by Slack /9/ heat conductivity should described by the Leibfried and Schlömann equation /10/

$$k \approx A / T \qquad (A = \text{constant}). \tag{1}$$

This equation describes an inverse dependency between heat conductivity k and temperature T, which is too strong variation with temperature compared with experimental results given in fig.3 .

If an impurity occupies lattice sites the dependence between k and T changes ,

$$k = B \cdot m / (\sqrt{T} \cdot \sqrt{\Gamma}) \qquad (2)$$

where B is constant, m is the average atomic mass in the lattice, Γ is the scattering factor given by Abeles /11/. Formulae (2) results of Ziman's variational method /12/. Important is that the value of the heat conductivity is varying with inverse square root of the temperature. The main impurities in the AlN lattice which have to be considered are oxygen, carbon and silicon /9, 2, 15/. While oxygen and carbon substitute nitrogen atoms in the lat tice, Al is replaced by Si, fig. 4. Because oxygen is the main impurity strong oxygen scattering is beliefed to be the most im portant mechanism in the materials. The scattering factor Γ of oxygen in the AlN lattice was given by Slack /9/ as

$$\Gamma = 0.310 \cdot x \cdot (1-x) \qquad (3)$$

which he calculated with the method of Abeles /11/. For low con centration of oxygen x is equal to the ratio of replaced nitrogen atoms to the total number of nitrogen lattice sites per cubcm. Equations (2) and (3) were used to estimate thermal conductivity curves A and B in figure 3. The curves are higher than the observed values. For the composition B measurement and theory would agree, if assuming a mixture of 10 vol.% oxynitrides with k= 25 W/(m*K) in a random distribution in a matrix material with the thermal conductivity of the closed line. For example at T=300K the value of the curve B of 86.8 W/(m*K) change to 76.7 W/(m*K) using the formulae published by B. Schulz /14/ with the assumptions used above. This value agrees with the observed values. Composition A is not as simple to explain, because polytypes were not identified in the microstructure. Calculating the conductivity of a material with 2.2 vol.% porosity and and 132.5 W/(m*K) heat conductivity of the matrix material the result is a composite with 125.6 W/(m*K) at 300 K. This value is still 10 W/(m*K) to high.

Conclusions

Two effects reduce the thermal conductivity in AlN ceramics. The presence of chemical impurities such as oxygen, which substitute lattice atoms, reduce the thermal conductivity of the grains. The formation of polytypes, which show lower heat conductivity than AlN, leads to further reduction of the thermal conductivity. To obtain AlN materials with high thermal conductivity the first aim should be to produce very pure matrix material and carefully avoid the formation of solid solutions between the sintering additive and AlN during sinter process.

/1/ J.A. Kohn, P.G. Cotter, R.A. Potter, Am. Mineral, 41(1956)355
/2/ K.M. Taylor, C.J. Lenie, J. Elektrochem. Soc., 107(1960)308
/3/ W. Werdecker, F. Aldinger, in: Proceedings of the 34th ECC, IEEE (1984)402
/4/ M. Kuramoto, H. Taniguchi, I. Aso, in: Proceedings of the 36th ECC, IEEE (1986)
/5/ T.R. Bhat, I.A. Khan, Indian J. Chem., vol.5, (1967)
/6/ J.W. McCauley, N.D. Corbin, J. of the Am. Cer. Soc., 62(1979)476
/7/ J. Weiss, P. Greil, L.J. Gauckler and G. Petzow, J. of Am. Cer. Soc. 65(1982) C68
/8/ G. Holland, in: Semiconductors and Semimetals, vol.2, 1966
/9/ G.A. Slack, J. Phys. Chem. Solids, 34(1973)321
/10/ G. Leibfried, E. Schlömann, Nachr. Akad. Wiss. Göttingen, Math.Phys., Klasse 4,(1954)71
/11/ B. Abeles, Phys. Rev., 131(1963)1907
/12/ R. Berman, D.T. Nettley, F.W. Sheard, A.N. Spencer, R.W.H. Stevenson and J.M. Ziman, Proc. Roy. Soc. London, A253(1959)403
/13/ D. Gerlich, S. L. Pole, G.A. Slack, Technical Information Series, Class 1, Report No.84CRD244, Oct. 1984
/14/ B. Schulz, High Temp. - High Press., 13(1981)649
/15/ G.A. Slack, T.F. McNelly, J. of Crystal Growth, 34(1976)263

1 a)

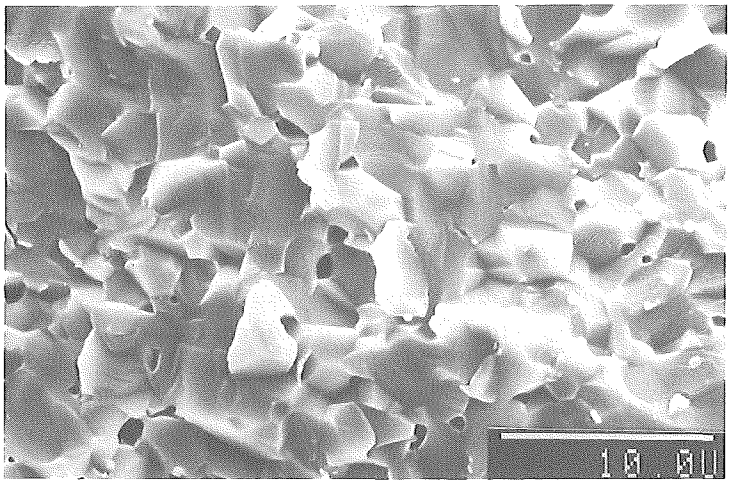

1 b)

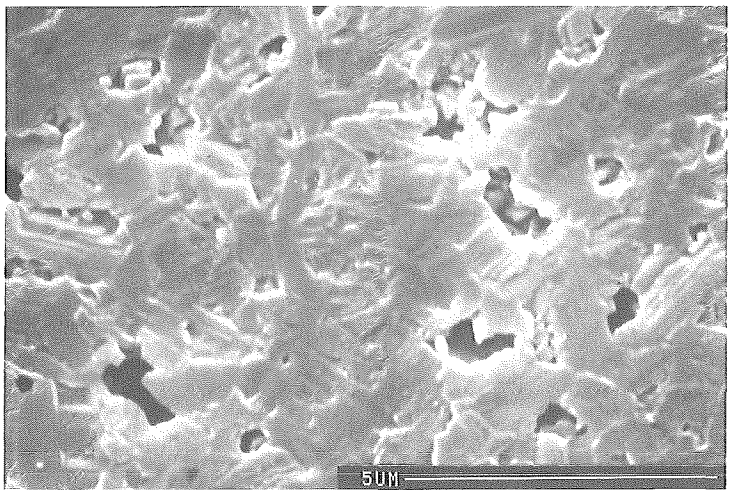

1 c)

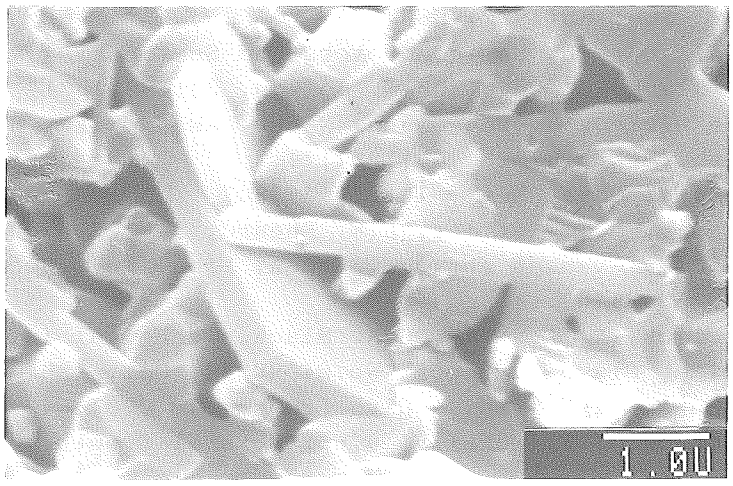

Figure 1: SEM micrograph of fracture surfaces of different AlN materials. (1a) ≡ AlN + 1 wt.% MgO, (1b) ≡ pure AlN with 3.4 wt.% oxygen, (1c) ≡ oxinitride plate within a porous matrix.

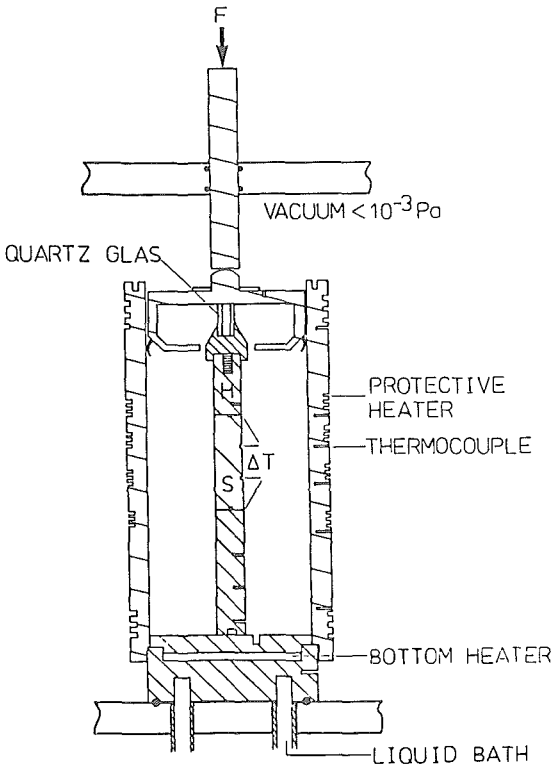

Figure 2: Cross section of the measuring cell.

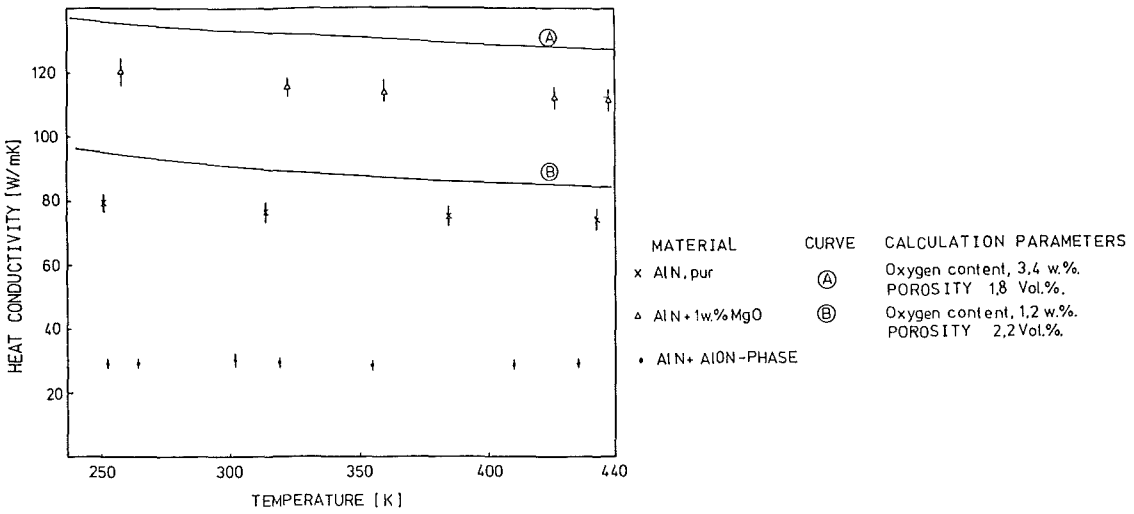

Figure 3: Observed and computed heat conductivities. The third composition is a mixture of AlN, $Al_9O_3N_7$ and $Al_{23}O_{27}N_5$.

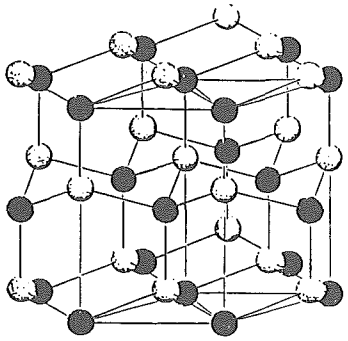

ATOM	LIMIT OF SOLUBILITY [cm^{-3}]	LATTICE PLACE	TYPE OF ELECTRICAL CONDUCTIVITY
O	$6.0*10^{21}$	N	n
C	LIKE O	N	p
Si	$8.8*10^{19}$	Al	n

Figure 4: AlN lattice (wurtzite type) and reported maximum impurity levels.

Preparation, Characterization and Thermal Diffusivity of Al_2TiO_5

M. Milosevski* and B. Schulz

Kernforschungszentrum Karlsruhe, IMF I, Karlsruhe, FRG
*** Guest scientist from Faculty of Technology and Metallurgy, Skopje, YU**

Abstract

The paper describes the technique of the preparation and characterization of crack free Al_2TiO_5 samples. The porosity range of the samples was between 10 and 18 %. On these crack free samples the thermal diffusivity was measured with a laser-flash technique. The data follow a temperature relationship as it is expected for electrical insulators.

1. Introduction

Al_2TiO_5 is of special interest because of its applicability for containing molten metals (uranium) without contamination of metals [1], for parts of engine in cars [2], as materials for tunnel gas burners [3], as good thermal insulating material for combustion engine systems, etc.

Al_2TiO_5 exhibits some very interesting properties that include:

1. its high refractoriness
2. its very low volume thermal expansion
3. its low thermal conductivity
4. its low strength and its strong anisotropic thermal expansion.

2. Properties of Al_2TiO_5

Several investigators [4,5,6] have studied the system Al_2O_3-TiO_2. Their phase diagrams show one compound, Al_2TiO_5, and eutectics with both component oxides. There are two allotropic forms of Al_2TiO_5, alpha, the high temperature and beta, the low temperature form, respectively. The eutectics are located at 1973 K at about 20 wt.% of Al_2O_3 and 2123 K at about 61.5 wt.% of Al_2O_3, Fig. 1.

- pure Al_2TiO_5 exists in equilibrium only above 1473 K. Below that temperature it decomposes eutectoidal into the Al_2O_3 and TiO_2.
  X-ray studies at high temperatures [7-12] proved that Al_2TiO_5 is characterized by a strong expansion anisotropy. Thermal expansion is negative in the c-direction and quite large in the a- and b-direction of the orthorhombic crystals.

Especially the decomposition of Al_2TiO_5 introduces many problems in determining properties of this compound at temperatures below the eutectoidal temperature. This together with the high anisotropy in the lattice thermal expansion means for the determination of the thermal expansion of bulk polycrystalline samples strong hysteresis effects and very low apparent thermal expansion coefficients.

This is due to the presence of a complicated system of internal cracks formed by internal stresses. During cooling, the contractions of the individual crystals are incompatible, and a complex system of stresses arises within each crystal. In

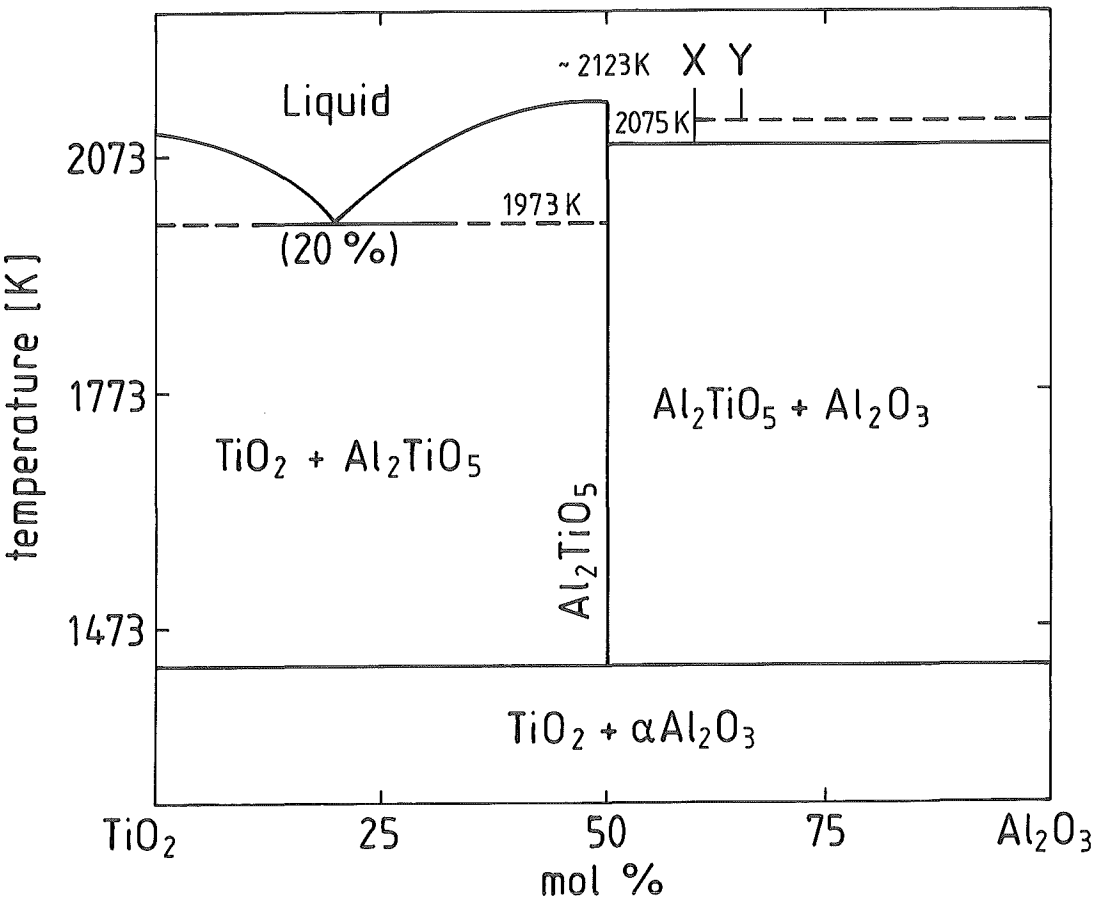

Fig. 1: Phase equilibrium of the Al_2O_3-TiO_2 quasibinary system [4].

general, high tensile stresses occur in directions of high thermal expansion (actually a contraction during cooling) and high compressive stresses in direction of low thermal expansion. When these stresses exceed the strength of the crystals or the bonds between crystals, fractures occur that tend to be oriented perpendicular to directions of high expansion [14]. Because the coherence of individual crystallites is destroyed, Al_2TiO_5 is very friable and mechanically weak.

The effect of anisotropic thermal expansion in polycrystalline systems has been investigated by several authors [7,13,14,15,16]. They observed microcracking only in specimens with large grain size. It is well documented that fine-grain-size ceramics remain crack-free, when cooled from high to room temperature [16,17,18,19].

As Al_2TiO_5 has a high thermal anisotropy, in order to reduce the grain boundary microcracking, that is obtain crack-free bodies of Al_2TiO_5, its grain size must be decreased under the value of its "transition grain size".

Cleveland and Bradt [20] estimated that the "transition grain size" for microcracking in Al_2TiO_5 ceramics was 1 - 2 μm. According to Hamano et al. [21] the "transition grain size" is 2.5 μm. Holcombre [22] reported a "transition grain size" of 1 μm.

To determine properties of Al_2TiO_5 which can be attributed to the compound Al_2TiO_5 it is thus important to prepare crack-free samples and evaluate those measuring conditions (heating rate), in which the non-equilibrium below 1473 K will not influence the data evaluated. Thus the proper preparation and characterization of crack-free Al_2TiO_5 samples and the determination of its thermal diffusivity is the main topic of this paper.

3. Experimental Procedures and Results

The compound used in this study was Al_2TiO_5 obtained from CERAC, USA. The chemical composition of this powder is shown in Table I.

Table I: Chemical composition of Al_2TiO_5 powder.

Al_2TiO_5 (wt.%)	99.5 + trace of Al_2O_3
impurities (wt.%)	Ca/Cu/Fe/Ga/Mg/V 0.005; Mn 0.001; Zr/Si 0.01

But, from X-ray analysis could be concluded that his powder contains large amounts of corundum and rutile. Fig. 2a. The average particle size of this powder was 37.7 μm. To obtain pure Al_2TiO_5 powder with sufficiently low grain size the following procedure was carried out:

The Al_2TiO_5 powder was hot pressed at 1723 K (30 MPa, 2 h). Obtained compacts which were cracked then were annealed at 1873 K for 4 h in air atmosphere to complete reaction between Al_2O_3 and TiO_2 ($Al_2O_3 + TiO_2 \rightarrow Al_2TiO_5$), what was confirmed by X-ray analysis, Fig. 2b. The compacts of Al_2TiO_5 then were milled in a mill with WC-balls for 21 days. Qualitative chemical analysis of the powder after milling showed a presence of W, Mo, Ni, Fe and Co. But, X-ray analysis showed only presence of α-Fe, Fig. 2c, what means that the other metals are

a - started Al_2TiO_5 c - after milling
b - after annealing at 1823 K for 4h d - after treating with 15 % HCl

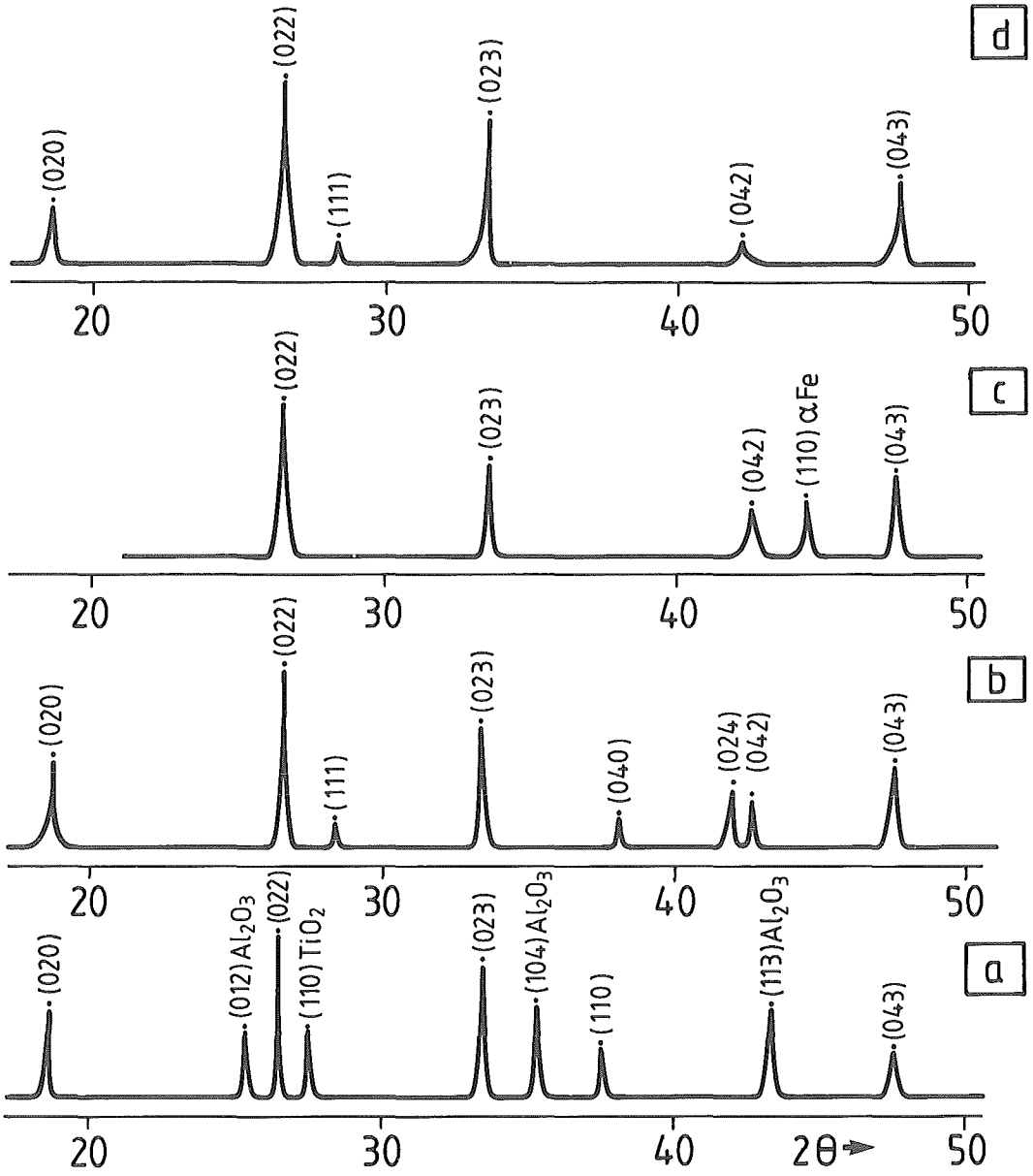

Fig. 2: X-ray interference of Al_2TiO_5 (2θ = 18 - 50); $Cu_{K\alpha}$.

present below the limit of detection of X-ray analysis. The powder was then treated with 15 % HCl to dissolve the present Ni, Fe and Co. Qualitative analysis of this powder showed the presence of W and Mo, whose content was below the limit of detection of X-ray analysis, Fig. 2d.

The particle size of Al_2TiO_5 after this treatment was 0.63 µm. The densification of this powder was made using hot-pressing. An axial hot-press equipment was used.

When we used powder with larger particle size, for example powder with particle size > 2 µm, we always got cracked bodies (grain size was larger than "transition grain size"). Hot-pressing of Al_2TiO_5 whose particles size was 0.63 µm, gave crack-free bodies (grain size smaller than "transition grain size"). Fig. 3a, Fig. 3b.

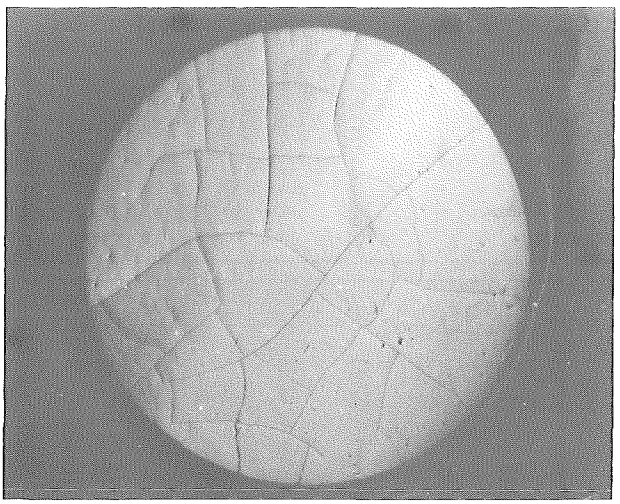

Fig. 3a: Compact of Al_2TiO_5 (particle size of the powder 3.3 µm) with crack.

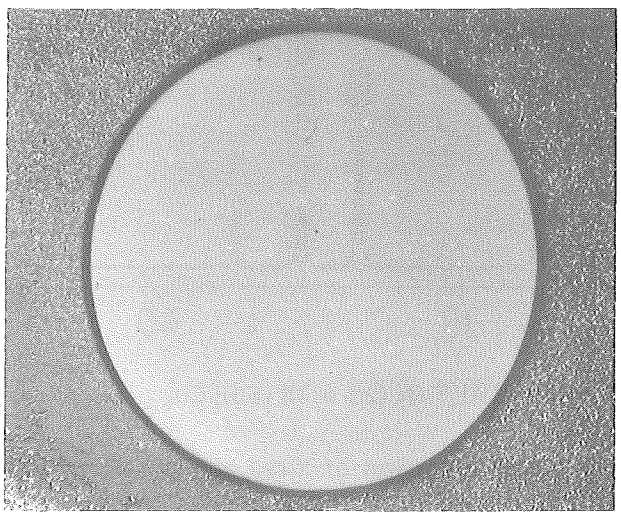

Fig. 3b: Compact of Al_2TiO_5 (particle size of the powder 0.63 µm) without crack.

Optimum hot-pressing parameters and characteristics of the obtained crack-free compacts are shown in Table II.

Table II: Optimum hot-pressing parameters and characteristics of the obtained crack-free compacts.

Temperature, K	1623	Second phase, wt.%	2.5 Al_2O_3
Pressure, MPa	30		2.5 TiO_2
Holding time, min	0.8	Porosity range (%)	10 - 18
		Carbon content, wt.%	0.054 ± 0.001

Even with this procedure samples with densities higher than 90 % of the theoretical density, cracked after some weeks. In our experiments we used crack-free compacts whose density was 82 - 89.5 % of the theoretical density.

The microstructure of crack-free Al_2TiO_5 is shown in Fig. 4. The grain size is estimated to be about 1 µm.

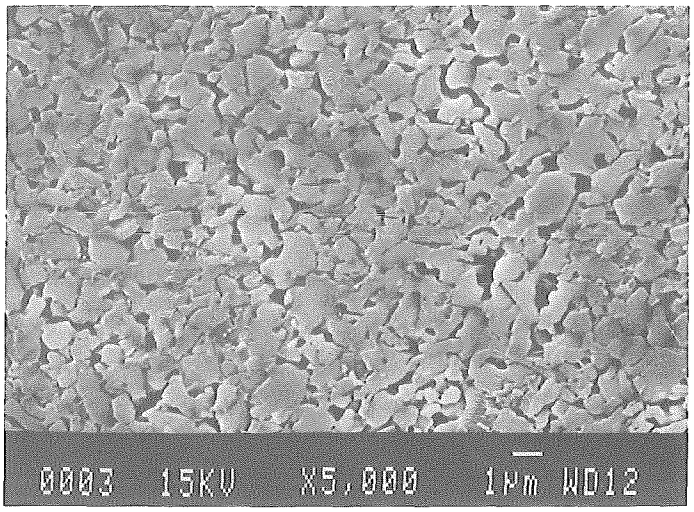

Fig. 4: Microstructure of crack-free Al_2TiO_5.

Measurement of thermal diffusivity

A laser flash equipment (Theta, New York) was used according to the theory of Parker et al. [25] and described in detail by R.E. Taylor [26]. The main principle is a homogeneous, adiabatic heating by a flash of the front face of a cylindrical shaped sample in a furnace heated to the measuring temperature. It is assumed that the energy is absorbed only in a depth being neglegible compared to the

thickness of the sample. The temperature raise at rear face is recorded by an infrared detector. Under ideal conditions the temperature in the sample is only a function of time and the coordinate along the axis of the cylindrically shaped sample. The thermal diffusivity was calculated from the specimen thickness and the time for the back surface temperature of the specimen, to reach one half of its final value. The ambient temperature of the specimen was changed by adjusting the temperature of a furnace containing the specimen. The heating rate up to the fixed temperature levels was always about 6 $Kmin^{-1}$. The thermal diffusivity was measured on heating as well as cooling from 293 - 1293 K.

One problem arises in measuring the thermal diffusivity of transparent samples. In this case the surfaces are manually covered with a Pt-coating, from a Pt-emulsion of thickness of about 10 µm. It was shown [27] that this causes an error of about less than 1 %. The standard deviation of the method is given as 3 - 5 %. The measuring temperature is determined with NiCrNi-thermocouple. Several samples were measured on heating and cooling. The equipment was checked with POCO graphite, which is not offical standard - there is none up to now - but is all over the world used as an internal standard.

In our experiment we used samples of Al_2TiO_5 with three different porosities: 10.5; 14.7 and 18.0 %. The temperature variation of the thermal diffusivity is shown in Fig. 5.

The thermal diffusivity of a sample with closed porosity is a definite function of the amount of porosity (P), the shape factor (F) and orientation ($\cos^2\alpha$) of the pores to the direction of heat flow [23]

$$\alpha_P = \alpha_0(1 - P)^n \tag{1}$$

$$n = f(F, \cos^2\alpha)$$

The subscripts P, 0 refer to the porous and dense sample. This means that in fact for each porous sample a quantitative microstructural analysis has to be performed to determine F and $\cos^2\alpha$, which whas not possible at the materials treated below. So it was decided to follow the results of the microstructure analysis as published in [23], from which follows Table III.

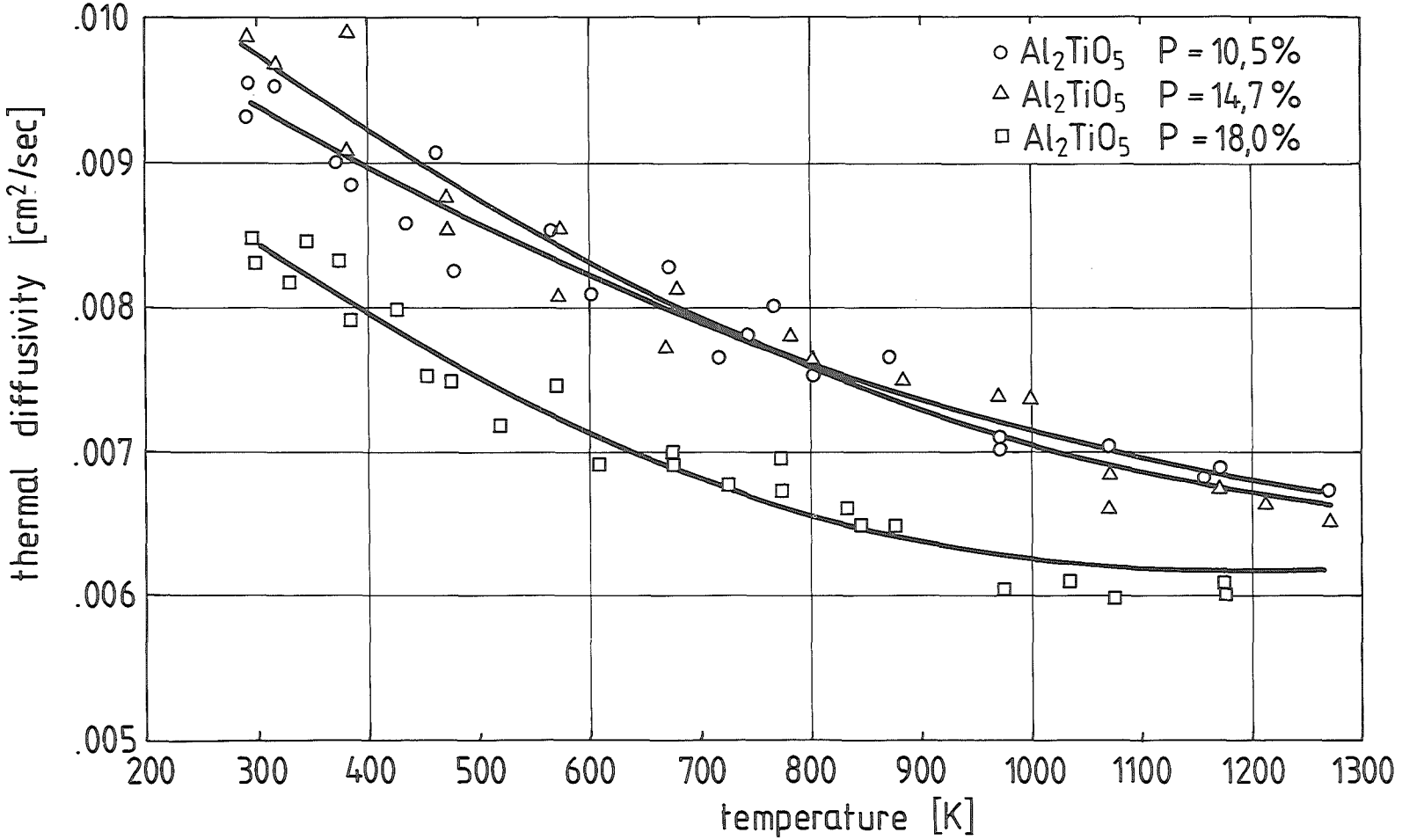

Fig. 5: Thermal diffusivity of Al_2TiO_5 with different porosity.

Table III: Exponent in equ. (1) for porosity correction of

Porosity %	n in equ. (1)
10.5	0.59
14.7	0.59
18.0	0.65

The variation of the thermal diffusivity with temperature for dense Al_2TiO_5 (P = 0) is shown in Fig. 6.

The thermal diffusivity of hot-pressed Al_2TiO_5 whose grain size is about 1 µm, exhibits a temperature dependence typical of a dielectric material in which heat transport occurs primarily by lattice conduction i.e. phonon transport. On heating and cooling, the thermal diffusivity does not exhibit any evidence of hysteresis which implies that in this fine grain size material there is no evidence of microcracking. The absence of hysteresis indicated also that over the duration of these measurements (heating rate/cooling rate about 6 $Kmin^{-1}$) there is no significant process of decomposition into the constituent oxides (corundum and rutile).

In the literature there is only one paper for thermal diffusivity of microcracked Al_2TiO_5 [24], Fig. 7.

On heating, the microcracked material exhibits decreased thermal diffusivity and goes on with constant thermal diffusivity, what may be attributed primarily to microcrack closure and healing. On cooling, the sample exhibits a pronounced hysteresis caused by irreversible crack opening and closing. (It is only for the first run, for the second run which is not shown in the figure, the hysteresis curve is closed).

Mechanical properties

Ultrasonic measurements for the determination of Poisson's ratio and Young's modulus were used. The value of Young's modulus is 1156 kbar (115, 6 GPa) and Poisson's ratio is 0.29 at porosity of 10 %.

According to the results of Carlsson [28] they got for Al_2TiO_5 microcracked, a Young's modulus of 11 GPa, what is about 10 times smaller than our value.

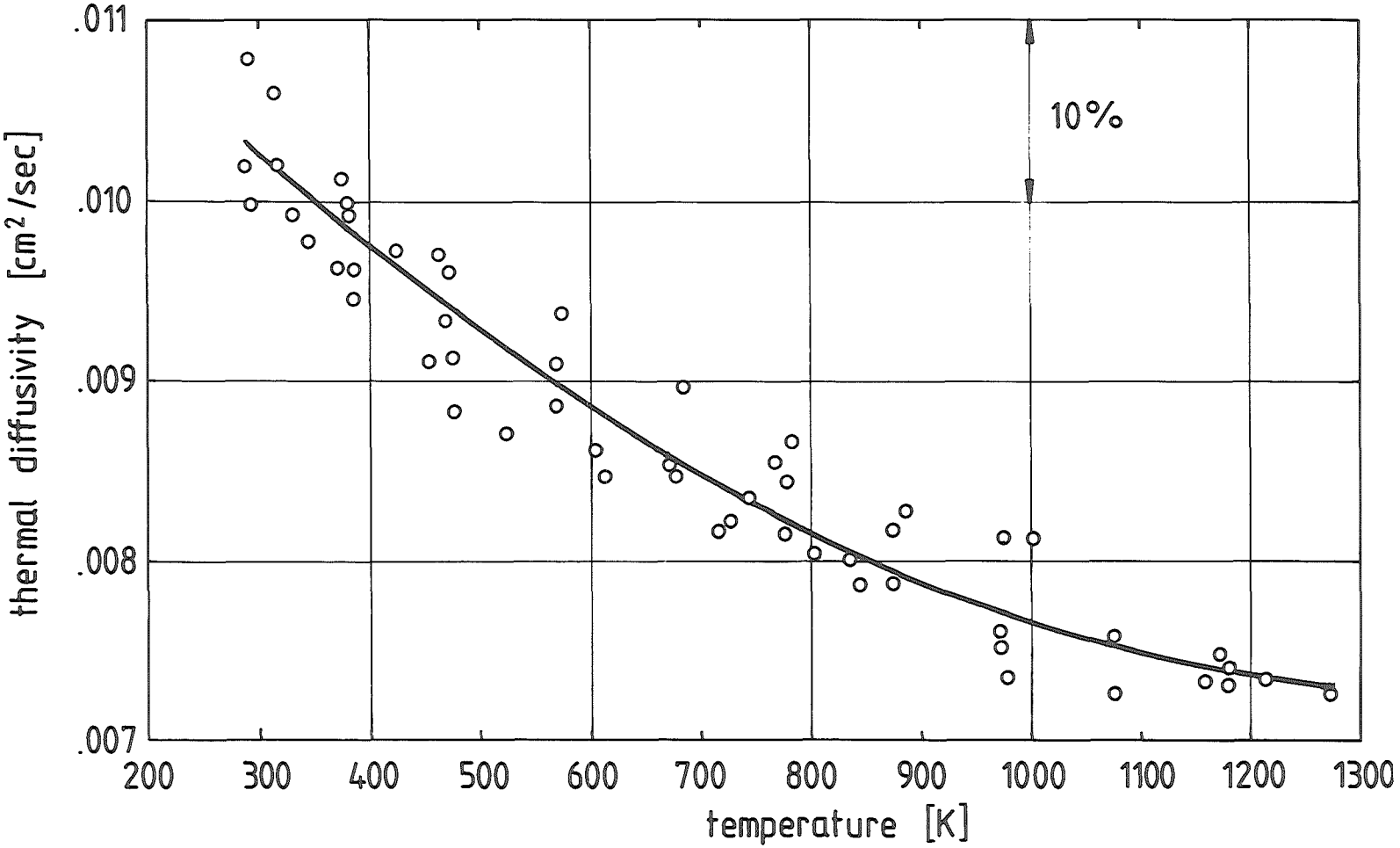

Fig. 6: Thermal diffusivity of Al_2TiO_5 corrected for porosity.

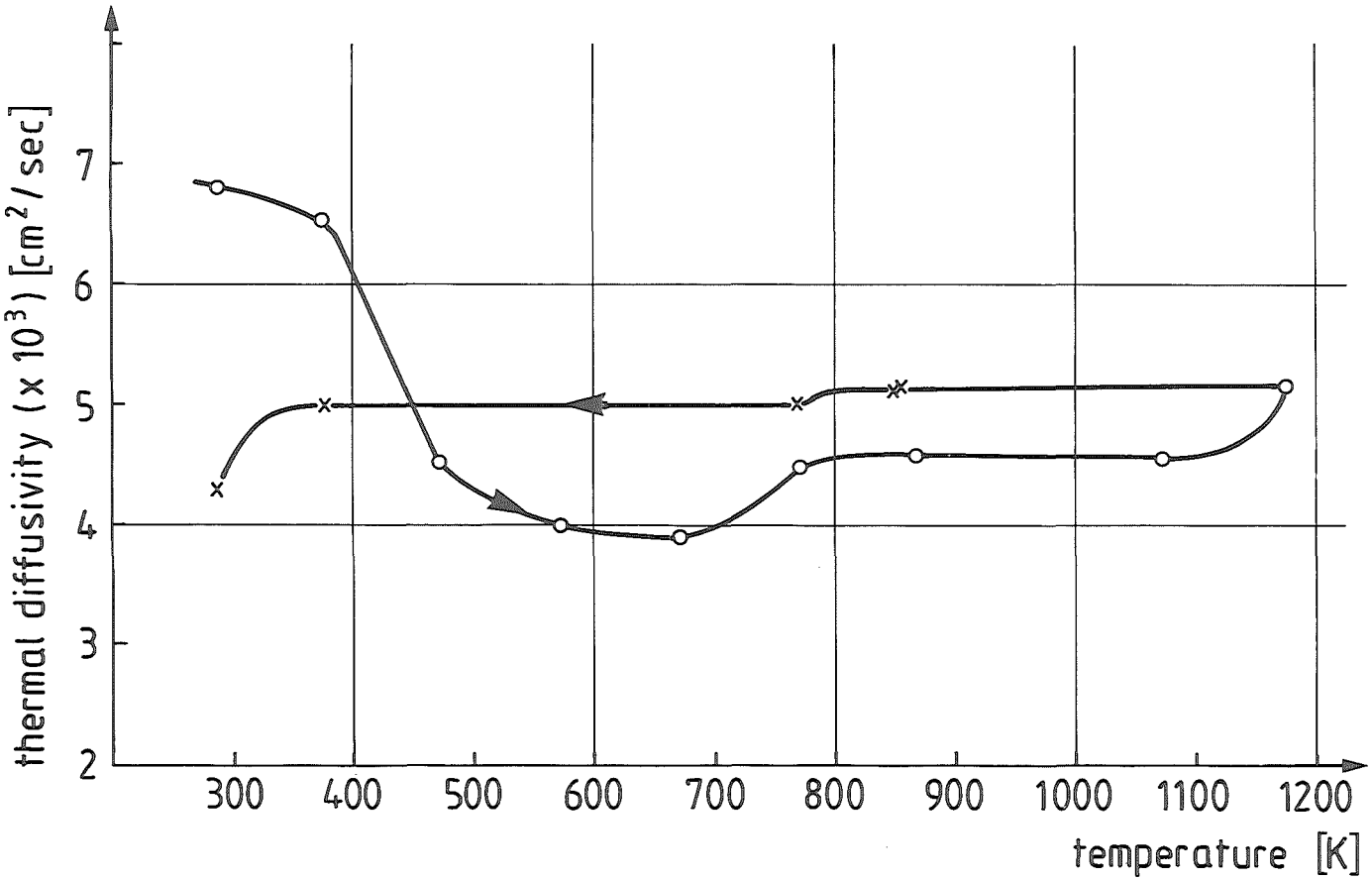

Fig. 7: Temperature variation of thermal diffusivity of microcracked Al_2TiO_5 [24].

Literature

[1] K. Morrow, E. Holcombre and A. Cramer, NTIS Y-1831, Sept. 29, 1972

[2] A. Diamont and M. Lafant, L'industrie Ceramique 743 (10) 669 (1980)

[3] Research Association (1963 - 64), Gas Council, Research Communication G.L. 111 p. 15 (quoted afer C. Han, Sprechsaal 118 (12) 1164 (1985))

[4] D. Goldberg, Rev. Int. Hautes Temp. et Refract. 5, 181 (1964)

[5] H. von Wartenberg and H. Reusch, Z. Anorg. Allgem. Chemie 207, 1 (1932)

[6] S. Lang, C. Fillmore and I. Maxwell, J. Res. Natl. Bur. Stds., 48 (4) 298 (1952)

[7] R. Buessem, N. Thielke and R. Sarakauskas, Ceramic Age, 60, 38 (1952)

[8] R. Thielke, USA, Air Force, Air Research Development Command WADC, Techn. Rept. 53-165, 1953

[9] L. Cartz, Anisotropy in single crystal refractory compounds Vol. I, p. 383. Ed. F. Wahldieck, New York, Plenum Press, 1968

[10] G. Bayer, J. Less Common Met. 24 (2) 129 (1971)

[11] B. Morosin and R. Lynch, Acta Cryst. B 28, 1040 (1972)

[12] E. Gugel and R. Schuster, Tonind. Ztg. 98, 315 (1974)

[13] R. Buessem and E. Lange, Interceram. 15 (3) 229 (1966)

[14] A. Bush and A. Hummel, J. Am. Ceram. Soc. 41 (6) 189 (1958)

[15] A. Bush and A. Hummel, J. Am. Ceram. Soc. 42 (8) 388 (1958)

[16] R. Manning, O. Hunter, W. Calderwood and W. Stacy, J. Am. Ceram. Soc. 55 (7) 342 (1972)

[17] R. McPherson, J. Australian Ceram. Soc., 3 (2) 43 (1967)

[18] A. Kuszyk and C. Bradt, J. Am. Ceram. Soc. 56 (8) 420 (1973)

[19] J. Blendel, R. Coble and R. Charles, Sixth International Symposium on Microstructure of Ceramic Materials, Berkeley, Calif. 1976

[20] J. Cleveland and C. Bradt, J. Am. Ceram. Soc. 61 (11-12) 478 (1978)

[21] K. Hamano, Y. Ohya and Z. Nakagava, Yoguo-Kyokai-Shi, 91, 289 (1983) (quoted after K. Hamano et al. Int. J. High Tech. Ceram. 1, 129 (1985))

[22] Holcombre, Private communication (quoted after J. Cleveland and Bradt, J. Am. Ceram. Soc. 61 (11-12) 478 (1978))

[23] B. Schulz and H. Wedemeyer, J. Nucl. Mat. 139, 35 (1986)

[24] H. Siebeneck, J. Cleveland, D. Hasselman and R. Bradt, In Ceramic Microstructure '76, Ed. R. Fulrath and J. Pask, Sixth International Symposium on Microstructure of Ceramic Materials, Berkeley, Calif. 1976

[25] W. Parker, R. Jenkins, G. Abbott, J. Appl. Phys. 32, 32 (1961)

[26] R. Taylor, High Temp. High Press. 12, 43 (1980)

[27] B. Schulz, Xth European Conference on Thermophysical Properties, September 1986, Frascati Italy

[28] R. Carlsson, S. Karlsson, Science of Ceramics, 11, 479 (1981)

Dilatometric Analysis of Al-, Ba-, Ca-Titanate

M. Milosevski*, B. Schulz

Kernforschungszentrum Karlsruhe
Institut für Material- und Festkörperforschung
Postfach 3640, 7500 Karlsruhe
Federal Republic of Germany

***Guest Scientist from University of Skopje, Yugoslavia**

Abstract

The titanates of aluminium, barium and calcium were chosen to perform dilatometry with respect to second order transitions and to hysteris effects in thermal expansion, well known in the literature. The relative thermal expansion of all three materials have been determined, after a detailed study of the method itself.

Introduction

Dilatometry is a well known method in materials science, applied especially in the area of sintering kinetics. Apart from this it is possible to measure the thermal expansion of materials as a physical property if detailed studies of possible systematic errors are performed. All investigations described below were carried out with a commercial Netzsch-Differential Dilatometer 402E.

Sample preparation and characterization

In the paper of the same authors in these proceedings [1] a detailed description of the preparation and characterization of Al_2TiO_5 crack free samples is presented. The methods applied there were also used for $BaTiO_3$ and $CaTiO_3$. Table 1 summarizes all data for the three titanates treated in the following. All samples were hot-pressed in graphite dies in Ar-atmosphere. The sample length was 25.00 mm for Ba-, $CaTiO_3$ and 9.00 mm for Al_2TiO_5.

Table 1: Optimum hot-pressing parameters of titanates.

Powder	$BaTiO_3$	$CaTiO_3$	Al_2TiO_5
Temperature (K)	1473	1723	1623
Pressure (MPa)	20	30	30
Holding time at temperature (min)	5	1.5	0.8
Particel size (µm)	0.84	10.0	0.63
Second phase	–	–	2.5 wt.% Al_2O_3 2.5 wt.% TiO_2
Porosity range (%)	0.03 - 3.8	5 - 10	10 - 18
Carbon content	0.011 ± 0.002	0.081 ± 0.013	0.084 ± 0.001

Systematic investigations with the dilatometer for thermal expansion measurements

If the temperature T and pressure P define as state properties the conditions of a thermodynamic system, its volume V is given by:

$$dV = \left(\frac{\partial V}{\partial T}\right)_P dT + \left(\frac{\partial V}{\partial P}\right)_T dP$$

only for the case that P = const. the toal change in volume dV is identical with the change in volume caused by temperature changes, then

$$\beta_{th} = \left(\frac{dV}{dT}\right) \cdot \frac{1}{V_0}$$

is the volume thermal expansion coefficient and for polycrystalline and isotropic materials

$$3\alpha_{th} = \beta_{th}$$

where α_{th}, the linear thermal expansion coefficient, is also defined by:

$$\alpha_{th} = \frac{1}{L_0}\left(\frac{dL}{dT}\right) = \frac{d\left(\frac{\Delta L}{L_0}\right)}{dT}$$

ΔL being the change in sample length with temperature referring to the starting length L_0 at room temperature ($\equiv$ 293 K).

Thus measuring the linear thermal expansion $\Delta L/L_0$ or its coefficient, it must be sure theat no other quantity acts on the sample in that way, that changes in length follow. Besides that the sample as well as the measuring system has to be in thermal and thermodynamic equilibrium.

The measuring system of the difference dilatometer allows the parallel adjustment of a standard reference sample and the sample itself. This means that the original quantity being registrated is the difference in length between the length of the standard and that of the sample at the sample temperature T, here

defined as Δl. The systematic investigations carried out all refer to this originally measured quantity. As the thermal expansion of the standard material is obviously a fact of major importance it is necessary to have two sets of standards the one for the measurement of thermal expansion of the sample, and the other for controlling the standards in use for possible contamination during measurements. The following standard reference materials are available, sapphire, copper, tungsten, silica, borosilicate glass (NBS) and an internal one stainless steel 1.4970 (thermal expansion data from the Physikalisch-Technische Bundesanstalt, Germany). The first parameter analyzed was the true resolution of the instruement. This is defined as the maximum deviation from the ideal straight line of the Δl if two standards of the identical material are mounted in the dilatometer. This resolution was determined as $\pm$ 1 µm. The next question arising is the role of the heating rate, if data are taken in dynamic mode, that is during heating or cooling. It is well known that many published data have their origin in experiments with heating rates up to 5 K/min. As a drastic example of the systematic shift of the measured Δl, results are presented for runs of $CaTiO_3$ against sapphire (Table 2).

Table 2: Role of heating rate in dilatometry (atmosphere vaccum 10^{-5} - 10^{-6} mbar).

$CaTiO_3$-Sapphire

true signal (static)	at 555 °C	72.4 µm ± 1 µm
0.5 K/min		65.4 µm
2 K/min		64.0 µm
5 K/min		41.6 µm

Obviously no thermal equiblibrium existed during dynamic measurements. The shift itself depends on many other physical properties of the sample, the standard and the measuring head, so, for example, on heat capacity, thermal conductivity and so on and cannot be foreseen. Even in static mode we made the experience that at T = const. the different properties of standard and sample determine the time at which the original signal Δl is by fact constant at constant T. From these results the conditions for dilatometric determination of the thermal expansion are as follows:

- calibration with standard reference materials
- stepwise heating and cooling
- data only at T = const.

- reproducibility within the true resolution of the instrument (± 1 µm)
- baseline (expansion at room temperature) must be equal on heating and cooling with ± 1 µm
- maximum time for one run ~ 60 h.

Results

Within our studies of the titanates, $BaTiO_3$ was chosen because it has a II-order transition (tetragonal-cubic) and it exists a recommended curve for its thermal expansion [2].

The II-order transition was measured in dynamic mode with 0.5 K/min. Our results given in Table 3 are compared with literature data. As can be seen we agree well with other authors which is especially true for the linear thermal expansion coefficient in the vicinity but above the transition temperature.

Table 3: Thermal expansion and II-order transition in $BaTiO_3$.

Temperature range (°C)	Method	Heating rate	α (K-1) ($T > T_T$)	Reference
95 - 120	Dil.	not given	$1.4 \cdot 10^{-5}$	v. Hippel et al. [3]
–	X	–	1.26	Panlener, Blumenthal [4]
100 - 133	Dil.	2.5 - 3 K/min	0.92	Bunting et al [5]
100 - 125	Dil.	2 K/min	1.12	Cook et al. [6]
99 - 110	Dil.	not given	–	Miyake, Ueda [7]
100 - 130	Dil.	not given	0.98	Shirane, Takeda [8]
95 - 115	Dil.	0.5 K/min	1.03	this work

Fig. 1 shows the thermal expansion in the transition region with a small shift in heating and cooling but no shift in the transition temperature, as often observed when too high heating rates are chosen. The comparison between the recommended curve for $BaTiO_3$ and our data above the transition temperature shows agreement within the ranges of accurcy of both data sets (Fig. 2).

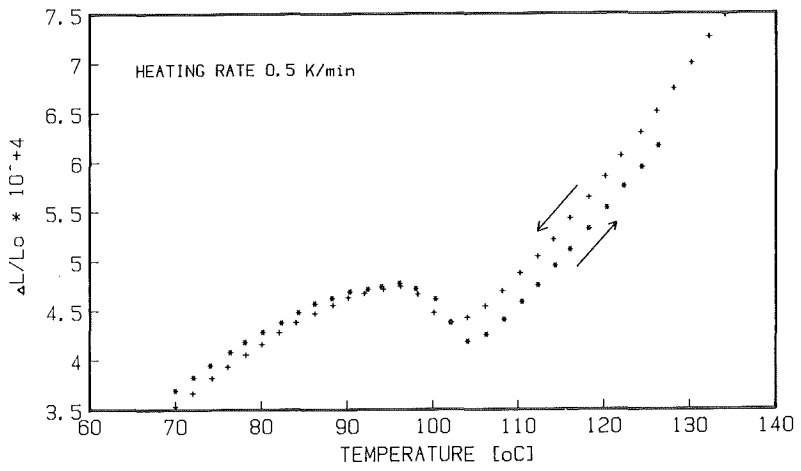

Fig. 1: Thermal expansion of $BaTiO_3$.

For $CaTiO_3$ no data were existing except very old ones by Eichelberger [9] without remarks on the measuring conditions. The situation is complicated by the fact that there is mentioned an orthorhombic to tetragonal transformation at about 600 °C [10], which later on was not confirmed. So as a first step differential scanning calorimetry was performed on $CaTiO_3$ with a Perkin-Elmer DSC2 in the sensivity range of 2 mJ/K and no sign of a transformation could be found up to the limiting temperature of the DSC (723 °C). Investigations with DTA were not successful because the sensivity of the DTA with 0.147 µV/mW was too low for studies above 1000 K. So X-ray measurements wer performed at room temperature, 600, 800 and 1000 °C, indicating indeed a phase transformation, which we attribute to take place at the temperatures between 723 and 800 °C (Fig. 3). This was confirmed by the fact that the splitting of the 200, 121, 002 X-ray peaks of the orthorhombic lattice diminishes when heating to 800 °C. In agreement to these facts the limiting measuring temperature for the thermal expansion according to the conditions mentioned above was 800 °C. The results from which we think that they represent the true linear thermal expansion of $CaTiO_3$ are presented in Fig. 4.

For Al_2TiO_3 many data are published for the thermal expansion. They all show strong hysteresis effects which (see [1]) may be attributed partially to the strong anisotropic lattice expansion of the Al_2TiO_3 and partially to the possible starting kinetics of the decomposition of this titanate into the constituent oxides. Our results as presented in Fig. 5 and measured with samples having a grain size of ~ 1 µm [1] showed up to 773 °C no hysteresis and good reproducibility. The curve

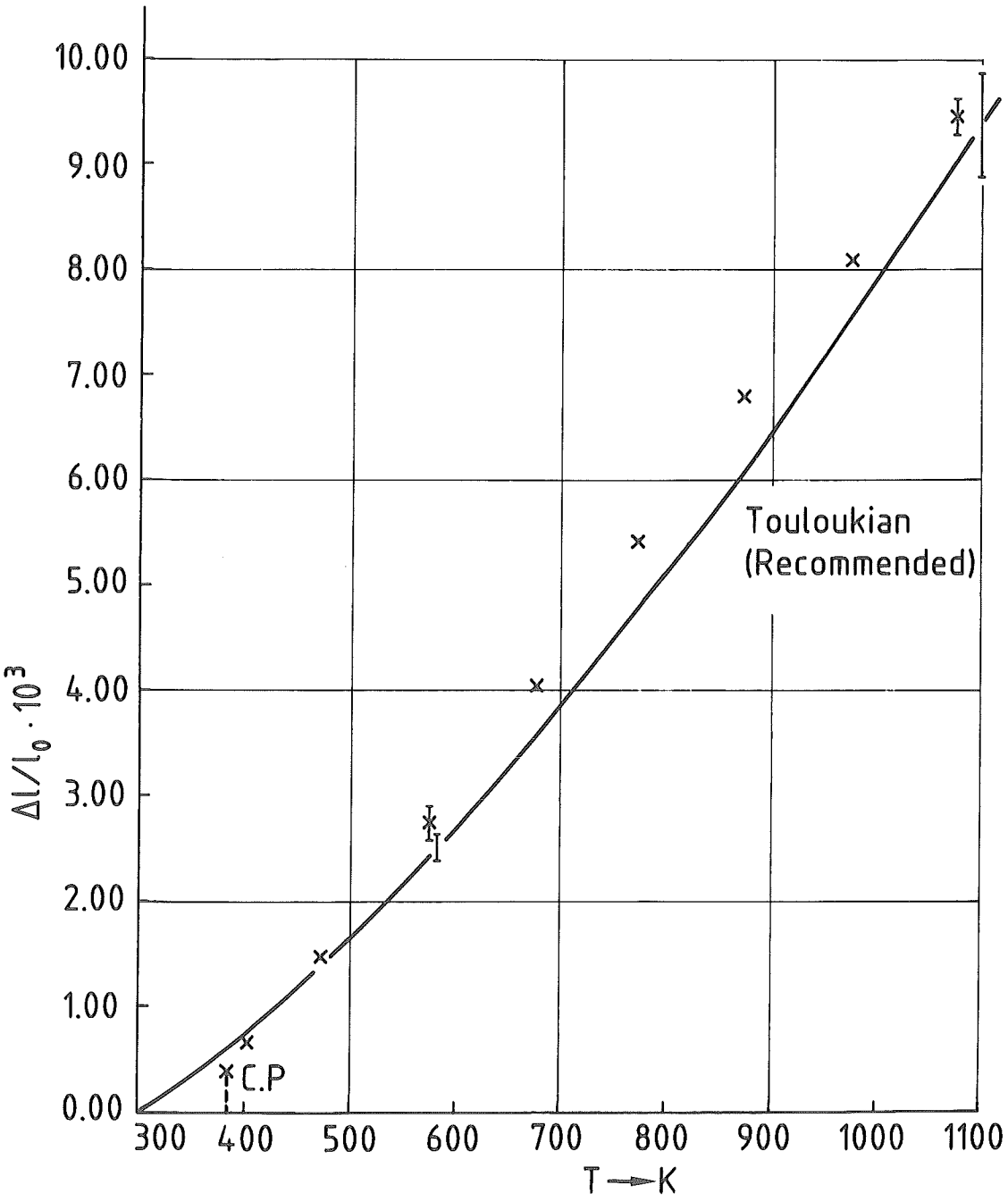

Fig. 2: Linear thermal expansion of $BaTiO_3$.

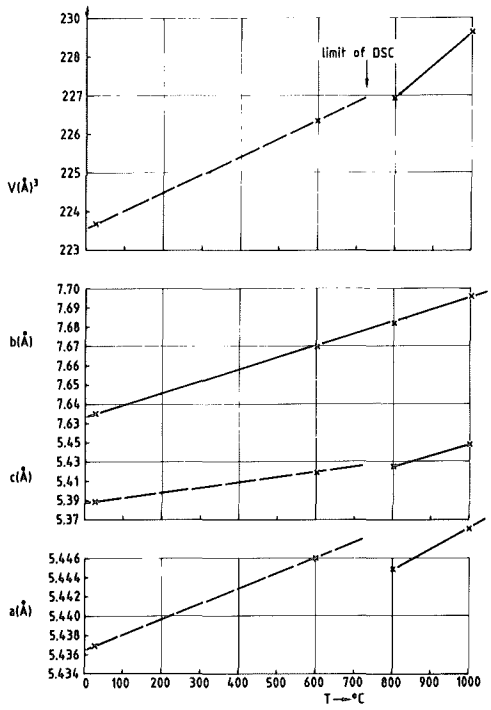

Fig. 3: Lattice constants and cell-volume of $CaTiO_3$.

of the linear thermal expanison is compared with the provisional curve as worked out in the Touloukian series of Thermophyiscal Properties of Matter [2]. There is no agreement between our data and the provisional one. We think our data to be correct.

The authors are indebted to Dr. A. Skokan, IMF I, who performed the X-ray measurements on $CaTiO_3$.

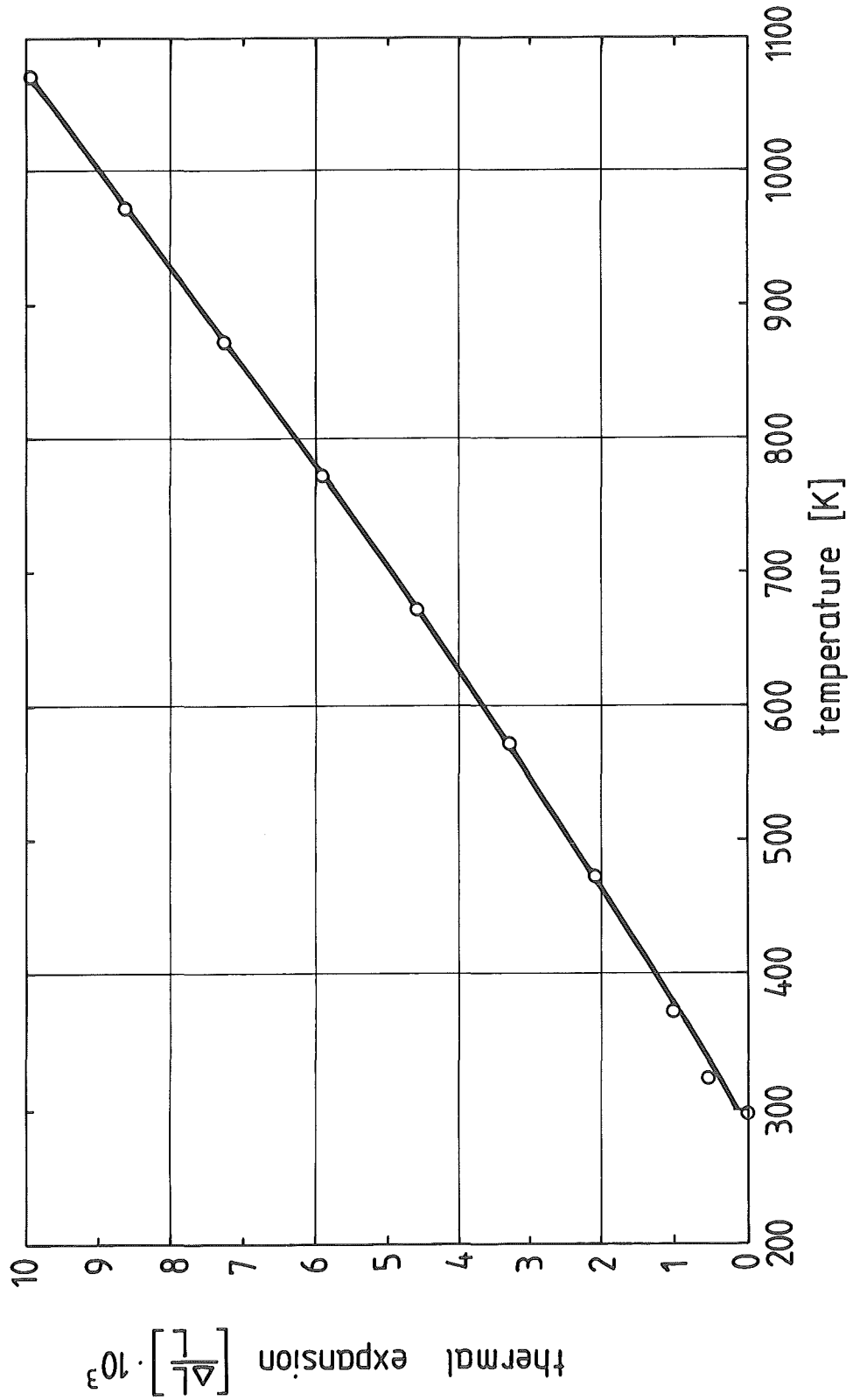

Fig. 4: Thermal expansion of $CaTiO_3$.

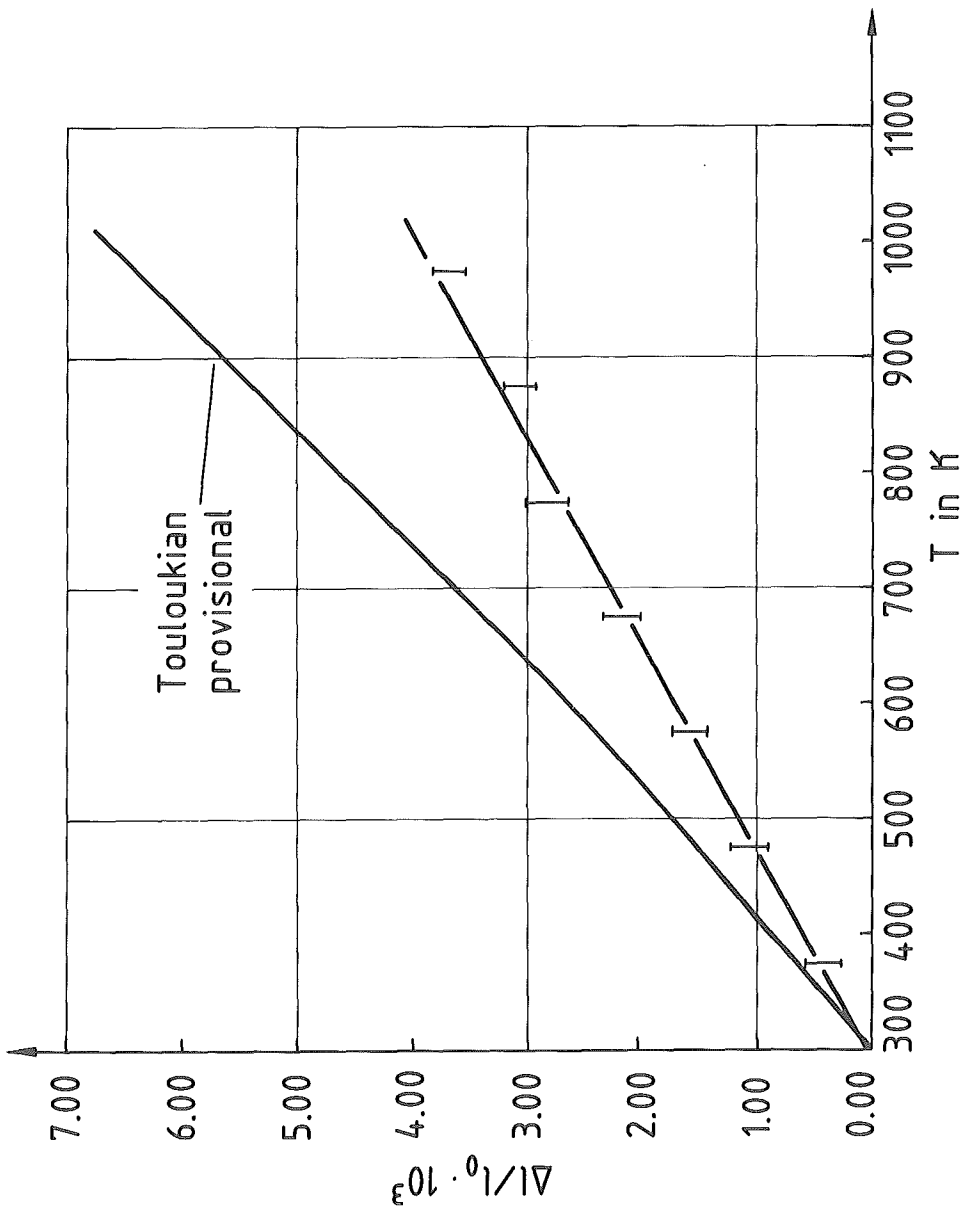

Fig. 5: Thermal expansion of Al_2TiO_5.

References

[1] M. Milosevski, B. Schulz, Proc. of the Meeting of the German-Yugoslav Cooperation, Ljubljana 1987

[2] Y. Touloukian, R. Kirby, R. Taylor, T. Lee, Thermophysical Properties of Matter, Vol. 13, IFI Plenum New York, 1973

[3] A. v. Hippel, R. Breckenbridge, F. Chesley, L. Tiskza, Ind. Eng. Chem. 38 (1946) 1097

[4] J. Panlener, N. Blumenthal, J. Am. Cer. Soc. 54 (1971) 610

[5] N. Bunting, R. Shelton, S. Creamer, J. Am. Cer. Soc. 30 (1947) 114

[6] W. Cook, G. Shirane, J. Phys. Soc. Jap. 4 (1949) 52

[7] S. Miyake, R. Ueda, J. Phys. Soc. Jap. 3 (1948) 177

[8] G. Shirane, A. Takeda, J. Phys. Soc. Jap. 7 (1952) 1

[9] L. Eichelberger, USAEC Publ. NP5432

[10] H. Kay, Report Brit. Electr. Res. Assoc. Ref. LT 257 (1951).

Investigations On Low Cement And Ultra Low Cement Refractory Castables

U. Schuhmacher*, W. Krönert*, A. Seltveit+

*Institut für Gesteinshüttenkunde der RWTH, Mauerstr. 5, D-5100 Aachen, West-Germany
+SINTEF, Div. of Metallurgy, N.-7035 Trondheim NTH, Norway

Introduction

During the last few years, there has been a steady increase in the use of refractory castables at the expense of prefired refractories. This is mainly due to improved chemical and physical properties of newly developed castables compared to traditional ones.

Traditional castables are mixtures containing 15-25% calcium aluminate cement and an aggregate. Direct moulding of castables into a form as well as setting and hardening without further processing is one of their main advantages. Setting and hardening can be explained by the hydration of the calcium aluminate phases /1-2/. Despite this advantage traditional castables have drawbacks which limit their use.The amount of water, required for casting is too high to obtain porosity similar to prefired bricks. Furthermore the mechanical strength decreases during heating up to 1000 - 1100° C, because of the dehydration of the hydrates / 3 /. Finally the high CaO content of the cement also weakens the resistance against acids, molten slags and metals strongly.

The cement contents of the new castables have been drastically reduced and are partly replaced by ultra fine powders, mostly amorphous silica. Low cement castables with 5-10% cement have increased mechanical stength between 300 -900° C and a much lower amount of water compared to traditonal castables, because of higher densities, different hydration products and the use of deflocculants. The presence of anorthite and / or gehlenite in the ternary phase diagramm Al_2O_3-SiO_2-CaO leads to formation of eutectica with low melting points, which are responsible for the drastic decrease in strength at temperatures higher than 1200°C even in castables containing 90% of tabular alumina as aggregate.

Further reduction of cement down to 1,0 - 2,0% and addition of reactive alumina is expected to improve the high temperature applications by mullite formation. Castables with only 1,0 - 2,0% cement are often classified as ultra low cement castables (ULCC).

In the experimental part properties of low cement and ultra low cement high alumina castables are investigated, with special emphasis on the influence of mullite formation on HMOR-values.

Experimental work

All test castables were made from commercial high alumina cement, refractory - grade amorphous silica and reactive alumina. Tabular alumina was used as aggregate in the specimens. Chemical datas are given in Table 1.

In order to study the mullite formation more closely , pastes from the fine ingredients of the later determined castables were studied experimentally. All specimens (Table 2) used for mineral phase studies have been prepared by hand mixing of 100 g powder with about 20 g of water. All samples were cured for 2 days at 20° C with humidity close to 100%. Drying was carried out for one day at 110° C. Firing and soaking conditions confirmed with PRE-standards and the soaking time took 12 hours.

All compositions of the castables are given in Table 3. The constituents were first drymixed for 5 min., then mixed for 5 min. with the respective proportion of water. Casting was done in steel molds on a vibration table; vibration time was 2 min.; amplitude 0,75 mm. The test pieces had 25 X 25 X 150 mm for HMOR - tests and 54 X 64 X 270 mm for CMOR - tests. Drying and hardening procedures were similar to those for pastes.

Analytical methods

Powder X - ray diffraction analysis were carried out with Cu K-α radiation and Ni - filter. Hot modulus of rupture was measured according to PRE / R 21 revised 1978. Rate of increase in bending strength for the samples tested on hot and cold modulus of rupture was 0,15 N mm^{-2} sec^{-1}.

Results and discussion

These castables are mostly interesting for application in the temperature range above 1200° C. The reactions that take place in this range are therefore critical. The results of powder X - ray diffraction of paste A fired at temperatures higher than 1000° C indicate strong formation of anorthite while past B and C form much less anorthite because of their lower cement content. In paste B and paste C a formation of mullite starts at 1300° C with simultanoues reduction of cristobalite and corundum content. The mullite formation in paste C, illustrated in Fig. 1, is however higher than in paste B. It appears from Fig. 1, that the mullite formation seems to be completed at 1400° C.

Fig. 2 compares the mineral phase compositions of the castables A - C at 1400° C after 12 hours soaking time. It can be seen clearly, that castable A contains anorthite in considerable amounts, whereas it decreases in castable B and is not detectable in castable C. However castable C has a high content of mullite, while there is none in castable B which is surprising.

The results from the measurements of the hot modulus of rupture show that castable C has considerably higher strength at 1400° C than the others. This is demonstrated in Fig. 3 where all castables are compared more closely. It is found that the strength of batch C is higher at temperatures above 1300° C. This is also the case around 1000° C, but the reduction in strength between 1000° C and 1300° C is more pronounced for castables C than for A and B. In order to improve the strength of castable C at 1300° C, the effect of longer soaking time was tested, because this is also a procedure applicable in an industrial environement. The positive effect can be seen in Fig. 4. This indicates that the strength is developed on kinetics of a reaction (mineralization). X - ray diffraction determinations on castable C fired 12 h and 48 h at 1300° C indicate higher amounts of mullite phase in those specimens fired for 48 h.

The high amount of mullite is however the probable reason for the low cold bending strength of castable C fired at temperatures higher than 1300° C (Fig. 5). Because of different expansion coefficients the cooling is likely to cause microcracks, while the high values at 1300° C indicate a glassy phase.

Conclusion

Low cement castables improve the lack of strength in the temperature range between 300 - 900° C compared to ordinary castables. For many applications their maximum operating temperature is restricted due to formation of liquids at higher temperatures. In order to improve the unsatisfactory properties at temperatures higher than 1300° C, the cement content was decreased to a minimumin in ultra low cement castables. An addition of reactive alumina combined with cement minimization reduces anorthite and melting phase formation. Mullite formation in ULCC improves strength at the temperatures higher than 1300° C.

References:

1) K.M. Parker, J.H. Sharp — Refractory Calcium Aluminate Cements. Trans. Brit. Ceram. Soc. 81(1982) 35

2) C.M. George — The hydration Kinetics of Refractory Aluminous cements and their Influence on Concrete Properties. Trans. Brit. Ceram. Soc. 79 (1980) 82-90

3) G.V. Givan, L.d. Hart, R.P. Heilich, G. Maczura — Curing and Firing High Purity Calcium Aluminate-Bonded Tabular Alumina Castables. Am. Ceram. Soc. Bull. 54 (1975) 710-713

4) B. Clavaud, J.P. Kiehl, R.D. Schmidt-Withley — 15 Years of Low Cement in Steelmaking. First Interantional Conference on Refractories, November 15-18, 1983, Tokio, Japan.

5) R. E. Fischer — New Developments in Monolithic Refractories. Advances in Ceramics Vol. 13, 1985

6) H. Boeß — Zementarme Feuerbetone - Ihre Eigenschaften und ihr Trockenverhalten. Ph. D. Thesis, TH Aachen (1985)

7) A. Seltveit, G.S. Dhupia, W. Krönert — Microstructural Aspects of Microsilica-Blended High Alumina Castables. Ceramic Engineering & Science Proc. Feb. 1986

Components (W-%)	Tabular Alumina	Reactive Alumina	Amorphous Silica	Cement
Al_2O_3	99,5	99,5	0,5	79
SiO_2	0,03	0,06	95,5	0,1
CaO	-	-	0,1	18-19
Fe_2O_3	0,05	0,06	0,25	0,3
Na_2O	0,2	-	0,1	0,5
MgO	-	0,02	0,4	0,4

Table 1 Chemical datas of the components

Components (W-%)	Paste A	Paste B	Paste C
Tabular Alumina -325 Mesh	42	46	34
Reactive Alumina	-	36	36
Amorphous Silica	20	12	24
Cement	28	6	6

Table 2 Compositions of the pastes

Components (W-%)	Castable A	Castable B	Castable C
Tabular Alumina	88	86,5	83,5
Reactive Alumina	-	9	9
Amorphous Silica	5	1,5	1,5
Cement	7	1,5	1,5
Water	4,5	3,75	3,5

Table 3 Compositions of the castables

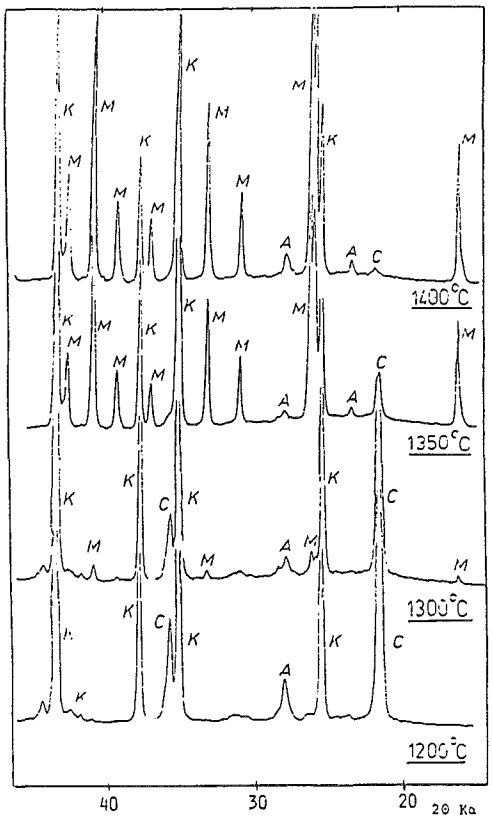

Fig. 1 Mullite formation of paste C

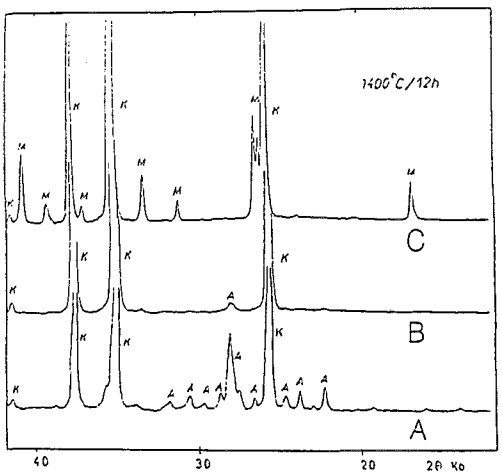

Fig. 2 Comparison o the mineralogical phases in castables A-C at 1400° C

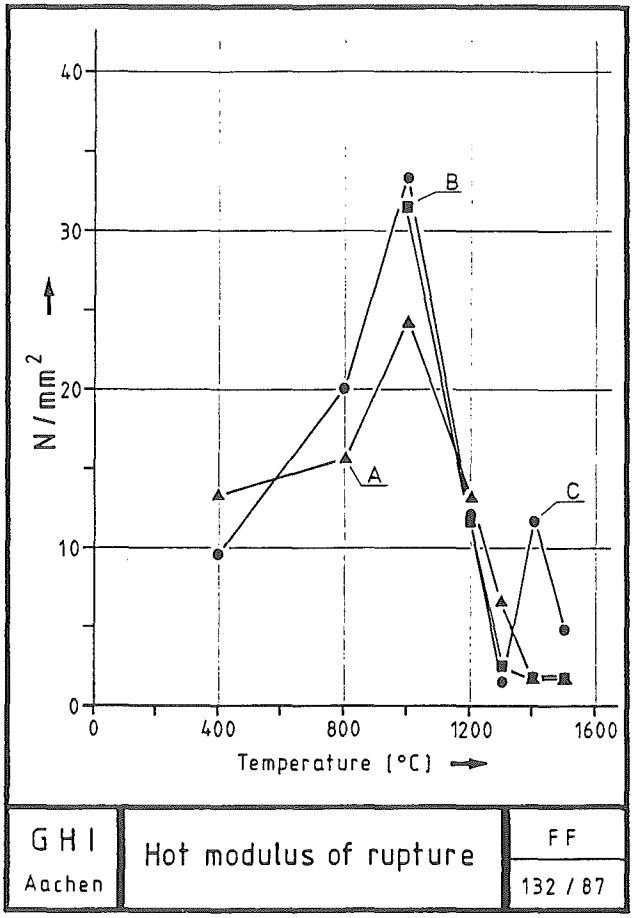

Fig. 3 Hot modulus of repture of castable A-C

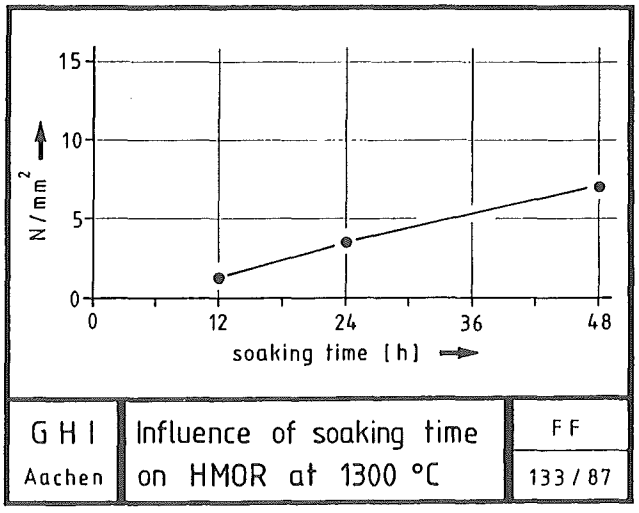

Fig. 4 Influence of holding time on hot modulus of rupture of castable C at 1300°C

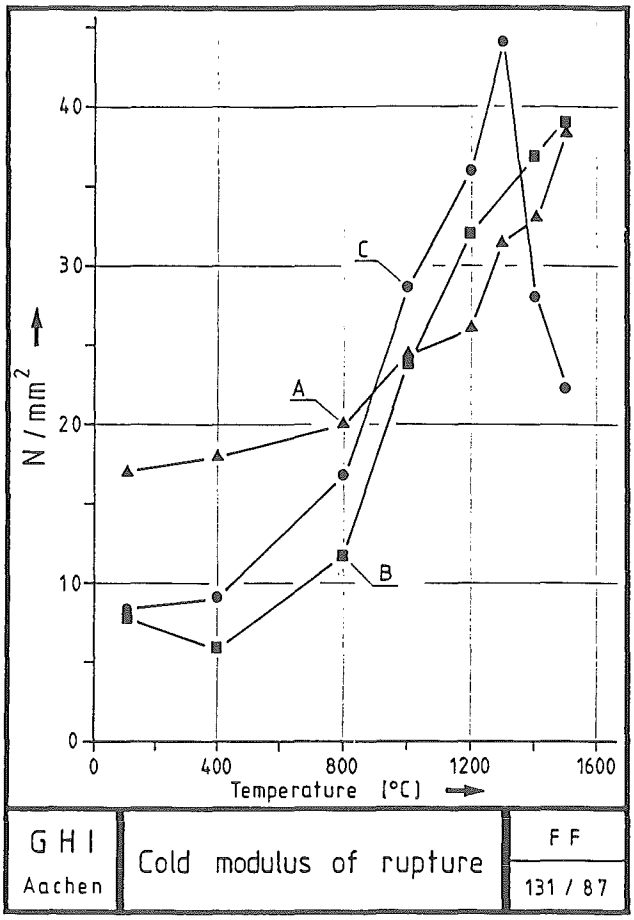

Fig. 5 Cold modulus of rupture of castables A-C

C E R A M I C S

SURFACES AND INTERFACES

CORROSION OF SILICON CARBIDE CERAMICS AT HIGH TEMPERATURES IN WATER VAPOR-CONTAINING ATMOSPHERES

R. Förthmann, E. Gyarmati, A. Naoumidis
Kernforschungsanlage Jülich GmbH, W.-Germany

The outstanding high temperature strength properties of silicon carbide ceramics make these materials interesting for applications as tubes for heat exchangers or chemical reactors at temperatures ranging from 1000 to 1400°C. For such applications it is necessary to know the influence of corrosive gases on the strength of these materials. Silicon carbide is known to be resistant to oxidizing atmospheres by forming protective silicon oxide layers. This paper gives first results of a series of corrosion tests with different silicon carbide qualities in water vapor and hydrogen-containing atmospheres at temperatures near 1400°C.

1. MATERIALS AND SAMPLE PREPARATION

For the hot gas corrosion experiments three varieties of industrial produced silicon carbide ceramics were investigated:

- Silicon-infiltrated silicon carbide (SiSiC) of the SIGRI Elektrographit GmbH, Meitingen, W.-Germany,
- Sintered silicon carbide (SSiC) of the SOHIO Engineered Materials Company, Niagara Falls NY, USA,
- Sintered silicon carbide of ESK: Elektroschmelzwerk Kempten GmbH, Kempten, W.-Germany.

Material	SiSiC (SK 5011)	SSiC (Hexoloy)	SSiC (EKASiC D)
Producer	SIGRI	SOHIO	ESK
Density/g cm^{-3}	3,05	3,10	3,13
Free silicon/%	12-15	0	0
Porosity/%	0	3,3	2,5
Bending strength/MPa (4-point, RT)	320	460	430

Table 1: Data of three silicon carbide varieties as given by the producer

The silicon carbide of SIGRI and SOHIO was obtained in form of tubes, that of ESK in form of plates. For corrosion testing the test specimens were cut from tube segments as shown in the figure, the test specimens were grinded and polished to the dimensions of about 60x3.5x4.5 mm ready for the 4-point bending strength test.

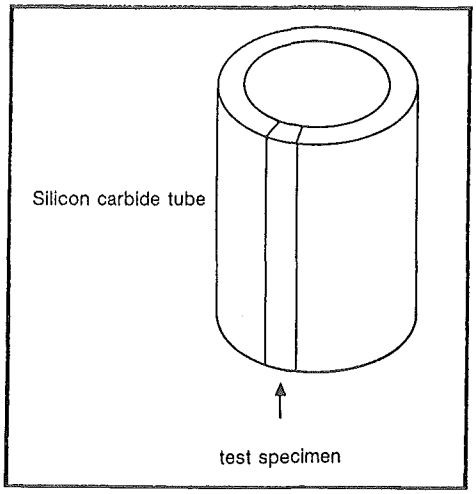

2. EXPERIMENTAL

The corrosion tests described in this paper were made at 1370 $\pm$ 10°C, this temperature is about 40°C below the melting point of the excess silicon in the SiSiC (SIGRI). The atmosphere consisted of 68 % water vapor and 1.3 % hydrogen with carrier gas which was either argon or nitrogen. The resulting oxygen partial pressures were calculated from the H_2O/H_2 ratio and were additionally measured by means of a ceramic oxygen sensor based on an oxygen ion conducting zirconia tube. After exposure the samples were unloaded for the following investigations:

- four-point bending strength measurement,
- X-ray diffraction analysis,
- optical microscopy,
- scanning electron microscopy,
- ceramography,
- electron microprobe analysis.

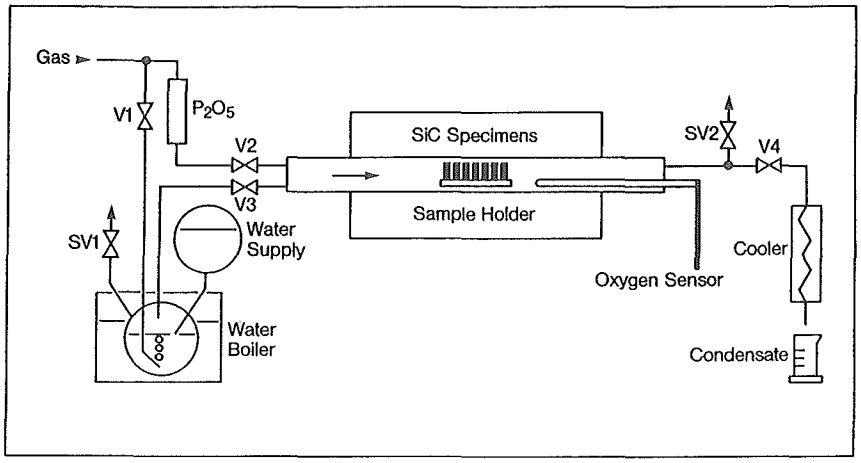

The silicon carbide test specimens were heated in a tube furnace capable of temperatures up to 1400°C. The furnace was supplied with argon or nitrogen (as a carrier gas) and hydrogen passing through a water boiler where the gas stream was saturated with water vapor.

3. RESULTS

3.1 Growth Rate of Silicon Oxide Layers

The exposed silicon carbide specimens were found to be covered with layers consisting of SiO_2 which was identified by X-ray diffraction to be α-cristobalite. Scanning electron microscopy resulted in thin and dense SiO_2 layers on SiSiC (SIGRI) and on SSiC (ESK), but very porous SiO_2 layers with much higher thickness on SSiC (SOHIO). As shown in the diagram, the porous oxide layer thickness (x) increased linear with time ($x \sim t$) but the dense oxide layer thickness on SiSiC (SIGRI) with the square root of time ($x \sim \sqrt{t}$). Such parabolic growth of oxide layers is typical for a diffusion-controlled growth kinetics. In this case the diffusion of oxygen in the dense silicon oxide controls the corrosion rate.

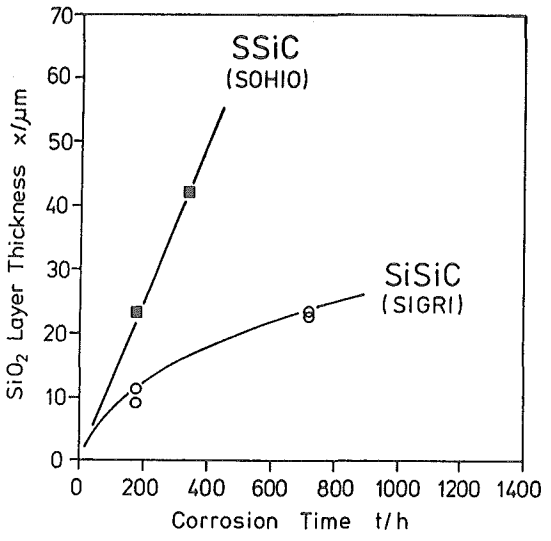

The dense silicon oxide layers on the surface of SiSiC (SIGRI) grows by a parabolic growth law, the porous silicon oxide layers on SSiC (SOHIO) by a linear growth law.

From the obtained parabolic constants of four corrosion tests the diffusion coefficient of oxygen in the dense SiO_2 layer of SiSiC at 1370°C were calculated by using the equations of K. MOTZFELD[1]:

Test Nr.	D/cm^2s^{-1}
3	1.2×10^{-7}
4	7.6×10^{-8}
6	1.4×10^{-7}
7	1.2×10^{-7}

The comparison of these results with literature data of oxygen diffusion in silicon oxide given by BARRER[2] and NORTON[3] confirm the interpretation of an oxygen diffusion-controlled growth rate of SiO_2 layers on SiSiC (SIGRI).

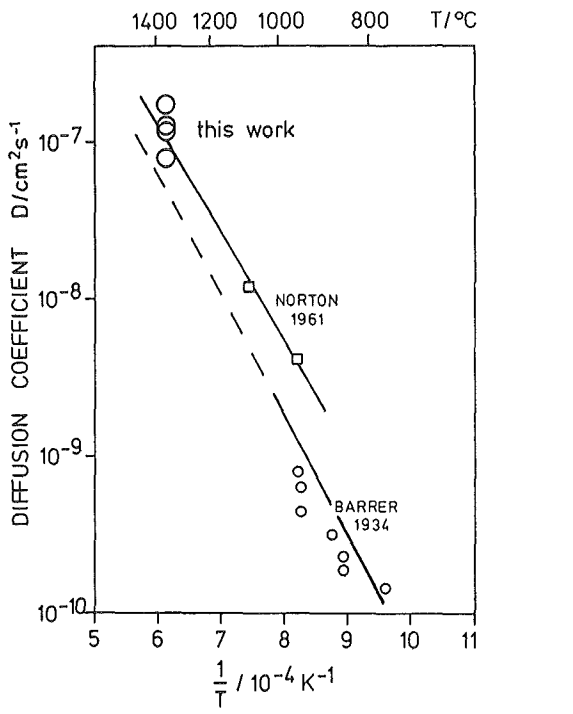

The diffusion coefficients of oxygen in the silicon oxide layer calculated from the parabolic growth rate are consistent with literature data.

In the case of SSiC (SOHIO) the oxygen reaches the silicon carbide surface directly by gas phase transport through the open porosity of the oxide layer, resulting in a linear growth with time and a much higher growth rate. The reason of the very different silicon oxide morphology is not yet clear, probably the behavior of the additives (e.g. B_4C and carbon in the SSiC of SOHIO) may play an important role.

3.2 Bending strength

From the measurements of the 4-point bending strength of three different silicon carbide ceramics before and after corrosion resulted a set of strength data which were evaluated by means of the Weibull statistics. The Weibull plots of SSiC (SOHIO) and SiSiC (SIGRI) are shown in the following diagram, the Weibull parameter was calculated from the slope of the least square fit of each curve. The results of seven corrosion tests are given in Table 2. They can be summarized as follows:

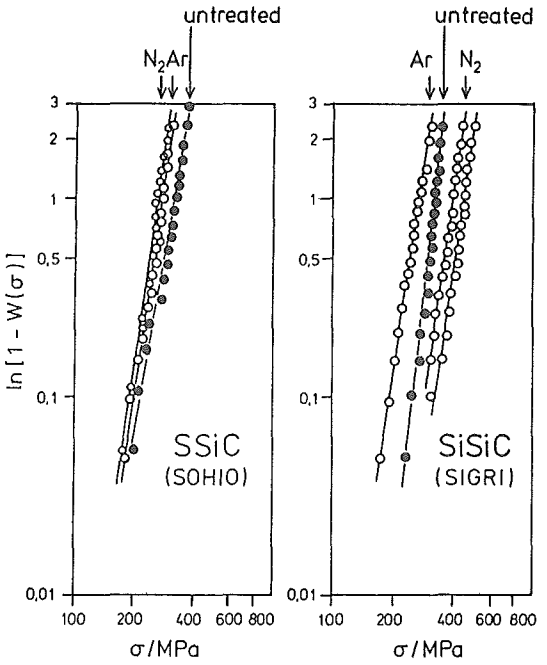

Weibull plots of the measured 4-point bending strength values show some decrease after 30 days exposure to water/hydrogen/argon atmospheres but increase of the SiSiC bending strength in nitrogen-containing atmospheres. This effects was not observed for the SSiC of SOHIO.

Material (Producer)	Corrosion conditions Time (days)	Carrier gas	Number of samples	4-Point Bending Strength Mean Strength (MPa)	Median Strength (MPa)	Weibull parameter m
SiSiC	0	- +)	20	309 ± 32	312	9.6
(SIGRI)	7	Ar	20	307 ± 46	311	6.0
	30	Ar	20	252 ± 42	255	6.4
	30	N_2	20	371 ± 57	376	6.1
SSiC	0	- +)	18	299 ± 52	303	5.6
(SOHIO)	30	Ar	20	268 ± 44	271	6.5
	30	N_2	19	251 ± 35	253	7.5
SSiC	0	- +)	16	275 ± 17	277	16.3
(ESK-D)	30	N_2	10	266 ± 21	268	11.9

+) untreated material

Table 2: Evaluation of the bending strength measurements (corrosion conditions: 1370°C/68 % H_2O/1.3 % H_2)

- The bending strength of silicon carbide is slightly decreased after exposure to H_2O/H_2-containing atmospheres with argon as carrier gas at 1370°C.
- The scatter of the measured bending strength data is increased after corrosion (i.e. the Weibull parameter is decreased), except the SSiC of SO-HIO which had a higher scatter of the strength data already before corrosion.
- The bending strength of SiSiC (SIGRI) is significantly increased, if the corrosive atmosphere contains nitrogen.

The observed strength decrease may be due to an observed pore formation in the SiC phase near to the SiC/SiO_2 interface. These pores are probably caused by the formation of carbon monoxide in this zone:

$$2\ SiC + 3\ O_2 \rightleftharpoons 2\ SiO_2 + 2\ CO$$

The pores may initiate the formation of microcracks during tensile load of the specimen. A similar effect is supposed to be caused by volatile silicon monoxide (SiO) formed at sufficiently low oxygen partial pressures:

$$Si + SiO_2 \rightleftharpoons 2\ SiO$$

The role of nitrogen is not yet clear and needs further investigation. From the measurements of BARRER[2] it is known that the diffusion coefficients of nitrogen in silicon oxide are comparable to those of oxygen. Although the silicon oxide layers on SiSiC (SIGRI) can be assumed to be gastight, the oxygen partial pressure at the $SiSiC/SiO_2$ interface will be much lower than in the gas phase, and is controlled by the equilibrium $Si/SiO_2/O_2$ at 1370°C. The equilibrium oxygen pressure at this temperature will be about 2×10^{-20} bar. This is sufficiently low for the formation of silicon nitride or oxinitride. The nitride may probably have an influence on the bending strength of silicon carbide.

3.3 Corrosion of SSiC joinings

Tubes of sintered silicon carbide (SSiC) were joined by means of very thin Co/Si films (thickness about 1 µm) which were sputtered by the PVD technique on the polished surfaces of a SSiC ring. Joining was achieved by an accelerated interaction between SiC and the metal silicide at sufficiently high temperature and pressure[4]. The joined tubes were separated into segments

and grinded to the dimensions of bending test specimens. The corrosion test was performed with these specimens at 1370°C for 30 days in an atmosphere of 67 % H_2O/1.3 % H_2/32 % Ar. These conditions are comparable to those given in Table 2.

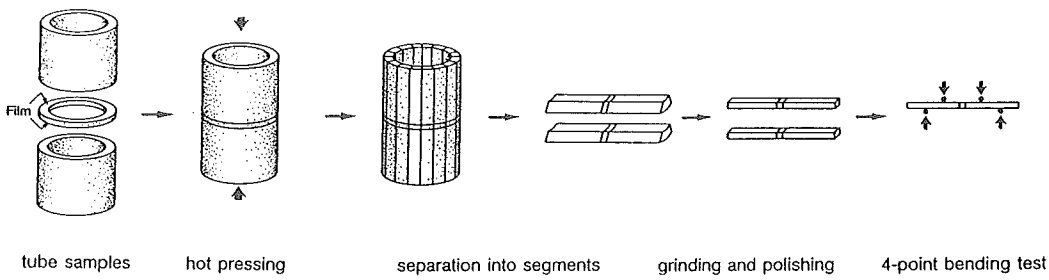

Method of joining SSiC tubes by using very thin sputtered metal films

From the mean values of the measured bending strength (Table 3) it can be concluded:

- At 1550°C joining temperature the bending strength of the joining is significantly lower compared with the SSiC itself, and it is further decreased by corrosion in the H_2O/H_2 atmosphere.
- At 1750°C joining temperature the bending strength of the joined specimens reaches nearly the SSiC strength, and no measurable decrease is observed after the corrosion test.

Sample	4-point bending strength/MPa	
	before corrosion	after corrosion
SSiC	299 ± 52	268 ± 45
SSiC joined at 1550°C	184 ± 35	119 ± 60
SSiC joined at 1750°C	234 ± 52	239 ± 45

Table 3: Mean strength of SSiC and joined SSiC before and after corrosion at 1370°C, 30 d, H_2O/H_2/Ar

4. THERMODYNAMIC CONSIDERATIONS AND FURTHER EXPERIMENTS

Thermodynamic calculations were done in order to make an assessment of active silicon carbide corrosion by forming the volatile compounds silicon monoxide (SiO) and silicon monsulfide (SiS). The results of these calculations based on the Gibbs free energy data given by KUBASCHEWSKI and ALCOCK[5] led to the following conclusions:

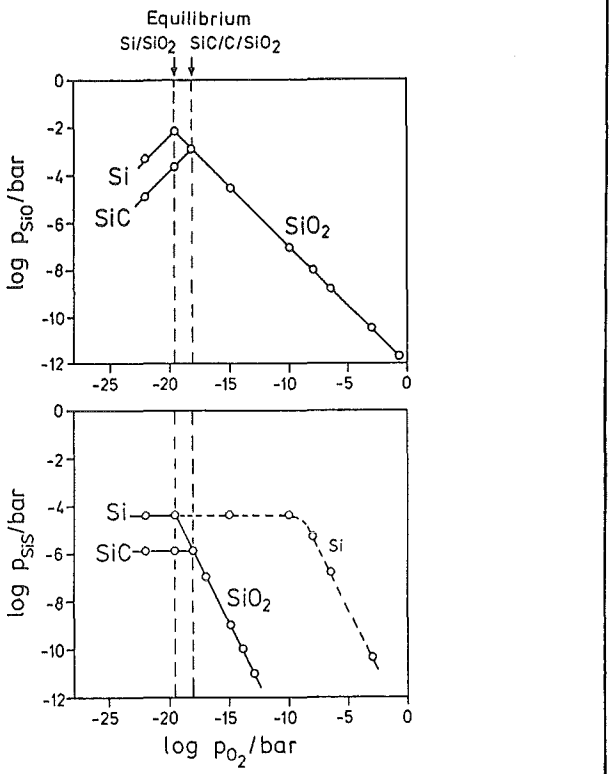

Calculated partial pressures of SiO and SiS over silicon, silicon carbide, and silicon oxide as a function of the oxygen partial pressure at 1370°C

- The partial pressure of SiO is increased with decreasing oxygen partial pressure: $p_{SiO} = 10^{-12}/\sqrt{p_{O_2}}$ (T = 1370°C, pressures in bar), until the equilibrium $Si/SiO_2/O_2$ is reached.

- The SiS partial pressure over Si is independent of the oxygen partial pressure at $p_{O_2} < 10^{-10}$ bar where in the gaseous phase H_2S is stable and SO_2 unstable (partial pressure of H_2S: 1 mbar).
- At $p_{O_2} > 10^{-10}$ bar, where SO_2 is the stable gaseous compound, the SiS partial pressure over Si decreases with increasing oxygen partial pressure.
- If the silicon carbide is covered by a dense SiO_2 layer, the SiS partial pressures are less by orders of magnitude, and even below the according SiO partial pressures. In this case any active sulfur corrosion can be excluded.

Further experiments are planned to clearify the influence of different oxygen partial pressures, the presence of sulfur compounds such as H_2S or SO_2, and the role of the silicon oxide layer morphology for the corrosion of silicon carbide ceramics at high temperatures.

5. SUMMARY

- The corrosion of different silicon carbide ceramics in water vapor/hydrogen atmospheres at high temperatures lead to different growth rates and structures of the silicon oxide layers.
- The growth rate of dense silicon oxide layers on exposed SiSiC specimens is controlled by the oxygen diffusion in the oxide layer.
- The 4-point bending strength of SSiC and SiSiC is slightly decreased by corrosion in water vapor/hydrogen, but increased, if SiSiC is exposed to nitrogen-containing atmospheres.
- The bending strength of specimens from joined SSiC tubes is not significantly decreased after exposure to water vapor/hydrogen atmospheres at high temperatures.
- The corrosion of SiSiC and SSiC in sulfur-containing atmospheres is expected to be mostly dependent on the oxygen partial pressure.

6. REFERENCES

1. K. Motzfeld, Acta Chem. Scand. 18 (1964) 1596-1606
2. R.M. Barrer, J. Chem. Soc. 136 (1934) 378-386
3. F.J. Norton, Nature 191 (1961) 701
4. E. Gyarmati, A. Naoumidis, H. Nickel, Proceedings of the Second International Symposium on "Ceramic Materials and Components for Engines", Lübeck-Travemünde, FRG, April 14-17 (1986) pages 449-457
5. O. Kubaschewski, C.B. Alcock, "Metallurgical Thermochemistry", 5. Ed. (1979)

INVESTIGATION OF ALPHA - SiC HOT CORROSION IN THE PRESENCE OF BASIC SLAG

V. Kevorkijan, M. Komac, T. Fetahagić, V. Štrumberger

"J. Stefan" Institute, 61000 Ljubljana, Yugoslavia

1. INTRODUCTION

Silicon carbide is a promising material for future gas turbines, high-temperature heat exchangers, diesel engine components, etc. Unfortunately, there are several factors which impede the faster application of SiC materials: problems encountered in manufacturing consistent products, problems of joining parts, structural reliability, etc. Additionally, high temperature corrosion in different combustion environments can severely affect the mechanical properties of SiC ceramics ([1]).

Papers on corrosion of SiC ceramics have appeared only recently. Thus enhanced corrosion in the presence of basic oxides, or formation of gaseous SiO and CO when the ambient partial pressure of oxygen is low, accelerate the degradation of the material ([2]). Furthermore, if SiC is exposed to coal slag the lowering of the effective oxygen pressure at the SiC/slag interface favours the formation of Fe-Ni-Si compounds, which could be responsible for corrosion of the SiC surface ([3,4]). The situation encountered in gas turbines has been simulated by reacting SiC with molten sodium salts ([5, 6]). The key variable in the corrosion reaction seems to be the sodium oxide activity, which in turn depends on the composition of the salt and the nature of the gaseous environment. Generally, it can be anticipated that in all cases mentioned above, corrosion will terminate or considerably slow down, when a dense protective SiO_2 layer is formed on the surface of SiC.

The purpose of our present work was threefold: (1) to develop a method to manufacture SiC tubes by pressureless sintering of α-SiC, (2) to study the corrosion of sintered α-SiC by basic coal slag, and (3) to ascertain the effect of corrosion on fracture strength and thermal shock resistance of sintered α-SiC.

2. EXPERIMENTAL PROCEDURE

2.1. Preparation of SiC tubes

The starting material was commercially available α-SiC powder (HCST A-10), with 0,5 wt % of B and 2 wt % of C added in order to facilitate sintering. Powders were isostatically pressed into tubes (wet-bag technique, centrally located mandrel between the two covers of the mold). After removing from the plastic mold the outer surfaces of tubes were machined in order to remove surface irregularities, thus obtaining uniform wall thickness. Sintering was performed in a furnace with a graphite heater in an argon atmosphere, for 30 min. at 2080°C. Under such conditions SiC samples sinter up to 98 % of the theoretical density.

2.2. Corrosion testing and post-test examination

SiC tubes (70 mm long, 19.5 mm OD and 11.4 mm ID) and rectangular bars for fracture strength determination were coated with a layer of powdered slag (for composition see Table I) and heated in air at 1250°C for different periods of time. In a separate set of experiments uncoated test specimens were heat treated under the same conditions. After exposure, C rings for diametral compression testing ([7]) were cut from the tube. Thermal shock tests were performed on corroded bars by heating the samples at different temperatures, with subsequent quenching in water at 20°C. Quenched samples were characterised by the measurements of retained bend strength (three-point bending test).

Table I. Chemical analysis of coal slag.

Equivalent oxide	Amont in coal slag (wt %)
SiO_2	45.2
Fe_2O_3	7.0
CaO	21.4
Al_2O_3	11.1
MgO	8.4
TiO_2	0.8
K_2O	0.7
MnO_2	0.1
Na_2O	0.2
NiO	traces
Loss on ignition	6.1
Base/acid*	66.02

*Defined as $(Fe_2O_3 + CaO + MgO + Na_2O + K_2O)/ (SiO_2 + Al_2O_3 + TiO_2)$

The microstructure of both as-prepared and exposed samples were characterised using optical, SEM/EDS, microprobe (EPMA) and Auger electron spectroscopy (AES) studies.

3. RESULTS AND DISCUSSION

3.1. Microstructural analysis

Observation of reference specimens which were heated in air in the absence of slag coating, revealed the formation of a layer identified by SEM/EDS and AES as consisting of SiO_2. The thickness of this layer first increased with the time of exposure. After 24 hours the scale was approximately 100 μm thick and then remained almost constant even after prolonged heating times. In addition, wedge-like penetrations of oxide phase could be observed on selected locations (Fig. 1). After 150 hours exposure these penetrations were some 50 μm deep. By employing SEM and AES they were identified as a cryptocrystalline mixture of SiC and SiO_2. Locally enhanced oxidation or corrosion of the sintered SiC in advance of the

reaction interface was also reported by other authors ([8]). The enhanced corrosion is believed to be mainly a consequence of processing defects, impurities and/or inclusions present in the ceramics. In the case of slag-coated specimens the formation of a glassy scale consisting of SiO_2, Al_2O_3, CaO, MgO and Fe_2O_3 could be observed (Fig. 2). Inside the scale, spherical voids and randomly oriented needle-like crystals 20-40 μm long could be detected as well. SEM/EDS analysis revealed that the crystals were SiO_2. The crystallization of tridymite in silica glass was reported by Jacobson ([6]) and was believed to have been promoted by the presence of sodium compounds. The concentrations of alkaline oxides in the slag which was used in present investigation was rather low, however, so it seemed quite probable that the crystallization of SiO_2 could be induced by other oxide components as well. The concentration of crystalline phases inside the glassy matrix increased with the time of exposure (Fig. 3, 4). As shown in Fig. 5, the coal slag corrosion was locally enhanced, too. However, in contrast to oxidation, the penetrations did not exhibit wedge-like form but were rather rounded off.

A layer which consisted of rather densely packed SiO_2 crystals extended along the SiC/slag interface (Fig. 6) and was observed also by other authors ([4]). This layer, which actually diminished the direct slag/substrate SiC contact surface and, therefore, acted as a protection, was not continuous. Disruptions detected in the layer appeared to be associated with enhanced corrosion. The SiO_2 scale at the slag/SiC interface may be eliminated either by reaction with SiC or by dissolution in the molten slag matrix. SiO_2 will react with SiC when the partial pressure of oxygen is below the critical value ($P^c_{O_2}$ = 1 Pa) ([9]):

$$2\ SiO_2 + SiC = 3\ SiO + CO \qquad (1)$$

Spherical voids observed on SiC/slag interface might thus be explained as the consequence of gaseous SiO and CO evolution

(Fig. 3). Due to elimination of the protective SiO_2, direct SiC/slag contact may result in formation of silicide phases, if O_2 partial pressure is sufficiently low ($P_{O_2} < 10^{-15}$ Pa) ([4]). In fact it has been found by AES studies that the rounded off penetrations were associated with small regions behind the SiC/slag interface which were oxygen depleted and consisted mainly of Fe and Si (Fig. 7). Thus, the reaction represented qualitatively by the equation:

$$x\ Me_{(slag\ matrix)} + y\ SiC = Me_xSi_y + y\ C \qquad (2)$$

my be responsible for locally progressive corrosion, if $P_{O_2} < 10^{-15}$ Pa in accordance with ([4]).

3.2. Mechanical and thermal shock behaviour

As shown in Fig. 8, the specimens investigated followed the thermal shock model of Hasselman ([10]) which shows a distinct discontinuity in the tensile fracture strength vs. T_C relationship, with considerable strength loss at a critical quentching temperature. The magnitude of the critical temperature difference T_C was 320°C, which is very near to literature data for T_C of the as-prepared sintered α-SiC ([11]). Since T_C is proportional to $k.\sigma_f/E.\alpha$ (k is thermal conductivity, σ_f fracture strength in bending, E Young's modulus, and α the coefficient of thermal expansion of the material under consideration), it is obvious that in spite of the strength degradation due to oxidation or corrosion, the changes of other parameters promote a constant value of the above quotient.

Fig. 9 shows the dependence of fracture strength of SiC specimens on the time of high-temperature exposure to air or slag attack. In both cases the strength first increases, which could be the consequence of the passivation of the surface.

With further increase in the exposure time, strength degradation occurs due to the phenomena described in the previous section. Obviously, slag attack considerably

increases the rate of strength degradation.

4. CONCLUSIONS

Hot corrosion mechanisms of sintered α-SiC depend on the environment during high temperature exposure. In the case of oxidation in an air atmosphere, a passive SiO_2 layer is formed on the surface of specimens which locally penetrates deeper into the SiC matrix. Most probably, these penetrations are associated with chemical or microstructural non-homogeneities in the substrate. In the case of basic slag coated specimens, a layer of dense packed SiO_2 crystals is formed on the slag/SiC interface. However, this layer may either dissolve in the slag matrix, or react due to low oxygen partial pressure with SiC to form gaseous products. Thus slag may come into direct contact with SiC which promotes the formation of metallic silicides.

As a consequence of corrosion attack, strength degradation of sintered α-SiC may be noted after extended exposure time. In contrast, thermal shock resistance remains unchanged.

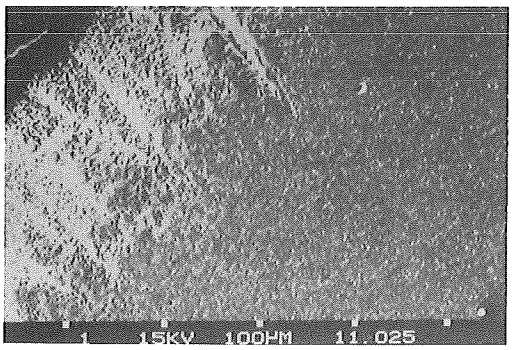

Fig. 1: Corrosion behaviour of α-SiC ceramic following 144 hours of air exposure at 1250°C.

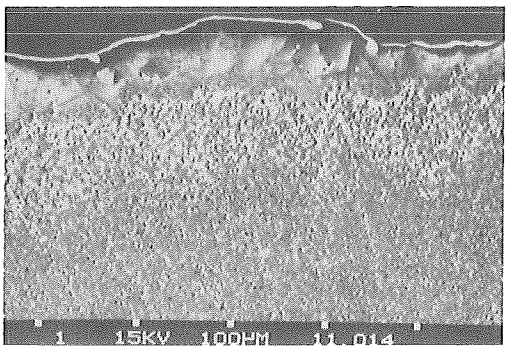

Fig. 2: Corrosion behaviour of α-SiC material following 24 hours of slag exposure at 1250°C.

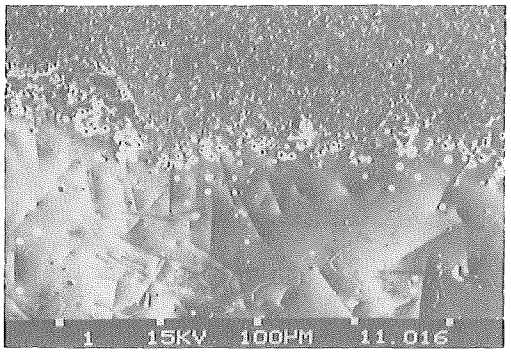

Fig.3: Appearance of crystalline phase inside the coal slag matrix and a film of bubbles on the SiC/coal slag interface. (After 168 hours at 1250°C).

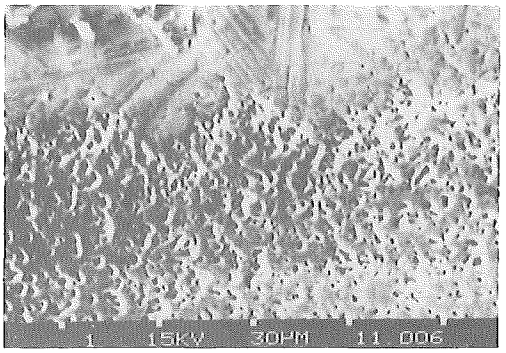

Fig.4: Randomly oriented wedge-like crystals of SiO_2 in the coal slag matrix. (After 120 hours at 1250°C).

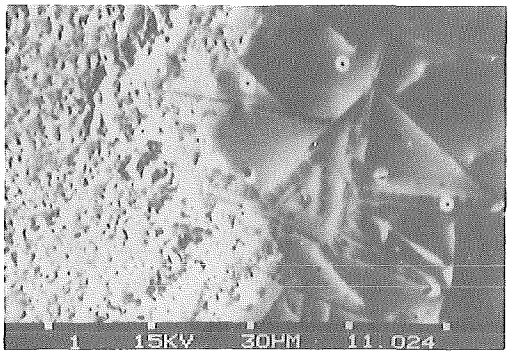

Fig.5: The penetration of coal slag into α-SiC. (After 120 h at 1250°C).

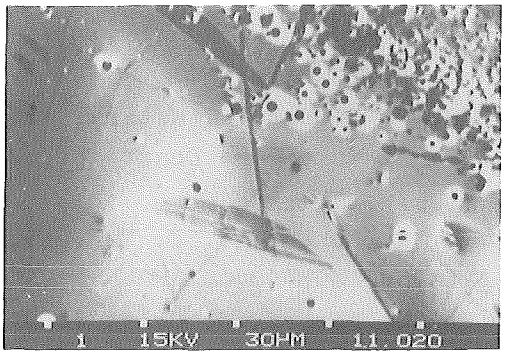

Fig.6: Appearance of a layer which consists of rather densely packed SiO_2 crystals.

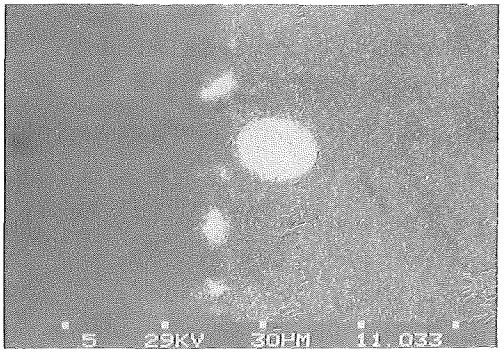

Fig.7: AES photograph of rounded off penetration: (a) SiO_2 map, (b) non-oxide silica map, (c) Fe map.

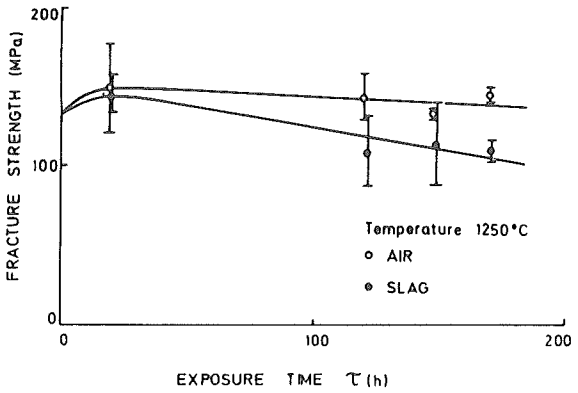

Fig. 8: Fracture strength as a function of quenching temperature difference for sintered α-SiC.

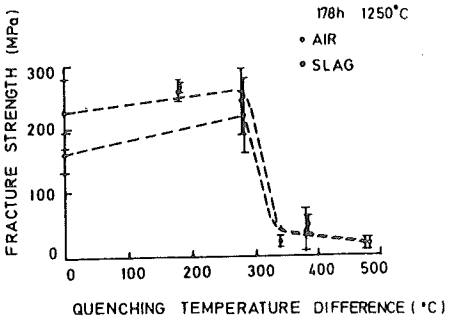

Fig. 9: Time dependence of C-ring fracture strength obtained for α-SiC samples exposed to both air and basic slag environments.

5. REFERENCE

(1) P. F. Becher, J. Mater. Sci., 19 (1984) 2805-2814

(2) D. W. McKee, D. Chatterji, J. Amer. Ceram. Soc., 59 (1976) 441-444

(3) M. K. Ferber, V. J. Ternery, Bull. Am. Ceram. Soc., 63 (1984) 898-904

(4) M. K. Ferber, J. Ogle, V. J. Tennery, T. Henson, J. Amer. Ceram. Soc., 68 (1985) 191-197

(5) N. S. Jacobson, J. L. Smialek, J. Amer. Ceram. Soc., 68 (1985) 432-439

(6) N. S. Jacobson, J. Amer. Ceram. Soc., 69 (1986) 74-82

(7) J. N. Cernica, Strength of Materials, Holt, Reinhart and Winston, New York, 1966, p.p. 205-206

(8) J. A. Costello, R. E. Tressler, Ceramics Int., 11 (1985) 39-44

(9) P. A. Gulbransen, S. A. Janssen, Oxid. Met., 4 (1972) 181-201

(10) D. P. Hasselman, J. Amer. Ceram. Soc., 52 (1969) 600-604

(11) J. C. Glandus, P. Boch, Proc. of the 4th E. C. F. Conference, (1982) 617-23

Oxygen Interaction with Metal Surfaces: Surface Science Approach

K.Wandelt

Fritz-Haber-Institut der Max-Planck-Gesellschaft,
Faradayweg 4-6, D-1000 Berlin 33, F.R.G.

and

P.Pervan and M.Milun

Institute of Physics of the University,
P.O.Box 304, 41001 Zagreb, Yugoslavia

I. Introduction

The interaction of oxygen with metallic surfaces is of fundamental technological and economical importance. Oxygen adsorption constitutes an elementary step in the formation of oxides, in corrosion processes, in catalytic oxidation reactions etc. In the USA an estimated 40% of the annual steel production are only to replace corroded parts. In turn, the controlled formation of thin oxide films plays an important role for protective passivation and coatings, for insulation in microelectronics and (in future) for thin film superconductors. Ceramics are oxides; and oxidation catalysts are important for pollution control.

In order to understand and control these global processes a detailed insight into the elementary reaction steps on the molecular level is required. This microscopic insight can be obtained by the so-called "surface science approach": Under ultrahigh vacuum (UHV) conditions ($\lesssim 10^{-10}$ Torr) atomically clean metal surfaces are exposed to well defined doses of pure oxygen. The

uptake and nature as well as the kinetics and energetics of the metal-oxygen interaction is then studied with highly surface sensitive analytical methods as a function of external parameters such as exposure, pressure and temperature as well as the surface composition and structure. The samples may range from single-component single-crystals to multicomponent polycrystalline surfaces. The surface specific analytical methods generally employed are based on the use of low energy ($\lesssim$3KeV) electron and ion beams (see Fig.1), because these particles exhibit only very short ($\sim$10 - 20Å) mean free path lengths in metals. For Auger Electron Spectroscopy (AES) the sample is bombarded with primary electrons of 2-3 KeV energy, which causes the emission of secondary electrons from the surface. The spectrum, that is the intensity versus energy curve, of these electrons is detected with an energy dispersive analyzer and contains characteristic signals arising from electronic Auger processes in atoms near the surface. Since such an Auger process involves three intra-atomic electron levels, any Auger signal is denoted by a triplet such as KLL, LMV etc., which means, for instance, that an initially created hole state in the K-shell is filled by an electron from the L-Shell, and that the energy gain of this transition leads to emission of another L-electron, which is detected. Auger signals provide qualitative and quantitative information about the chemical nature of the surface (see Figs.4 and 16). Photoelectron Spectroscopy (PES) to a first approximation is based on a single electron process: The surface is irradiated with soft X-rays (XPS) of e.g. 1253,6 eV(MgK_α) or 1486,6 eV (AlK_α) energy or with UV-light (UPS) of e.g. 21.22 eV (He I) or $h\nu$= 40.81 eV (HeII) energy, which again causes the emission of characteristic electrons. The kinetic energy E_K of these electrons is measured and is given by $E_K = h\nu - \varphi - E_B$. Since the energy of the primary photons $h\nu$ and the work function φ are known, atom-specific electron binding energies E_B can be determined, and the signal intensity is again a quantitative measure of the respective atomic species (see Figs.3,5 and 8). Finally, due to the wave nature of electrons, coherent beams of low energy electrons (20 - 1000 eV) are diffracted by the regular lattice of a single crystal surface. The diffracted beams are made visible by means of a fluorescence screen and form a so-called LEED (low energy electron diffraction) pattern which shows the crystallographic symme-

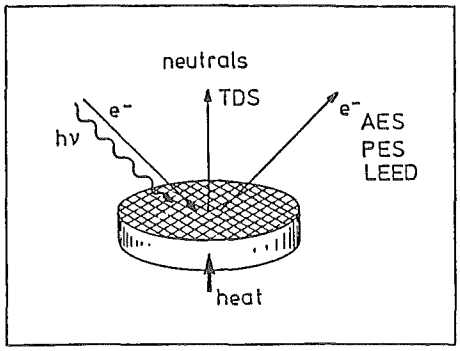

Fig.1 Illustration of the socalled "surface science approach" for the investigation of the properties of solid sufaces. The surface is exposed, for instance, to beams of primary electrons and photons of different energy. The energetic and spatial distributions of emitted secondary electrons from the surface carry information about the qualitative and quantitative composition of the surface as well as about the crystallographic and electronic structure. Simple heating of the sample may lead to desorption characteristics of adsorbed particles, which are typical for the nature of the adsorption bond.

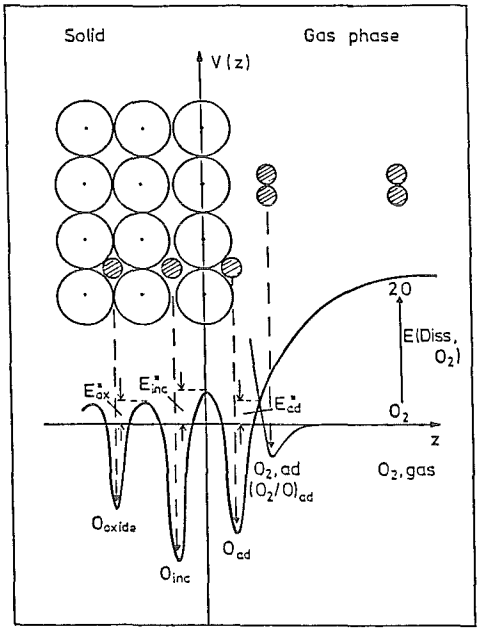

Fig.2 Schematic representation of the potential energy of an oxygen molecule (or oxygen atom) approaching a surface along the surface normal (z-axis). An oxygen molecule may be trapped in a shallow "physisorption" minimum (O_2,ad) if the activation energy E^*_{ad} for "chemisorption" into the deeper O_{ad}-minimum is positive. Likewise, activation barriers E^*_{inc} and E^*_{ox} will control the incorporation of atomic oxygen below the surface or into the final bulk oxide.

try of the surface (see e.g. Fig.7). Simple heating of the sample may lead to thermally induced desorption of adsorbed surface species; in Thermal Desorption Spectrometry (TDS) the desorbing species are monitored with a mass-spectrometer and the temperature at which desorption occurs reflects the adsorptive bonding strength. For more detailed informations about the methods mentioned the reader is refered to the Refs. 1-3. The intent of the present contribution is to review briefly the use of these surface sensitive techniques in order to investigate some kinetic, energetic, structural and electronic aspects of the oxygen-metal interaction.

Fig.2 illustrates the various possible interaction channels between oxygen and a metal in the form of a diagram: potential energy V versus (vertical) distance z between a gas-phase oxygen molecule and the metal surface (z=0). At large oxygen-surface separation ($z \longrightarrow \infty$) the interaction is zero; $V(\infty) = 0$ is taken to be the energy reference. Dissociation of an oxygen molecule in the gas phase "costs" the dissociation energy $E(Diss,O_2)$. Approach and chemisorptive adsorption of the two obtained oxygen atoms lowers the total energy of the combined system by $E(Diss, O_2) + 2E(O_{ad})$ (see Fig.2). The energy gain of $E(O_{ad})$ per atom is the driving force for atomic oxygen adsorption O_{ad} <u>on</u> the metal surface. If the oxygen is not predissociated in the gas phase the oxygen molecule O_2 approaches the surface nearly along the z-axis and may be "trapped" in molecular form by a physisorptive energy minimum (O_2,ad) being held by long-range van der Waals forces. Thermal activation of the thus physisorbed O_2 molecule over the "activation barrier" E^*_{ad} may then again lead to dissociative chemisorption into the O_{ad}-minimum at shorter bond distance. In this direct process the activation energy E^*_{ad} is much smaller than $E(Diss,O_2)$ in the previous case and $O_{2,ad}$ may be regarded as a "precursor" for chemisorption into the final O_{ad}-state. In fact, E_{ad} may even be negative, so that the intermediate $O_{2,ad}$--state can not be isolated. O_2 physisorption may also occur above surface regions which are already covered by atomic oxygen (see $(O_2/O)_{ad}$ state in Fig. 2). Eventually the metal-oxygen interaction may lead to the formation of thick oxide films and bulk oxides, which means that oxygen atoms are incorporated (O_{inc}) below the surface or bound in deeper layers to form a metal oxide

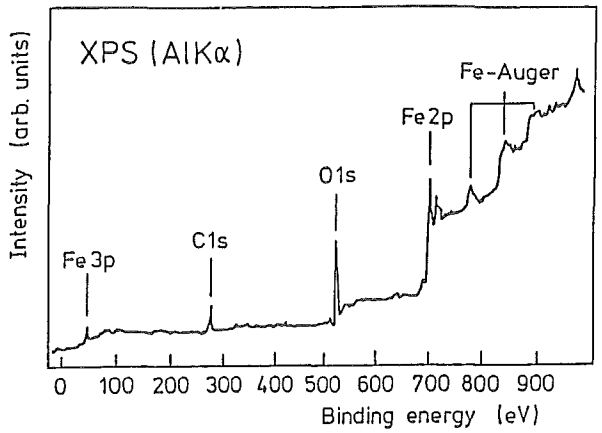

Fig.3 XPS spectrum (intensity versus energy curve) of an iron surface excited with photons of 1486,6eV (AlK_α -radiation). The various peaks correspond to the emission of Fe(3p)-, C(1s)-, O(1s)-, Fe(2p)- and Fe-Auger electrons. The binding energy is refered to the Fermi level of the sample. The presence of the C(1s)- and O(1s)-signal points to surface contamination by carbon and oxygen.

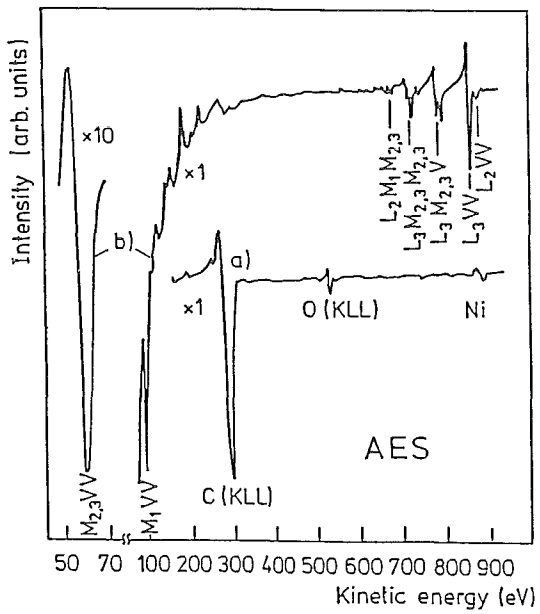

Fig.4 Auger electron spectrum (AES) of a heavily oxygen (O) and carbon (C) contaminated nickel (Ni) surface (a) and of the same surface after cleaning (b). The triplets KLL, MVV, etc. denote the respective Auger transitions (see text).

(O_{oxide}). These processes are again controlled by the occurence of corresponding activation barriers, E^*_{inc} and E^*_{ox}, and energy minima of O_{inc} and O_{oxide}. The "surface science approach" allows to investigate the formation and the characteristics of these various stages of oxygen-metal interaction /4/.

2. Representative results

2.1 Single-component single-crystal surfaces

Fig.3 shows the X-ray excited photoelectron (XPS) spectrum (electron intensity versus binding energy) of a carbon (C) and oxygen (O) contaminated iron (Fe) surface. The origin of the energy axis corresponds to the Fermi level E_F of the metal substrate. The peaks correspond to direct Fe(3p)-, C(1s)- and Fe(2p)-core electron or Fe(Auger)-electron emission. The intensity (height) of the C(1s) and O(1s) signal is a quantitative measure of the concentration of these surface contaminants; a few percent of a monolayer can easily be detected. Fig.4 displays the AES spectrum of a nickel (Ni) surface which is again heavily contaminated with carbon (C) and oxygen (O) (see curve a)). Ion bombardment of this sample under UHV-conditions finally may lead to a nickel surface the AES spectrum of which shows only signals corresponding to pure Ni (curve b)). (The triplets MVV, KLL, LVV, etc. designate Auger electron transitions characteristic of the corresponding chemical species /1-3,5/.) The presence of only a few percent of a monolayer of any surface species can again be easily detected by this spectroscopy.

The thus prepared atomically clean metal surface can then be exposed to controlled doses of oxygen gas (exposures are measured in units of 1 Langmuir (L) = 1 sec x 10^{-6} Torr), and the amount of oxygen adsorbed on the surface can be detected, for instance, by the intensity of the O(1s) core electron emission peak. A set of O(1s) signals as measured at 300K sample temperature are shown in Fig.5. Fig.6 shows a plot of the O(1s) intensity as a function of oxygen exposure (in Langmuir) to a (100)-oriented single-crystal surface of nickel at 300K. The O(1s) intensity increases rapidely at low exposures (regime I), goes through a plateau

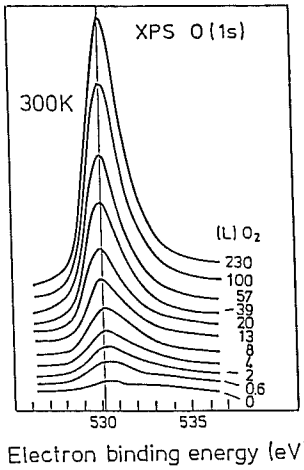

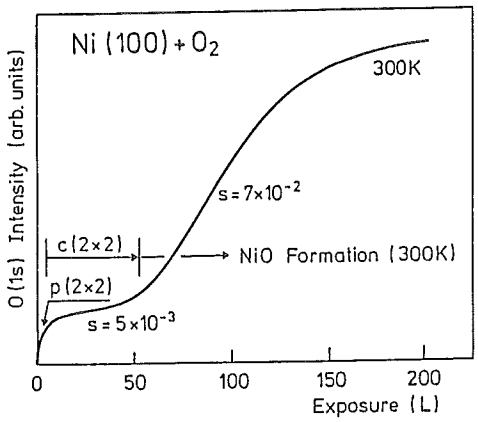

Fig.5 O(1s) XPS peak of oxygen adsorbed on nickel at room temperature. The intensity of the peak is proportional to the amount of adsorbed oxygen which in turn is a function of the oxygen exposure (1L = $1x10^{-6}$ Torr x 1sec).

Fig.6 Plot of the O(1s) intensity as a function of oxygen exposure to a Ni(100) surface at 300K. s denotes the sticking coefficient (see text) and p(2x2) and c(2x2) refer to the observed LEED pattern (see Fig.7) in the respective exposure regime.

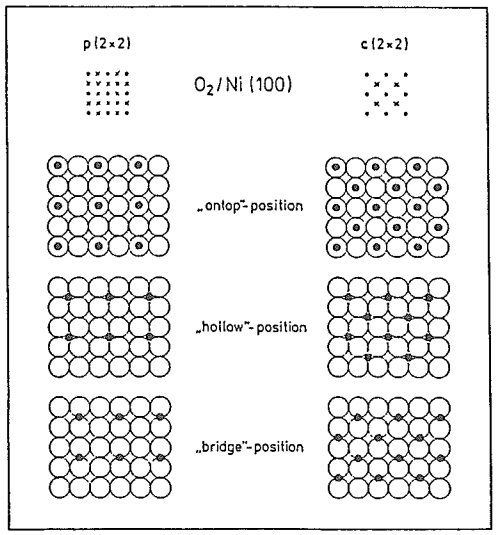

Fig.7 LEED (Low Energy Electron Diffraction) pattern (reciprocal lattice) and structure models of the p(2x2) and c(2x2) oxygen adsorption structures on Ni(100). In the LEED pattern (top) the full dots represent the Ni-substrate lattice, the crosses are oxygen induced extra spots. The structure models (below) illustrate possible positions for the oxygen atoms (black), namely ontop of a nickel atom (white), in the hollow between four nickel atoms or in the bridge position between two nickel atoms.

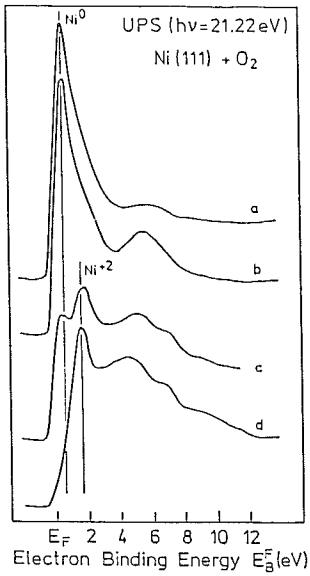

Fig.8

Representative UPS valence band spectra of a) a clean Ni(111) surface; b) after adsorption of 6L O_2; c) after adsorption of 100L O_2, and d) of bulk NiO.

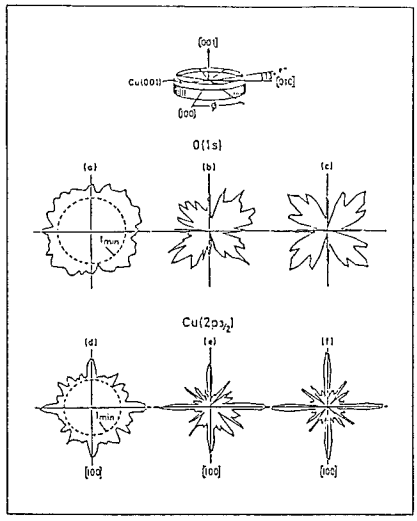

Fig.9

Azimuthal angular distributions of absolute XPS intensities for the O(1s) (a) and $Cu(2p_{3/2})$ (d) core levels from a Cu(100) surface exposed to 1200L oxygen. A polar emission angle of 13° with respect to the surface was used. The O(1s) data are a sum of three complete scans; $Cu(2p_{3/2})$ is one single scan. In (b) and (e), the minimum value I_{min} has been subtracted from the data in order to amplify anisotropies. In (c) and (f) the data have been fourfold averaged (see text) in order to reduce spurious sources of non-fourfold anisotropy. (Kono et al. /9/)

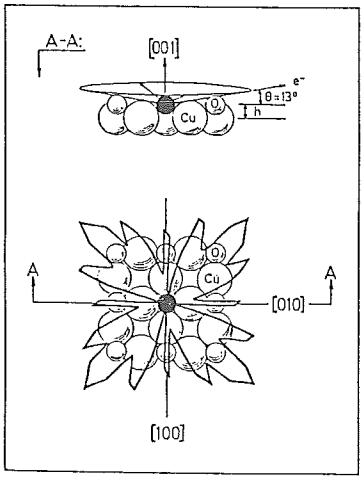

Fig.10

Side- and top-view of an $O_{ad}c(2x2)/Cu(100)$ structure model showing the geometry of detection of the O(1s)- and $Cu(2p_{3/2})$-azimuthal anisotropies (top) and a superposition of the O(1s)-anisotropy on a fourfold hollow site (bottom).

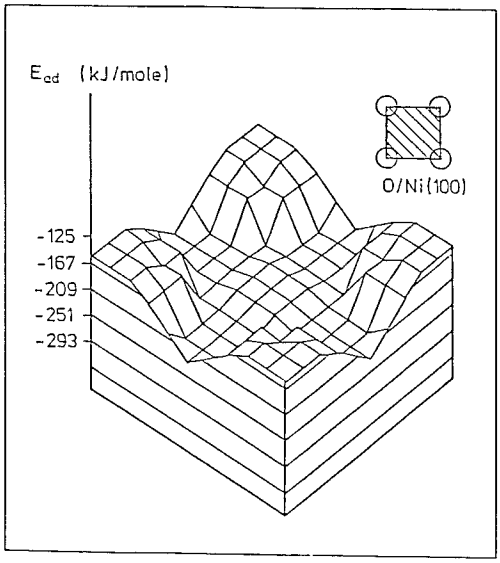

Fig.11 Theoretically calculated adsorption energy (E_{ad}) hypersurface for different positions of an oxygen atom within a square unit cell between 4 Ni atoms.

between ~5L and ~50L (regime II), and then continues to rise less steeply (regime III). The O(1s) intensity is a measure of the number of adsorbed oxygen atoms, while the exposure is proportional to the number of oxygen molecules impinging on the surface, not all of which necessarily stick to the surface. The sticking coefficient s is thus given by the derivative (slope) of the intensity vs. exposure curve. While the sticking coefficient s_o (exposure $\rightarrow$ 0) is assumed to be unity /6/ it decreases to s = 5×10^{-3} between ~5L and ~50L, and re-increases to s = 7×10^{-2} around 100L exposure. A detailed statistical analysis of this variation of s suggests that one impinging O_2 molecule requires a cluster of 8 empty Ni sites on the surface in order to adsorb dissociatively /7/.

The three exposure regimes are also characterized by the occurrence of different oxygen-induced extra spots in the corresponding LEED-pattern of the surface. In the first regime (at very low exposures) a so-called p(2x2) LEED picture is observed as sketched in Fig.7, while a c(2x2) LEED picture (see Fig.7) is typical for the regime between ~5L and ~50L (plateau). Beyond 50L any regular diffraction pattern fades away. This latter regime corresponds to the incorporation of oxygen and the formation of bulk nickel oxide (NiO), while the first two exposure regimes correspond to oxygen atoms adsorbed in registry on the Ni(100) surface (see Fig.7). This can be concluded from valence band photoelectron spectra (excited with UV-photons of 21.22 eV; UV--photoelectron spectroscopy (UPS)) An example is shown in Fig.8 /8/, where spectrum a) corresponds to the valence electron emission of a clean Ni(111) surface. At moderate oxygen exposures (10L) the leading signal hardly changes, indicating no strong electronic interaction of the oxygen with the Ni(3d) valence electrons. Only the growth of a small peak at ~6eV below E_F due to emission of O(2p) electrons indicates the presence of adsorbed oxygen atoms on the surface. After higher exposures (e.g. 100L) the spectrum changes drastically (see curve c), and now corresponds to a superposition of spectra from bulk NiO (see curve d) and from the Ni(111) surface covered with adsorbed oxygen. Very similar data are obtained for the Ni(100) surface.

A combination of such UPS data with the LEED observation from Ni(100) suggests that for the first two exposure regimes oxygen atoms are adsorbed on the Ni(100) surface in p(2x2) and c(2x2) registry with the substrate surface lattice. This, however, still leaves open the relative lateral orientation between the Ni-surface lattice and the O_{ad}-adsorbate lattice. Three possible models are shown for both the p(2x2) and the c(2x2) structures in Fig.7 in which the oxygen atoms are placed, for instance, "ontop" of a nickel atom, in the "hollow-position" between four nickel atoms, or in the "bridge-position" between two Ni-atoms. Additional information is required to pin-down the true location, which can be obtained (besides from LEED-intensity measurements) from angular resolved PES studies. Figs.9 a) and d), show azimuthal anisotropies of the O(1s) and Cu($2p_{3/2}$) photoemission intensities as measured from a Cu(100) surface, covered with a c(2x2) oxygen overlayer, at a polar emission angle of $\theta = 13^{o}$ off the surface (see top sketch in Fig.9) by rotating the crystal by 360^{o} about the surface normal /9/. After subtraction of the respective isotropic background I_{min} the characteristic anisotropies are accentuated in Figs.9 b) and e). Finally, in order to minimize spurious experimental sources of anisotropy like surface imperfections and heterogeneous fields around the sample, the pattern b) and e) are fourfold averaged through $\overline{I(\phi)} = I(\phi) + I(\phi+90^{o}) + I(\phi+180^{o}) + I(\phi+270^{o})$ resulting in the appealing "flower patterns" of Fig.9 c) and f). These latter azimuthal intensity distributions exhibit excellent fourfold symmetry with maxima in the Cu($2p_{3/2}$) emission coinciding with minima of the O(1s) distribution. The fourfold symmetry appears immediately incompatible with oxygen atoms (being the source of the O(1s) emission) in bridge-positions which exhibit twofold symmetry (see Fig.7). A detailed analysis, namely of azimuthal anisotropies measured at different polar angles θ, in fact, suggests that the oxygen atoms occupy fourfold hollow-sites /4/. Fig.10 illustrates a superposition of the O(1s) pattern from Fig.9 c) with an atomistic model showing the oxygen atoms in hollow-sites between four Cu-atoms. Intensity maxima are pointing in the direction of "valleys" between adjacent Cu-atoms, which, indeed, may be regarded as the most natural "channels" for electron emission. The same kind of reasoning rules out the "ontop"-position (see Fig.7).

The reason why the adsorbed oxygen atoms prefer to sit in the hollow-sites is obvious: The fourfold coordination results in the highest chemical bonding strength (four bonds). This argument based on the coordination number is supported by chemisorption theory. Fig.11 displays the threedimensional plot of a theoretically /10/ calculated adsorption energy (E_{ad}) hypersurface for various positions of an oxygen atom within a square unit cell between four Ni surface atoms (see inset). Minima in this hypersurface correspond to sites of highest energy gain and, hence, highest bond strength. Such calculations mainly yield relative adsorption energies, and Fig.11 clearly suggests stronger adsorption between the four Ni-atoms than ontop of a Ni-atom (at each corner). The absolute bonding energy of an oxygen atom in the most favorable adsorption site can be determined by means of Thermal Desorption Spectrometry (TDS) as mentioned in the Introduction.

2.2 Single-component poly-crystalline surfaces

Of course, differently oriented single-crystal surfaces offer sites of different adsorption symmetry and coordination, and, hence, different relative adsorption energy. In this respect, a single - component, but poly - crystalline surface represents a structurally heterogeneous surface with crystallites of different crystallographic orientation as well as defects in the form of grain boundaries. Adsorbed oxygen atoms, always seeking for sites of highest adsorption energy, will populate such a polycrystalline surface (as a function of increasing coverage) in the order of decreasing E_{ad}. This appears, indeed, to be reflected in the set of TDS spectra of oxygen from polycrystalline palladium (Pd) shown in Fig.12a) and b). The polycrystalline Pd foil was first exposed to a given amount of oxygen at 510K /11/. Its temperature was then raised linearly and the partial pressure of desorbing molecular oxygen was monitored as a function of sample temperature. Fig.12a) shows such desorption curves for initial coverages θ_o as given in the figure. The continuous shift of the curve maximum to lower desorption temperature is compatible with the above notion of the successive population of surface sites in the order of decreasing E_{ad}. Fig.12b) represents a continuation of

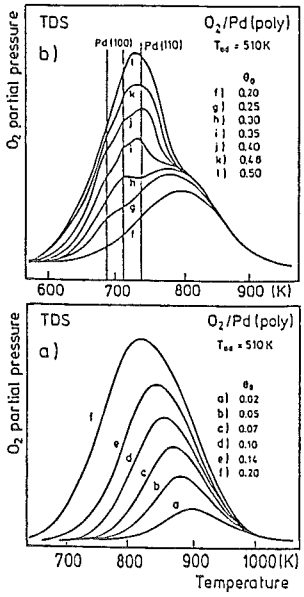

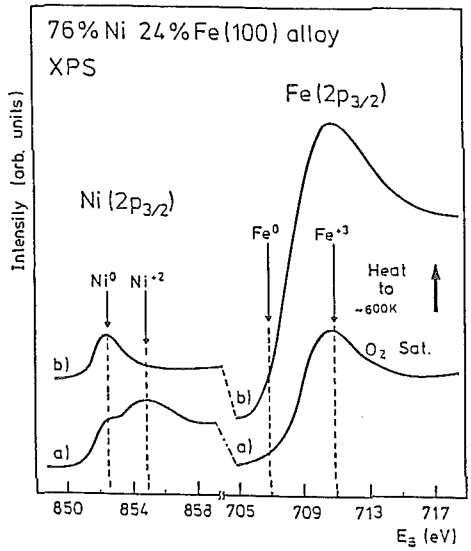

Fig.12 Thermal desorption spectra of oxygen from a Pd foil after adsorption of different amounts of O_2 at 510K. θ_o denotes the initial oxygen coverage. Panel b) is a continuation from panel a).

Fig.13 XPS $Ni(2p_{3/2})$- and $Fe(2p_{3/2})$-spectra from the (100) surface of a 76%Fe24%Ni single crystal alloy a) after saturation with oxygen at 300K and b) following heating of this surface to 600K (after Brundle et al. /13/).

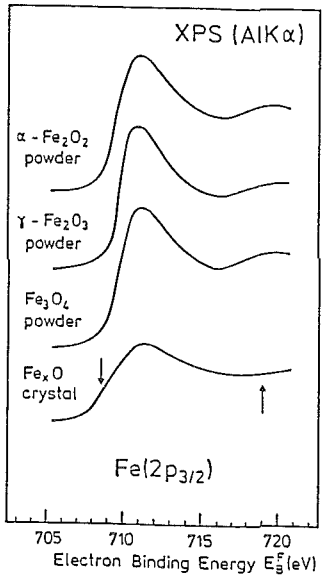

Fig.14 XPS $Fe(2p_{3/2})$ core level spectra of various iron oxides, taken from the air-exposed samples as received.

Fig.12a); at these higher coverages θ_o with $0.20 \lesssim \theta_o \lesssim 0.5$ of oxygen the desorption traces even begin to show features which are characteristic for oxygen desorption from Pd(110) and Pd(100) single crystal surfaces, suggesting the presence of such patches at the surface of this polycrystalline foil. Analysis of the temperatures corresponding to the peak maxima in Fig12a) using established methods /12/ yield an initial adsorption energy of E_{ad} = 230 kJ/mole at $\theta_o \lesssim 0.1$. This value is of the same order of magnitude as the one calculated theoretically in Fig.11.

2.3 Two-component single-crystal surfaces

Fig.13 reproduces /13/ $2p_{3/2}$ core level electron spectra of Ni and Fe from a (100) surface of a 76%Ni24%Fe alloy single crystal which was exposed to oxygen at room temperature (curves a)) and then heated to $\sim$600K without further oxygen supply (curves b)). After saturating the surface with oxygen at room temperature the Ni($2p_{3/2}$) signal shows two peaks which correspond to Ni^{2+}-ions of the NiO overlayer formed and to metallic nickel (Ni^o) underneath. In turn, the Fe($2p_{3/2}$) signal exhibits only one peak corresponding to Fe^{3+}-ions of the iron oxide. The absence of an Fe^o-signal indicates that the iron component is completely oxidized, in contrast to the nickel near the surface. Heating this surface oxygenated at room temperature to $\sim$600K leads to significant spectral changes. The nickel oxide is quantitatively reduced to metallic nickel and the oxygen is transfered to iron resulting in more iron oxide formation. Note the loss of the Ni^{2+} signal and the increase of the Fe^{3+} intensity. This transformation is in agreement with the higher heat of formation of (any) iron oxide than that of nickel oxide.

The assignment of the peaks in Fig.13 to Ni^o, Ni^{2+}, Fe^o, Fe^{3+}, of course, is based on reference measurements with pure nickel and iron as well as with various possible oxide samples (standards). The detection of such "standard spectra", however, is much less trivial as it may appear /14/. For instance, iron is known to form three different stable oxides, Fe_xO ($x \approx 0.95$), Fe_3O_4 and Fe_2O_3. Because of their different content of Fe^{2+} and Fe^{3+}-ions one may expect characteristic differences between the Fe($2p_{3/2}$)

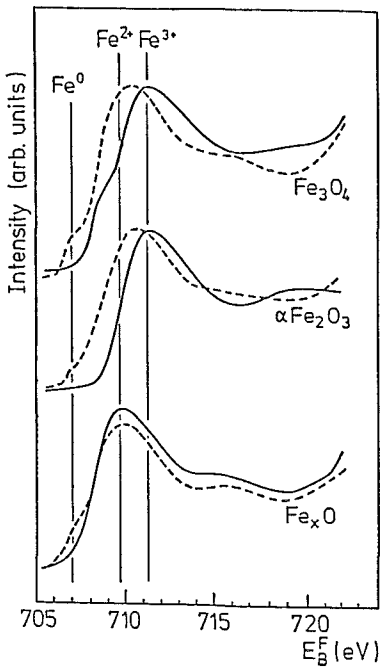

Fig.15 High resolution Fe($2p_{3/2}$) XPS spectra showing the effect of Ar^+ bombardment (1keV, 10μA) on iron oxide surfaces. The full lines are the standard spectra from the perfect single crystal oxides. The dashed spectra are measured with the bombarded surfaces: Fe_3O_4, Ar^+ for 10 min; Fe_2O_3, Ar^+ for 7 min; Fe_xO, Ar^+ for 3 min).

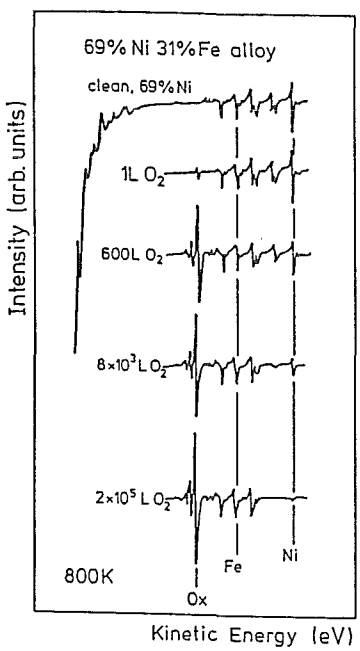

Fig.16 Auger spectra of a successively oxidized polycrystalline 69%Ni31%Fe sample. The oxidation was performed at 800K and 5×10^{-5} Torr O_2.

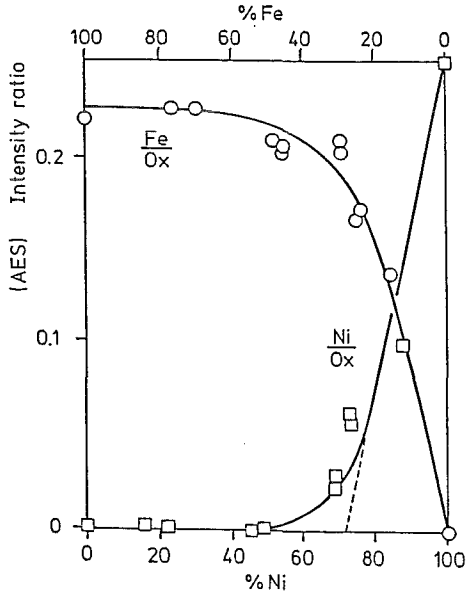

Fig.17 Ratios of the Auger peak heights Fe(650)/O(515) and Ni(850)/O(515) of completely oxidized NiFe alloys as a function of the initial alloy composition. Oxidation was performed at 800K and 5×10^{-5} Torr O_2.

photoemission spectra. Fig.14 shows Fe($2p_{3/2}$) spectra from various commercial iron oxide samples inserted into the spectrometer as received. The spectra look disappointingly similar; the peak maxima occur at very similar electron binding energies, solely the Fe_xO spectrum shows some deviations in the intensity distribution (see arrows). It has been shown, that the similarity of these spectra arises from the simple fact, that all air-exposed oxide surfaces are covered with a layer of the same oxide, namely α-Fe_2O_3, because it is the thermodynamically most stable one. The true reference spectra of the different iron oxides could only be measured if single-crystal samples were crushed or cleaved in situ or under an inert (oxygen-free) argon atmosphere prior to measurement /4/. The thus obtained standard spectra are shown in Fig.15 (full lines). In these spectra not only the Fe^{2+}-ions of Fe_xO are clearly distinguishable by their $2p_{3/2}$ peak shift, but also the presence of both kinds of ions in Fe_3O_4 manifests itself by the occurrence of the pronounced Fe^{2+}-shoulder within the low energy edge of the Fe^{3+} peak.

A comparison of these standard spectra (full lines in Fig.15) with those from Fig.14 seems to suggest that simple removal of the Fe_2O_3-overlayer from all air-exposed iron oxides should enable the detection of the desired standard spectra. The most frequently employed technique to remove disturbing and contaminating overlayers is ion-bombardment. The surface is exposed to a beam of inert gas ions (e.g. Ar^+) of 1 - 3KeV energy, and this ion beam "erodes" surface material away. This so-called "sputtering" method, however, has the serious disadvantage, that the sputter--coefficient (number of removed surface atoms per incident ion) strongly depends on the atomic mass of the sputtered surface species. For a given ion mass and energy, lighter surface atoms are sputtered more easily than heavier surface atoms. This means in the present case that the lighter oxygen atoms are sputtered more efficiently than the heavier iron atoms. Consequently, the substrate stoichiometry is seriously modified. This becomes most apparent from a comparison between the full and dashed curves in Fig.15. As mentioned before the full lines are the standard spectra of the single-crystalline and stoichiometric oxides Fe_xO, Fe_3O_4 and α-Fe_2O_3, while the dashed spectra were monitored from the same samples after a few minutes of argon ion bombardment. In

all cases intensity is shifted to lower electron binding energies corresponding to the emission from lower valent states of iron, namely Fe^{2+} and even metallic Fe^{o}. These new spectra have no resemblance what so ever with the original (standard) spectra of the stoichiometric starting materials. In view of such dramatic modifications of the surface composition due to selective sputter effects spectra from ion-bombarded multi-component surfaces and, in particular, the interpretation of composition profiles normal to surfaces of multi-component samples must be regarded with extreme caution (if not doubt).

2.4 Two-component polycrystalline samples

In this paragraph we carry the discussion one final step further towards an understanding of the interaction of oxygen with more realistic surfaces, namely polycrystalline surfaces of binary alloys /4,14/. The upper spectrum in Fig.16 corresponds to the Auger electron spectrum (AES) of a clean polycrystalline 69%Ni 31%Fe alloy surface. This composition is determined from the relative intensity of the Ni- and Fe-AES signals (see Fig.16). The surface was then heated to ~800K and exposed to increasing doses of oxygen gas: the exposures are given in the figure. The spectra exhibit a strong oxygen signal (Ox), but simultaneously the Ni- and Fe-signals show significant changes in relative intensity. The Fe-signal increases slightly while the Ni-signal finally fades away. This observation is in agreement with that from Fig.13 and suggests segregation of iron oxide to the surface. This iron oxide eventually grows to such a thickness that due to the finite information depth of the emitted Auger electrons the metallic nickel from the alloy underneath is no longer seen. Fig.17 finally shows a plot of the Fe/Ox- and Ni/Ox-Auger intensity ratios as obtained after heavy oxidation at 800K of polycrystalline FeNi alloys of different composition. This plot suggests that alloys with an initial nickel concentration of less than 60 - 70% are finally covered with an overlayer of pure iron oxide, namely Fe_2O_3, while alloy samples containing more than 60 -70% nickel are finally covered with an overlayer of Ni-ferrite, which contains both Ni- and Fe-ions. The enhanced enrichment of iron oxide at the surface is again expected due to the higher

heat of formation of (any) iron oxide than that of nickel oxide. Such stable surface oxides may play an important role as passivation layers which protect the metallic material against further corrosive attack.

3. Concluding remarks

In this paper we have presented a brief outline of the so-called "surface science approach" to systematic oxidation studies of metallic surfaces. The examples were chosen in the order of increasing complexity. The simplest and therefore most defined case is the adsorption of oxygen on well defined single-crystal surfaces of pure metals. In this case the structural, electronic and vibrational (not discussed here) properties of adsorbed oxygen atoms can be determined in great detail using various surface sensitive spectroscopies. The results of these well-defined model studies may then serve to understand the oxidation process at more complex surfaces. As such we have addressed polycrystalline surfaces of pure metals (here Pd), binary alloy single-crystal surfaces (here FeNi(100)) and polycrystalline FeNi samples of various compositions. This approach of successive generalization appears to be the only way to reach ultimately an understanding of surface oxidation in particular, and corrosion in general.

Acknowledgements

This work was in part supported by both the BMFT through the Internationale Büro of the KFA - Jülich, and the SIZ za znanstveni rad SRH, through the ZAMTES office Zagreb, under the auspices of the bilateral Yugoslav-German research project "Surface Physics", No. 32.2.A.F., as well as by the Deutsche Forschungsgemeinschaft through Sonderforschungsbereich 128 (München) and 6 (Berlin) and the SIZ za znanstveni rad SRH (Project 24.8). The International Atomic Energy Agency, Vienna, supported part of this work through the research contracts No. 3227 and 4527. The authors are also indebted to G.Ertl, C.R.Brundle, G.Doyen and C.S.Fadley for the permission to use their figures.

References

/1/ "Practical Surface Analysis", Eds. D.Briggs and M.P.Seah (John Wiley & Sons, New York, 1983)

/2/ D.P.Woodruff and T.A.Delchar, "Modern Techniques of Surface Science" (Cambridge University Press, 1986)

/3/ G.Ertl and J.Küppers, "Low Energy Electrons and Surface Chemistry" (Verlag Chemie, Weinheim, 1985)

/4/ K.Wandelt, "Photoemission Studies of Adsorbed Oxygen and Oxide Layers", Surface Sci. Rep. 2 (1982) 1, and references therein

/5/ R.Weissmann and K.Müller, "Auger Electron Spectroscopy - A Local Probe for Solid Surfaces", Surface Sci. Rep. 1 (1981) 251

/6/ C.R.Brundle and H.Hopster, J.Vac.Sci.Technol. 18 (1981) 63

/7/ C.R.Brundle, R.J.Behm and J.A.Barker, J.Vac.Sci.Technol. A2 (1984) 1038

/8/ H.Conrad, G.Ertl, J.Küppers and E.E.Latta, Solid State Commun. 17 (1975) 497

/9/ S.Kono, C.S.Fadley, N.F.T.Hall and Z.Hussain, Phys.Rev. Lett. 41 (1978) 117

/10/ G.Doyen, Ph.D. - Thesis, München, 1975

/11/ M.Milun, P.Pervan and K.Wandelt, Surface Sci. 189/190 (1987) 466

/12/ The relevant methods have been refered to and discussed in
a) P.Pervan and M.Milun, Fizika 18 (1986) 47
b) P.Pervan, M.Milun and K.Wandelt, Appl. Surface Sci. 29 (1987) 271

/13/ C.R.Brundle, E.Silverman and R.J.Madix, J.Vac.Sci.Technol. 16 (1979) 474

/14/ K.Wandelt and G.Ertl, Surface Sci. 55 (1976) 403

STABILITY AND INSTABILITY OF ANODICALLY FORMED LAYERS ON METALLIC SURFACES

Lj.D.Arsov

Faculty of Technology and Metallurgy, University "Kiril and Metodij"
9100 Skopje, Yugoslavia

Stability and instability of anodical surface layers formed on aluminium, titanium and their alloys was investigated. It is shown that surface colour varies with the layer depth and (in the case of titanium) the uniform dissolution of the coloured layers is possible. The effect of $CuSO_4$ and $NiSO_4$, on the formation and dissolution of anodic layers on aluminium, has been also investigated. When the sulphate concentration was increased, kinetic viscosity of the electrolyte became higher, hardness of the film generally increased, at the first and then decreased, and the uniformity of the film was decreased.

Introduction

Stability and instability of many metals depend on the state of their surface, i.e. clean metal surface, presence of natural oxyde or passive layers etc. Some metals such as titanium and aluminium, when exposed to atmospheric conditions form a natural oxide layers that protects the basic from corrosion. The thickness of these layers can electrochemically be increased by means of anodic oxidation. The aim of electrochemical formation of surface layers is to increase the corrosion stability of metal surfaces in many corrosive medias. Some metals like titanium, molibdenum zirconium tantal etc. gets colored during the formation of passive layers[1].

Aluminium gets colored during the electrochemical treatment if in the basic electrolyte there is some additions as: $CuSO_4$, $NiSO_4$, $MgSO_4$ etc. Increase in the concentration of the sulphate suppresed chemical dissolution of the anodic layer and the uniformity of the anodic layer was decreased. During the electrolysis if the porous film dissolves; - the pore base by field assisted dissolution so that Al^{3+} ions accumulates in the sulphuric acid bath. Besides, it was also investigated the mechanism of electrochemical formation of anodic oxide layers, their colorations in dependence of additions in basic electrolyte, applied voltage and current density. The chemical and electrochemical reactions which take place in acid medias on metallic surfaces were in-

vestigated by means of elliptically polarized electromagnetic waves.

The physico-chemical and optical characteristics of anodic oxide layers have been determined using the: potentiostatic, potentiodynamic, galvanostatic, metallographic, interferometric and electron diffraction methods.

Experimental

The electrochemical treatment of pure aluminium and aluminium's alloy S.10.6063 (USA) surfaces were investigated. By spectroscopic analyses the chemical composition of S.10.6063 (USA) aluminium's alloy has been determined (Fe - 0.27 % ; Cu - 0.03 % ; Si - 0.48 % ; Mg 0.58 % ; Mn - 0.02 % and Ti - 0.027 %). The Al samples of cylindric form with diameter of 25 mm were firstly mechanicaly tretaed by emery paper 600. After that the electrodes were cleaned ultrasonically with alcohol and than introduced into the cell with suitable bath for electropolishing. A platinium or carbon counter electrode with surface area more than 5 orders of magnitude greater than Al sample was used. By registration of potentiostatic j-E curves in various baths for electropolishing of aluminium and aluminium's alloys, the chemical composition of bath and optimal electrochemical conditions are determined, in which could be obtained the maximal reflectivity and minimal surface roughness. The quality of electropolished Al surface was tested ellipsometrically and interferometrically[2,3]. By measurements of elliptically polarized electromagnetic waves at normal incidence the maximal reflectivity of 91.1 % is obtained for electropolished S.10.6063 (USA) aluminium surfaces in bath with chemical composition of 100 cm^3 $HClO_4$ and 400 - 500 cm^3 C_2H_5OH during 20 min. and voltage of 20 V, current density about 170 mA/cm^2 and bath temperature between 20-25^oC. The root mean square denivelation of that surface measured interferometrically was about 4 nm.

Titanium samples with purete 99.7 % were also prepared and electropolished like aluminium samples but in other solutions and conditions of electropolishing described in ref.[4] Firstly, on titanium surface in H_2SO_4 oxide layers are formed with all possible spectral colours and their shades, in the volatge range between 0 and 100 V. The thickness of oxide layers is linear function of applied voltage and the growth low is 2.5 nm/V . After that, for every thickness of anodic oxyde layers the chemical and electrochemical dissolution was investigated. The Chemical and electrochemical dissolution of anodic oxide layers with time were followed by in-situ measurements of elliptically polarized electromagnetic waves. For this purpose was used an optical-ellectrolytic cell adapted for in-situ ellipsometric and electrochemical measurements .

Results and Discussion

The electrochemical colorations of electropolished and non electropolished aluminium's surfaces were performed by means of alternative currents at voltage range between 10-20 V in solutions of H_2SO_4 with concentrations between 10-40 % and various concentrations of additions $CuSO_4$ (0.005 % - 0.06 %) and $NiSO_4$ (0.5 - 6 %). During all the investigations time, the ratio between the volume of electrolyte and electrode surface was about 10 lit/dm^2.

Thanks to a great number of performed experiments, it is confirmed that the colour of aluminium's surfaces will depend on concentration of H_2SO_4, concentration of addition, values of applied voltage and current density, bath temperature and time of electrochemical treatment. By change of these parameters it can be obtain the various colorations and shaides as: clear yellow, yellow, yellow old or, braun, black,clear green, green, dark green etc. In the first step of investigations we took pains to keep the constant values in the majority of changable parameters and change only one parameter. This precedure was repeated many times and in each case was change only one parameter while the others were constant. When it was constated which of changable parameters had greater influence to the quality of surface colour and which ones only of the surface shades the further investigations were performed in such a manner that less influently parameters as: time of treatment and bath temperature were kept constant, while concentrations were changed of H_2SO_4, concentration of additions, applied voltage and current density.

Table 1.

Electrochemical coloration of aluminium's alloy S.10.6063(USA) with alternative current in 20%H_2SO_4 with 0.035% $CuSO_4$ as addition: I_o - start current density : I - terminal current density after 30 min.

number of sample	I_o(mA/cm^2)	I(mA/cm^2)	colour	bath temperature
1	45	40	clear green	20 - 27^{o}C
2	50	45	green	20 - 28^{o}C
3	55	40	green	20 - 28^{o}C
4	60	10	dark green	20 - 29^{o}C
5	65	35	dark green	20 - 30^{o}C

It is proved that the current density change its values with time at

constant voltage as a result of formation the surface layer whose thickness grow with time of polarisation. The special attention we have paid to obtain the green colours and their shades.

In Table 1. are given the influence of current density on the surface colour shades. From Table 1. it is evident that, if the current density increses the bath temperature also increases.

In the Table 2. are given the influence of voltage and current density on the surface colour.

Table 2.

Electrochemical colorations of non electropolished aluminium's alloy S.10.6063 (USA) with alternative current, in 20 and 30 % H_2SO_4. I_0 - start current density : I - terminal current density after 30 min. As addition are utilized different concentrations of $NiSO_4$

Conc. $NiSO_4$ %	Voltage (V)	I_o(mA/cm²)	I(mA/cm²)	Colour
		20 % H_2SO_4		
0.1	16	234.6	130.6	clear yellow
0.1	25	279.6	142.8	yellow
0.2	25	373.4	367.3	yellow old gold
0.2	12	153.6	122.4	not colored
		30 % H_2SO_4		
0.1	17	279.5	214.2	clear green
0.1	19	193.8	214.7	dark green
0.1	20	296.0	214.2	black
0.1	22	312.7	271.5	black
0.1	30	357.1	197.9	braun black

It should to mention that we have investigated as addition the different concentration of mixtures containing $CuSO_4$ and $NiSO_4$, but the results will be presented in our next report.

From all our experiments it is ascertained that at constant conditions of treatment it could be obtained stable colours with the same shades. From time to time it should be controled the concentration of addition ($CuSO_4$ and

$NiSO_4$) because with time it decreases and when it takes some critical value, generally, the surface colorations take more clear shades.

By electrochemical coloration of electropolished aluminium's surfaces it will be obtained the surfaces with greater shiness and brightness, i.e. with better decorative properties. Moreover, this process of double electrochemical treatment is chipper and could be utilized only for luxous parts of some building yerad.

Titanium exposed in atmospheric conditions, spontaneusly builton his surface, the natural oxide layer which protects the basic metal from corrosion in many corrosive medias. By measurments by elliptically polarized electromagnetic waves it is shown that this layer can reduce at cathodic potentiels from -0.4 to -0.9 V. The fastest cathodic reduction takes place at potentiels of -0.6 and -0.7 V (sce). Moreover, it hasn't yet a ceratin proof if, with cathodic reduction the whole natural oxide layer is dissolved or no. The simultaneous potentiostatical-ellipsometric measurements were shown that the cathodic reduction is possible also for thicker anodically formed oxide layers and in more concentrated solutions of H_2SO_4 the chemical dissolution has a remarquable participation. Moreover, the chemical dissolution has bed influence on surface homogenity and the surface becomes optically irreversible, so it isn't possible to follow the quantitative diminuation of layer thickness with elliptically polarized electromagnetic wave. According to these reasons the formation and electrochemical dissolution of anodic oxide layers is performed in lower concentrations of H_2SO_4 when the chemical dissolution is neglected related to the electrochemical, too.

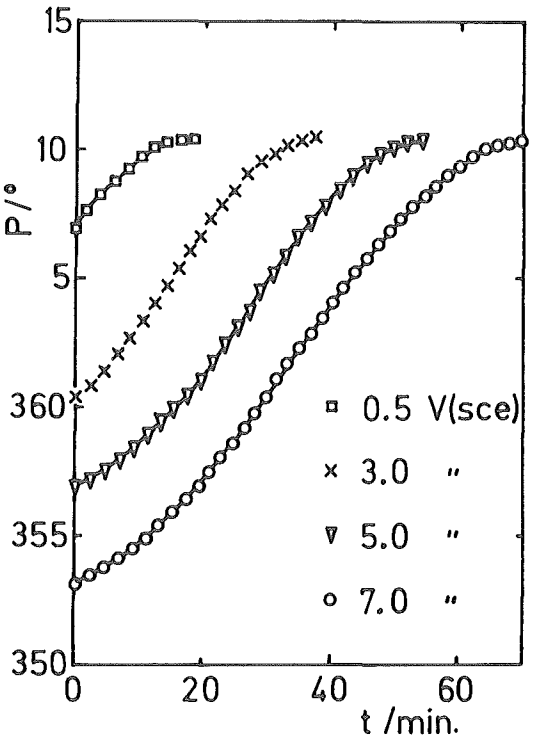

Fig.1. Polarizer-time dependence during electrochemical dissolution at -0.6 V (sce) of anodic layers formed between 0.5 and 7 V(sce)

Electrochemical reduction of anodic oxide layers is possible for cathod potentiels between -0.4 and -0.9 V (sce)

In Fig.1. is shown the electrochemical dissolution rate, at potentiel of -0.6 V for

anodic oxide layers with differents thickness formed at 0.5 : 3 : 5 and 7 V(sce) The electrochemical dissolution is followed by variations of polarizer position settings during the succesive diminuation of film thickness. From Fig.1. it is evident that the tima of dissolution depend of film thickness. After the dissolution of anodic oxide layer, the polarizer position settings take the same values, of 10.27 degre for every thickness of anodic oxide layers. This phenomen shown that the anodic oxide layer could be completely dissolved.

In the Fig.2. are shown the variations of polarizer and analiser position settings during the electrochemical dissolution of a thicker film of 125 nm formed on titanium surface at 50 V. From the course of P and A curves it can be concluded that there exists the differential relation between these two curves.

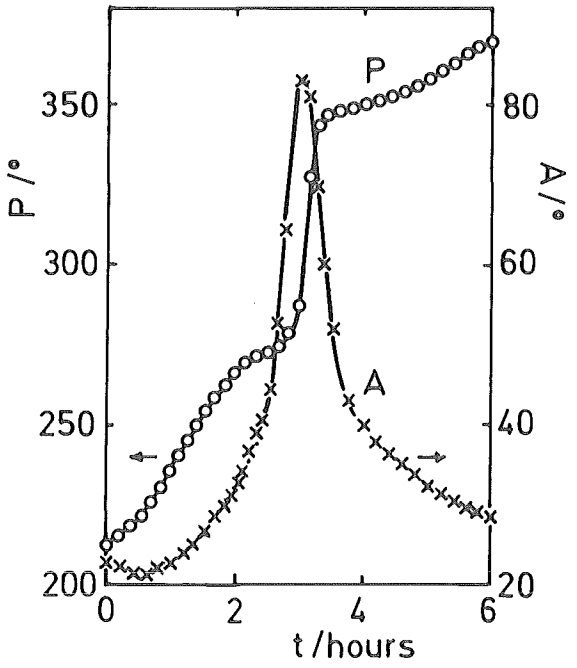

Fig.2. Polarizer-analiser dependence during the cathodic dissolution of anodic film formed at 50 V, at potential of -0.6 V(sce) in 0.5 mol/dm³ H_2SO_4

Taking into account the nature of elliptically polarized electromagnetic waves and thickness of anodic oxide layers we have succeded to establish a mathematical relationship between the parameters of elliptically polarized electromagnetic waves and the time of cathodic reduction of anodic oxide layers. With this relationship is possible to calculate all optical parameters of anodic oxide layers.

R e f e r e n c e s

1. L.Young - Anodic oxide films, Academic Press (1961), New York

2. Lj.Arsov - J.eng.Phys. 20, (1979), 5

3. R.Lignon - Rev. Metallurgy, 61, (1964), 85

4. Lj.Arsov, M.Froelicher, M.Froment et A.Hugot-Le Goff, J.Chim.Phys. 3, (1975), 275

THE ADHESION BETWEEN GLASS AND ENAMEL

O. Seide, H. Röcker

Institut für Gesteinshüttenkunde der RWTH Aachen,
Mauerstr. 5, D-5100 Aachen

1. Introduction

Enamel is not a material by itself, but finds its use combined with other materials. While the enamelling of metal in order to protect the surface of the metal has been a common practice for a long time, the enamelling of glass is still quite a new field with new applications in the study of enamel /1/.

In order to save energy, major car-manufacturers **adhere** the front and rear windshield to the body so that both parts are even (**Fig. 1**). The total weight of the car can thus be reduced and aerodynamics improved. One enamels the border of the windshield in order to protect the organic glue from

Fig. 1: Example for an enamelled front windshield (Audi AG, D-Ingolstadt)

destruction by the ultraviolet radiation and also in order to give the windshield a nice finish. One adheres the glue on the enamel.

2. Basic Theory

The basic requirement for the production of a compound glass-enamel is the wetting of the glass by the enamel. During the bending-process of the windshield, which happens at the determined temperature of 630°C, the glass support has a viscosity of about $5 \cdot 10^{10}$ dPa·s, and can be considered as a solid /2/. Consequently, the enamel during the firing must have such a low viscosity, that it acts as the wetting liquid in the whole process.
Accordingly, the viscosity of the enamel on the glass support should be clearly less than the viscosity of the glass. The viscosity of the enamel is at the maximum of $1.5 \cdot 10^{6}$ dPa·s by the given baking temperature /2₁/.

One can describe this wetting of a glass surface with enamel with Young's equation, which explains the wetting of a solid surface with a liquid (**Fig. 2**).

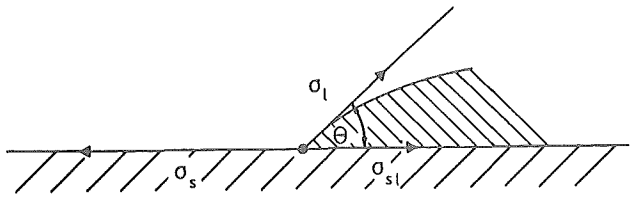

$$\sigma_s = \sigma_{sl} + \sigma_l \cos \theta$$

$$\sigma_s - (\sigma_l + \sigma_{sl}) > 0$$

σ_s : Surface tension of the solid phase
σ_l : Surface tension of the liquid phase
σ_{sl}: Interfacial surface tension
θ : Contact angle

Fig. 2: Wetting

A wetting of the support exists, if the contact angle θ is smaller than 90^{o}. In this case the difference between σ_s and $\sigma_{sl} + \sigma_s$ is greater than zero.

Because the interfacial surface tension σ_{sl} of the new formed interfacial surface always has a positive value, the wetting can then only succeed, if the surface tension of the liquid has a greater value than that of the interfacial surface one and also a smaller one than the surface tension of the solid phase.

This means, that for the enamelling of glass one can only use enamels which have a low surface tension.
The fulfillment of the requirement for an enamel with low surface tension goes together with the fulfillment of the requirement for low-melting enamels, because normally the components, which decrease the viscosity of the enamel, decrease at the same time the surface tension (compare /3/ with /4-6/).
A wetting is consequently the base for an adhesion.

3. Experimental

The adhesion between glass and enamel itself depends on the forming of a boundary layer produced by diffusion process during the firing of the enamel on the glass support. Silicon-Oxygen-Silicon-bondings guarantee in the boundary layer the adhesion of the two compounds.

In order to prove the diffusion, a self-produced fine grinded enamel was laid on float glass by a screen printing process and fired in layers of about 10µm thick.
Table 1 shows the chemical composition of the enamel and the glass support used.

In addition to this, a further glass sample was coated with a stannic oxide before the enamel was laid on it and fired. Both samples were fired for a period of 12 hours. Namely SnO_2 coatings work as diffusion blockade for the ions of glass and enamel. This explains a comparison of the two X-ray line profiles in **Fig. 3.**

	FLOAT GLASS	ENAMEL
SiO_2	70.13	55.00
B_2O_3	--	9.50
Al_2O_3	0.88	0.10
PbO	--	18.33
Alkali Oxides	14.84	8.01
MgO	5.15	0.40
CaO	9.00	0.30
ZnO	--	4.80
SnO_2	--	1.00
Colouring Oxides	--	2.56
SiO_2/PbO	--	3.0

Table 1:

Chemical composition of the components (mol%)

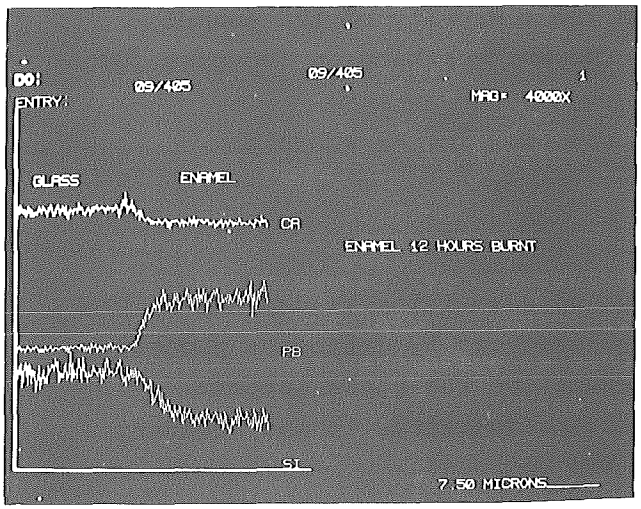

Fig. 3: X-Ray Line Profiles:

above: Enamel fired 12 hours on uncoated glass support

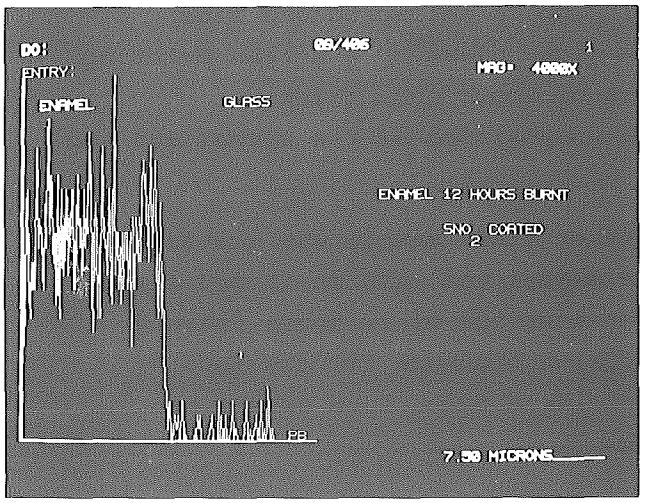

below: Enamel fired 12 hours on with SnO_2 coated glass support

The uncoated sample has a large diffusion region, that means that a gradual assimilation of the concentration level took place between the glass and enamel during the firing.
On the other hand, using this as a representative example one can look at the case of lead, in which the glass had been coated with stannic oxide; one can see that the concentration level drasticly drops if one scans from the enamel into the glass.

That proves that a layer of tin dioxide prevents diffusion under the given conditions.*

The mechanism of adhesion of enamel on glass itself depends on Si-O-Si-bondings.

This is investigated in the following comparing experiment. For the experiment, two glass supports were enamelled; one of the glass support had been coated with stannic oxide and the other one remained uncoated. This happened under conditions that were more comparatively similar to the industrial ones, that means in this case 30 minutes firing time.

Both samples were then boiled in concentrated hydrogen chloride acid for a period of 8 hours. **Fig.4** shows the result.

The enamel on the SnO_2 coated glass support was totally dissolved by the acid. Consequently this result happened due to the non production of Si-O-Si-bondings. Contrary to this

---

* Note:

The diffusion layer was investigated with a Scanning Electron microscope, which is connected to an energy dispersive X-ray analyser which can acquire line profiles. In order to acquire line profiles one has to restrict the choice of elements to silicon, calcium and lead because of the concentration contents and the technical measuring possibilities.

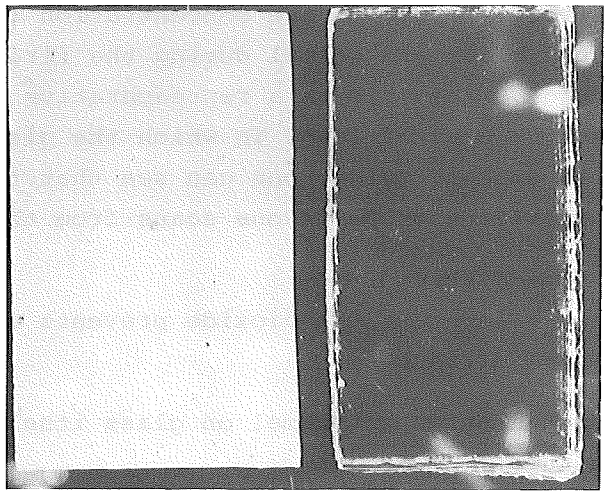

Fig. 4: Enamel after 8 hours boiling in conc. HCl:

left side: Relicts of enamel on uncoated glass support
right side: Enamel is totally eliminated from the SnO_2 coated glass support

the acid could not completely damage the uncoated sample, because in this case the ions could diffuse and produce Si-O-Si-bondings.

Fig. 5 shows a SEM-picture of the acid treated enamel and the glass support.
One can observe the seriously damaged enamel. One can see that the attack is particularly intensive on the grain boundaries.

The enamel surface and the uncoated glass surface were both analysed by an energy dispersive X-ray analyser. The results are shown in **Fig. 6.**
One can see that the enamel surface contains only Silicon dioxide. That means that only the SiO_2 structure has resisted to the attack by the acid.

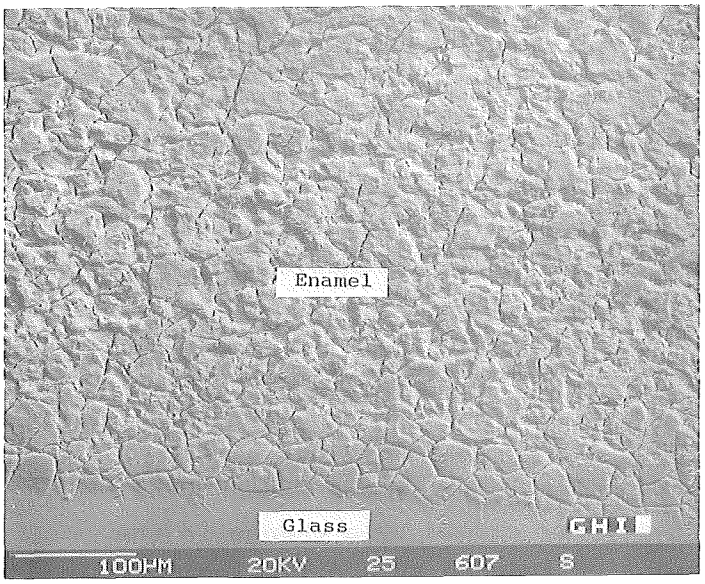

Fig. 5:

Uncoated glass support: Enamelled glass surface after 8 hours in the acid solution and the glass support itself

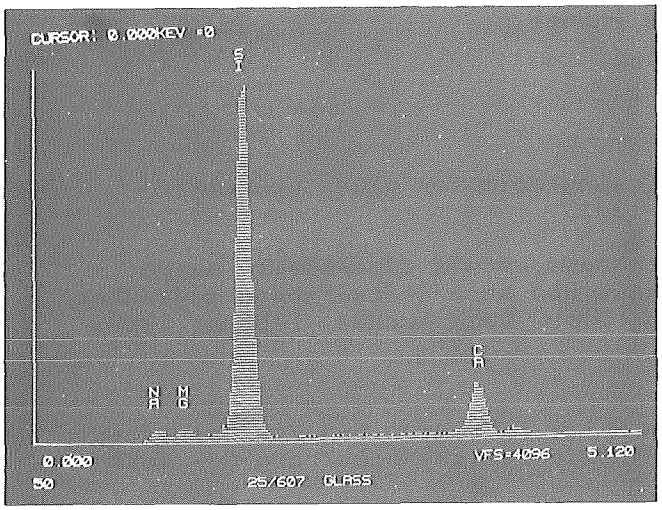

Fig. 6:

EDX-Spectra of enamel and the uncoated glass surface after 8 hours in acid solution

above: Glass surface

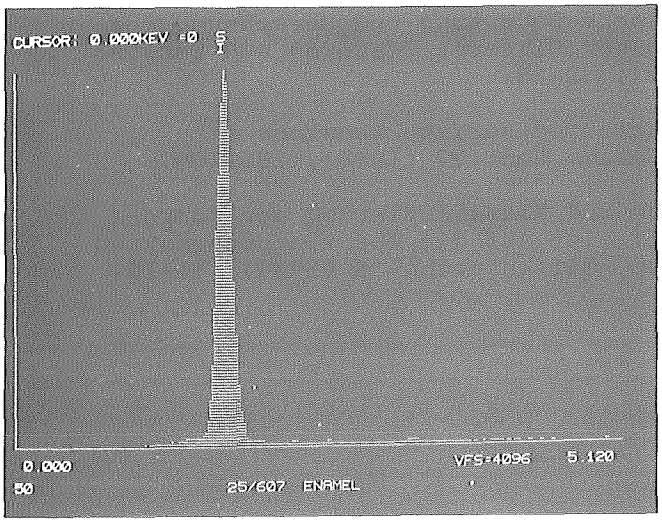

below: Enamel surface

4. Summary

The adhesion between enamel and glass depends on the Si-O-Si-bondings. The really critical point of the compound material glass-enamel is not the adhesion between the two compounds itself, but the decrease of the mechanical strength caused by the enamelling.

The decrease of the mechanical strength is caused by the non homogeneous nature of the enamel layer (e.g. pores, crystallizations, phase separations) and in this case can also be caused by thermal induced tensions in the phase boundary of the compound. Thermal tensions are caused by a change in the coefficient of thermal expansion induced by a diffusion process during baking the enamel.

5. References:

/1/ Young, E.S.: The growing role for glass enamels; Glass Ind. (1983), 13-15.

/2/ Röcker, H.: Der Verbundwerkstoff Glas-Email, seine mechanische Festigkeit und sein Haftvermögen gegenüber organischen Klebern; Diss. RWTH Aachen, Februar 1987.

$/2/_1$ ibid.: p. 156.

/3/ Scholze, H.: Glas - Natur, Struktur und Eigenschaften; 2. Aufl., Springer-Verl., Berlin-Heidelberg-New York 1977, 128-140.

/4/ Dietzel, A.: Praktische Bedeutung und Berechnung der Oberflächenspannung von Gläsern, Glasuren und Emails; Sprechsaal **75** (1942), 82-85.

/5/ Lyon, K.C.: Calculation of surface tensions of glasses; J. Amer. Ceram. Soc. **27** (1944), 186-189.

/6/ Appen, A.A.: Versuch zur Klassifizierung der Komponenten nach ihrem Einfluß auf die Oberflächenspannung von Silikatschmelzen; Silikattechn. **5** (1954), 11-12.

TEMPERATURE DEPENDENCE OF INTERFACIAL ENERGIES BETWEEN SOLID OXIDES AND LIQUID METALS

P. Nikolopoulos, D. Sotiropoulou

University of Patras, Institute of Physical Metallurgy, Dpt. of Chemical Engineering, GR.-26110 Patras, Greece.

U. Jauch, G. Ondracek

Kernforschungszentrum Karlsruhe, Institut für Material-und Festkörperforschung, D-7500 Karlsruhe, Fed. Rep. Germany.

Introduction

The determination of interfacial energies between ceramic and liquid metal phases is of importance in the technology of cermets. In the presence of a liquid phase during sintering of metal-ceramic powder composite material, the density, microstructure and mechanical properties are influenced by the wetting behaviour at the interface.

The wetting in a solid- liquid- vapour system, in thermodynamic equilibrium, is characterized by the wetting angle. Its magnitude depends on the temperature and the surface as well as on the interfacial energies of the phases in contact.

An established method for studying the interfacial phenomena is that of a sessile drop of liquid metal lying on a substrate of the relevant metal-oxide (Fig 1). In this case the following equation holds

$$\gamma_{SV} = \gamma_{SL} + \gamma_{LV} \cos \Theta \qquad (1)$$

where γ_{SV}, γ_{LV} are the surface energies of the solid and liquid phases respectively, γ_{SL} the interfacial energy of solid-liquid and Θ the wetting angle.

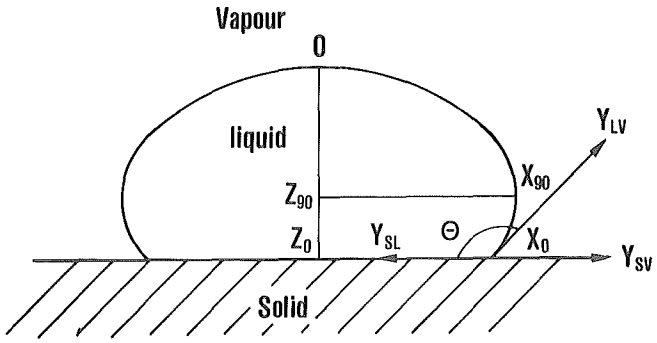

Fig. 1. Wetting angle (Θ) in solid-liquid- Vapour system in equilibrium.

The work of adhesion (W_a) is given by

$$W_a = \gamma_{LV}(1+\cos\Theta) \qquad (2)$$

In this work we describe the experiments that have been carried out in order to determine the temperature functions of the interfacial energies in the Al_2O_3-Bi, Pb, Cu, Ni and ZrO_2-Cu, Co, Ni systems. Additional literature data about wetting angles in the systems Al_2O_3-Sn, Al_2O_3-Co [1] and ZrO_2-Sn, ZrO_2-Pb [2] supplement the experimentally determined quantities.

Experimental procedure

Polycrystalline alumina AL23 (tradename of Friedrichsfeld Co., West Germany) with a purity of 99.7% and polycrystalline zirconia ZR23 (stabilised with 5 wt% CaO) with a purity of 99% were used in the wetting experiments. The as-received Al_2O_3 and ZrO_2 had a density of 3.7 to 3.95 $Mg.m^{-3}$ and 5.0 to 5.4 $Mg.m^{-3}$ respectively. The grain size of Al_2O_3 varies between 10 to 20 µm and for ZrO_2 between 30 to 50 µm. Discs of 20 mm diameter and 3 mm thickness were used in the experiments. The purity of the metals (Fa. Ventron G.m.b.H., W. Germany) was in wt%, Sn = 99.9985%, Bi = 99.99995%, Pb = 99.9985%, Cu = 99.999%, Ni = 99.99% and Co = 99.998%.

The measurements were carried out in a purified argon atmosphere. The samples were heated with an induction coil and the wetting angles were measured from the photographs of the sessile drops.

Experimental results

Owing to the fact that the wetting angle (Θ) in all the systems examined was greater than 90°, the sessile drop has the form of ellipsoid of revolution. From the values of X_{90}, Z_{90}, X_0, Z_0 (Fig. 1) and by using the tables of Bashfort and Adams [3], the wetting angle can be determined.

For each system and temperature, two to four experiments were carried out. Each experiment lasted for about 20-30 min. Photographs of the sessile drops were obtained in 5 min intervals. The results showed that the wetting angle is time independent in all systems examined.

Fig. 2 and 3 show the temperature dependence of the wetting angle in the systems Al_2O_3-Sn, Bi, Pb, Cu, Ni, Co and ZrO_2-Sn, Pb, Cu, Ni, Co respectively. The values of the measured wetting angles agree reasonably well with the most literature data obtained for the same systems under inert gas conditions.

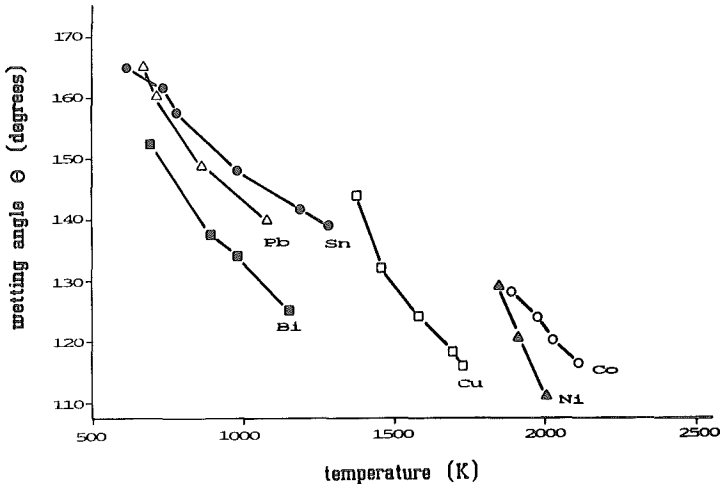

Fig. 2. Effect of temperature on wetting angles formed by liquid metals on Al_2O_3.

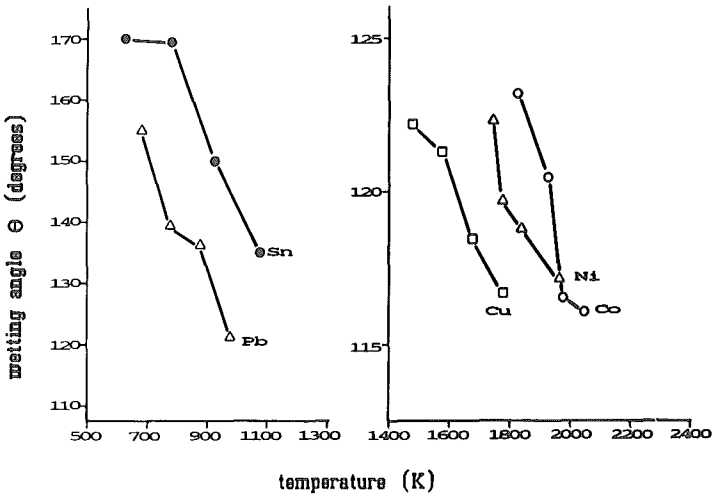

Fig. 3. Effect of temperature on wetting angles formed by liquid metals on ZrO_2.

The results indicate that the liquid metals, for the investigated temperature range, do not wet the ceramic oxides. This is often attributed to the domination of the ceramic surface by the oxygen anions. The wetting angle decreases with increasing temperature and melting points of the metals. Moreover the angles (Θ) indicate that the wettability is not sufficient for high densification of composites during liquid phase sintering.

Interfacial energy and work of adhesion

The measured wetting angles in the Al_2O_3- and ZrO_2- liquid metal systems, together with literature data of the surface energies of solid ceramics (Al_2O_3 [1], ZrO_2 [4]) and of the surface energies of liquid metals in inert gas atmosphere or vacuum [1,5,6,7,8], were used for the calculation of the interfacial energies (eq. 1) and of the work of adhesion (eq. 2).

The temperature coefficient of the surface energy of ZrO_2 was estimated as $d\gamma_{SV}/dT = -0.3\ 10^{-3}\ J.m^{-2}.k^{-1}$. This value compares well with the corresponding temperature coefficients of the oxides ThO_2 ($-0.24\ 10^{-3}\ J.m^{-2}k^{-1}$)[9] and UO_2 ($-0.35\ 10^{-3}\ J.m^{-2}k^{-1}$)[10] which have similar crystal structure. The linear

temperature functions of surface energies are given in Tabl. I.

Table I. Linear temperature functions of surface energies for solid ceramics and liquid metals.

Material	Surface energy ($J.m^{-2}$)	
Al_2O_3	$2.559-0.784\times10^{-3}$ T	$0 \leqslant T < 2323$ K
ZrO_2	$1.227-0.3\times10^{-3}$ T	$0 \leqslant T < 2893$ K
Sn	$0.544-0.07\times10^{-3}(T-T_m)$	$T \geqslant T_m = 505$ K
Bi	$0.372-0.09\times10^{-3}(T-T_m)$	$T \geqslant T_m = 544$ K
Pb	$0.468-0.13\times10^{-3}(T-T_m)$	$T \geqslant T_m = 600$ K
Cu	$1.311-0.20\times10^{-3}(T-T_m)$	$T \geqslant T_m = 1356$ K
Ni	$1.754-0.28\times10^{-3}(T-T_m)$	$T \geqslant T_m = 1726$ K
Co	$1.610-0.29\times10^{-3}(T-T_m)$	$T \geqslant T_m = 1768$ K

The influence of metal vapours, existing in the furnace atmosphere, has proved to be of minor importance for Al_2O_3 and ZrO_2 surface energies and the value of the wetting angle and therefore, has been neglected.

The results of the measurements of wetting angles as well as the calculated values of the work of adhesion and the interfacial energies in the investigated systems are given in Tables II and III. Table IV shows the linear temperature functions of interfacial energies and the coefficients of correlation.

In Figs. 4 and 5 the data of interfacial energies of Al_2O_3- liquid metals and ZrO_2- liquid metals respectively, are plotted versus the homologous temperature (T/T_m). These figures, together with Table IV, show that the interfacial energies, depending on the ceramic substrate, vary in a restricted region at the metal's melting point. The mean values and the standard deviations of the interfacial energies are given as:

- $\gamma_{SL} = 2.538 \pm 0.139$ $J.m^{-2}$ for the Al_2O_3- liquid metal systems and

Table II. Wetting angles (Θ), work of adhesion (W_a), interfacial energies (γ_{SL}) in the Al_2O_3 - liquid metal systems.

System	T (K)	Θ (deg)	Standard deviation	W_a ($J.m^{-2}$)	γ_{SL} ($J.m^{-2}$)
Al_2O_3 - Sn	611	165.24	± 4.06	0.018	2.599
	726	161.74	± 2.68	0.027	2.492
	772	157.74	± 7.86	0.039	2.440
	975	148.26	± 4.37	0.076	2.230
	1183	141.96	± 1.71	0.106	2.023
	1280	138.95	± 2.67	0.120	1.925
Al_2O_3 - Bi	689	152.73	± 4.95	0.040	2.338
	890	137.38	± 2.99	0.090	2.112
	965	134.33	± 1.90	0.101	2.035
	1144	125.24	± 1.86	0.135	1.845
Al_2O_3 - Pb	667	165.30	± 3.05	0.015	2.480
	711	160.48	± 7.15	0.026	2.430
	860	149.00	± 5.18	0.062	2.257
	1073	139.82	±10.05	0.096	2.029
Al_2O_3 - Cu	1370	143.87	± 2.82	0.252	2.541
	1450	131.86	± 2.66	0.430	2.284
	1575	123.97	± 2.30	0.559	2.032
	1695	118.42	± 1.42	0.651	1.822
	1720	116.10	± 1.19	0.693	1.756
Al_2O_3 - Ni	1843	129.28	± 2.98	0.631	2.204
	1908	121.20	± 1.34	0.821	1.945
	2003	111.30	± 0.66	1.067	1.598
Al_2O_3 - Co	1888	128.20	± 2.81	0.601	2.053
	1973	123.91	± 2.12	0.686	1.877
	2023	120.10	± 1.53	0.766	1.743
	2113	116.68	± 0.88	0.832	1.580

- $\gamma_{SL} = 1.599 \pm 0.064\ J.m^{-2}$ for the ZrO_2- liquid metal systems.

By considering the above results and from the literature data for the UO_2- liquid metal systems [11] ($\gamma_{SL} = 1.676 \pm 0.142\ J.m^{-2}$) one can conclude that, by using an average value for the interfacial energy between ceramic and liquid metals at the metal's melting point, this provides a reasonable

Table III. Wetting angles (Θ), work of adhesion (W_a), interfacial energies (γ_{SL}) in the ZrO_2-liquid metal systems.

System	T (K)	Θ (deg)	Standard deviation	W_a ($J.m^{-2}$)	γ_{SL} ($J.m^{-2}$)
ZrO_2 - Sn	623	170.04	± 0.63	0.008	1.568
	773	169.40	± 0.88	0.009	1.511
	923	149.73	± 5.93	0.070	1.395
	1073	134.92	± 2.87	0.148	1.261
ZrO_2 - Pb	673	154.88	± 2.73	0.043	1.441
	773	139.73	± 0.87	0.106	1.335
	873	136.36	± 0.53	0.120	1.278
	973	121.55	± 3.81	0.200	1.155
ZrO_2 - Cu	1473	122.18	± 1.28	0.602	1.471
	1573	121.31	± 2.43	0.609	1.414
	1673	118.38	± 1.09	0.655	1.318
	1773	116.73	± 2.07	0.676	1.247
ZrO_2 - Ni	1740	122.33	± 0.81	0.814	1.641
	1773	119.71	± 1.85	0.878	1.558
	1833	118.82	± 1.65	0.893	1.508
	1953	117.15	± 1.69	0.919	1.412
ZrO_2 - Co	1823	123.21	± 1.78	0.721	1.553
	1923	120.38	± 0.57	0.774	1.441
	1973	116.53	± 0.69	0.858	1.328
	2043	116.06	± 0.52	0.858	1.286

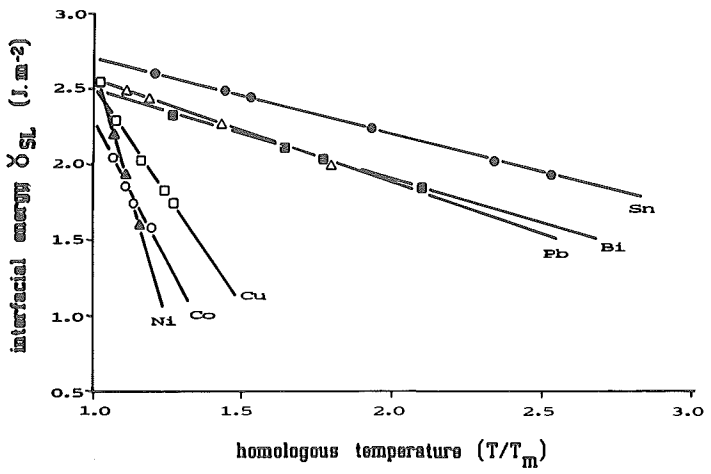

Fig. 4. The temperature dependence of Al_2O_3- liquid metal interfacial energies.

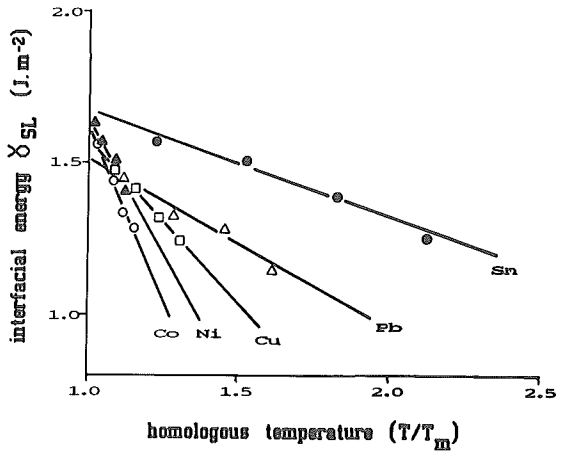

Fig. 5. The temperature dependence of ZrO_2- liquid metal interfacial energies.

Table IV. Linear temperature functions of the interfacial $\left|\gamma_{SL}(T) = \gamma_{SL}(T_m) - \frac{d\gamma_{SL}}{d_T}(T-T_m)\right|$ in the Al_2O_3- and ZrO_2 - Liquid metal systems (R = correlation coefficient).

System	Interfacial energies ($J.m^{-2}$)	R
Al_2O_3 - Sn	$2.710-1.014\times10^{-3}(T-505)$	0.9999
- Bi	$2.492-1.083\times10^{-3}(T-544)$	0.9998
- Pb	$2.552-1.112\times10^{-3}(T-600)$	0.9998
- Cu	$2.528-2.141\times10^{-3}(T-1356)$	0.9943
- Ni	$2.641-3.778\times10^{-3}(T-1726)$	0.9997
- Co	$2.305-2.126\times10^{-3}(T-1768)$	0.9978
ZrO_2 - Sn	$1.671-0.691\times10^{-3}(T-505)$	0.9857
- Pb	$1.506-0.915\times10^{-3}(T-600)$	0.9914
- Cu	$1.568-0.768\times10^{-3}(T-1356)$	0.9957
- Ni	$1.628-0.992\times10^{-3}(T-1726)$	0.9715
- Co	$1.622-1.274\times10^{-3}(T-1768)$	0.9818

approach to wettability in such systems. This approach seems to be independent of the type of metal and is applied, in particular, for those metals with high melting point and high surface energy.

Acknowledegmement

The present work was financially supported by Deutsche Forschungsgemeinschaft and performed in the frame of the bilateral Greek-German cooperation.

References

[1] P. Nikolopoulos, J. mater. Sci. 20 (1985) 3993
[2] B. Grau. Studienarbeit, Universität Karlsruhe, 1986
[3] F. Basfort, S.C. Adams. "An attempt to test the theories of capillary action" (University Press, Cambridge, 1883) p. 63.
[4] W.D. Kingery, J. Amer. Ceram. Soc. 37 (1954) 42
[5] G. Lang, P. Laty, J. Ch. Joud, P. Desré, Z. Metallkunde 68 (1977) 113
[6] B.C. Allen "Liquid Metals" ed. by S.Z. Beer (Dekker, New York, 1972), p. 161
[7] G. Lang, Z. Metallkde 67 (1976) 549
[8] A.R. Miedema, R. Boom, Z. Metallkde 69 (1978) 123
[9] T. Inoue, Hj. Matzke, J. Amer. Ceram. Soc. 64 (1981) 355
[10] P. Nikolopoulos, S. Nazaré, F. Thümmler. J. Nucl. Mater. 71 (1977) 89.
[11] P. Nikolopoulos, G. Ondracek, J. Mater. Sci. 98 (1981) 306

CHARACTERIZATION OF A PHASE BOUNDARY IN Ni-Al_2O_3 SINTERED UNDER PRESSURE

M.K.Pavićević, G. Burri*, H. Schmid** and R. Gotthard**

Faculty of Mining and Geology, University Laboratory for Electron Microanalysis, 11ooo Belgrade, Djušina 7, Yugoslavia

*Faculte des Sciences, Institut de Physique experimentale, CH-1o15 Lausanne, Darigny

**Ecole Polytechnique Federale de Lausanne, Institut de Genie Atomique, CH-1o15 Lousanne, Dorigny

Abstract

The nature of bond in Ni-Al_2O_3 system exposed to pressure ranging from 5o-6oo MPa has been investigated in vacuum at temperature of 135o°C. We used EMPA, SEM + X-ray, Auger, ESCA and TV-TEM as methods for characterization. The existence of intermetal Ni_2Al_3 phase was proved only on the basis of properties of X-ray emission spectra of a valent-conductive Al bond.

Introduction

We have investigated, for a longer period of time, a phase boundary in Ni-Al_2O_3 system that was sintered under the pressure and we applied the method of electron microanalysis with wave-dispersive spectrometry (1-3). The samples obtained under the pressure of 5o MPa (sample o,5) and 6oo MPa (sample 6) were selected for our research work.

We chose the method for our study on the basis of already published papers showing that K_b-band of aluminium as well as SK_a satellite lines ranging from 827o to 83o5 ppm are good indicators in determining the nature of aluminium bond in compounds with oxygen or in alloys of aluminium binary system with other metals.

Both energetic position of a K_b-band and profiles are undoubtedly a solid indicator in determination of a difference between metal aluminium and its oxides. On other hand the relative maximum intensities ratio of SK_{a4}/SK_{a3} satellite lines changes together with the nature of aluminium bond. This ratio represents a linear function of atomic concentration of aluminium, and the slope of a streight line is the function of electropositivity of another component (5).

On the basis of investigated spectra we made a presumption that aluminium-nickel bond in the studied system represents a ionic-covalent and a metal bond. Electronic structure of interatomic bond is, according to its configuration, similar to the alloy of Ni_2Al_3 type, but is not identical. We tried to confirm this statement by applying both complementary and comparative methods.

Experiment

During development of new materials by sintering, a particulat attention should be paid to the following stages: the choice of material, sintering conditions, determination of properties of new materials and explanation of phemonema occurring along phase boundary. In case of a nickel-based composite material, all these sta - ges are given in Fig. 1.

The choice of the relative material and the sintering process are described in papers (1-3), as well as the investigation of a bond nature between a metal and cheramic phase that was carried out by method of high-resolution X-ray spectrometry and electron microexcitation (EMPA+HR X-ray).

Registration of X-ray profiles by scanning electron microscopy (SEM+X-ray) was performed at the Institute for experimental physics in Lausanne. Characterization of materials by the Auger and photoelectron spectrometry (ESCA) as well as the registration of ultrathin samples by method of a high-voltage transmission electron microscopy (HV-TEM) were done at the Institute for physics , EPF-Lausanne.

The theory on the bond nature of $Ni-Al_2O_3$ was considered by K.I. Portnoy with his collaborators (4) who gave two alternative proposals.

The Ni and Al concentration profiles for samples No. o,5 and 6 are given in Figs. 2a and 2b.

If a reaction zone of compounds of Ni_2Al_3 or $NiAl_2O_4$ type, value order of at least 1/um, exists along Ni and Al_2O_3 phase boundary, the concentration profiles would not have a "sharp" transfer from one phase into another. This indicates the conclusion that the reaction zone either does not exist or is considerably below 1/um.

Having analysed the LMM-Auger spectra of nickel and the KVV-Auger spectra of oxygen we could not confirm the presence of other substances except metal nickel and Al_2O_3 in the sample.

The same results were obtained by registration of XPS-spectra of Ni 2s, 2p, 3s and 3p levels and Al 2s and 2p level and O 1s and 2s level. Therefore the application of HV-TEM proved to be the only possible alternative. Figs. 3a and 3b represent the photos of inner foils of samples No. o,5 and No. 6. The metal phase (nickel) is marked by "m" and a ceramic one (Al_2O_3) by "o". The results of these investigations proved no existence of a reaction zone at phase boundary, although, in case of sample No 6, the possibility of its appearance is not eliminated.

The results obtained by a repeated tilting at the twice greater magnification, give the possibility of existence of a reaction zone between a metal and non-metal phase.

Conclusion

At present, the results obtained make the following conclusions possible:

1. A reaction zone between a metal (Ni) and a non-metal (Al_2O_3) phase was not proved to exist as a measurable "Physical thickness".
2. X-ray spectrometry of a valent-conductive band (K_b and SK_a-spectra) confirmed only the existence of Al in form of Ni_2Al_3 what might result from diffusion processes. However, Ni L-spectra would have certainly confirmed this presumption.

3. Investigation of new samples sintered under strictly controlled conditions can provide us with the sound answer on the bond nature of both aluminium and nickel in Ni-Al_2O_3 system.

Acknowledgement

The authors would like to thank Dr Irina Arsentijevna from Moscow Institute of Metallurgy, Dept. of Metallophysics, USSR, Moscow E-25o, Lefortovskii Val 26 for the preparation of investigated samples and Mrs V.Vukčević from the Faculty of Mining and Geology, ULEMA, Belgrade for the English version of this paper.

References

1. Pavićević M.K., Ristić M.M. and Arsentijeva I. (1981): Determination of the nature of aluminium bonding in Ni-Al_2O_3 system sintered under pressure. Beutr. elektronenmikroskop. Direktabb. Oberfl. 14, 81-84 Münster.
2. Ristić M.M. and Pavićević M.K. (1982): The influence of electronic structure and interatomic bond on X-ray emission spectra of aluminium in Ni-Al_2O_3 system. Buletin de l'Akademic Serb des Science of Arts, Class des Science technique (2o); 71-78, Beograd.
3. Pavićević M.K. (1983): The influence of a bond nature on Roentgen emission spectra of aluminium in Nickel-Corundum system in M.K. Pavićević, El Goresy, I.B. Borowskii and L. Rindered (Eds.): Microbeam methods and application, Faculty of Mining and Geology: 117-128, Beograd.
4. Portnoy I.K. i dr. Kompozionnie materiali na nikelvoi osnove, Metallurgia, Moskva, 1979.
5. D.W.Fischer and W.L.Bann in Advances in X-ray analysis, Vol. lo Plenum Press, New York, 1966 pp. 374-388.

Dispersively reinforced material $Ni-Al_2O_3$

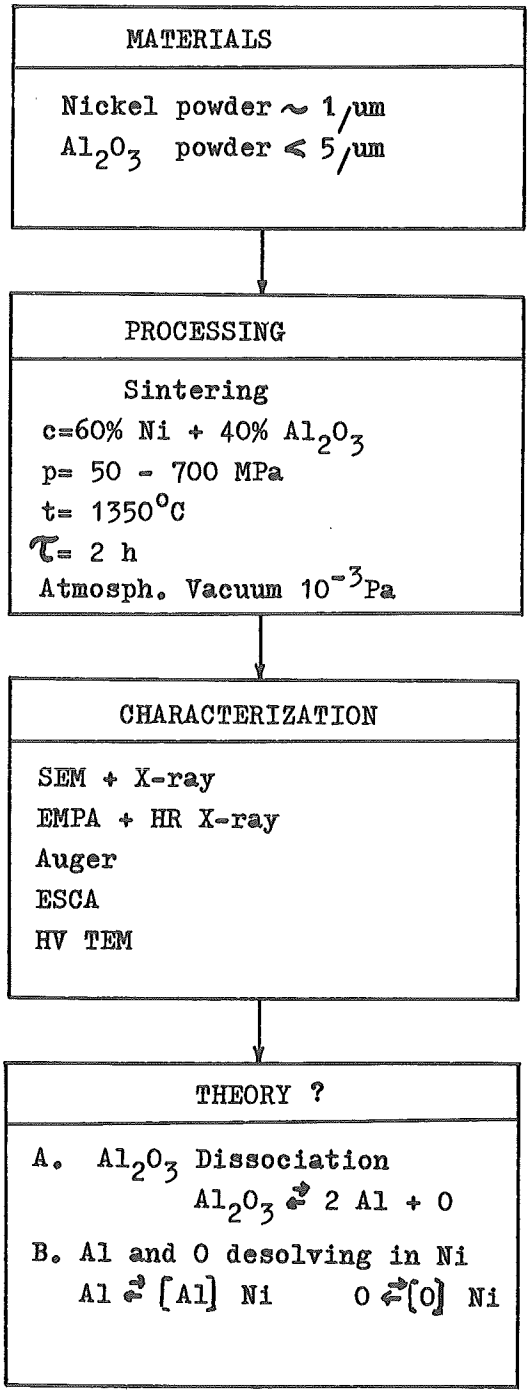

Fig. 1 New materials development

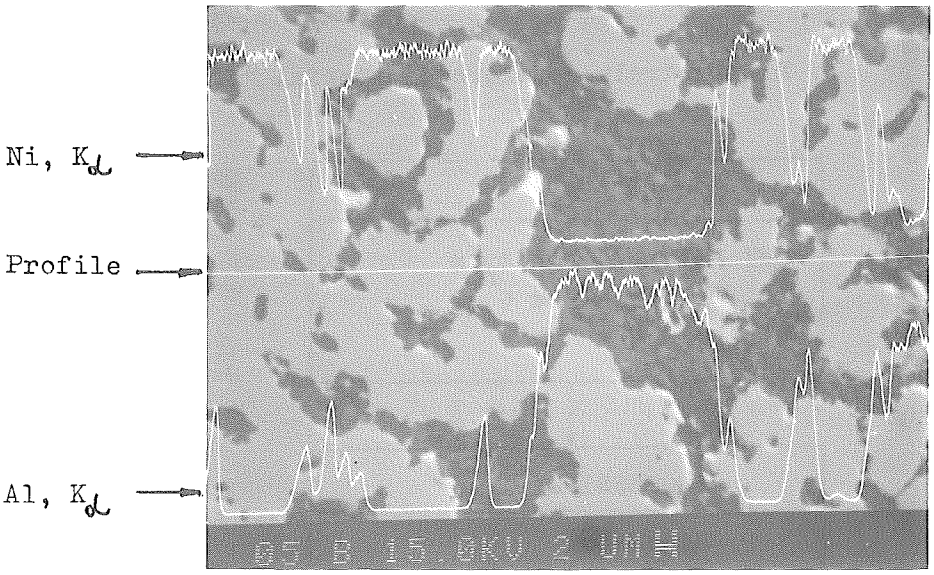

Fig. 2a SEM photo of background electrons and X-ray concentration profiles of Ni and Al Kα-lines in sample No. 0,5, magnification 2 x 10^3.

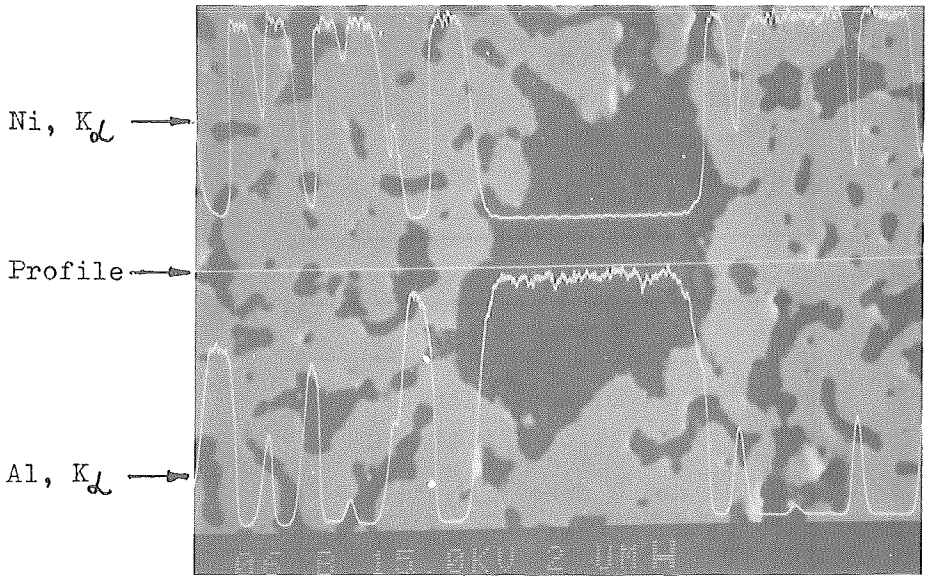

Fig. 2b SEM photo of background electrons and X-ray concentration profiles of Ni and Al Kα-lines No. 6, magnification 2 x 10^3.

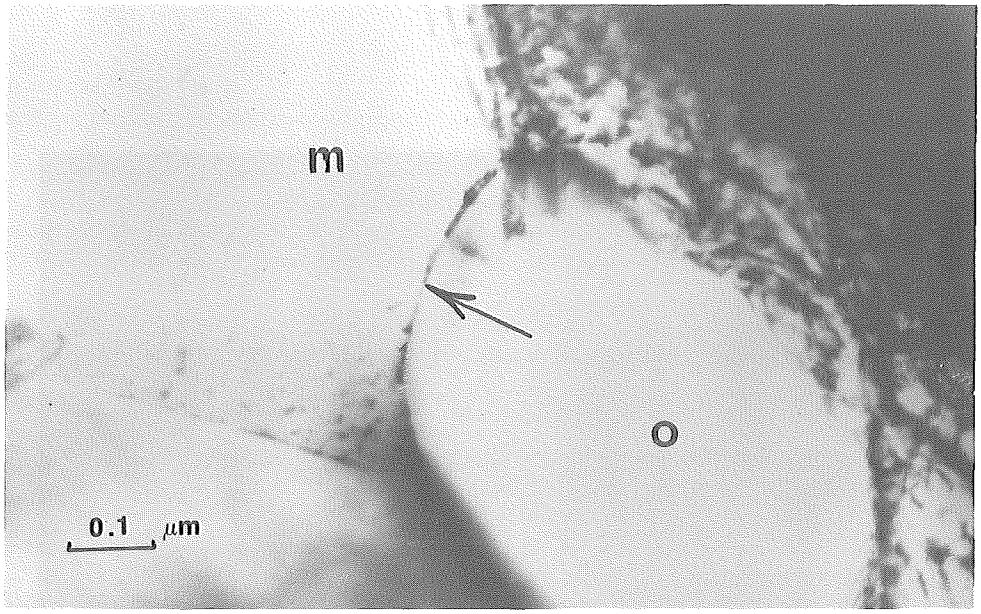

Fig. 3a TEM-photo of sample No. 0,5. The arrow marks Ni-Al_2O_3 boundary phase. Orthogonal geometry of electron beam.

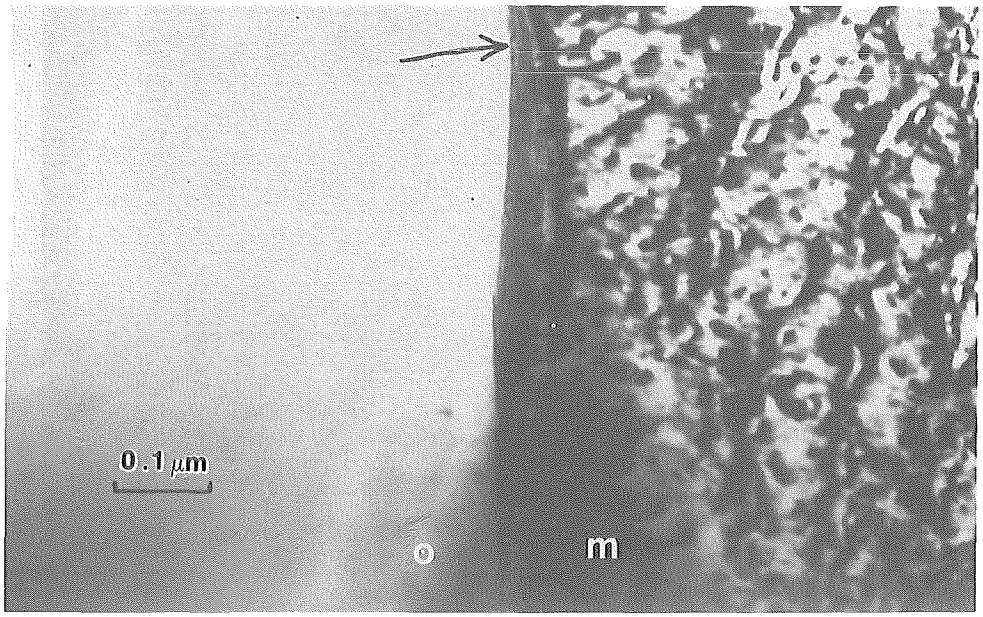

Fig. 3b TEM-photo of sample No. 6. The arrow marks Ni-Al_2O_3 boundary phase. Orthogonal geometry of electron beam.

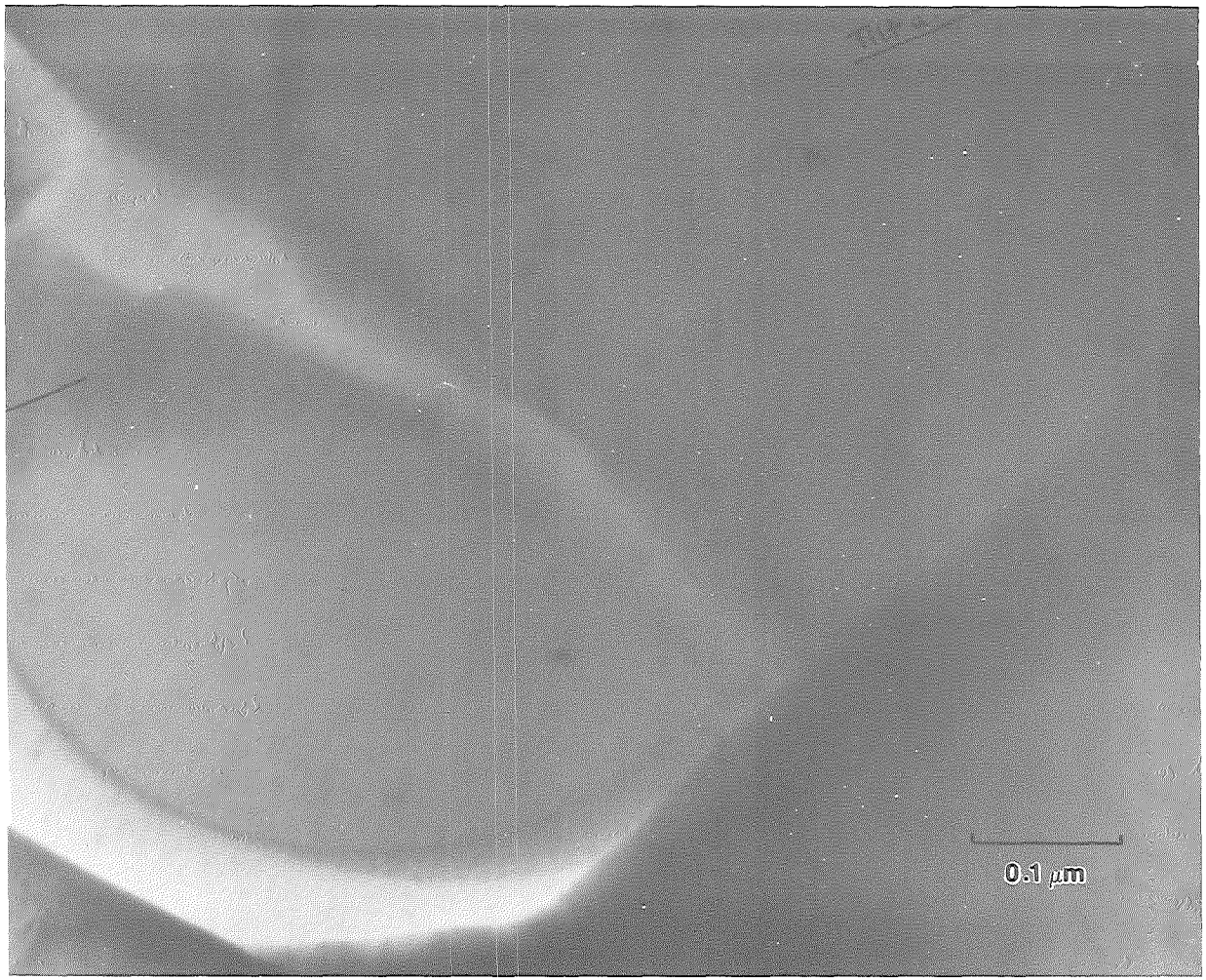

Fig. 4 TEM-photo of sample No. 6. Angular geometry of electron beam (tilting).

NEUTRAL PRIMARY BEAM SIMS ANALYSIS OF CERAMIC MATERIALS

G. Borchardt[1], S. Scherrer[2], and S. Weber[2]

[1] Technische Universität Clausthal, Fachbereich Metallurgie und Werkstoffwissenschaften
D-3392 Clausthal-Zellerfeld, Federal Republic of Germany
[2] Ecole des Mines, Laboratoire de Physique du Solide (U.A. 155),
F-54042 Nancy, France

INTRODUCTION

The chemical as well as the physical properties of interfaces and surfaces often determine the behaviour of materials in a given application: typical examples are all kinds of corrosion, semiconductor and sensor technology, wear and friction, adhesion of coatings, joining processes, sintering, and many other phenomena which are rather common in the field of "interfacial engineering" whose continuously increasing importance requires special interdisciplinary efforts. While one of the papers in this volume [1] gives a survey of what surface analysis can teach on the initial stages of the interaction between a metal surface and a gas atmosphere, it is the aim of this contribution to give a better understanding of the potentials and the risks of applying modern surface analysis methods to materials with low room temperature electrical conductivity like most ceramics, glasses or polymers. Secondary Ion Mass Spectrometry (SIMS) has been chosen as an example: but the conclusions obtained should in principle be also valid for all other methods which use primary or secondary beams consisting of charged particles.

CHARGE EFFECTS AND MOBILE SPECIES IN THE SOLID

While the primary effects on the stability of the secondary signal (which generally provides the information on the surface) are more or less different for different analytical methods and different types of experimental set-ups for a given analytical method in the wide field of surface analysis one feature common to all methods deserves special attention: this is the influence of surface charges on the distribution of very mobile species in the near surface region of the matrix to be analyzed. The origin of the surface charge and its order of magnitude as a function of the experimental parameters can be deduced from charge

balance considerations [2,3,4]. The main result is that for SIMS "self adjusting" methods should be most favourable, especially if primary beams of neutral particles were used. Independently, Devienne et al. [5] (mass spectra only) and our group (chemical and isotopic concentration profiles) first published SIMS analyses of insulators with primary beams consisting of neutral particles. In the meantime, neutral primary beam techniques have been adapted to their respective experimental facilities by other groups [9, 10] under different acronyms. Recently, specially designed neutral particle sputter guns have become available for this type of investigation [11]. While a promising indirect feedback technique which monitors the residual charge and optimizes the secondary signal has been developed for one individual instrument [12], it has until now been impossible to achieve a zero net charge on the surface under consideration. It must therefore be discussed if the electric field due to the residual charges may influence the distribution of (charged) mobile species in the subsurface region of the sample. An undisturbed SIMS analysis will be necessary to study for example fracture phenomena, the kinetics of heterogeneous reactions, the structure of interfaces, diffusion profiles, and many other related phenomena.

For this purpose the space charge layer in the solid which compensates the surface charge is studied with respect to its dynamics as compared to the sputter rate. The solution of the linearized Poisson-Boltzmann equation [13] yields for the electrical potential $\Psi(x)$ in the solid the well-known expression (for the symbols see the list below)

$$\Psi(x) = \Psi(0)\, e^{-x/d} \tag{1}$$

with $d = [\varepsilon\varepsilon_0 kT/2c(\infty)\, z_i^2\, e_0^2]^{1/2}$ as a "screening length". The relaxation time τ which is necessary to build up the space charge layer is estimated as follows:

$$\int_0^d \rho(x)\, dx = \int_0^\tau i(d,t)dt = F \int_0^\tau \left(\sum_1^n z_i j_i\right)_d dt \tag{2}$$

with $j_i = -(D_i c_i/RT)\partial(\mu_i + F\, z_i \Psi)/\partial x$ as the flux of the species i.

Taking only the most mobile species into consideration and neglecting the diffusional term in the flux equation, we find

$$\varepsilon\varepsilon_0(\partial\Psi/\partial x)_0 \leq (z^2e_0^2/kT)\int_0^\tau c(t)D(t)E(t)_d\,dt \qquad (3)$$

$$\approx (z^2e_0^2c(\infty)\ D/kT)(\partial\Psi/\partial x)_d\ \tau$$

For $(\partial\Psi/\partial x)_d \simeq (\partial\Psi/\partial x)_0 = \Psi(0)/d$

we have as a lower limit for the relaxation time

$$\tau \simeq \varepsilon\varepsilon_0 kT/c(\infty)z^2e_0^2D = 2\ d^2/D \qquad (4)$$

If the relaxation velocity d/τ is sufficiently low as compared to the sputter rate dx/dt, the analysis should not be hindered. For most practical cases (s. Table 1)

$$dx/dt > 5\ d/\tau = 5\ D/2d \qquad (5)$$

will be sufficient if the other parameters, especially the sample temperature, can be kept constant. Because of the fact that the temperature dependence of D/d is given by

$$D/d \sim T^{-1/2} \exp\ [-\Delta h/kT] \qquad (6)$$

a typical value for the activation enthalpy of $\Delta h \simeq 1$ eV means that at about room temperature a temperature rise of 10 K roughly quadruples the value of D/d.

		$D/\frac{cm^2}{s} = 10^{-14}$		$D/\frac{cm^2}{s} = 10^{-16}$		$D/\frac{cm^2}{s} = 10^{-20}$	
$c(\infty)/cm^{-3}$	d/Å	τ/s	$\frac{d}{\tau}/\frac{Å}{s}$	τ/s	$\frac{d}{\tau}/\frac{Å}{s}$	τ/s	$\frac{d}{\tau}/\frac{Å}{s}$
10^{20}	3	0.14	20	14	0.2	$1.4 \cdot 10^5$	10^{-5}
10^{18}	16	14	2	1400	0,02		
10^{16}	260	1400	0.2	$1.4 \cdot 10^5$	10^{-3}		
10^{14}	1600	$1.4 \cdot 10^5$	0.02				

Table 1. The application of the working equation (4) to practically relevant values of the bulk concentration of one mobile ionic species $c(\infty)$ and its average diffusivity D (T = 300 K, ϵ = 10).

From Table 1 it can be easily deduced that experiments with $d/\tau > 0.2$ Å/s cannot be recommended. And if the investigations require low sputter rates e.g. in order to improve the depth resolution, even further restrictions on the tolerable d/τ range will have to be respected.

For very low concentrations of mobile species the screening length d is of the same order of magnitude as the sample dimensions and the "external field" produced by the surface charge is unaffected by any space charge layer. A simplified treatment is possible. No falsification of the analysis will occur if the inequality $\dot{x} > (D/kT)\ z\ e_o\ E$ can be maintained.

For T = 300 K, $\dot{x} \simeq 1$ Å/s, z = 1 this condition yields for the critical product $D\ E \leq 10^{-10}$ V cm s^{-1}.

List of symbols

c_i concentration of a mobile species i in the bulk
d screening length ("Debye length")
D_i; D diffusivities of the charged species; mean value

e_o	elementary electric charge
E	electric field
Δh	enthalpy of activation
i	electric current density
j_i	molar flux density of a charged species i
k	Boltzmann's constant
t	time
T	(absolute) temperature
x	coordinate normal to the sample surface
$\dot{x}$	sputter rate
z_i, z	absolute charge number
ε_o	permittivity of the vacuum
ε	relative dielectric constant of the sample
$\rho(x)$	space charge density
$\Psi(x)$	electric potential in the sample

EXPERIMENTAL APPLICATIONS OF NPB-SIMS IN MATERIALS SCIENCE RESEARCH

Experimental results on a variety of poorly conducting surfaces such as corroded or fresh (i.e. as cleaved) glass surfaces [14,15] (see Figs. 1 and 2), oxide scales on silicon nitride (see Fig. 3), and a bioceramic material demonstrate that even in the most unfavourable case of the rather mobile hydrogen (deuterium) or sodium in glass ($D \approx 10^{-16}$ cm^2/s) at room temperature the resulting electric field in NPB-SIMS analysis is too weak to hinder the analysis.

ACKNOWLEDGEMENTS

We are obliged to P. Shipley, Qi Cai, and E. Ebeling for their help with the typescript. We very much appreciated the collaboration with U. Gross who supplied the bioceramic samples. The financial support of the Deutsche Forschungsgemeinschaft (DFG) for part of this work is gratefully acknowledged.

REFERENCES

1 K. Wandelt, this volume
2 H.W. Werner, A.E. Morgan
J. Appl. Phys. 47 (1976) 1232 - 1242
3 H.W. Werner, N.J. Warmoltz
J. Vac. Sci. Technol. A2 (1984) 726 - 731
4 T. Richter, G.H. Frischat, G. Borchardt, S. Scherrer, S. Weber
Mikrochim. Acta Suppl. 11 (1985) 163 - 170
5 F.M. Devienne, J.C. Roustan
C.R. Acad. Sci. Paris t. 276, Série C (1973) 923 - 925
6 S. Scherrer, F. Naudin
Proc. XI Glass Congress, Prague 1977, Vol. 3 p. 301 - 310
7 G. Borchardt, H. Scherrer, S. Weber, S. Scherrer
Jnt. J. Mass Spectrom. Ion Phys. 34 (1980) 361 - 373
8 G. Borchardt, S. Scherrer, S. Weber
Mikrochim. Acta II (1981) 421 - 432
9 A. Iino, A. Mizuike
Bull. Chem. Soc. Japan 54 (1981) 1975 - 1977
10 F. Degrêve, J.M. Lang
Surface Interface Anal. 7 (1985) 177 - 187
11 A. J. Eccles, J.A. van den Berg, A. Brown, J.C. Vickerman
J. Vac. Sci. Technol. A4 (1986) 1888 - 1892
12 G. Stingeder, M. Grasserbauer, K. Traxlmayer, E. Guerrero, H. Pötzl
Mikrochim Acta. Suppl. 11 (1985) 171 - 185
13 J. O'M Bockris, A.K.N. Reddy
Modern Electrochemistry, Vol. 2, ch. 7, Plenum Press, New York 1973
14 G.H. Frischat, T. Richter, G. Borchardt, S. Scherrer
Advances in Ceramics (in press)
15 T. Richter, G.H. Frischat, G. Borchardt, S. Scherrer
Phys. Chem. Glasses 26 (1985) 208 - 212

FIGURES

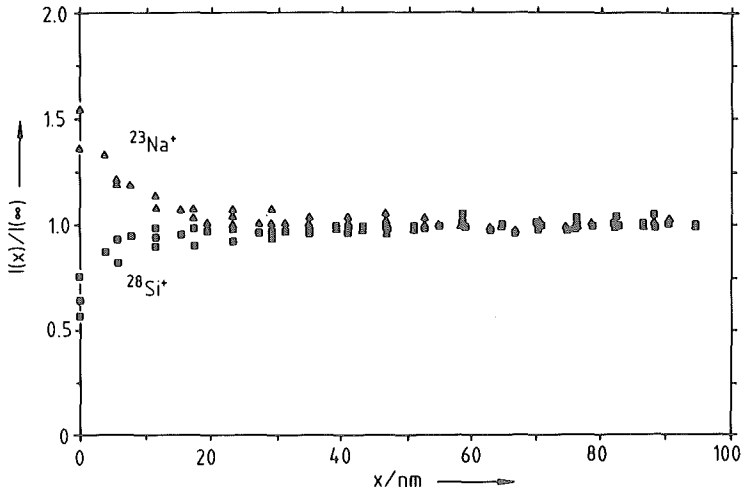

Fig. 1 Normalized intensity profiles of ^{23}Na and ^{28}Si of an as cleaved soda zirconia silicate glass surface (molar composition of the bulk SiO_2 : (Na_2O + Li_2O) : ZrO_2 ≃ 74 : 16 : 10); intensities normalized to the bulk intensities [14].

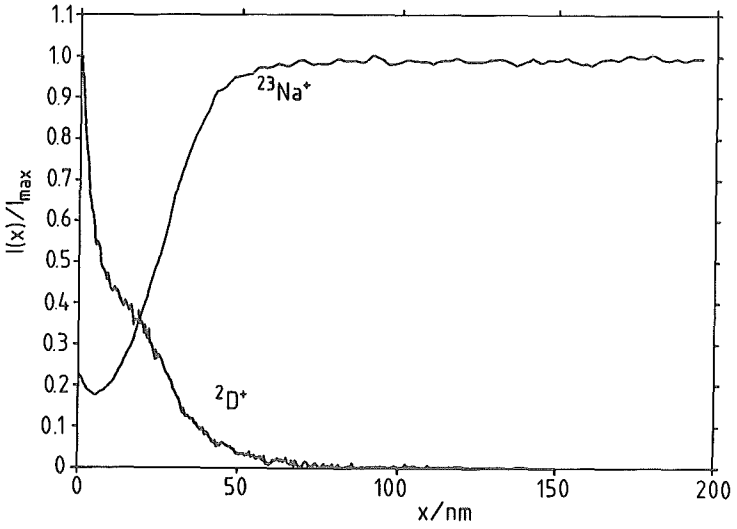

Fig. 2 Normalized intensity profiles of ^{2}D and ^{23}Na of an as cleaved soda lime silicate glass surface (molar composition of the bulk SiO_2 : Na_2 : CaO = 74 : 16 : 10) after a treatment in D_2O for 15 min at 85 °C; intensities normalized to the maximum intensities [15].

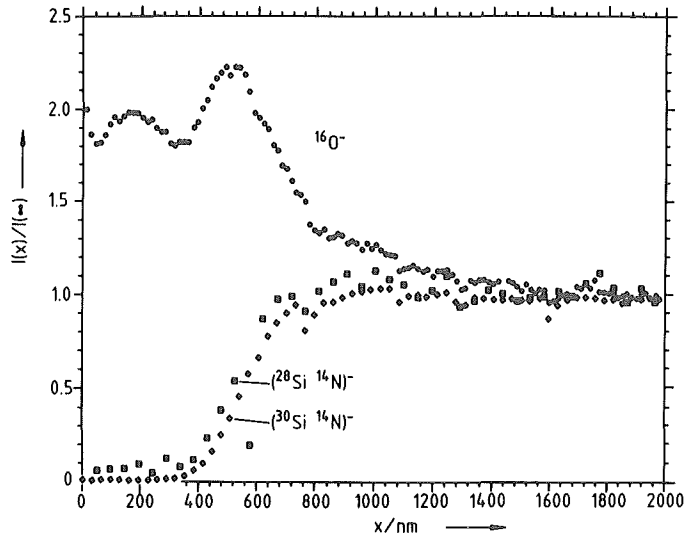

Fig. 3 Normalized intensity profiles of characteristic species of a Si_3N_4 surface after oxidation in air (950 °C, 30 min); intensities normalized to the bulk intensities.

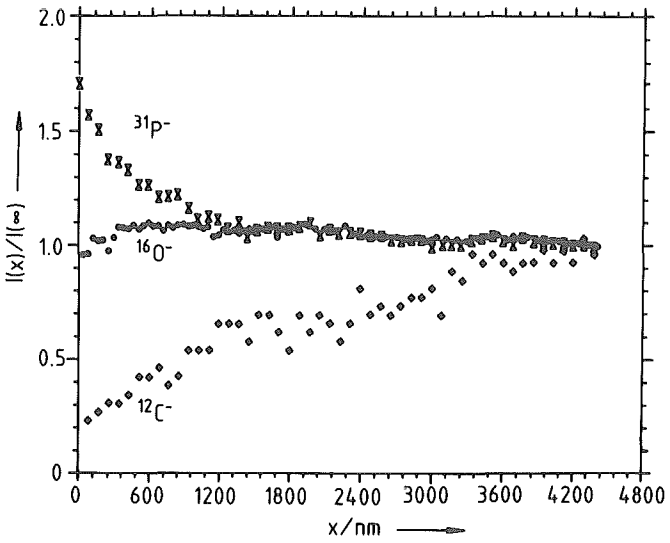

Fig. 4 Normalized intensity profiles of ^{12}C, ^{16}O, and ^{31}P of a polished surface of a bioceramic material (intensities normalized to the bulk intensities).

C E R A M I C S

ELECTRICAL AND MAGNETIC PROPERTIES

MICROSTRUCTURE-PERMEABILITY RELATION IN MnZn FERRITES PREPARED OF IRON OXIDE WITH CHLORINE IMPURITIES

H.INTIHAR,M.DROFENIK,D.KOLAR,M.LIMPEL *

J.Stefan Institute, Edvard Kardelj University, Ljubljana
Iskra IEZE, Ljubljana*

INTRODUCTION

High permeability ferrites are in spite of their relatively long application still important materials, particularly in contemporary electronic devices. They can be used as filter cores, linear broad band transformers, loading coils and power converters. The magnetic properties of MnZn ferrites depend on composition, stoichiometry and microstructure. The most pronounced influence on magnetic properties and hence on applicability, have the composition and impurities present in starting oxides, especially in Fe_2O_3 (1).

The production costs of high purity iron oxides are relatively high, thus the application of low cost Fe_2O_3 would decrease the production costs of high permeability ferrites (2). However, these oxides usually contain a relatively high amount of SiO_2, Na_2O, CaO and chlorine. Among them, make chlorine impurities production of MnZn ferrites more pretending and determine the final properties of high permeability ferrites.

The major amount of chlorine impurities is released during the firing and induces a highly corrosive atmosphere which corrodes the production equipment. However, the rest of chlorine impurities even if present in small concentrations, in sintered samples, degrade the magnetic permeability of MnZn ferrites (3), (4), (5).

The aim of this investigation was to study the influence of small

amount of chlorine on the ferrite microstructure and, consequently, on the magnetic permeability.

EXPERIMENTAL WORK

Oxides of industrial quality were used as starting materials: Mn_2O_3 (98%), ZnO (99%) and two different types of Fe_2O_3 (Table I).

Table I: Some data about chemical composition of two different iron oxides used in our experiments

Fe_2O_3	Fe_2O_3(wt.%)	MnO(wt.%)	SiO_2(wt.%)	Na_2O(wt.%)	Chlorine(wt.%)
(A)	99,1-99,4	0,280	0,016	0,036	0,154
(B)	99,1-99,4	0,007	0,008	0,020	0,080

Standard ceramic procedure was used to prepare samples of MnZn ferrite. Mixtures of oxides were wet homogenized in an attritor 4 hours and afterwards calcined at 900°C, four hours. The calcined powder was wet milled in attritor 3 hours, dried and agglomerated with the addition of 2 wt.% of binder. Torroids with the dimension of: d(o)=20 mm, d(i)=16 mm were pressed at pressure of 0.1 MPa, and presintered at 650°C , at a heating rate of 1°C/min. Samples were sintered in controlled atmosphere at two different temperatures (T_1=1350°C, T_2=1300°C) and three different times (3, 13, 25 hours).

The temperature dependence of initial magnetic permeability (hereon named magnetic permeability) was determined using a test chamber and impedance admittance bridge at 100 kHz. Grain boundaries were examined using TEM, while surfaces of intergranular fracture were analysed with AES.

RESULTS AND DISCUSSION

In order to study the influence of chlorine impurities on the microstructure development and, consequently, on the magnetic permeability of MnZn ferrites, the sintering temperature and time during the preparation of ferrites were varied.

The magnetic permeability vs. temperature of samples, sintered at 1350^{o}C, is shown in Figs. 1, 2. Magnetic permeability of samples B, prepared from iron oxide containing a lower amount of impurities, show a pronounced peak in magnetic permeability, accompanied by an exaggerated grain growth (large grains with entrapped porosity, Fig.1). Contrary, samples A prepared from more contaminated iron oxyde exhibit predominantly a normal microstructure of approximately equal grain size and intergranular porosity (Fig.2).

Comparing the microstructures of samples A and B, sintered at 1350 deg.C, one can see that samples prepared from purer iron oxide (B) are more prone to the exaggergated grain growth. In these samples a microstructure with overestimated grain size and entrapped porosity is readily formed in comparison with more contaminated samples, where such microstructure was rarely observed. One is justified to assume that at least one of the impurities present in both samples A and B, effectively decreases the grain boundary mobility and, hence, inhibits the formation of giant grains with entrapped pores. Samples B, which are more prone to the formation of giant grains with entrapped porosity, contain a lower amount of impurities such as SiO_2 and Na_2O, which are believed to form a liquid phase during sintering and thus promote the exaggerated grain growth (6).

Since the amount of chlorine impurities in samples A is relatively high, and since particularly these samples exhibit a normal microstructure with intergranular porosity, it was

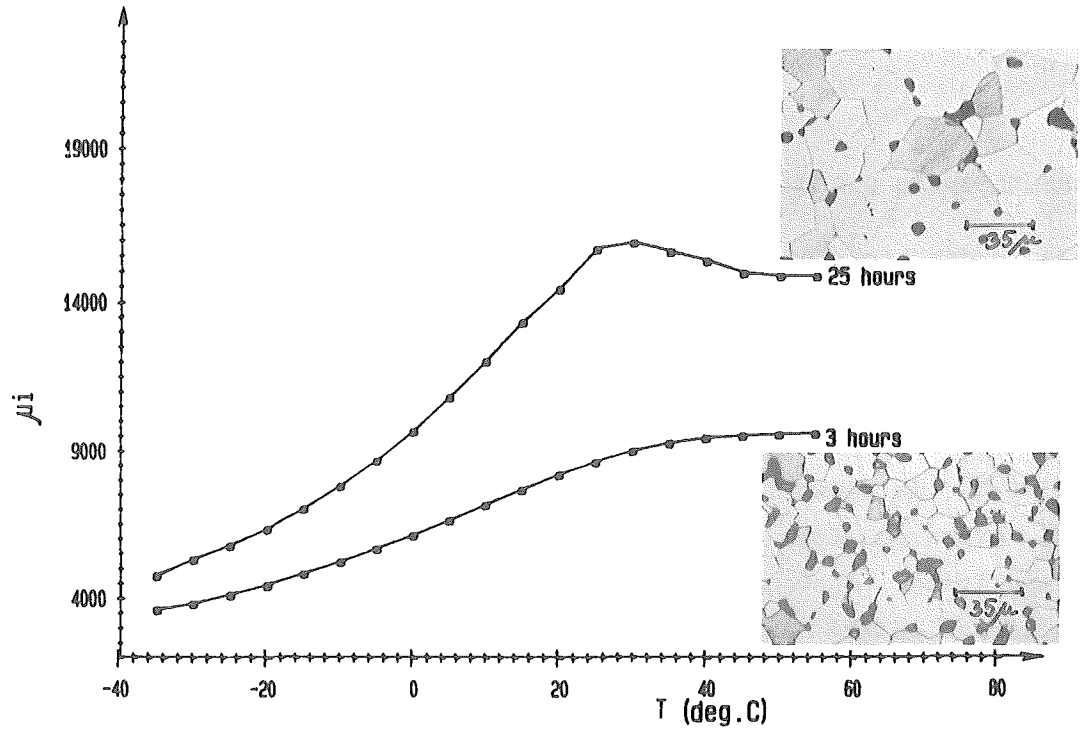

Fig.1 : Typical temperature dependence of magnetic permeability for samples with Fe_2O_3 (A), sintered at 1350°C, 3 and 25 hours

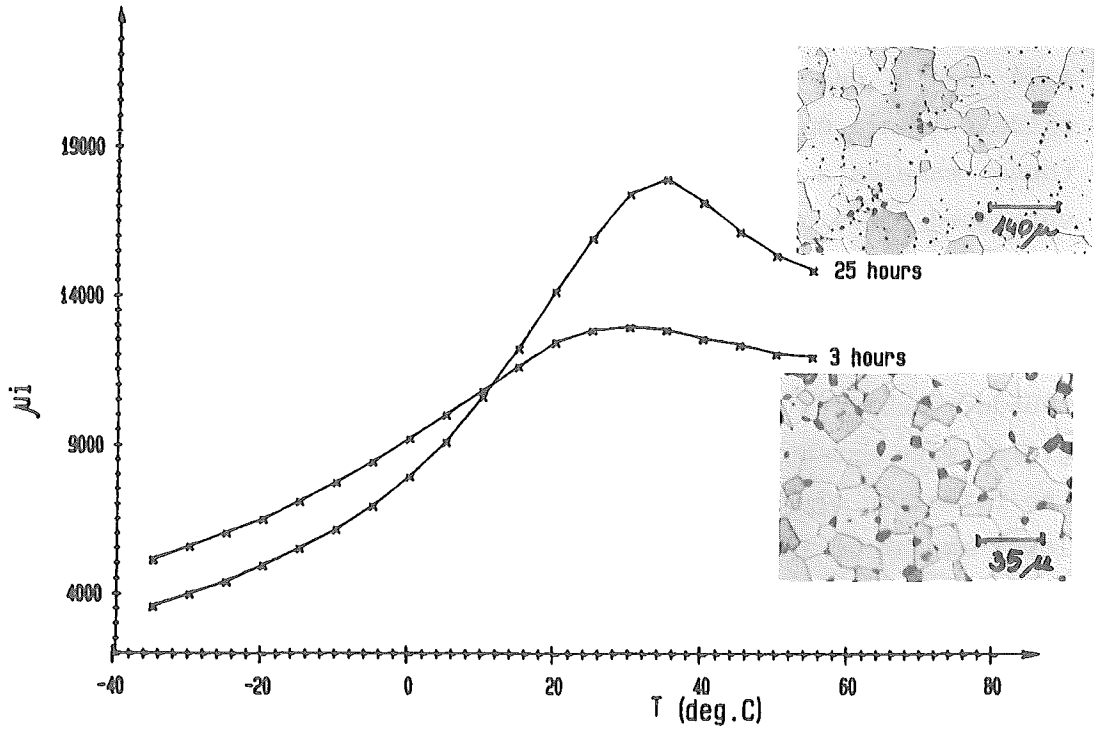

Fig.2 : Typical temperature dependence of magnetic permeability for samples with Fe_2O_3 (B), sintered at 1350°C, 3 and 25 hours.

assumed that the chlorine impurities play a predominant role during the microstructure developement of studied ferrites. The chemical analysis indicate that after 3 hours of sintering at 1350^{o}C chlorine is still retained in sintered samples (prepared of Fe_2O_3 (A)). The concentration determined was 0.006 wt.%. In order to estimate the role of chlorine during the development of microstructure, samples A were subjected to TEM and AES. Figs.3 a,b show TEM images of the grain boundaries of ferrite containing 0,006 wt.% chlorine.

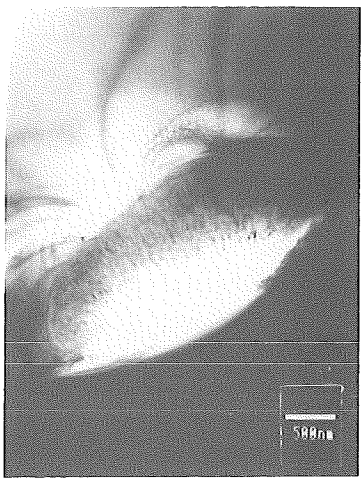

a)

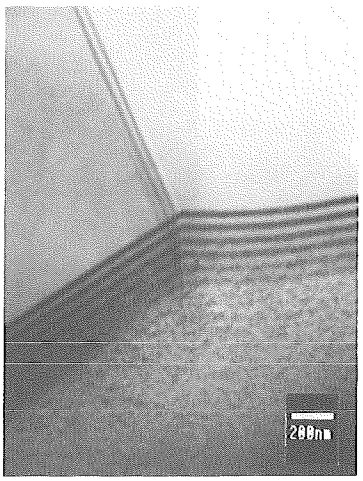

b)

Fig.3 : TEM images of grain boundaries of ferrite sintered at 1350^{o}C, 3 hours.

The review of grain boundaries indicates that:
- a SiO_2-rich liquid phase was found on the grain boundaries and was located discontinuously along them, as shown in Fig.3a.
- the rest of grain boundaries were found to be free from second phases as seen in Fig.3b, which shows a triple grain junction.

In order to get some more evidence concerning the composition of the grain boundary, the fractured surface of sample A (T sintering = 1300^{o}C, time = 3 hours) was characterized with the use of AES. Only areas showing the intergranular fracture were analysed.

Figs.4 a, b, c show typical Auger electron images of the fractured surface of sample A.

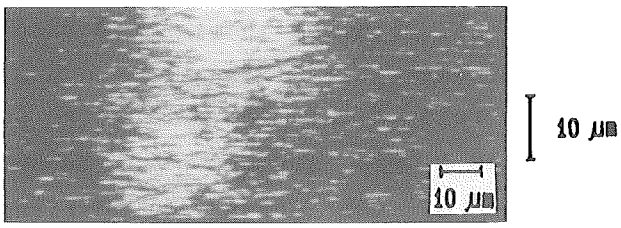

a) Image of chlorine

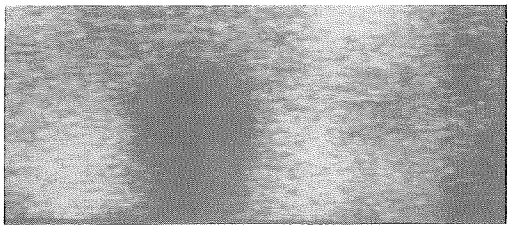

b) Image of oxygen

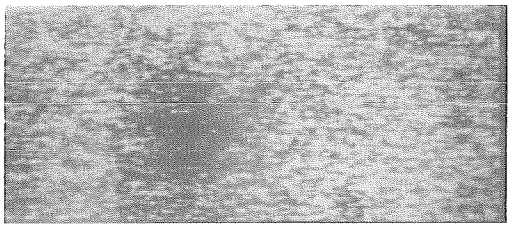

c) Image of iron

Fig.4 : Typical Auger electron images of (the same area) fractured surface of sample with Fe_2O_3 (A) sintered at 1300°C, 3 hours.

This analysis indicates a good evidence about the existence of chlorine layer on the grain boundary surface of sample analysed. Further it was found that even a very short time of treating the fractured surface of sample with an excitating electron beam ($E_{(p)}$ = 3keV), completely removes the chlorine layer. Fig.5 shows two spectra of Auger electrons, before and after treating the surface with electron beam.This indicates a

presence of a very thin layer, composed of chlorine on the grain boundaries.

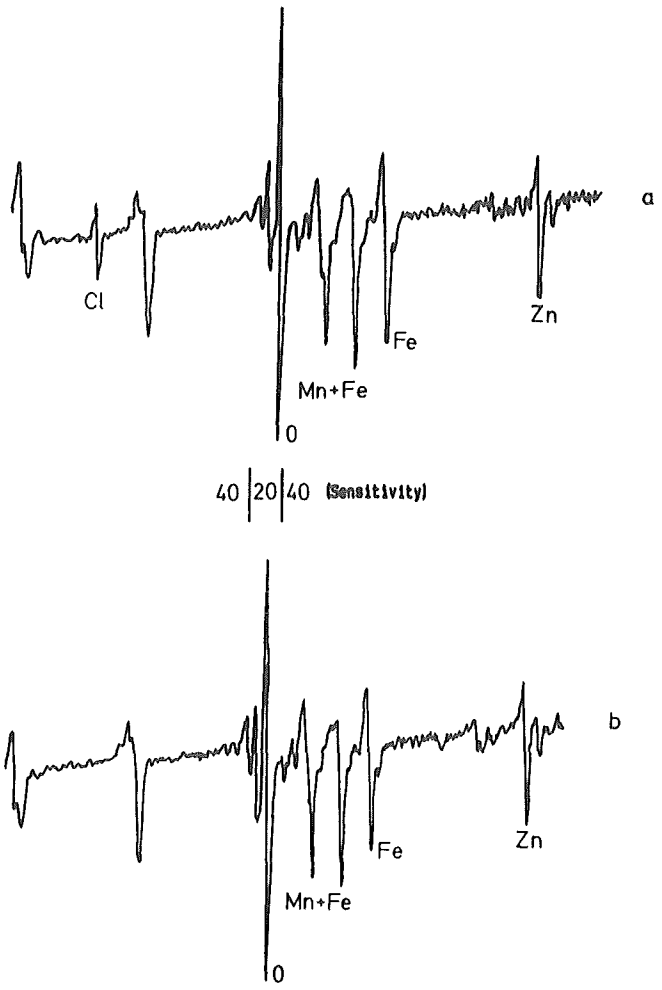

Fig.5 : AES spectra of fractured surface of sample with Fe_2O_3 (A) sintered 3 hours at 1300°C:

a) spectra with chlorine peak

b) spectra of the same area of surface as in "a" after 10 minutes of treating with an excitating electron beam

The study of the grain boundary chemistry of ferrite grains applying AES reveals that a very thin layer of chlorine can be detected on the grain boundary surface of samples studied, regardless on the thermal procedure undertaken during the preparation of the samples A.

CONCLUSIONS

On the basis of the results presented above, it can be concluded that a very thin layer of chlorine which encloses the ferrite grains in sample A during sintering, effectively retards the grain boundary mobility, and retards the promotion of grains with overestimated size and entrapped porosity, which gives rise to the formation of the normal microstructure.
In other words, the chlorine impurities compensate the influence of a higher amount of impurities Na_2O and SiO_2, present in samples prepared with Fe_2O_3 (A), making them less prone to the exaggergated grain growth, even at higher temperatures.

LITERATURE

(1) GALLAGHER,D.W.JOHNSON Jr.,F.SCHREY, Am.Ceram.Bul., vol.55, No 6, (589-593), 1976

(2) E.ROESS, Adv.in Cer., vol.15, 4th int.conf.on ferrites, part 1, (39-49), 1985

(3) B.B.GHATE, Adv.in Cer., vol.1, (477-493), 1980

(4) K.SUGANUMA,T.OBI,G.FURUSHO, Adv.in Cer., vol.15, (81-85), 1985

(5) B.B.GHATE,R.J.HOLMES,C.E.PASS, Am.Ceram.Bul., vol. 60, (484-490), 1981

(6) A.D.GILES,F.F.WESTENDORP, J.de Phisique, Colloque C-1, supplement au No 4, Tome 38, Avril 1977, page C-1 317-320

Electron Conducting Ceramics as Sensor Material for Noise Thermometry

H. Häußer*, D. von Mallinckrodt**, H. Brixy***

Summary

The ohmic resistance of $LaCrO_3$ is diminished by substituting Sr, Ca or Mg for La and becomes nearly independent of temperature above 600°C. While temperature independence is advantageous for the application in question, the resistance value is too low. The resistance can be enhanced through a second, electrically nonconducting phase ($MgAl_2O_4$). The volume fraction of spinel was varied between 10% and 90%, and the resultant effect on resistance was plotted as a temperature function.

Introduction

Noise in an ohmic resistor, caused by statistical thermal agitation of electrons, is described on the basis of the Nyquist theory; the differential mean square noise voltage is a direct function of the absolute temperature and resistance value:

$$dV^2 = 4kT\, R_e\, \{Z(f)\}\, df \qquad (1)$$

with V as the voltage, k as Boltzmann's constant, T the absolute temperatur, RE {Z(f)} the real part of impedance Z, and f the frequency. Since the electrical resistance is determinable, a temperature sensor operating on a noise-level basis can be used to measure the absolute temperature.

* Institut für Gesteinshüttenkunde, RWTH Aachen, Mauerstr. 5, 5100 Aachen
** Friedrichsfeld GmbH, 6800 Mannheim 71
*** Institut für Reaktorentwicklung; KFA-Jülich GmbH, 5170 Jülich

Unlike thermocouples, where material changes can lead to faulty temperature indications, the material variable of the sensor of a noise thermometer, i.e. the resistance R. is always ascertainable and, hence, does not affect the accuracy of the temperature reading. The measuring range extends from 1 k to 2500 k with a potential accuracy of 0.1 %. In principle, any electrical resistor could serve as a temperature sensor. For practical reasons, however, the resistance should be situated somewhere between 1 Ohm and 50 Ohm, and the resistor should have as low a temperature coefficient as possible, white noise in the frequency range of interest, high thermal stability and high chemical resistance. The applications for noise thermometers are cases in which very accurate temperature readings are required and/or in which thermocouples cannot be used due to the possibility of thermal-stress drift sensors have been made of thin wires consisting of high-melting metals such as Pt, Rh, W or Ta.

Their biggest drawback is a mostly short service life. Ceramic sensors offer several advantages over metal sensors: greater freedom of material selection, higher chemical stability, maximum-temperature serviceability and a more robust and compact type of construction.

What was needed was a ceramic material that would satisfy all metrological requirements and surpass prior-art sensors with regard to thermal stability, temperature range and robustness. Of all the various materials that were investigated, especially $LaCrO_3$ displayed suitable eletrical properties; its resistance drops to a useful level at about 900°C, and the temperature coefficient is relatively small. The service-temperature range peaks at about 1800°C.

The resistance can be further lowered through partial substitution of Sr for La, which yields a simultaneous drop in the resistor's temperature coefficient (see figs. 1 and 2). Substituting Ca or Mg for Sr produces very similar resistance behavior.

$LaCrO_3$ is a semiconductor. Thermal excitation makes the polyvalent chromium ion change its valence.

This produces bivalent and tetravalent, or even sexavalent, chromium ions. Doping with Sr, Ca or Mg provides a quasi substitute for thermal excitation, i.e. part of the chromium ions are forced into a state of binary or quaternary valence, thus creating free charge carriers.

$$La_{1-x}\ Sr_x(Cr^{3+}_{1-x}\ Cr^{4+}_x)\ O_3 \qquad (2)$$

Thusly doped $LaCrO_3$ ceramics display a favourably low thermal coefficient in combination with very low resistance. In order to raise the resistance, i.e. to ensure proper electrical accommodation, a second, electrically nonconducting phase was built into the $LaCrO_3$.

The system $(LaCrO_3)_{1-x}\ (MgAl_2O_4)_x$ with x denoting the volume fraction, was investigated. Figures 3, 4 and 5 shows the resistance curves obtained for various volume fractions of spinel (10% - 90%). Unfortunately, not only the resistance was increased, but also the temperature coefficient, which became unsuitibly high. The resistance curves of specimen 8 and 9 approximate that of a thermistor, while specimen 5 appears to be more suitable.

Figures 6, 7 and 8 are scanning eletron micrographse of the investigated two-phase ceramics containing 20%, 40% and 70% spinel, respectively.

An alternative way to raise the resistance is to substitute Al for Cr. Replacing some of the chromium ions with trivalent aluminum ions forces the resistance up by reducting the number of polyvalent chromium ions, so that the number of excitable chromium ions automatically decreases.

$$LaAl_x Cr^{3+}_{1-x-2y} (Cr^{2+}_y Cr^{4+}_y) O_3 \qquad (3)$$

Where x is the part of substitution and y a funktion of the temperature. The above considerations were, however, only confirmed for alumina contents of 20 mol% and 40 mol%, and then only for temperatures exceeding 800°C (see fig. 9).

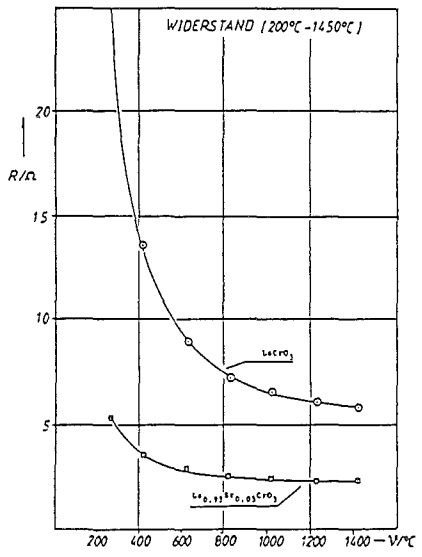

Fig.1 Resistance of $LaCrO_3$ and Sr-doped $LaCrO_3$ as a function of temperature

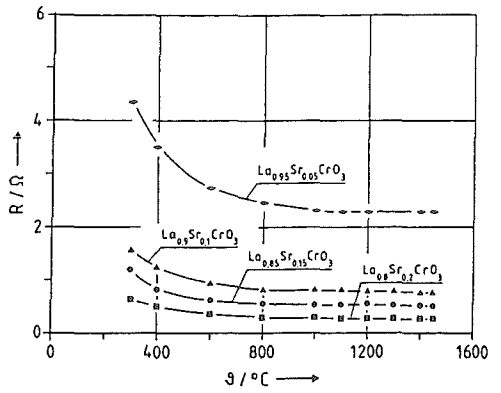

Fig.2 Resistance curves obtained for $LaCrO_3$ doped with various amounts of Sr

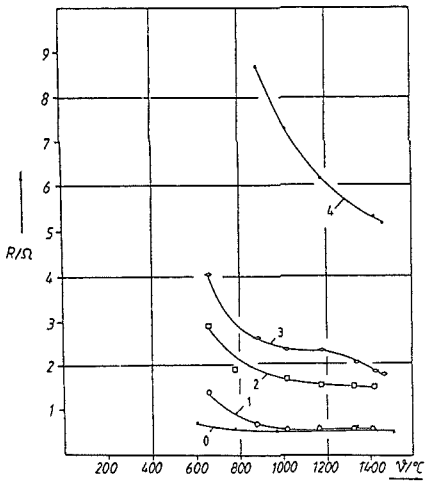

Fig.3,4 and 5 resistance curves obtained for the system $(La_{0.85}Sr_{0.15}Cr\ O_3)_{1-x}\ (MgAl_2O_4)_x$ with various volume fractions of spinel (specimen 0: none; specimen 1:10%, specimen 2:20%, etc.)

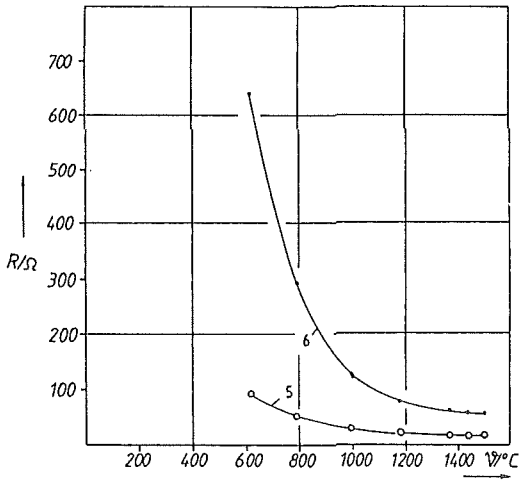

Fig.4

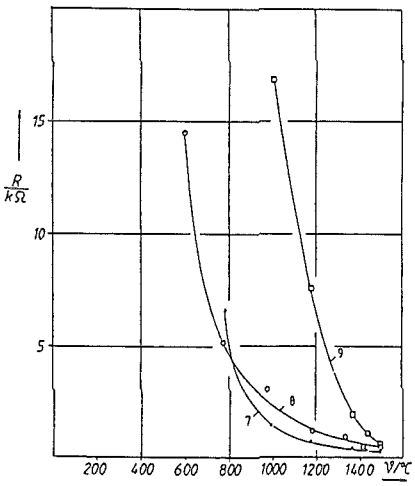

Fig.5

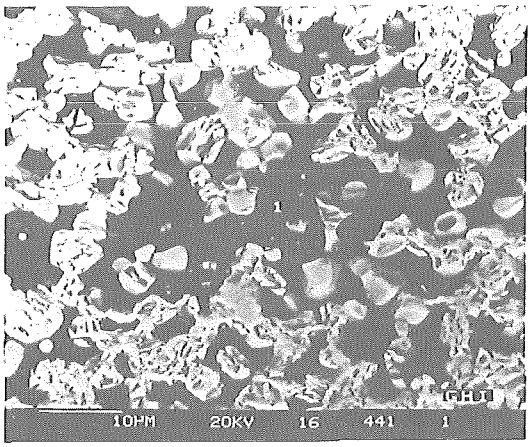

Fig.6 Phase distribution of specimen 2 (20% spinel)

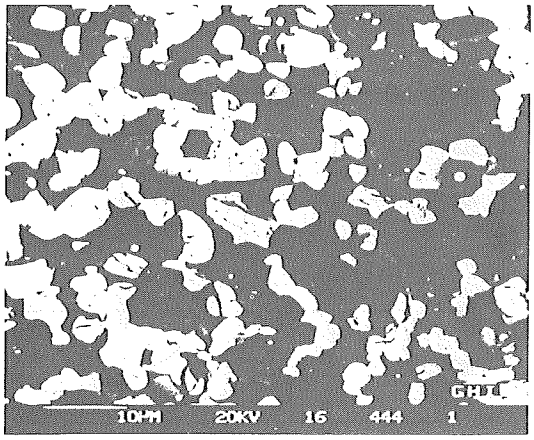

Figure 7:

Phase distribution of specimen 4 (40% spinel)

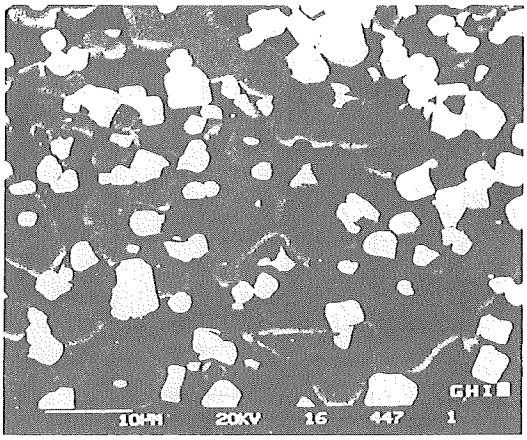

Figure 8:

Phase distribution of specimen 7 (70% spinel)

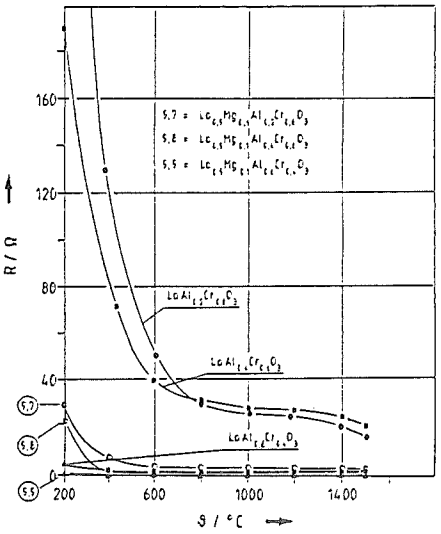

Fig.9 Temperature-dependent resistance of the systems $La(Al_xCr_{1-x})O_3$ and $La_{0.9}Mg_{0.9}(Al_xCr_{1-x})O_3$, with x= 0.2, 0.4 and 0.6, respectively

References

Anderson R L, Lyons J D, Kollie T G, Christie W H, Eby R, 1982 in *Temperature, Its Measurement and Control in Science and Industry* volume 5 Ed. J P Schooley (New York: American Institute of Physics) pp 977-1077

Anthony A M, 1969 in *High Temperature Technology* (Sevenoaks, Kent: Butterworth) pp 214-233

Bansal K P, Kumari S, Das B K, Jain G C, 1981 *Trans. J. Brit. Ceram. Soc.* 80 215-219

Baumard J F, Tani E, 1977a *Phys. Status Sol. A* 39 373-382

Baumard J F, Tani E, 1977b *J. Chem. Phys.* 67 857-860

Brixy H, 1972 *Die Rauschthermometrie als Temperaturmessmethode in Kernreaktoren* Jül-885-RG Jülich, FRG: Kernforschungsanlage)

Brixy H, Hecker R, Rittinghaus K F, 1975 *Chemie-Technik* 4 113-118

Brixy H, Oehmen J, Rittinghaus K F, Wegener H P, 1978 *Technisches Messen* atm 10 351-354

Brixy H, Hecker R, Rittinghaus K F, 1982 in *Temperature, Its Measurement and Control in Science and Industry* volume 5 Ed. J P Schooley (New York: American Institute of Physics) pp 1225-1237

Brixy H, Mallinckrodt D von, Lynen A, 1983 *High Temp.-High Pressures* 15 139-146

Fenton A W, 1969 *Proc. IEE* 116 1277-1280

Groupp L, Harlan U, Anderson R L, 1976 *J. Am. Ceram. Soc.* 59 449-450

Howng W Y, Thorn R J, 1980 *J. Phys. Chem. Solids* 41 75-81

Johnson G H, 1953 *J. Am. Ceram. Soc.* 36 97

Johnson J B, 1928 *Phys. Rev.* 32 97-101

Khattak C P, Cox D E, 1977 *Mat. Res. Bull.* 12 463-471

Matsumoto K, Sata T, 1981a *Yogyo Kyokai Shi* 89(2) 68-73

Matsumoto K, Sata T, 1981b *Yogyo Kyokai Shi* 89(3) 124-129

Meadowcroft D B, Wimmer J M, 1979 *J. Am. Ceram. Soc.* 58 610-615

Micheli A L, 1984 *Am. Ceram. Soc. Bull.* 63 694-698

Morgan P E D, 1977 *Am. Ceram. Soc. Bull.* 56 432

Nyquist H, 1928 *Phys. Rev.* 32 110-116

Tien T Y, Stadler H L, Gibbon E F, Zacmanidis P J, 1975 *Am. Ceram. Soc. Bull.* 54 280-282

Vu Tien, Cabannes L F, Anthony A M, 1975 *Ceramurgia International* 1 134-135

MICROSTRUCTURE AND PHASE DEVELOPMENT IN MULTICOMPONENT ZnO BASED VARISTOR CERAMICS

O.Milosevič, P.Kostič, Lj.Karanovič, V.Petrovič and D.Uskokovič

Institute of Technical Sciences of the Serbian Academy of Sciences and Arts, Belgrade, Yugoslavia

ABSTRACT

The application of varistors for protection of apparatus both in electronics and energetic understands a very precise control of quality when a high degree of non-linearity is concerned, as well as a high conductivity, low leakage currents and a negligible degree of degradation. As electrical properties of such multi-component ceramics are distinctly correlated by the main structure it was established a general concept of both the phase and microstructure development in order to make a complete design of the shape of current-voltage characteristics.

1. INTRODUCTION

Metal-oxide varistors, obtained by the sintering of zinc oxide with small additions of Bi_2O_3 and other metal oxides, represent a new family of electronic ceramics with high nonlinear characteristics of the current-voltage relationship /1/.

According to the mechanisms which dictate the conduction process, the current-voltage characteristic is divided into four distinct regions as denoted at Fig.1.

At extremely low voltages (region I), a varistor shows the Ohmic behaviour. Till the moment of reaching the stationary conditions with the voltage values of 1/20 U_c approximately, the varistor exhibits non-ohmic properties. Within this region marked as a prebreakdown region (II), the current-voltage characteristic shows the strong temperature dependence which can be well described by activation energy value. Regarding from the point of designing, this fact proved to be of outstanding importance as it points to the presence of mobile charged carriers which destruct the shape of current-voltage characteristics. This influences on increment in the leakage current i.e. on a degradation property of a varistor. Thus, this fiels is closely connected with the zinc oxide grains and is a function of the charged carriers concentration in the grains which can be impurity ions, native defects of zinc oxide as well as ions of some substitutional oxides that are being used in technology of ZnO varistors.

On the other hand, the conduction mechanisms in this field put very precise

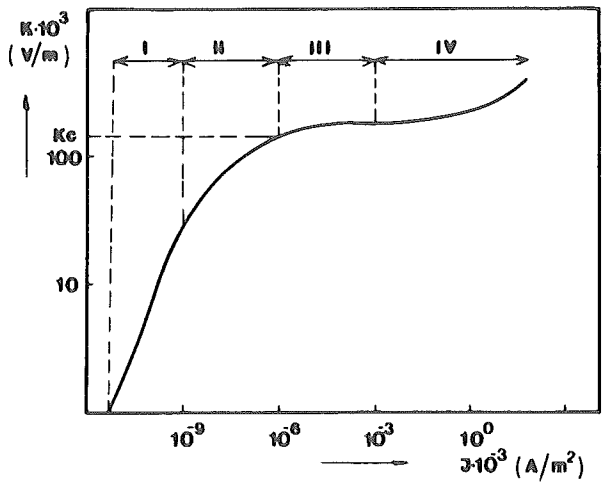

Fig. 1. Scheme of a current-voltage characteristic of ZnO varistor.
I - Ohmic region; II - Low current prebreakdown region;
III - The breakdown region; IV - High current linear region

requirements concerning conductivity of intergranular layer. The very fact that the intergranular phase contains Bi_2O_3 known by its polymorphic forms, points to the necessity of controlling the phase composition of intergranular layer. Having this in mind, as well as a demand for obtainment of varistor ceramic for protection of apparatus both in electronics and energetic, the aim of this paper is to present a concept of ZnO varistors production concerned microstructure and phase development and thus contributes to a more complete recognition and understanding of some basic processes concerning formation of non-linear varistor ceramics.

2. EXPERIMENTAL

All the experiments were performed in the multicomponent varistor ceramics containing ZnO as the main component /2/. A reagent grade of ZnO, Bi_2O_3, Sb_2O_3, MnO_2, Co_3O_4, NiO, SnO_2, Al_2O_3, K_2O and Cr_2O_3 powders were mixed by wet ball milling. After being dried and calcined at 1273 K, each mixture was pressed into a disc diameter of $8 \cdot 10^{-3}$ m and $3.4 \cdot 10^{-2}$ m. The samples were formed either by uniaxial or by a cold isostatical pressing to about 60% of their theoretical densities. The pellets were then sintered within the temperature interval ranging from 1273-1673 K for 0-240 m under the controlled heating and cooling rates. The obtained ceramics were polished planparallely and coated by silver electrodes and insulating layer.

The grain sizes of ZnO matrix were estimated by means of the light and electron microscope.

The phase analysis was carried out by X-ray diffractometer and energy dispersive X-ray analyser (EDAX).

3. RESULTS AND DISCUSSION

3.1. Microstructure

The microstructure of investigated varistor systems based on zinc oxides with Bi_2O_3, Sb_2O_3, CoO, MnO_2, Cr_2O_3 and other components is formed during liquid phase reactive sintering.

The present investigations based on both the light and scanning microscopy showed that the main constituents of microstructure are, in general, independent from the varying composition within the framework of investigated system and that the same can be generalized in the following way:

- the grains of ZnO present a predominating ceramic phase and consists of semi-conductive ZnO crystals the lattice parameters of a = $3.24951 \cdot 10^{-10}$ m, c = $5.20684 \cdot 10^{-10}$ m and the size of which ranges between 20.0 - 30.0 · 10^{-6} m depending on the very purpose of a varistor and the sintering conditions. The grains are of the polygonal shape and the twinning boundaries are noticed along them;

- spinel particles as inclusions, size of $1.0\text{-}3.0 \cdot 10^{-6}$ m, and of a lattice parameters in the range of $8.5466\text{-}8.5779 \cdot 10^{-10}$ m are localized along grain boundaries or in multiple grain junctions between several ZnO grains. Investigation results obtained by techniques of both light and scanning electron microscopy confirmed a high density of spinel particles discontinually distributed along grain boundaries, being not in equilibrium configuration and showing a considerable surface curvature. This indicates a possible pinning of spinel particles along grain boundaries during sintering what, from the point of a total surface energy of a system, prevents a further boundary migration. Thus, a spinel phase presents an inhibitor of a grain growth i.e. it hinders a discontinual grain growth and influences on a homogeneous distribution of microstructure;

- the areas being within grain boundaries separate the neighbouring ZnO grains and correspond to an intergranular phase (Fig.2). Crystal phases based on Bi_2O_3 were identified in its composition and in regard to its nature and origin, they can influence on the process of non-linear conduction. It was established by method of X-ray diffraction that sintered varistor ceramics contain a pyrochlore phase lattice parameters in the range $10.109\text{-}10.132 \cdot 10^{-10}$ m and $\delta\text{-}Bi_2O_3$ with lattice parameter a = $5.445 \cdot 10^{-10}$ m. Subsequent heat treatment up to 1273 K causes formation $\gamma\text{-}Bi_2O_3$ lattice parameter of a = $10.132 \cdot 10^{-10}$ m.

Starting from the basic composition of crystal phases /3/ which are the constituents of varistor ceramics, and taking, on the basis of the same, the Sb/Zn /2/ concentration ratio as x-axis, being the quantitative index of grain, spinel and intergranular phase then it is obvious from Fig.3 that the basic components are for grains-zinc oxide, spinel-zinc and antimony, while the three basic components of the mentioned phases (bismuth, zinc and antimony) are distributed in an intergranular phase.

The concentration profiles of additives are shown in Fig.4, from which it is obvious that a spinel phase is mainly dopped by additives as the maxima of concentration parabolas correspond to this phase.

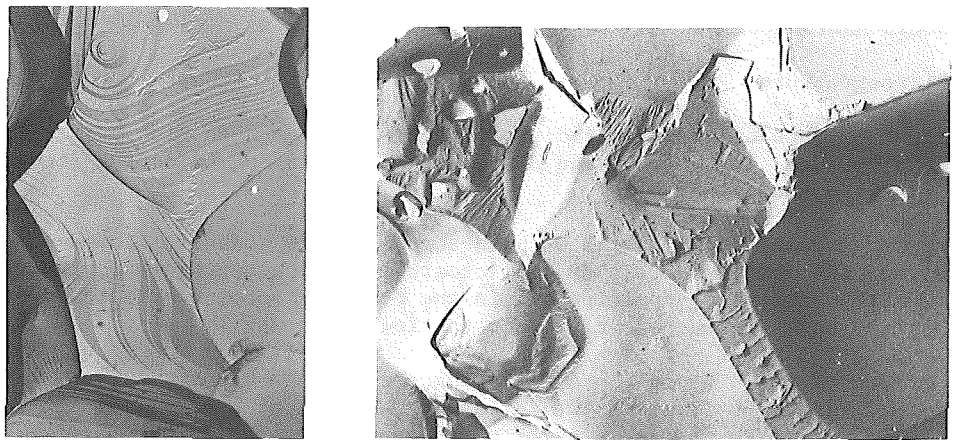

(a) (b)

Fig.2. Electron micrographs of fracture sections of ZnO based ceramic sintered at 1473 K (magnification 6000 (a) and 13000 (b)).

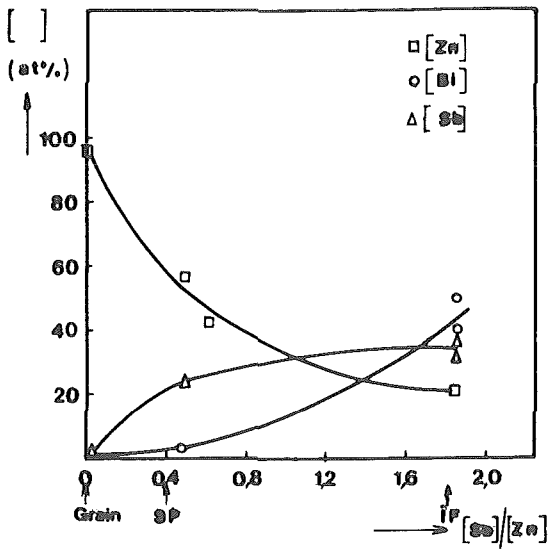

Fig.3. The main components of grain, spinel and intergranular phase.

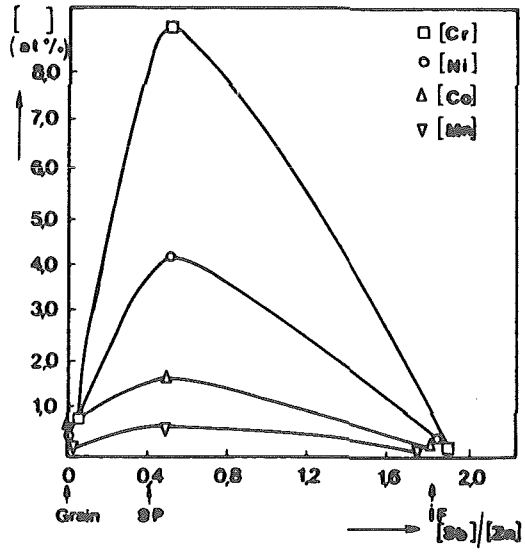

Fig.4. Concentration profiles of additives in investigated varistor systems.

3.2. Phase development

In multicomponent systems based on zinc oxide, the development of phases i.e. microstructure is performed through several parallel processes which are mutually interfered. In this connection we can accept that the sintering

process is a dominating factor in ZnO phase formation, while formation of spinel phases (SP) and that of pyrochlore (PYR) result from solid and liquid phases reaction. Both melting, evaporation and crystallization of Bi_2O_3 phase and their polymorphic modifications condition formation of intergranular layer, while thermally activated diffusion motion of intrinsic defects of zinc oxide and cations of additive oxides influence on formation of solid solutions on the basis of the main constituents. A hypothetical scheme of phases development derived on the basis of numerous results and analyses of structure of multicomponent varistor systems based on ZnO /2/ containing the following additives (mol %): Bi_2O_3 (0.5-2.0), Sb_2O_3 (0.5-2.0), CoO (0.5-1.0), MnO_2 (0.5-1.0), SnO_2 (0.0-1.0), Al_2O_3 (0.0-0.4), NiO (0.0-1.0), Cr_2O_3(0.0-1.0), K_2O (0.0-0.5), is given in Fig.5.

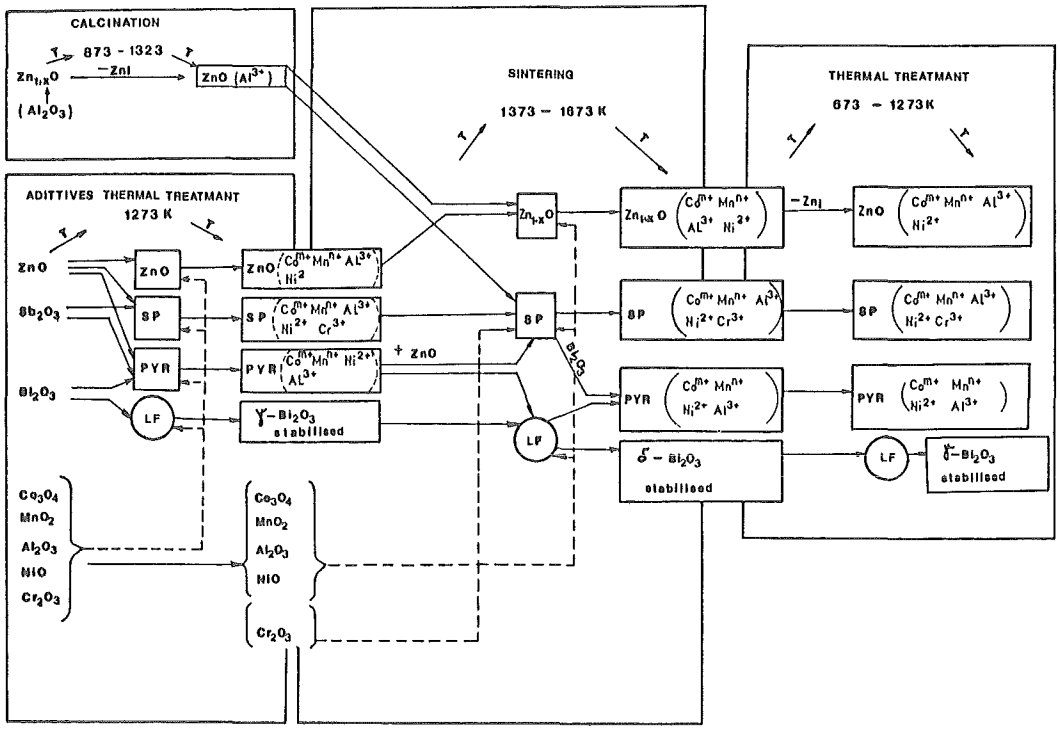

Fig.5. Hypothetical scheme of varistor ceramic phases development.

3.3. Control of a phase composition of an intergranular layer

As the non-linearity characteristic is extremely sensitive to a very small variation of conductivity in prebreakdown region, the requirements appearing during production of varistor ceramic refer to the realization of high insulating intergranular layer which prevents a free ions migration under the influence of applied voltage thus influencing on the height of the formed barrier voltage and possibility of a varistor to degrade.

Having in mind the fact that phase transformations of Bi_2O_3, which mainly form the intergranular phase, are followed by a momentary change in

conductivity, when its high temperature polymorphs show a high ionic conductivity, a requirement for obtaining a high quality varistors ceramic understands a controlled synthesis of intergranular layer's phases.

A polymorphic shape of γ-Bi_2O_3 represents a phase of high specific resistivity and, at that, its stable shape shows the resistivity of $5 \cdot 10^{11}$ Ωm and has a dielectric constant $\varepsilon = 56$ /4, 5/. Owing to the choice of the way of cooling, and either the presence of impurities we can have influence on the retaining of this high-resistant γ-modification to a room temperature what makes the realization of a required shape of current-voltage characteristic of ZnO varistor, possible. However, due to its very low content in ceramic (< 10%) the identification of this phase was less possible and consequently the results obtained were not quite reliable.

As the sintered varistor ceramics of investigated systems contain a δ-Bi_2O_3/2/ phase within intergranular region, it is possible to influence on the very control of its phase composition in sense of stabilizing the γ-phase being of less ionic conductivity than δ-Bi_2O_3 phase, by the corresponding heat treatment.

A schematic presentation of transformation of Bi_2O_3 phase within intergranular layer, the result of which was the obtainment and stabilization of a high-resistant γ-shape, is given in Fig.6. It was formed on the basis of obtained results /2/ and literature data for obtaining of γ- and δ-polymorphous modification /6, 7/.

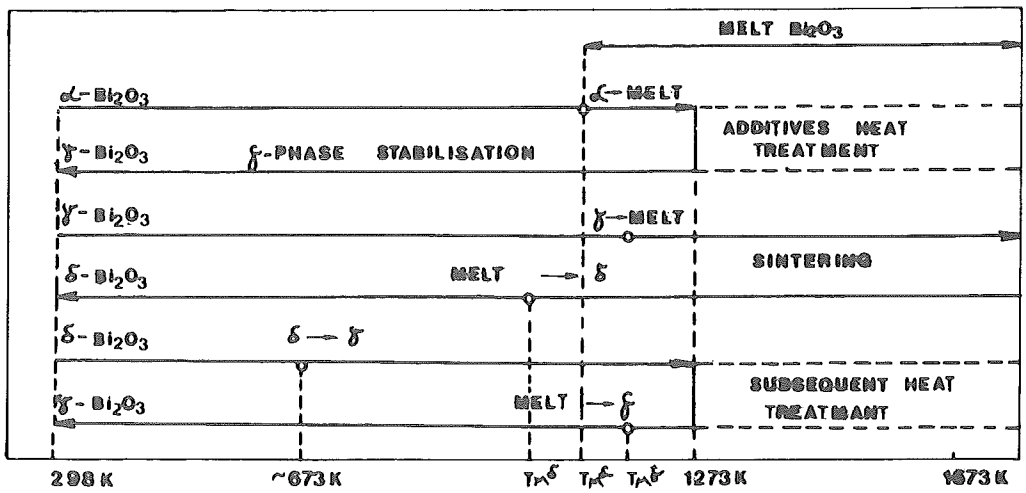

Fig.6. A derived hypothetic scheme of polymorphous transitions of Bi_2O_3 during the whole procedure of obtaining ZnO varistors. T_M^{α}, T_M^{δ} and T_M^{γ} are the melting temperatures of particular phases. According to literature data for pure phases, they are 1093, 1023 and 1173 K /6, 7/, respectively. These points represent only the indices of the particular phase transformations in context of multicomponent varistors ceramic.

When we insert γ-Bi_2O_3 phase formed during the heat treatment of additives into the initial composition of the varistors ceramic /8/ we shall notice

that during sintering this phase will melt. After the cooling of this melt with the adequate stabilizing effect of additives, δ-form will appear.

The fact that a metastable δ-form is formed more easily from the melt than the γ-form can be explained by the extremely similar structure existing between δ-form and the melt, as well as by a great difference in the structure of γ-forms and the melt. Apart from this, the appropriate reduction conditions, established the ZnO grain boundaries due to evaporation of Bi_2O_3 during sintering, stimulate the stabilization of δ-forms regarding its known defective structure with oxygen vacancies /9/.

After re-heating the ceramic during subsequent heat treatment at temperatures of 673 K approximately, a polymorph transfer from δ into γ- form /6, 7/ took place, what can be connected with the appearance of the maximum amplitude of the EPR signal g = 4.3 and the minimum degree of deformation /10/ with the samples of the system that was thermally treated at the same temperature. This phase has been retained, due to the corresponding stabilizing influence of additives, to the room temperature.

As is the case with δ-Bi_2O_3 phase, the effect of atmosphere is of extremely great importance for the formation of γ-phase. Enrichment of atmosphere by oxygen during a subsequent heat treatment provides for the necessary conditions for both its formation and stabilization. The action of oxydation atmosphere stimulates this transformation regarding a defective structure of γ-Bi_2O_3 phase containing the excess of oxygen and has the form of Bi_2O_{3+x}/11/. This fact is also important from the point of the conductivity mechanism in varistor ceramic as it considers the γ-Bi_2O_3 phase to be a supplyer of oxygen ions along ZnO grain boundary. Regarding to literature data, the components such as are Sb_2O_3, CoO, Cr_2O_3 and SiO_2 behave as stabilizators of the mentioned phase. The results of electrical characteristics of varistors that were thermally treated within temperature interval 773-1273 K in atmosphere of air and oxygen, given elsewhere /8/, strongly support the above statement. The appropriate increment in non-linearity in the low current region and the breakdown field is the result, as we have already noticed /8, 12/, of a reduced concentration of interstitial Zn_i ions through their diffusion to grain boundary, on the one hand and of a phase transformation of intergranular δ-Bi_2O_3 phase existing in a sintered ceramic, in γ-Bi_2O_3 and its stability to the room temperature, on the other hand. A certain evidence on the influence of stability of γ-Bi_2O_3 phase on reduction of a leakage current we can also find in results obtained by A.Iga /13/ and M.Trontelj /14/.

4. CONCLUSION

The present investigations of multicomponent varistor ceramics based on ZnO shows that the main constituents of microstructure (ZnO grains, spinel and intergranular phase) are in general independent from the varying composition within the framework of investigated systems. Based on different experimental methods, a hypothetical scheme of microstructure and phase development in such multicomponent systems was derived.

Starting from a current-voltage characteristic and a mechanism of a potential barrier formation, as well as from a microstructure formation mechanisms, it was established that the requirements for obtainment of highly resistant intergranular layer can be reached through the control of polymorphous

transformations of Bi_2O_3 within an intergranular phase and by intentional synthesis and stabilization of a cubic γ-shape.

ACKNOWLEDGEMENT

The investigations presented in this paper were financially supported by the Republic Committee for the Science of Serbia through the project "Physical chemistry of condensated systems", as well as by the Committee for the Science in Belgrade and MINEL through the project "Investigation and development of non-linear resistors based on ZnO of highly non-linear characteristics and stability". The authors aknowledge their indebtedness to the mentioned institutions.

LITERATURE

1. M.Matsuoka, "Nonohmic properties of zinc oxide ceramics", Jpn.J.Appl. Phys., 10 (16) (1971) 736.
2. O.Milosevič, "The change of crystal phases and the grain growth during the final sintering stage of zinc oxide varistors", M.Sc.Thesis, University in Belgrade, 1986.
3. M.Inada, "Crystal phases of nonohmic zinc oxide ceramics", Jpn.J.Appl. Phys., 17 (1978) 1.
4. R.E.Aldrich, S.L.Hou and M.L.Harvill, "Electrical and optical properties of $Bi_{12}SiO_{20}$", J.Appl.Phys., 42 (1971) 493.
5. S.L.Hou and D.S.Oliver, "Pockels readout optical memory using $Bi_{12}SiO_{20}$", Appl.Phys.Lett., 18 (1971) 325.
6. S.Ito, T.Kokubo and M.Tashiro, "Formation of metastable δ-form of $6Bi_2O_3 \cdot SiO_2$ crystal from its melt", Bull.Inst.Chem.Res.Kyoto Univ., 55 (1977) 447.
7. S.Ito, T.Kokubo and M.Tashiro, "Transformation of metastable δ-form of $6Bi_2O_3 \cdot SiO_2$ and its melt into stable γ-form induced by mechanical tapping", Bull.Inst.Chem.Res.Kyoto Univ., 55 (1977) 457.
8. O.Milosevič, P.Kostič and D.Uskokovič, "Essential problems occuring in obtainment of ZnO varistors connected with the correlation between current-voltage characteristics and structures", to be published.
9. J.W.Medernach and R.L.Snyder, "Powder diffraction patterns and structures of the bismuth oxides", J.Am.Ceram.Soc., 61 (1978) 494.
10. M.V.Vlasova, N.G.Kakazey, P.Kostič, O.Milosevič and D.Uskokovič, "EPR study of the influence of defect structure on electrical properties of ZnO varistors", J.Mat.Sci., 20 (1986) 1660.
11. L.P.Fomcenkov, A.A.Majer and N.A.Graceva, "Polimorfizm okisi vizmuta", Neorganiceskie materiali, 10 (1974) 2020.
12. O.Milosevič, P.Kostič and D.Uskokovič, "Structure recovery of hot-isostatically pressed varistor ceramics based on ZnO", Proceedings of the International Conference on Hot Isostatic Pressing-Theories and Applications", Lulea, 1987.(to be published).
13. A.Iga, M.Matsuoka and T.Masuyama, "Effect of phase transition of intergranular Bi_2O_3 layer in nonohmic ZnO ceramics", Jpn.J.Appl.Phys., 15 (1976) 1161.
14. M.Trontelj, "Electrical properties of ZnO varistors", XXVII Jug.Conf. ETAN, Struga (1983).

AMORPHOUS MAGNETS

B.Leontić
Faculty of Natural Sciences, Zagreb

1. Introduction

Paramagnetic and diamagnetic properties of solids are readily explainable in simple quantum-mechanical terms. Ferromagnetism however is still described by several models and even so semi-quantitatively.

Efforts to explain ferromagnetism date from the early "crystal field" theory of Weiss. Actually it soon became evident that any dipole-dipole interaction in solids would result in Curie temperatures of the order of 1 K. We now know that electron spin alignment results from the nature of the electron wave function.

Although the Hartree-Fock equation:

$$\left[-\frac{\hbar^2}{2m}\nabla^2 + V(\vec{r}) + \sum_j e^2 \int \frac{\psi_j^*(\vec{r}\,')\psi_j(\vec{r}\,')d\tau'}{|\vec{r}-\vec{r}\,'|}\right]\psi_i(\vec{r}) - e^2\sum_j \psi_j(\vec{r}) \int \frac{\psi_j^*(\vec{r}\,')\psi_i(\vec{r}\,')d\tau'}{|\vec{r}-\vec{r}\,'|} = \varepsilon_i\psi_i(\vec{r}) \tag{1}$$

tells us qualitatively haw the exchange energy causes spin orientation, the real picture is more complicated.

Amorphous magnets being metallic, may be viewed through itinerant electron model where electrons are considered as residing in energy bands. The tight binding approximation[1] gives the electron energies as:

$$\varepsilon_k = E_0 + A + B\sum e^{i\vec{k}\cdot\vec{R}_i} \tag{2}$$

where

$$A = \int |\phi(\vec{r})|^2 \Delta V d\vec{r} \tag{3}$$

and

$$B = \int \phi(\vec{r})\,\phi(\vec{r}-\vec{R}_i)\,\Delta V d\vec{r} \tag{4}$$

Here $\Delta V<0$ is the interaction of the itinerant electrons where R_i is the nearest neighbour distance and the summation in (2) is over nearest neighbours. We note that the relationship between the electron wave functions $\psi_k(\vec{r})$ and the atomic wave function ϕ at a position $\vec{r}$ is given by the usual relation

$$\psi_k(\vec{r}) = \sum_i \phi\,(\vec{r} - \vec{R}_i)\, e^{i(\vec{k}_i - \vec{R}_i)} \tag{5}$$

In amorphous ferromagnets we must consider the charge transfer between the 3d-electrons in the transition-metal atoms and the s- and p- electrons of the metalloid. This changes the effective number of d- electrons in the system.

The exchange term in H - F equation gives too large an effect since it is a very simple approximation of reality. If we denote this term by I_0 a more appropriate value[2)3)] of the exchange term can be written as:

$$I = I_0/(1 + \gamma I_0/W) \tag{6}$$

where γ is of order of unity and W is the band width.

Simple quantities can be computed and compared with the experiment. Thus the Curie temperature T_c is given by:

$$I \int_0^\infty N(\varepsilon) \left| \frac{\partial f(\varepsilon, T_c)}{\partial \varepsilon} \right| d\varepsilon = 1 \tag{7}$$

where $N(\varepsilon)$ are the electron densities of states and $f(\varepsilon, T_c)$ is the electron energy distribution at temeprature T_c ($f(\varepsilon,T) = \left[e^{(\varepsilon-\mu_c)/kT} + 1\right]^{-1}$, where μ_c is the chemical potential) while the temperature dependence of the magnetisation M(T) is given for most cases as:

$$\left(\frac{M(T)}{M(O)}\right)^2 = 1 - \frac{T^2}{T_c^2} \tag{8}$$

2. Systems of Interest

A quantity of great practical interest is the saturation magnetisation $M_s(0)$ given by a simple relation:

$$M_s(0) = N\mu = N\, n_B\, \mu_B \tag{9}$$

where N is the number of magnetic atoms per unit volume, n_B is the number of Bohr magnetons μ_B per magnetic atom ($\mu_B = 9{,}27 \cdot 10^{-24}$ JT^{-1}). This quantity will depend on the electron concentration and is often represented by the Slater-Pauling curve. Fig.1 shows such a curve for a number of systems. Note that the values of μ for all amorphous systems fall below those for pure transition metal crystalline alloys. Another interesting diagram is shown in Fig.2 where μ-values for FeB and FeP amorphous alloys are shown together with relevant Curie temperatures as a function of the metalloid concentration[4]. A very useful diagram is shown in Fig.3 where the values of μ and T_C for Fe atoms in systems $Fe_{80}B_{20}M$ and $Fe_{80}P_{20}M$ are plotted as a function of other metalloid additions such as M = C,Si,Ge,B,P,As. A similar diagram[5] pertaining to Co is shown in Fig.4.

The results presented indicate that the charge transfer between the metalloid s- and p- electrons and the 3d- electrons of the transition metal greatly influences the average magnetic moment per atom of the system. An atom of boron should contribute[5] about 1.6 electrons to the transition metal 3d band, while phosphorous will contribute 2.4. Evidently such a large charge transfer cannot take place spatially without serious Coulomb forces being set up. What probably happens is that s - d and p - d hybridisation takes place in the form of covalent bonds and the average magnetic moment is reduced.

The diagrams shown in Fig.3 and 4 shaw that Fe and Co behave inversely as part of the glazing metalloid is substituted by elements P, Si, C and Ge. The reason is that B and C are small atoms that tend to go into the matrix interstitially while the larger ones go in substitutionally. The former thus do not affect the coordination number while the latter do. The exchange interaction in Fe tends thus to decrease with interatomic distance while for Co the reverse is true.

While the Fe - metalloid systems are of great interest for large-scale applications in power systems, another category of amorphous magnets are of great significance in electronics. These are mostly cobalt based quaternary alloys which, due to a high initial permeability, can successfully substitute mu-metal and similar more expensive materials.

3. Soft Ferromagnetism. Anisotropy and Magnetostriction.

In crystalline ferromagnets anisotropy is present since ease of magnetisation depends on crystal orientation. In amorphous material this anisotropy is greatly supressed. Indeed amorphous ferromagnets are remarkably isotropic although not entirely so.

On the microscopic scale anisotropies exist due to preferential cooling of the material as it is rapidly solidified and also due to the intrinsic randomness of the structure. Thus hard magnetisation and Berkhausen noise are present as evidenced[7] on Fig.5. The hard magnetisation present is due to the so-called maze domains. By annealling as-obtained ribbons at 350 -400°C Luborsky et al.[8] have shown that remanent magnetisation decreases together with residual stresses of the matrix. More quantitatively we can define the magnetisation energy[9]:

$$E_a = \int_0^{H_s} (M_s - M)\,dH \qquad (10)$$

and show that the compositional dependence of E_a for Fe - Ni - B alloy is linearly related to the saturation magnetostriction λ_c. Many authors have shown that E_a decreases as stress is applied to amorphous ribbon and λ_s rises in the same proportion. The same relationship is found in the temperature dependence. Fujimori et al.[10] have shown that for systems such as $(Fe_{1-x}Co_x)_{80}M_{20}$, where M stands for pairs of metalloid glazers such as (P,C) and (Si,B), λ_s, anisotropy field H_a and the field necessary to make the maze domains disappear, depend on the concentration x with a vanishing λ_s in the Co- rich region. It is this property of the alloy that is responsible for high quality high permeability, low anisotropy etc. materials mentioned earlier.

4. Production Techniques

First amorphous alloys purposely made were produced by P.Duwez at Caltech in the early 60's by rapid solidification from the melt. Such techniques are greatly developed. Those that are in greater or lesser use are shown in Fig.6. The most frequent and economically most attractive technique is the so-called metal spinning on a single roll.

Ribbons as wide as 50 cm or more are now rutinely produced although the more expensive alloys are usually manufactured in narrower sizes.

The methods of ribbon manufacture impose limitations on the amorphous magnet applications since complicated shapes have to be manufactured by stamping from the ribbon.

A more versatile technique proposed for our joint Project would entail a splat cooling technique where flakes of the amorphous material would be produced by an atomisation technique in conjUnction with a cool substrate. Powders thus produced may then be compacted by a number of techniques one of which is polymer bonding under pressure.

5. Conclusion

Amorphous ferromagnets are highly useful low-loss materials ideally suited for a variety of applications ranging from power--distribution tranformers to sophisticated devices in electronic circuits, computer memories, etc. One major field of application thus far has been left out, namely the medium-frequency magnetic cores and similar devices where an insulated bulk material is desirable. It is in this applicative field where we intend to make a contribution.

References

1) See for example, G.C.Fletcher: "Electron Band Theory of Solids". North Holland, Amsterdam (1971)
2) J.Kanamori, Prog.Theor.Phys., Osaka 30, 275 (1963)
3) J.Hubbard, Proc.Phys.Soc. 85, 455 (1964)
4) R.Hasegawa and R.Ray, Jour.Appl.Phys. 50, 1586 (1979)
5) N.S.Kazama et al., Jour.Magn.Mat. 15-18, 1331 (1980)
6) K.Yamauchi, T.Mizoguchi, Jour.Phys.Soc.Jap. 39, 541 (1975)
7) H.Fujimori et al., Jap.J.Appl.Phys., 13, 1889 (1974)
8) F.E.Luborsky et al., IEEE Trans.Magn. MAG-11, 1644 (1975)
9) R.C.O´Handley, IEEE Trans.Magn. MAG-11, 206 (1975)
10) H.Fujimori et al., Mat.Sci.Engng. 23, 281 (1976)

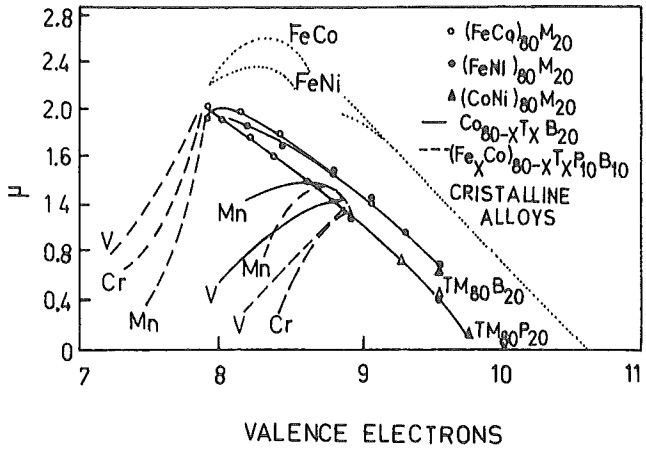

Fig. 1 Slater-Pauling curves for the (Fe, Co, Ni)-B and (Fe, Co, Ni)-P Crystalline alloys are shown as dotted lines.

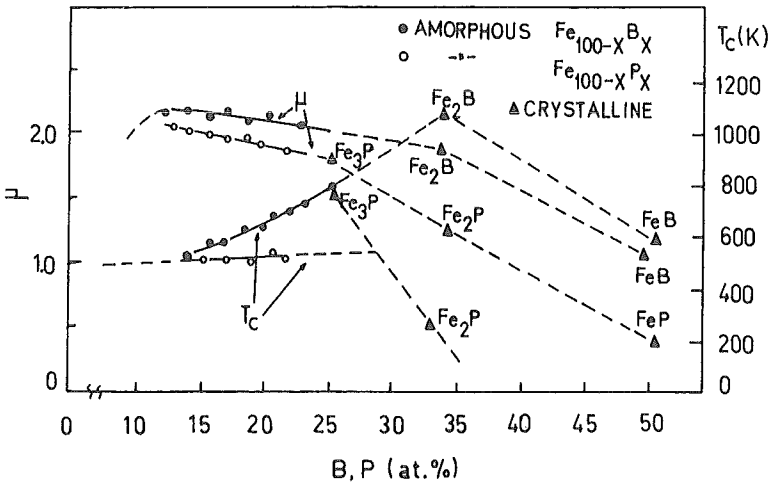

Fig. 2 Magnetic moment per Fe atom in Bohrs magnetons for FeB and FeP is ploted as a function of metalloid content. Corresponding Curie temperatures are plotted on the right.

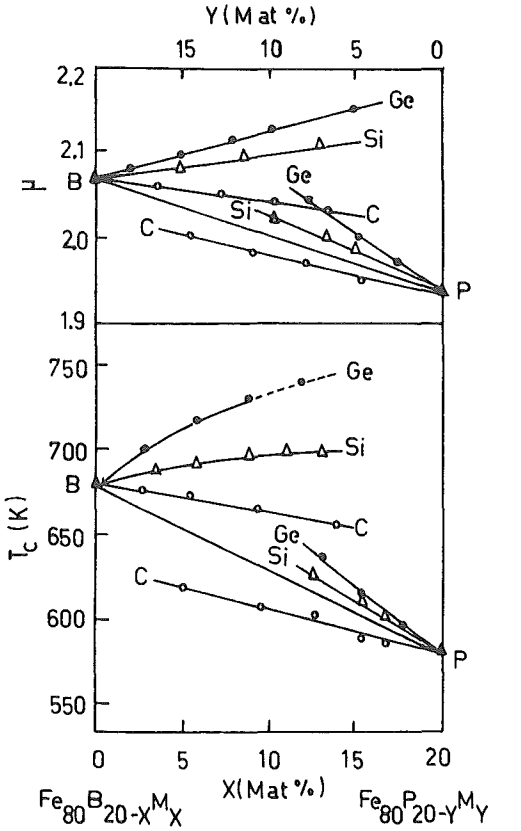

Fig. 3 Magnetic moment per Fe atom and Curie temperatures are plotted against the percentage of substitution of B and P by Ge, Si and C atoms.

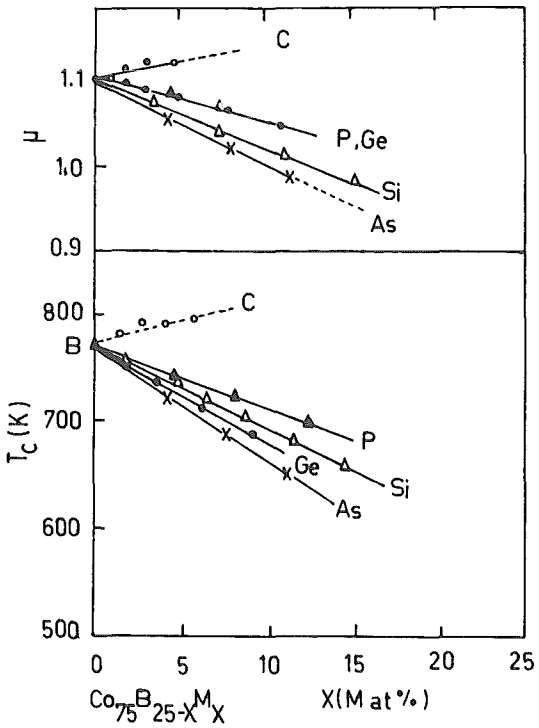

Fig. 4 Same plot as in Fig. 3, but for Co-based alloys.

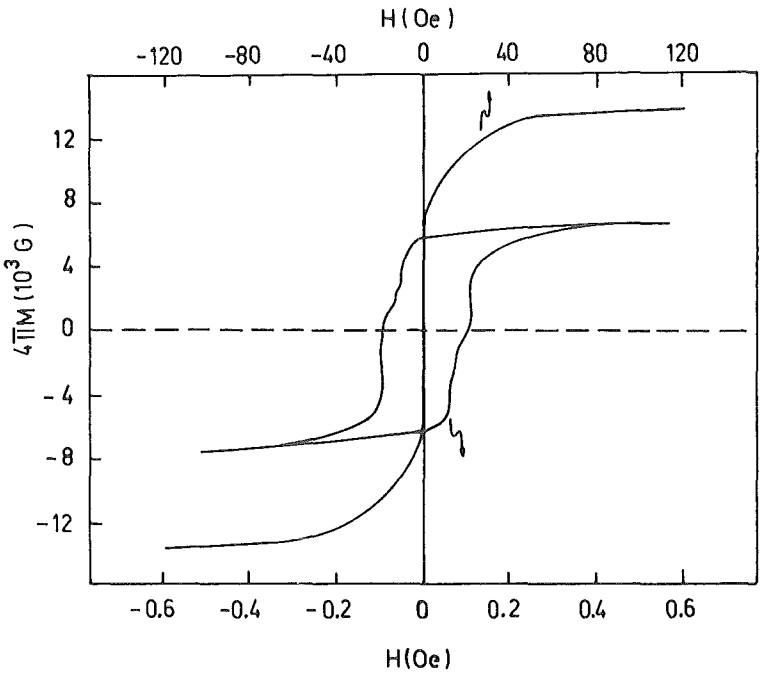

Fig. 5 A typical hysteresis curve of a soft amorphous ferromagnet (in this case $Fe_{80}P_{13}C_7$) before annealing. The hard magnetisation part is shown on amplified scale.

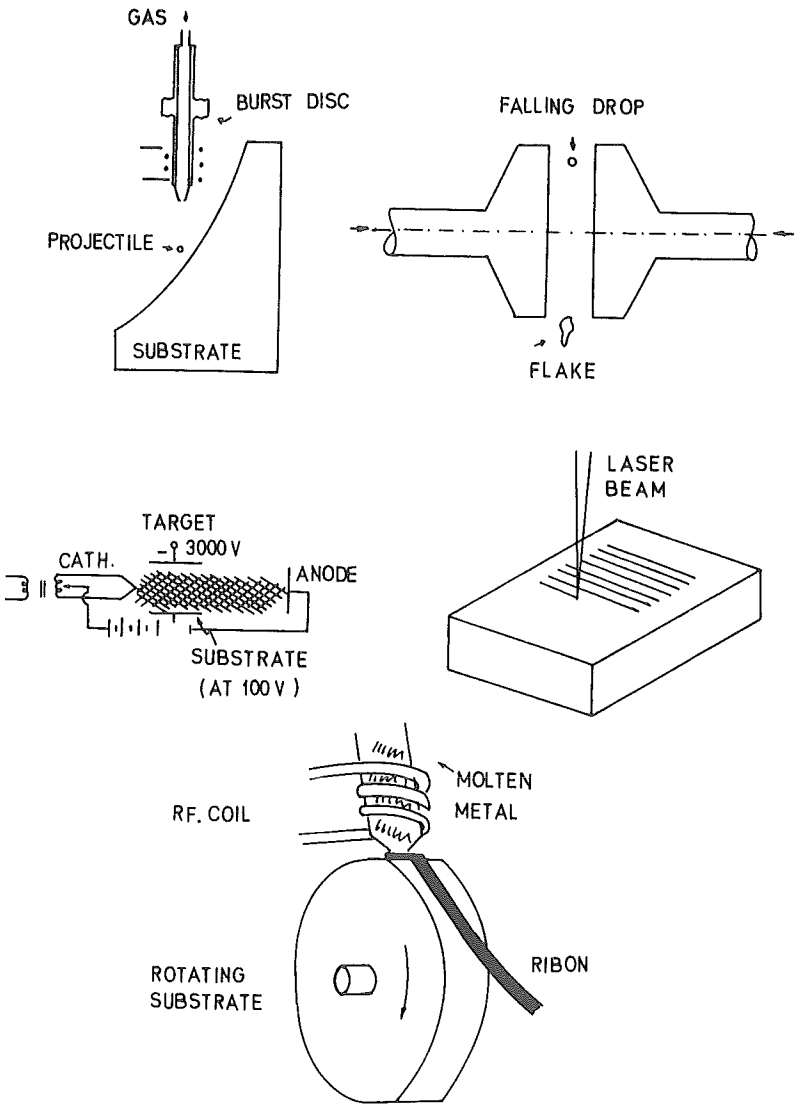

Fig. 6 Illustration of various techniques of amorphous alloy production. Top left and right are the gun and the piston methods respectively. In the middle left a schematic diagram shows cathode sputtering and on the right laser glazing. Bottom: Metal spinning.

on the correlation between microstructure and magnetic induction of porous iron and iron-$Ni_{0.4}Zn_{0.6}Fe_2O_4$-composites

E. Remane

Kernforschungszentrum Karlsruhe
Institut für Material- und Festkörperforschung
Postfach 3640, 7500 Karlsruhe
Federal Republic of Germany

Abstract

The dependence of the magnetic induction from the microstructure of sintered iron toroids and sintered iron-NiZn ferrite toroids was investigated. Compacting pressures, sintering temperature and sintering time were varied over a wide range in order to obtain cores with very different microstructures. The microstructures were characterized by a computerized imaging system. A theory was applied which used the measured microstructural parameters to calculate the induction behaviour. These theoretical results are in good agreement with the experimental results.

1. Introduction

The achievable saturation induction of a porous magnetic solid is on the one hand dependent on the volume fraction of the magnetic material. On the other hand the pores themselves cause demagnetizing fields which also influence the induction [1,14,15]. A linear relationship between induction and macroscopic density of the type:

$$B = B_0 \cdot \frac{\rho}{\rho_0} = B_0(1 - c_D)$$

B, ρ = induction and density of the porous sample
B_0, ρ_0 = induction and density of a dense sample
c_D = volume fraction of the pores

was used in the past [2,3] but it neglects the demagnetizing effects. Some authors noticed that by introducing pores into a sample the induction decreases more than proportionally with the density [12,13]. This is why Warlimont and Stäblein [4,5] suggest another approach

$$B = B_0(1 - c_D)^{1.5}$$

to take the additional demagnetizing effects into account where the exponent 1.5 is an empirical value.

The influence of the demagnetizing fields is not only dependent on the volume fraction of the pores, but also on their shape and orientation. Needleshaped pores oriented parallel to the H-field have practically no influence on the induction whereas lenseshaped pores with the rotation axis parallel to the H-field have a high influence. A theory which enables us to calculate the magnetic behaviour in dependence on the concentration, shape and orientation of the pores is the "quantitative microstructure-field property correlation for two phase materials" from Ondracek [6].

2. Microstructure-field property correlation (MPC)

The calculation of material properties with the MPC is based on the knowledge of the values of concentration, shape and orientation of the inclusions, which can be evaluated by a computerized image analyzing system. For detailed information concerning the evaluation of these parameters see [6]. Briefly, the method functions as follows: Polished cuts of a sample are viewed by a TV-camera, the picture is digitized by an imaging system. With this system the area, the greatest diameter and the circumference of each pore is measured. An implemented software substitutes each pore by an ellipse of the same area and a main axis A equal to the greatest diameter of the pore. The secondary axis B of this substitutional ellipse is calculated. The ratios A/B of all ellipses are averaged and by means of stereological functions a spheroid can be calculated. Each pore is substituted by this average spheroid, the volume fraction of pores and spheroids are equal. By means of three polished cuts, perpendicular to each other, the average orientation of the pores can be estimated. The ratio of the rotation axis and secondary axis X/Z is used to derive the shape factor F, the area fraction of the pores within a TV-picture is used as concentration factor c_D, the estimated angle α between the rotation axis and the magnetic field direction is used to obtain the orientation factor $\cos^2\alpha$.

The MPC for inclusion structure with very different properties of the matrix and dispergent ($\lambda_M/\lambda_D \gg 1$) is [6]

$$\lambda_C = \lambda_M (1 - c_D)^{\frac{1 - \cos^2\alpha}{1 - F} + \frac{\cos^2\alpha}{2F}} \qquad (2)$$

λ_C, λ_M = property of the composite and matrix, respectively
c_D = dispergent concentration, volume fraction
F = shape factor
$\cos^2\alpha$ = orientation factor

If both phases are continuous - in the following the terminology "continuous structure" is used - the MPC equation is [7]

$$(1 - c_D)(\lambda_M - \lambda_C)\left[\frac{2(1 - \cos^2\alpha)}{\lambda_M + \lambda_C} + \frac{\cos^2\alpha}{\lambda_C}\right] = c_D(2 - \cos^2\alpha) \qquad (3)$$

λ_C and λ_M are unspecifically denoted as "property" and they are representing properties like electrical permittivity ε, magnetic permeability μ in the case of para- and diamagnetic materials or electrical conductivity σ. In former studies it was derived that for ferromagnetic materials a substitution of the "property" by the induction B is permitted when comparing the inductions of different materials at a same fixed field strength H.

3. Investigations with pure sintered iron

3.1 Description of the samples and analytical evaluation of the microstructure

Iron toroids were produced by varying compacting pressure, sintering temperature and -time in order to obtain porous samples with different microstructures.

Water atomized iron powder, Mannesmann Ltd, MAG 400, was pressed at various compacting pressures into ring cores with green densities between 6.02 g/cm³ and 7.52 g/cm³. Subsequently the cores were sintered for four hours in pure H_2-atmosphere at various temperatures. The sintered densities achieved are listed in table 1. The dimensions of the toroids were: height: 5.05 mm, $\varnothing_{outer}$: 50.0 mm, $\varnothing_{inner}$: 39.5 mm. The toroids were wrapped with copper wire, $\varnothing_{wire}$ = 0.71 mm, number of turns 1330 on the prime winding, 20 turns on the secondary winding. The analytical investigation on the microstructure led to an orientation factor of $\cos^2\alpha$ = 0.33, that means there is a random orientation of the pores. The evaluated shape factor F combined with $\cos^2\alpha$ = 0.33 led to x-values (equation (2)) as they are listed in table 1.

3.2 Magnetic field measurements

A static method is used although the prime D.C. is continously increased from -7 A to +7 A and vice versa to produce the virgin curve and the full hysteresis loop. With an integrating fluxmeter the continuous induction change is summed. The signals of the H- and B-fields are hooked to a x-y-recorder. For demagnetizing the cores are brought into an A.C. coil with decreasing amplitude.

3.3 Results

As comparable material property value to be used in MPC (equation (2)) the achieved induction at a field strength of H = 50 A/cm was taken for each toroid. These induction values are listed in table 1 in the column denoted as B_{gem}. Together with the listed values for (1 - c_D) and x the induction of the iron matrix of each toroid B_M is calculated with the equation (2); the results are listed in the sixth column of table 1. If the theory holds, these values must be constant for all cores, because B_M

describes the achieved induction at H = 50 A/cm of the pure matrix material of each toroid if there were no demagnetizing influences of the pores. As can be seen in table 1 the values for the cores with high porosities deviate more from the average than others do. This is explainable by the fact that equation (2) holds for the inclusion microstructure only, whereas at porosities of 20 vol.-% and more the continuous microstructure begins gradually.

Toroid code	G	1 850 °C	2 1000 °C	3 1300 °C	4 1400 °C	5 1400 °C
Code 2	6.02	5.84	5.85	6.11	6.34	6.52
Code 3	6.35	6.40	6.41	6.46	6.75	6.80
Code 4	6.78	6.75	6.80	6.81	7.06	7.14
Code 5	7.14	7.21	7.14	7.34	7.37	7.33
Code 5K	7.52	7.49	7.46	7.47	7.58	7.57

Table 1: Sintered iron toroids. Description see text.

To demonstrate the agreement between theory and experiment the B_C-values of the cores are calculated by introducing the average value B_M = 1.64 T into equation (2).

The results are listed in table 1 in the last column. In fig. 1 the calculated and measured values of B_C are shown. Additionally shown is the calculated behaviour when a linear dependence between induction and density is assumed. The significant difference of both curves is due to the additional effect caused by the demagnetizing field as mentioned before.

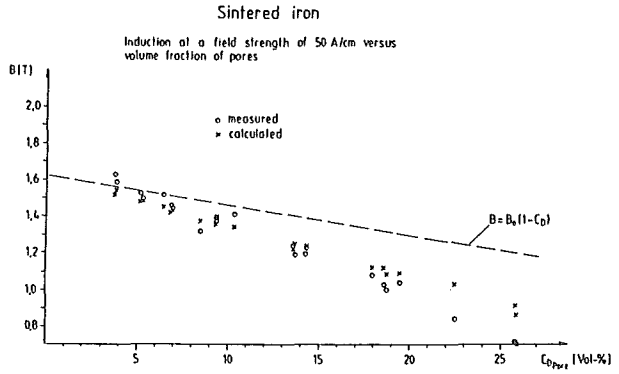

Fig. 1: Induction B of sintered iron toroids versus pore volume fraction.

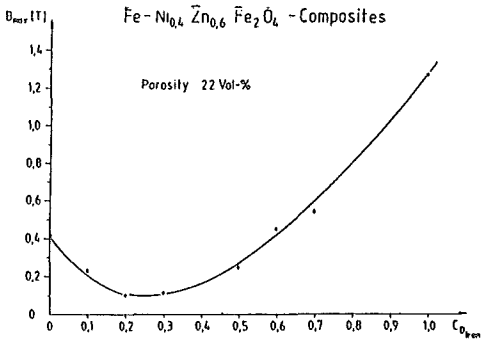

Fig. 2: Induction B at H = 535 A/cm of toroids with pore volume fractions of 22 %.

4. Investigations of Iron-NiZn ferrite cores

4.1 Description of the cores

$Ni_{0.4}Zn_{0.6}Fe_2O_4$-powder (Vogt Electronic Ltd., Passau) and iron powder (Höganäs ABC 100.30), were homogeneously mixed in eleven different ratios iron/ferrite. The weight-% amount of one component with respect to the whole mass was varied from 0 % to 100 % in 10 %-steps. These mixtures were pressed into toroids using six different compacting pressures from 2 t/cm² up to 12 t/cm² in steps of 2 t/cm²; PVA was used as lubricant. The dimensions of the toroids were $\varnothing_{outer}$ = 50 mm, $\varnothing_{inner}$ = 32 mm, height = 6 mm.

The toroids were dewaxed at 420 °C for one hour with a temperature increase of 50 °C/h, atmosphere = N_2, cooled by switching off the furnace. Sintering was carried out in pure argon at 850 °C for four hours. The magnetic field measurements were made as described in the experiment above, but the number of turns of the prime coil was 500.

The toroids are denoted with n-m. m stands for the compacting pressure in t/cm². n stands for the weight fraction of iron in the powder mixture. n = 1 means 0 % iron, n = 2 means 10 % iron and so on up to n = 11 = 100 % iron. In table 2 the weight fraction of iron is denoted with c_{m_1} and its volume fraction with c_{v_1}.

4.2 Experimental results

The induction achieved at a field strength of H = 535 A/cm was taken as the comparable property. The first measurements on cores with a nearly constant pore fraction provided an unexpected result, see fig. 2. Iron and $Ni_{0.4}Zn_{0.6}Fe_2O_4$ have a saturation induction of about 2.15 T and 0.38 T, respectively. So it was expected although not a linear but a continously increasing behaviour. Further physical investigations showed, that contrary to all experiences the composites were thermodynamically unstable at these sintering conditions.

With respect to the magnetic properties these results mean that the iron crystallites at a concentration of 20 - 30 wt.% iron or more are embedded in or surrounded by nonmagnetic phases. I.e. there is a continous change from an inclusion into a continuous microstructure, what provides the opportunity to prove the application of the MPC for inclusion and continuous microstructure and the convergence of both models. In table 2 the volume fraction of the nonmagnetic phases is denoted with c_{v_2}.

The results of X-ray diffractometry, microprobe analysis, scanning elelctron microscopy and Mößbauer spectroscopy led to the conclusion: if an amount of upt to 20 - 30 wt.% iron powder is added to the pure NiZn ferrite powder, the spinell lattice of the ferrite is broken up completely during sintering. The added iron as well

toroid	c_{m_1}	c_{v_1}	c_{v_2}	B_C [T]
1-2	0.0	0.0	1.0	0.31
1-4	"	"	"	0.33
1-6	"	"	"	0.40
1-8	"	"	"	0.42
1-10	"	"	"	0.41
1-12	"	"	"	0.4
2-2	0.1	0.049	0.951	0.19
2-4	"	0.052	0.948	0.23
2-6	"	0.053	0.947	0.23
2-8	"	0.055	0.945	0.17
2-10	"	0.056	0.944	0.22
2-12	"	0.057	0.943	0.18
3-2	0.2	0.101	0.899	0.1
3-4	"	0.103	0.897	0.09
3-6	"	0.104	0.896	0.09
3-8	"	0.108	0.892	0.1
3-10	"	0.109	0.891	0.1
3-12	"	0.111	0.889	0.09
4-2	"	0.149	0.851	0.1
4-4	"	0.157	0.843	0.1
4-6	"	0.162	0.838	0.12
4-8	"	0.163	0.837	0.12
4-10	"	0.168	0.832	0.11
4-12	"	0.169	0.831	0.11
6-2	"	0.289	0.711	0.24
6-4	"	0.307	0.693	0.23
6-6	"	0.303	0.967	0.25
6-8	"	0.308	0.692	0.25
6-10	"	0.316	0.684	0.28
6-12	"	0.311	0.689	0.25

toroid	c_{m_1}	c_{v_1}	c_{v_2}	B_C [T]
7-2	0.6	0.359	0.641	
7-4	"	0.381	0.619	
7-6	"	0.410	0.59	0.45
7-8	"	0.418	0.582	(defect)
7-10	"	0.417	0.583	0.46
7-12	"	0.428	0.572	
8-2	0.7	0.475	0.525	0.54
8-4	"	0.495	0.505	0.66
8-6	"	0.516	0.484	0.63
8-8	"	0.518	0.482	(defect)
8-10	"	0.531	0.469	"
8-12	"	0.514	0.486	0.57
9-2	0.8	0.601	0.399	0.645
9-4	"	0.664	0.336	1.01
9-6	"	0.672	0.338	1.025
9-8	"	0.682	0.318	1.08
9-10	"	0.670	0.33	0.97
9-12	"	0.686	0.314	1.08
10-2	0.9	0.738	0.262	1.07
10-4	"	0.793	0.207	1.25
10-6	"	0.82	0.18	1.46
10-8	"	0.827	0.173	1.48
10-10	"	0.833	0.167	1,37
10-12	"	0.838	0.162	1.53
11-2	1.0	0.78	0.22	1.27
11-4	"	0.88	0.12	1.64
11-6	"	0.93	0.07	1.85
11-8	"	0.95	0.05	1.95
11-10	"	0.961	0.039	1.98
11-12	"	0.965	0.035	1.97

Table 2:
Iron-Ni-Zn-ferrite toroids.
Description see text

as the iron atoms of the ferrite reacts with the oxygen to FeO. Other iron compounds do not exist. If the iron content is further increased the phases FeO, α-Fe, (FeNi)-solid solution with 5 at.% Ni in solution and $FeZnO_2$ are formed and they do not change their chemical and crystalline structure with a further increase of iron powder amount. During the investigations an interesting result was obtained: Mößbauer data of $FeZnO_2$, not existing in the literature up to now, could be determined. The quadrupole splitting is 0.8 mm/sec, the isomere shift is 0.165 mm/sec, a ^{37}Co-Rh-source was used. One of the spectra used for determination is shown in Fig. 3.

What do these results mean with respect to the magnetic behaviour? The two phases FeO and $FeZnO_2$ are not ferromagnetic. α-Fe and (FeNi) solid solution behave similar. So one can say that the iron crystallites are embedded in a nonmagentic material when the iron powder amount of 20 - 30 wt.% has passed over, that means a real iron inclusion microstructure. At high iron concentration a real iron continuous microstructure is existing. In the concentration range between, there is a gradual change from one microstructure type to the other.

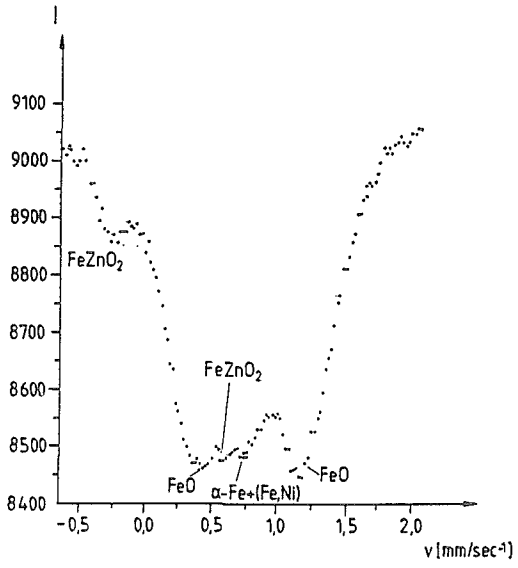

Fig. 3:
Mösbauer spectrum of the sample with 40 wt.% iron.

4.3 MPC and comparison with the experimental results

The MPC were completed with respect to the application on continuous microstructure by Schulz [7] (equation (3) in chapter 2).

With an orientation factor of $\cos^2\alpha = 0.33$ this equation can be rewritten as

$$B_C = \frac{B_M}{10}\left\{(4 - 9c_K) + \sqrt{(4 - 9c_K) + 20\,(1 - c_K)}\right\} \qquad (4)$$

In table 2 the measured B_{535} values are listed. The value for the matrix induction was calculated with the B_{535} values of the pure iron toroids: $B_M = 2.15$ T.

In fig. 4 the calculated B_C-values after equation (4) are plotted together with the measured B_C-values. The deviation of the calculated and meausred values for the cores 3-x, 2-x and 1-x with 20 %, 10 % and no iron, respectively, is due to the fact that here in contrast to the other toroids the magnetic ferrite phase is still existing.

If those cores with inclusion microstructure of iron, that means a volume fraction of less than 20 %, are considered separately and if one applies the MPC for inclusion microstructure like in chapter 3.3, then B_C-values are calculated as they are listed in table 3. There is again a good agreement with the experimental results. The convergence between both MPC models is obvious.

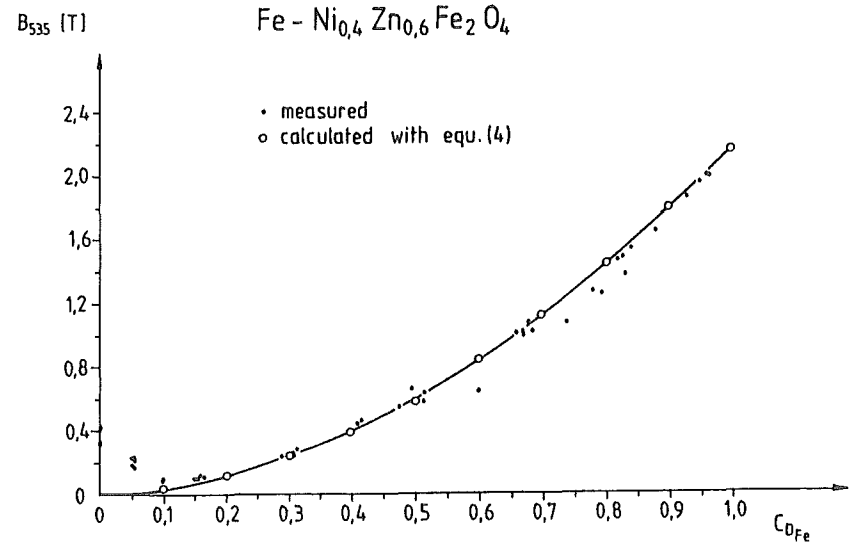

Fig. 4: Induction B at H = 535 A/cm versus volume concentration of iron.

Table 3: Induction of the toroids with a volume fraction of iron of more than 20 %.

Toroid code	B_C [T]		Toroid code	B_C [T]	
	measured	calculated		measured	calculated
11-2	1.27	1.27	10-2	1.07	1.13
11-4	1.64	1.64	10-4	1.31	1.32
11-6	1.85	1.84	10-6	1.46	1.41
11-8	1.95	1.93	10-8	1.48	1.44
11-10	1.98	1.97	10-10	1.37	1.46
11-12	1.97	1.97	10-12	1.53	1.48

5. Conclusions

30 sintered iron toroids of different microstructures were investigated with regard to microstructure and magnetic induction behaviour. The application of the MPC leads to a good agreement between theoretical and experimental results. It can be pointed out that by characterizing the microstructure the induction behaviour can be calculated. Or vice versa, for a magnetic composite when knowing the magnetic behaviour of one component the microstructure can be calculated to achieve a required magnetic property of the composite. The application of the MPC enables us to produce magnets of a certain induction behaviour without involving great expense of experiments concerning composition and production procedures.

132 Fe-$Ni_{0.4}Zn_{0.6}Fe_2O_4$-toroids with various ratios of powder mixture were produced and investigated concerning microstructure and induction. In dependence on the amount of added iron powder the ferrite spinell is destroyed and different unmagnetic phases are formed. The application of the MPC for continous microstructure could be proved. The result is a good agreement between calculated and experimental results concerning the induction behaviour.

Mösbauer spectroscopy data for a $FeZnO_2$-phase were obtained. The isomere shift is 0.165 mm/sec, the quadrupole splitting is 0.8 mm/sec, using a ^{57}Co-Rh-source.

Literature

[1] U. Stille, Archiv für Elektrotechnik 38. Band (1944) 91-101

[2] B.A. James, G. Williams, Powder Metallurgy Vol. 22, No. 2 (1979) 75-85

[3] K.H. Moyer, M.J. Topolski, M.J. McDermatt, P. Wisniewski, Progress in Powder Metallurgy Vol. 34 + 35 (1980) p. 133 - 151

[4] H. Warlimont, Pulvermetallurgie Tagung, Düsseldorf (1986)

[5] H. Stäblein in E.P. Wohlfarth (ed.), "Ferromagnetic Materials", Vol. 3, North-Holland Publishing Co. (1982)

[6] G. Ondracek, KfK 3648 (1982/83) (German) and Review in Powder Metallurgy and physical ceramics (1988) (English) in print

[7] B. Schulz, KfK 1988 (1974)

[12] G. Jangg, M. Drozda, H. Danninger, R.E. Nad, Powder Metallurgy International Vol. 15, No. 4 (1983) 173-177

[13] J.M. Capus, Metal Powder Report Vol. 36, No. 1 (1981) 112-113

[14] J. Fischer, Elektrodynamik, Springer-Verlag Berlin Heidelberg New York, (1976)

[15] E. Kneller, Ferromagnetismus, Springer Berlin Göttingen Heidelberg, (1962)

M E T A L S (1)

WEAR RESISTANT SINTERED STEEL WITH HIGH CARBIDE CONTENT

R.Klausmann*), R.Oberacker, F.Thümmler

Nuclear Research Center and University of Karlsruhe
D 7500 Karlsruhe 1, Postfach 3640

ABSTRACT

Sintered steels with 10-30 vol-% of special carbides have been developed by mechanical alloying, pressing and liquid phase sintering. The best results have been achived with systems, where the carbide phase is added as fine carbide powder, which does not take part in liquid phase formation, but is provided by addition of P or P+C. Especially in Fe-NbC-P and Fe-NbC-P-C systems very high densification and equal and fine distribution of the carbide phase in the heat treatable matrix have been reached. These alloys provide some advantages compared with HSS T15 as well as Astaloy E with 2.5% C.

Introduction

The most important wear resistant metallic alloys are the high speed steels, which contain 20 - 30% of various carbide forming alloying elements. Part of them are manufactured by PM methods, providing advantages with respect to fine and equal carbide distribution (Fig. 1) and to manufacture near-net-shaped parts /1,2/ without milling procedure. On the other hand, a very exact and costly sintering regime (± 2°C, vacuum) has to be provided. A different PM-development are multicomponent alloys used in Japanese integrated camshafts /3/. These alloys containing Cr, Cu, Si, Mo, P and C can be sintered in common belt type furnaces. They are offered as a prealloyed powder (ASTALOY E) by a European powder manufacturer /4/. The microstructure of this material consists of coarse and irregular carbide phases in a martensitic matrix (Fig. 2).

In this work, a systematic study for developing of wear resistant PM steels by using transition metal carbides is described /5/. It follows the lines of:

- high densification by sintering under normal protective gas atmospheres, and at temperatures up to max. 1300°C
- fine and even distribution of carbides in a hardenable matrix
- mechanical and wear properties, which meet the requirements for working of "elastohydrodynamic contacts", where adhesive wear, abrasive wear and surface fatigue take place /5/.

Manufacturing and properties of the newly developed alloys shall be compared with the commercial materials mentioned above in order to look after advantages of the new systems.

---

*) Now with W.C. Heraeus, Hanau

Starting materials and selection of systems

The basic iron powder was water atomized ASC 100.29 from Höganäs, the hard phase was added in form of MC(or M_2C) by powder mixing technique (M = transition metal). The alternative way was to add M (in form of ferroalloy powder) and C separately, with in-situ-formation of MC (or other types of carbide) during sintering. Green density after die pressing (500 MPa) was only about 80% of theoretical, therefore a liquid phase sintering process was necessary to achieve high densification.

In the Fe-M-C systems, permanent liquid phase formation at moderate temperature occurs, e.g. in the following: Fe-Cr-C, Fe-V-C, Fe-Mo-C, Fe-W-C, in most cases due to eutectics, which show melting points between 1080°C (Fe-20% W-1.5% C) and 1290°C (Fe-8.2% VC) /6/. From these systems, Fe-Mo-C (resp. Fe-Mo_2C) has been choosen for detailed investigation.

Fe-M-C-systems, which do not form liquid phases below ∿1300°C, are e.g.Fe-Nb-C and Fe-Ti-C /6/. For sintering to high densities in an "acceptable" temperature range, they need additives like B, P of P+C. In this case, transient liquid phases are formed which enhance sintering drastically.

Sintering studies

In order to investigate the principle sintering behaviour, dilatometer experiments with powder compacts have been performed in H_2-atmosphere (dew point < -50°) up-to 1300°C. Fig.3 shows α-γ-transformation and thermal expansion in Fe-Mo_2C-compacts below 1290°C. At this temperature, the occurring liquid phase leads to additional swelling, but no shrinkage occurs during isothermal sintering at 1300°C. In Fe-Ferromolybdenum-C compacts with the same nominal composition one observes no α-γ-transformation due to solid solution formation during heating-up period. Above 1050°C carbide formation (M_3C and $M_{23}C_6$) compensates thermal expansion. At 1260°C liquid phase formation leads to some volume increase and during isothermal sintering to strong shrinkage, i.e. high densification. Fig.4 shows, that thermal expansion and isothermal sintering behaviour is strongly influenced by the carbon content (0.7 - 2.0%). The densification curves are pretty complicated, mainly in the range of heating-up, and the isothermal sintering behaviour is very sensitive on composition, particle characteristics and temperature.

In this system, the permanent liquid phase, occurring above a certain temperature, is formed by the main alloying constituents. The formation of mixed carbides as well the carbide solubility in the matrix results in a not defined content of carbide phase in the microstructure. The system is easy to oversinter, showing dimensional instability or, as the opposite, incomplete densification. Furthermore, decarburisation takes place during H_2-sintering, which can be overcome only by addition of hydrocarbons (CH_4) in the protective atmosphere.

In Fig. 5 dilatometer curves of Fe-Nb-C and Fe-NbC-compacts are presented. Only thermal expansion and γ-α-transformation is visible during heating-up in Fe-NbC, in Fe-Ferroniobium-C additionally a volume effect from NbC formation takes place. In fact no strong reaction between matrix and NbC or Nb, resp., occurs. Only little shrinkage can be seen during isothermal sintering. Compacts of Fe-Ti-C and Fe-TiC behave similar, but even more indifferent /5/. No liquid phase occurs in both systems as the eutectic melting points are 1420 and 1380°C, resp. /6/.

The addition of B or P can change the densification-behaviour completely which was elaborated mainly in the system with NbC. With B, a permanent liquid phase is present above 1060°C with P a transient one >1050°C. The addition of P as a sintering aid was more successful than B with respect to the resulting microstructure. Fig.6 show the dilatometer curves of the basic powder compacts*) ASC 100.29, PASC 60 (=ASC with 0.6% P, added as Fe_2P) and mixtures with NbC. PASC exhibits a larger thermal expansion than ASC 100.29, very little α-γ-transformation due to partial Fe-P-solid solution, but strong shrinkage above 1200°C and during isothermal sintering at 1300°C. The same is valid for the PASC-NbC-compact. The relatively good wetting behaviour of NbC by the P-containing liquid phase /5/ results in a sintered density of 93.5%, compared with 94% without NbC.

In order to get a hardenable matrix, the addition of C is advisable, which is also very favorable for sintering. In Fe-P-C-system a permanent liquid phase occurs, the amount depending on C-content. In Fig. 7 , the thermal expansion and sintering behaviour of Fe-NbC-P-C can be seen. In these experiments the isothermal sintering was adjusted to the C-content, ranging from 1320 to 1280°C. The onset of strong shrinkage is within the heating-up period in all compositions and lies as low as 1160°C in the compacts with 0.9% C. Final densities between 98 and 98.5% of theoretical have been achieved.

*) These compacts were pressed at 600 MPa to green densities of ∿90%.

It has to be emphasized that their is very little solid solubility of NbC in the Fe-based liquid phase and, consequently, NbC does not essentially take part in the liquid phase formation. The dilatometer curves are easy to survey and to explain. Variations of sintering temperature of ±10°C have no significant influence on final density as well as on microstructure, unlike in Fe-Mo_2C-system and in HSS. The amount and type of carbide phase in the sintered product is well defined.

Microstructural optimisation by mechanical alloying

Fig. 8 and 9 show the microstructures achieved with samples in the Fe-Mo-C and Fe-NbC-P-C systems in the as-sintered state. They contain grain boundary carbides, uneven carbide distribution and large residual pores in the Fe-Mo-C system. Although it was possible to improve the microstructure of Fe-Mo-C-specimen by heat treatment to some extent, it was decided to focus the following experiment on Fe-NbC-P-C due to its principle advantage in processing as mentioned above. Mechanical alloying was choosen for microstructural improvement.

For mechanical alloying a 1 h -treatment in a laboratory attritor in n-heptene has been applied. Tank, rotor and balls were made from unalloyed steel. In order to get an optimized distribution of NbC in Fe, the application of Carbonyl Iron instead of ASC was necessary, with mechanical addition of ferro phosphorous. A post-annealing of the powder at 600°C, followed by treatment in a tumbling device was advisable for improving the cold pressing behaviour, because the compressibility and tap density was decreased by attritoring as a consequence of deformation of the powder particles to thin plates and due to particle-particle welding effects.

After cold pressing (600 MPa) and sintering 1 h at 1280°C densities of >98% have been reached, independent on NbC-content between 10 and 30 vol-%. As shown in Fig.10, microstructure has been improved dramatically and meet the requirements much better than without attritor treatment. Similar results have been obtained with TiC as the hard component, but the densification is somewhat more difficult due to the worse wetting behaviour compared wit NbC.

Properties of Fe-NbC-P-C-alloys

Fig.11 shows some mechanical properties of mechanically alloyed Fe-10% NbC-0.6% P-C systems (C = 0.45; 0.6; 0.9%) in dependence on C-content and an nealing temperature. Their is a strong influence of carbon content on strength properties and the higher carbon containing materials exhibit very good properties after 450°C treatment. In the unannealed state a maximum in hardness

occurs at 0.6% C, due to the higher amount of residual austenite with higher C-content. In Fig. 12 two examples of long term strength data are shown as Wöhler diagrammes. Endurance limits of 335 and 385 MPa have been measured, which are pretty high values for sintered steels. Mechanical alloying is indispensable for high endurance limit, as seen in this figure. Preliminary abrasive wear and Vickers hardness data are collected in Fig.13 which shows an adequate low level of wear for the new alloys, generally less than Astalloy E.

Conclusions

Fe-MC-systems can be sintered to high densities, when a liquid phase takes place in the process. In case when the MC phase does not take part in liquid phase formation, P or P+C addition can take over this role, being very effective for densification. Fe-10-30% NbC-P-C alloys have been manufactured by powder route including mechanical alloying and investigated with respect to a perspective use as wear resistant material. Systems like this are not sensitive for change in MC-content and small variations in sintering temperature. Microstructure and mechanical properties of this system are promissing for further investigations.

Literature

/1/ R.Wähling, P.Beiss, W.J.Juppmann: Sintering Behaviour and Performance Data of HSS-Components, PM-Group-Meeting, Harrogate, Oct. 1984, 151

/2/ P.Beiss: PM-Methods for the Production of High Speed Steels, Metal Powder Report 38 (1983) 185

/3/ T.Suganuma: Development of Sintered Integral Camshaft, Metal Powder Report 38 (1983) 433

/4/ Höganäs-Information, Astaloy E, Febr. 1985

/5/ for more detailed description see:
R.Klausmann: Entwicklung von carbidhaltigen Sinterstählen mit hoher Verschleißfestigkeit (Dr.-Ing.-Dissertation), KfK 4137, Oct. 1986, Kernforschungszentrum Karlsruhe

/6/ H.Holleck: Binäre und ternäre Carbide und Nitride der Übergangsmetalle und ihre Phasenbeziehungen, KfK 3087 B, January 1981, Kernforschungszentrum Karlsruhe; Gebr. Borntraeger Verlag Berlin-Stuttgart, 1984

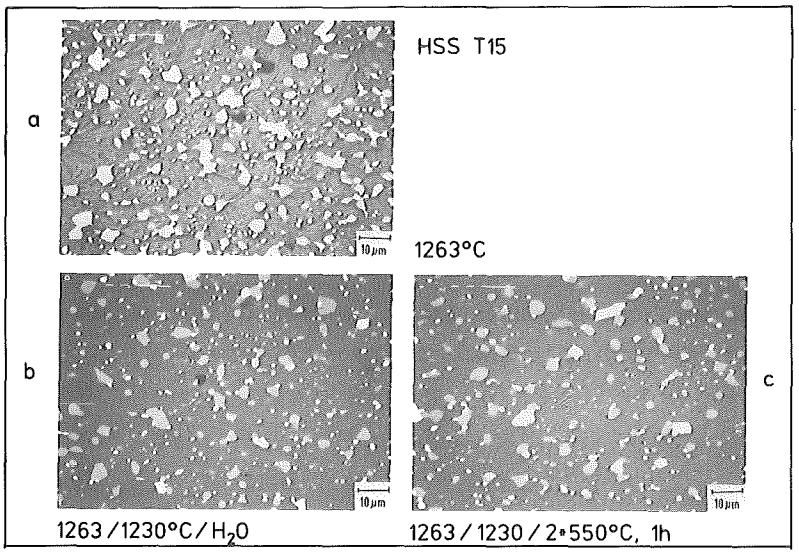

Fig. 1: Microstructure of PM HSS T15 after different heat treatments

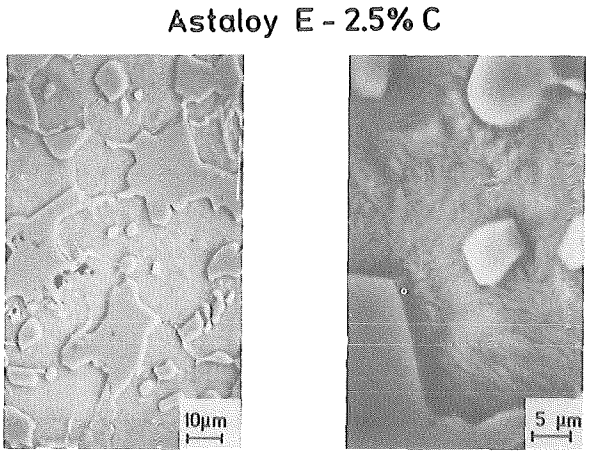

Fig. 2: Microstructure of Astalloy E with 2.5% C

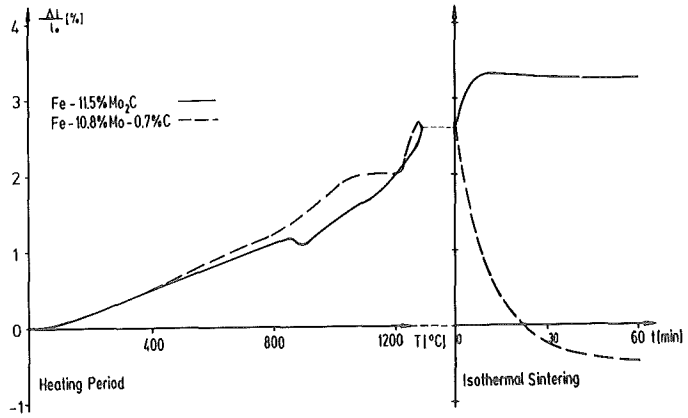

Fig. 3: Dilatometer experiments on Fe-Mo_2C and Fe-Mo-C mixtures

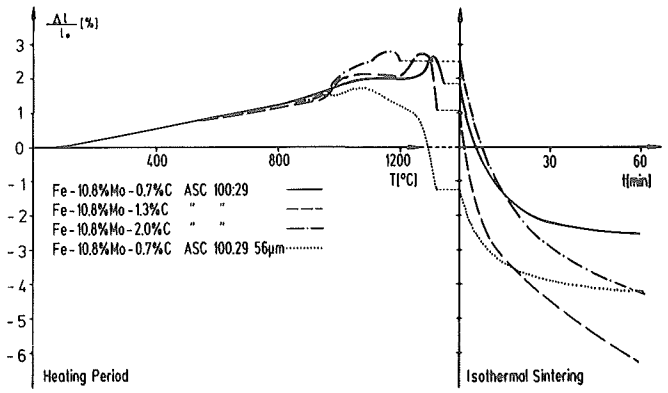

Fig. 4: Dilatometer experiment on Fe-Mo-C mixtures with different C-content

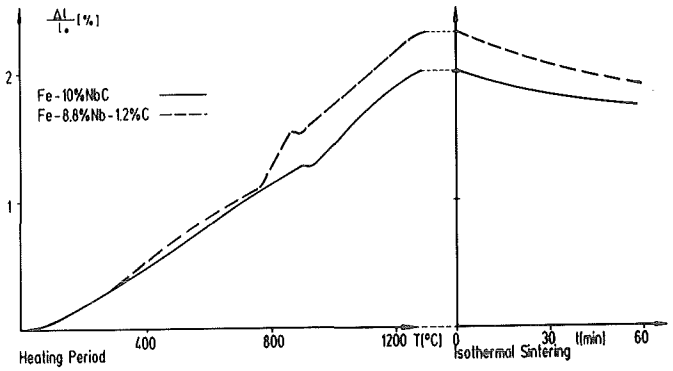

Fig. 5: Dilatometer experiments on Fe-NbC and Fe-Nb-C mixtures

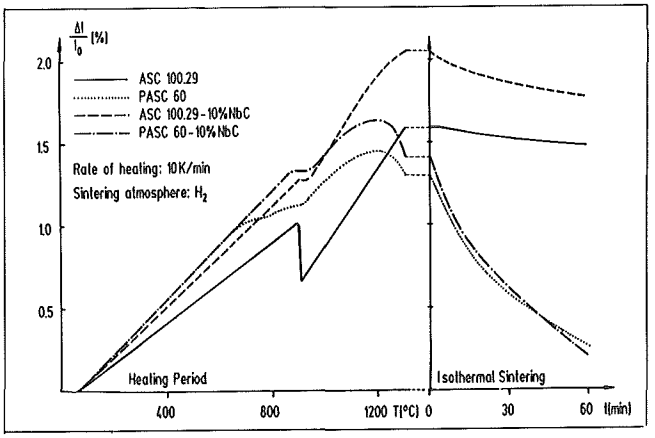

Fig. 6: Dilatometer experiments on Fe, Fe-P and Fe-NbC-P

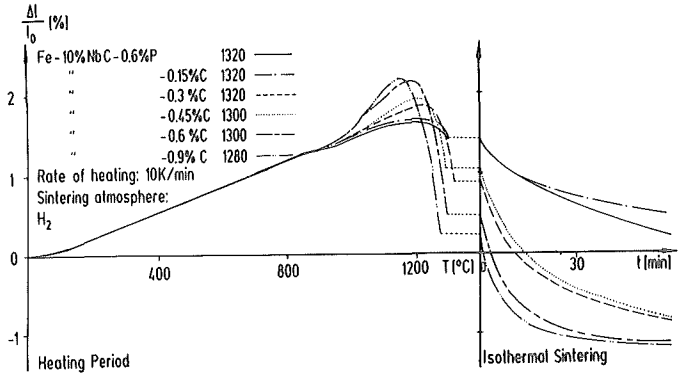

Fig. 7: Dilatometer experiments on Fe-NbC-P-C mixtures with different C-content

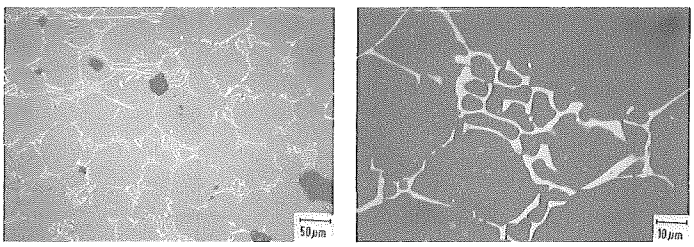

Fig. 8: Microstructure of Fe-10.8% Mo-2%C after sintering at 1170°C

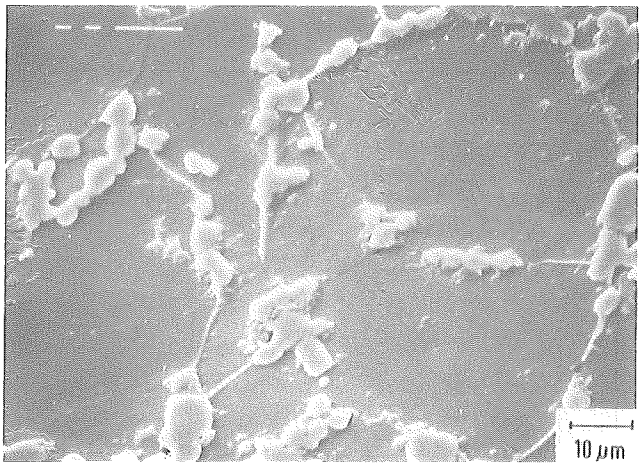

Fig. 9: Microstructure of Fe-NbC-P (PASC 60 + 10% NbC) after "normal" mixing, pressing and sintering (1 h/1320°C) procedure

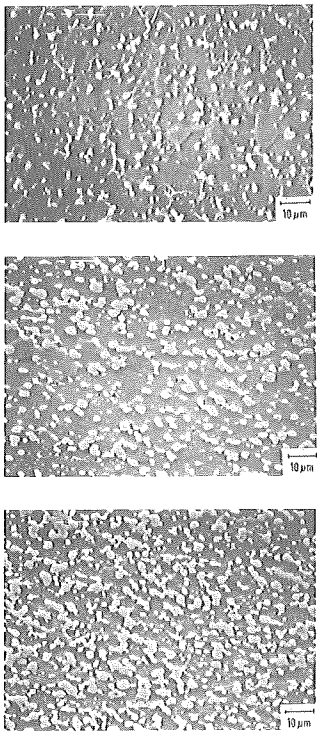

Fig.10: Microstructure of mechanically alloyed Fe-NbC-0.6%-P-materials

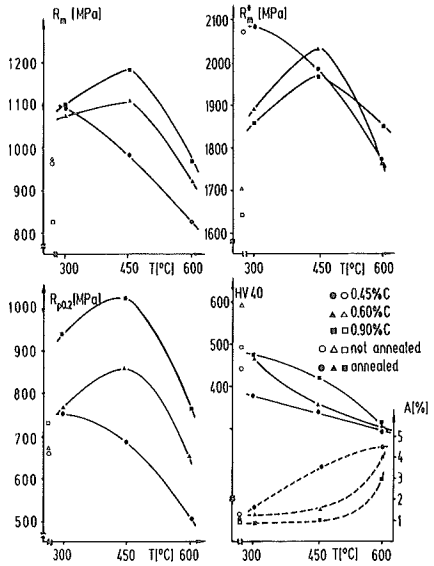

Fig.11: Tensile strength, bend strength, yield strength, hardness and elogation at fracture of mechanically alloyed Fe-10% NbC-0.6% P-C-systems with different C-contents without and after heat treatment

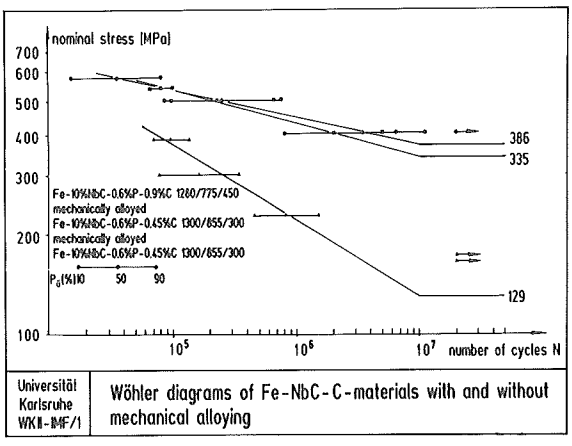

Fig.12: Wöhler diagrams of Fe-NbC-C-materials with and without mechanical alloying

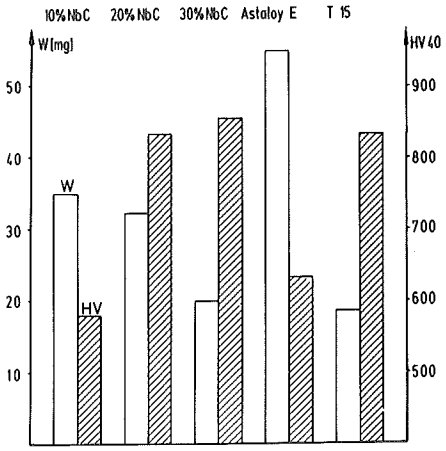

Abb.13: Abrasive wear and Vickers hardness of Fe-NbC-0.6% P-0.9% C-alloys, compared with Astaloy E and PM HSS T 15

PRODUCTION OF METAL POWDERS BY ROTATING ELECTRODE PROCESS

M.Zdujić, V.Petrović, L.Nelević* and D. Uskoković

Institute of Technical Sciences of the Serbian Academy of Sciences and Arts, Belgrade

*Institute of Aluminium, Titograd

ABSTRACT

The fabrication of metal powders the thermophysical properties of which differ considerably, can be performed by the rotating electrode process. The properties of molybdenum, titanium and aluminum powders were discussed. Some results of theoretical calculations concerning both droplets motion and solidification in helium and argon were given.

INTRODUCTION

Gas, water, vacuum and centrifugal atomization are the most frequently used processes in powders production by disintegration of liquid metal. Among the centrifugal atomization, the rotating electrode process (REP) is certainly the best known one. Various modifications of the above mentioned process have been developed till these days, but the basic principle of liquid disintegration, applying centrifugal energy, is the same. The electric arc discharge, plasma, electric beam and laser was used as the source for the metal melting. The review of different types of centrifugal atomization is given in literature /1/. Owing to the fact that the droplets are formed directly from the solid bar, the relative process is often utilized in titanium alloys powder production.

The purpose of this paper is to present experimental results obtained during atomization of different metals and alloys by the rotating electrode process. Apart from this, the theoretical calculations concerning simultaneous momentum and heat transfer as well as solidification of droplets are given.

MOMENTUM AND HEAT TRANSFER

As the control of REP operating parameters proved to be very good, the phenomena occuring in the course of atomization can be theoretically described to a certain degree.

The velocities of droplets, i.e. particles in function of time are presented in Figure 1. The initial velocity by which the droplets leave the electrode is defined by the equation: $u_o = \omega D/2$, where ω - angular velocity (rad/s) and D - electrode diameter (m). It was assumed that the atmosphere in the

atomization chamber was stangant. The equations defining the particles motion were given previously /2/. As the density of argon is higher when comparing to helium, the velocity drop in argon is greater than it is in helium. The particles not exceeding 50 μm in size, reach the therminal (free falling) velocity rapidly.

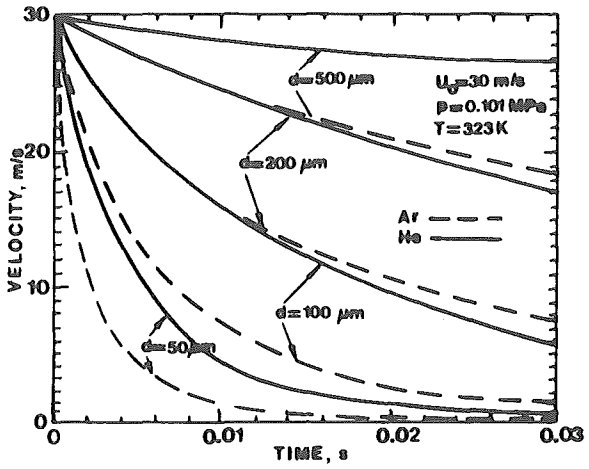

Fig.1. Calculated particle velocity in argon and helium as a function of time of the titanium REP powders.

The calculation of the solid-liquid position being the function of time is carried out when assuming that the temperature is uniform inside solidificating droplets and that the heat is extracted from the droplets surface both by convection and radiation (so called Newtonian cooling). The equations describing this approximative solidification conditions can be found in the reference /3/.

The convective heat transfer coefficients for each droplet in argon and helium was calculated from the Nusselt number. It is obvious from Fig.2 that a solid-liquid interface velocity increases with the progress of solidification.

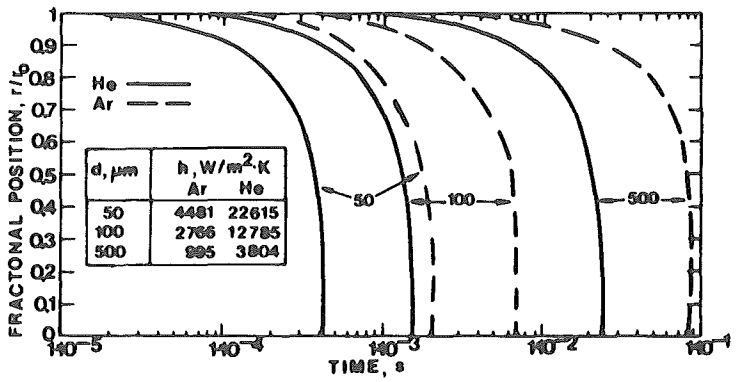

Fig.2. Calculated fractional position of the solid-liquid interface as a function of solidification time for the titanium REP particles.

The influence of the particle diameter and its initial velocity on the required solidification path length is shown in Fig.3. The details of the calculation can be found in our previous work /2/.

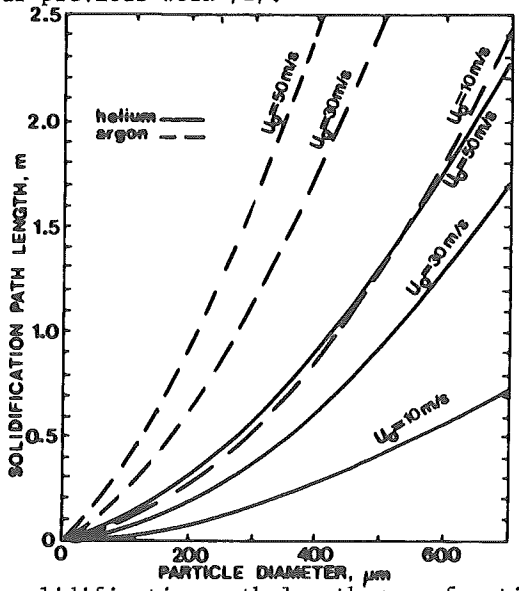

Fig.3. Calculated solidification path length as a function of particle diameter and initial velocity for the titanium REP powders.

EXPERIMENTAL

All the experiments presented in this paper were performed at the laboratory apparatus constructed and installed in the Institute of Technical Sciences of the Serbian Academy of Sciences and Arts. The lay-out of this equipment was described previously /2/. The rotating electrode diameter and the angular velocity can be changed within the range 0.01 - 0.04 m and 500 - 2200 rad/s, respectively.

The electric arc melting was carried out by a direct current power supply. Either helium or argon was used as the inert atmosphere. Molybdenum, titanium alloys, iron alloys and aluminum with its alloys have been the materials which were successfully atomized up to the present days.

The experimental results for each atomization run were compared to the literature correlations which predict disintegration mechanisms, the mean particle diameter and the particle size distribution /4, 5/. In all these cases good agreements were obtained.

The protuberances from which the droplets were formed off are shown in Fig.4 and it is obvious that their number increases with the rise in angular velocity.

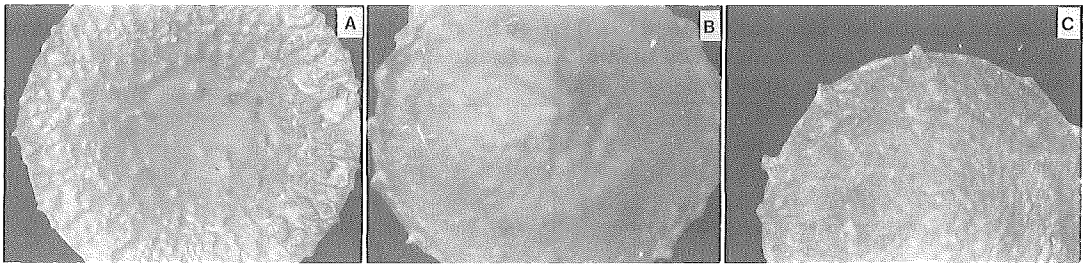

Fig.4. Solidified protuberances at the edge of the rotating electrode: a) ω = 2094 rad/s; b) ω = 1047 rad/s; c) ω = 524 rad/s (high speed steel; D = 0.01 m).

RESULTS AND DISCUSSION

The morphology of different powders obtained by rotating electrode process are shown in Figs.5, 6 and 8. Molybdenum powders obtained under two different operating parameters are shown in Fig.5. In both cases the powders produced have very narrow particle size distribution (defined by geometric standard deviation σ_g). The powder particles are spherical and have no satellites. Smaller particles are of finer structure (dendrite size is small) compared to the large ones, what results from a higher cooling rate. The surfaces of two particles being different in size are shown at the bottom of Fig.5 (under the same magnification). The rise in particle size is followed by increase in dendrite and grain size /6/, and this dependence is presented in Fig.9. It should be noted that the dendrite size (grain size) is smaller at the surface than it is inside particles. It certainly is connected with solidification parameters such as are temperature gradient in the liquid phase, solid-liquid interface velocity and the cooling rate.

The powder morphology of Ti-5Al alloy is given in Fig.6. The particles are also spherical in shape although are somewhat smaller when compared to molybdenum powder. The particle size distribution is broader what has a higher apparent density and a tap density, as a result. The particle surfaces are smooth (Fig.6. bottom left),although the grain boundaries can be recognized on some of them (Fig.6. bottom right). The microstructure of the powder is martensitic thus indicating a rapid solidification. The comparisson of microstructure of the starting ingot with the obtained powder from the same, is shown in Fig.7. Our observations show that the pores are present, to a certain degree in Ti-5Al powder but they are very rare in molybdenum powder.

With the aim to investigate the rapidly solidified aluminum alloys and the possibilities of their production by rotating electrode process, some atomization experiments of technical pure aluminum and Al-5Mg alloy were performed. A characteristic fine dendritic structure of aluminum powders is given in Fig.8. According to the direction of the primary dendrites visible on the larger particles (Fig.8.b), it can be concluded that the previously solidified smaller particle (satelite) acts as a nucleating agent. However, as the satellites proved not to be typical for REP powders, it seems that the mentioned mode of nucleation is not characteristic for these particles

POWDER	d_m, μm	σ_g	APPARENT D.(%T.D.)	TAP D. (%T.D.)	FLOW RATE(s/50g)
a	209	1.17	60.0	63.8	9
b	602	1.07	60.8	63.9	13

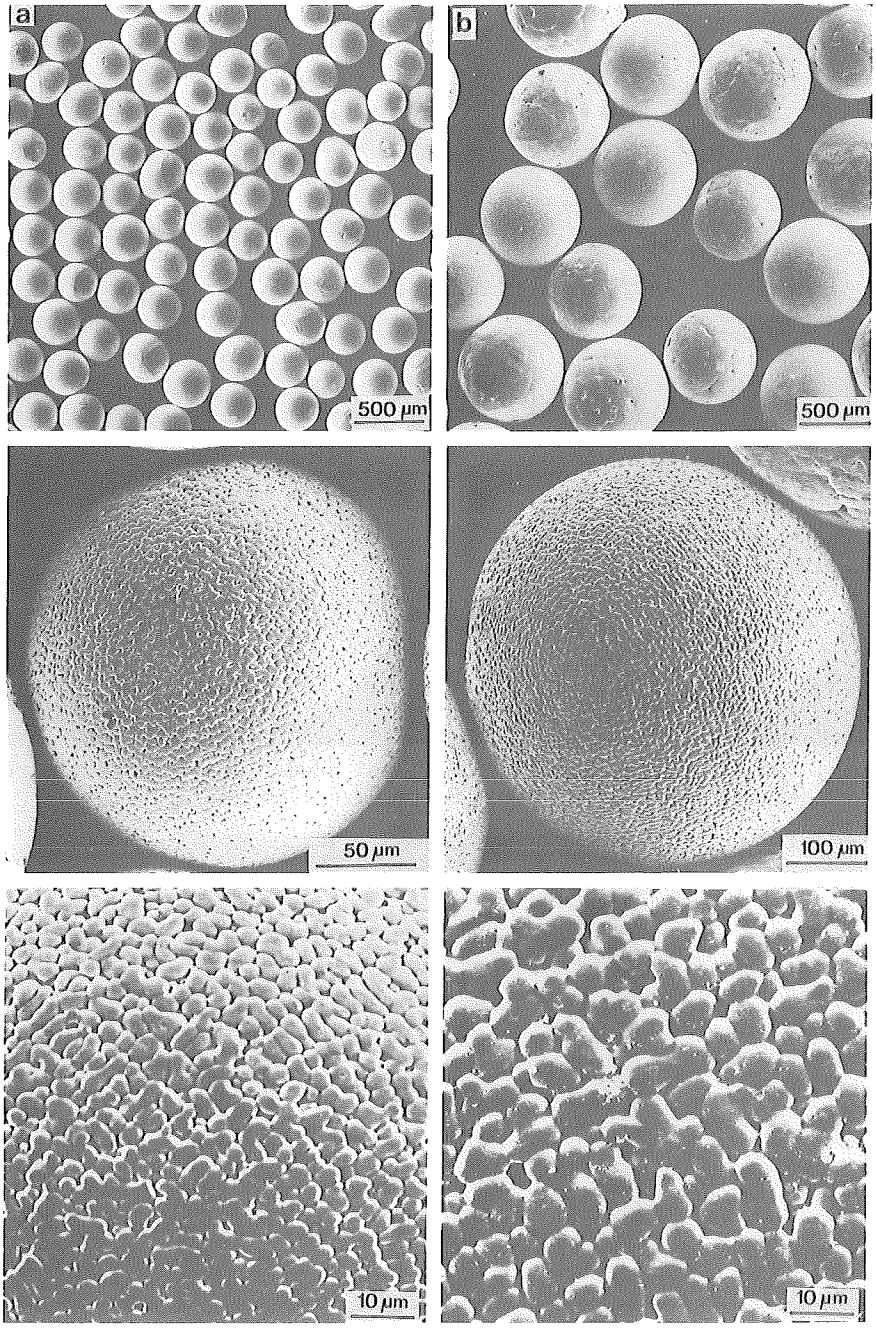

Fig.5. Particle morphology of the molybdenum powders produced by the rotating electrode process: a) D = 0.015 m, ω = 1885 rad/s; b) D = 0.02 m, ω = 524 rad/s.

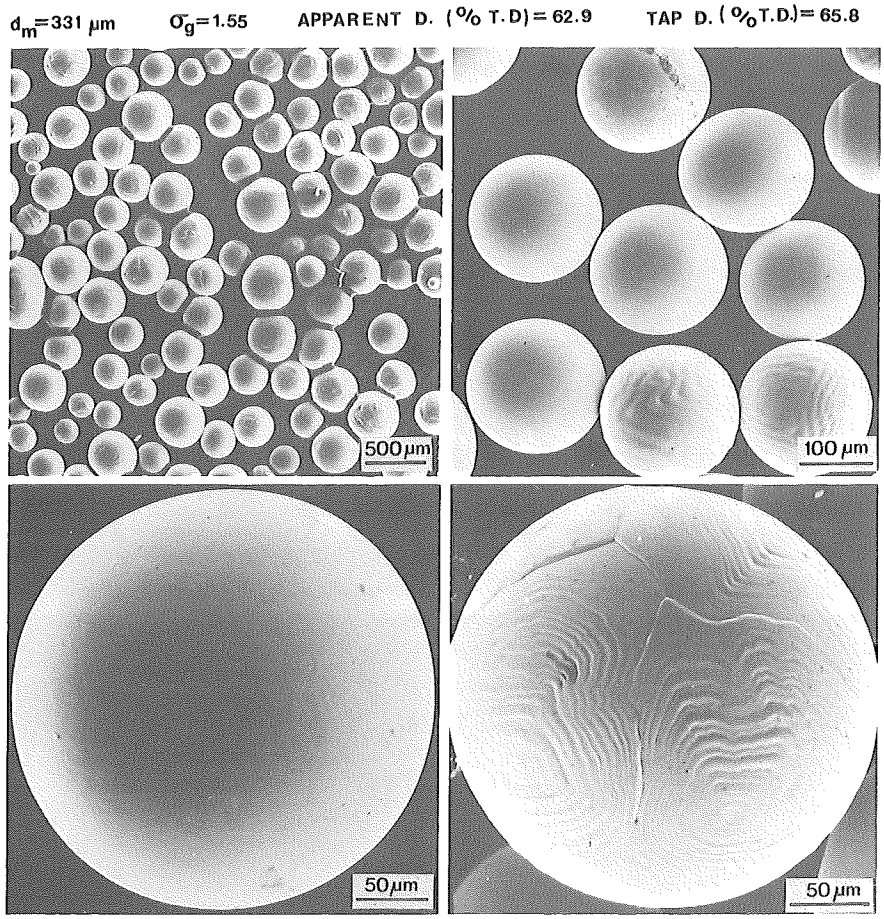

Fig.6. Particle morphology of the Ti-5Al powder produced by the rotating electrode process: D = 0.015 m, ω = 1466 rad/s.

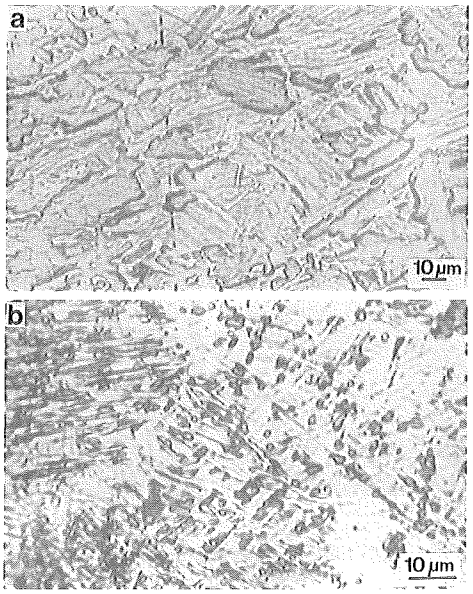

Fig.7. Microstructure of a) Ti-5Al ingot and b) obtained powder.

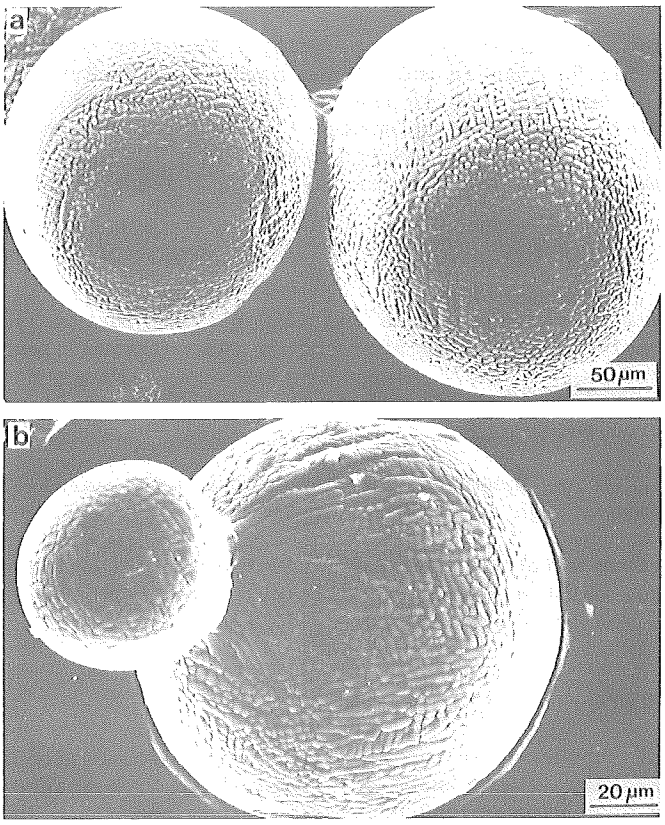

Fig.8. Particle morphology of the aluminum powder produced by the rotating electrode process; a) fine dendritic structure: b) particle with a satellite as a nucleating agent.

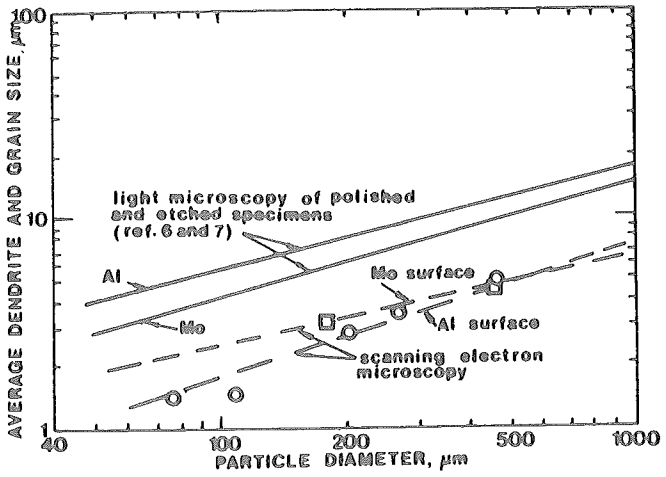

Fig.9. Dendrite arm spacing and grain size as a function of particle diameter, for pure molybdenum and technical pure aluminum powder obtained in helium and argon, respectively.

solidification. A dendrite spacing, being a function of a particle size, is presented in Fig.9. Like in molybdenum powders, a dendrite spacing is also smaller on the surface than in the particle body itself. The cooling rate of aluminum powders, estimated by means of a dendrite spacing is in the range 10^1 - 10^3 K/s for the particle size range 600 - 100 μm, and is an order of magnitude smaller that the theoretical calculation predict /7/.

CONCLUSION

a) The powders of various metals and alloys which thermophysical constants differ considerably can be produced by the rotating electrode process,

b) The mean particle size as well as the particle size distribution can be well controlled,

c) The particles are spherical in shape and have no satellites; thus the powders have a high apparent and tap density,

d) For the given material, the solidification structure changes with a particle size, being a result of different conditions under which the particles of various diameters are solidificated.

ACKNOWLEDGEMENTS

This work was supported by the Serbian Research Foundation and Prvi Partizan, Hard Metal Factory. The authors are grateful to Dr.B.Novaković and to Dr.B. Radonjić for supplying molybdenum and aluminum rods.

REFERENCES

1. S.J.Savage and F.H.Froes. "Production of Rapidly Solidified Metals and Alloys", Journal of Metals 36 (1984) 20-33.
2. M.Zdujić, M.Sokić, V.Petrović, D.Uskoković, "The Study of Properties and Cooling Rates of Steel Powders Obtained by Rotating Electrode Process, Part I and II", Powder Metallurgy International 18 (1986) 275-277,325-329.
3. C.G.Levi and R.Mehrabian, "Heat Flow in Atomized Metal Droplets", Metallurgical Transactions B 11B (1980) 21-27.
4. B.Champagne and R.Angers, "REP Atomization Mechanisms", Powder Metallurgy International 16 (1984) 125-128.
5. B.Champagne and R.Angers, "Size Distributions of Powders Atomized by the Rotating Electrode Process", Modern Development in Powder Metallurgy 12 (1980) 83-104.
6. M.Zdujić, V.Petrović, D.Uskoković, "Preparation of Molybdenum Powders by Rotating Electrode Process", Sintering '85, Proceedings of the VI World Round Table Conference on Sintering, Edited by G.C.Kuczynski et al.(1987) 101-108.
7. M.Zdujić, V.Petrović, D.Uskoković, "Properties of Titanium and Aluminum Powders Centrifugally Atomized by Rotating Electrode Process", Presented at the Conference Theory and Practice of Sintering, Zlatibor, 3-6 September 1986 (to be published).

COOLING RATE, UNDERCOOLING AND RAPID SOLIDIFICATION BY ATOMIZATION

K. Rzesnitzek, W.A. Kaysser and G. Petzow

Max-Planck-Institut für Metallforschung
Institut für Werkstoffwissenschaften
Heisenbergstr. 5, D-7000 Stuttgart

INTRODUCTION

Rapid Solidification Processing received scientific interest since the experiments of P. Duwez in 1960, due to advantages as:

- refinement of microstructures
- decreased segregation
- formation of metastable and new phases
- increased solid-solubility ranges

Gas or water atomization are valuable methods for producing rapidly solidified powders for high performance materials in large quantities. The paper presents part of an investigation on some fundamental aspects of powder production in a semipilot scale. The obtained microstructures depend on cooling rate, undercooling and nucleation conditions of the molten droplets.

EXPERIMENTAL EQUIPMENT

The principal arrangement of the atomizer is shown in fig.1. The alloys are induction molten in a graphite crucible. After reaching the temperature the orifice at the lower end of the crucible is heated up and the melt starts to flow. After passing the nozzle the melt stream is hit by the atomizing gas and thereby divided into small droplets which solidify during their flight by convective heat transfer to the surrounding gas. The cooling rates are up to 10^5 K/s.

UNDERCOOLING

One important factor controlling the microstructural development is the degree of undercooling. The degree of undercooling in our experiments was estimated by comparing the x-ray diffraction analysis of the powders produced to the equilibrium phases. Figure 2 shows the Cu-Sn phase diagram and the phases obtained in the particle size fraction < 30 µm of different alloy compositions.
For droplets smaller than 30 µm an undercooling by 150 K and more is usual.

Fig. 3 shows the microstructure of an atomized Cu-20Sn alloy. The particles larger than 80 µm in diameter (fig. 3a) consist of dendritic α-phase. In the particle size range between 30 and 80 µm (fig. 3b), both the dendritic α-phase and the segregation free β-phase appear. Doubling the magnification (fig. 3c) shows, that the segregationfree β-phase particles, contain more or less spherical areas that solidified most likely at first. Minor segregations can be seen in the rest of these particles, which developed radially from the first solifified zones.

COOLING RATE

An important aspect of the atomization is the knowledge of the cooling rate. The calculation of the cooling rate from the thermal data is based on several assumptions:

- the melt stream is divided into spherical droplets, with diameter d, by the gas jet
- the droplets are accelerated by the gas stream and thereby the relative velocity between the particle and the gas changes
- the heat transmission is calculated from the relative gas velocities and the thermal data of the melt droplets and the atomizing gas using the Nusselt number Nu.
- as the dimensionless Biot number Bi is << 0.01 the Newtonian cooling conditions are valid. This means that no temperature gradients appear within the particles. For the calculation of the Biot number the thermal conductivity K and the heat transfer coefficient h must be known.
- when the temperature of undercooling is attained, nucleation starts instantaneously. The cooling rate is calculated using the specific weight and the heat capacity c_p of the particle.
- the cooling rate during the removal of the latent heat of fusion is called the "local solidification rate" /1/

$$\frac{\Delta T_p}{\Delta t} = \frac{6\,k\,Nu\,(T_p - T_g)}{d^2\,\rho\,c_p} \qquad Bi = \frac{h\,d}{K}$$

The cooling rate vs. time of an Cu-7Sn droplet 10 µm in diameter is shown in fig. 4. After droplet formation the relative velocity between gas and droplet is high and the cooling rate is one order of magnitude higher than during actual solidification. Solidification is indicated by a small peak due to the latent heat of fusion. So the "local solidification rate" is determined mainly by the type of the gas and not by the gas velocity at the nozzle. A high gas velocity at the nozzle of course leads to smaller particles and thereby to higher cooling rates, as the cooling rate is depending on the square of the particle diameter.

MEASUREMENT OF THE COOLING RATE

The formation of the microstructure depends on the local solidification rate. For alloys with dendritic solidification the Secondary Dendritic Arm Spacing (SDAS) is a measure for the cooling rate. Fig. 5a-c shows different dendritic structures of Cu-7Sn solidified at different cooling rates.

The SDAS becomes smaller with increasing cooling rate. Kattamis developed a model that describes the SDAS controlled by a ripening process during the time the dendrites and the melt are in contact /2/. Fig. 6 shows 3 mechanisms for the ripening of secondary dendrite arms. The first was developed by Kattamis. One dendrite arm has a smaller radius than his neighbours and therefore its melting point is lower than the melting point of the remaining arms. In an isothermal melt the small arm will disappear by transport of material to the larger arms. The local dendrite arm spacing increases. In the second model, from Chernov et. al., the root of a dendrite is smaller than its remainder. The necked region melts off and the remaining rest may be swept back into the melt and act as a nucleus. The third model, from Kahlweit, considers a single dendrite arm with a twofold radius of curvature at its tip. Here the material is transported back to the cylindrical surface by diffusion /3/.

The model of Kattamis is described by the equation:

$$\dot{T} = (5.5/\lambda_2) M \Delta T$$

$$M = \frac{\sigma D \ln(c_l/c_0)}{\Delta S^m m(1-k_0)(c_0-c_l)}$$

M = coarsening factor
k_0 = equilibrium partition coefficient
D = diffusion coefficient
σ = specific interface energy
m = slope of liquidus line
ΔS^m = entropy of fusion
c_l = composition of the melt
c_0 = initial composition of the melt

With the knowledge of the thermodynamic data of the alloy system the correlation between SDAS λ_2 and cooling rate $\dot{T}$ is given.
We calculated the cooling rate of Cu-7Sn particles for atomization and splat-cooling. For the condition of furnace cooling the cooling rate was measured directly by a thermocouple. In fig. 7 these cooling rates are compared with the ripening model of Kattamis. It is in good agreement with the calculated cooling rates. Our method for calculation of the cooling rate seems to be, hence valid, we are able to calculate the cooling rates for other alloys without measuring the microstructural features.

NUCLEATION

During normal cooling of an alloy droplet always multiple heterogeneous nucleation occurs. This can be seen by the different growth directions in the particle shown in fig. 8.
If an undercooled droplet is hit by a single potent nucleus, e.g. a satellite, nucleation starts at once and an apparently directed solidification occurs, actually it is an isotropic growth (fig. 9). Different orientations are visible due to etching with Klemm III and the use of polarized light.

A method to increase undercooling is to minimize the number of potent nuclei. The nuclei in our alloy melts are thought to be metal oxides. If these nuclei are converted into inert oxides, the nuclei density will strongly decrease. With the addition of Al the metal oxides will be transformed into inert, fine dispersed aluminumoxide particles. Since aluminumoxide does not act as nucleus in bronze alloys this method should lead to large undercoolings.

With an initial undercooling large enough to allow the particle to be its own heat sink, very rapid solidification velocities are realized. If the particle reaches, due to the latent heat of fusion, the solidus temperature again before solidification is completed, the remaining liquid solidifies by the normal external heat flow.
Boettinger gave a hierarchy of equilibrium (fig. 10) /4/. In the normal metallurgical practice condition III is required. Condition IV shows a significant loss of interfacial equilibrium. This is important for simple metallic phases when the crystal growth rate exceeds the diffusive speed of solute atoms in the liquid phase. In this case solute trapping occurs and leads to a segregation free solidification.

The large Cu-7Sn particle in fig. 11 generated from a purified melt shows an area where solidification occured segregation free. The rest of the particle shows the usual microstructure due to solidification by external heat flow. The SEM photograph in fig. 12 shows a similar Cu-7Sn particle also with a large area of segregation free solidification. The small white points herein are the fine dispersed aluminumoxide particles.

Segregation free solidification is possible if the growth velocity v_E of the solidification front is larger than the diffusional speed of the solute atoms. In the above example a solidification front velocity of about 4 m/s is required. The usual solidification front velocity in our particles by cooling by convective heat transfer without initial undercooling can be calculated with /4/:

$$V_E = \frac{6 \cdot h_i \cdot \Delta T}{L}$$

Which results in a front velocity of 2.4 cm/s. In this case the latent heat of fusion L is only diminished by the external heat transfer to the atomizing gas. In the case of large undercoolings the solidification front velocity can become some orders of magnitude higher. Unfortunately no data are available for the system Cu-Sn.

CONCLUSIONS

In our atomizer we obtained undercoolings of the droplets smaller than 30 µm by 150 K and more. The calculation of the cooling rate from thermal data is in good agreement with the dendrite ripening model from Kattamis based on thermodynamical data. The resulting dendritic microstructures are a product of the time the dendrites and the melt are in contact. The gas velocity at the nozzle determines the particle size. During the solidification of the droplet there is only a minor relative velocity between the gas and the particles. So the cooling rate is mainly determined by the type of gas and the droplet diameter.

The nucleation conditions normally generate a dendritic microstructure. By cleaning the melt from heterogeneous nuclei large undercoolings are obtainable and solidification can occur in a segregation free manner.

REFERENCES

/1/ T.W.Clyne, R.A.Ricks, P.J.Goodhew, "The Production of Rapidly-Solidified Aluminum Powder by Ultrasonic Gas Atomization. Part I: Heat and Fluid Flow", Int. Jour. Rapid Solidification, 1, 59-80(1984).

/2/ T.Z.Kattamis, J.Coughlin, M.C.Flemings, Trans. Met. Soc. AIME, 239: 1504(1967).

/3/ M.Flemings,"Solidification Processing", McGraw-Hill Series in Materials Science and Engineering, New York, 1974.

/4/ W.J.Boettinger, S.R.Coriell, "Microstructure Formation in Rapidly Solidified Alloys" in Science and Technology of the Undercooled Melt, Eds. P.R.Sahm, H.Jones, C.M.Adam. NATO ASI Series E; no.114. 81-110,1986

Acknowledgement: This work was supported by Deutsche Forschungsgemeinschaft.

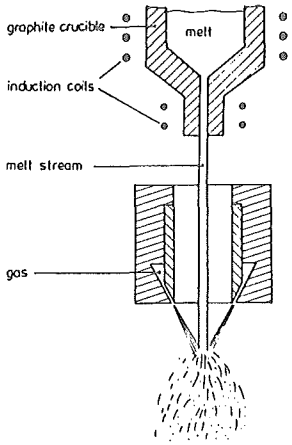

Fig. 1. Principal arrangement of the atomizer

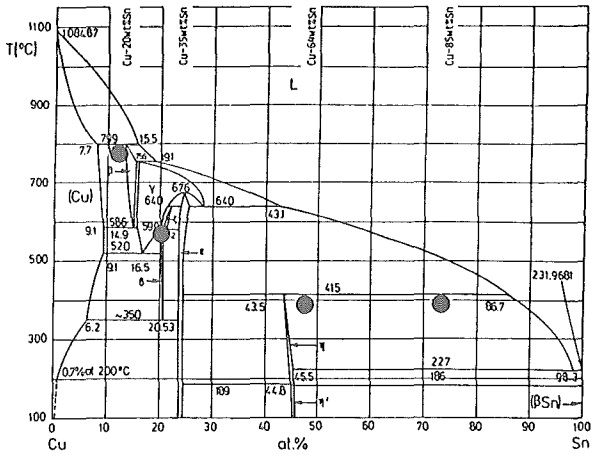

Fig. 2. Phase diagramm Cu-Sn. Phases obtained by atomization (<30µm)

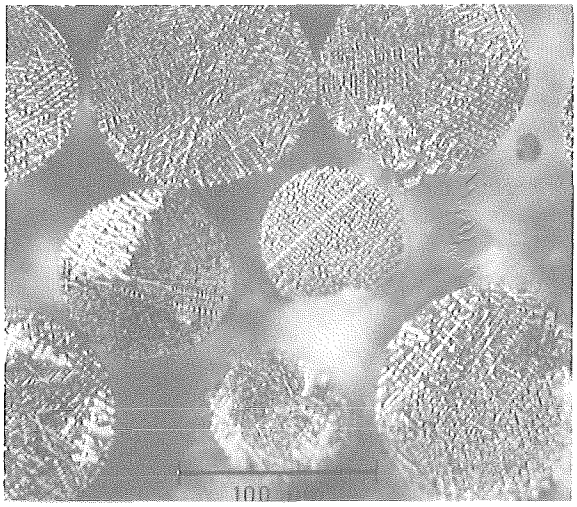

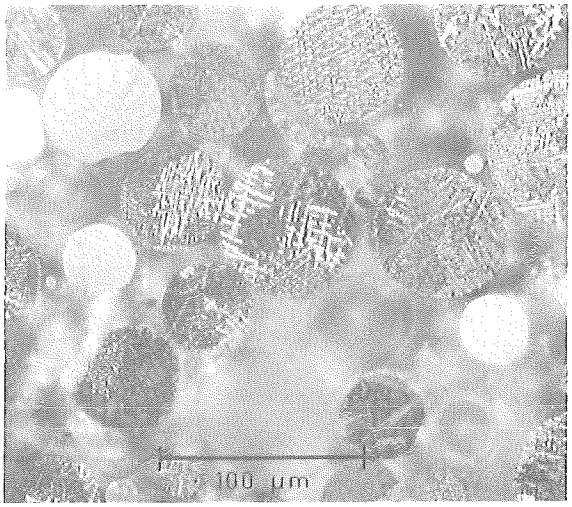

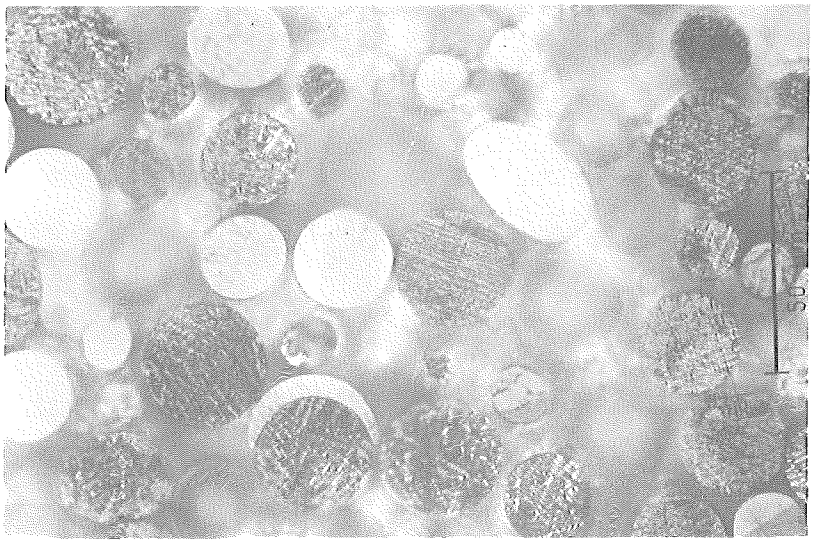

Fig. 3. Microstructure of atomized Cu-20Sn. α-dendritic, β-light phase.

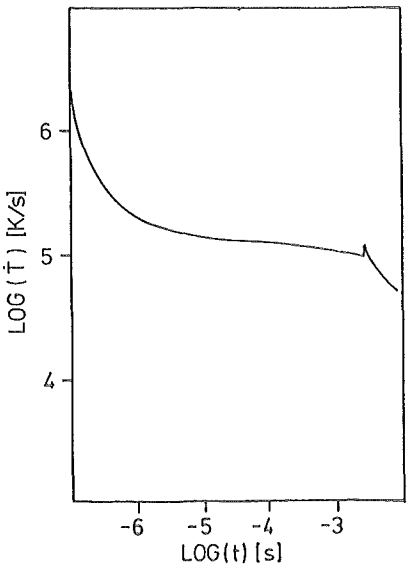

Fig. 4. Cooling rate vs. time of a Cu-7Sn particle 10 µm in diameter during atomization

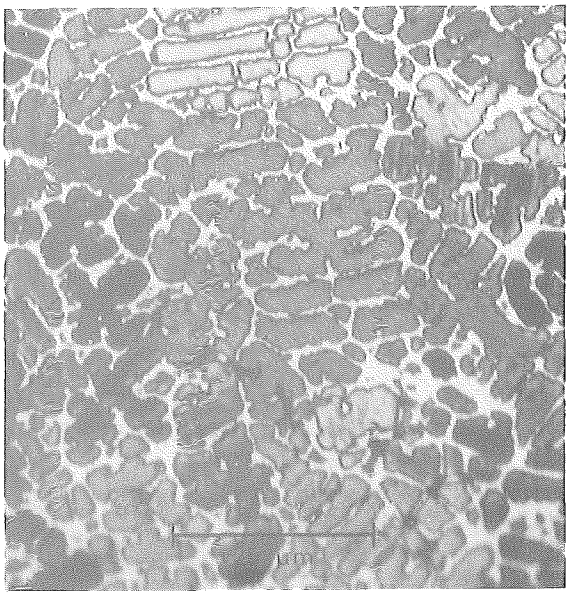

Fig. 5. Microstructure of Cu-7Sn
a. 2 mm droplet, waterquenched 500 K/s
b. atomized particles, 10^4 k/s - 10^5 K/s
c. splat-cooled particle, 10^7 K/s

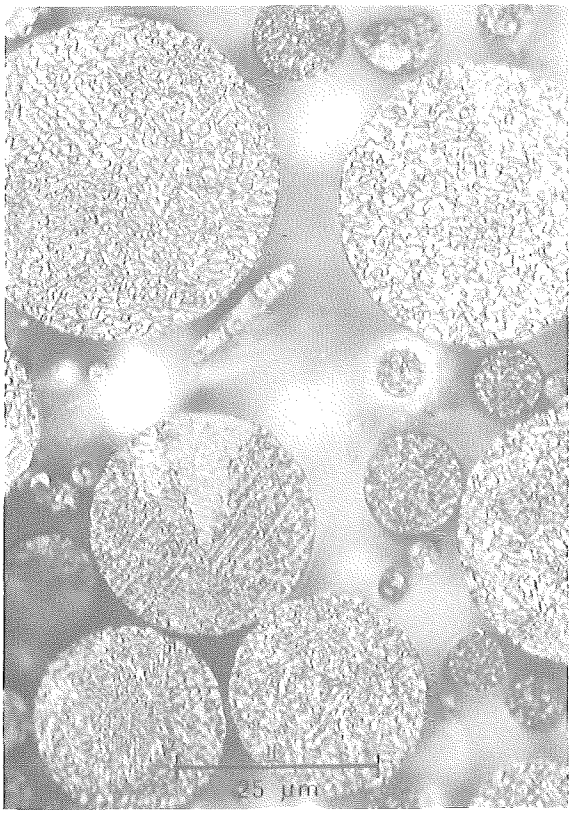

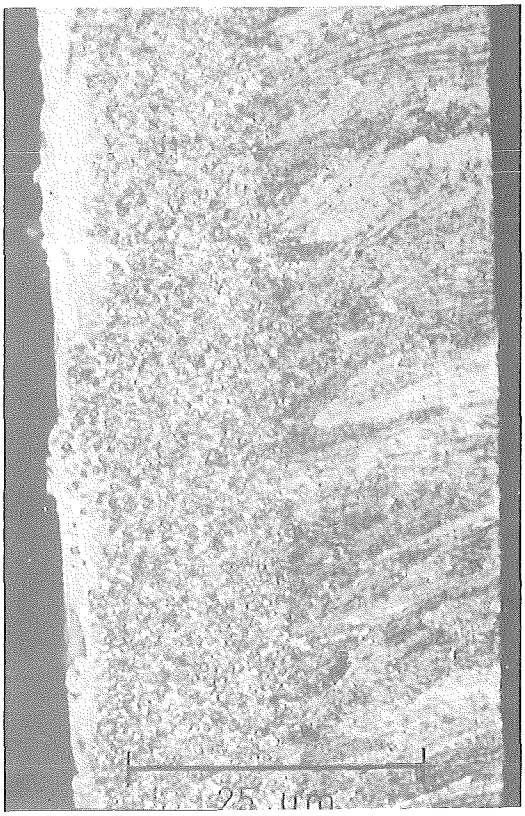

Fig. 6. Ripening of secondary dendrite arms

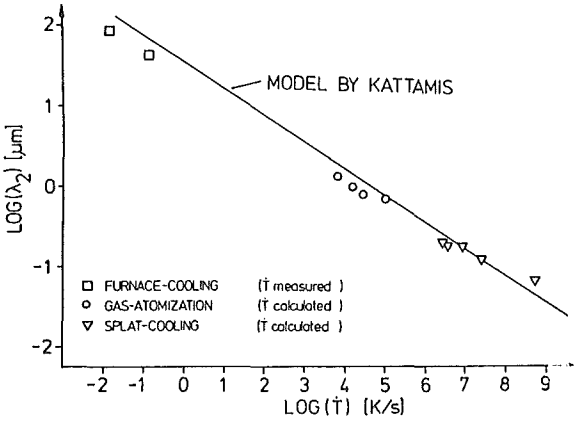

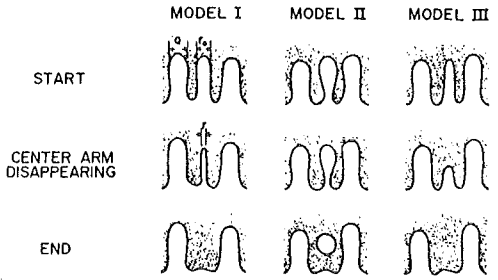

Fig. 7. Comparison of calculated cooling rates and the model of Kattamis

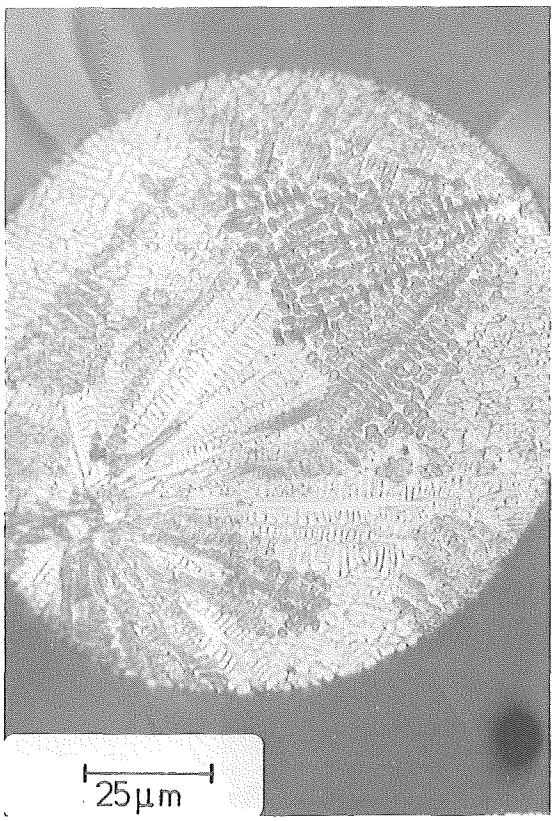

Fig. 8. Multiple heterogeneous nucleation in Cu-7Sn

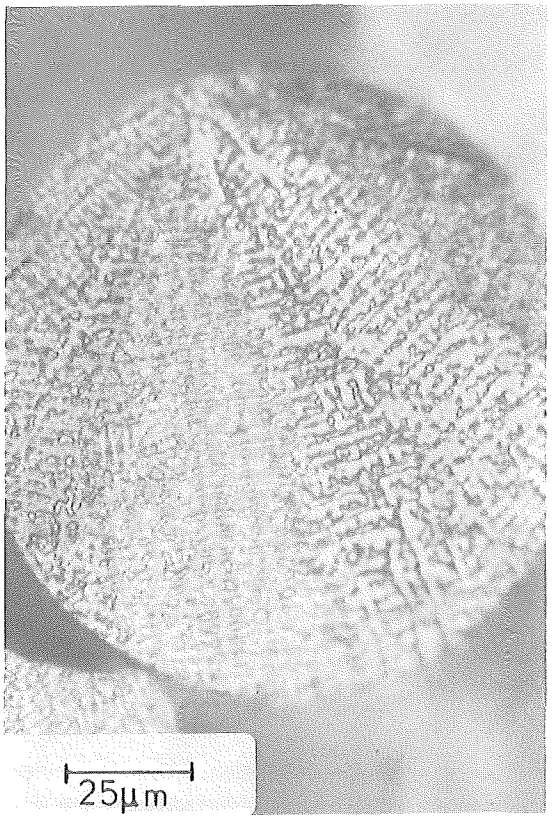

Fig. 9. Single nucleation event in Cu-7Sn

Increasing Solidification Rate ↓

I. Full Diffusional (Global) Equilibrium

A. No chemical potential gradients (composition of phases are uniform)
B. No temperature gradients
C. Lever rule applicable

II. Local Interfacial Equilibrium

A. Phase diagram gives compositions and temperatures only at liquid-solid interface
B. Corrections made for interface curvature (Gibbs-Thomson Effect)

III. Metastable Local Interfacial Equilibrium

A. Stable phase can not nucleate or grow sufficiently fast
B. Metastable phase diagram (a true thermodynamic phase diagram missing the stable phase or phases) gives the interface conditions

IV. Interfacial Non-Equilibrium

A. Phase diagram fails to give temperature and compositions at interface
B. Chemical potentials are not equal at interface
C. Free energy functions of phases still lead to criteria for the impossible

Fig.10. Hierarchy of equilibrium

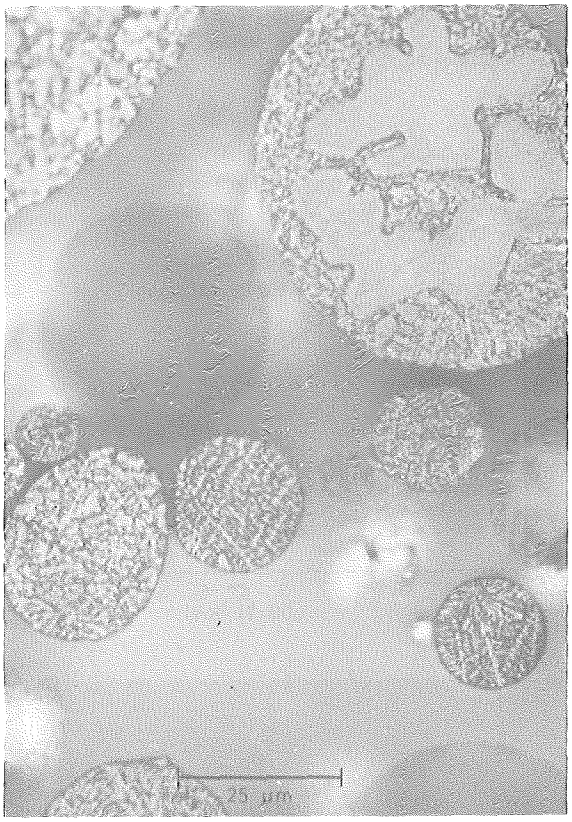

Fig.11. Cu-7Sn with segregation free solidified areas

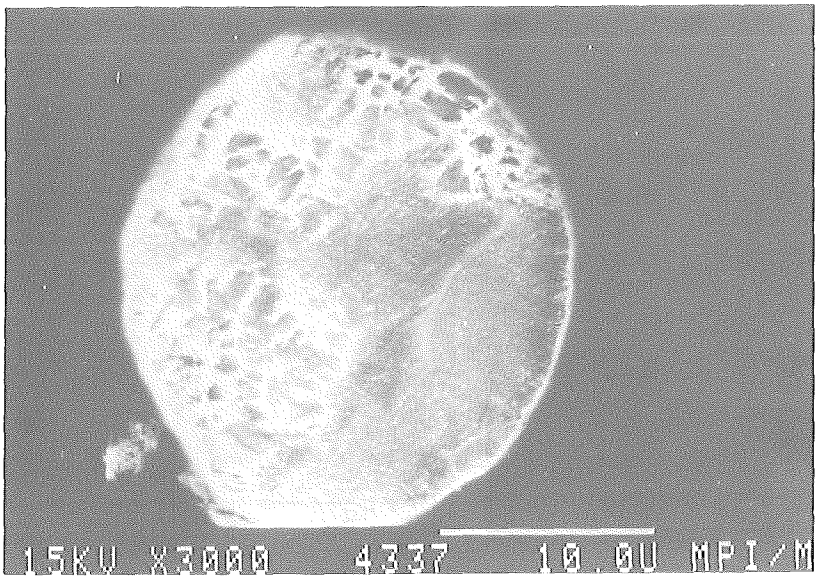

Fig.12. SEM micrograph of Cu-7Sn, partial segregation free. The white dots are entrapped Aluminumoxide particles

MECHANICAL PROPERTIES OF GAS ATOMIZED Cu-Ti AND Cu-Ti-B ALLOYS

D.Bosic[§*], R.Laag[*], W.A.Kaysser[*] and M.Mitkov[§]

[*]Max-Planck-Institut für Metallforschung
Institut für Werkstoffwissenschaften
Heisenbergstr.5, D-7000 Stuttgart 80, West Germany

[§]Institute Boris Kidric, 11001 Beograd, Jugoslavia

INTRODUCTION

Alloys of Cu-Ti are mainly used as:

- Electric conductors and contact materials with increased microhardness and only slightly decreased electrical conductivity compared to unalloyed Cu.
- Wear-resistant materials, with a high amount of the intermetallic phase Cu_4Ti.
- Dispersion hardened copper-alloys for welding-machines, where a high microhardness is obtained by additional dispersion strengthening /1/.

Alloying copper with titanium increases the hardness by the formation of Cu_4Ti precipitates from the supersaturated α-Cu(Ti) solid solution during ageing. The specific resistivity increases slightly due to the precipitation. As shown schematically in Fig.1a, part of the Ti remains in solid solution due to considerable solid solubility of Ti in Cu at the ageing temperatures.

In our investigation we tried to improve the mechanical and electrical properties of Cu-Ti by the addition of boron. If equivalent amounts of B and Ti are added to Cu, extremely stable TiB_2 precipitates form during ageing which should provide an increased hardness. The solubility of titanium and boron in α-Cu solid solution in equilibrium with TiB_2 is expected to be extremely small which leads to a high electrical conductivity. However, during slow cooling of ternary Cu-Ti-B melts the primary solidification of TiB_2 yields precipitates, which were too coarse for effective precipitation hardening (Fig. 1a,b). The intention of our experiments was to avoid primary precipitation of TiB_2 during solidification and to keep Ti and B in a supersaturated Cu solid solution (Fig. 1c). For this purpose the Cu-Ti-B alloys were cooled and solidified rapidly. The supersaturated solid solutions were aged to obtain the complete depletion of the Cu solid solution from Ti and B by the precipitation of fine TiB_2 (Fig. 1d).

EXPERIMENTS

Prealloys of Cu-Ti-B were molten in boron nitride crucibles and subsequently cast into a copper-mold. The prealloys were heated to 1400 °C and Ar-atomized. The usual metallographic techniques were applied.

EXPERIMENTAL RESULTS

Figure 2a shows cast Cu-4Ti (all concentrations are in weight percent). Solidification at a cooling rate of approximately 100 Ks^{-1} resulted in a dendritic

microstructure with interdendritic Cu_4Ti precipitates (arrows). The microstructure of a cast ternary Cu-2Ti-1B alloy was very inhomogeneous. Cu-B, Cu_4Ti and TiB_2 were found by X-ray analysis. Dendritic areas with extended agglomerations of Cu_4Ti and TiB_2 (arrow in Fig. 2b) agglomerations were characteristic of all cast alloys.

Figure 3a shows an Ar-atomized Cu-0.5Ti-0.1B powder. The powder contains 0.2 wt.% TiB_2 which formed during cooling. The solid solution contains 0.35 wt.% Ti and almost no B. The dendritic and cellular microstructure is free of Cu_4Ti or TiB_2 agglomerations. Figure 3b shows the microstructure of atomized Cu-2.35Ti-1.45B. 2.5 wt.% of TiB_2 had formed during cooling and 1.0 wt.% Ti and 0.7 wt.% B were in solid solution. Even at the high volume fraction of primary TiB_2 precipitates the microstructure is free of agglomerations.

Figure 4 shows the microhardness of the Cu-Ti-B and Cu-Ti alloys after ageing at 300 °C. For small Ti and B concentrations the hardness is low. It does not change considerably during annealing. Alloys with higher concentrations of Ti provide higher initial hardness and a characteristic hardness maximum after annealing for 20 min.

DISCUSSION

Atomization of Cu-Ti-B alloys results in homogeneous microstructures which are free of TiB_2 agglomerations. The fine primary TiB_2 precipitates are dispersed in the Cu dendrite matrix and in the interdendritic areas. Up to 1 wt.% Ti and up to 0.7 wt.% B could be kept in supersaturated solid solution. In atomized powders the simultaneous presence of Ti and B was more effective for hardening than the presence of an equivalent amount of Ti alone.

The hardness of the atomized Cu-Ti and Cu-Ti-B powders increases rapidly during initial stage of age hardening. Prior observations on hardening of Cu by formation of Cu_4Ti precipitates exclude a fast hardeness increase at 300 °C /2/. The start of a measurable hardening effect in a homogenized Cu-Ti alloy was reported by /2/ only after annealing 60 min.

From the slow formation of Cu_4Ti an equally slow formation of TiB_2 can be deduced. A simple extrapolation to 300 °C of the partial diffusion coefficent of Ti and B in Cu which were measured by /3/ at 800 °C and 900 °C, indicates that the diffusion of B is 10^3 times faster than the diffusion of Ti. As a result the diffusion of Ti should control the formation of TiB_2 in Cu in a similar way as the diffusion of Ti controls the formation of Cu_4Ti. As a consequence, the fast initial hardening is neither due to the formation of TiB_2 nor due to the formation of Cu_4Ti precipitates.

It is thought that the first hardness maximum in the atomized powders results from arranging Ti atoms near to the dislocations in the lattice in a periodical structure. This so called 'modulated structure' was observed earlier in Cu-Ti by /4/. During prolonged annealing dislocation annihilation results in the homogenization of the modulated structure. Simultaneously coarsening of the dendrites occurs. Both effects lead to a decrease of the microhardness during prolonged annealing.

During future work ageing at higher temperatures will be investigated. The electrical conductivity of HIPped and swaged Cu-Ti-B material from atomized powders will be measured.

Acknowledgement: The authors gratefully acknowledge the financial support of the International Bureau of KFA-Jülich.

References:

/1/ H.Schreiner; "Pulvermetallurgie von Werkstoffen der Elektrotechnik", in: Mitteilungen aus dem Ausschuß für Pulvermetallurgie Eds.: W.J.Huppmann, H.Hassel; Powder Met.Int. -17-, 1985, 195-198.

/2/ U.Heubner, G.Wassermann; Z.Metallkde., -53-, 1962, 152-161.

/3/ J.Rexer; Z.Metallkde., -63-, 1972, 745-751.

/4/ A.Datta, W.A.Soffa; Acta.Metall., -24-, 1976, 987-1001.

Figures:

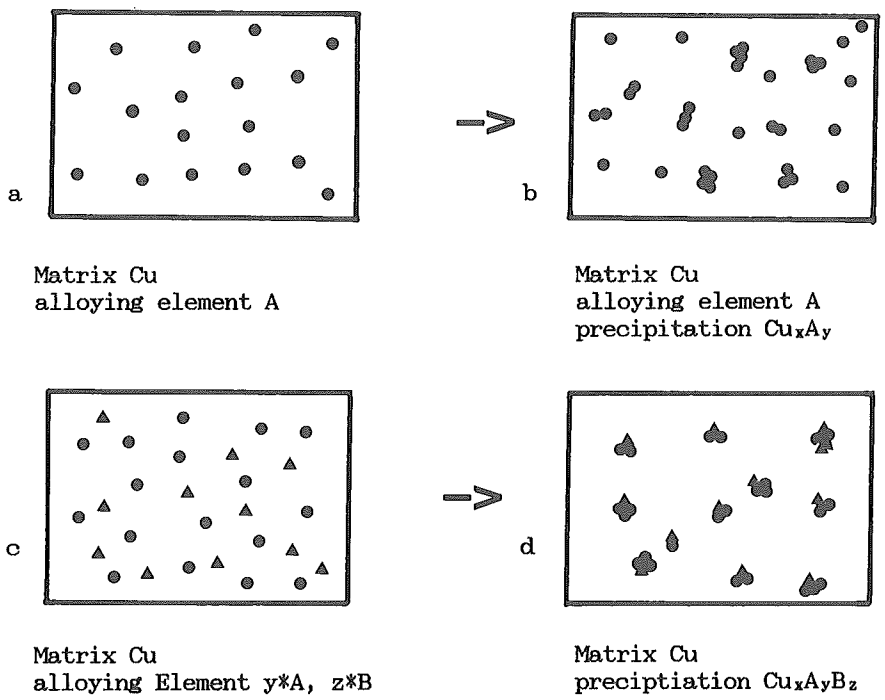

Fig. 1: The experimental procedure to form finest TiB_2-particles in the lattice. ● A, ▲ B, ⬬ Cu_xA_y, ⬬ $Cu_xA_yB_z$

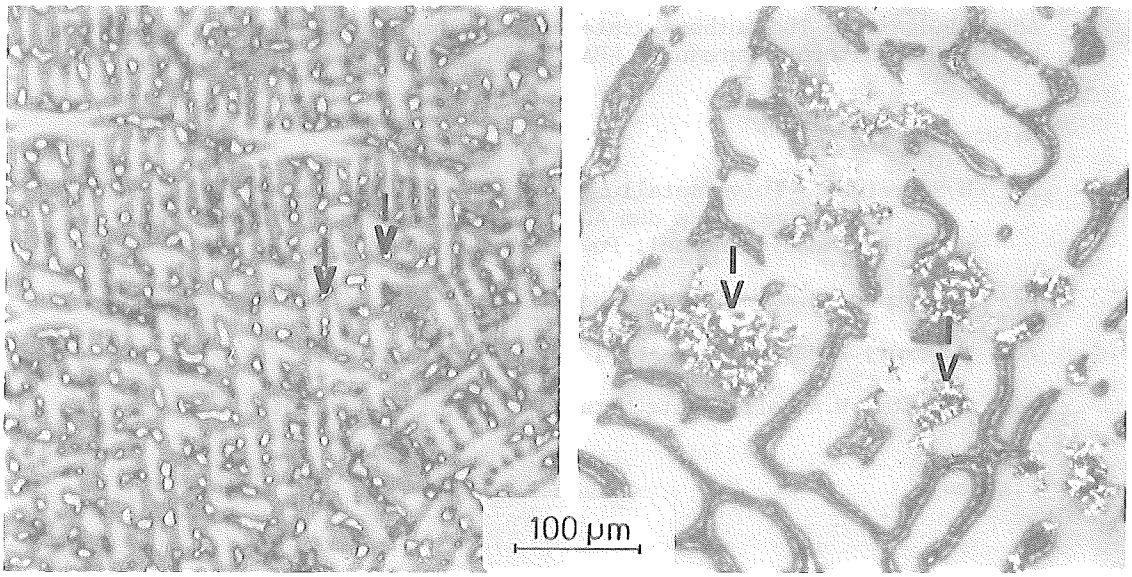

a b

Fig. 2: Cu-4Ti (a) and Cu-2Ti-1B (b) in as cast condition. Large interdendritic precipitations of Cu_4Ti (arrows) in (a) and a very inhomogeneous distribution of Cu_4Ti and TiB_2 (arrows) in (b) are a result of slow cooling.

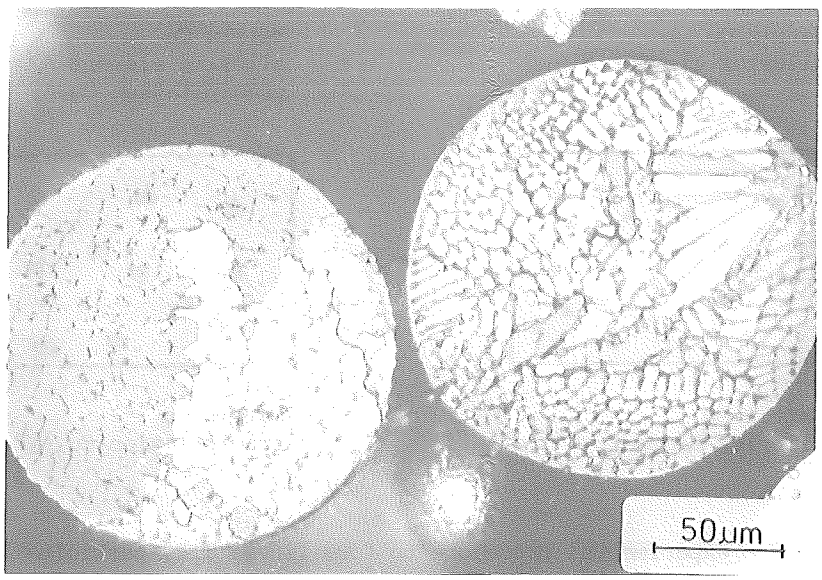

Fig. 3a: Microstructure of Ar-atomized Cu-0.5Ti-0.1B powder.

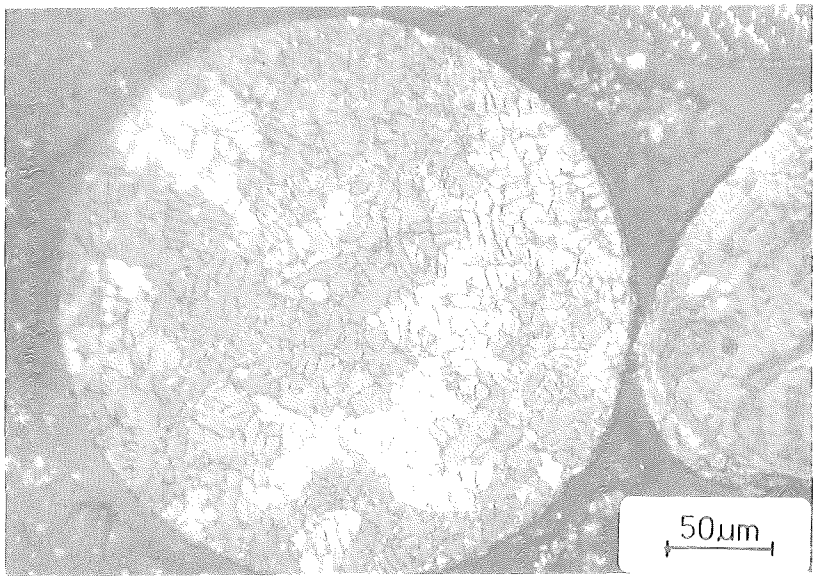

Fig. 3b: Microstructure of Ar-atomized Cu-2.35Ti-1.45B powder.

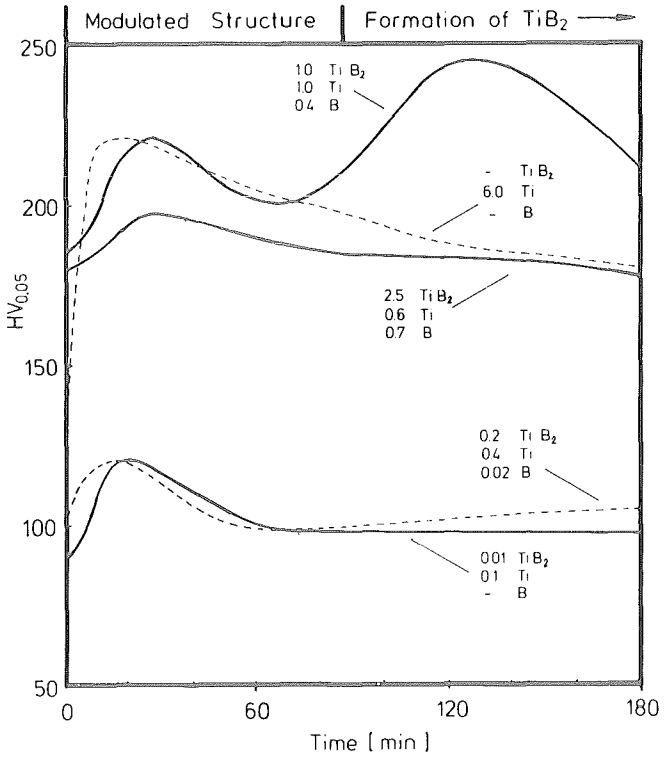

Fig. 4: Microhardness of Cu-Ti-B and Cu-Ti alloys after ageing at 300 °C.

Mechanical Properties of Rapidly Solidified Iron-Based Alloys

B. L. Mordike, H. D. Burchards, K. U. Kainer
Institut für Werkstoffkunde und Werkstofftechnik
Technische Universität Clausthal
Agricolastraße 2
D-3392 Clausthal-Zellerfeld

Introduction

Conventional high carbon cast irons are renowned for their brittleness and low strength. Attemps to improve these properties led to alloying development for grain refinement and heat treatments to form bainite /1-3/. An alternative approach is that of thermomechanical treatment to produce a fine microstructure /4/. A further possibility is to combine powder metallurgical with rapid solidification techniques /5-9/. Consolidation of rapidly quenched powder can produce material with superplastic properties in the temperature range of the α-γ transformation (650 - 700°C) at low strain rates /5-7/. It is also possible to consolidate without destroying the rapidly quenched structure by avoiding classical consolidation techniques /9,10/. This leads to remarkable properties i.e. extremely high strength with acceptable ductility. This work discribes the properties of such alloys which were produced in powder form by gas or water atomization and subsequently consolidated by extrusion or hipping and submitted to a thermomechanical treatment.

Experimental Details

Three alloys were chosen on the basis of previous experience for investigation (see Table 1). The first alloy was essentially a high carbon iron with small additions of silicon and manganese. The second alloy contained chromimum to stabilize cementite and encourage carbide formation. The third alloy was an iron-silicon alloy. The carbon and silicon contents were kept at a modest level

to prevent graphitisation. Melts of these compositions were converted to powder by water and gas atomization. For the atomizing parameters chosen the mean sizes are as given in Table 2.

alloy	C %	Si %	Mn %	Cr %	Mo %	P %	S %
12	3.0	0.5	0.6	0.04	0.06	0.03	0.14
52	2.9	0.5	0.6	1.70	0.08	0.03	0.15
55	1.9	1.0	0.5	0.04	-	0.02	0.10

Table 1: Chemical analysis of the investigated alloys

alloy	condition	mean particle size d_{50} (µm)	standard deviation	O_2-content ppm	N_2-content ppm
12 (3.0 % C)	water atomized	52	1.40	2900	120
	gas atomized	58	2.17	370	100
52 (2.9 % C; 1.7 % Cr)	water atomized	56	1.43	4000	160
	water atomized and desoxidized	33	1.29	1830	200
	gas atomized	81	2.68	840	140
55 (1.9 % C; 1.0 % Si)	water atomized	48	1.29	3400	200
	gas atomized	71	1.86	840	130

Table 2: Properties of the atomized powders

Experiment Results and Discussion

The form of the powder depends on the type of atomization employed (Fig. 1). Water atomizing produces irregularly shaped particles whereas in gas atomizing they are essentially spherical. The higher oxygen content for the water atomized particles is due in part to the atomizing medium but also in part to the higher surface area. The quenching rate and hence form of solidification depends on the particle size. Fig. 2 (a) shows four particle sizes for a water atomized 2.9 C% , 1.7 % Cr. The 10 µm particle shows dendritic

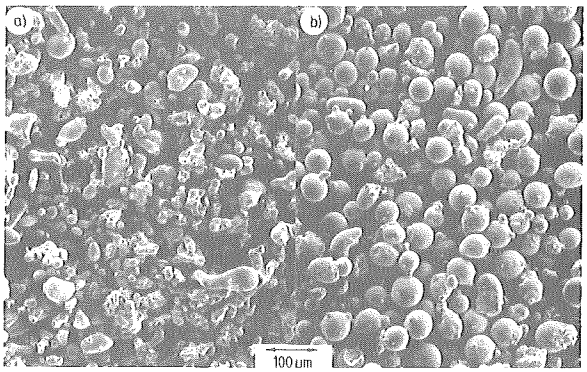

Fig. 1: Typical powder shapes of water atomized (a) and gas atomized (b) iron carbon alloys

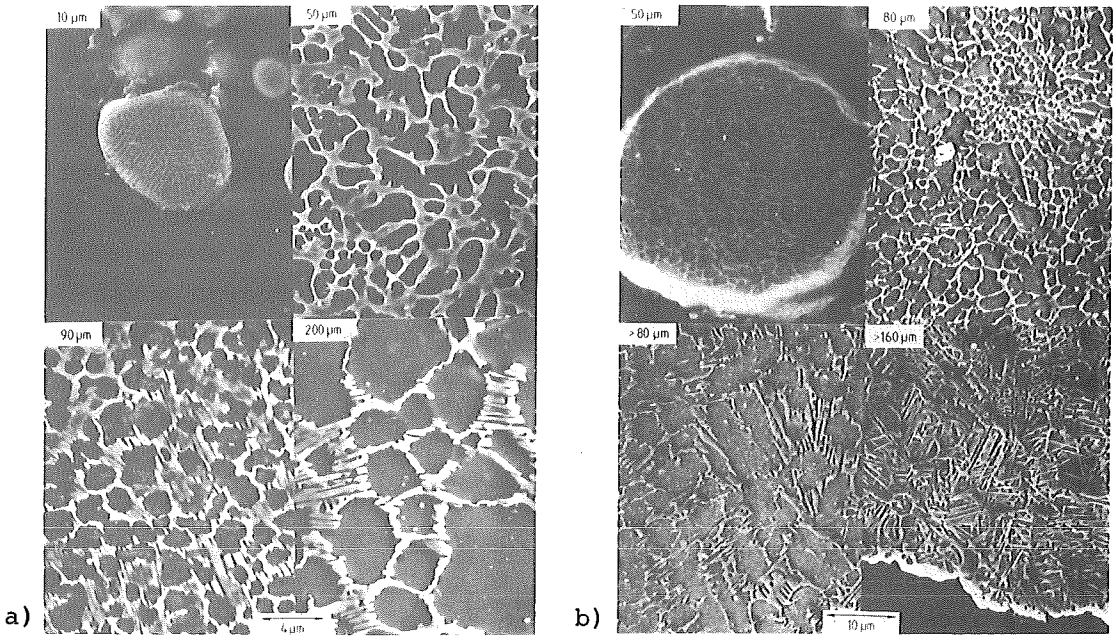

Fig. 2: Microstructure of water atomized (a) and gas atomized (b) iron alloy powder with 2.9 % C and 1.7 % Cr depending on the particle size

solidification which becomes with increasing particle size more cellular until at 200 µm, large cells with grain boundary eutectic can be observed. The trend for gas atomization is similar but there is evidence of bainite formation for the larger particle sizes because of the higher vessel temperature. The cooling rate can be calculated from the secondary dendrite arm spacing and this is shown for the two processes as a function of particle size in Fig. 3. As expected water atomization produces a more rapid quench.

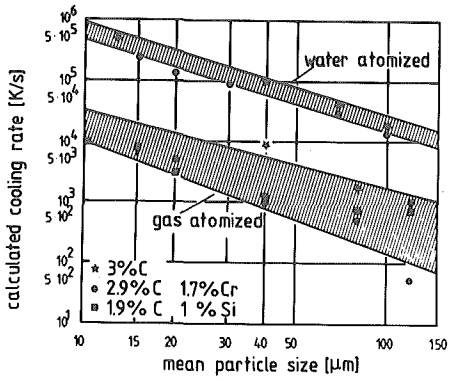

Fig. 3: Cooling rate of atomized powders calculated from the secondary dendritic arm spacing /11/

The mechanical properties depend on the composition and the microstructure. Fig. 4 shows the range of microhardness for both gas and water atomized particles of a mean size of 33 µm. The hardness of gas atomized material was always lower than that of gas atomized material. Heat treatment reduced the absolute hardness and also the difference between them. Fig. 5 shows the possible methods of consolidation. The aim is to produce a consolidated material without losing any of the benefits derived from rapid quench. Simple sintering is thus unacceptable. Extrusion or hipping at the lowest possible temperatures must be attempted. Fig. 6 and 7 shows the microstructure for material consolidation by extrusion and hipping and also after thermomechanical treatment. The initial mean particle size for both extrusion and hipping was 33 µm and in both cases the alloy shown is gas atomized 2.9 % C, 1.7 % C. 6 a and b are as extruded at

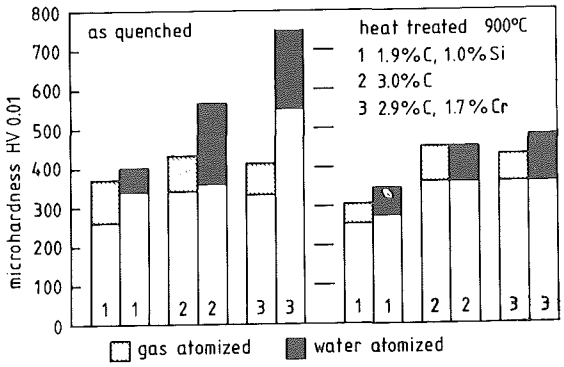

Fig. 4: Microhardness of as quenched and treated powders (900°C, 30 min)

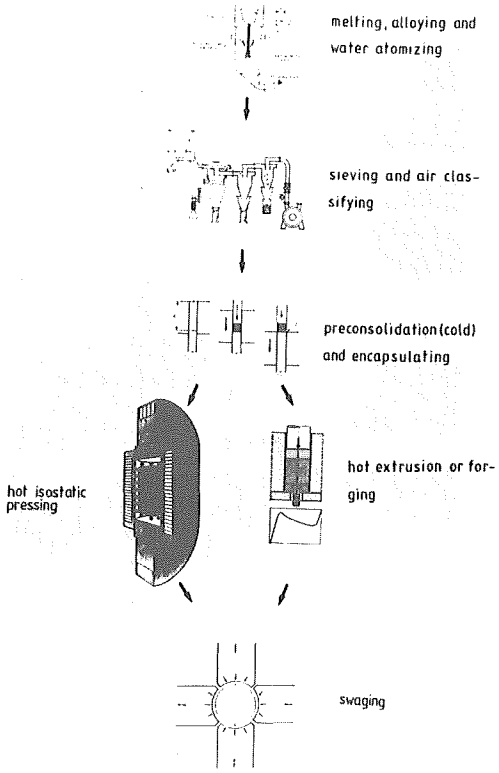

Fig. 5: Flow chart of the consolidating and treating process of the microcrystalline material

950°C with ϕ = 2.7. 6 (b) has also been heat treated: 1000°C for 15 minutes and oil quenched followed by tempering at 250°C for 2 ours. The difference is that some coagulation has taken place on heat treatment. Figs. 6 c and d show that swageing at 950°C resulting in total deformation of ϕ = 4.0 and ϕ = 4.6 prevents coarsening of the structure. The hipped structure has experienced only a modest degree of deformation γ = 0.5. The hipping treatment of 700°C for six hours has not produced such a good compact as extrusion. It was chosen as the highest temperature at which superplasticity was observed without thermal decomposition. There is evidence that the oxide film has not been broken down. Only after swageing are the compaction and properties improved. Again there was a final heat treatment and temper. Fig. 8 shows how the hardness various as a function of deformation ratio for

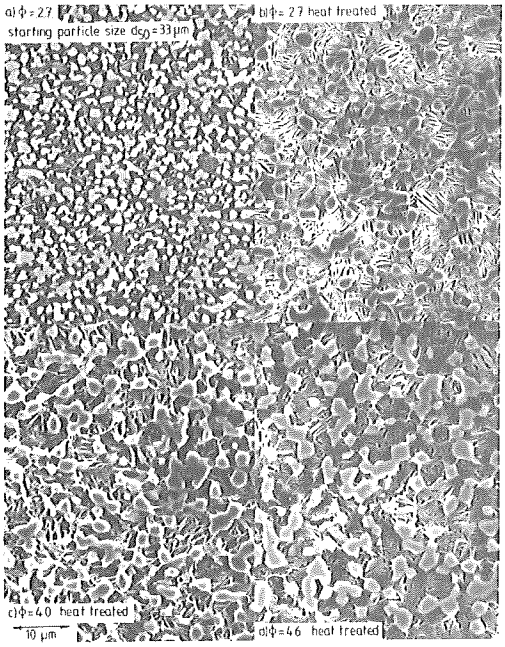

Fig. 6: Microstructure of the 2.9 % C, 1.7 % Cr iron alloy powder dependent on the deformation ratio (ϕ = ln A_o/A): a,b) extruded; c,d) extruded and swaged

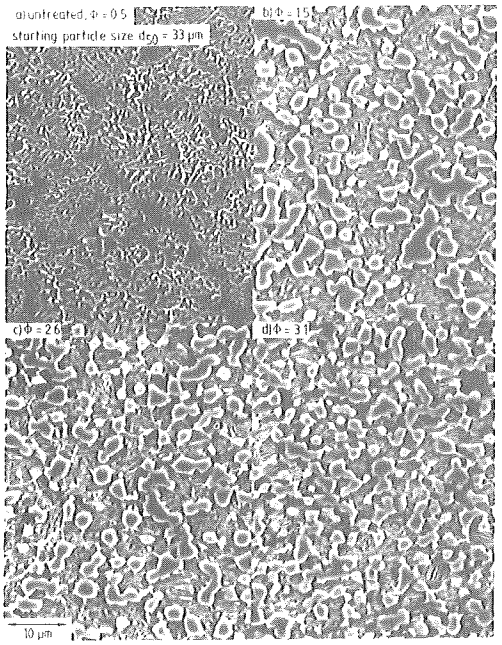

Fig. 7: Microstructure of consolidated 2.9 % C, 1.7 % Cr iron alloy powder dependent on the deformation ratio: a) HIPped b-d) HIPped and swaged, heat treated

various alloys with mean initial particle size of 33 µm. The strength is derived from carbide formation, bainite formation and microstructural refinement. The proportion of carbide is highest in the chromium containing alloys. Fig. 9 shows that the hardness is a function of particle size and degree of deformation but that the differences which existed initially after atomization between the water, gas and deoxidized and water atomized powders have disappeared. Fig. 10 shows again for 2.9 % C, 1.7 % Cr that high tensile strengths can be obtained. The ultimate strength attainable is not very dependent on initial mean particle size although there is a trend. Only in the case of deoxidized melts at high degree of deformation is a strong increase in strength with decreasing initial particle sized observed. The influence of de-

gree of deformation on the tensile strength for the three alloys, with initial particle size 33 µm is shown in Fig. 11. Values in excess of 2400 N/mm² can be obtained for 1.9 % C, 1 % Si and 3 % C alloys. Gas atomized alloys would appear to be generally better although it is clear that these results can be improved by optimizing the thermomechanical treatment.

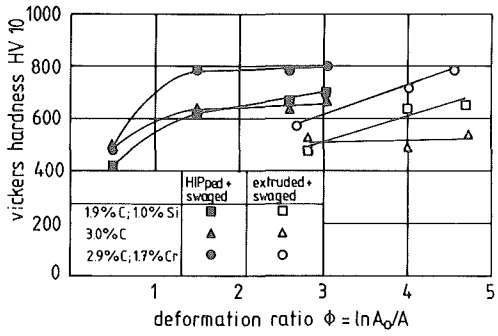

Fig. 8: Vickers hardness as function ot the deformation ratio for different starting powders, extruded and swaged or HIPped and swaged (heat treated)

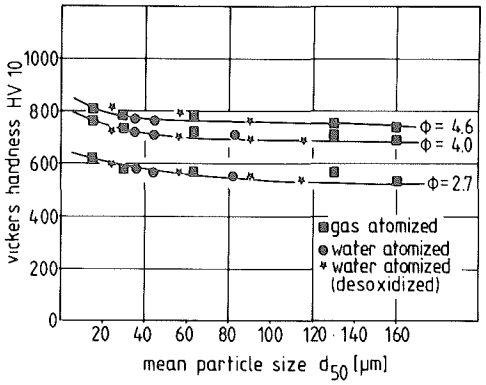

Fig. 9: Vickers hardness vs mean particle size of consolidated atomized 2.9 % C; 1.7 % Cr iron powders

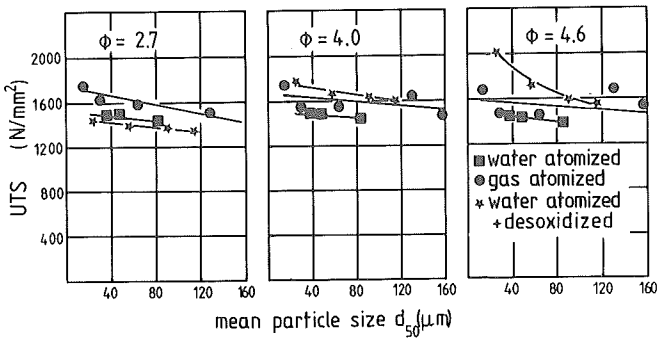

Fig. 10: Ultimate stress of extruded and swaged Fe 2.9 % C and 1.7 % Cr powder

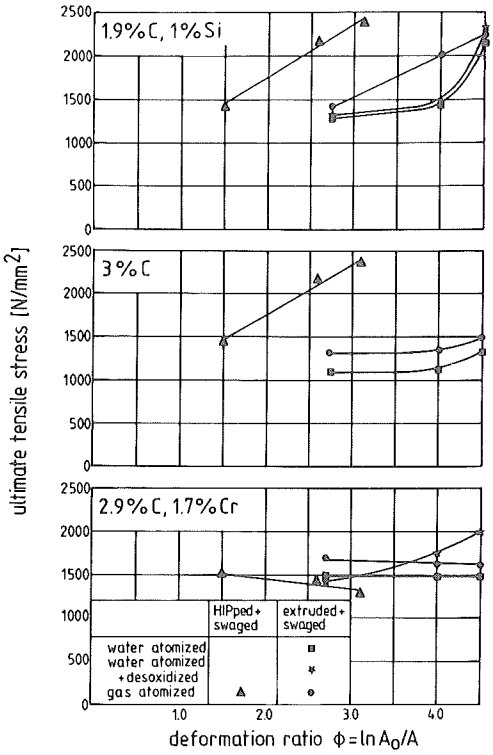

Fig. 11: Ultimate tensile stress of the consolidated iron-carbon powders with different compositions

References:

/1/ B.P.J. Sandvik, Metallurgical Transaction 13 A, (1982) 777.

/2/ B.P.J. Sandvik, ibid, 789.

/3/ K. Röhrig, Gießerei Praxis (1983), 1.

/4/ T. Oyama, O.D. Sherby, J. Wadsworth and B. Walsen, Scripta Met. 18 (1984), 799.

/5/ O.R. Ruano, L. Eiselstein, O.D. Sherby, Met. Trans. A., 13 A (1982), 355.

/6/ O.R. Ruano, L. Eiselstein, O.D. Sherby, ibid, 1785.

/7/ L.E. Eiselstein, O.A. Ruona, O.D. Sherby, J. Mat. Science 18 (1983), 483.

/8/ G. Frommeyer, Z. Metallkunde 76 (1985), 662.

/9/ H.D. Burchards, Diss. University Clausthal 1987.

/10/ B.L. Mordike, D. Burchards, K.U. Kainer, Powder Met. International 18 (1986), 437.

/11/ H. Jones, Rapid Solidification of Metals and Alloys, The Institution of Metallurgists, London (1982).

M E T A L S (2)

INTERMETALLIC PHASES FOR HIGH TEMPERATURE APPLICATIONS

R.Laag and W.A.Kaysser

Max-Planck-Institut für Metallforschung
Institut für Werkstoffwissenschaften
Heisenbergstr.5, D-7000 Stuttgart 80, West Germany

INTRODUCTION

Iron aluminide and nickel aluminide intermetallics have recently been the object of considerable interest as a potential structural material for moderate to high temperature applications. The cubic DO_3 (Fe_3Al), $L1_2$ (Ni_3Al) and B2 (FeAl, NiAl) lattice structures yield special properties as a low specific weight (compared to the superalloys) and a high strength modulus which make them interesting for mass-critical applications in aircraft and space industry. Excellent corrosion-resistance up to 800°C with high yield strength, open a wide field in coatings especially in oxygen-rich hot gases with an optimum relation of price to performance. The component area is still under development. Here the ductility, creep resistance and corrosion resistance are important for fast rotating parts like turbine blades rotors and turbochargers.

A major problem of coarse grained intermetallics is their extreme brittleness, whereas single crystals and polycrystals with grain sizes smaller 20 µm display considerable ductility at room temperature /1//2/. The reasons are weak grain boundary structures and the sensitivity of grain boundaries to segregation of impurity atoms /3/. Several remedies exist to improve the unfavoured properties to a certain degree: Macroalloying, microalloying and rapid solidification.

THEORETICAL APPROACH

It is possible to modify the chemical bonding in the lattice by macroalloying with third elements. This must be done carefully because it runs the risk of sacrificing the advantages of high ordered structure by changing the complex lattice structure and by forming large precipitations in the lattice. A more adequate way seems to be microalloying which modifies the grain boundaries and prevents the segregation of impurity atoms by forming fine

inert precipitations inside the grains. Grain refinement increases the specific grain boundary area and dilutes the impurities at the boundaries.

Investigations of /2/,/3/ show that in Ni_3Al the major reason for weak grain boundaries is a positive valency difference between ternary additions like Cr and substituted elements. The weakening is caused by modified metal-metal-bonds in the grain boundary which are reduced by the presence of Cr to a smaller number of strong directional covalent bonds. These covalent bonds result in a reduced number of metallic bonds in the lattice adjacent to the grain boundary. In contrast the addition of Ti as a substitutional element for Al should result in a negative valency difference and hence should enhance grain boundary strength. Figure 1 shows schematically the predicted effect of minor concentrations of ternary additions on the fracture mode. Increasing amounts of ternary alloying elements enhance the strength of the bulk, but weaken the grain boundaries in case of a negative valency difference and increase the grain boundary strength less effectively than the bulk strength in the case of positive valency difference. One intention of this investigation was to substitute a number of lattice atoms by microalloying with Cr and Ti until the grain boundaries and the bulk material have nearly the same strength.

EXPERIMENTS

The experimental work focused on the Fe-rich side of the Fe-Al system. Table 1 shows the chemical composition of the alloys. The alloys 1,2 and 3 were molten in a Al_2O_3 crucible under Ar, homogenized for 5 min and solidified by furnace-cooling with approximately 50 Ks^{-1}. The alloys 4,5 and 6 were molten under the same conditions and then cast in a Cu mold with 15 mm in diameter and 120 mm in length. To increase the cooling rate the alloys 7,8 and 9 were cooled as a thin film between two Cu bars. Alloy 10 was atomized with 40 bar Ar pressure. The microhardness of all specimens was measured in a Leitz microhardness tester. In addition specimens 18 mm in length and 9 mm in diameter of the alloys 4,5 and 6 were tested in a compression test. For each alloy 10 samples were tested.

RESULTS

A precipitous ductile-brittle transition was found between

40at.% and 42at.% Al, the exact transition-concentration was dependent on the cooling rate. Figures 2 and 3 show the microstructure of the alloys 1 to 6. The increased cooling rates of the alloys 7,8 and 9 resulted in a microstructure shown in Fig. 4. The atomized alloy 10 is shown in Fig. 5. From x-ray diffraction the presence of $FeAl_2$ was found in all specimen except in alloy 10. A reference specimen of $FeAl_2$, molten and cooled as alloy 1 is shown in Fig. 1c.

Specimens, etched with molybdenum acid show a network-like structure with a cooling rate dependent netsize. The largest netsize was found in furnace cooled specimens. Argon-atomized powder shows no network. The microstructures of alloys with Cr or Ti additions show fine networks in the interior of the grains and in coarser networks additional greyish precipitates are found (Fig. 3b, 4b,c).

From the microstructures it is concluded that the addition of 1 at.% Cr or Ti removes the same number of Al-atoms from its lattice sites. Because of the high electronegativity the excess Al atoms form Al_2Fe.

The average curves of the compression tests are shown in Fig. 6. The length reduction by plastic deformation was almost equal for all specimens. The maximum compression strength is slightly reduced by the ternary addition of Cr.

The refinement of the microstructure at higher cooling rates, shown in Fig. 4, results in finer distributed Al_2Fe precipitates. Compared to the Ti addition, an addition of 1 at.%Cr yields finer grains accompanied with a larger network size, and a decreased number of coarse Al_2Fe precipitates.

Gas atomized powder of Fe-11at.%Al is dendritic. The cooling rate is estimated to $10^4 Ks^{-1}$. The needle-like crystals inside the grains are of Fe_3Al. The absence of Al_2Fe is a result of extending the solubility of Fe for Al. The secondary dendrite arm spacing reduces with a decreasing particle size (Fig. 5a,b).

CONCLUSIONS

Fig. 7 shows a summary of the solidification experiments. Higher cooling rates increase the microhardness more effectively than higher Al-concentrations or a decrease in the grain size. There is hardly any difference at higher cooling rates between

ternary additions of Cr and Ti. At higher cooling rates ternary additions considerably increase the microhardness caused by the increasing amount of Al_2Fe precipitates. Due to the precipitation of Al_2Fe the predictions of the valency difference model on the influence of microalloying by Cr and Ti in Fe-Al-alloys are not applicable.

From this initial investigations we found an increased solidification rate very suitable to produce Fe aluminides with finer microstructure and better properties. In our future work we intend to continue the fast cooling path by Ar-atomization. From the present results we expect an improved mechanical behaviour due to the absence of Al_2Fe precipitations at the grain boundaries in a material with further reduced grain size.

REFERENCES

/1/ E.M.Schulson; J.of Powder Metallurgy, -23-, 1, (1987).
/2/ T.Tagasuki, N.Masahashi, O.Izumi; Acta.Metall.,-33-,(1985).
/3/ Losch; Acta.Metall.,-27-,(1979).

Acknowledgement: The authors gratefully acknowledge the financial support of Deutsche Forschungsgemeinschaft.

FIGURES

Alloy	Chemical Composition in At.-%				
No.	Fe	Al	Cr	Ti	Cooling
1	60	40	--	--	Furnace
2	58	42	--	--	Furnace
3	33	66	--	--	Furnace
4	60	40	--	--	Kokilla
5	60	39	1	--	Kokilla
6	60	39	--	1	Kokilla
7	60	40	--	--	Splat
8	60	39	1	--	Splat
9	60	39	--	1	Splat
10	89	11	--	--	Ar-atom.

Table 1: Alloys and their cooling conditions. All concentrations are verified by a chemical analysis.

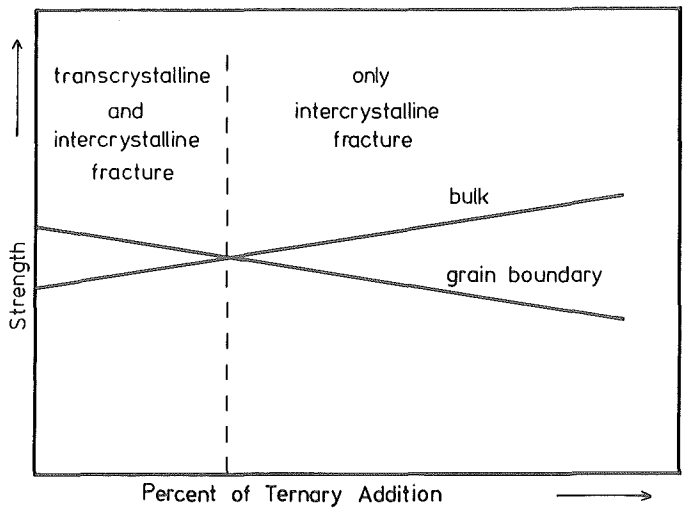

Fig.: 1 Effect of microalloying on the bulk and grain boundary strength.

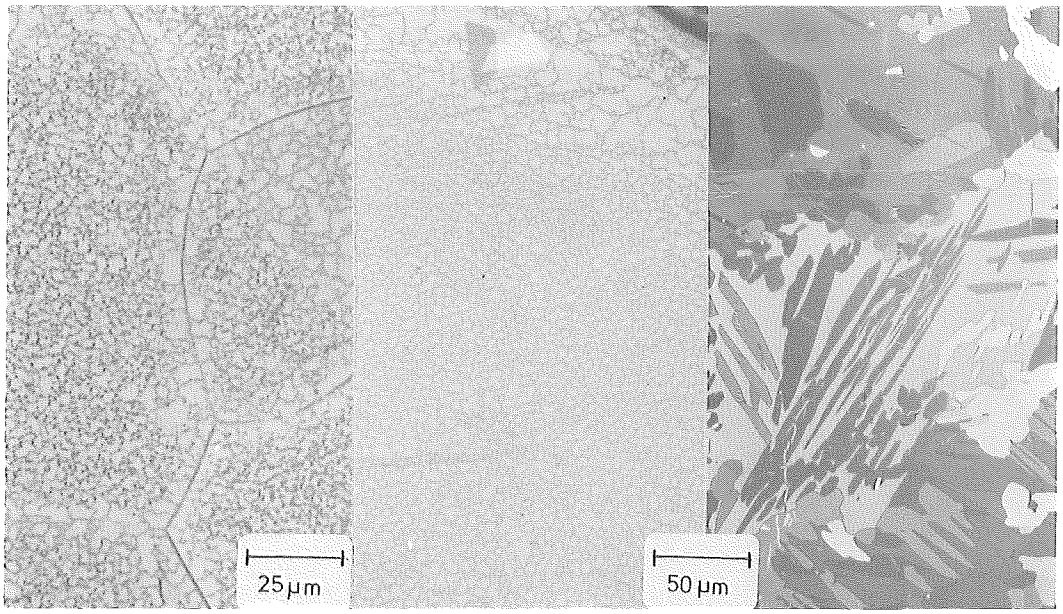

a.) b.) c.)

Fig.: 2 Microstructure of furnace cooled Fe-Al alloys; a.) alloy 1, b.) alloy 2, c.) alloy 3; the cracks formed during metallographic preparation (from Tab. 1).

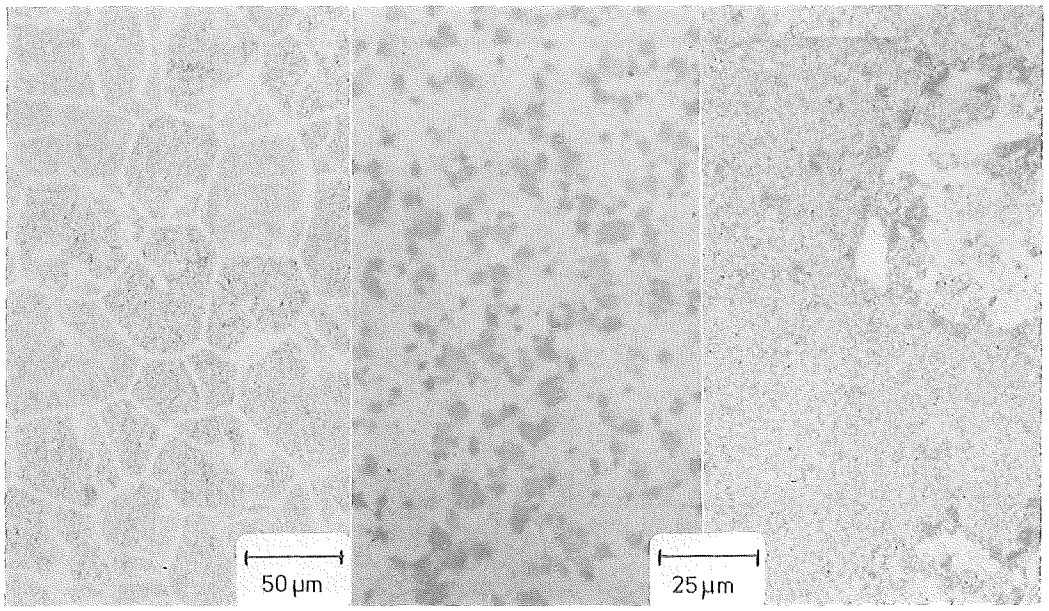

a.) b.) c.)

Fig.: 3 Microstructure of mould-cooled alloys; a.) alloy 4, b.) alloy 5, c.) alloy 6 (from Tab. 1).

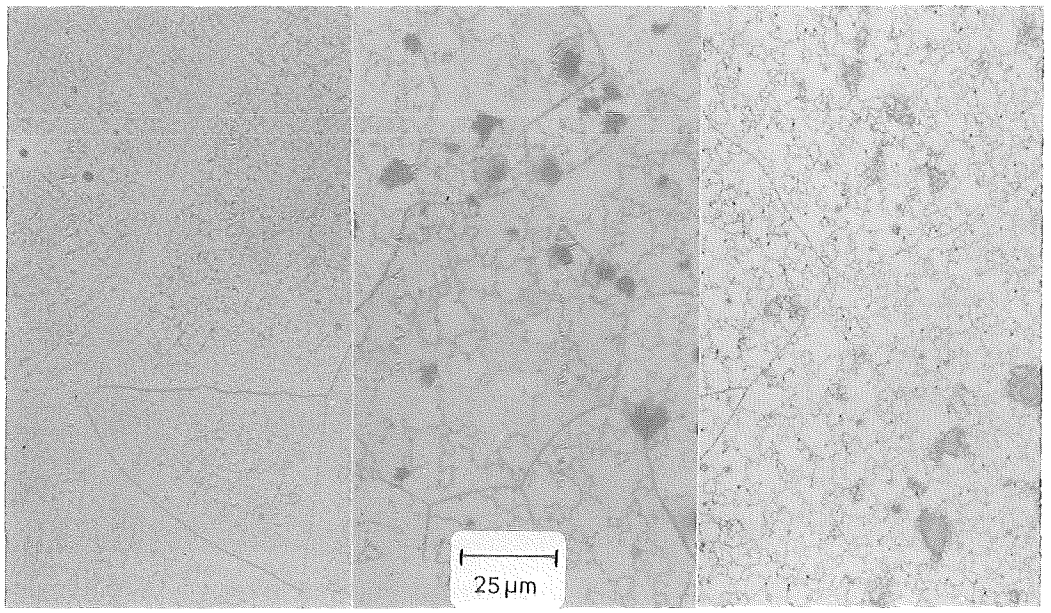

a.) b.) c.)

Fig.: 4 Microstructure of a.) alloy 7, b.) alloy 8, c.) alloy 9 (from Tab. 1).

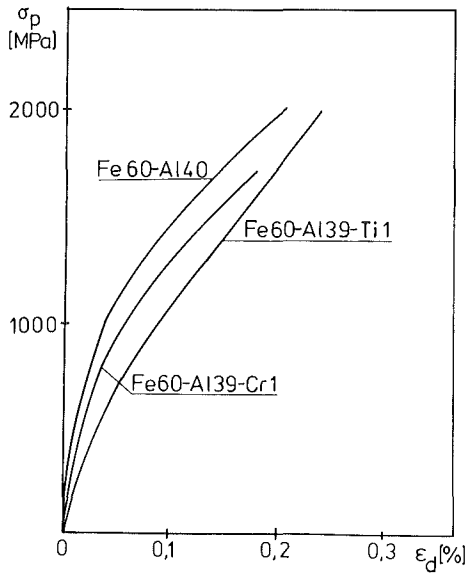

Fig.: 5 The compression tests of alloys 4,5 and 6.

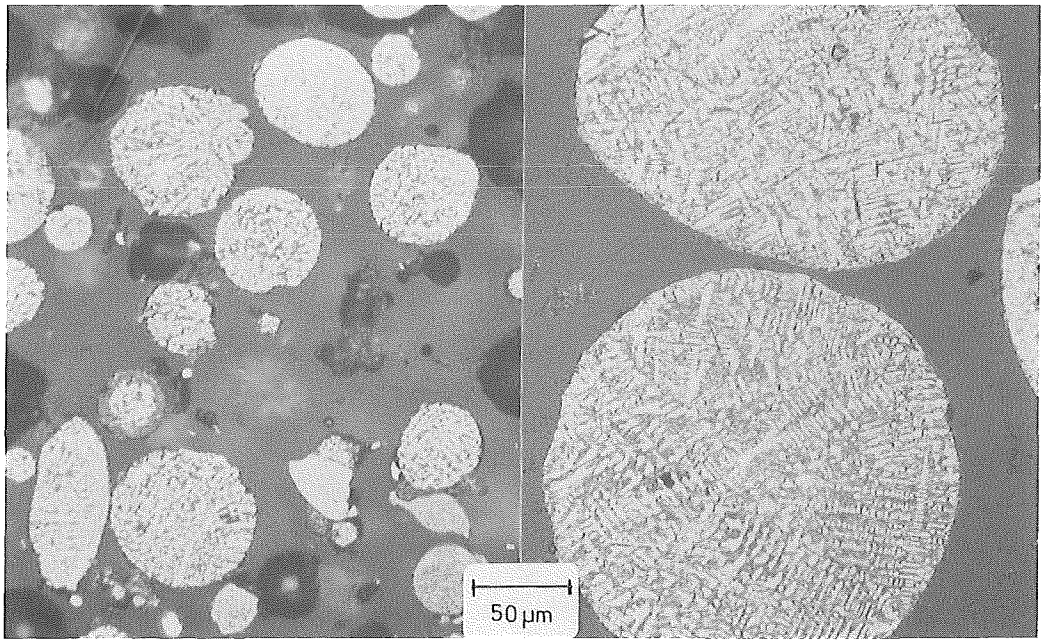

a.) b.)

Fig.: 6 Microstructure of Ar- atomized Fe-11at%.Al powder; a.) particles < 80 µm, b.) particles between 150 and 200 µm.

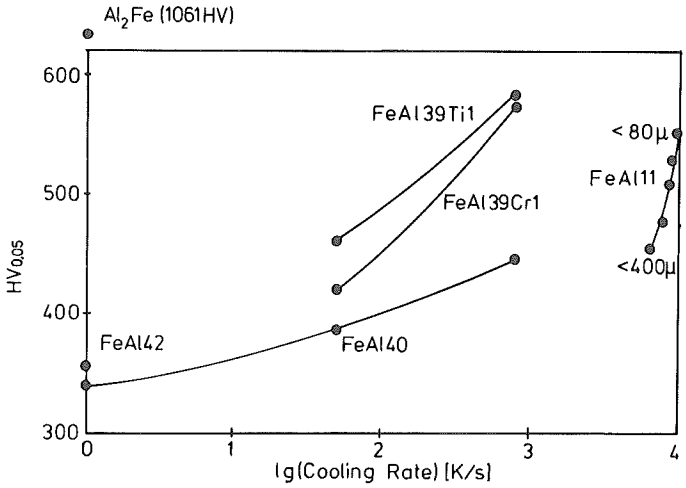

Fig.: 7 Effect of cooling rate on microhardness.

Behaviour of metals during hot rolling processes, Part I : Mathematical models.

by Paul Funke, Technical University Clausthal (FRG)

Research and development of the optimization of hot rolling processes take into consideration only the thermomechanical parameters in correlation to the final properties of the hot rolled products. This way of reflection is dependent on the actual production conditions for preheating, rolling, cooling, and coiling. The behaviour of metals in the hot deformation process in combination with strengthening will influence the distribution of yield stress in single rolling passes or in a sequence of passes for a continuous hot strip mill. The mechanisms in combination with thermomechanical treatment will primary change the state of structure during and after a deformation process; therefore there is a chance to interpret the yield stress distribution within the roll gap in terms of strengthening and softening effects.

Introduction: The adaption of roll pass schedules for high strength, low alloyed structural steel grades will be influenced by lower rolling temperatures, higher yield strength of the rolled materials, decreasing recristallization rates, and different strengthening effects like austenite and precipitation hardening. The resultant hot deformation behaviour needs higher roll forces and roll torques which surpass the installed power of continuous hot strip mills or of reversing heavy plate mills. Therefore the necessity to study the hot deformation behaviour of new steel grades to optimize the roll pass schedules within the limits of the loading capacity and to fulfill the specification of properties under controlled conditions.

During the last decades you will find many papers and results determinded under industrial conditions/1/ to answer the second question: the influence of heating conditions, the distribution of single strains in a sequence of roll passes, the strategy of temperature conditions, and the cooling rate after the final pass on the specific properties of the rolled materials. Otherwise it must be the target to describe the state of struc-

ture after the final pass in combination with the actual behaviour of the metals during every pass of the hot deformation process.

Possible mechanisms during hot deformation: During the plastic deformation under higher temperatures the following effects of hardening are important

- the yield stress of a metal will be influenced by the state of structure, character and distribution of precipitations (grain size, grain shape, grain size distribution, non-metallic inclusions) and the temperature of the material before deformation
- during hot deformation the strain hardening effect influences the local yield stress dependent on temperature, strain, and strain rate
- during or after hot deformation possibly a transformation takes place dependent on the temperature an the phase diagram of the deformed metals; the yield stress within the transformation range (existence of two phases) is often higher than in the single-phase neighbourhood
- after the hot deformation and during the cooling process precipitation hardening is possible dependent on temperature, cooling rate and the content of soluted elements.

Because the energy of plastic deformation will be transformed into heat the temperature will rise in the whole volume or locally in regions with higher strain concentrations. The effect of higher temperatures will be the favour of thermal reactions which will influence the structure and the properties of the material especially during or after the deformation process. Some of these reactions are hardening mechanisms like precipitation hardening or strain hardening, the most important thermal activated reactions are recovery and recristallization with a softening effect.

A softening effect during hot deformation of most of the metals can be the result of strain dependent on the temperature and strain rate

- dynamic recovery, i.e. the yield stress will be influenced by strain hardening and by a continuous recovery effect as a superposition of strengthening and softening

- dynamic recristallization dependent on temperature, strain and strain rate; the yield stress will be influenced by strain hardening, but the spontaneous recristallization can eliminate the strain hardening effect.

A softening effect after hot deformation can be the result of

- static recovery dependent on temperature, strain and strain rate
- static recristallization also dependent on temperature, strain and strain rate.

The effects of softening mechanisms are illustrated schematically in Fig. 1a and 1b.

Indicators of different strengthening and softening mechanisms: Strengthening and softening mechanisms affect normally the mechanical properties, but these indicators are integral properties, for the different components of the structure and the chemical composition of a metal. It is therefore necessary to simulate the hot deformation process and to determine the deformation forces and lately the yield stress under different deformation conditions. The starting point are common test methods like tensile test, compression test, torsion test, plane strain compression test, and bending test. Most of these methods are able to determine the material behaviour during the deformation in single or multiple steps. The test process must be controlled in strains, strain rates, temperature, and intermediate times between successive deformation steps; finally it must be possible to heat up or to cool down the specimens before, during and after one deformation step. In some versions of equipment the controlled deformation process is combined with a dilatation measuring unit and/or with a device for diferentional thermal analysis (DTA) to study simultaneously the transformation behaviour of the appearance of endothermic or exothermic reactions in the solid state. For the ajustment of the whole simulation process and for the evaluation of all datas there exist computer programs. Besides the determination of actual yield stress, differences of yield stress as a result of strengthening and softening mechanisms during or after deformation, and of correlations between yield stress and the deformation parameters there is a chance to calculate the activation energy of different mechanisms. In the last decades publications describe the

technique and results of controlled tensile or compression /2/ and/3/, torsion tests /4,5/ and plane strain compression tests /6/.

Development of mathematical models: In the Dr.Engr.thesis by I.Piorko /7/ there was tried to describe the hot deformation behaviour of steels for a hot rolling process in contiuous hot strip mills with the following assumptions:

- in all passes only strengthening takes place, no softening effects
- in every rolling pass there assumed a different, but constant, average temperature
- the strengthening effect can be described by an exponential-relation with the strain rate $\dot{\varphi}$ as a factor and the strain φ as the exponent
- the mean yield stress of every pass is a mean value of the strengthening curve of the metal
- the starting value for the behaviour of the material at the beginning of each pass is a calculating value k_o - no physical value with the character of a yield stress
- the softening between two passes can be described as a recovery effect dependent on strain and strain rate in the pass before
- the roll forces in every rolling pass result from the mean yield stress, the geometry of the roll gap (contact length) and an estimable for efficiency for the deformation process
- the starting value k_o can be calculated for the first pass on the measured roll force; k_o contends all informations about the hot deformation behaviour of the used steel.

These assumptions will not consider the effects of dynamic recovery and recristallization. On the other side the strain rates of an industrial rolling process are too high to cause dynamic recristallization.

The increase of strain, strain rate and yield stress in the roll gaps of five stands of an industrial hot rolling mill, calculated by this model of piorko is shown in Fig.2, the yield stress after the passes dependent of φ and $\dot{\varphi}$ in Fig.3.

J.Hertel /8/ developed a mathematical model for dynamic recovery during hot deformation starting with a differential equation of the dislocation density ϱ under constant shear rate and temperature for a softening effect only by dynamic recovery

$$\frac{d\varrho}{dt} = a' \dot{\gamma} - K_E' \varrho^2$$

with a' = strengthening modulus, K_E' = velocity constant of dynamic recovery, and $t = \gamma / \dot{\gamma}$. With this description the fundamental mechanisms of hot deformation with softening effects only by dynamic recovery is in good agreement with the actual behaviour during hot rolling. In Fig.4 the correlation between the velocity constant and the temperature for a selected steel grade gives the chance to determine the activation energy for dynamic recovery.

It will be usefull to modify the mathematical model with the assumption, that strengthening and dynamic recovery must be taken into account for most of the technical steel grades.

References

/1/ Straßburger, Chr.: Entwicklungen zur Festigkeitssteigerung der Stähle
Düsseldorf (1976)

/2/ Turk, R.: Ein Modell für die Beurteilung der Warmformgebungseigenschaften der Metalle
(Dr.-Diss. Univ.Ljubljana) Ljubljana (1983)

/3/ Lueg, W., Krause, U.: Stahl u.Eisen 80(1960) S.1061/67

/4/ Rossard, C., Blain, P.: Rev.Métallurg. 56(1959) S.175/80

/5/ Preiser, H.: Der Warmtorsionsversuch und seine unterschiedlichen Verfahren zur Aufnahme von Fließkurven
(Dr.-Diss. TU Clausthal) Clausthal (1972)

/6/ Pawelski, O., Kaspar, R.: Simulation des Warmwalzens zur Untersuchung des Werkstoffverhaltens von Stählen. in: Werkstoff- und Bauteilprüfung sowie Betriebslastensimulation (ed. Jacoby, G.)
S.87/98; Karlsruhe (1981)

/7/ Piorko, I.: Ein neues Verfahren zur Berechnung der Walzkräfte in mehrgerüstigen Warmbreitbandstrassen unter besonderer Berücksichtigung des Formänderungsfestigkeitsverhaltens
(Dr.-Diss. TU Clausthal) Clausthal (1970)

/8/ Hertel, J.: Z.Metallkde. 71(1980) Nr.10, S.673/80 and Nr.11, S.735/80

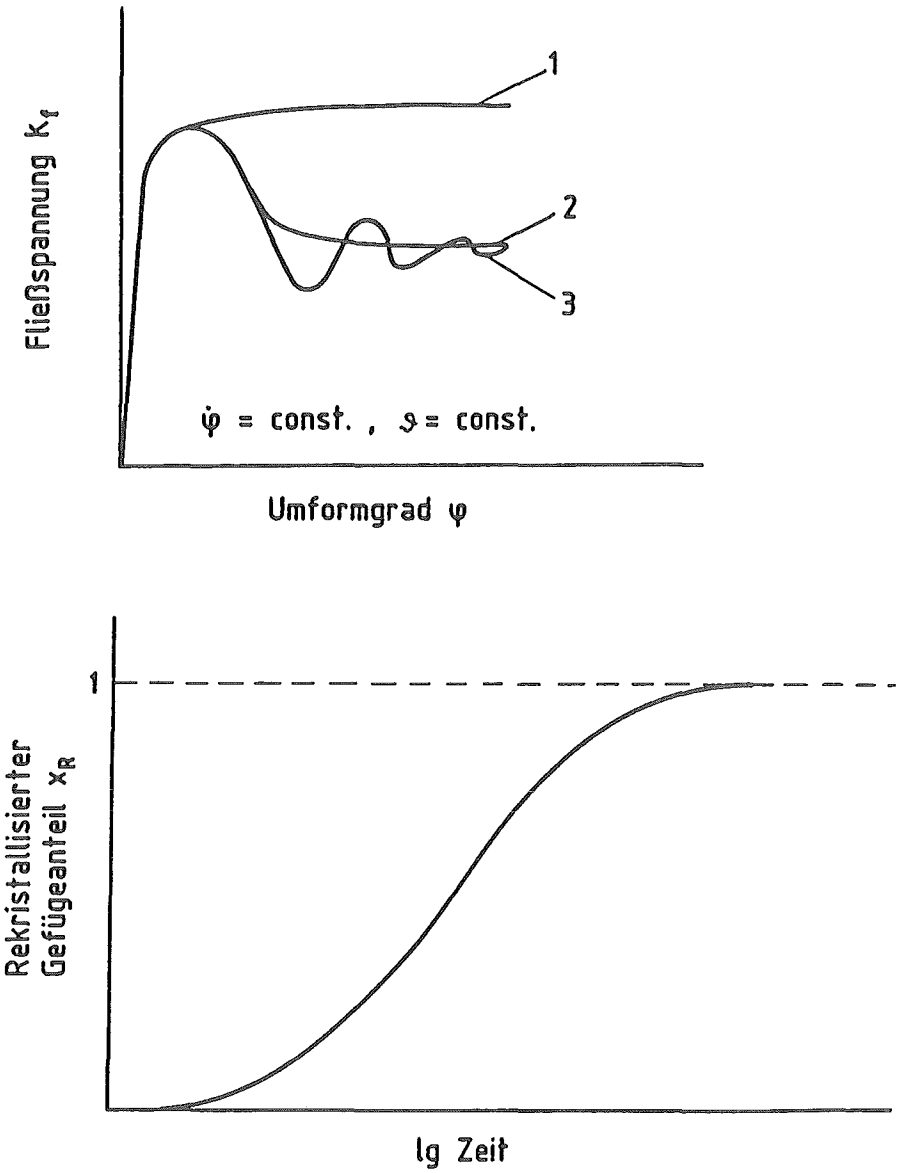

Fig.1 - Possible yield stress behaviour during hot deformation (a) and softening effect of static recristallization (b)

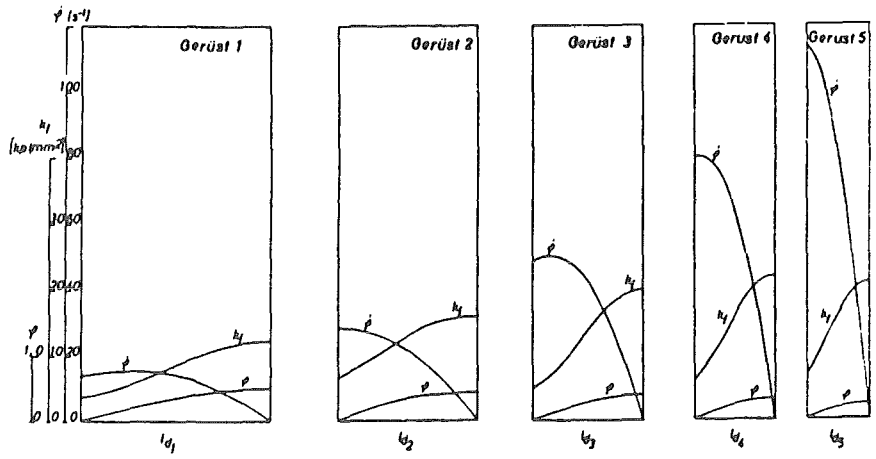

Fig.2 - Calculated distribution of strain, strain rate, and yield stress in the roll gaps of a continuous hot strip mill (after I.Piorko)

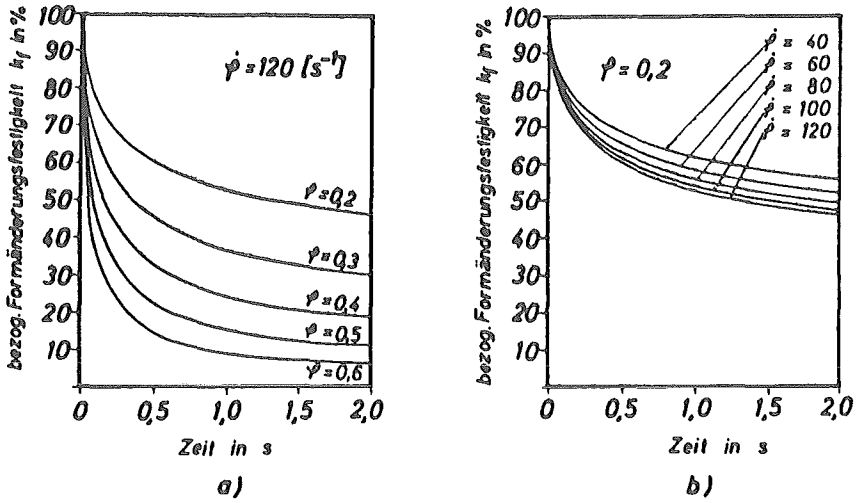

Fig.3 - Calculated distribution of the yield stress between two stands of a continuous hot strip mill dependent on the strain and strain rate during the pass before (after I.Piorko)

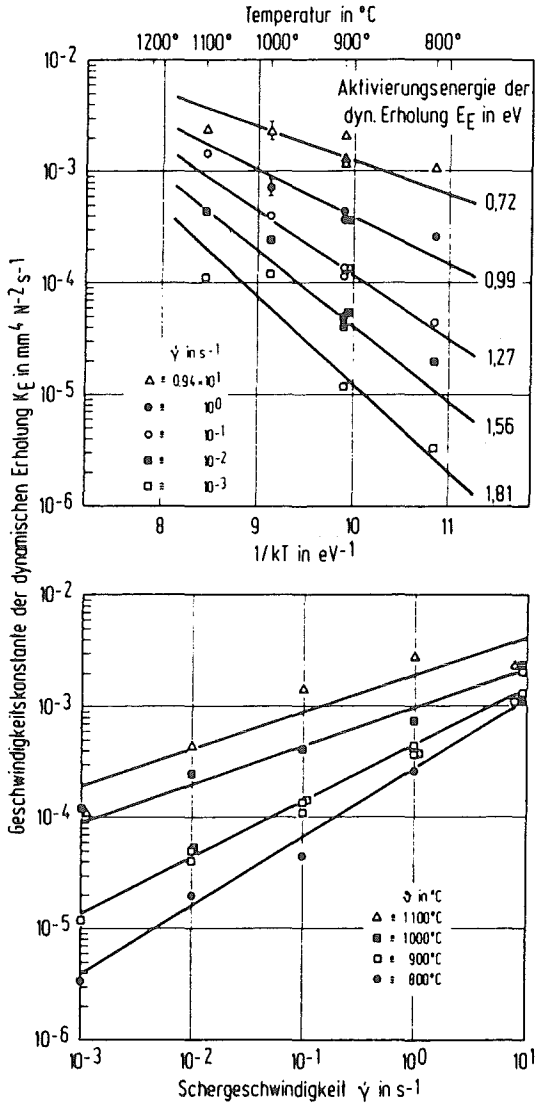

Fig.4 - Correlation between the speed constant of dynamic recovery and the temperature (a) and the strain rate (b) after J.Hertel

BEHAVIOUR OF METALS DURING HOT ROLLING PROCESSES

Part II

Experimental Methods for Flow Stress Determination and Calculation of the Two-Dimensional Temperature-Field in the Roll Gap

by R.Krengel

Institut für Werkstoffumformung
Technische Universität Clausthal

BEHAVIOUR OF METALS DURING HOT ROLLING PROCESSES

Part II

Experimental Methods for Flow Stress Determination and Calculation of the Two-Dimensional Temperature-Field in the Roll Gap

by R.Krengel

Institut für Werkstoffumformung
Technische Universität Clausthal

ABSTRACT

This report deals with an experimental technique to determine the course of the deformation parameters in the roll gap with the aid of the visioplasticity method. These parameters are mainly the strain-rate, the strain and the deformation temperature.
The strain rates and strains can be determined in the whole deformation zone by making the metal flow visible with a square grid on a flow plane of the material. The two-dimensional temperature field inside the metal is calculated by a finite difference method.
From this analysis the deformation parameters can be obtained to determine the course of the mechanical properties and the structure in the hot rolling process by a subsequent simulation with material tests.

INTRODUCTION

In hot rolling processes a great variation of the deformation parameters can occur over the cross sections of the rolled material and this can produce different structures and different mechanical properties. Therefore it is of great interest to get an exact description of the local processes in the roll gap to ensure well defined final products.

The information of the course of the local process parameters can only be obtained by experimental investigations of the metal flow, because an exclusive mathematical description of the whole process is not yet possible due to the complex physical mechanisms of this process.
The knowledge of the local process parameters allows an analysis of the local mechanisms in the hot rolling process, as for example the dynamic recristallisation. As well it allows an investigation of the correlations between the forming- and cooling- conditions on one side and the differences of the structure and the mechanical properties on the other side.

LOCAL AND GLOBAL PROCESS PARAMETERS

In the scope of plasto-mechanics /1/ the rolling process is often supposed as a process with a plane-strain state and it is described by the strip-model of the elementary theory.

In this strip-model a plane cross section moves through the roll gap as a flat strip without any buckling, that means that a plane cross section remains a plane during the whole deformation process. To simplify the calculations the process parameters, the stresses and the material properties inside a cross section are assumed to be constant. Therefore these global parameters are integral average values (picture-1). The consideration of global process parameters is only justified, if the gradients in the spatial distribution of these parameters are not too extensive.

The determination of the real material flow in the deformation zone by experimental methods give informations about the distribution of local process parameters for the examination of material properties.

THE VISIOPLASTICITY METHOD

The rolling process is a stationary deformation process. Therefore the flow lines and the stream lines coincide in a flow plane. By interrupting the rolling process with a sudden stop, it is possible to receive the whole deformation state in the roll gap by using a material, provided with measuring marks.

In the scope of visioplasticity many experimental methods had been developed to apply measuring marks inside the material or on the surface of the specimen /2/.
Investigations of the deformation state in the rolling process were carried out just in the beginning of this century by filling bore-holes in the material with prepared pins and screws or by engraving a coarse grid on the surface or inside a flow plane of the material (picture-2).

With theses experiments only limited informations about the deformation parameters could be obtained, because of the great distance of grid marks in the material. On the other side these marks could affect the metal flow in the roll gap.
The method of filled bore-holes was extended to a three-dimensional analysis /3/ of profile rolling processes by filling fine bore-holes with pins adjusted to the rolling direction.

As well there is some research of metal flow in the flat cold rolling process by using very fine grids engraved or etched on flow planes in the midline of the specimen (picture-3).

In the hot rolling process similar investigations had not been carried out, becuase of the destruction of the fine grids by scale formation or by pressure welding of both specimen parts.

METHODS FOR ENGRAVING GRIDS FOR HOT WORKING

At our institute a new method had been developed to use fine grids with squares of 1 mm square length in the hot rolling process.
The visioplasticity method with grids on the flow plane of a separated specimen has some restrictions :
- the choosen plane for engraving the grid must characterize the whole deformation process
- between both parts of the specimen tensile stresses or shear stresses should not occur, because of the separation of the material
- the velocity of the rolling process cannot be high to guarantee a sudden stop of the rolling mill.

These considerations make it favourable to engrave the grid in the midplane of the specimen.

For the experiments an austenitic stainless steel was used to reduce the scale formation during the heating to receive an exellent visible grid after the hot rolling process.
The rolling specimens had a thickness of 24 mm, a total length of 400 mm and a width of 70 mm for each specimen part. In the entrance and exit zone weld edges were shaped for joining two specimen parts together (picture-4).

Before engraving a grid the lateral face of the specimen was polished to get a plane surface. The square grid was applied to this lateral face by photochemical etching with an ultra-violet sensitive photo-varnish.
It is important to coat the lateral face of the specimen with an even and stable varnish film with a sufficient thickness to secure a good quality of the grid.

A pattern with the desired grid was adjusted to this side face and exposed to a Xenon-pulse lamp. The grid-pattern had a square length of 1 mm with a line width of 0.050 mm and a very accurate sectioning of the lines.
A finer grid was not advisable, because the inhomogenities of the structure with respect to the grain size of the material leads to oscillations of the flow lines. Therefore a finer grid would not give a greater accuracy of the data. With the choosen grid it was possible to get about 1846 grid points of intersections onto the lateral face.

By developing this varnish the light-exposed parts of the film form a acid-resistant layer. The not exposed grid lines are dissolved from this layer and after etching the grid onto the lateral face of the specimen the varnish layer was removed.
The grid was coated with a protective layer of a special glass suspension to prevent a pressure welding of both specimen parts in the rolling process and to prevent a scale formation on the grid.
Then two specimen parts were welded together in the area of the entrance and exit zone to get the final rolling piece. The material was heated in an electrical furnace with an inert-gas chamber filled with Argon to minimize a scale formation during heating at 1150 Celsius.

HOT ROLLING EXPERIMENTS

The specimens were rolled on a duo-rolling mill with a roll diameter of about 300 mm (picture-5).
In the first rolling tests the specimens presented an additional penetration of the roll into the specimen after the sudden stop of the rolling process and this leads to an undesired distortion of the grid. This phenomena is effected by the just persisting static roll pressure and was as well observed by other scientist, who could not abolish this effect.

To remove the static pressure just in the moment of stopping the rolling process, a new hydraulic system was projected and installed in the roll housing. Two additional hydraulic cylinders (with a pressure force of 630 KN each) were installed between the screw downs and the upper roll neck bearings.
Before starting the rolling process these cylinders are lifted to the full stroke of 10 mm by a pressure of 500 bars. Then the screw downs are moved to the initial pass position and the other hydraulic cylinders press the upper roll neck bearings with the new cylinders against the screw downs.
Just in the same moment when the rolling process is stopped, the magnetic valves of the upper hydraulic cylinders are opened to drop their pressure. The other cylinders get a pressure of 500 bars by a motor-pump to open the roll gap.

This new hydraulic system gave the desired results and no penetration of the rolls after stopping the rolling process could be observed furtheron.

MEASURING EQUIPMENT

During the hot rolling process the following data had been measured to get essential informations of the rolling process:
- the roll force
- the torques of the upper and lower rolls
- the number of revolutions of the electic drives
- the entrance and exit velocity of the specimen
- the surface temperatures of the specimen in the entrance and exit area of the rolling mill by pyrometers
- the temperature inside the specimen at three heights of the thickness by Ni-CrNi thermoelements.

The measured values were recorded by a light-beam-oscillograph to observe the dynamic processes in the stage of stopping.

MEASURMENT OF THE DEFORMED GRID

The whole state of deformation can be derived out of these experiments, if the specimen is stopped in the roll gap just in the area of the engraved grid (picture-6).
After seperating the rolled specimen at the midline into both specimen parts and after removing the protective glass layer, the deformed grid is put under a measuring-microscope (ZEISS UMM 200 DIGITAL) with an optical resolution of about 0.001 mm.

The x/y-coordinates of the grid were measured by the points of intersections and these data were stored directly on a micro-computer. From the measurd coordinates of the specimen the velocities in the x- and y- directions can be calculated and after carring out a surface approximation with bicubic spline-functions the strain rates in the defromation zone can be derived.
After the determination of equivalent strain rates along the flow lines the equivalent strains can be calculated by integration over the time step.

CALCULATION OF THE TWO-DIMENSIONAL TEMPERATURE-FIELD

The strain-rates and strains had been calculated along the flow lines of the grid at the points of intersections. Equally the temperatures inside the specimen should be calculated at the same points to get also the course of the third process parameter along these flow lines.

To solve an instationary heat condution problem in this given irregular network the Finite-Element-Method (FEM) can be used, due to its flexibility for complex geometrical forms in irregular meshes.
This practicability is not considered to belong to the Finite-Difference-Method (FDM), that is widely applied, due to its simplicity in solving complex mathematical problems. Also it does not require as much storage capacity as FEM.

Partial differential equations are approximated with the Finite-Difference-Method usually by using a square or rect-angular stencil with standard central difference formulas. Although a great variety of regions can be approximated by square meshes, particulary if a very fine mesh is used, there remains the problem of treating curved boundaries and irregular meshes.

With a new mathematical procedure /4/ general difference approximations can be generated for any configuration of nodes, that is similar to a slightly distored, square stencil by treating the entire stencil with shape functions of a Lagrangian finite element. This flexible stencil, which is curvilinear in the physical (x,y)-plane, is mapped onto a corresponding square element in a local reference plane by a coordinate-transformation (picture 7).

This flexible stencil is in fact the finite difference analogue of a parent element, which can be deformed into a curved isoparametric element, and it allows the calculation of the temperatures along the flow lines in the roll gap.
The boundary conditions for this problem are the heat transfer by radiation and convection outside the roll gap and the heat conduction to the roll inside the roll gap with regard to a surface layer formed by scale.

FINAL REMARKS

The determination of the local process parameters strain-rate strain and temperature in the deformation zone by experimental methods give important informations for the simulation of the structure and the mechanical properties in material tests. Theses informations of local process parameters allow more precise investigations of the real deformation mechanisms then a simulation with global parameters, that are normally used in material tests.

LITERATURE

/1/ H.Lippmann , O.Mahrenholtz
Plastomechanik der Umformung metallischer Werkstoffe
Springer-Verlag, Berlin/Heidelberg 1967

/2/ L.Eberlein
Methoden zur Ermittlung des Werkstoffflusses beim Umformen / Neue Hütte 29(1984)7, p.251-254

/3/ H.Osterburg
Ein Beitrag zur Ermittlung lokaler Prozeßparameter beim Walzen in Streckkalibern mit Hilfe der dreidimensionalen visioplastischen Methode / Umformtechnische Schriften Band 1 , Verlag Stahleisen, Düsseldorf 1986

/4/ W.H.Frey
Flexible Finite-Difference Stencils from Isoparametric Finite Elements
Intern.Journal Num.Methods in Eng. 11(1977), p.1653-1665

Methods for determination of material flow in metal forming processes

	method	material flow quality	material flow quantity	determination of deformation parameters	stream-lines	conditions
indirect methods	vickers-hardness	+	+	-	-	cold forming
	recristal-lisation	+	-	-	-	cold forming
	polarisation	+	+	-	+	optical active
direct methods with characteristic structures	grain boundaries	+	-	-	-	cold forming
	structural components	+	-	-	-	below transf. temperatures
	segregations	+	-	-	-	
direct methods with foreign structures	filled bore-holes	+	+	local possible	+/-	
	laminated material	+	+	conditional pos.	+/-	
	surface grids	+	+	local possible	-	
	optical sensit coatings	+	+	possible	+/-	deformation at room temp.
	grids on seperated planes	+	+	+	+	planes without tensile or shear stresses

Picture 2: Methods for determination of material flow with experimental techniques

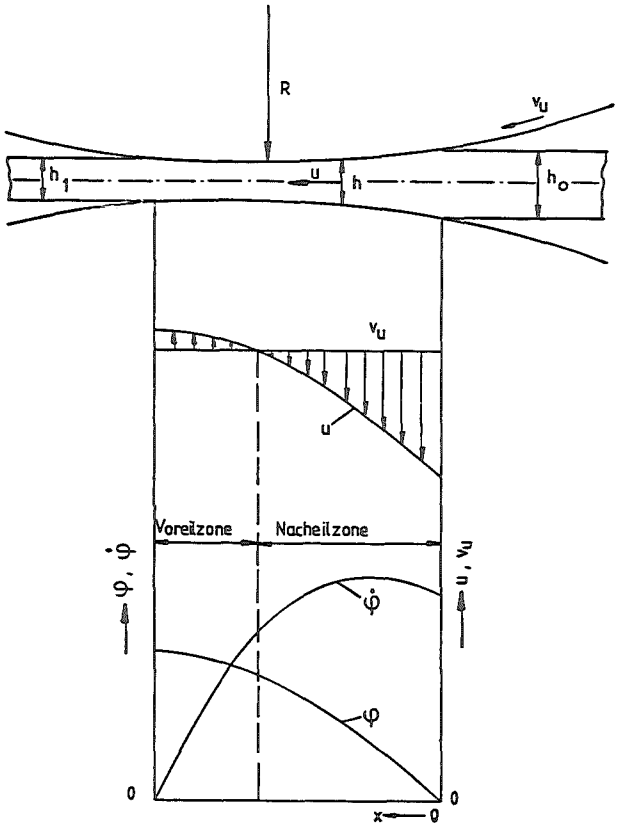

Picture 1: Course of global process parameters in the roll gap

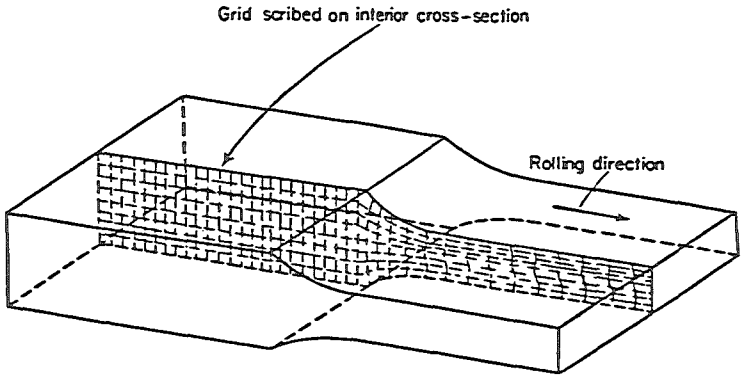

Picture 3: Deformation of an engraved grid on a flow plane of the roll specimen

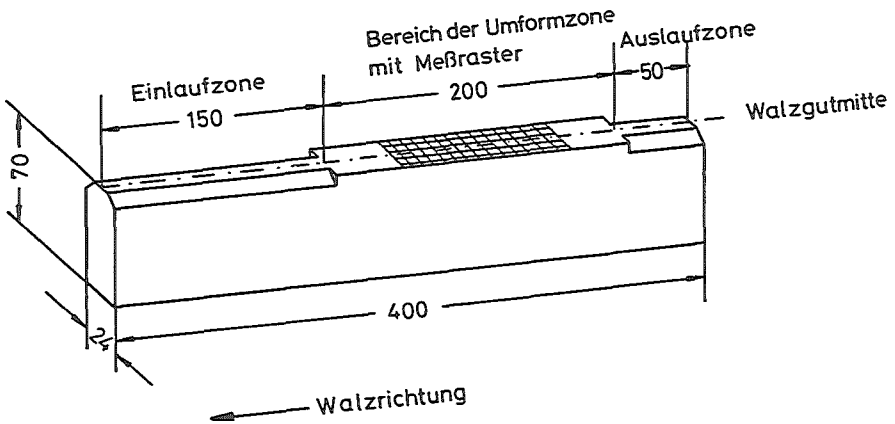

Picture 4: Preparation and size of the roll specimens

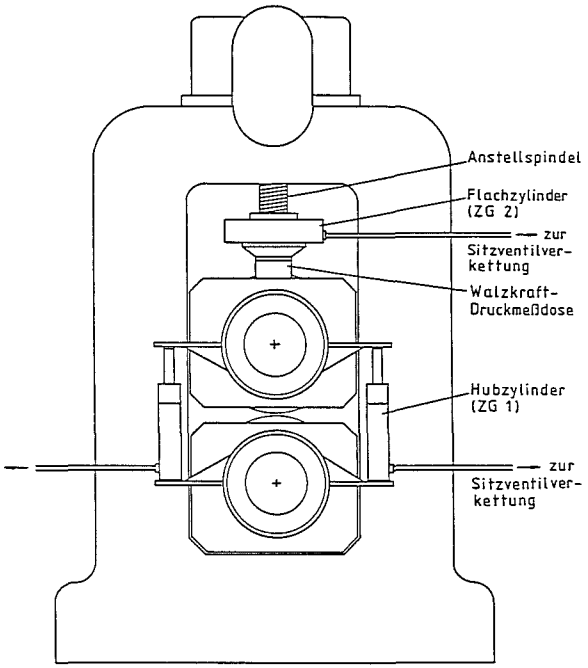

Picture 5: Schematic view of the rolling mill with the installed hydraulic cylinders

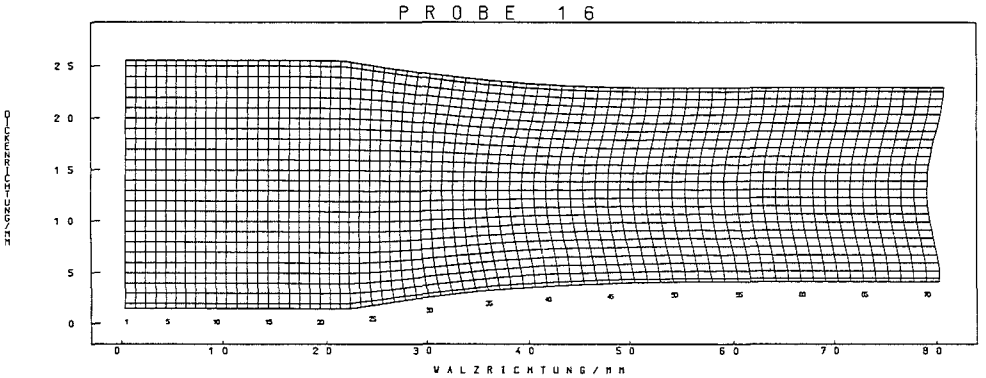

Picture 6: Measured points of intersections on a hot rolled specimen stopped in the grid area

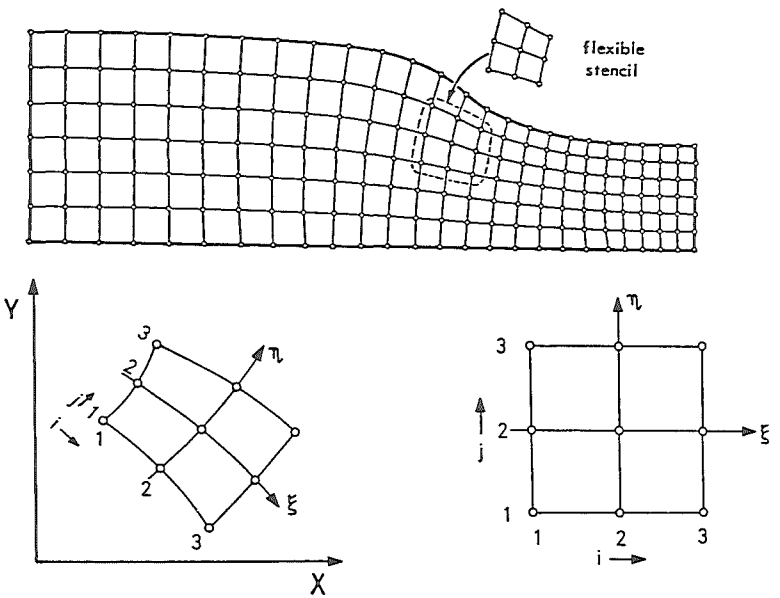

Picture 7: Mapping of a curvilinear flexible stencil onto a corresponding square element in a local reference plane

INTERFACIAL REACTIONS DURING CLADDING OF STEEL BY HOT ROLLING

T. Večko[1], R. Turk[1], H.-R. Priebe[2], G. Borchardt[2]

[1] Univerza E. Kardelja v Ljubljani, VTOZD Montanistika, YU-61000 Ljubljana, Yugoslavia

[2] Technische Universität Clausthal, Fachbereich Metallurgie und Werkstoffwissenschaften, D-3392 Clausthal-Zellerfeld, Federal Republic of Germany

SUMMARY

Cladding of commercial steels (tool steel Č.4850 and construction steel Č.4321 according to YUS norm) was studied by laboratory hot rolling experiments under the same thermomechanical conditions at which commercial rolling of compound strips is performed, i.e. at a temperature of 1150 °C with a degree of deformation of up to 0.5 and a slow cooling rate. The relations between the thermomechanical conditions during hot rolling and the mechanical properties of the compound strip are discussed in terms of the properties of the interfacial layer.

INTRODUCTION

Various phenomena arise during the hot plastic deformation of compound steel which are interesting from both a fundamental and a commercial point of view. From the fundamental point of view the influence of simultaneous plastic deformation and diffusion on the formation of the cladding zone are important, whereas the commercial point of view is concerned more with the preparation of the contact surfaces, the welding of the compound pack and the behaviour of the interfacial layer during cooling to room temperature. For the purpose of commercial rolling of strips it is important that laboratory rolling also takes place in the plain strain state and with similar thermomechanical parameters. The cladding is considered to be successful if a good quality joint is already ensured at the first pass - thus avoiding oxidation of the contact

surfaces at the following deformations - and if the joint strength at room temperature equals at least that of the basic metal.

EXPERIMENTS

Both steels (for the compositions see Table 1) were received as hot rolled plates with a thickness of 25 mm. Wedges were made out of these plates. Their basic surfaces were planed to the desired degree of roughness (< 1 µm). The wedges of both steels were welded together at the outside just before heating (see Figure 1a). The plain strain state was achieved with an appropriate starting geometry [1]. As the elongation of both steels is different, the local values of the average strain and strain rate were determined separately for each layer of the deformed wedge. The rolled compound plates were cooled in the furnace at a well defined rate (see Figure 2). The clad layers of the wedge were metallographically analyzed with an optical microscope. The diffusion of the alloying elements was analyzed using an electron microprobe and Auger electron spectroscopy (for carbon only). The clad strength of the compound plate was determined in a microtensile test, as shown in Figure 1b.

RESULTS

Microstructures: The microstructures of the as received steels are shown in Figures 3a and 3b. The final microstructure is the result of the three processes through which the compound passes during its production (see Figure 4a).

Heating: During heating transport of C, Cr, Mn, V, and Mo occurs only in places where both steels are in direct contact and not via the gas phase. An adhesive clad of weak strength already appears in this stage. Weakness of the joint is due to the presence of surface contaminations, incomplete metal contact because of the roughness of both surfaces, and growth of grains as a result of secondary recrystallisation.

Rolling: During the hot rolling process, direct contact between the surfaces is only possible in places which are free of oxides. So-called "anchor places" are formed where the atoms of both

surfaces reach an interatomic distance so that a metallic bond between them becomes possible. These are areas where the joining of both metals starts. As the deformation continues, the anchor places spread into cohesive bridges and the free surface area gradually decreases. The process is completed when a common intermediate layer has been formed. The unjoined places are filled by atomic diffusion parallel to the surface which is favoured by voids, dislocations, and other microstructural faults in anchor places and in cohesive bridges.

Cooling: Diffusion also continues during the cooling process. Finally, a microstructure is obtained at room temperature, which consists of perlite, fine lamellar perlite, and ferrite (see Figure 4a). The quantity of perlite in the construction steel (I) increases towards the boundary with the tool steel (II). The actual contact layer of the construction steel consists of a ferrite zone of 80 to 100 µm thickness with very finely precipitated carbides (III). The tool steel consists of dispersed perlite and carbides, and directly on the contact layer there is a highly carburized zone with an increased quantity of carbides (IV). The thickness of the carburized layer both in the construction steel and in the tool steel is independent of the degree of deformation. That is why both layers are considered to be formed during the cooling stage.

Microhardness: The microhardness of the cross section of the compound sample is in accordance with the structural changes in the intermediate layer (see Figure 4b).

Concentration profiles: The overall concentration profiles for Cr, Mo, V, Mn, and C agree with the microstructure and the microhardness, respectively (see Figures 5a and 5b).

Tensile strength: The tensile strength of the compound increases slightly during deformation from 620 N/mm² to 680 N/mm². Microtensile test samples broke down outside the contact surface in the ferrite layer, which was formed by the diffusion of carbon from the construction steel to the tool steel during the cooling process. (Details of the carbon migration will be given in another paper [2].)

CONCLUSIONS

The experiments demonstrate that cladding of the two steels is achieved. The moderate tensile strength of the compound material is due to a pure ferrite layer in the contact zone. In further cooperative investigations we shall try to optimize the cooling conditions in order to avoid excessive uphill diffusion of carbon.

ACKNOWLEDGEMENTS

We very much appreciated the skilfull help of Chr. Wolf, E. Ebeling, H.-J. Mauch, W. Schulz and P. Shipley with the type-script, the sample preparation, and the metallographical work, and of R. Görke and of T. Zalar with the electron microbeam analysis and the Auger spectroscopy work. Financial support from the Deutsche Akademische Austauschdienst for one of us (T.V.) and from the Internationales Büro der KFA Jülich formed an essential basis for this international cooperative study.

REFERENCES

1 A. Rekar, Dissertation, Technische Universität Clausthal, 1984

2 T. Večko, R. Turk, H.-R. Priebe, G. Borchardt (in preparation)

TABLES AND FIGURES

	Alloying elements (composition in weight %)						
Steel	C	Si	Mn	Cr	Mo	Ni	V
Č.4321	0.19	0.22	1.30	1.33	0.044	0.16	0.014
Č.4850	1.52	0.26	0.28	11.82	0.65	0.28	0.91

Table 1 The composition of the two steels used in this investigation (see text).

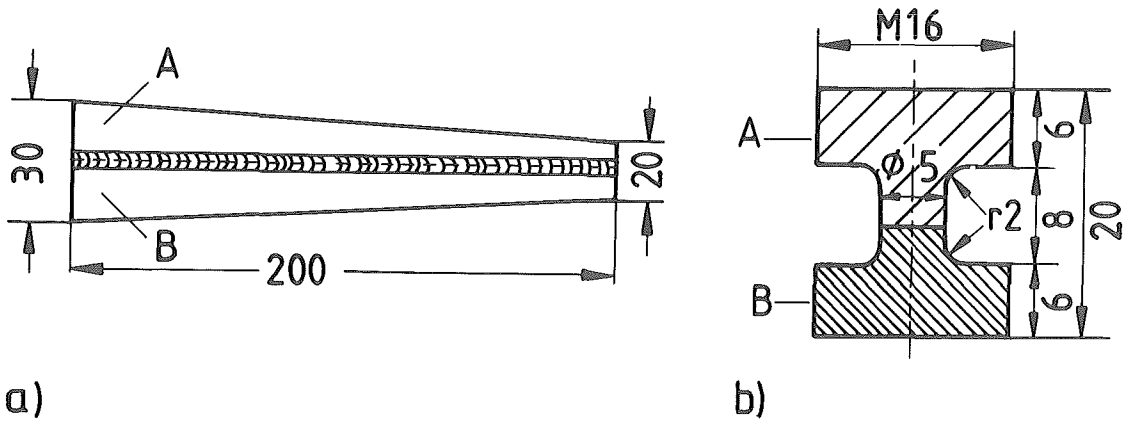

Figure 1 a) Geometry of the welded sample for the laboratory rolling experiment; b) Geometry of the sample for the microtensile experiment: I, II are the construction steel and the tool steel, respectively. (Dimensions are given in millimeters.)

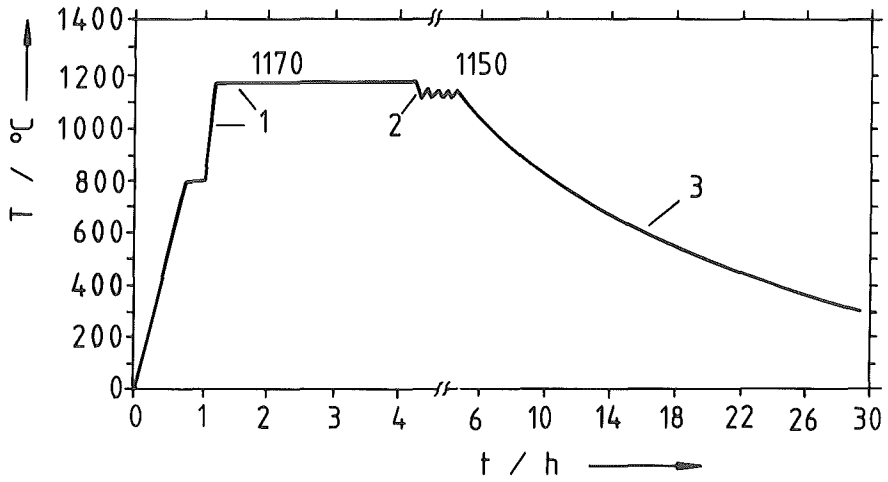

Figure 2 Temperature programme for the cladding experiment: 1 heating, 2 rolling, 3 cooling.

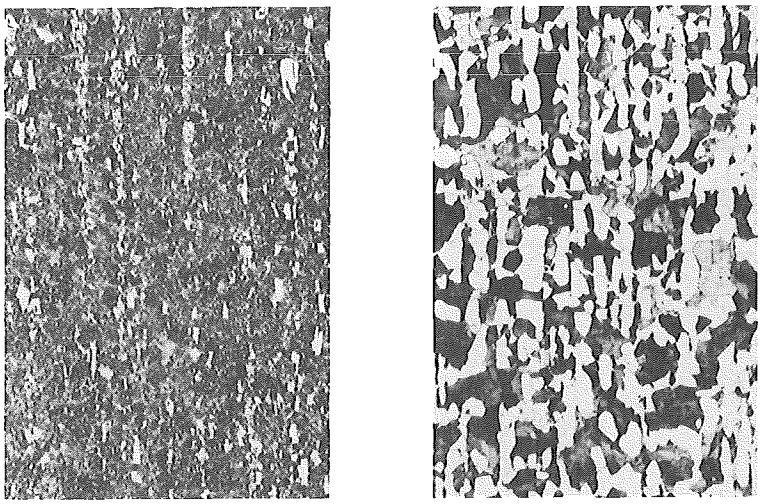

Figure 3 Microstructure of the as received steels: a) tool steel; b) construction steel.

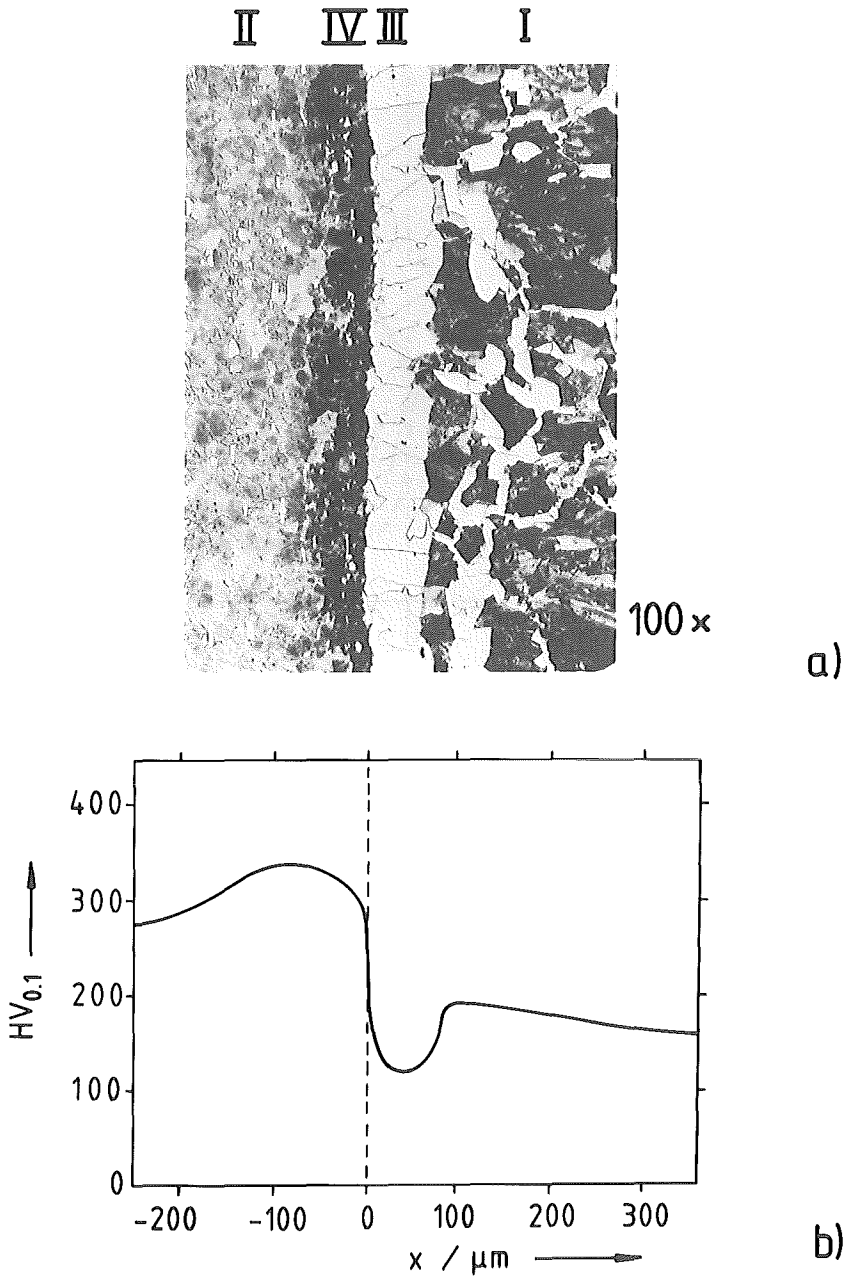

Figure 4 a) Microstructure of the contact zone between the two steels after the cladding experiment (see text); b) microhardness profile of the contact zone.

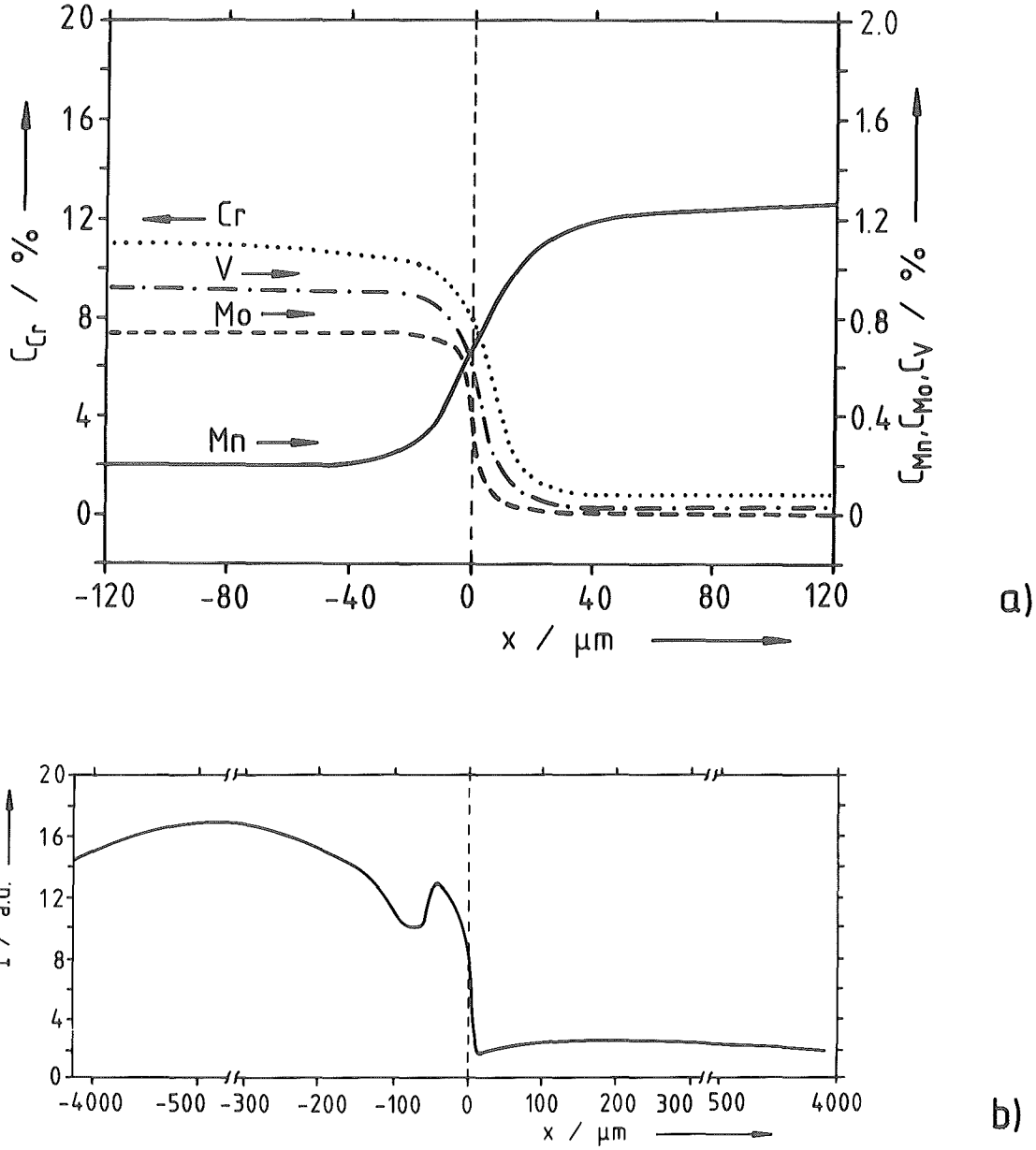

Figure 5 Concentration profiles after the cladding experiment: a) Cr, Mn, Mo, V; b) C.

INFORMATIONS ABOUT HOT FLOW-STRESS CURVES AND THE RESULTING STRUCTURAL CHANGES

I. Bizjak[1], R. Turk[1], P. Funke[2]

[1] Univerza E. Kardelja v Ljubljani, FNT, VTOZD Montanistika, YU-61000 Ljubljana, Yugoslavia
[2] Technische Universität Clausthal, Institut für Werkstoffumformung, D-3392 Clausthal-Zellerfeld, Federal Republic of Germany

SUMMARY

On the basis of the experimental data by a tension testing machine it is possible to apply new numerical method to determinate the continuous changes of the necking of the tensile bars, to construction of a thermomechanical controlled true stress-elongation diagram and new computer programs for the evaluation of all data during the hot tensile test was developed. The results will be compared with the running structural changes; therefore the interpretation of special effects could be improved for the hot deformation behaviour.

INTRODUCTION

The test method for studying of hot workability of methods must enable us to determine the necessary stress for plastic deformation of test material at the given conditions of testing, i. e. temperature, deformation rate and degree of deformation. Secondly it must find the extend of deformation, which can be stood by the test probe without fracture - again at known test conditions. In adition the test must permit an accurate simulation of the intermittend deformation cycles, corresponding to the practical operations of hot deformations. To understand what´s going on with the structure of material at any period of testing, i. e. during and after the deformation we have to ensure rapid cooling of probes in order to keep the high temperature structure down to the room temperature.
So, the test method must permit the determination of workability informations in the range of temperatures, strain rates and strain degrees which are of interest. Because of the direct dependency between the structure changes and the plastic state maintenance conditions and vice versa it is not possible to extrapolate the experimental conditions to the others. The test conditions also depend on the material and the hot forging process, which we are interested in. In this manner the strain rate with the modern hot rolling can be up to 500 s^{-1}.

Among the four main test methods, which are tensile test, compression test (axially symmetric and plane), and torsion test, the tensile test has its peculiarity. It is a non-friction test, the test bar geometry changes under the outer load as determined by the structure changes in the test materials, which are caused by the deformation. Therefore the comparison between the numerically forecasted changing of the bar shape (while numerically simulating tensile test) and experimentally proved changing during the tensile test could be the measure of control of the law of plastic flow and resulting structural changes. This comparison can be the best proof of knowing and controling processes inside plastically deformed materials.
The strain rate varies during the tensile testing. It is a great deficiency of the test because we never know what is the proportion of influence of the increased strain and what is the proportions of influence of the strain rate change on the flow stress change.
At the high speed tensile tests we have to solve the problem of the reconstruction of geometrical changes of the test bar on one side; on the other one we have to follow the change of the actual strain rate. For this purpose a model for the reconstruction of forming of the necking has been developed, which is based on the shape of the deformed bar when the experiment is finished. The model was experimentally tested by photographing the whole test. The shots were compared with the reconstructed shape for the same moment of the test. The reconstructed shapes with those obtained by photo shows the validity of the model. We used the reconstructed states to correct the load-elongation curve respectively engineering stress-strain curve into the true stress - true strain curve. At the same time the model enable us to follow the changes of strain and strain rate.
Let us refer to the true stress-extension curve, equipped with the flow of true strain and true strain rate - as a thermomechanically controlled (TMC) true curve. It contains all the middle value informations in lateral and longitudinal direction of the test bar. Thermomechanically controlled true curve is the base for:

- mathematical form of plastic flow law and for
- understanding of structure changes taking place during the plastic state maintenance or the changes which are the consequence of it.

RECONSTRUCTION OF THE CYLINDRIC BAR DEFORMATION IN NECKING ZONE

The shape of the contour only depends on movement of the cross-section, separating the plastically stressed and plastically unstressed area. The movement of the separating surface depends on fulfilment of the yielding condition.

The shape and the resulting structure of the deformed bar mirror the whole process of its plasic working. All point on the surface on the bar except those, which are in plastic state at the moment, the testing is interrupted, were in a certain moment on the separating surface. In the first aproximation let the corresponding cross-section define separating surface, and let the volume with all lesser cross-sections define the instanttaneous corresponding plasticaly loaded volume (it's size is known from the tested bar). Next we only have to determine the shape of this volume, which gives the instanttaneous length of bar; by that the position on the engineering curve (force-extension) is known. The smallest cross-section of this volume is the starting point for the calculation of the middle true stress and the length of this volume is the starting point for the calculation of the middle logitudinal strain rate.

The complete procedure of the correction of the technical diagram into the true diagram is as follows:
The test being completed, we first measured precisely the contur of the bar with the measuring microscope. We avoited the discontinuity by using splines. On the conture of the bar we chose a sequence from the begining of the bar to the point of breakdown. Analogously an equivalent sequence of points of corresponding cross-section has been set on the remaining part of the bar. The reconstruction of the instantaneous shapes of the bar is done iteratively. At each step we acquire two new points (one from each sequence) in adition to the points acquired in the previous step. We take that these two corresponding points were in a given moment of the deformation on the separating surfaces between the plastically loaded and plastically unloaded area. We fixed the points of the first sequence and we let the points from the second sequence to move along the bar axis. We do linear or nonlinear regression on all the acquired points - depending on the assumed function model for the shape of the bar. From the calculated function model we can compute the volume between the separating surfaces of the bar. This volume has to be equal to the one measured with the microscope. Because generally it is not true yet, we have to move the mavable set of the regression points (at each step doing regression again of course) until the volumes are equal. From the final position of the points and from the eventual function model we compute instantaneous bar extension, the length of the plastic area and the radios of curvature at the thinest part of the bar. These data serve later for the correction of the engineering curve (force - extension) into the thermomechanically controlled true stress - extension curve.

RESULTS

The reconstruction of the necking zone contour change:

The sequence of Figures 1a and 1b shows the comparison between the reconstructed and photographed contour.We treat whole area of the homogenous strains on the basis of the validaty of volume conservation of a cylindrical shape. We start with a nonhomogeneous necking, when the convergence of stepwise regression of the function medel is present. The reconstruction procedure is well conditioned because at each step we start from the deforming contour.

The construction of thermomechanically controlled true diagram and database for the mathematical formulation of yield stress curves:

A number of results on different materials showed, that the model keeps all the refinements of the changes of forces and stresses, wich are necessary for the maintenance of the plastic state. With these refinements we mean the ones, wich are the consequence of the structural changes or the processes in connection with it.

For the study of formability a shape of true stress - extension curve equiped with the strain and strain rate flow is more suitable. The flow of strain rate precisely defines the deformation of transition from homogeneous into the nonhomogeneous area. This deformation determines the transformation from the true diagram into the yielding curve by Gridgeman. The transformation i.e. correction of the true diagram can be done in which case the curvature of the contour at this point of necking is needed. This data are given by the recontruction model. The series of such diagrams (see Figure 2) for differnt testing conditions constitutes the data base for the mathematical definition of the yield stress curves.

Structural changes during and after the plastical deformation:

The starting point for the development of hot structures is the delivered thermical and working energy. Therfore the recorded interdependence between force and extension shown in the coordinates flow stress - strain or flow stress - temperature must clearly determinate the causes for the structure changes, which are present during the plastic deformation (dynamic process) or which follow it (static process). The development of hot structures leads to new characteristics of materials for the reason we have to know and control that process. With hot formability we are interested in determination of:
- the parameters of dynimic softening,chiefly recristalization and
- the parameters of static softening.

The begining of the dynamic recristalization is agreed upon to be determined by the strain at which the curves flow stress - strain instantaneously doesn't rise with the increasing strain (see Figure 2). The dynymic recristalization occurs during the fall of flow stress.

The static softening of material subjected to hot loading in the sequence of deformation, holding period on deformation can be roughly determined - for the needs of designing the forming technology - by mean of softening coefficient; this can be defined as follows (see Figure 3a):

Y_k^1 is the yield stress at interruption of the first deformation cycle

Y_{o2}^1 is the offset yield stress of the first deformation cycle

Y_{o2}^2 is the offset yield stress in the second deformation cycle.

Example of evolution is here formulation of the softening characteristic of low carbon steel Č.o147. The curves on the diagram softening - holding time show the static softening (see Figure 3b): the first at the temperature of lo5o°C and the second at the temperature of 95o°C. The strain of the first cycle equals the end of the first cycle of dynamic recristalization. The softening degree of the first cycle of dynamic recristalization equal E = o.3lo at temperature lo5o°C and at strain o.187. But this degree eguals E = o.2o8 at temperature 95o°C and at strain o.299. Therfore more of stored working energy remains at temperature 95o°C after the deformation. This energy is parially freed through post dynamic recristalization. The static recristalization starts only after 12 sec. and ends after 27 sec.. At temperature lo5o°C so much of energy of the deforming metal has been consumed by dynymic recristalization, that the post dynamic softening has no essential effect anymore. The static recristalization starts after 6 sec. already and ends 17 sec. after the dinished deformation.

CONCLUSIONS

We have shown the posibilities of construstion of a thermomechanicaly controlled diagram true stress-elongation, equipped with no stable flow of strain rate as it is the only good basis for studying the formability of metals. The model of reconstruction of plastic necking zone is based on the data of deformed bar and therfore the reconstruction is independent on how fast the test is performed.

A number of experiences showed that the usage of the model keeps all the changes of the stress during the deformation and therefore the true diagrams are useful for the study of the causes of structur

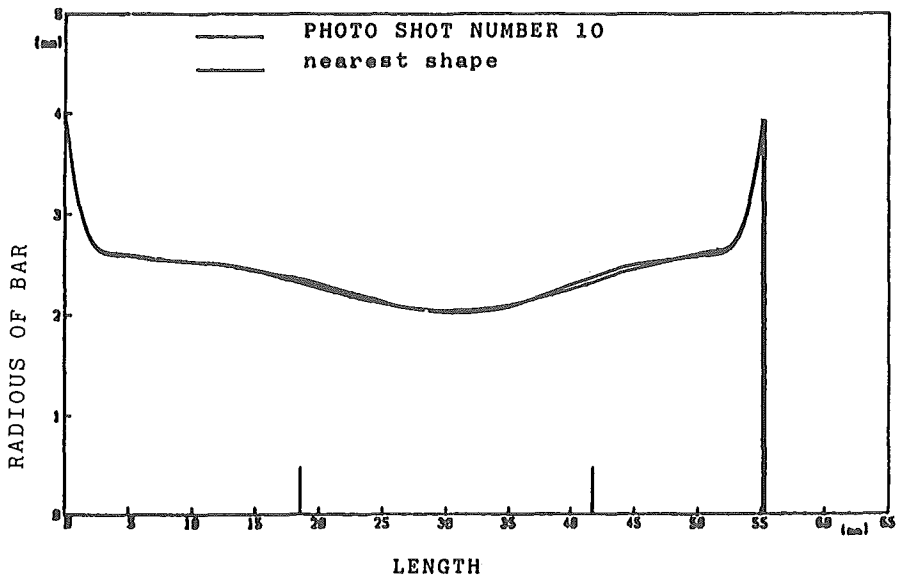

a

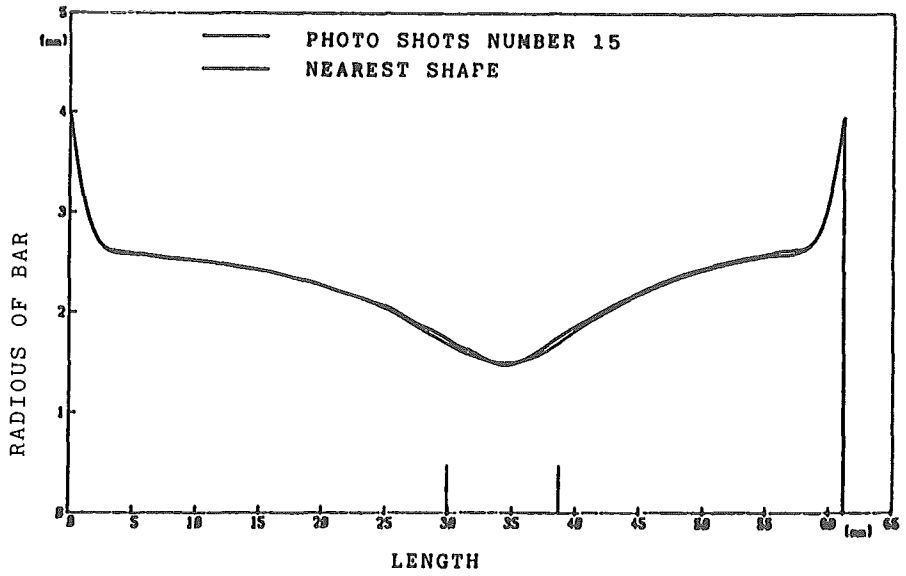

b

Fig. 1a and 1b: Comparison between the reconstructed and photographed contour by cylindrical bars

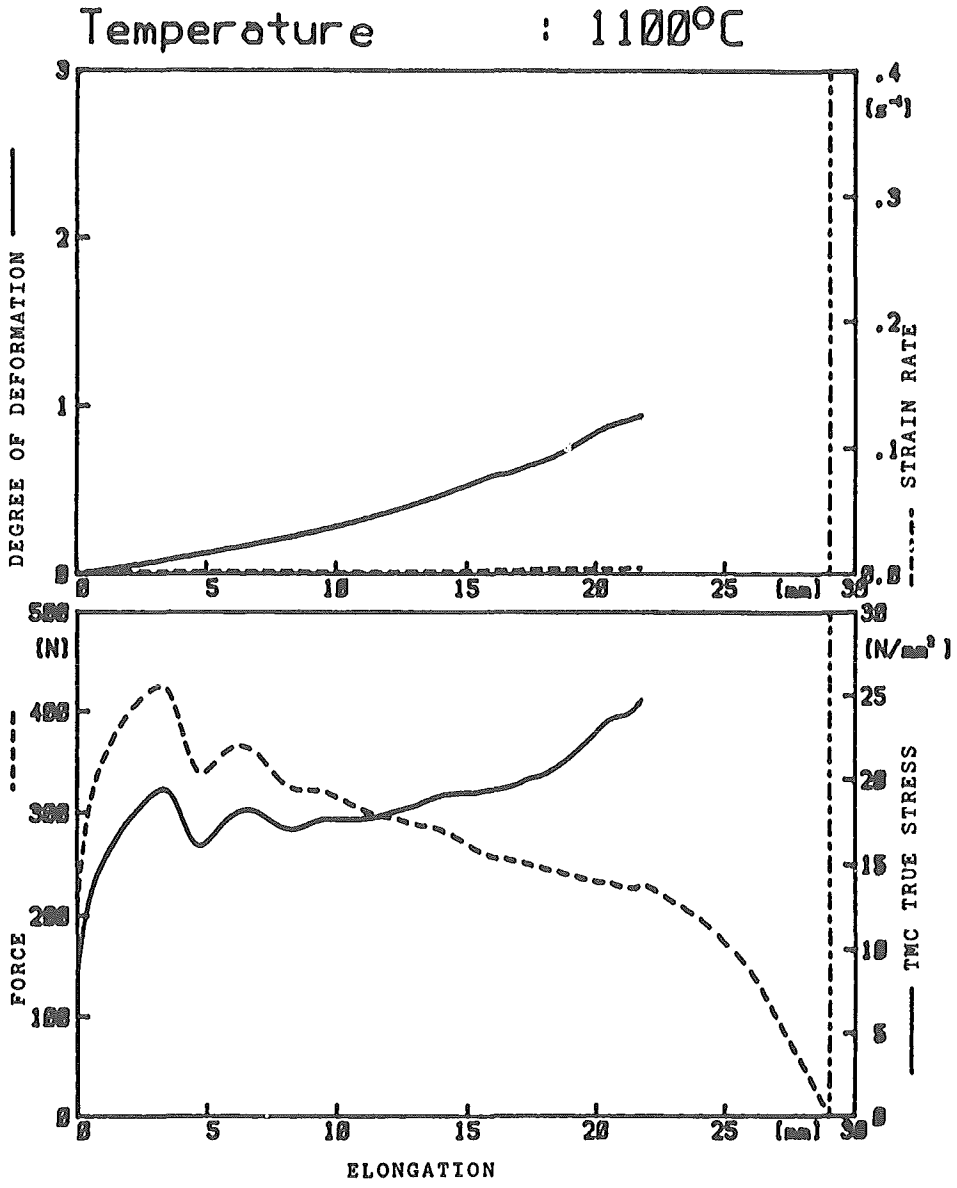

Fig. 2: Thermomechanically controlled yielding curve

changes during and after the hot plastic deformation. The model of forecasting the effects of plastic deformation using the finite elements method as the superstructure of the reconstructing results is under development.

ACKNOWLEDGEMENT

The presented work has been suported by internationalen Büro der Kernforschungsanlage Jülich. This is gratefully acknowledged.

REFERENCES

1 R.Turk, Dissertation FNT Ljubljana 1983, Ein Modell für die Beurteilung der Warmformgebungseigenschaften der Metalle.

2 R.Turk, I.Bizjak, International symposium on the plasticity, Herceg Novi 1986, The reconstruction of geometrical transformation of a cylindrical bar by a hot tensil test.

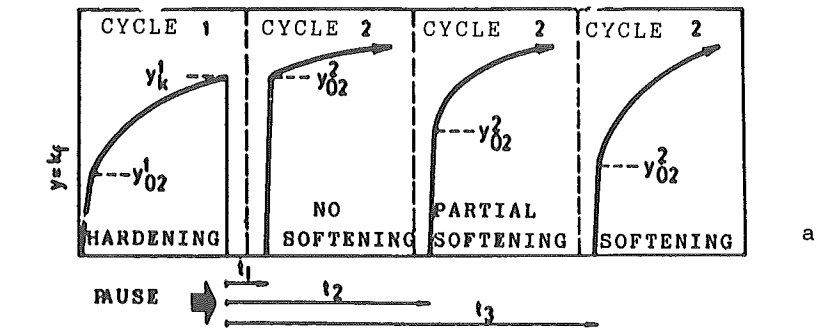

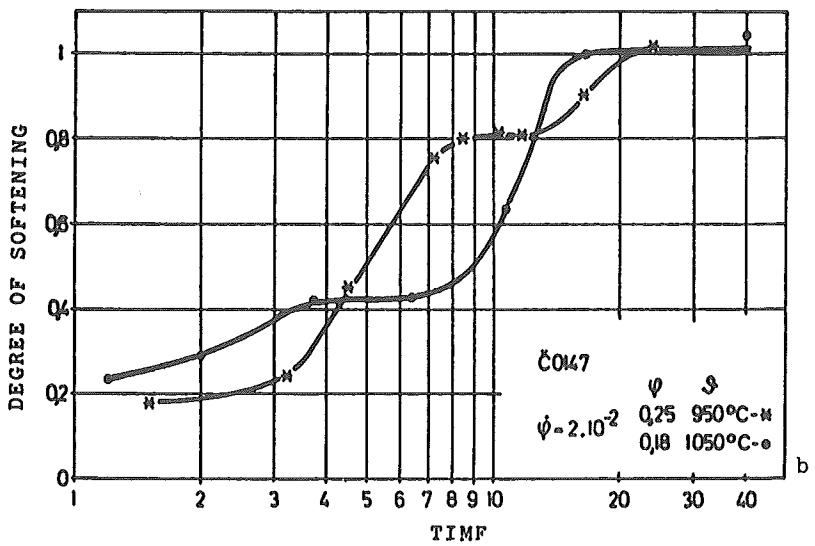

Fig. 3: Softening-holding time diagram of low carbon steel

M E T A L S (3)

PHYSICO-MATHEMATICAL INVESTIGATION OF THE CONSOLIDATION OF IRON POWDER

R.Agatonović, R.Novaković, D.Stefanović* and M.M.Ristić

Serbian Academy of Sciences and Arts, Department of Physical Chemistry, Knez Mihailova 35, 11000 Beograd, Yugoslavia

* Electronic Faculty, University in Niš, Niš, Yugoslavia

Abstract

Consolidation of iron powder has been investigated in this paper. The results obtained by measuring the changes of the TEMF in function of pressure give the possiblility for the process of consolidation to be considered from the point of new electron configuration model.

Introduction

Following the classic attitudes of the sintering physics, all up-to-date investigations of the consolidation process were mainly focused to the estabilshment of the correlation between the properties, on the one hand and structure on the other.

However, the very following of the essence of a transport process occurring in a solid body, imposes the necessity of the consolidation process to be considered from electron point of view. Development of the quantum theory of a solid body offers different models for the explanation of physical properties of different materials, as well as for the changes occurring in materials exposed to different processes.

In our experimental work we studied the changes which were evident in the course of consolidation of iron powder and con-

nected with the change in pressure. We measured the change of the TEMF in function of pressure and came to the conclusion that this complex dependence can be only explained by electronic theory of a solid state.

EXPERIMENTAL

During experimental work we used iron powder purity of 99,9% and grain size of 1-5 $/$um.

The powder was pressed by two-sided pressing method within pressure interval 0,1 GPa - 1,2 GPa in the matrix Ø 10 mm.

Having applied the method, previously developed (1), we measured the influence of the pressing pressure on the change of thermoelectromotive force at the contact Fe (sample) - constantant. The results obtained are presented in Table I.

Table I. The values of TEMF depending on the pressing pressure

p	ρ	TEMF
MPa	g/cm^3	mV
1	2	3
41.97	4.413	9.929
50.58	4.500	10.082
66.49	4.616	10.184
75.75	4.690	10.142
101.53	4.880	9.870
120.53	5.018	9.858
129.49	5.037	10.145
153.25	5.180	9.908
156.96	5.220	10.243
171.12	5.268	9.746
181.16	5.342	9.626
185.30	5.390	9.396
200.56	5.411	9.157
243.50	5.647	9.935
250.70	5.684	9.860
278.66	5.740	10.074
315.32	5.908	10.114
369.08	6.058	10.088

Table I. - continued

1	2	3
374.18	6.128	10.069
393.80	6.188	10.101
443.97	6.353	9.842
494.14	6.486	10.001
552.63	6.552	9.840
573.07	6.593	9.816
622.12	6.653	9.850
694.16	6.823	9.909
728.24	6.833	10.016
784.80	6.963	9.966
800.30	7.007	9.859
855.65	7.022	9.797
891.03	7.083	9.985
934.39	7.157	10.070
997.71	7.189	9.967
1084.97	7.269	10.010
1187.86	7.295	10.013

DISCUSSION

The TEMF method proved to be very suitable for characterization of the state of a porous system, particularly when estimating the role of the Fermi level in the analysis of the state of the given system.

It is known that during the pressing process of disperse powders, the sintering occure at the particles contacts. The cause of the sintering results, in essence, results from electrons tunnelling at the given potential baririer what has been previously established (2).

The change in electron structure takes place at pressures of 10^8-10^9 Pa order and is manifested by s-d and s-d-f transitions of valent electrons. However, these pressures can be obtained even at the initial stage of pressing, as the specific surfaces are very small at particles contacts.

The results we obtained by measuring the change of the TEMF in function of pressure enable us to consider the consolidation process from the point of electron configuration model, based on the principle of redistribution of collectivized and

localized electrons, as well as on the change in spectrum of localized electrons. Thus, the increment in localized electrons caused formation of covalent bonds between the neignbouring atoms in material (at particles contacts) when a part of a covalent bond dominates over the metal one. Increment in number of localized electrons leads to decrement of the Fermi level, what is caused by electrons transition into a lower, non-occupied zone, thus causing the value of the TEMF to rise.

The explanation of the electron process occurring along the boundary of the initial and medium stages of the cold sintering of iron powder, by this model is also possible. As the pressures that correspond to the beginning of the medium stage are almost equal to the boundary of a material plastic flow ($p \approx \sigma_{0,2}$) this means that the particles plastic deformation, being followed by a constant formation of dislocations, takes place. The process of dislocations formation causes electrons delocalization, breaks covalent bonds and leads to the rise in concentration of collectivized electrons, concentrated within dislocations surrounding. This causes the Fermi level to shift towards higher energies, i.e. the corresponding reduction of the TEMF.

As is known, the charge carriers transport is possible in case when two materials are closely connected. In our experiments, the samples of iron powder were in close contact with constantant and the change in the TEMF with pressure was measured by the method described in Ref.1. As the TEMF depends on concentration of electrons in both materials and on temperature of contact, the following can be determined on the basis of the known equation (3):

$$E = \frac{kT}{q_o} \ln\left(\frac{n_2}{n_1}\right) \qquad (1)$$

where: E - TEMF,
n_2 - concentration of electrons in iron,
n_1 - concentration of electrons in constantan,
k - Bolcman's constant,
T - temperature at iron-constantan contact, and
q_o - electron charge.

Starting from equation (2) we determined n_2/n_1 ration, given in Table II.

Table II. The ratio of concentration of electrons in iron and that in constantan depending on the pressing pressure

p	$\frac{n_2}{n_1}$
MPa	-
41.97	1.0401
50.58	1.0707
66.49	1.0411
75.75	1.0409
101.53	1.0398
120.53	1.0398
129.49	1.0410
153.25	1.0400
156.96	1.0414
171.12	1.0393
181.16	1.0388
185.30	1.0379
200.56	1.0369
243.89	1.0401
250.70	1.0398
278.66	1.0407
315.32	1.0408
369.08	1.0407
374.18	1.0406
393.80	1.0408
443.97	1.0397
494.14	1.0404
552.63	1.0397
573.07	1.0396
662.12	1.0397
694.16	1.0400
728.28	1.0404
784.80	1.0402
800.30	1.0399
855.65	1.0395
891.03	1.0403
934.39	1.0407
997.71	1.0402
1184.97	1.0404
1187.86	1.0404

A mathematical model, which at the same time connect the mutual dependence of E, p and n_2/n_1 was established owing to the analysis of the obtained values for the TEMF, by the ratio of concentration of electrons in iron and that in constantan and by the pressing pressure. This model confirms the existance of three stages during iron powder consolidation which were determined by our previous experimental results (1,5). When testing the functional dependences E, the optimum agreement was obtained by linear regression model of the first order (4) for single pressing stage.

The general form of this mathematical model is given by equation:

$$E = a_o + a_1 p + a_2 \frac{n_2}{n_1} \qquad (2)$$

Table III presents the values for coefficient of a mathematical model, given by equation (2) and the mean square error G(%) after the stages of the consolidation process of iron powder.

Table III. Coefficients and the mean square error of equations of linear regression model of the first order, describing the consolidation process of iron powder after stages.

stages	a_o	a_1	a_2	G(%)
I_a	-252,3	$2{,}93 \cdot 10^{-4}$	252,1	0,013
I_b	-234,8	$4{,}89 \cdot 10^{-6}$	235,3	0,022
II	-245,2	$2{,}55 \cdot 10^{-6}$	245,3	0,034
III	-231,3	$1{,}06 \cdot 10^{-5}$	232,0	0,031

From the mathematical point of view, the applied model presents a plane in space. This means that a physical dependence of TEMF in function of pressure and electrons concentration, regarded from mathematical point of view, is presented by planes in space. Having thoroughly analysed the model in question, we came to the conclusion that different values of pressure and electrons concentration, that might belong to different stages, correspond to particular values of the TEMF. In other words, the conditions of consolidation system i.e. the mechanisms that dictate a transport processes, periodically repeat with the change in pressure.

CONCLUSION

It was established that the processes at electron level control the consolidation process of iron powder. The mathematical model connecting the mutual dependence of the pressing pressure, thermoelectromotive force (TEMF) and electrons concentration, has been developed. The physical essence of the TEMF occurrence during consolidation of iron powder has been presented on the basis of this model.

REFERENCES

1. D.Stefanović, M.M.Ristić, A study of the consolidation process by measurement of the work function of electrons, Science of Sintering, Vol. 8, No. 2, pp.163-168, 1976
2. Van der Ziel, Solid state physical electronics, Prentice-Holl, New Jersey, 1968
3. A.M.Vasiljev, A.T.Glazunov, V.A.Fobrikont, Fizika i Tehnika, Znanie, Moskva, 1977
4. E.Förster, B.Rönz, Methoden der korrelations-und Regressionsanalyse, Berlin, 1979
5. R.Agatonović, D.Stefanović, V.Petrović, M.M.Ristić, Horizons of Powder Metallurgy, Part II, Diseldorf, 1986

P-T DIAGRAMS OF TRANSITION ELEMENTS

R.Novaković and M.M.Ristić

Serbian Academy of Sciences and Arts,
Department of Physical Chemistry,
Knez Mihailova 35, 11000 Beograd, Yugoslavia

Abstract

The mathematical-physical analysis of phase transformation in function of temperature and pressure has been done in this paper. The analytical expressions characterizing the phase transformations have been obtained. The initial thermodynamic conditions can be defined in advance on the basis of these analytical expressions in order that the desired phase can be obtained.

Introduction

The analytical descriptions of the curves that characterize the behaviour of elements when exposed to high pressures can be given by different methods. The methods of approximations by polynoms require a great number of information on a curve and they have limited possibilities of interpolation concerning narrow intervals of definition.

Mathematical formulation of P-T state diagrams

One of the approximative methods of curves describing the behaviour of elements under high pressures is given by exponential functions in fragmentary system of coordinates (Fig.1). On the basis of this method, the general types of equations for approximation of curves can be obtained, as well as for the prognosis of the shape of curves in systems of any type. A fragmen-

tary system of P'-T' coordinates where P'-pressure and T'- temperature corresponds to any type of curves. In this coordinate system, the curves are described by equations of the following type:

$$T' = k\ (P)^{Q} \tag{1}$$

When a fragmentary system is changed for Cartesian coordinates, the equation (1) changes into the following:

$$T = k\ (P-P_o)^{Q} + T_o \tag{2}$$

where $T_o < T_1 < T_2$ and $P_o < P_1 < P_2$

$$Q = \frac{\ln\ (T_1 - T_o) - \ln\ (T_2 - T_o)}{\ln\ (P_1 - P_o) - \ln\ (P_2 - P_o)} \tag{3}$$

$$k = \frac{T_1 - T_o}{(P_1 - P_o)^{Q}} \tag{4}$$

or

$$T = T_o - k\ (P-P_o)^{Q} \tag{5}$$

where $T_2 < T_1 < T_o$, $P_o < P_1 < P_2$

$$Q = \frac{\ln\ (T_o - T_2) - \ln\ (T_o - T_1)}{\ln\ (P_2 - P_o) - \ln\ (P_1 - P_o)} \tag{6}$$

$$k = \frac{T_o - T_2}{(P_2 - P_o)^{Q}} \tag{7}$$

In this paper we shall consider one-component state diagrams of IV Vand VI groups of transition elements. Table I. gives the values of parameters of equation (2), SWASK (d^5), the points of melting and entropy for the mentioned elements.

Table I. Values of $\underline{k}$, $\underline{Q}$ and T_o parameters after (2), (3) and (4) and SWASK (d^5), $T_{melt.}$ and S^o_{298} for transition metals of IV, V and VI groups of the Periodic systems of elements

No. of element	name of element	k	Q	T_o [K]	SWASK (d^5)	$T_{melt.}$ [K]	Entropy S^{298}
22	Ti	0,000125 1,24 0,107	1,61 0,56 0,992	1153 908 305	43	1933	30,5578
40	Zr	-0,0269 0,3	1,006 0,95	1133 303	52	2133	38,9298
72	Hf	-0,007 0,065 0,149	1 0,997 1	2010 1800 160	55	2498	54,8366
23	V				63	2083	29,302
41	Nb				76	2741	36,5437
73	Ta	0,053	1	3285	81	3273	41,4414
24	Cr				73	2123	23,77648
42	Mo	0,01	0,96	2893	88	2883	28,5904
74	W	0,072	1	3693	96	3653	33,488

The method of Fisher's linear discriminant and classification of P-T state diagrams

In order to prognosis the shape of curves that describe the unknown P-T state diagrams given in Table I, we shall use the classification method from theory pattern recognition, known as the method of Fisher's linear discriminant [5]. The essence of this method is in the following: The set X consisting of

n,d- dimensional samples $x_1 \ldots\ldots x_n$, that each x_i has d-coordinates, which characterise it. These samples shape of $x_i = (x_{i1} \ldots\ldots x_{id})$ should be mapped from R^d space on R^1 line in set Y in order that the projected sampels are well separated. The initial classes X_1 and X_2 must be defined according to well marked properties. The purpose of the whole procedure is to determine the Fisher's discriminant (classifier) to obtain the scalar as follows:

$$Y_i = W^T \cdot X_i \tag{8}$$

where Y_i are projections of X_i vector at direction of W vector. The sample means of set X is given by expression:

$$m_i = \frac{1}{m_i} \sum_{XEX_i} X \tag{9}$$

and that of Y

$$\tilde{m}_i = \frac{1}{n_i} \sum_{YEY_i} Y$$

$$= \frac{1}{n_i} \sum_{XEX_i} W^T X = W^T \cdot m_i \tag{10}$$

$$\bar{S}_1 = \sum_{YEY_i} (Y - m_i)^2 \tag{11}$$

The difference $/\tilde{m}_1 - \tilde{m}_2/ = /W^T(m_1 - m_2)/$ is the between-class scatter, and
$S_1^2 + S_2^2$ is called the total within-class scatter.

The Fisher's linear discriminant is defined as a linear $W^T X$ function for which a criterion function

$$I\ (W) = \frac{/\tilde{m}_1 - \tilde{m}_2/^2}{\bar{S}_1^2 + \bar{S}_2^2} \tag{12}$$

has a maximum, namely the ratio of the between-class scatter to the within-class scatter is maximum. To obtain I (W) as an explicit function of W, we should define within-class matrices S_i and S_w:

$$S_i = \sum_{XEX_i} (x - m_i)(x - m_i)^T \tag{13}$$

and

$$S_W = S_1 + S_2 \tag{14}$$

When connecting (12), (13) and (14) we obtain

$$\tilde{s}_i^2 = W^T S_i W \tag{15}$$

and consequently we have

$$\tilde{s}_1^2 + \tilde{s}_2^2 = W^T S_W W \tag{16}$$

Similar to (12) we have

$$(\tilde{m}_1 - \tilde{m}_2)^2 = W^T S_B W \tag{17}$$

where S_B is a matrix of between-class scatter. As it is an outer product of two vectors its rank is at most 1. In particular, for any W, $S_B W$ is the direction of $(m_1 - m_2)$, and S_B is quite singular. The expression (12) can be now written in the following form:

$$I(W) = \frac{W^T S_B W}{W^T S_W W} \tag{18}$$

It is casy to show that a vector W maximising I must satisfy

$$S_B W = \lambda S_W W \tag{19}$$

which is a generalized eigenvalue problem. As matrix S_B is regular and $S_B W$ is always in direction $(m_1 - m_2)$ the solution W can be found direction from

$$W = S_W^{-1}(m_1 - m_2) \tag{20}$$

The general laws of unknown P-T state diagrams of transition elements

The above mentioned method was applied according to data given in Table I. The initial classification was done according to the number of phases shown in P-T diagrams (Fig. 2). The first

subset X_1 consists of P-T state diagrams of IV group of transition elements being of complex shape. The second subset X_2 is consisted of P-T state diagrams of V and VI transition elements of simple shape. In this paper we shall perform mapping of R^3 space into R^1 space. Three components: SWASK, $T_{melt.}$ and S^o_{298} form a measure vector. Mean vectors in X_1 and X_2 are:

$$X_1: m_1 = \begin{bmatrix} 79,5 & 2782,67 & 32,19 \end{bmatrix}^T$$
$$X_2: m_2 = \begin{bmatrix} 50 & 2188 & 41,4419 \end{bmatrix}^T \qquad (21)$$

The matrix within-class scatter in:

$$S_W = \begin{bmatrix} 83.5 & 3905.77733 & 25.548 \\ 3905.77733 & 233105.926 & 2195.57267 \\ 25.548 & 2195.57267 & 55.8336667 \end{bmatrix} \qquad (22)$$

The matrix between-class scatter is:

$$S_B = \begin{bmatrix} 870.25 & 17837.76 & -292.92 \\ 17837.76 & 367625.81 & -5594.04 \\ -272.92 & -5594.04 & 85.59 \end{bmatrix} \qquad (23)$$

The vector according to which the mapping is performed is:

$$W = \begin{bmatrix} 1,007 & -0,016 & -0.0995 \end{bmatrix}^T \qquad (24)$$

The mappings of R^3 space into R^1 space according to vector W are given in Fig. 3, while the corresponding numerical values are shown in Table II.

$I(W) = \frac{439}{21}$ shows a good relations of class scatter.

Table II. Numerical values of mapping of R^3 space into R^1 space for transition elements of IV, V and VI group of the Periodic system of elements.

ELEMENT	Ti	Zr	Hf	V	Nb	Ta	Cr	Mo	W
MAPPING	9,7	14,8	10,4	27,6	29,6	25,7	37,6	40,2	35,6

Due to the comparative analysis of the obtained results (Table II), (Fig. 2) and (Fig. 3) we can obtain the intervals in which are the unknown parameters k and Q of equation (2). Thus we can make prognosis for unknown P-T state diagrams for V, Nb and Cr. The distance between points is a criterion function. The estimation of intervals of unknown parameters from (2) are given in Table III.

Table III. Intervals of parameters k, Q and T_o for unknown P-T state diagrams of V, Nb and Cr.

parameter	k	Q	T_o K
element			
V	0,03-0,04	0,98-0,99	2083
Nb	0,04-0,05	0,96-0,97	2741
Cr	0,03-0,04	0,97-0,99	2123

Conclusion:

The mentioned theoretical considerations represent contribution to phenomenological approach of state diagrams. This classification method can be also applied on multicomponents systems, but requires much more informations about corresponding characteristics.

References

1. M.M.Ristić, Osnovi nauke o materijalima, Naučna knjiga,1982
2. R.M.Novaković, F.V.Skripnik, S.M.Radić, M.M.Ristić, Dijagrami stanja elemenata u oblasti visokih pritisaka, CMS BU, Beograd, 1985.
3. M.Bertolino, Numerička analiza, Naučna knjiga,1977, Beograd
4. K.Fukunaga, Intraduction to statistical pattern recognition, Academic Press, New York and London, 1972.

5. R.O.Duda, P.E.Hart, Pattern classification and scene analysis, John Wiley & Sons, New York, 1973.

6. M.M.Ristić, F.V.Skripnik, L.F.Pryadko, Estimation of Physical Properties of Transition Metals Based on a Configuration Model of Solids, Monatschefte für Chemice 118, 323-328 (1987)

7. A.N.Krestovnikov, L.P.Vladimirov, B.S.Guljanicki, A.Ya.Fišer, Spravočnik po rasčetam ravnovesii metalurgičeskiih reakcii, Moskva, 1963.

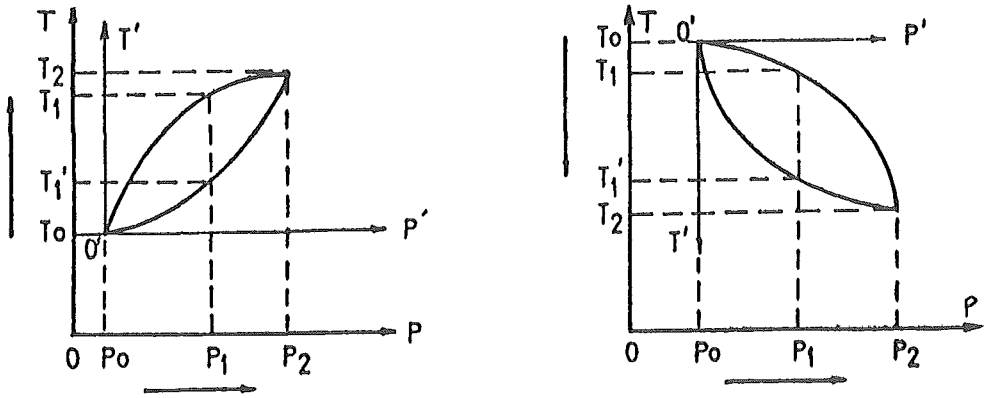

Fig. 1

Exponential curves in fragmentary system of coordinates

Fig. 3

The mappings of R^3 space into R^1 space according to vector W

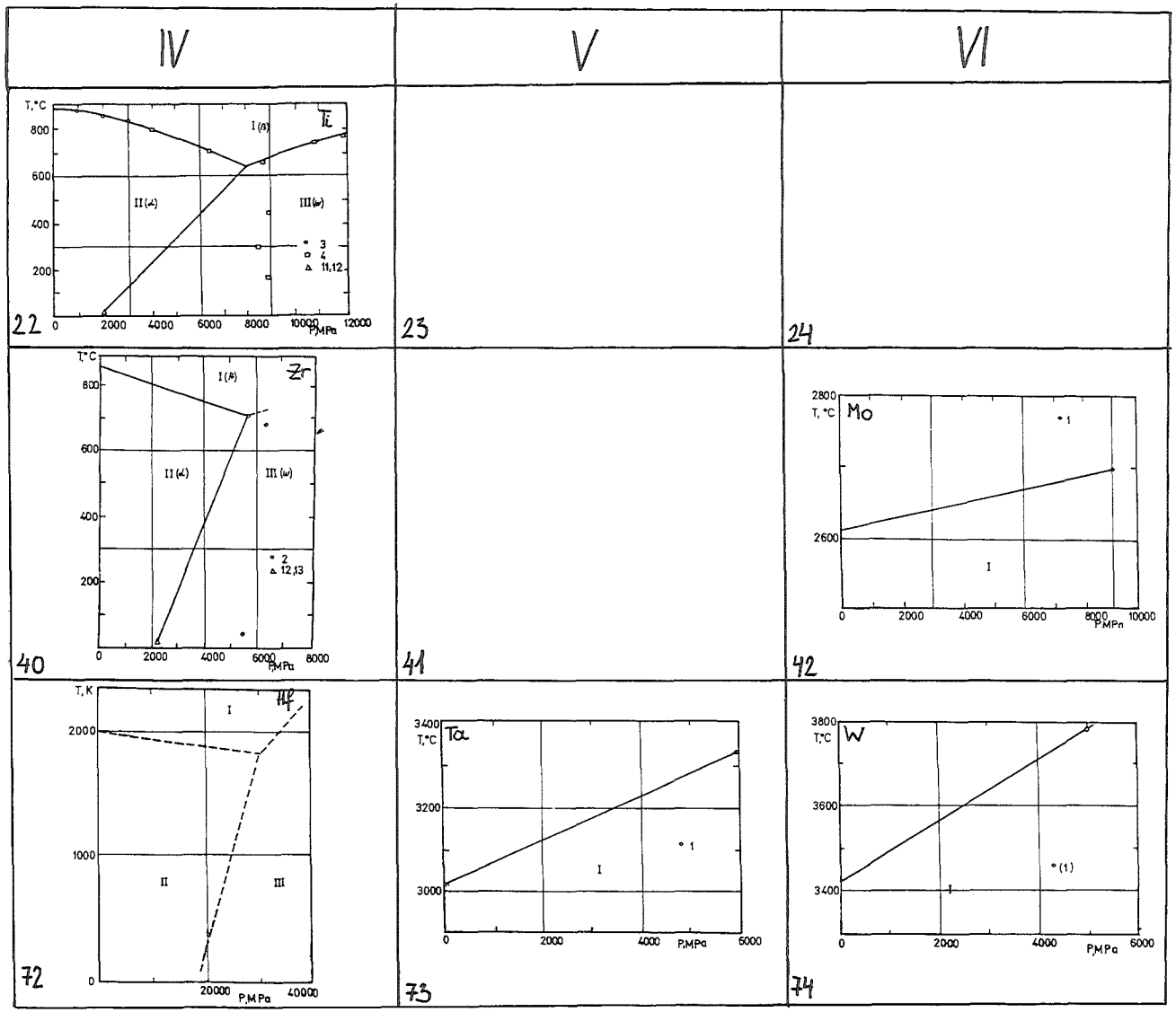

Fig. 2

P-T state diagrams of transition elements of IV, V and VI groups

L I S T O F P A R T I C I P A N T S:

Agatonović, Ratomir, MSc.
Serbian Academy of Sciences and Arts
Department of Physical Chemistry
Knez Mihajlova 35, 11000 Beograd, YU

Arsov, Ljubomir, Prof.Dr.
"Kiril i Metodij" University of Skopje
Faculty of Technology and Metallurgy
P.O.B. 580, 91000 Skopje, YU

Bernik, Slavko, Dipl.Ing.
"Jožef Stefan" Institute
"Edvard Kardelj" University, Ljubljana
Jamova 39, P.O.B. 100, 61111 Ljubljana, YU

Bizjak, Ivan, Dipl.Ing.
"Edvard Kardelj" University, Ljubljana
Faculty of Natural Science and Technology
Aškerčeva 20, 61000 Ljubljana, YU

Borchardt, Günter, Prof.Dr.-Ing.
Technische Universität Clausthal
Fachbereich Metallurgie und Werkstoffwissenschaften
D-3392 Clausthal-Zellerfeld

Bošković, Snežana, Dr.
"Boris Kidrič" Institute of Nuclear Sciences, Vinča
Institute of Materials
P.O.B. 522, 11001 Beograd, YU

Božić, Dušan, MSc.
"Boris Kidrič" Institute of Nuclear Sciences, Vinča
Institute of Materials
P.O.B. 522, 11001 Beograd, YU
Present Address
Max-Planck-Institut für Metallforschung
Institut für Werkstoffwissenschaften
Heisenbergstr.5, D-7000 Stuttgart 80

Buh, Marjan, MSc.
ETA Cerkno, 65282 Cerkno, YU

Čeh, Miran, Dipl.Ing.
"Jožef Stefan" Institute
"Edvard Kardelj" University, Ljubljana
Jamova 39, P.O.B. 100, 61111 Ljubljana, YU

Djurić, Branko, Dr.
"Boris Kidrič" Institute of Nuclear Sciences, Vinča
Institute of Materials
P.O.B. 522, 11001 Beograd, YU

Drofenik, Miha, Prof.Dr.
"Jožef Stefan" Institute
"Edvard Kardelj" University, Ljubljana
Jamova 39, P.O.B. 100, 61111 Ljubljana, YU

Fandel, Thomas, Dipl.Ing.
Institut für Gesteinshüttenkunde der RWTH Aachen
Mauerstr.5, D-5100 Aachen

Fetahagić, Arifa, MSc.
Energoinvest
Center for Research and Development of Materials
Stup, Tvornička 3, P.O.B. 53, 71000 Sarajevo, YU

Fetahagić, Tarik, MSc.
Energoinvest
Center for Research and Development of Materials
Stup, Tvornička 3, P.O.B. 53, 71000 Sarajevo, YU

Förthmann, Rudiger, Dr.
Institut für Reaktorwerkstoffe
Kernforschungsanlage Jülich
P.O.B. 1913, D-5170 Jülich

Funke, Paul, Prof.Dr.
Technische Universität Clausthal
Institut für Werkstoffumformung
D-3329, Clausthal-Zellerfeld

Grathwohl, Georg, Dr.
Universität Karlsruhe
Institut für Keramik im Maschinenbau
P.O.B. 6980, D-7500 Karlsruhe 1

Greil, Peter, Dr.
Max-Planck-Institut für Metallforschung
Institut für Werkstoffwissenschaften
Heisenbergstr.5, D-7000 Stuttgart 80

Häusser, Helmut Heinz, Dipl.Ing.
Institut für Gesteinshüttenkunde der RWTH Aachen
Mauerstr.5, D-5100 Aachen

Intihar, Heda, Dipl.Ing
"Jožef Stefan" Institute
"Edvard Kardelj" University, Ljubljana
Jamova 39, P.O.B. 100, 61111 Ljubljana, YU

Ivanković, Hrvoje
University of Zagreb
Faculty of Technology
Marulićev trg 20/I, P.O.B. 177, 41000 Zagreb, YU

Kainer, Karl Urlich, Dr.Ing.
Technische Universität Clausthal
Institut für Werkstoffkunde und Werkstofftechnik
Agricolastr.2, D-3392 Clausthal-Zellerfeld

Kaysser, Wolfgang , Dr.
Max-Planck-Institut für Metallforschung
Institut für Werkstoffwissenschaften
Heisenbergstr.5, D-7000 Stuttgart 80

Keuthen, Mathias, Dr.
Institut für Chemische Technik der Universität Karlsruhe
Kaiserstr.12, D-7500 Karlsruhe 1

Kevorkijan, Varužan, MSc.
"Jožef Stefan" Institute
"Edvard Kardelj" University, Ljubljana
Jamova 39, P.O.B. 100, 61111 Ljubljana, YU

Kićević, Dušan, Dipl.Ing.
"Boris Kidrič" Institute of Nuclear Sciences, Vinča
Institute of Materials
P.O.B 522, 11001 Beograd, YU

Kiss, Šandor, Dr.
"Boris Kidrič" Institute of Nuclear Sciences, Vinča
Institute of Materials
P.O.B 522, 11001 Beograd, YU

Kolar, Drago, Prof.Dr.
"Jožef Stefan" Institute
"Edvard Kardelj" University, Ljubljana
Jamova 39, P.O.B. 100, 61111 Ljubljana, YU

Komac, Miloš, Dr.
"Jožef Stefan" Institute
"Edvard Kardelj" University, Ljubljana
Jamova 39, P.O.B. 100, 61111 Ljubljana, YU

Kosec, Marija, Dr.
"Jožef Stefan" Institute
"Edvard Kardelj" University, Ljubljana
Jamova 39, P.O.B. 100, 61111 Ljubljana, YU

Kosmač, Tomaž, Dr.
"Jožef Stefan" Institute
"Edvard Kardelj" University, Ljubljana
Jamova 39, P.O.B. 100, 61111 Ljubljana, YU

Kostić, Emilija, Dr.
"Boris Kidrič" Institute of Nuclear Sciences, Vinča
Institute of Materials
P.O.B. 522, 11001 Beograd, YU

Kostić, Petar, MSc.
Serbian Academy of Sciences and Arts
Institute of Technical Sciences
Knez Mihajlova 35, 11000 Beograd, YU

Kranzmann, Axel, Dipl.Phys.
Max-Planck-Institut für Metallforschung
Institut für Werkstoffwissenschaften
Heisenbergstr.5, D-7000 Stuttgart 80

Krawczynski, Johanna, Dr.
International Bureau, Kernforschungsanlage Jülich
P.O.B. 1913, D-5170 Jülich

Krengel, Ronald, Dipl.Ing.
Technische Universität Clausthal
Institut für Werkstoffumformung
D-3329 Clausthal-Zellerfeld

Laag, Rainhard, Dipl.Ing.
Max-Planck-Institut für Metallforschung
Institut für Werkstoffwissenschaften
Heisenbergstr. 5, D-7000 Stuttgart 80

Leontić, Boran, Prof.Dr.
University of Zagreb, Faculty of Natural Sciences
Institut of Physics
Bijenička cesta 46, P.O.B. 304, 41001 Zagreb, YU

Marinković, Slobodan, Dr.
"Boris Kidrič" Institute of Nuclear Sciences, Vinča
Institute of Materials
P.O.B. 522, 11001 Beograd, YU

Mickovski, Jovan, Dr.
Ironworks Skopje, 91000 Skopje, YU

Milošević, Olivera, MSc.
Serbian Academy of Sciences and Arts
Institute of Technical Sciences
Knez Mihajlova 35, 11000 Beograd, YU

Miloševski, Milosav, Prof.Dr.
"Kiril i Metodij" University of Skopje
Faculty of Technology and Metallurgy
P.O.B. 580, 91000 Skopje, YU

Milun, Milorad, Dr.
University of Zagreb, Institute of Physics
P.O.B. 304, 41001 Zagreb, YU

Mordike, Barry Leslie, Prof.Dr.
Technische Universität Clausthal
Institut für Werkstoffkunde und Werkstofftechnik
Agricolastr.2, D-3392 Clausthal-Zellerfeld

Naoumidis, Aristides, Dr.
Kernforschungsanlage Jülich
Institut für Reaktorwerkstoffe
P.O.B.1913, D-5170 Jülich

Nikolopoulos, Panajotis, Prof.Dr.
University of Patras, Institute of Physical Metallurgy
Dept. of Chemical Engineering
26110 Patras, Greece

Novak, Saša, MSc.
"Jožef Stefan" Institute
"Edvard Kardelj" University, Ljubljana
Jamova 39, P.O.B.100, 61111 Ljubljana, YU

Novaković, Rada, MSc.
Serbian Academy of Sciences and Arts
Dept. of Physical Chemistry
Knez Mihajlova 35, 11000 Beograd, YU

Ondracek, Gerhard, Prof. Dr.
Universität und Kernforschungszentrum Karlsruhe
Institut für Material-und Festkörperforschung
P.O.B.3640, D-7500 Karlsruhe 1

Pavićević, Miodrag, Prof.Dr.
University of Beograd
Faculty of Mining and Geology
D. Jušina 7, 11000 Beograd, YU

Pavlovski, Blagoj, Prof.Dr.
"Kiril i Metodij" University of Skopje
Faculty of Technology and Metallurgy
P.O.B. 580, 91000 Skopje, YU

Pejovnik, Stanko, Prof.Dr.
"Boris Kidrič" Institute of Chemistry
Hajdrihova 19, 61000 Ljubljana, YU

Pervan, Petar, Dipl.Ing.
University of Zagreb, Institute of Physics
P.O.B.304, 41001 Zagreb, YU
Present Address
Fritz-Haber-Institut der Max-Planck-Gesellschaft
Faradayweg 4-6, D-1000 Berlin 33

Petzow, Günter, Prof.Dr.
Max-Planck-Institut für Metallforschung
Institut für Werkstoffwissenschaften
Heisenbergstr.5, D-7000 Stuttgart 80

Pirš, Jože, Prof.Dr.
Technical Faculty of Rijeka
Ulica Narodnog Ustanka 58, 51000 Rijeka, YU

Pristavec, Matjaž, Dipl.Ing
"Jožef Stefan" Institute
"Edvard Kardelj" University, Ljubljana
Jamova 39, P.O.B. 100, 61111 Ljubljana, YU

Reijnen, Piet, Prof.Dr.
Institut für Gesteinshüttenkunde der RWTH Aachen
Mauerstr.5, D-5100 Aachen

Remane, Edmund, Dipl.Phys.
Kernforschungszentrum Karlsruhe
Institut für Material-und Festkörperforschung
P.O.B. 3640, D-7500 Karlsruhe 1

Rzesnitzek, Klaus, Dipl.Ing.
Max-Planck-Institut für Metallforschung
Institut für Werkstoffwissenschaften
Heisenbergstr.5, D-7000 Stuttgart 80

Schuhmacher, Uwe, Dipl.Ing.
Institut für Gesteinshüttenkunde der RWTH Aachen
Mauerstr.5, D-5100 Aachen

Schulz, Brigitte, Dr.
Kernforschungszentrum Karlsruhe
Institut für Material-und Festkörperforschung
P.O.B.3640, D-7500 Karlsruhe 1

Schulz, Hans, Dipl.Ing.
Kernforschungszentrum Karlsruhe
Institut für Material-und Festkörperforschung
P.O.B.3640, D-7500 Karlsruhe 1

Seide, Otmar, Dipl.Min.
Institut für Gesteinshüttenkunde der RWTH Aachen
Mauerstr.5, D-5100 Aachen

Sigulinski, Feodor, Dipl.Ing
"Boris Kidrič" Institute of Nuclear Sciences, Vinča
Institute of Materials
P.O.B. 522, 11001 Beograd, YU

Slokan, Milan, MSc.
"Jožef Stefan" Institute
"Edvard Kardelj" University, Ljubljana
Jamova 39, P.O.B. 100, 61111 Ljubljana, YU

Stamenković, Ivan, Dr.
"Boris Kidrič" Institute of Nuclear Sciences, Vinča
Institute of Materials
P.O.B. 522, 11001 Beograd, YU

Suvorov, Danilo, Dr.
"Jožef Stefan" Institute
"Edvard Kardelj" University, Ljubljana
Jamova 39, P.O.B.100, 61111 Ljubljana, YU

Tecilazić-Stevanović, Marija, Prof.Dr.
University of Beograd
Faculty of Technology and Metallurgy
Karnedžijeva 4, P.O.B. 494, 11000 Beograd, YU

Thümmler, Fritz Ernst, Prof.Dr.-Ing.
University and Nuclear Research Center Karlsruhe
P.O.B. 3640, D-7500 Karlsruhe 1

Tozon, Mili, Dipl.Oec.
"Jožef Stefan" Institute
"Edvard Kardelj" University, Ljubljana
Jamova 39, P.O.B. 100, 61111 Ljubljana, YU

Trubelja, Fabijan, Prof.Dr.
Academy of Sciences and Arts of Bosnia and Hercegovina
Ul.6.Novembra 7, P.O.B. 01-54, 71000 Sarajevo, YU

Turk, Radomir, Prof.Dr.
"Edvard Kardelj" University, Ljubljana
Faculty of Natural Science and Technology
Aškerčeva 20, 61000 Ljubljana, YU

Uskoković, Dragoljub, Dr.
Serbian Academy of Sciences and Arts
Institute of Technical Sciences
Knez Mihajlova 35, 11000 Beograd, YU

Večko, Tatjana, Dipl.Ing.
"Edvard Kardelj" University, Ljubljana
Faculty of Natural Science and Technology
Aškerčeva 20, 61000 Ljubljana, YU

Wandelt, Klaus, Prof.Dr.
Fritz-Haber-Institut der Max-Planck-Gesellschaft
Faradayweg 4-6, D-1000 Berlin 33

Windelberg, Dirk, Dr.
Institut für Mathematik
Universität Hannover
Welfengarten 1, D-3000 Hannover 1

Zdujić, Miodrag, MSc.
Serbian Academy of Sciences and Arts
Institute of Technical Sciences
Knez Mihajlova 35, 11000 Beograd, YU

Vertrieb: KFA Jülich GmbH, Zentralbibliothek
Postfach 1913 · D-5170 Jülich
Telefon: 02461/61-5367 · Telex: 833556-70 kfa d

ISBN 3-89336-001-8